Wilhelm Zwerger *Editor*

The BCS-BEC Crossover and the Unitary Fermi Gas

Springer

Lecture Notes in Physics

Volume 836

For further volumes:
http://www.springer.com/series/5304

The Lecture Notes in Physics

The series Lecture Notes in Physics (LNP), founded in 1969, reports new developments in physics research and teaching—quickly and informally, but with a high quality and the explicit aim to summarize and communicate current knowledge in an accessible way. Books published in this series are conceived as bridging material between advanced graduate textbooks and the forefront of research and to serve three purposes:

- to be a compact and modern up-to-date source of reference on a well-defined topic
- to serve as an accessible introduction to the field to postgraduate students and nonspecialist researchers from related areas
- to be a source of advanced teaching material for specialized seminars, courses and schools

Both monographs and multi-author volumes will be considered for publication. Edited volumes should, however, consist of a very limited number of contributions only. Proceedings will not be considered for LNP.

Volumes published in LNP are disseminated both in print and in electronic formats, the electronic archive being available at springerlink.com. The series content is indexed, abstracted and referenced by many abstracting and information services, bibliographic networks, subscription agencies, library networks, and consortia.

Proposals should be sent to a member of the Editorial Board, or directly to the managing editor at Springer:

Wilhelm Zwerger

Editor

The BCS–BEC Crossover and the Unitary Fermi Gas

Springer

Wilhelm Zwerger
Physik-Department
Fakultät für Physik
Technische Universität München
James-Franck-Straße
85747 Garching
Germany
e-mail: zwerger@ph.tum.de

Cover design: eStudio Calamar, Berlin/Figueres

Printed on acid-free paper

Preface

The Fermionic many-body problem has been a major theme in physics since the early days of quantum mechanics. Its applications span the range from the microscale in nuclei and atoms to the macroscopic scale in condensed matter physics and even beyond e.g. in the physics of neutron stars. Within the last ten years, a completely new area has developed, in which some of the most basic models that have been used to deal with the fermionic many-body problem can be studied in an unprecedented clean manner: ultracold atoms, whose interactions can be tuned over a wide range via Feshbach resonances. Despite the extreme diluteness of these gaseous systems, ultracold atoms allow to reach a regime of strong interactions once the scattering length exceeds the average interparticle distance. In particular, ultracold Fermi gases near a Fesbach resonance provide a perfect realization of the crossover between superfluids of the BCS type and a Bose–Einstein-Condensate of strongly bound pairs, a subject that had been discussed theoretically for decades but had never been accessible in practice before. The special case of the unitary gas at infinite scattering length exhibits additional symmetries like scale and conformal invariance that have lead to new developments in both many-body physics and field theory. Moreover, the universality that is connected with the fact that the interaction range is much shorter than the average interparticle distance implies that results obtained with ultracold gases also apply in a quite different context, e.g. to strongly interacting nucleons in the core of neutron stars. Ultracold atoms thus provide a novel model system in which basic questions in many-body physics can be addressed and—most importantly—a quantitative comparison between theory and experiment is possible. The results thus serve as a benchmark for judging the accuracy of methods used in many-body theory as applied to the more complex problems that are of relevance in condensed matter and nuclear physics. Ultracold atoms have opened a completely new area in many-body physics whose implications reach far beyond the particular context of dilute gases. In a situation, where an ever increasing specialization makes it more and more difficult to see beyond the boundaries of one's own subfield, such a new field that spans a bridge between different areas of physics, is clearly extremely valuable.

The present book provides an overview of the present status of this field from the ultracold atoms perspective. It covers a broad range of topics, including some of the most recent experimental results as well as novel field-theoretic or numerical methods developed in this context or the issue of a minimum viscosity to entropy ratio that is deduced from the scaling flows of expanding atomic clouds. Special efforts have been taken to make the individual chapters of the book self-contained and accessible to non-experts in the field. It should be stressed that despite a lot of progress over the last few years, many problems are still open, in particular the issue of imbalanced Fermi gases and possible unconventional superfluid phases as well as dynamical properties both near and far from equilibrium. Hopefully, the contributions to this book will provide a valuable introduction not only to the present state of knowledge but also to the still open problems, perhaps providing motivation to address some of the many challenges which remain.

It is a pleasure to thank Wolfram Weise for the initiative to edit a book on this subject within the Lecture Notes in Physics series. My special thanks and appreciation go to all the authors, who have taken off time from research, teaching and many other obligations to write a chapter for this book which provides a self-contained and up-to-date account of their original contributions to the subject. I think they have all done an excellent job.

Contents

Contributors

Aurel Bulgac Department of Physics, University of Washington, Seattle, WA, USA, e-mail: bulgac@uw.edu

Eric Braaten Department of Physics, The Ohio State University, Columbus, OH 43210, USA, e-mail: braaten@mps.ohio-state.edu

Yvan Castin Laboratoire Kastler Brossel, Ecole normale supérieure, CNRS and UPMC, Paris, France, e-mail: yvan.castin@lkb.ens.fr

C. Chafin , Department of Physics, North Carolina State University, Raleigh, NC, 27695, USAe-mail: cechafin@ncsu.edu

F. Chevy Laboratoire Kastler Brossel, École Normale SupérieureCNRS, UPMC, 75005, Paris, France, e-mail: frederic.chevy@lkb.ens.fr

J. M. Diederix Institute for Theoretical Physics, Utrecht UniversityLeuvenlaan 4, 3584 CE , Utrecht, The Netherlands, e-mail: J.M.Diederix@uu.nl

A. E. Feiguin Department of Physics and Astronomy, University of Wyoming, Laramie, WY 82071, USA, e-mail: afeiguin@uwyo.edu

Michael McNeil Forbes Department of Physics, Institute for Nuclear Theory, University of Washington, Seattle, WA, USA, e-mail: mforbes@uw.edu , T-2, Los Alamos National Laboratory, Los Alamos, NM, USA

F. Heidrich-Meisner Department of Physics, Arnold Sommerfeld Center for Theoretical Physics, and Center for NanoScience, Ludwig-Maximilians-Universität München, 80333, München, Germany, e-mail: heidrich-meisner@lmu.de

Henning Heiselberg Applied Research, DALOLautrupbjerg 1-5, 2750, Ballerup, Denmark, e-mail: heiselberg@mil.dk

A. J. Leggett Department of Physics, University of Illinois at Urbana-Champaign, Champaign, IL, USA, e-mail: aleggett@illinois.edu

Piotr Magierski Faculty of Physics, Warsaw University of Technology, Warsaw, Poland, e-mail: Piotr.Magierski@if.pw.edu.pl

Yusuke Nishida Center for Theoretical Physics, Massachusetts Institute of Technology Cambridge, Cambridge, MA 02139, USA, e-mail: nishida@mit.edu

G. Orso Department of Physics, Arnold Sommerfeld Center for Theoretical Physics, and Center for NanoScience, Ludwig-Maximilians-Universität München, 80333, München, Germany, e-mail: giuliano.orso@lmu.de

M. Randeria Department of Physics, Ohio State University, Columbus, OH 43210, USA, e-mail: randeria@mps.ohio-state.edu

Alessio Recati Dipartimento di Fisica, Università di Trento and CNR-INO BEC CenterPovo, 38121, Trento, Italy, e-mail: recati@science.unitn.it

Subir Sachdev Department of Physics, Harvard University, Cambridge, MA 02138, USA, e-mail: sachdev@physics.harvard.edu

C. Salomon Laboratoire Kastler Brossel, École Normale Supérieure CNRS, UPMC, 75005, Paris, France, e-mail: salomon@lkb.ens.fr

T. Schäfer Department of Physics, North Carolina State University, Raleigh, NC 27695, USA, e-mail: tmschaef@unity.ncsu.edu

Dam Thanh Son Institute for Nuclear Theory, University of Washington, Seattle, WA 98195, USA, e-mail: son@phys.washington.edu

H. T. C. Stoof Institute for Theoretical Physics, Utrecht University, Leuvenlaan 4, 3584 CE, Utrecht, The Netherlands, e-mail: H.T.C.Stoof@uu.nl

G. C. Strinati Dipartimento di Fisica, Università di Camerino, 62032, Camerino, Italy, e-mail: giancarlo.strinati@unicam.it

Sandro Stringari, Dipartimento di Fisica, Università di Trento and CNR-INO BEC Center, Povo, 38121, Trento, Italye-mail: stringar@science.unitn.it

Felix Werner Department of Physics, University of Massachusetts, Amherst, MA, USA, e-mail: werner@lkb.ens.fr

S. Zhang Department of Physics, The Ohio State University, Columbus, OH, USA, e-mail: szhang@mps.ohio-state.edu

W. Zwerger Physik Department, Technische Universität München, 85747, Garching, Germany, e-mail: zwerger@ph.tum.de

M. Zwierlein Department of Physics, MIT-Harvard Center for Ultracold Atoms and Research Laboratory of Electronics, MIT, Cambridge, MA 02139, USA e-mail: zwierlei@mit.edu

Chapter 1
The BCS–BEC Crossover
and the Unitary Fermi Gas

M. Randeria, W. Zwerger and M. Zwierlein

1.1 Introduction

There has been great excitement about the recent experimental and theoretical progress in elucidating the Bardeen-Cooper-Schrieffer (BCS) to Bose Einstein condensation (BEC) crossover in ultracold Fermi gases. Prior to these cold atom experiments, all known, and reasonably well understood, superconductors and superfluids were firmly in one of the two limits. Either they were well described by the celebrated BCS theory of pairing in Fermi systems, or they could be understood in terms of the BEC of bosons, with repulsive interactions. For the first time, the ultracold Fermi gases exhibited behavior that, with the turn of a knob, could be made to span the entire range from BCS to BEC. While such a crossover had been theoretically predicted, its actual realization in the laboratory was a major advance [1, 2], and led to intense investigation of the properties of the very strongly interacting, unitary regime that lies right in the middle of the crossover. We now understand that the unitary Fermi gas has remarkable universal properties, arising from scale invariance, and has connections with fields as diverse as nuclear physics and string theory.

Our goal in this introductory chapter is to convey the excitement of all these new developments, and to give a brief overview of the field which should also serve to

M. Randeria (✉)
Department of Physics, Ohio State University,
Columbus, OH 43210, USA
e-mail: randeria@mps.ohio-state.edu

W. Zwerger
Physik Department, Technische Universität München,
D-85747 Garching, Germany
e-mail: zwerger@ph.tum.de

M. Zwierlein
Department of Physics, MIT-Harvard Center for Ultracold Atoms and
Research Laboratory of Electronics, MIT, Cambridge, MA 02139, USA
e-mail: zwierlei@mit.edu

put the contributions in the rest of the book in proper context. Our emphasis is on the theoretical developments, that are the focus of the rest of the book, but we also mention some of the key experimental results.

It is appropriate to begin our discussion with the BCS theory of pairing in a Fermi gas which has been one of the major paradigms of many-body physics since its invention more than 50 years ago [3]. Despite the idealized nature of this model, the BCS theory of fermionic superfluidity has proven to be remarkably successful. In addition to providing a *quantitative* theory of conventional superconductors [4], it has also given a successful *qualitative* description of many other more complex systems. For example, it describes well the pairing interactions in atomic nuclei [5] or in neutron stars [6]. Moreover, it can easily be generalized to nonconventional superfluids, for instance to p-wave, spin-triplet pairing that occurs in Helium-3 [7], some heavy Fermion compounds [8] or in the Ruthenates [9]. The basic physics of BCS has even been applied to pairing of quarks in color superconducting phases expected in the QCD phase diagram at high densities [10].

In quite simple terms, the BCS state of N fermions might be thought of as condensation of $N/2$ fermion pairs that can all occupy the same state: a bound pair with zero center-of-mass momentum. This naive picture of superconductivity as a BEC of pairs has to be treated with great caution, however. Indeed, in the weak coupling regime considered by BCS, the attractive interaction between electrons is much smaller than the Fermi energy. Thus the size of a Cooper pair is larger than the average interparticle spacing by a factor that is of order 10^3 in conventional superconductors. Within the volume occupied by a single pair, there are thus about a billion other pairs. It is therefore impossible to picture the Cooper pairs of BCS theory as bosonic particles. Historically, an explanation of superconductivity in terms of BEC of pairs was put forward by Blatt, Butler and Schafroth [11, 12]. Their theory, however, did not apply to superconducting metals known at that time. In particular, it implied a critical temperature on the order of the Fermi temperature instead of the much smaller observed T_c. It is a legitimate question, however, to ask whether there was something fundamentally wrong with this idea and, if not, whether there are systems in nature that actually have an attractive interaction comparable to or even larger than the Fermi energy.

The idea that a continuous crossover exists between the BCS and BEC limits first arose in the 1960s with the work by Keldysh on exciton condensation (see the contribution by Keldysh in [13]), although the long range Coulomb interaction in that problem makes it somewhat different. In a pioneering paper, Eagles [14] studied superconductivity in metals with a very low electron density, where the attraction between electrons was no longer small compared with the Fermi energy. Independently, Leggett attacked the problem of the BCS–BEC crossover in the context of Helium 3 [15]. Although He-3 is very much in the BCS limit, Leggett wanted to understand to what extent its properties, e.g., the total angular momentum of the superfluid, might be similar to a BEC of diatomic molecules.

In these early papers [14, 15], which are discussed in the contribution by Leggett and Zhang to this volume, it was shown that the BCS-wavefunction continues to provide a qualitatively correct variational description of the pairing correlations

for arbitrary strength of the attractive interaction. The $T = 0$ crossover mean field theory differs from the standard BCS analysis in only one way. Unlike standard BCS, where the chemical potential μ is essentially the non-interacting Fermi energy ε_F, in the crossover theory one has to solve for μ self-consistently, together with the gap equation. One finds that μ decreases monotonically with increasing attraction, going from ε_F in the BCS limit to a *negative* value in the BEC limit, that is one-half the pair binding energy. Thus one obtains a smooth crossover from the weak-coupling BCS limit with large, overlapping Cooper pairs all the way to the strong-coupling BEC regime of tightly bound dimers. There is no singularity in the many-body ground state even at the threshold for a bound state in the two-body problem; collective Cooper pairs have already formed well before that in the many-body problem. In fact, Leggett pointed out that the only possible singularity occurs when the chemical potential goes through zero as a result of strong attraction. More precisely, there is a critical coupling strength on the BEC-side of the crossover, beyond which the fermionic quasiparticle excitations above the superfluid ground state have their minimum at zero rather than at finite momentum.[1] This change in the nature of the fermionic excitation spectrum is of relevance for population imbalanced gases, where it determines the location of the so-called splitting point [17]. For the balanced gas, in turn, no thermodynamic singularities show up at this point unless pairing occurs in a non-zero angular momentum channel. In this case, there is a true quantum phase transition along the crossover from weak to strong coupling, separating a phase where part of the Fermi surface has no gap to one with a gap in the fermionic excitation spectrum for all momenta [18–20].

The evolution of the critical temperature T_c across the BCS–BEC crossover was first addressed by Nozieres and Schmitt-Rink [21], who also argued that pairing preempts a possible gas-liquid instability that might be expected for strong attractive interactions. With the discovery of high temperature superconductors in 1986 and the realization that the pairing interaction in these systems is rather strong in the sense that the pair size is only slightly larger than the average interparticle spacing, the crossover from a BCS picture of fermionic superfluids to a BEC of strongly bound pairs became of interest again [22]. The fact that superconductivity in the cuprates appears upon doping a Mott-insulator with antiferromagnetic order [23], indicates, however, that simple models which start from a Fermi gas with strong attractive interactions are unable to describe these systems in any quantitative manner.

The qualitative structure of the phase diagram of the BCS–BEC crossover in a dilute Fermi gas in the standard three dimensional (3D) case is shown in Fig. 1.1 and was obtained well before the era of cold atom experiments [21–24, 26] (the situation in two dimensions is similar, yet there are fundamental differences compared to the 3D situation. This is due to the fact that the superfluid transition in 2D is of the Berezinskii-Kosterlitz-Thouless type and, moreover, that there is no equivalent of the unitarity limit in 2D, since pair binding appears at arbitrary weak

---

[1] Within meanfield theory, this occurs when the chemical potential reaches zero. More precise calculations, however, show that the critical coupling strength $1/(k_F a) \simeq 0.8$ beyond which fermionic excitations have their minimum at zero momentum appears at $\mu \simeq -0.54\varepsilon_F$ [16].
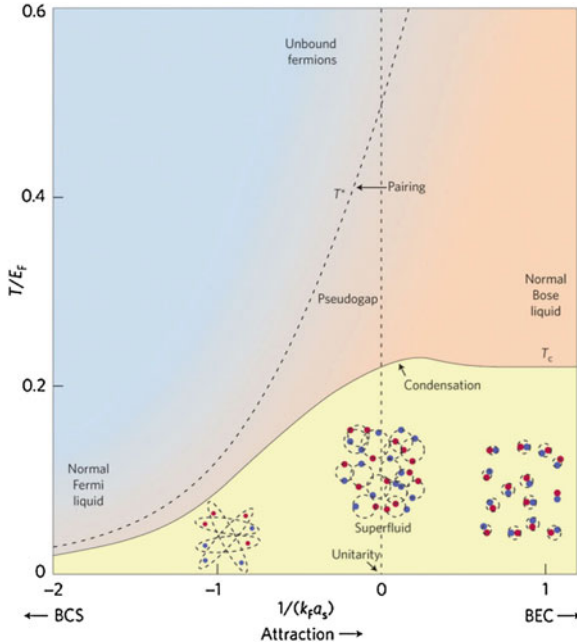
Fig. 1.1 Qualitative phase diagram [24] of the BCS to BEC crossover as a function of the temperature T/T_F and the dimensionless coupling $1/(k_F a)$, where k_F is the Fermi momentum and a the scattering length. The pictures show schematically the evolution of the ground state from the BCS limit with large, spatially overlapping Cooper pairs to the BEC limit with tightly bound molecules. The ground state at unitarity $1/(k_F a) = 0$ has strongly interacting pairs with size comparable to $1/k_F$. As a function of increasing attraction, the pair-formation crossover scale T^* diverges away from the transition temperature T_c below which a condensate exists (Figure from Ref. [25])

attractive interactions [19, 27, 28]). As will become evident from the contributions to these Lecture Notes, many of its features have now been tested experimentally. Moreover, substantial progress has been made within the last few years in understanding the crossover problem on a much deeper level, both in quantitative terms and also conceptually. In dilute Fermi gases, where the range of the potential is much smaller than the interparticle distance k_F^{-1}, the interaction is characterized by a scattering length a. The experimental method for changing a—the Feshbach resonance—is explained in the following Section. At this point, we may simply think of a as being tuned by varying the depth of an attractive square well. For weak attraction one has a negative scattering length and for $1/k_F a \rightarrow -\infty$ we are in the BCS limit. The scattering length diverges at the threshold for bound state formation in the two-body problem; this is the unitary point $1/k_F a = 0$. Finally, for strong attraction, $a > 0$ is in fact the size of the two-body bound state in vacuum and in the many-body problem, one is in the BEC limit when $1/k_F a \rightarrow +\infty$.

An important point to emphasize here is that although the attraction increases monotonically going from the BCS to BEC regimes (moving from left to right in

Fig. 1.1), both limiting cases are actually weakly interacting. This is clear in the weak attraction BCS limit, but less obvious in the BEC limit, where the strong attraction is resolved by the formation of tightly bound dimers. They have a residual *repulsive* interaction that basically results from the Pauli exclusion of their constituents [24, 27]. The associated scattering length $a_{dd} = 0.6a$ has been determined from an exact solution of the four-body Schrödinger equation [29] and vanishes in the deep BEC limit.[2] The genuinely strongly interacting regime is therefore in the middle of the crossover, near the unitary point $|a| = \infty$. At this point, the superfluid transition temperature $T_c/T_F \simeq 0.22$ is expected to be an appreciable fraction of the Fermi temperature [21, 24]. While more precise calculations based on standard Green function techniques [32, 33], field theoretic expansions around the upper and lower critical dimension [34, 35] or on quantum Monte Carlo methods [36–38] give values $T_c/T_F \simeq 0.16$ that are smaller than these early predictions, the point still remains that such large ratios of the superfluid or superconducting T_c to the bare Fermi energy are unheard of in known condensed matter systems. The unitary gas, which is still basically a fermionic system, in fact has the highest T_c in units of the bare Fermi temperature T_F of all known fermionic superfluids.

A second point that should be stressed is that—as far as the ground state problem is concerned—the BCS–BEC crossover problem is just a simple, smooth evolution from a state with very large pairs to one with small, non-overlapping pairs that behave like point Bosons. By contrast, the normal (i.e., non-superfluid) state crossover is in many ways more subtle. On the BCS-side the formation of pairs and their condensation appears simultaneously. Superfluid order is lost by breaking pairs and—since $T_c \ll T_F$—the corresponding normal state is an ordinary Landau Fermi liquid. By contrast, superfluid order on the BEC side is lost by depleting the condensate but *not* by destroying the bosons. Thus the state above T_c in this limit is a normal Bose gas, where "pairing" still persists. One has to go to a much higher temperature scale T^*, determined by the binding energy, up to logarithmic entropy corrections [22, 24], where the molecular bosons break up into their atomic constituents. The question of how the system above T_c evolves from a normal Fermi liquid to a normal Bose liquid is quite nontrivial and reliable experimental results on this problem have become available only very recently (see the contribution by F. Chevy and C. Salomon in this volume). It was proposed early on that it does so via a pairing pseudogap [39–41] between T_c and T^*. The existence of a pseudogap would be particularly exciting near unitarity where the system can be in a degenerate regime and yet show marked deviations from Fermi-liquid behavior in the temperature range between the phase transition T_c and the the pairing crossover scale T^*. We will say more about this question in Sect. 1.7, where we discuss observable consequences and recent experimental progress. We also discuss there the extent to which these considerations relate to the more complex set of phenomena observed in high T_c superconductivity in the copper-oxide based materials.

---

[2] A similar result is obtained also in one dimension [30] not, however, in two dimensions, where the repulsive interaction between strongly bound dimers stays finite in the BEC-limit [27, 31].

An independent line of investigation of the problem to understand Fermi gases with strong attractive interactions was started by G. Bertsch in 1999 in the nuclear physics context [42]. As will be discussed in detail in the contribution by Heiselberg, Bertsch suggested to study an attractive Fermi gas with an infinite value of the scattering length as a model to describe low density neutron matter, e.g., in neutron stars. He thus focussed attention on the unitary gas in particular, realizing that–as a result of the zero range nature of the interaction–the Pauli pinciple still guarantees stability despite the infinitely strong attractive interaction and, moreover, that the ground state energy of the unitary gas is necessarily a universal number times the bare Fermi energy [43]. Knowledge of the thermodynamics of the unitary gas realized with ultracold atoms at typical densities $n \simeq 10^{-12}\,\mathrm{cm}^{-3}$ thus has implications for understanding the equation of state of neutron stars at densities that are about twentyfive orders of magnitude larger [44]!

1.2 Feshbach Resonance

Although conceptually important, the BCS–BEC crossover problem was of little direct experimental interest before the era of ultracold atoms, largely because in condensed matter and nuclear physics one has to live with whatever interaction nature provides and there is no way to change it. This situation changed dramatically with the realization that dilute gases of fermionic alkali atoms, such as ^{40}K and ^{6}Li, can be cooled into the degenerate regime [45–50] and that their interatomic interaction can be tuned via a Feshbach resonance [51, 52].

In the following we describe the basic physics of magnetically tunable Feshbach resonances which allow to change the interaction between two different (hyperfine) species of fermions simply by changing a magnetic field. For a more detailed presentation of this subject see, e.g., the recent review by Chin et al. [53]. As we shall see below, in general, one needs a two-channel model to describe a Feshbach resonance: two fermions in the "open channel" coupled to a bound state in the "closed channel". However, essentially all crossover experiments are in the so-called 'broad' Feshbach resonance limit where the width of the resonance is much larger than the Fermi energy. In this limit, an effective single-channel model is sufficient. The two-body interaction is then described by a scattering amplitude of the form $f(k) \simeq -a/(1 + ika)$ that only depends on the scattering length a as a single parameter. Typically the scattering length between neutral atoms is of the order of the van der Waals length $r_0 \simeq 50a_0$ and thus much smaller than the typical interparticle spacing $n^{-1/3} \simeq 0.5\,\mu\mathrm{m}$ in cold gases. Near a Feshbach resonance, however, it is possible that these lengths become comparable.

Quite generally, a Feshbach resonance in a two-particle collision appears whenever a bound state in a closed channel is coupled resonantly with the scattering continuum of an open channel. The ability to tune the scattering length by a change of an external magnetic field B [54] relies on the difference in the magnetic moments of the closed and open channels. Varying B thus changes the position of closed channel bound states relative to the open channel threshold. On a phenomenological
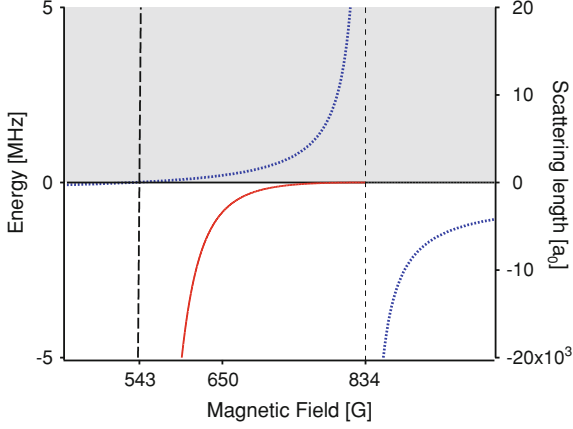
Fig. 1.2 Magnetic field dependence of the scattering length (*blue curve*) between the two lowest magnetic sub-states of ^{6}Li with a Feshbach resonance at $B_0 = 834$ G and a zero crossing at $B_0 + \Delta B = 534$ G. The background scattering length $a_{\text{bg}} = -1405\, a_0$ is exceptionally large in this case (where a_0 is the Bohr radius). The energy of the bound state causing the Feshbach resonance is shown in *red*

level, Feshbach resonances are described by an effective pseudopotential between atoms in the open channel with scattering length

$$a(B) = a_{\text{bg}}\left(1 - \frac{\Delta B}{B - B_0}\right). \tag{1.1}$$

Here a_{bg} is the off-resonant background scattering length in the absence of the coupling to the closed channel while ΔB and B_0 describe the width and position of the resonance expressed in magnetic field units (see Fig. 1.2).

Taking the specific example of fermionic ^{6}Li atoms, which have electronic spin $S = 1/2$ and nuclear spin $I = 1$, for typical magnetic fields above 500 G, the electron spin is essentially fully polarized by the magnetic field, and aligned in the same direction for the three lowest hyperfine states. Thus, two lithium atoms collide with their electron spins aligned, hence in the triplet configuration. The "incoming" state or open channel is thus part of the triplet interatomic potential. The closed channel consists of states in the singlet potential. Due to the hyperfine interaction, that can trade electron spin for nuclear spin, the two atoms can resonantly tunnel from the triplet into bound states of the singlet potential. This coupling is described by an off-diagonal potential $W(r)$, whose range is on the order of the atomic scale.

As a result of the finite difference $\Delta\mu$ of the magnetic moments in the open and closed channels, a change in the magnetic field by δB amounts to shifting the closed channel energy by $\Delta\mu\delta B$ with respect to the open channel (see Fig. 1.3). Provided that the magnetic field is close to a resonant value B_0 at which a bound state $\phi_{\text{res}}(r)$ of the closed channel potential has an energy $E_{\text{res}}(B) = \Delta\mu(B - B_0)$ close to zero, this state is resonantly coupled to the open channel scattering state at
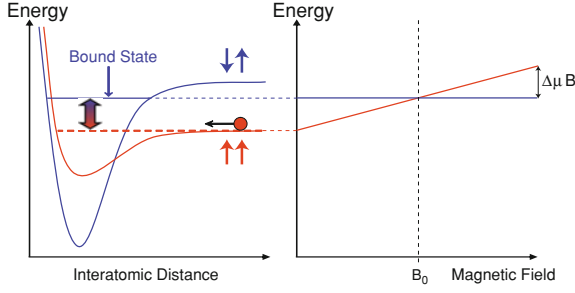
Fig. 1.3 Atoms prepared in the open channel, corresponding to the interaction potential (*in red*), undergo a collision at low incident energy. In the course of the collision the open channel is coupled to the closed channel (*in blue*). When a bound state of the closed channel has an energy close to zero, a scattering resonance occurs. The position of the closed channel can be tuned with respect to the open one, e.g., by varying the magnetic field B

low energies. This coupling leads to a resonant contribution

$$\tan \delta_{\text{res}}(k) = \frac{\hbar^2 k}{m r^\star v} \tag{1.2}$$

to the scattering phase shift at small momenta $k \to 0$ which is inversely proportional to the detuning $v = \Delta\mu(B - B_0)$ away from resonance [55]. The associated characteristic length $r^\star > 0$ is determined by the overlap between the open channel scattering state $|\phi_0\rangle$ and the closed channel bound state $|\phi_{\text{res}}\rangle$. More precisely, it is connected to the off-diagonal coupling potential $W(r)$ via [56]

$$\langle \phi_{\text{res}} | W | \phi_0 \rangle = \frac{\hbar^2}{m} \sqrt{\frac{4\pi}{r^\star}}. \tag{1.3}$$

Its inverse $1/r^\star$ is therefore a measure of how strongly the open and closed channels are coupled. Including the phase shift $\tan \delta_{\text{bg}}(k) = -k a_{\text{bg}}$ due to scattering in the open channel potential, the total scattering length $a = -\lim_{k\to 0} \tan(\delta_{\text{bg}} + \delta_{res})/k$ is of the form

$$a = a_{\text{bg}} - \frac{\hbar^2}{m r^\star v} \tag{1.4}$$

as given in Eq. 1.1. In particular, the phenomenological width parameter ΔB is determined by the combination $\Delta\mu\Delta B = \hbar^2/(m r^\star a_{\text{bg}})$ of the two characteristic lengths a_{bg} and $r^\star$.

In addition to the tunability of the scattering length, Feshbach resonances also allow to form weakly bound dimers by an adiabatic change in the magnetic field that starts from the side with $a < 0$ and slowly crosses the resonance into the regime $a > 0$, where the pseudopotential exhibits a bound state at energy $\varepsilon_b = \hbar^2/(m a^2)$ [53]. The corresponding bound state has a finite closed channel

admixture $\sqrt{Z}\ \phi_{\text{res}}$. Close to the resonance, where the scattering length is dominated by the resonant contribution in Eq. 1.4, the binding energy

$$\varepsilon_b = \frac{\hbar^2}{ma^2} = \left(\Delta\mu(B - B_0)\right)^2/\varepsilon^\star + \ldots \qquad (1.5)$$

of the weakly bound state vanishes quadratically, with characteristic energy $\varepsilon^\star = \hbar^2/m(r^\star)^2$. The associated closed channel admixture Z is thus given by

$$Z = -\frac{\partial\varepsilon_b}{\partial\nu} \simeq = 2\frac{|\nu|}{\varepsilon^*} = 2\frac{r^*}{|a_{\text{bg}}|}\frac{|B - B_0|}{|\Delta B|}, \qquad (1.6)$$

remaining much smaller than one over the magnetic field range $|B - B_0| \lesssim |\Delta B|$ for the typical Feshbach resonances that obey $r^\star \ll |a_{\text{bg}}|$ [55].

The discussion so far is based on two-body scattering only. In order to define the notion of a broad Feshbach resonance, however, we have to take into account that at a finite density of the fermionic atoms, the typical relative momenta are of order k_F. Now, the two-particle scattering amplitude

$$f(k) = \frac{1}{k\cot\delta_0(k) - ik} \rightarrow \frac{-1}{1/a + r^\star k^2 + ik}. \qquad (1.7)$$

near a Feshbach resonance has the parameter $r^\star$ introduced in Eq. 1.2 as an effective range parameter [56]. The condition that the scattering amplitude $f(k_F)$ near the Fermi energy is only determined by the scattering length a and the universal contribution ik that limits the scattering cross section to its maximum value $4\pi/k^2$ at $a = \infty$, therefore requires $k_F r^\star \ll 1$. This is the condition for a 'broad' Feshbach resonance, which only involves the many-body parameter $k_F r^\star$ [56]. In quantitative terms, the Fermi wavelength $\lambda_F = 2\pi/k_F$ of dilute gases is of order μm, while $r^\star$ is typically on the order of or even smaller than the effective range r_e of the interaction. The condition $k_F r^\star \ll 1$ is therefore very well obeyed and characterizes the *low density* limit that is relevant in ultracold gases. A very important point to realize in this context is that the broad Feshbach resonance limit is precisely opposite to that encountered in conventional superconductors. In the latter case, the role of the characteristic energy $\varepsilon^\star$ beyond which the attractive interaction is cutoff is played by the Debye energy $\hbar\omega_D$. Since the ratio $\hbar\omega_D/\varepsilon_F$ is typically very small, pairing in conventional superconductors is described by a model with $k_F r^\star \gg 1$, i.e. one is in the *high-* rather than in the low-density limit. There is again a kind of universality in this limit provided one is the weak coupling regime where the resulting pairs are much larger than the interparticle distance. This is connected with the fact that in weak coupling only properties right *at* the Fermi surface are relevant. Then, a reduced BCS model is applicable for which mean field theory becomes exact and dimensionless ratios like the $2\Delta/k_B T_c = 3.52$ are universal.

Experimentally, a crucial requirement for reaching the regime $k_F|a| \gg 1$ in practice is the stablity of fermionic gases near a Feshbach resonance. If two-body losses are negligible, the lifetime of ultracold gases is limited by three-body losses, where

two of the colliding atoms fall into a deeply bound state. To ensure energy-momentum conservation, a third atom has to be present in order to take away the large excess binding energy. For bosons, the three-body loss rate $K_3 \sim (na^2)^2$ increases strongly with density and scattering length, thus preventing one from reaching the strongly interacting regime $n^{1/3}a \gg 1$ with Feshbach resonances. Fortunately, for fermions the situation is reversed. In fact, their lifetime is particularly *large* near Feshbach resonances because the Pauli principle forbids two fermions of the same kind to be at the same place [29]. Typical lifetimes can in fact reach over half a minute for ^{6}Li [57].

1.3 Universality and Scale Invariance

As described above, the BCS–BEC crossover in dilute Fermi gases can be tuned by changing the scattering length a. Since the interaction in the broad Feshbach resonance limit has a as the single parameter, purely dimensional arguments imply that all measurable quantities can be written in a "universal" form; for instance the free energy per particle must be the form $F(T, V, N)/N = \varepsilon_F \mathscr{F}(T/T_F, 1/k_F a)$. Here $\mathscr{F}(\theta, x)$ is a dimensionless function of the scaled temperature $\theta = T/T_F$ and the dimensionless coupling $x = 1/k_F a$, where $k_B T_F = \varepsilon_F = \hbar^2 k_F^2/2\mathrm{m}$ is the non-interacting Fermi energy (or temperature), and $k_F = (3\pi^2 n)^{1/3}$ is the Fermi momentum corresponding to a density n. In concrete terms, universality in this context implies that functions like $\mathscr{F}(\theta, x)$ are independent of any microscopic details up to corrections of order $(k_F r^*)^2$. Thus, for example, the equation of state of ^{40}K and ^{6}Li, which are both in the broad Feshbach resonance limit $k_F r^\star \ll 1$, should be identical across the entire crossover if expressed in scaled variables θ and x.

More generally, the notion of universality is usually associated with physics near a continuous phase transition, where a diverging length scale gives rise to a behavior that is insensitive to microscopic details. Phrased in these terms, the origin of universality of strongly interacting fermions near a Feshbach resonance was elucidated by Nikolic and Sachdev [58]. As explained in detail in the contribution by Sachdev to this volume, universality is tied to the existence of a quantum critical point at unitarity when the chemical potential vanishes, i.e. the gas is at zero density. Associated with the three relevant perturbations around this fixed point, the complete thermodynamics and phase diagram is then a universal function of temperature T, the deviation from unitarity, the chemical potential μ and the external field h that is conjugate to an imbalance in the density of the two spin components [58].

As pointed out by Bertsch, a subject of particular interest in itself is the unitary gas at infinite scattering length. At the two-body level, this is the critical coupling for the appearance of a bound state. In the many-body problem, this point seems not to have any special significance at first sight, since all the thermodynamic properties are continuous across the particular value $1/k_F a = 0$ of the dimensionless coupling constant. A closer look however, reveals that there are additional symmetries precisely at infinite scattering length. In fact, if the interaction near a Feshbach resonance is modelled by a two-channel description in which two atoms are transformed

into a closed channel 'molecule' and vice versa, the bosonic field associated with the closed channel is massless at zero detuning $v = 0$. As a result, the unitary gas is a non-relativistic field theory which is scale-invariant at $k_F a = \infty$, as realized by Son and Nishida and by Werner and Castin [59–61]. The origin and consequences of scale invariance, in particular in the presence of a harmonic trapping potential, are discussed in detail in the contribution by Castin and Werner. In a homogeneous situation, scale invariance implies that the kinetic and interaction energy terms in the Hamiltonian have identical scaling dimension. A rescaling $\mathbf{x} \rightarrow \lambda\mathbf{x}$ of the coordinates by an arbitrary factor λ thus results in a simple change of the Hamiltonian by $H \rightarrow H/\lambda^2$, as if the two-body interactions were of a pure power law form $\sim 1/r^2$. Note, however, that in systems with pure $1/r^2$-interactions scale invariance holds for any value of the interaction strength and for *any* dimension. For contact interactions $\sim g\delta(\mathbf{x})$ in turn, scale invariance in three and also in one dimension requires either zero or infinite coupling $g = \infty$, while in *two* dimensions it again holds for arbitrary coupling strength, as pointed out earlier by Pitaevskii and Rosch [62]. Within a space-time formulation, scale-invariant, non-relativistic many-body problems are invariant under the transformation $\mathbf{x} \rightarrow \lambda\mathbf{x}$ and $t \rightarrow \lambda^2 t$. More precisely, the full symmetry group of the unitary gas is known as the Schrödinger group which is the analogue, for Galilean invariant systems, of the conformal group.

Being a continuous symmetry, scale invariance leads to a conservation law by Noether's theorem. The associated conservation of the 'dilaton current' implies that the trace of the energy-momentum tensor vanishes. As a result, the pressure $p = 2\varepsilon/3$ of the non-relativistic, unitary Fermi gas is simply proportional to its energy density ε, a relation which has first been derived using thermodynamic arguments by Ho [63]. Note that the relation holds at arbitrary temperature and is identical to that which is usually associated with an ideal (quantum or classical) gas, even though the system is very strongly interacting. Apart from the simple relation between pressure and energy density, the combination of scale and conformal invariance also has the surprising consequence that the bulk viscosity ζ of the unitary gas vanishes identically [64, 65]. As a result, a unitary gas in an isotropic trap will expand without any generation of entropy after the trap potential is removed. This is discussed in detail in the contributions by Castin and Werner and by Nishida and Son.

1.4 Thermodynamics and Critical Temperature

Following the first experimental realizations of degenerate Fermi gases in the strongly interacting regime near a Feshbach resonance [1, 2, 66–69], quite a lot of effort has been spent to measure the thermodynamic properties and to precisely determine the universal numbers that characterize the unitary gas in particular. From the theory point of view, this is the most interesting and also challenging problem due to the absence of a small expansion parameter. The ground state of a balanced gas with equal densities of the two spin components is a superfluid which is adiabatically connected to the BCS-type superfluid in the weak coupling limit $k_F a \rightarrow 0^-$. On purely dimensional grounds, the ground state energy density $\varepsilon = \xi_s \varepsilon^{(0)}$ is a pure number $\xi_s < 1$—called

the Bertsch parameter—times the energy density $\varepsilon^{(0)} = 3n\varepsilon_F/5$ of the non-interacting Fermi gas with the same density n (the subscript in ξ_s is a reminder of the fact that the parameter refers to the superfluid state). Due to the relation $p = 2\varepsilon/3$ and the Gibbs-Duhem relation $N\mu = F + pV$, the universal number ξ_s also determines the factor by which the ground state pressure or the chemical potential of the unitary gas is reduced compared to its value in an ideal, non-interacting Fermi gas. Moreover, the zero temperature compressiblity $\kappa = \partial n/\partial \mu$ is enhanced by a factor $1/\xi_s$. As a result, the ratio $c_s = v_F\sqrt{\xi_s/3}$ between the speed of sound and the Fermi velocity is again fixed by the single parameter ξ_s. Superfluid properties, in turn, are associated with new and independent universal ratios. Of particular interest are the critical temperature for the superfluid transition T_c/T_F and the zero temperature gap Δ/ε_F for fermionic quasiparticles.

There are a number of ways to determine the Bertsch parameter ξ_s experimentally, for instance from a measurement of the release energy after expansion of the gas in a trap [70] or—most directly—from in-situ absorption imaging of the density distribution [66]. Indeed, the density profile at unitarity is that of a free Fermi gas with a rescaled size. Due to the inhomogeneous density, the chemical potential μ_{trap} in the trapped gas is decreased by $\sqrt{\xi_s}$ and not by ξ_s as in the homogeneous case. Since the radius $R \sim \sqrt{\mu_{\text{trap}}}$ of the atomic cloud scales with the square root of the chemical potential, attractive interactions at unitarity give rise to a reduction of the cloud radius by a factor $\xi_s^{1/4}$. The values of ξ_s obtained from this and other measurements [71–73] have a considerable uncertainty $\xi_s = 0.4 \pm 0.1$, however, in part due to the difficulty in extrapolating to zero temperature. An extensive analysis of the thermodynamics of both the balanced and the imbalanced gas near unitarity has recently been performed by the group at ENS [74, 75]. As discussed in the contribution by Chevy and Salomon, these measurements indicate a value $\xi_s = 0.41(1)$ for the Bertsch parameter which is close to that obtained from a variety of analytical approximations [43, 76]. They include diagrammatic techniques like the pair fluctuation approach discussed in detail in the contribution by Strinati [77, 78] or Gaussian functional integrals [79, 80]. Very similar values for ξ_s are obtained from both $T = 0$ fixed-node Monte Carlo calculations [81–83] and also from finite temperature Monte Carlo calculations [84]. The latter method is discussed in detail in the contribution by Bulgac, Forbes and Magierski to this volume. The accuracy of this value is challenged, however, both by recent precision experiments of the equation of state at MIT which give $\xi_s = 0.37 \pm 0.01$ and also by quantum Monte Carlo calculations which indicate an upper bound $\xi_s < 0.38$ [85].

A remarkable consequence of the symmetries of the unitary gas that were mentioned above is that, beyond the derivation of some exact relations, they also provide an unexpected route to calculate its thermodynamic properties from a systematic expansion around an upper and a lower critical dimension. This idea is due to Nishida and Son [34] and is explained in detail in their contribution to this volume. It is based on the observation [86] that the unitary gas in four dimensions is an ideal Bose gas while in two dimensions, it is an ideal Fermi gas. Both, in $d = 4$ and in $d = 2$, the unitary Fermi gas is therefore an exactly soluble problem. This surprising

statement can be understood in physical terms by noting that in four dimensions a two-particle bound state in a zero range potential only appears at infinitely strong attraction. Thus, already at an arbitrary small value of the binding energy, the associated dimer size vanishes, in strong contrast to the situation in $d = 3$, where the size of the two-particle bound state is infinite at unitarity. The unitary Fermi gas in four dimensions is thus a non-interacting BEC, similar to the limit $a \rightarrow 0^+$ in three dimensions. The $d = 4 - \varepsilon$ expansion may be complemented by an expansion around the lower critical dimension, which is two for the present problem [35, 86, 87]. Indeed, for $d \leq 2$ a bound state at zero binding energy appears for an arbitrary weak attractive interaction and an expansion around $d = 2 + \varepsilon$ is thus effectively one around the non-interacting Fermi gas. For quantitatively reliable results in the relevant case $d = 3$, the $\varepsilon = 4 - d$ expansion has been extended up to three loops [88]. Within a Pade resummation that takes into account the known behavior in the limit $d \rightarrow 2^+$, the resulting value is $\xi_s = 0.36 \pm 0.02$ [89] which agrees very well with the most precise experimental number available at this point. The result $\xi_s = 0.36$ has in fact been obtained within a diagrammatic calculation based on the Luttinger-Ward approach [33]. The conserving nature of the approximation guarantees that all thermodynamic relations are obeyed. Moreover, the approximation respects the exact Tan relations that hold for Fermions with contact interactions, as discussed in the following section. The Luttinger-Ward formulation thus provides an internally consistent and quantitatively reliable picture of the thermodynamics along the full BCS–BEC crossover, both in the normal and in the superfluid phase and at arbitrary values of the coupling $1/k_F a$.

With increasing temperature, superfluidity will eventually be lost. In the balanced gas, the transition to the normal state is continuous along the full BCS–BEC crossover and the associated critical exponents are those of the 3D XY-model. At unitarity, the ratio T_c/T_F between the critical temperature and the bare Fermi temperature is again a universal number. Early calculations, based on including Gaussian fluctuations beyond mean field theory, gave values $T_c/T_F \simeq 0.22$ [21, 24]. They are close to the result $T_c/T_F = 0.218$ reached in the BEC-limit, where strongly bound dimers undergo an ideal Bose-Einstein condensation. More precise results, which take into account the interaction between non-condensed pairs, have been obtained by Haussmann within the Luttinger-Ward approach [32, 33]. Depending on whether the superfluid transition is approched from above or below, the critical temperature of the unitary gas is found to be $T_c/T_F = 0.15$ or 0.16, The apparent first order nature of the transition is clearly an artefact of self-consistent Green function methods but, fortunately, the range of temperatures where the normal state still appears stable in the presence of a finite superfluid order parameter is rather small except on the BEC-side near $k_F a \simeq 1$ [33]. In fact, it is an unsolved challenge to develop conserving approximations that properly account for both the gapless nature of excitations in the symmetry broken phase and the continuous nature of the superfluid transition, a problem that appears already in the classic theory of weakly interacting Bose gases [33, 90]. The value $T_c/T_F \simeq 0.16$ is close to that obtained by quantum Monte Carlo methods, which give $T_c/T_F = 0.152(7)$ [36, 37] or $T_c/T_F = 0.171(5)$ in more recent calculations [38]. Note that in a trap, due to the

increased density at the center, the ratio between T_c and the Fermi temperature of the trap $\widetilde{T}_F$ is higher, close to $T_c/\widetilde{T}_F \simeq 0.21$ [91]. Similarly, since the local value of T_F decreases upon approaching the trap edge, the gas becomes less degenerate there. The critical entropy $S(T_c) \simeq 1.6Nk_B$ necessary for reaching the superfluid transition is therefore considerably larger than the universal value $S(T_c) \simeq 0.7Nk_B$ of the homogeneous gas [33]. As a final example of the universal numbers which characterize the unitary gas, we mention the zero temperature excitation gap Δ for fermionic excitations. The theoretically predicted value $\Delta \simeq 0.46\varepsilon_F$ from both the Luttinger-Ward approach [33] and Monte Carlo calculations [92] agrees rather well with the experimental result $\Delta \simeq 0.44\varepsilon_F$ obtained by RF-spectroscopy [93], as discussed further in Sect. 1.7.

We conclude this Section with qualitative insights on why and how the quantitative results on crossover thermodynamics discussed above differ from those obtained from the simplest BCS-Leggett mean field theory (MFT). In the BCS limit $1/k_F a \to -\infty$ there are two features that MFT fails to capture. First, the numerical pre-factor in the gap $\Delta \simeq \varepsilon_F \exp(-\pi/2k_F|a|)$ is overestimated. The polarization of the medium, described diagramatically by particle-hole (p-h) fluctuations, effectively weakens the attractive interaction [94, 95]. This reduces both the gap and the critical temperature by a factor $(4e)^{1/3} \simeq 2.2$, leaving the ratio $2\Delta/T_c$ unchanged. (Remarkably, it seems that p-h fluctuations may not have a significant effect on T_c [96] at unitarity.) Secondly, the weak-coupling MFT ground state energy omits corrections perturbative in $k_F|a|$ but includes the exponentially small, non-perturbative pairing contribution. The perturbative "Fermi liquid" corrections are correctly described by Gaussian fluctuations [79] about mean field theory. They have the same form as the classic Lee-Yang-Huang and Galitskii results for the repulsive Fermi gas, but now with a negative scattering length.

In the opposite BEC limit $1/k_F a \gg 1$, MFT does lead to dimers with a binding energy $\hbar^2/ma^2$. However, the dimer-dimer scattering length is found to be [24, 26] $a_{\mathrm{dd}}^{\mathrm{MFT}} = 2a$ as compared to the exact result $a_{\mathrm{dd}} = 0.6a$ obtained by the solution of the four-fermion problem [29]. This directly impacts the compressibility and the speed of sound in the BEC limit. Gaussian fluctuation theories [79, 80, 97], that work across the entire crossover, are able to approximately account for this renormalization in the BEC limit.

At unitarity, MFT gives a value of $\xi_s^{\mathrm{MFT}} = 0.59$ [26] that is much larger than the best estimates ξ_s. This reduction in ground state energy [79] can be attributed to zero point motion of the collective mode and virtual scattering of gapped quasiparticle excitations missing in MFT. Simlarly, at unitarity, the MFT plus Gaussian fluctuation $T_c \simeq 0.2T_F$ [24] neglects critical fluctuations, and thus exceeds the best numerical estimates of T_c.

1.5 Universal Tan Relations

The effort to understand strongly interacting Fermi gases near infinite scattering length has led to a remarkable development in many-body physics that started in a

series of papers by S. Tan in 2005 [98]. He found a number of relations that apply quite generally to two-component fermions with an interaction that has zero range. In particular, Tan has shown that the momentum distribution of each spin-component falls off like C/k^4 at large momenta. The associated constant C, which is called the 'contact', has a simple physical meaning: it is a measure for the probability that two fermions with opposite spin are close together. The contact determines the change of the energy with respect to the interaction strength by a Hellmann-Feynman like relation, the Tan adiabatic theorem. It also allows to calculate the energy from the momentum distribution [99]. A crucial feature of the Tan relations is the fact that they apply to *any* state of the system, e.g., both to a Fermi-liquid or a superfluid state, at zero or at finite temperature and also in a few-body situation. The only change is the value of the contact C. The origin of this universality was elucidated by Braaten and Platter [100]. As described in detail in the contribution by Braaten to this volume, the Tan relations are a consequence of operator identities that follow from a Wilson-Kadanoff operator product expansion of the one-particle density matrix.

The Tan relations have been tested in a number of experiments recently. In a rather direct manner, they may be verified by observing the tail of the momentum distribution obtained in a time-of-flight measurement [101]. Moreover, the fact that a change in the magnetic field results in a linear shift of the closed channel eigenenergy implies, via the Tan adiabatic theorem, that the contact C is proportional to the number of closed channel molecules [102, 103]. As discussed in the contribution by Castin and Werner, this allows to infer the value of the contact along the BCS–BEC crossover from earlier measurements of the closed channel fraction at Rice [104]. A different way of getting access to the contact is via rf-spectroscopy, a method discussed in more detail in Sect. 1.7 In particular, it turns out, that the average shift of the transition frequency compared with those in a free atom due to the effects of interaction, is directly proportional to C [105, 106]. The so-called 'clock-shift' thus basically measures the probability for two atoms to be close together. This probability is not very sensitive as to whether one considers a superfluid or a normal state. In fact, for the unitary gas, the contact C is almost unchanged between the balanced superfluid phase and a normal phase at strong imbalance [106]. This observation provides an understanding of the observation that the average clock-shift hardly changes with imbalance [107]. The contact also shows up as the coefficient of $\omega^{-3/2}$ power-law tail in the rf-spectrum at high frequencies [16, 108, 109], as discussed in the contribution by Braaten. In the presence of non-vanishing final state interactions, the proportionality to the contact still holds. The power law, however, is changed to $\omega^{-5/2}$, which leads to a finite value of the average clockshift obtained from the first moment of the rf spectrum [105, 106]. The consistency of the value for C obtained from either the asymptotics of the momentum distribution or the high frequency part of the rf-spectrum has been verified nicely in experiments performed at JILA [101].

An analog of the Tan relations also hold for Fermi gases in one dimension [110]. Similar to the 3D case, there is again a special value of the coupling where the system is scale invariant, implying an equation of state with $p = 2\varepsilon$. Apart from the trivial non-interacting gas, this appears at both infinite repulsion or attraction. In either one of these limits, the thermodynamics is like that of a single component

Fermi gas: in the repulsive case, the effective Fermi wave vector is doubled because the many-body wave function has to vanish at coincident coordinates not only for Fermions with equal but also for those with opposite spin. In the attractive case, the resulting bound pairs are like hard core bosons due to the underlying Pauli exclusion of their constituents. As discussed in detail in the contribution by Feiguin et al. on the BCS–BEC crossover in one dimension, this is a Tonks-Girardeau gas of dimers.

An extension of the Tan relations has recently also been derived for Bosons with zero range interactions [111]. In addition to the contact, which is a two-body observable, the extended form of the Tan relations for Bosons also involves a three-body parameter that is associated with a—sub-dominant—$1/k^5$-tail of the momentum distribution.

1.6 The Unitary Fermi Gas as a Perfect Fluid?

A quite surprising connection between the physics of ultracold atoms and recent developments in field theory has opened up with the realization that not only equilibrium but also transport properties of the unitary Fermi gas should exhibit universal features. These connections are motivated by the fact that the unitary gas is a non-relativistic field theory which is both scale and conformally invariant [59, 60]. In the relativistic domain, such field theories exhibit quite unique features in their dynamical properties. For example, it has been shown by Policastro, Son and Starinets [112] that the shear viscosity η and the entropy per volume s in a $\mathcal{N} = 4$ supersymmetric Yang-Mills theory in the limit of infinite't Hooft coupling $\lambda = g^2 N \to \infty$ are simply proportional to each other. Their ratio $\eta/s = \hbar/(4\pi k_B)$ is a universal constant independent of temperature. The supersymmetric version of Yang-Mills theory is related by a duality transformation to a theory that involves gravity in a five dimensional space with constant negative curvature called Anti-de Sitter space (AdS-CFT correspondence). Perturbations away from this exactly soluble model typically give rise to larger values of η/s. This observation has prompted Kovtun, Son and Starinets (KSS) to conjecture that the constant $\hbar/(4\pi k_B)$ is a lower bound on the shear viscosity to entropy ratio for a large class of strongly interacting quantum field theories [113] and has motivated the search for the 'perfect fluid' which realizes, or at least comes close to, this bound [114]. A nontrivial example in this context is the standard *SU(3)* Yang-Mills theory for which the associated η/s ratio turns out to be rather close to the KSS bound [115]. Adding fermions to the pure gauge theory, the ratio η/s becomes an experimentally accessible quantity in high-energy, non-central collisions of heavy nuclei. The experimental estimate for the ratio η/s of the quark-gluon plasma is around $0.4\hbar/k_B$, i.e., a factor five above the KSS bound [114]. In fact, the quark-gluon plasma appears to be the most perfect *real* fluid known so far. Surprisingly, ultracold atoms near a Feshbach resonance, at temperatures almost twenty orders of magnitude below that of the quark-gluon plasma, seem to be equally perfect. Questions that were first raised in a string-theory context have thus become of relevance for ultracold atoms. In particular, the unitary Fermi gas provides a
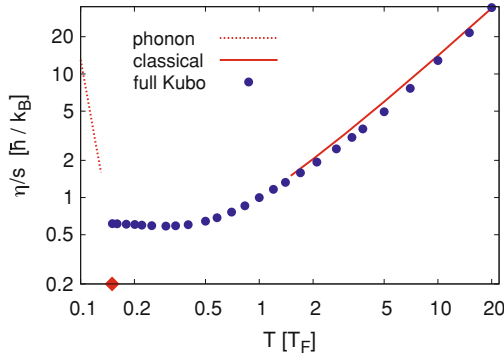
Fig. 1.4 Shear viscosity to entropy ratio η/s (*blue circles*) in comparison with known asymptotes. The *dashed red line* on the left is the phonon contribution $\eta/s \sim (T/T_F)^{-8}$ deep in the superfluid, the *solid red line* on the right the classical limit $\eta(T) \sim T^{3/2}$ divided by the associated entropy from the Sackur-Tetrode formula. The *red* diamond indicates $T_c \simeq 0.15 T_F$. (From Ref. [123])

motivation to search for gravity-duals of non-relativistic, conformally invariant theories, currently an active subject in field theory [116, 117].

In the high-temperature limit $T \gg T_F$, the transport properties of the unitary gas may be described in terms of a Boltzmann equation, which predicts a power law $\eta(T) \sim T^{3/2}$ for the shear viscosity at unitarity [118]. This power law dependence, including the theoretical prediction for the associated prefactor, has recently been verified in the temperature range between T_F and about $7T_F$ by measuring the expansion dynamics of an anisotropic gas released from an optical trap [119], thus extending earlier measurements of η based on the damping of the radial breathing mode [120]. Extraction of the viscosity from the 'elliptic' flow that appears in the transverse expansion from a deformed trap is discussed in detail in the contribution by Schäfer and Chafin to this volume. At low temperatures, in the superfluid regime, a finite viscosity arises from the presence of a normal fluid component. Asymptotically, phonon-phonon collisions dominate, giving rise to a rapid increase $\eta(T) \sim T^{-5}$ of the viscosity as the temperature approaches zero [121]. In fact, this behavior is completely analogous to that of superfluid ^{4}He, a problem that had been solved by Landau and Khalatnikov in 1949 [122]. Unfortunately, the superfluid regime and the expected rise in η have so far not been accessible experimentally. It is certain, however, that both the viscosity and the ratio η/s of the unitary gas necessarily exhibit a minimum, a behavior, which is in fact typical for any fluid [114]. Quantitative predictions for the viscosity of the unitary gas down to the superfluid transition temperature have been obtained recently by Enss et al. [123]. They are based on a diagrammatic evaluation of the exact Kubo-formula within a Luttinger-Ward approach. The formalism respects all symmetries of the problem, in particular scale invariance, and thus gives a vanishing bulk viscosity. Moreover, it also obeys an exact sum rule for the frequency dependent shear viscosity $\eta(\omega)$ derived by Taylor and Randeria [65].

The sum rule implies that $\eta(\omega)$ decays like $\sim C_\eta/\sqrt{\omega}$ at large frequencies with a prefactor C_η that is proportional to the Tan contact density C. The ratio η/s of the unitary gas is shown in Fig. 1.4. It exhibits a shallow minimum just above the critical temperature of the superfluid transition. The associated value $\eta/s \simeq 0.6\hbar/k_B$ is a factor of about seven above the KSS bound, slightly larger than that found for the relativistic quark-gluon plasma [114]. The unitary gas in fact appears to be the most perfect of all *non*-relativistic fluids known so far!

A closely related issue is the behavior of shear- and spin-diffusion of a scale invariant fluid. Indeed, as was shown by Hohenberg and Martin [90], there is a simple Einstein relation $\eta = \rho_n D_\eta$ that connects the shear viscosity η to the shear diffusion constant D_η via the normal fluid mass density ρ_n. The minimum value $\eta \simeq 0.5\hbar n$ of the shear viscosity in the normal state just above the superfluid transition [123] thus implies that the shear diffusion constant has a minimum value $D_\eta \simeq 0.5\hbar/m$ that only depends on fundamental constants. A similar result has been found recently in an experiment which measures the spin diffusion constant D_s from the equilibration dynamics of two initally separated spin components of the unitary gas [124]. This diffusion constant is related to a spin conductivity σ_s by an Einstein relation of the form $D_s = \sigma_s/\chi_s$, where χ_s is the equilibrium spin-susceptibility. At temperatures close to, but still above, the superfluid transition, D_s attains a minimum value $D_s \simeq 6.3\hbar/m$ [124].

1.7 RF Spectroscopy: Pairing Gap and Pseudogap

Atomic gases offer many internal (hyperfine) states. Superfluid mixtures are prepared in two of these, which are labeled "up" and "down" or $|1\rangle$ and $|2\rangle$, while all other internal states are empty. A radiofrequency pulse, properly tuned to the energy difference between an occupied and an empty state, say state $|3\rangle$, can transfer atoms among internal states. For a single atom or a non-interacting collection of atoms, these internal transition frequencies are known with the precision of atomic clocks—in fact, atomic clocks probe such a hyperfine transition in cesium to keep our standard of time. However, if the atom in the initial state, say $|2\rangle$ interacts with other atoms in $|1\rangle$, for example forming a molecular bound state, the rf photon has to first supply the binding energy of the molecule before it can break the bond and transfer the atom from state $|2\rangle$ to state $|3\rangle$. Even in the absence of molecular binding, the atom experiences an energy shift as it interacts with the surrounding gas, and the RF pulse will have to be detuned by the difference in energy shifts between the final and intial state. In atomic clocks, such density-dependent interaction shifts are a major source of systematic error and are thus called clock shifts.

RF spectroscopy has given access to microscopic information on the strongly interacting gas in the BEC-BCS crossover. Initial experiments traced the evolution of the molecular spectrum all the way across resonance [125]. Although two-body physics no longer supports a bound state beyond the resonance, the spectra were still shifted and broad. However, interpretation of the spectra was made difficult by the

fact that the final state $|3\rangle$ employed in these experiments was still strongly interacting with atoms in state $|1\rangle$. In addition, the averaging over the inhomogeneous density in a trap and the associated spatial variation of the fermionic excitation gap Δ did not allow to measure Δ directly. These problems were avoided in experiments that employed locally resolved and 3D reconstructed rf spectroscopy [126]. Working with a $|1\rangle-|3\rangle$ mixture and a rf-transfer to state $|2\rangle$ moreover allowed to essentially eliminate the final state effects [127]. In this manner, the pairing gap $\Delta = 0.44 \pm 0.02\varepsilon_F$ of the unitary gas was measured by injecting unpaired atoms into the superfluid in a slightly imbalanced Fermi mixture [93]. Paired and unpaired atoms responded at different frequencies, allowing to read off the pairing gap.

Detailed information about the excitation spectrum of strongly interacting Fermi gases is provided by momentum resolved rf spectroscopy, first realized by the JILA group [128]. This is the cold atom analog of angle-resolved photoemission spectroscopy (ARPES) [129, 130], one of the most powerful probes of correlated electrons in solid-state materials. The energy and momentum of the excitation are deduced by measuring energy and momentum of the outcoupled atoms, similar to the situation in an ARPES experiment which determines both the energy and momentum of the outgoing electrons. On a microscopic level, the information gained by such an experiment is the occupied or 'hole' part $A_-(\mathbf{k}, \varepsilon)$ of the full single-particle spectral function $A(\mathbf{k}, \varepsilon)$ of the initial, strongly correlated state [16, 108, 131]. The function $A_-(\mathbf{k}, \varepsilon)$, which is just the Fermi function times the $A(\mathbf{k}, \varepsilon)$, has a rather simple physical interpretation: it is the probability density for removing a particle with given momentum $\mathbf{k}$ in the many-body system with an energy ε. For free particles and at zero temperature, therefore, $A_-(\mathbf{k}, \varepsilon) = \delta(\varepsilon - \varepsilon_k)$ for $\varepsilon_k = \hbar^2 k^2/2m < \mu$ while it vanishes for $\varepsilon_k > \mu$. The spectral function thus directly reveals the energy-momentum relationship of a fermionic excitation in the many-body system, including the appearance of an energy gap. The rf spectrum $I(\omega) \sim \sum_k A_-(\mathbf{k}, \varepsilon_\mathbf{k} - \hbar\omega)$ then follows by integrating over all possible momenta of the outgoing atom.

We expect that the hole spectral function in the $T = 0$ superfluid state has a sharp peak

$$A_-(\mathbf{k}, \varepsilon) = Z_\mathbf{k}\delta(\varepsilon - E_\mathbf{k}^{(-)}) \tag{1.8}$$

at an energy

$$E_\mathbf{k}^{(-)} = \mu - \sqrt{\left(\hbar^2 k^2/2m^* - \widetilde{\mu}\right)^2 + \Delta^2} \tag{1.9}$$

with a weight $Z_\mathbf{k}$ and renormalized dispersion similar in form to the usual Bogoliubov quasiparticles with gap Δ. In the Leggett-BCS mean field theory of the crossover, the parameter $m^* = m$, the bare fermion mass, and $\widetilde{\mu} = \mu$, the chemical potential, with the weight $Z_\mathbf{k} = v_\mathbf{k}^2$, the occupation number. Thus the minimum in the dispersion is at $k_\mu = \sqrt{2m\mu}/\hbar$ for $\mu > 0$ (and $k = 0$ for $\mu < 0$) within MFT. Note that, in contrast to the normal state, the fact that v_k^2 is nonzero at *arbitrary* momentum in the superfluid state, gives a finite probability to create a hole even for momenta above k_μ. Moreover, due to the sum over final momenta, the sharp onset of the rf-spectrum in the $T = 0$

MFT appears at $\hbar\omega_{\min} = \sqrt{\mu^2 + \Delta^2} - \mu$, and not at the energy gap scale. In fact, in the BCS limit $\hbar\omega_{\min} \simeq \Delta^2/2\mu$, the condensation energy per particle, which is much less than the gap. Beyond the crossover MFT, interaction effects lead to [16, 83, 92] $\widetilde{\mu} = \mu - U$, shifted away from the chemical potential, and $m^* \neq m$. The predicted negative shift in $\widetilde{\mu}$ of $U \simeq -0.43\varepsilon_F$ at unitarity has been seen in the rf experiments [93].

An important question is whether the energy gap, or more precisely, a strong suppression of spectral weight near the chemical potential, called the pseudogap, persists above T_c in the unitary regime. In this context, a crucial parameter is the crossover temperature scale $T^\star$ (see Fig. 1.1), below which pairing correlations become manifest [39–41]. In the BCS limit, $T^\star$ coincides with T_c, so that the formation of pairs and their condensation occur simultaneously. In the opposite extreme, the BEC limit, $T^\star$ is the temperature scale for molecular dissociation, which is much larger than the Bose condensation T_c. The key quantitative issue near unitarity is the extent of the temparature window $T_c < T < T^\star$, in which various anomalies in spectroscopy and thermodynamics, arising from pairing correlations above T_c, are predicted [39–41]. Since $T^\star$ is a crossover scale, its estimate depends on the observable being probed, in marked contrast with a phase transition. Early estimates [24] and quantum Monte Carlo calculations [132, 133] indicate that $T^\star$ is roughly $0.5T_F$ for the unitary gas, which is about three times T_c. Other theoretical approaches, discussed below, suggest a much smaller window of temperatures [16] at unitarity, though these effects can only increase as one moves to the BEC side. The experiments at present are also not unequivocal on the extent of the temperature range or the size of the pseudogap anomalies. The extent to which both theory and experiment provide clear evidence for the existence of a well-defined a pseudogap regime in the unitary gas is a subject of current debate, as we discuss next.

We first discuss angle-resolved rf spectroscopy above T_c. At a phenomenological level [39, 134], one expects the spectral function in the pseudogap regime to still show an energy gap, and a bending-back of the dispersion (analogous to the Bogoliubov dispersion in the superfluid state) as in Eq. 1.9. This arises because of the persistence of pairing correlations, or 'preformed pairs', above T_c. However, the sharp peak in Eq. 1.8 will be greatly broadened, because one expects quasiparticles to be quite ill-defined in this strongly interacting regime. The very short mean free path, or equivalently short lifetime of fermionic excitations, is closely related to the anomalously low shear viscosity $\eta \simeq 0.5\hbar n$ of the unitary gas in the regime just above T_c discussed in the previous section.

Gap-like features and the associated back-bending of the dispersion *near k_F* have been observed in a recent angle-resolved rf experiment [135]. Note that back-bending *far from k_F*, with small but non-zero spectral weight, is predicted to be a universal feature [109] of Fermi gases with contact interactions in all phases, normal and superfluid. This is a direct consequence of the $1/k^4$-tail in the momentum distribution discussed in Sect. 1.5 This is indeed what the experiments [135] find, with the back-bending at large momenta persisting up to very high T, even when the near-k_F behavior no longer exhbits a pseudogap. A quantitative estimate of the energy gap, either the pseudogap above T_c or the superconducting gap below T_c, requires
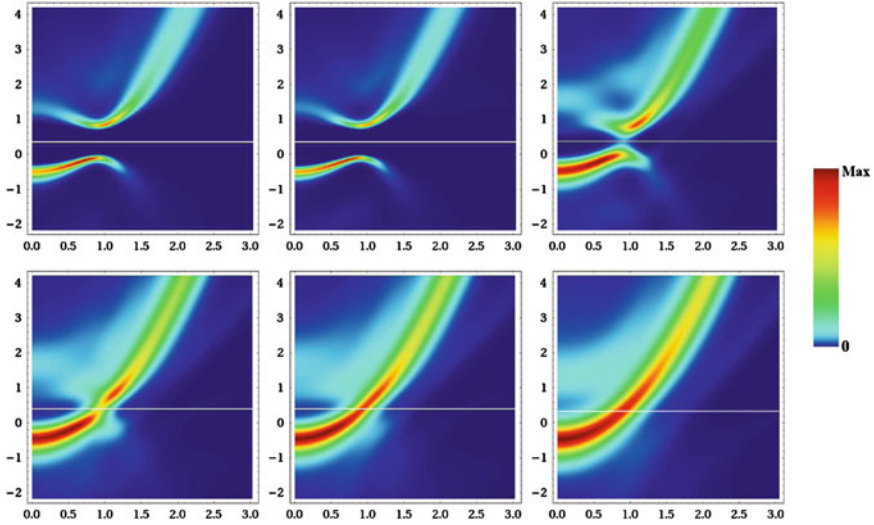
Fig. 1.5 Density plots of the spectral function $A(\mathbf{k}, \varepsilon)$ at unitarity for different temperatures. Momentum and energy are in units of k_F or ε_F respectively. From top left to bottom right: $T/T_F = 0.01,\ 0.06,\ 0.14,\ 0.160(T_c),\ 0.18, 0.30$. The white horizontal lines mark the chemical potential μ (From [16])

measuring the near k_F feature with respect to the chemical potential. Eventually, such measurements could help to answer the question whether or not sharp quasiparticle excitations exist in the normal fluid regime above T_c.

The contributions by Strinati and by Bulgac, Forbes and Magierski, describe two different microscopic approaches—the pair-fluctuation approach to the BCS–BEC crossover [108, 131, 136] and quantum Monte Carlo calculations [133], respectively—both of which lead to characteristic pseudogap spectral features.

The full spectral functions of the unitary gas as a function of momentum and energy for temperatures across the superfluid transition as obtained from the Luttinger-Ward approach [16] is shown in Fig. 1.5. Deep in the superfluid state, the dispersion of both the hole (below μ) and particle branch (above μ) exhibits a BCS-Bogoliubov-like dispersion, as expected from Eq. 1.9. The shift of $\widetilde{\mu}$ from the chemical potential by the interaction-induced shift $U \simeq -0.46\varepsilon_F$. is also observed. With increasing temperature the gap closes and the two branches gradually merge. Apparently, in this approach, the backbending very quickly disappears above $T_c \simeq 0.16 T_F$ and there is no pronounced pseudogap regime.

Pairing corelations above T_c are also of relevance in understanding the thermodynamics of the BCS–BEC crossover in the normal state. It was predicted [40, 41] in early calculations of two dimensional lattice models of the BCS–BEC crossover that in the temperature range $T_c < T < T^\star$ (see Fig. 1.1), there is a strong suppression of the spin susceptibility χ_s with lowering T, while the compressibility $dn/d\mu$ is T-independent. This qualitative difference between the behaviors of χ_s and $dn/d\mu$

represent a marked deviation from conventional Fermi liquid behavior in a strongly interacting, degenerate Fermi system. Whether these effects are significant in the three dimensional continuum problem at unitarity depends on the separation between T_c and $T^\star$, as already noted.

The expected strong reduction of the spin susceptibility below $T^\star$ due to the formation of singlet pairs can, in principle, be measured with ultracold atoms by observing the displacement of the two spin-components induced by a trapping potential which acts differently on both hyperfine states [137]. In practice, unfortunately, this is difficult because in the case of ^{6}Li, the polarizabilities are essentially equal at the magnetic fields of interest. A quite different method to determine the spin susceptibility has opened up recently with the measurement of the spin diffusion constant D_s mentioned above. Indeed, an independent mesasurement of D_s and the associated spin conductivity σ_s allows to extract the equilibrium spin susceptibility $\chi_s = \sigma_s / D_s$ as their ratio. The resulting $\chi_s(T)$ of the unitary gas shows no clear suppression in the regime above the superfluid transition, indicating that the characteristic temperature $T^\star$ may not be much higher than T_c at unitarity.

To conclude this section, it seems appropriate to point out similarities and differences between the pairing pseudogap in the BCS–BEC crossover and the much discussed—but still not well understood—pseudogap phase in underdoped high-T superconductors. In fact, the early work [39–41] on pseudogaps in the crossover problem was motivated by the desire to see if the normal state of a short coherence length superconductor, with pair size comparable to interparticle distance, might generically show deviations from Fermi liquid behavior. As emphasized in the introduction, the high Tc superconductors (HTSC) differ from the ultracold Fermi gases in essential microscopic details. In the HTSC the electrons live in the two-dimensional copper-oxygen planes of a highly anisotropic crystal, and the dominant interactions arise from Coulomb repulsion. d-wave pairing and superconductivity arises upon doping—i.e., adding mobile carriers to—a parent antiferromagnetic Mott insulator. The superfluid phase competes with a variety of different order parameters, including antiferromagnetism and charge ordering. By contrast, the neutral atoms in a Fermi gas have manifestly attractive interactions, the only instability is to s-wave pairing and the superfluid state is free from competing order parameters or a proximity to a Mott transition.

Despite these differences, there are insights from the much better understood problem of the BCS–BEC crossover that may be useful for the HTSC cuprates. In both systems one can be in strong interaction regimes where (1) the pair size is comparable to interparticle spacing, (2) a simple mean-field description of the phase transition fails, and (3) T_c is determined by the superfluid stiffness rather than the pairing gap. In the underdoped cuprates, that lie between the highest T_c optimally doped superconductor and the parent Mott Insulator, there is clear evidence for a normal state pseudogap [23]. The associated loss of spectral weight above T_c has a strong angular anisotropy revealed by ARPES measurements [129, 130]. Although there are striking similarities between the anisotropy of the pseudogap above T_c and the d-wave superconducting gap below T_c, the connection between the two gaps gap remains controversial. The pseudogap regime in the HTSC exhibits features arising

from competing order parameters, local pairing above T_c, and proximity to the Mott insulator. The problem of the unitary Fermi gas, in turn, is in many ways simpler with a single instability to s-wave pairing. Thus if a gap exists above T_c, it can only be related to precursor pairing correlations.

1.8 Spin Imbalance and the Fermi Polaron

In standard BCS theory, pairs are formed in an s-wave state between fermions with opposite spins. The question of what happens if not every spin up fermion can find a spin down partner has intrigued physicists ever since the early days of BCS theory. In conventional superconductors, unequal populations of up and down-spin electrons are very difficult to create, essentially because superconductivity is destroyed by the orbital effects in the presence of a magnetic field long before the Zeeman splitting is able to induce an appreciable imbalance. In an early study, however, Chandrasekhar and Clogston independently considered what would be the maximum critical field if it enters a superconductor at all and no orbital effects were present [138, 139]. Such a field would imbalance the chemical potentials of spin up and spin down electrons by the Zeeman energy $\pm\mu_B B$, where μ_B is Bohr's magneton. Eventually, it would be energetically more favorable to form an imbalanced normal state than to force atoms with vastly different Fermi energies to pair up. The critical field is reached when the Zeeman energy overcomes the pairing gap, $\mu_B B > \Delta/\sqrt{2}$. In the weak coupling limit, where $2\Delta = 3.52\, k_B T_c$, this gives $B = 18.5$ Tesla for $T_c = 10$ K. Conventional superconductors do not reach such high critical fields, but heavy fermion superconductors [8, 140] or layered organic superconductors [141] may be in this "Pauli limited" regime.

In atomic gases, the population imbalance can be chosen at will. In fact, imbalance is yet another way, besides increasing the temperature or reducing the scattering length, to probe how stable the superfluid is. A detailed discussion of the present state of knowledge about the set of questions associated with imbalanced gases is given in the contributions by Chevy and Salomon from an experimental and by Diederix and Stoof as well as by Recati and Stringari from a theoretical perspective. It turns out, that there is a critical value of the imbalance beyond which the superfluid turns into a normal Fermi liquid. For the homogeneous unitary gas, the critical imbalance $\sigma_c = (n_\uparrow - n_\downarrow)/(n_\uparrow + n_\downarrow) \simeq 0.4$ in the ground state has been determined from quantum Monte Carlo calculations by comparing the energy of the balanced superfluid with that of an imbalanced normal state [142]. The superfluid-to-normal transition at $T = 0$ is, to current knowledge, first order in nature as long as $1/k_F a$ is less than a critical value close to 0.8 [16]. This is the location of the splitting point mentioned in the introduction. Beyond this point, on the BEC-side, single Fermions can be added to a balanced superfluid in a continuous manner. With increasing imbalance the system thus stays superfluid, effectively as a Bose-Fermi mixture up until full polarization, where the gas is a trivial non-interacting Fermi gas. The breakdown of superfluidity with increasing imbalance in a trap has been measured by observing the disappearance of a vortex lattice [143]. As shown in Fig. 1.6, for
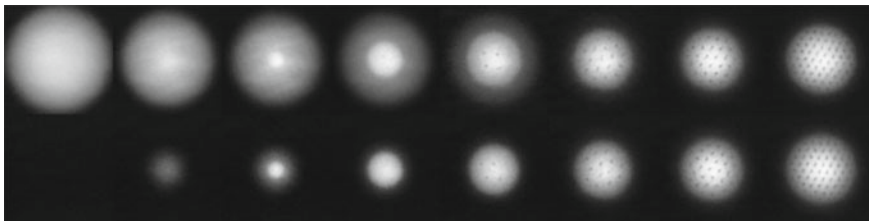
Fig. 1.6 Observation of vortices in a strongly interacting Fermi gas with imbalanced spin populations. The population imbalance $(N_\uparrow - N_\downarrow)/(N_\uparrow + N_\downarrow)$ was (from left to right) 100, 90, 80, 62, 28, 18, 10 and 0%. From [143]

Fig. 1.7 Critical population imbalance $\delta = (N_\uparrow - N_\downarrow)/(N_\uparrow + N_\downarrow)$ between the two spin states for which the superfluid-to-normal transition is observed. The profiles indicate the distribution of the gas in the harmonic trap. Data from [143]
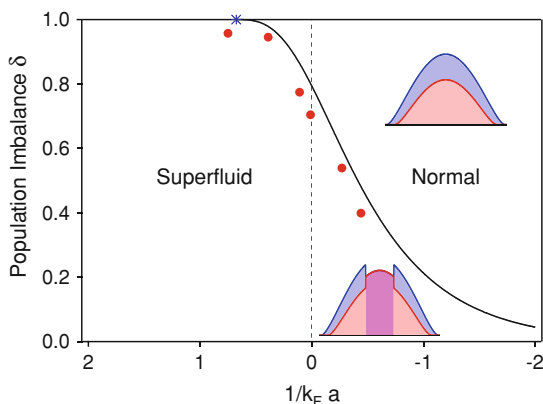
the unitary gas superfluidity breaks down beyond a ratio of 85%/15% between the two spin states.

Since vortices are difficult to create and observe near the phase boundaries, the superfluid phase diagram has also been mapped out by using pair condensation as an indicator for superfluidity. The resulting phase diagram is shown in Fig. 1.7. As was mentioned above, on the BEC side the critical value of the imbalance where superfluidity is destroyed by the Chandrasekhar-Clogston mechanism of a mismatched Fermi sphere between the two components approaches 100%. This can be understood by noting that in this regime even a tiny concentration of minority atoms in a majority Fermi sea will form bosonic molecules with the majority atoms, which then give rise to a Bose-Einstein condensate.

The first order transition between the superfluid at equal spin population and the imbalanced normal mixture gives rise to phase separation. First hints for phase separation between the normal and superfluid phase were seen in Refs. [72, 143, 144]. Using tomographic techniques, a sharp separation between a superfluid core and a partially polarized normal phase was found [145] (see Fig. 1.8). Finally, the phase diagram of a spin-polarized Fermi gas at unitarity was obtained, by mapping out the superfluid phase versus temperature and density imbalance [146]. Using tomo-
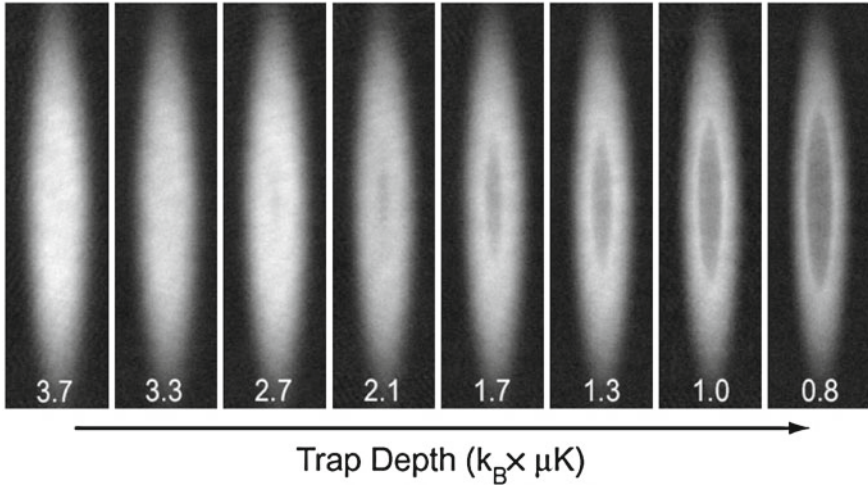
Fig. 1.8 Direct observation of the phase transition in imbalanced gases. The images are of the column density difference between spin up and spin down atoms. Below a critical temperature, an "empty" core opens up, signalling superfluid pairing at equal densities [145]

graphic techniques, spatial discontinuities in the spin polarization were revealed. This is the signature of a first-order phase transition which disappears at a tricritical point, in agreement with theoretical predictions [142, 147]. A detailed discussion of the structure of the phase diagram of the imbalanced unitary gas is given in the contributions by Diederix and Stoof and by Recati and Stringari.

While a detailed understanding of whether imbalanced Fermi gases with strong attractive interactions exhibit more complex phases than a normal Fermi liquid or a mixed superfluid/normal Fermi gas is still missing (see section 9 below and the contributions by Bulgac, Forbes and Magierski for a discussion of possible exotic phases in this context), considerable progress has been made within the last few years in the limit of a very large imbalance. In this limit, the two component Fermi gas can be viewed as a small number of spin down, minority impurities swimming in a Fermi sea of spin up particles. For a weakly-attractive interaction between the impurity and the Fermi sea, the impurity propagates freely through the medium, experiencing only a mean field energy shift $4\pi\hbar^2 an_\uparrow/m$ from forward-scattering, where n is the majority density, a the scattering length between spin up and spin down. However, as interactions increase and the mean free path becomes comparable to the interparticle distance, momentum changing collisions become important. In the strong coupling regime, the impurity dresses itself with a polarization cloud of majority atoms, giving rise to a new type of quasiparticle: the Fermi polaron. The question of whether a single added down-spin behaves like a proper quasiparticle can be addressed by calculating the quasiparticle residue, the probability that an added bare particle with momentum **p** will propagate with this very momentum for an arbitrary long time [148, 149]. For very strong attraction, this picture is expected to break down: Here, an added
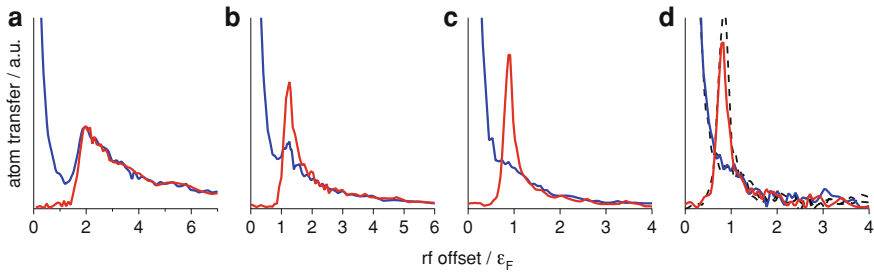
Fig. 1.9 RF spectroscopy on polarons. Shown are spatially resolved, 3D reconstructed rf spectra of the environment (*blue*, state $|1\rangle$) and impurity (*red*, state $|3\rangle$) component in a highly imbalanced spin-mixture. **a** Molecular limit. **b**, **c** Emergence of the polaron, a distinct peak exclusively in the minority component. **d** At unitarity, the peak dominates the impurity spectrum. For the spectra shown as dashed lines in **d** the roles of states $|1\rangle$ and $|3\rangle$ are exchanged. Impurity concentration was $x = 5(2)\%$ for all spectra, the interaction strengths $1/k_F a$ were **a** 0.76(2), **b** 0.43(1) c) 0.20(1), d) 0 (Unitarity)

down-spin will form a spin-zero, mobile molecular bound state with the up-spin Fermi sea. The fermionic quasiparticle will therefore vanish beyond a critical value of the coupling $1/(k_{F\uparrow}a)$, via a discontiuous transition first predicted by Prokof'ev and Svistunov [150].

Polarons have been observed via locally resolved RF spectroscopy [151]. In the case of molecular binding, one finds the characteristic onset at the molecular binding energy, and fully coincidal spectra for both the spin up and spin down atoms-as binding is a purely two-body affair. For the polaron, a characteristic bimodal spectrum is observed: A narrow, coherent quasi-particle peak, centered at the polaron binding energy, which emerges from a broad, incoherent background (see Fig. 1.9).

The results for the ground state energy of the Fermi polaron are in quite good agreement with the result of a variational Ansatz for the ground state wave function due to Chevy, in which the single down spin is dressed with particle-hole excitations of the up-spin Fermi sea [152, 153]. This approximate treatment is supported by a more detailed analysis including multiple particle-hole pairs [154], and also by Quantum Monte-Carlo calculations [150, 155]. The effective mass of Fermi polarons at unitarity has been deduced from density profiles [156]. As discssed in the contributions by Chevy and Salomon and by Recati and Stringari, it can be determined in a direct manner from a dynamical measurement, by extrapolating frequencies of collective excitations in strongly imbalanced Fermi mixtures to the single-impurity limit [157]. The result of $m^* = 1.20(10)m$ is in good agreement with theoretical predictions [150]. The polaron energy was observed to be largely independent of the impurity density, i.e. interaction effects between the dressed particles must be weak.

At a critical interaction strength $1/(k_{F\uparrow}a) = 0.76$, the Fermi Polaron peak vanishes and a transition towards two-body binding is observed [151]. The disappearance of the Fermi polaron as a spin *1/2* quasiparticle beyond a critical value of the coupling was predicted by diagrammatic Monte Carlo calculations [148, 150]

and was later studied by variational methods [149, 158]. At this point, a Fermi liquid of polarons is replaced by a Bose liquid of molecules. At low enough temperatures, this molecular cloud will form a Bose condensate that fully phase separates from the normal state of unpaired atoms, as observed in [159]. Even further away from the Feshbach resonance, when the interactions between molecules and atoms become weaker, one might be able to observe fermionic atoms moving in a bath of bosons. This would be an example of the "classical" polaron, a fermion (electron) dressed by a boson bath (phonons).

1.9 FFLO Phases and Outlook

A remarkable proposal of what might happen in a fermionic superfluid in the presence of a finite spin-imbalance was put forward almost fifty years ago by Fulde and Ferrell and independently by Larkin and Ovchinnikov [160, 161]. The novel type of super-fluidity, now often abbreviated as FFLO or LOFF states, predicts that Cooper pairs acquire a non-vanishing center-of-mass momentum. As a result, the superfluid order parameter exhbits a nontrivial periodic modulation in space, thereby spontaneously breaking translation invariance. Due to the coexistence of fermionic superfluidity and periodic order such a state has also been called a 'Fermi supersolid' [162]. In solid state materials, the orbital effect of an external magnetic field usually overwhelms the Zeeman effect causing spin imbalance. Despite decades of intensive search, there are very few systems in which there is now some indirect experimental evidence for the occurrence of FFLO order: layered organic superconductors with a strong parallel magnetic field [141] and certain heavy fermion materials [8, 140]. A quite different context where superfluid states with additional periodic order might show up are color superfluids that are expected in the core of neutron stars [10]. In this case, the imbalance arises as a result of the different chemical potentials due to different quark masses.

  As disussed in the previous section, ultracold atoms provide an ideal model system to study attractive Fermi gases with an adjustable value of the spin-imbalance. For a Fermi gas near unitarity, one expects in fact that for small imbalances the ground state exhibits FFLO order. This conclusion is supported both on general grounds [17] and also on a generalization of density functional theory that includes superfluid ordering and a finite spin imbalance, as discussed in the contribution by Bulgac et al. Unfortunately, in the 3D case, neither the precise type of spatial order, nor the relevant range of stability of an FFLO phase with respect to temperature are known. In addition, the inhomogeneous density in the trap leads to a situation where an FFLO phase would appear sandwiched between a balanced superfluid in the center and a polarized normal phase around it. This makes an observation very difficult if not impossible. As is discussed in detail in the contribution by Feiguin et al. the situation is much more promising in a one-dimensional configuration for two reasons: First of all, it turns out that in one dimension and for negative 3D scattering lengths (i.e. essentially on the BCS-side of the crossover) the ground state of the attractive

Fermi gas exhibits FFLO order at *arbitrary* values of the polarization. As a second point, in contrast to the 3D case, the interesting phase with finite imbalance appears in the center of the trap and not in its wings. From a theory point of view, the 1D case has the additional advantage that a number of exact results are available through the Bethe-Ansatz. For instance, a complete analytic solution can be given for the BCS–BEC crossover of the balanced gas [163, 164]. Moreover, efficient numerical methods like the density matrix renormalization group allow to obtain quantitatively reliable results for realistic system sizes without the Fermionic sign problem.

Experimentally, attractive Fermi gases confined in 1D tubes have been realized by the Rice group [165]. The observed spin-resolved density profiles show the predicted phase separation into an imbalanced gas in the center and a balanced superfluid at the edge of the trap. Unfortuately, so far experiments have not demonstrated that the phase in the center of the trap indeed corresponds to a paired state with FFLO order. This is not a trivial task and requires e.g. to resolve spin density modulations on a rather small length scale or a time-of-flight measurement that reveals the momentum distribution of the pairs. Due to their finite center-of-mass momentum, peaks should appear at a nonzero momenta $\pm Q$ with Q increasing linearly with the imbalance.

As a result of a breathtaking sequence of experiments and new theoretical insights over a short period of time, ultracold Fermi gases have developed into an exciting new form of matter with unexpected properties. The realization of the BEC-BCS crossover, the observation of vortex lattices in neutral fermionic superfluids and precision measurements of universal numbers in the thermodynamics of the unitary Fermi gas have come alongside with new theoretical concepts like the ε-expansion for scale invariant many-body systems, the Tan relations or the Fermi polaron as a novel type of a quantum impurity problem. Unconventional superfluids like the FFLO phase or a quite subtle liquid of trions in a mixture of three-component Fermi gases [166, 167] that resembles the hadrons of QCD [168] appear in reach within the coming years. Ultracold Fermi gases present us with a model textbook system, that did not exist before, with simple and controllable interactions, dimensionality and spin composition. Eventually, the goal is to deepen our understanding of fermions, the building blocks of matter, in the presence of strong interactions. The field has taken the first important steps, but this is only the beginning.

References

1. Regal, C.A., Greiner, M., Jin, D.S.: Phys. Rev. Lett. **92**, 040403 (2004)
2. Zwierlein, M., Stan, C., Schunck, C., Raupach, S., Kerman, A., Ketterle, W.: Phys. Rev. Lett. **92**, 120403 (2004)
3. Bardeen, J., Cooper, L.N., Schrieffer, J.R.: Phys. Rev. **108**, 1175 (1957)
4. Tinkham, M.: Introduction to Superconductivity, 2nd edn. Dover, Mineola (2004)

5. Bohr, A., Mottelson, B.R., Pines, D.: Phys. Rev. **110**, 936 (1958)

6. Migdal, A.B.: Nucl. Phys. **13**, 655–674 (1959)

7. Vollhardt, D., Wölfle, P.: The Superfluid Phases of Helium 3. Taylor and Francis, London (1990)

8. Pfleiderer, C.: Rev. Mod. Phys. **81**, 1551 (2009)

9. Mackenzie, A.P., Maeno, Y.: Rev. Mod. Phys. **75**, 657 (2003)

10. Alford, M.G., Schmitt, A., Rajagopal, K., Schäfer, T.: Rev. Mod. Phys. **80**, 1455–1461 (2008)

11. Schafroth, M.R., Butler, S., Blatt, J.: Helv. Phys. Acta **30**, 93 (1957)

12. Schafroth, M.R.: Phys. Rev. **111**, 72 (1958)

13. Griffin, A., Snoke, D., Stringari, S.: Bose-Einstein Condensation. Cambridge University Press, Cambridge (1995)

14. Eagles, D.M.: Phys. Rev. **186**, 456 (1969)

15. Leggett, A.: Diatomic molecules and Cooper pairs. In: Modern Trends in the Theory of Condensed Matter. Proceedings of the XVIth Karpacz Winter School of Theoretical Physics, Karpacz, Poland, Springer, Berlin 13–27 (1980)

16. Haussmann, R., Punk, M., Zwerger, W.: Phys. Rev. A **80**, 063612 (2009)

17. Son, D., Stephanov, M.: Phys. Rev. A **74**, 013614 (2006)

18. Klinkhamer, F.R., Volovik, G.E.: JETP Lett. **80**, 343 (2004)

19. Randeria, M., Duan, J., Shieh, L.: Phys. Rev. B **41**, 327 (1990)

20. Read, N., Dmitry Green, D.: Phys. Rev. B **97**, 10267 (2000)

21. Nozières, P., Schmitt-Rink, S.: J. Low Temp. Phys. **59**, 195–211 (1985)

22. Randeria M.: Crossover from BCS theory to Bose-Einstein condensation. In: Griffin, A., Snoke, D., Stringari, S. (eds.) Bose-Einstein Condensation. Cambridge University Press, Cambridge 355– 392 (1995)

23. Lee, P.A., Nagaosa, N., Wen, X.-G.: Rev. Mod. Phys. **78**, 17 (2006)

24. Sade Melo, C.A.R., Randeria, M., Engelbrecht, J.R.: Phys. Rev. Lett. **71**, 3202 (1993)

25. Randeria, M.: Nature Phys. **6**, 561 (2010)

26. Engelbrecht, J.R., Randeria, M., Sade Melo, C.A.R.: Phys. Rev. B **55**, 15153 (1997)

27. Drechsler, M., Zwerger, W.: Annalen der Physik **1**, 15–23 (1992)

28. Randeria, M., Duan, J.-M., Shieh, L.: Phys. Rev. Lett. **62**, 981 (1989)

29. Petrov, D., Salomon, C., Shlyapnikov, G.: Phys. Rev. Lett. **93**, 090404 (2004)

30. Mora, C., Komnik, A., Egger, R., Gogolin, A.O.: Phys. Rev. Lett. **95**, 080403 (2005)

31. Petrov, D.S., Baranov, M.A., Shlyapnikov, G.V.: Phys. Rev. A **67**, 031601 (2003)

32. Haussmann, R.: Phys. Rev. B **49**, 12975 (1994)

33. Haussmann, R., Rantner, W., Cerrito, S., Zwerger, W.: Phys. Rev. A **75**, 023610 (2007)

34. Nishida, Y., Son, D.T.: Phys. Rev. Lett. **97**, 050403 (2006)

35. Nishida, Y., Son, D.T.: Phys. Rev. A **75**, 063617–22 (2007)

36. Burovski, E., Prokof'ev, N., Svistunov, B., Troyer, M.: Phys. Rev. Lett. **96**, 160402 (2006)

37. Burovski, E., Kozic, E., Prokof'ev, N., Svistunov, B., Troyer, M.: Phys. Rev. Lett. **101**, 090402 (2008)

38. Goulko, O., Wingate, M.: Phys. Rev. A **82**, 053621 (2010)

39. Randeria M.: Precursor pairing correlations and pseudogaps. In: Iadonisi, G., Schrieffer, J.R., Chiafalo, M.L. (eds.) Proceedings of the International School of Physics "Enrico Fermi" Course CXXXVI on High Temperature Superconductors. IOS Press, Amsterdam 53–75 (1998)

40. Randeria, M., Trivedi, N., Moreo, A., Scalettar, R.T.: Phys. Rev. Lett. **69**, 2001 (1992)

41. Trivedi, N., Randeria, M.: Phys. Rev. Lett. **75**, 312 (1995)

42. Bertsch G.: Proceedings of the tenth international conference on recent progress in many-body theories. In: Bishop, R., Gernoth, K.A., Walet, N.R., Xian, Y. (eds.) Recent Progress in Many-Body Theories. World Scientific, Seattle (2000)

43. Baker, G.A.: Phys. Rev. C **60**, 054311 (1999)

44. Schwenk, A., Pethick, C.J.: Phys. Rev. Lett. **95**, 160401 (2005)

45. DeMarco, B., Jin, D.: Science **285**, 1703–1706 (1999)

46. Granade, S.R., Gehm, M.E., O'Hara, K.M., Thomas, J.E.: Phys. Rev. Lett. **88**, 120405 (2002)
47. Hadzibabic, Z., Stan, C.A., Dieckmann, K., Gupta, S., Zwierlein, M., Grlitz, A., Ketterle, W.: Phys. Rev. Lett. **88**, 160401 (2002)
48. Roati, G., Riboli, F., Modugno, G., Inguscio, M.: Phys. Rev. Lett. **89**, 150403 (2002)
49. Schreck, F., Khaykovich, L., Corwin, K.L., Ferrari, G., Bourdel, T., Cubizolles, J., Salomon, C.: Phys. Rev. Lett. **87**, 080403 (2001)
50. Truscott, A.G., Strecker, K.E., McAlexander, W.I., Partridge, G.B., Hulet, R.G.: Science **291**, 2570–2572 (2001)
51. Courteille, P., Freeland, R., Heinzen, D., van Abeelen, F., Verhaar, B.: Phys. Rev. Lett. **81**, 69–72 (1998)
52. Inouye, S., Andrews, M.R., Stenger, J., Miesner, H.J., Stamper-Kurn, D.M., Ketterle, W.: Nature **392**, 151–154 (1998)
53. Chin, C., Grimm, R., Julienne, P., Tiesinga, E.: Rev. Mod. Phys. **82**, 1225 (2010)
54. Tiesinga, E., Verhaar, B., Stoof, H.: Phys. Rev. A **47**, 4114–4122 (1993)
55. Bloch, I., Dalibard, J., Zwerger, W.: Rev. Mod. Phys. **80**, 885 (2008)
56. Bruun, G., Pethick, C.: Phys. Rev. Lett. **92**, 140404 (2004)
57. Ketterle W., Zwierlein, M.: Making, probing and understanding ultracold Fermi gases. In: Inguscio, M., Ketterle, W., Salomon, C. (eds.) Ultracold Fermi Gases, Proceedings of the International School of Physics "Enrico Fermi", Course CLXIV, Varenna, 20–30 June 2006. IOS Press, Amsterdam (2008)
58. Nikolic, P., Sachdev, S.: Phys. Rev. A **75**, 033608–0336014 (2007)
59. Nishida, Y., Son, D.T.: Phys. Rev. D **76**, 086004 (2007)
60. Son, D.T., Wingate, M.: Ann. Phys. **321**, 197–224 (2006)
61. Werner, F., Castin, Y.: Phys. Rev. A **74**, 053604 (2006)
62. Pitaevskii, L.P., Rosch, A.: Phys. Rev. A **55**, R853 (1997)
63. Ho, T.-L.: Phys. Rev. Lett. **92**, 090402 (2004)
64. Son, D.T.: Phys. Rev. Lett. **98**, 020604–4 (2007)
65. Taylor, E., Randeria, M.: Phys. Rev. A **81**, 053610 (2010)
66. Bartenstein, M., Altmeyer, A., Riedl, S., Jochim, S., Chin, C., Hecker-Denschlag, J., Grimm, R.: Phys. Rev. Lett. **92**, 120401 (2004)
67. Bourdel, T., Cubizolles, J., Khaykovich, L., Magalh"aes, K.M.F., Kokkelmans, J.M.F., Shlyapnikov, G.V., Salomon, C.: Phys. Rev. Lett. **91**, 020402 (2003)
68. Gehm, M.E., Hemmer, S.L., Granade, S.R., O'Hara, K.M., Thomas, J.E.: Phys. Rev. A **68**, 011401 (2003)
69. O'Hara, K.M., Hemmer, S.L., Gehm, M.E., Granade, S.R., Thomas, J.E.: Science **298**, 2179 (2002)
70. Bourdel, T., Khaykovich, L., Cubizolles, J., Zhang, J., Chevy, F., Teichmann, M., Tarruell, L., Kokkelmans, S., Salomon, C.: Phys. Rev. Lett. **93**, 050401 (2004)
71. Kinast, J., Turlapov, A., Thomas, J.E., Chen, Q., Stajic, J., Levin, K.: Science **307**, 1296–1299 (2005)
72. Partridge, G.B., Li, W., Kamar, R.I., Liao, Y., Hulet, R.G.: Science **311**, 503 (2006)
73. Stewart, J.T., Gaebler, J.P., Regal, C.A., Jin, D.S.: Phys. Rev. Lett. **97**, 220406 (2006)
74. Nascimbène, S., Navon, N., Jiang, K.J., Chevy, F., Salomon, C.: Nature **463**, 1057–1060 (2010)
75. Navon, N., Nascimbene, S., Chevy, F., Salomon, C.: Science **328**, 729 (2010)
76. Heiselberg, H.: Phys. Rev. A **63**, 043606 (2001)
77. Hu, H., Drummond, P.D., Liu, X.-J.: Nat. Phys. **3**, 469–472 (2007)
78. Perali, A., Pieri, P., Strinati, G.C.: Phys. Rev. Lett. **93**, 100404 (2004)
79. Diener, R.B., Sensarma, R., Randeria, M.: Phys. Rev. A **77**, 023626 (2008)
80. Hu, H., Liu, X.-J., Drummond, P.: Europhys. Lett. **74**, 574–580 (2006)
81. Astrakharchik, G.E., Boronat, J., Casulleras, J., Giorgini, S.: Phys. Rev. Lett. **93**, 200404 (2004)

82. Carlson, J., Chang, S.-Y., Pandharipande, V.R., Schmidt, K.E.: Phys. Rev. Lett. **91**, 050401 (2003)
83. Carlson, J., Reddy, S.: Phys. Rev. Lett. **95**, 060401 (2005)
84. Bulgac, A., Drut, J.E., Magierski, P.: Phys. Rev. A **78**, 023625 (2008)
85. Forbes, M.M., Gandolfi, S., Gezerlis, A.: Phys. Rev. Lett. **106**, 235303 (2011)
86. Nussinov, Z., Nussinov, S.: Phys. Rev. A **74**, 053622–053629 (2006)
87. Randeria, M., Duan, J.-M., Shieh, L.-Y.: Phys. Rev. Lett. **62**, 981 (1989)
88. Arnold, P., Drut, J.E., Son, D.T.: Phys. Rev. A **75**, 043605 (2007)
89. Nishida, Y.: Phys. Rev. A **79**, 013627–5 (2009)
90. Hohenberg, P.C., Martin, P.C.: Ann. Phys. **34**, 291–359 (1965)
91. Haussmann, R., Zwerger, W.: Phys. Rev. A **78**, 063602 (2008)
92. Carlson, J., Sanjay, R.: Phys. Rev. Lett. **100**, 150403 (2008)
93. Schirotzek, A., Shin, Y., Schunck, C.H., Ketterle, W.: Phys. Rev. Lett. **101**, 140403 (2008)
94. Gor'kov, L., Melik-Barkhudarov, T.: Zh. Eskp. Theor. Fiz. **40**, 1452 (1961)
95. Heiselberg, H., Pethick, C.J., Smith, H., Viverit, L.: Phys. Rev. Lett. **85**, 2418 (2000)
96. Floerchinger, S., Scherer, M., Diehl, S., Wetterich, C.: Phys. Rev. B **78**, 174528 (2008)
97. Diener, R.B., Randeria, M.: Phys. Rev. A **81**, 033608 (2010)
98. Tan, S.: Ann. Phys. **323**, 2971–2986 (2008)
99. Tan, S.: Ann. Phys. **323**, 2952–2970 (2008)
100. Braaten, E., Platter, L.: Phys. Rev. Lett. **100**, 205301 (2008)
101. Stewart, J.T., Gaebler, J.P., Drake, T.E., Jin, D.S.: Phys. Rev. Lett. **104**, 235301 (2010)
102. Werner, F., Tarruell, L., Castin, Y.: Europ. Phys. J. B **68**, 401–415 (2009)
103. Zhang, S., Leggett, A.J.: Phys. Rev. A **79**, 023601 (2009)
104. Partridge, G.B., Strecker, K.E., Kamar, R.I., Jack, M.W., Hulet, R.G.: Phys. Rev. Lett. **95**, 020404 (2005)
105. Baym, G., Pethick, C.J., Yu, Z., Zwierlein, M.W.: Phys. Rev. Lett. **99**, 190407 (2007)
106. Punk, M., Zwerger, W.: Phys. Rev. Lett. **99**, 170404 (2007)
107. Schunck, C., Shin, Y.-I., Schirotzek, A., Zwierlein, M., Ketterle, W.: Science **316**, 867 (2007)
108. Pieri, P., Perali, A., Strinati, G.C.: Nat. Phys. **5**, 736–740 (2009)
109. Schneider, W., Randeria, M.: Phys. Rev. A **81**, 021601 (2010)
110. Barth, M., Zwerger, W.: Ann. Phys. (NY) **326**, 2544–2565 (2011)
111. Braaten, E., Kang, D., Platter, L.: Universal relations for identical bosons from 3-body physics. Preprint arXiv:1101.2854 (2011)
112. Policastro, G., Son, D.T., Starinets, A.O.: Phys. Rev. Lett. **87**, 081601 (2001)
113. Kovtun, P.K., Son, D.T., Starinets, A.O.: Phys. Rev. Lett. **94**, 111601 (2005)
114. Schafer T., Teaney D.: Rep. Prog. Phys. **72**, 126001 (2009)
115. Meyer, H.B.: Phys. Rev. D **76**, 101701 (2007)
116. Balasubramanian, K., McGreevy, J.: Phys. Rev. Lett. **101**, 061601–061604 (2008)
117. Son, D.T.: Phys. Rev. D **78**, 046003–7 (2008)
118. Bruun, G.M., Smith, H.: Phys. Rev. A **75**, 043612 (2007)
119. Cao, C., Elliott, E., Joseph, J., Wu, H., Petricka, J., Schaefer, T., Thomas, J.E.: Science **331**, 58 (2011)
120. Turlapov, A., Kinast, J., Clancy, B., Luo, L., Joseph, J., Thomas, J.: J. Low Temp. Phys. **150**, 567–576 (2008)
121. Rupak, G., Schafer, T.: Phys. Rev. A **76**, 053607–9 (2007)
122. Landau, L., Khalatnikov, I.: Sov. Phys. JETP **19**, 637 (1949)
123. Enss, T., Haussmann, R., Zwerger, W.: Ann. Phys. **326**, 770–796 (2011)
124. Sommer, A., Ku, M., Roati, G., Zwierlein, M.W.: Nature **472**(7342), 201–204 (2011)
125. Chin, C., Bartenstein, M., Altmeyer, A., Riedl, S., Jochim, S., Hecker-Denschlag, J., Grimm, R.: Science **305**, 1128 (2004)
126. Shin, Y., Schunck, C.H., Schirotzek, A., Ketterle, W.: Phys. Rev. Lett. **99**, 090403 (2007)
127. Schunck, C.H., Shin, Y., Schirotzek, A., Ketterle, W.: Nature **454**, 739–743 (2008)
128. Stewart, J.T., Gaebler, J.P., Jin, D.S.: Nature **454**, 744–747 (2008)

129. Campuzano J., Norman M., Randeria M.: Photoemission in the high-tc superconductors. In: Bennemann, K., Ketterson, J. (eds.) The Physics of Superconductors: Vol II: Superconductivity in Nanostructures, High-Tc and Novel Superconductors, Organic Superconductors. Springer, Berlin (2004)
130. Damascelli, A., Hussain, Z., Shen, Z.-X.: Rev. Mod. Phys. **75**, 473 (2003)
131. Chen, Q., Levin, K.: Phys. Rev. Lett. **102**, 190402 (2009)
132. Akkineni, V.K., Ceperley, D.M., Trivedi, N.: Phys. Rev. B **76**, 165116–165116.6 (2007)
133. Magierski, P., Wlazowski, G., Bulgac, A., Drut, J.E.: Phys. Rev. Lett. **103**, 210403 (2009)
134. Norman, M.R., Randeria, M., Ding, H., Campuzano, J.C.: Phys. Rev. B **57**, R11093 (1998)
135. Gaebler, J.P., Stewart, J.T., Drake, T.E., Jin, D.S., Perali, A., Pieri, P., Strinati, G.C.: Nat. Phys. **6**, 569 (2010)
136. Chen, Q., He, Y., Chien, C., Levin, K.: Rep. Prog. Phys. **72**, 122501 (2009)
137. Recati, A., Carusotto, I., Lobo, C., Stringari, S.: Phys. Rev. Lett. **97**, 190403 (2006)
138. Chandrasekhar, B.: Appl. Phys. Lett. **1**, 7 (1962)
139. Clogston, A.: Phys. Rev. Lett. **9**, 266 (1962)
140. Bianchi, A., Movshovich, R., Capan, C., Pagliuso, P., Sarrao, J.L.: Phys. Rev. Lett. **91**, 187004 (2003)
141. Lortz, R., Wang, Y., Demuer, A., Bttger, P.H.M., Bergk, B., Zwicknagl, G., Nakazawa, Y., Wosnitza, J.: Phys. Rev. Lett. **99**, 187002 (2007)
142. Lobo, C., Recati, A., Giorgini, S., Stringari, S.: Phys. Rev. Lett. **97**, 200403–4 (2006)
143. Zwierlein, M.W.A., Schunck, C.H., Ketterle, W.: Science **311**, 492–496 (2006)
144. Zwierlein, M.W., Schunck, C.H., Schirotzek, A., Ketterle, W.: Nature **442**, 54–58 (2006)
145. Shin, Y., Zwierlein, M., Schunck, C., Schirotzek, A., Ketterle, W.: Phys. Rev. Lett. **97**, 030401 (2006)
146. Shin, Y., Schunck, C., Schirotzek, A., Ketterle, W.: Nature **451**, 689 (2007)
147. Gubbels, K., Stoof, H.: Phys. Rev. Lett. **100**, 140407 (2008)
148. Prokof'ev, N., Svistunov, B.: Phys. Rev. B **77**, 020408 (2008)
149. Punk, M., Dumitrescu, P.T., Zwerger, W.: Phys. Rev. A **80**, 053605–10 (2009)
150. Prokof'ev, N.V., Svistunov, B.V.: Phys. Rev. B **77**, 125101 (2008)
151. Schirotzek, A., Wu, C.-H., Sommer, A., Zwierlein, M.W.: Phys. Rev. Lett. **102**, 230402–230404 (2009)
152. Chevy, F.: Phys. Rev. A **74**, 063628 (2006)
153. Combescot, R., Recati, A., Lobo, C., Chevy, F.: Phys. Rev. Lett. **98**, 180402 (2007)
154. Combescot, R., Giraud, S.: Phys. Rev. Lett. **101**, 050404 (2008)
155. Bulgac, A., Forbes, M.M.: Phys. Rev. A **75**, 031605 (2007)
156. Shin, Y.: Phys. Rev. A **77**, 041603–041604 (2008)
157. Nascimbène, S., Navon, N., Jiang, K.J., Tarruell, L., Teichmann, M., McKeever, J., Chevy, F., Salomon, C.: Phys. Rev. Lett. **103**, 170402–170404 (2009)
158. Mora, C., Chevy, F.: Phys. Rev. A **80**, 033607–033610 (2009)
159. Shin, Y., Schirotzek, A., Schunck, C.H., Ketterle, W.: Phys. Rev. Lett. **101**, 070404 (2008)
160. Fulde, P., Ferrell, R.: Phys. Rev. **135**, A550 (1964)
161. Larkin, A., Ovchinnikov, Y.: Zh. Eksp. Teor. Fiz. **47**, 1136 (1964)
162. Bulgac, A., Forbes, M.M.: Phys. Rev. Lett. **101**, 215301–215304 (2008)
163. Fuchs, J.N., Recati, A., Zwerger, W.: Phys. Rev. Lett. **93**, 090408 (2004)
164. Tokatly, I.V.: Phys. Rev. Lett. **93**, 090405 (2004)
165. Liao, Y.-a., Rittner, A.S.C., Paprotta, T., Li, W., Partridge, G.B., Hulet, R.G., Baur, S.K., Mueller, E.J.: Nature **467**, 567 (2010)
166. Huckans, J.H., Williams, J.R., Hazlett, E.L., Stites, R.W., O'Hara, K.M.: Phys. Rev. Lett. **102**, 165302–165304 (2009)
167. Ottenstein, T.B., Lompe, T., Kohnen, M., Wenz, A.N., Jochim, S.: Phys. Rev. Lett. **101**, 203202–203204 (2008)
168. Rapp, A., Zarand, G., Honerkamp, C., Hofstetter, W.: Phys. Rev. Lett. **98**, 160405 (2007)

Chapter 2
The BEC–BCS Crossover: Some History and Some General Observations

A. J. Leggett and S. Zhang

Abstract While the experimental realization in ultracold Fermi alkali gases of the phenomenon we now call the "BEC–BCS crossover" was attained only in the last few years, theoretical considerations of this issue go back a lot further, and refer to other systems as well. In the first part of this chapter we review some of this history, while in the second half we make some general comments on the current theoretical situation with respect to the specific ultracold-gas implementation.

2.1 Introduction

It is by now well accepted that a system of Fermi particles with two different "species" equally populated, and an attractive interspecies interaction, may exhibit a behavior that as the strength of the interaction is decreased varies continuously from a Bose-Einstein condensate of tightly bound di-fermionic molecules to Cooper pairing of weakly attracting independent fermions. While the experimental realization, in dilute ultracold Fermi alkali gases, of this so-called "BEC–BCS crossover" has been attained only in the last few years, related theoretical considerations have a much longer history and have been put forward also in the context of systems other than the dilute ultracold gases (excitons, metallic superconductivity, nuclear matter ...). In the first half of this chapter, we shall give a brief review, which is not claimed to be exhaustive, of the early history of the theory, and in the second half make some general comments on the current theoretical situation with respect to the specific alkali-gas implementation.

A. J. Leggett
Department of Physics, University of Illinois at Urbana-Champaign,
Champaign IL, USA
e-mail: aleggett@illinois.edu

S. Zhang (✉)
Department of Physics, The Ohio State University, Columbus OH, USA
e-mail: szhang@mps.ohio-state.edu

At the outset we would like to emphasize an important aspect in which the ultracold Fermi gases that have been the subject of intense experimental study in the last few years differ from the other physical systems in which a "BEC–BCS crossover" has been studied theoretically: they are "naturally" *dilute*, in the sense that the inter-fermion interaction is short-ranged, with an effective radius r_0, which under typical experimental conditions is orders of magnitude smaller than the average inter-fermion separation. This permits a kind of theoretical simplification that does not in general apply to these other systems, and is part of the subject of the second half of this chapter.

2.2 Some Prehistory

While the many people who worked on the theory of Bose-Einstein condensation (hereafter BEC) in liquid helium in the years between London's proposal of this phenomenon in 1938 and the work of BCS in 1957 were presumably conscious, in the back of their minds, that the ^{4}He atom is actually a composite of six fermions, no particular attention seems to have been paid to this state of affairs; with hindsight this is hardly surprising, since the minimum energy scale relevant to dissociation of the atom into its fermionic components (tens of eV) is several orders of magnitude greater than that involved in BEC of the liquid (a few K), and thus it is usually an excellent approximation, in the context of the latter, to treat the atom as a simple structureless boson. The first person to make the explicit suggestion that pairs of fermions (electrons) with an effectively attractive interaction might form a molecular-like object with bosonic statistics and thus undergo BEC appears to have been Ogg [1], in the context of a very specific superconducting system (an alkali metal-ammonia solution); however, Ogg speculated that this mechanism might more generally be the explanation of superconductivity. This idea was taken up a few years later by Schafroth [2] and amplified in the paper of Schafroth et al. [3]; however, it proved very difficult to use this approach to calculate specific experimental quantities. Following the work of Bardeen et al. [4] (hereafter BCS), further work was done, mainly by Blatt and coworkers, along the lines developed in ref. [3]; see for example ref. [5]. This work emphasized the point of view that Cooper pairing in a weakly interacting Fermi gas could be viewed as a form of BEC (of pairs of electrons); the qualitative considerations developed in it foreshadow some of those that resurfaced subsequently in the context of the crossover problem. However, following the successful explanation by the BCS theory of most of the experimental properties of the then-known superconductors and its consequent rapid acceptance by the community, there seems to have been a tendency in the late 1950s and early 1960s to emphasize the differences rather than the similarities between the phenomena of BEC and of Cooper pairing.

One important development that, at least with hindsight, pulls rather strongly in the opposite direction is the seminal paper of Yang [6] on off-diagonal long-range order (ODLRO). We will discuss the application of this idea (or rather of a closely

related one) to the crossover problem in the second part of this chapter, but here note that Yang in effect showed that the generalized definition of BEC given by Penrose and Onsager [7] for a simple Bose system such as ^{4}He could be generalized to apply to a fermionic system provided one replaces the single-boson density matrix by the two-fermion one. (For details, see below). However, it seems to have been some time before the full significance of this observation was appreciated by the community.

Meanwhile, attempts were being made to apply BCS-like ideas to Fermi systems other than the electrons in metals. In the case of liquid ^{3}He and heavy nuclei, the situation seemed to be fairly close to that envisaged in the original BCS work, in the sense that the pairing interaction was likely to be so weak that the radius of any pairs formed would be much greater than the inter-fermion distance, just as it is in (pre-1970s) superconducting metals; in modern terminology, one is automatically in the "BCS limit." In the present context, a more interesting case is that of excitons in semimetals or semiconductors. That the tightly-bound excitons in a semiconductor are effectively bosons and might therefore undergo (nonequilibrium) BEC had been pointed out in the early 1960s by Moskalenko [8] and by Blatt et al. [9]; however, in 1965 Keldysh and Kopaev [10], and independently des Cloizeaux [11], pointed out that in a semimetal (a crystal in which the groundstate corresponds to partial filling of the conduction band with partial depletion of the valence band), or in a narrow-gap semiconductor where the exciton binding energy exceeds the gap, a process analogous to Cooper pairing can take place, the components of the pair now bring an electron and a hole. The resulting state is not superconducting (since the pair is electrically neutral) but rather forms an "excitonic insulator." It was appreciated that in a real solid one might be in a regime intermediate between the "exciton BEC" and "excitonic insulator" regimes, and in 1968 Keldysh and Kozlov [12] studied the problem of exciton condensation taking explicit account of the fermionic nature of the component electrons and holes. While they mainly concentrated on the corrections to simple BEC behavior arising from the fermionic statistics, their technique, which is diagrammatic in nature, can in principle be applied for arbitrary density of the electron-hole liquid. Since then a great deal of work has been done along similar lines for this system.

In the context of the ultracold alkali gases, however, it turns out that a rather simple, and as far as present experiments go, at least qualitatively correct picture can be obtained by a very simple generalization of the original BCS technique, which we will refer to as the "naïve ansatz". The motivation for this approach is the following observation, which was certainly appreciated from very early days (see e.g. ref. [13], and references cited therein), that the coordinate-space form of the standard BCS wave function is formally identical to that of a Bose condensate of tightly bound di-fermionic molecules, the only (but crucial!) difference being that the ratio of the pair radius to the mean interparticle spacing is very small in the BEC case and very large in the BCS one. In hindsight this might seem to lead naturally to the conjecture that a reasonable description of the intermediate regime (the "crossover") might be obtained by simply using this form of wave function (or the corresponding BCS particle-nonconserving one) as a variational ansatz over the whole of the range of coupling.

The first person to implement this program explicitly was Eagles in 1969 [14]. He was motivated by experiments that showed that the semiconductor $SrTiO_3$ become superconducting when doped with Zr. Eagles argued that in such a case the electron gas might be very dilute, so that the size of any pairs formed might be much smaller than the mean inter-electron distance; in that case the system would look like a Bose condensate of tightly-bound di-electronic "molecules." Using the BCS form of inter-electron attraction with a cutoff that is tied to the chemical potential μ ("Fermi energy" in the language of ref. [14]) he wrote down the BCS gap equation for an arbitrary strength of interaction, and also the equation expressing the conservation of total (average) particle member; he then solved this pair of equations numerically over the whole crossover regime (in his notation the point where the quantity A of Eq. 2.7 goes through zero is what would nowadays be called the unitarity limit). While the specific choice of the form of interaction, which for $\mu > 0$ depends explicitly on the Fermi energy and hence on density, makes it difficult to compare Eagles' results quantitatively with those obtained subsequently in the context of the dilute ultracold alkali gases, all the qualitative factors that appear in the latter—the change in sign of μ on the "BEC" side of unitarity, the different significance of the "gap" Δ on the two sides of this point, the fact that over much of the crossover regime the superconducting transition temperature T_c is of the order of the free-gas Fermi temperature, and the existence, in the BEC limit, of a wide temperature range where pairing occurs without superconductivity—are to be found in this early paper.

By the late 1970s there had been a couple of experimental developments that tended to focus attention on the crossover problem. First, the long-predicted phenomenon of Cooper pairing in liquid ^{3}He had been experimentally realized, and it was discovered that there were not one but three different paired states, with different structures of their internal wave functions; this tended to re-focus attention on the similarities, rather than the differences, between diatomic molecules and Cooper pairs. Secondly, since dilute spin-polarized atomic hydrogen (a Bose system) was being cooled into a regime close to degeneracy, it was plausible that in the future it would also be possible to cool atomic deuterium, a Fermi system, into the degeneracy regime and possibly even down to the temperature for onset of pairing. (In the event, deuterium turned out to be notoriously refractory in a cryogenic context, and to this day it has not to our knowledge even been cooled into the quantum regime.)

Motivated by these considerations, and unaware at the time of Eagles' work, one of the present authors (A. J. L.) considered [15, 16] in 1980 the crossover problem in the context of a dilute ultracold Fermi gas. The model studied was of a dilute degenerate gas of fermions with the two spin species equally populated, interacting by an interatomic potential that has a strong but finite short-range repulsion but a fairly weak attraction at larger distances, and is tuned so that one is close to the onset of a two-body bound state; thus the low-energy s-wave scattering length a_s is large compared to the range r_0 of the potential and can have either sign. It is intuitively clear that in this limit there is only one physically relevant dimensionless ratio in the problem, namely that of a_s to the mean interparticle spacing, or equivalently $k_F a_s$ where k_F is the Fermi wave vector of the noninteracting atomic gas, so that rather generally one would expect that at $T = 0$ both the chemical potential μ and

the gap (pairing field) Δ could have the form $\varepsilon_F f(k_F a_s)$, where ε_F is the Fermi energy of the noninteracting gas. To obtain approximate forms of $f(k_F a_s)$, ref. [15] wrote down explicitly the "naïve" ansatz for the many-body wave function (see part 2 of this chapter), argued that the Hartree and Fock terms in the energy contribute only uninteresting constants and thus arrived at the standard BCS gap equation, with however the more general form of the pairing matrix element $V_{kk'}$ corresponding to the (semi)realistic form of interatomic potential. Eliminating the high-momentum part of $V_{kk'}$ in favor of the experimentally measurable quantity a_s by a standard renormalization procedure, and solving the resulting gap equation simultaneously with the equation expressing number conservation in a way similar to that done by Eagles earlier, one is able to obtain the general behavior of the dimensionless functions $f_\mu(k_F a_s)$ and $f_\Delta(k_F a_s)$. As we will see in part 2, these results of the naïve ansatz appear to contribute a good starting point for discussion of the realistic alkali gas problem at $T = 0$.

At around the same time there occurred a development that, although little noticed at the time, foreshadowed a central theme in the study of the BEC–BCS crossover: in his thesis, Modawi [17] suggested the use of a Feshbach resonance to enhance the transition temperature of atomic deuterium by several orders of magnitude (although even after the enhancement it would still be depressingly low). For reasons unconnected with physics, this work was never published (though cf. [18], pp. 626–627).

In 1985 Nozières and Schmitt-Rink [19] returned to the crossover problem and generalized the earlier work to consider both the effects of a crystalline lattice and the behavior of the critical temperature in the intermediate regime. They pointed out that while in the BCS limit the presence of a lattice makes no qualitative difference, in the BEC limit it changes the situation enormously, since the tightly-bound pairs then sit on individual lattice sites and can move only by a "correlated hopping" process involving as an intermediate stage the virtual ionization of a pair; for the "negative-U Hubbard model" that they use the matrix element for motion of the bosons is thus t^2/U, which in this limit is much smaller than that (t) for the original fermions, in contrast to the continuum case where the two quantities are of the same order of magnitude. As to the behavior of the critical temperature, they carried out a calculation that combines a simple "ring" approximation for the thermodynamic potential with the standard Thouless criterion for the instability of the normal state so as to obtain the behavior of T_c as a function of the coupling strength; while they recover the expected results that T_c is given in the weak-coupling (BCS) limit by the standard BCS formula and in the opposite limit by the expression for the condensation temperature of a dilute Bose gas, their most important conclusion is that the transition is, at least in this approximation, a *continuous* function of the coupling strength.

As is well known, a new ingredient was added to the mix with the discovery in 1986 of the cuprate (high-temperature) superconductors, an electronic system in which the (presumed) formation of Cooper pairs seems to take place at intermediate values of coupling strength. This prompted an explosion of work on the crossover problem that we will not attempt to review here; much of this work prior to 1995 is reviewed in [20].

2.3 Some General Remarks on the Crossover Problem

In this section we will discuss the "standard" model of the BEC–BCS crossover problem, by which we mean the following. We consider an ultracold gas of N fermionic atoms with two hyperfine species equally populated, in volume V, and take the standard thermodynamic limit $N, V \rightarrow \infty, N/V \equiv n = $ const.; as is conventional, we label the two relevant hyperfine species by a spin index $\sigma = \pm 1$. The atoms are taken to interact via an interatomic central potential $V(r)$, which will typically consist of a strongly repulsive hard core, an attractive region of depth 1–5 eV at 2–3 Å, and a more weakly attractive Van der Waals tail of the form $-C/r^6$; the "van der Waals length" $l_{\mathrm{VdW}} \equiv (mC/\hbar^2)^{1/4}$, which determines the "typical" radius of the most weakly bound molecular state, will be taken to be 50–100 Å. We assume that we can apply a variable uniform static magnetic field to the system so as to tune it through a Feshbach resonance, that is, a value H_{res} of the field at which the zero-energy scattering state of our two hyperfine species (which together define the "open" channel) is degenerate with the most weakly bound molecular state of a second pair of hyperfine species (the "closed" channel), which may or may not have one species in common with the open channel; the detuning between these two states will be denoted $\delta(H) = $ const.$(H - H_{\mathrm{res}})$. For simplicity we shall assume that the resonance is "broad", i.e. that the Fermi energy of the gas calculated in the absence of interaction is much smaller than the characteristic "width" δ_c of the two-body resonance (for details, see e.g. ref. [21], Chap. 4); when this condition is satisfied, there is a wide interval ($\delta_c \ll \delta < 0$) of magnetic field close to the resonance where although molecules are formed, they are almost entirely in the open channel (see e.g. Fig. 4.2 of ref. [21]); we will always assume unless otherwise noted that $|\delta| < \delta_c$. Thus, except when we are explicitly considering the "closed-channel fraction," it will be adequate to eliminate the closed channel from the problem entirely, in favor of an extra magnetic-field-dependent term in the open-channel potential $V(r)$. The resulting zero-energy s-wave scattering length in the open channel, which is of course a function of δ (or H) and tends to $\pm \infty$ at the position of the (normalized [21]) resonance (the "unitary limit"), will be denoted simply a_s.

It is convenient to introduce the dimensionless parameter $\xi \equiv -1/(k_{\mathrm{F}} a_s)$, where $k_{\mathrm{F}} \equiv (3\pi^2 n)^{1/3}$ is the Fermi wave vector of the noninteracting gas; then the "BEC limit" corresponds to $\xi \rightarrow -\infty$ and the "BCS limit" to $\xi \rightarrow +\infty$, and generally speaking we expect the "crossover" to correspond to the regime $|\xi| \lesssim 1$. In the following we shall always assume the dilute-gas limit, i.e. that $k_{\mathrm{F}} l_{\mathrm{VdW}} \ll 1$ (it would probably actually be adequate for most of our purposes to assume another weaker condition, but we may as well play safe). As we shall see, this condition simplifies some aspects of the problem considerably; since the highest densities so far obtained in the ultracold Fermi gases have been only $\sim 10^{-13} \mathrm{cm}^{-2}$, it has certainly been well satisfied in all experiments to date.

A convenient general description of the crossover behavior, which does not assume any particular ansatz for the many-body wave function or density matrix, may be given in terms of the formalism developed by Yang [6]. Suppose that the energy

eigenstates of the N-body system are $\Psi_N^{(n)}(\mathbf{r}_1\sigma_1\mathbf{r}_2\sigma_2\ldots\mathbf{r}_N\sigma_N)$ with energies E_n and the system is in thermal equilibrium at some inverse temperature $\beta \equiv (k_B T)^{-1}$. (We could generalize the formalism also to discuss nonequilibrium states, but this is not necessary for our present purposes). Then define the reduced two-body density matrix

$$
\rho_2(\mathbf{r}_1\sigma_1\mathbf{r}_2\sigma_2 : \mathbf{r}_1'\sigma_1'\mathbf{r}_2'\sigma_2') \equiv Z^{-1}(\beta) \sum_n \exp(-\beta E_n) \left\{ \sum_{\sigma_3\ldots\sigma_N} \iint \ldots d\mathbf{r}_3\ldots d\mathbf{r}_N \right.
$$

$$
\left. \times \Psi_N^{(n)}(\mathbf{r}_1\sigma_1\mathbf{r}_2\sigma_2\ldots\mathbf{r}_N\sigma_N)\Psi_N^{*(n)}(\mathbf{r}_1'\sigma_1'\mathbf{r}_2'\sigma_2'\ldots\mathbf{r}_N'\sigma_N') \right\}
$$

$$
\equiv \left\langle \psi_{\sigma_1}^\dagger(\mathbf{r}_1)\psi_{\sigma_2}^\dagger(\mathbf{r}_2)\psi_{\sigma_2'}(\mathbf{r}_2')\psi_{\sigma_1'}(\mathbf{r}_1') \right\rangle, \tag{2.1}
$$

where $Z(\beta)$ is the partition function. The quantity ρ_2, regarded as a matrix function of its indices, is Hermitian and thus can be diagonalized with real eigenvalues:

$$
\rho_2(\mathbf{r}_1\sigma_1\mathbf{r}_2\sigma_2 : \mathbf{r}_1'\sigma_1'\mathbf{r}_2'\sigma_2') = \sum_i n_i \chi_i(\mathbf{r}_1\sigma_1\mathbf{r}_2\sigma_2)\chi_i^*(\mathbf{r}_1'\sigma_1'\mathbf{r}_2'\sigma_2'), \tag{2.2}
$$

where the eigenfunctions $\chi(\mathbf{r}_1\sigma_1, \mathbf{r}_2\sigma_2)$ must be antisymmetric under the exchange $\mathbf{r}_1\sigma_1 \leftrightarrows \mathbf{r}_2, \sigma_2$.

As shown by Yang, the n_i must satisfy the condition

$$
\sum_i n_i = N(N-1). \tag{2.3}
$$

Intuitively, the eigenvalue n_i can be interpreted as "the number of atomic pairs which occupy the two-particle state $\chi_i(\mathbf{r}_1\sigma_1\mathbf{r}_2\sigma_2)$." Assuming that the translational symmetry of the Hamiltonian is not spontaneously broken, the quantity ρ_2 must be invariant under the total translation operation $\mathbf{r}_i \to \mathbf{r}_i + \eta, \mathbf{r}_j' \to \mathbf{r}_j' + \eta (i, j = 1, 2)$, and hence the eigenfunctions χ_i can be chosen to be eigenstates of the center-of-mass momentum:

$$
\chi_i(\mathbf{r}_1\sigma_1\mathbf{r}_2\sigma_2) = \exp i\mathbf{K} \cdot (\mathbf{r}_1 + \mathbf{r}_2)/2\widetilde{\chi}_i(\mathbf{r}_1 - \mathbf{r}_2, \sigma_1\sigma_2). \tag{2.4}
$$

By a similar argument they can be chosen to be eigenfunctions of the total spin and its z-component:

$$
\widetilde{\chi}_i(\mathbf{r}_1 - \mathbf{r}_2, \sigma_1\sigma_2) = \widetilde{\widetilde{\chi}}_i(\mathbf{r}_1 - \mathbf{r}_2)\zeta_i(S, m), \tag{2.5}
$$

where $\zeta_i(S, m)$ is one of the four simultaneous eigenstates of total spin $S(= 0, 1)$ and total z-projection of spin $m(= 0, 1)$ of a pair of spin-1/2 particles. (It would also be possible to use the rotational invariance of ρ_2 to choose the functions $\widetilde{\widetilde{\chi}}_i(\mathbf{r}_1 - \mathbf{r}_2)$ to be eigenstates of the relative orbital angular momentum, but it is convenient not to do so, at least for the moment.) Evidently, one would expect not only the eigenvalues

n_i but also the eigenfunctions χ_i (or at least the $\overset{\approx}{\chi}_i$-components thereof) to depend both on the temperature and on the detuning δ (which controls the scattering length $a_s(\delta)$).

We can divide the possible forms of the eigenfunctions $\chi(\mathbf{r}_1\sigma_1, \mathbf{r}_2\sigma_2)$ (Eq. 2.4) into three classes according to the center of mass momentum $\mathbf{K}$ and whether the relative wave function $\widetilde{\chi}(\mathbf{r}_1 - \mathbf{r}_2)$ is or is not bound as a function of $|\mathbf{r}_1 - \mathbf{r}_2| \equiv r$ (i.e. whether or not it tends to zero faster than r^{-2} as $r \to \infty$). (A) $\widetilde{\chi}$ unbound, $\mathbf{K}$ any (B) $\widetilde{\chi}$ bound, $\mathbf{K} = 0$ (C) $\widetilde{\chi}$ bound, $\mathbf{K} \neq 0$. It should be noted that the number of eigenfunctions with eigenvalue ~ 1 in class A is always of order N^2, even in the extreme BEC limit; this is simply because even in this limit, if we pick two fermions at random it is highly likely that they will belong to different molecules and will be uncorrelated. Classes (B) and (C) together intuitively describe any bound pairs that form in the system, and the number of relevant eigenfunctions in these two classes can be at most of order N; crudely speaking, the onset of pairing, e.g. with decreasing temperature, corresponds to the point at which the sum of eigenvalues N_{BC} in these two classes becomes of order N. The onset of condensation corresponds to the point, if any, at which the quantity N_B becomes of order N; the usual assumption is that there is then only a single relevant form of $\widetilde{\chi}$, i.e. one gets "simple" BEC or a generalization of it. In this case the onset of condensation is equivalent, in our infinite geometry, to the onset of off-diagonal long-range order as defined by Yang [6]. With these definitions it is clear that there is no fundamental conceptual distinction between BEC and Cooper pairing; the only differences (which are of course crucial in a practical sense) lie in the ratio of the pair radius to the mean interparticle spacing and in the nature of the low-lying excitation spectrum.

Before we enter the general discussion using Yang's formulation, it is instructive to revisit briefly the standard model of the BEC–BCS crossover at $T = 0$. There we write the ground state wave function as

$$
\begin{aligned}
&\Psi_N^{(0)}(\mathbf{r}_1\sigma_1, \mathbf{r}_2\sigma_2, \ldots, \mathbf{r}_N\sigma_N) \\
&= \mathscr{A}\left[\phi(\mathbf{r}_1\sigma_1, \mathbf{r}_2\sigma_2)\phi(\mathbf{r}_3\sigma_3, \mathbf{r}_4\sigma_4)\ldots\phi(\mathbf{r}_{N-1}\sigma_{N-1}, \mathbf{r}_N\sigma_N)\right],
\end{aligned}
\tag{2.6}
$$

where $\mathscr{A}$ is the antisymmetrization operator. The two-body wave function $\phi(\mathbf{r}_1\sigma_1, \mathbf{r}_2\sigma_2)$ is regarded as a variational parameter. At this stage, no constraint has yet been put on the form of $\phi(\mathbf{r}_1\sigma_1, \mathbf{r}_2\sigma_2)$ except that we require it to be antisymmetric with respect to simultaneous exchange of $(\mathbf{r}_1\sigma_1)$ and $(\mathbf{r}_2\sigma_2)$. In the following, we take the spin structure of $\phi(\mathbf{r}_1\sigma_1, \mathbf{r}_2\sigma_2)$ to be a singlet and write the relative spatial wave function as

$$
\phi(\mathbf{r}_1 - \mathbf{r}_2) = \sum_{\mathbf{k}} c_{\mathbf{k}} \exp i\mathbf{k} \cdot (\mathbf{r}_1 - \mathbf{r}_2)
\tag{2.7}
$$

where $c_{-\mathbf{k}} = c_{\mathbf{k}}$ and $a_{\mathbf{k}\uparrow}^{\dagger}$ is the fermion creation operator for momentum state $\mathbf{k}$ with spin up. Now, if we follow the BCS trick and relax the constraint on the number of particles, we can write the equation which results from minimizing the energy as a

function of the coefficients $c_{\mathbf{k}}$, i.e. the gap equation, in the form (possibly unfamiliar, but completely equivalent to the standard form)

$$2E_{\mathbf{k}}F_{\mathbf{k}} + \sum_{\mathbf{k}'} V(\mathbf{k} - \mathbf{k}')F_{\mathbf{k}'} = 0, \tag{2.8}$$

where $E_{\mathbf{k}} = \sqrt{(\varepsilon_{\mathbf{k}} - \mu)^2 + |\Delta_{\mathbf{k}}|^2}$ is the quasiparticle excitation energy and $\varepsilon_{\mathbf{k}} = \frac{\hbar^2 k^2}{2m}$ is the free particle kinetic energy. $F_{\mathbf{k}} \equiv \frac{c_{\mathbf{k}}}{1 + |c_{\mathbf{k}}|^2}$ is the pair wave function. If we compare this with the two-body Schrödinger equation with energy E:

$$(2\varepsilon_{\mathbf{k}} - E)\psi_{\mathbf{k}} + \sum_{\mathbf{k}'} V(\mathbf{k} - \mathbf{k}')\psi_{\mathbf{k}'} = 0, \tag{2.9}$$

we find that for large $|\mathbf{k}|$, $F_{\mathbf{k}}$ has the same structure as $\psi_{\mathbf{k}}$, which suggests that the short-range form of the pair function $F(\mathbf{r}) = \sum_{\mathbf{k}} F_{\mathbf{k}} \exp(i\mathbf{k} \cdot \mathbf{r})$ is the same as that of the two-body wave function. (We shall give a more general argument concerning the short-range form of many-body wave function in the following.) The gap equation (2.9) can be conveniently written in terms of scattering length a_s by a standard renormalization procedure,

$$\frac{1}{V} \sum_{\mathbf{k}} \left[\frac{1}{\varepsilon_{\mathbf{k}}} - \frac{1}{E_{\mathbf{k}}} \right] = \frac{m}{2\pi \hbar^2 a_s}. \tag{2.10}$$

This provides one equation for the gap $\Delta_{\mathbf{k}}$ (which we will take to be independent of $\mathbf{k}$) and the chemical potential μ. Another equation can be obtained by requiring that the average number of particles be N, namely

$$\frac{1}{V} \sum_{\mathbf{k}} \left[1 - \frac{\varepsilon_{\mathbf{k}} - \mu}{E_{\mathbf{k}}} \right] = n. \tag{2.11}$$

The solution of these two equations can be obtained easily in the BEC or BCS limits and in the intermediate regime by numerical means. In the BEC limit, we find that $\mu \to -\frac{\hbar^2}{2ma_s^2}$ and $\Delta \to \frac{4\varepsilon_{\mathrm{F}}}{\sqrt{3\pi k_{\mathrm{F}} a_s}} \sim \sqrt{n}$. In the BCS limit, $\mu \to \varepsilon_{\mathrm{F}}$ and $\Delta \to 8\varepsilon_{\mathrm{F}} e^{-2} \exp\left[-\frac{\pi}{2k_{\mathrm{F}}|a_s|} \right]$, the standard BCS results. At unitarity, we find that the chemical potential $\mu = 0.59\varepsilon_{\mathrm{F}}$ and $\Delta = 0.68\varepsilon_{\mathrm{F}}$. The chemical potential μ goes through zero in the BEC side of the resonance at a value $\xi \sim 1$. The qualitative behavior of the BEC–BCS crossover sketched above is quite satisfactorily tested in experiments. However, there are important effects which are not accounted for in the naïve ansatz even in the BEC and BCS limits. For example, in the BEC limit, the scattering length between molecules turns out to be $0.6a_s$ rather than $2a_s$ as one would get from the naïve ansatz [22]. In the BCS limit, as Gor'kov and Melik-Barkhudarov have shown, there are important polarization contributions to the zero temperature gap parameter [23].

To go beyond the naïve ansatz and discuss the general crossover problem, we first have to examine the sort of approximations that one is allowed to make

in the context of ultracold Fermi gases. In the BEC–BCS crossover model, the scattering length a_s can assume an arbitrarily large value and thus the conventional perturbative calculation using the small gaseousness parameter $\eta \equiv k_F a_s$ is clearly inapplicable. On the other hand, as was pointed out earlier, the actual range of the interaction potential l_{VdW} is small such that $k_F l_{VdW} \ll 1$ is always guaranteed. This suggests that an expansion in binary collisions should be possible. In fact, as we shall see momentarily, such a formulation is exact to the extent that one can describe the system entirely in terms of the s-wave scattering length a_s.

Let us consider then the energy eigenstates $\Psi_N^{(n)}(\mathbf{r}_1\sigma_1, \mathbf{r}_2\sigma_2, \ldots, \mathbf{r}_N\sigma_N)$ of the system and ask the following question. Suppose we take two atoms of opposite spin, say at positions $\mathbf{r}_1$ and $\mathbf{r}_2$ with $\sigma_1 \neq \sigma_2$, close together such that $|\mathbf{r}_1 - \mathbf{r}_2| \lesssim l_{VdW}$ while far away (compared with l_{VdW}) to all the other atoms, what will the many-body wave function $\Psi_N^{(n)}(\mathbf{r}_1\sigma_1, \mathbf{r}_2\sigma_2, \ldots, \mathbf{r}_N\sigma_N)$ look like? Obviously, in this case, since atoms 1 and 2 cease to interact with the other atoms, the wave function factorizes and we can write it as

$$\Psi_N^{(n)}(\mathbf{r}_1\sigma_1, \mathbf{r}_2\sigma_2, \ldots, \mathbf{r}_N\sigma_N) = \mathscr{A}\phi(\mathbf{r}_1\sigma_1, \mathbf{r}_2\sigma_2)\Psi_{N-2}'^{(n)}(\mathbf{r}_3\sigma_3, \mathbf{r}_4\sigma_4, \ldots, \mathbf{r}_N\sigma_N)$$
(2.12)

where $\mathscr{A}$ is the antisymmetrization operator. $\phi(\mathbf{r}_1\sigma_1, \mathbf{r}_2\sigma_2)$ is determined by solving the two-body Schrödinger equation in the region $|\mathbf{r}_1 - \mathbf{r}_2| \lesssim l_{VdW}$. Any corrections arise only if a third atom is within a distance $\sim l_{VdW}$ from atoms 1 and 2. Such an event is unlikely for two reasons. Firstly, the phase space associated with this event is a factor $(k_F l_{VdW})^3$ less than that for the two-body encounters. Secondly, in the spin-$\frac{1}{2}$ system we are considering here, two of the three atoms close together must have the same spin orientation, the probability of which is suppressed by the Pauli principle. In fact, by the very formulation of the problem, we have already neglected the higher partial wave scattering, which makes a contribution of order $(k_F l_{VdW})^2$ or higher. Thus, to be consistent, we need not consider three-body processes and the binary expansion becomes exact.[1]

Next, we have to discuss the form of the two-body wave function $\phi(\mathbf{r}_1\sigma_1, \mathbf{r}_2\sigma_2)$. We first note that in the crossover model, the spin part of $\phi(\mathbf{r}_1\sigma_1, \mathbf{r}_2\sigma_2)$ is necessarily a singlet and will be of no further interest to us. The spatial part of $\phi(\mathbf{r}_1\sigma_1, \mathbf{r}_2\sigma_2)$, which we denote as $\widetilde{\phi}(\mathbf{r}_1, \mathbf{r}_2)$, will have a complicated nodal structure in its relative coordinates $\mathbf{r} = \mathbf{r}_1 - \mathbf{r}_2$. However, its short-range form ($|\mathbf{r}| \lesssim l_{VdW}$) should be insensitive to the energy scales of the problem, namely the Fermi energy ε_F and the characteristic width δ_c of the Feshbach resonance. The reason for this is simple: The form of $\widetilde{\phi}(\mathbf{r}_1, \mathbf{r}_2)$ in the region $|\mathbf{r}_1 - \mathbf{r}_2| \lesssim l_{VdW}$ is determined by the competition between the kinetic energy and the deep potential energy, each of which is much larger than ε_F and δ_c. In the region $l_{VdW} \ll r \lesssim a_s, k_F^{-1}$, the form of $\widetilde{\phi}(\mathbf{r}_1, \mathbf{r}_2)$ is fixed by the scattering length. Up to a normalization constant, it is given by

$$\widetilde{\phi}(\mathbf{r}_1 - \mathbf{r}_2) = \text{const.} \times \frac{1}{|\mathbf{r}_1 - \mathbf{r}_2|}\left(1 - \frac{|\mathbf{r}_1 - \mathbf{r}_2|}{a_s}\right),$$
(2.13)

---

[1] However, in discussing the stability of the system with respect to decay into deeply bound molecular states, such processes are of primary importance.

where we have suppressed the centre of mass dependence which is of no relevance in the discussion below. The whole of the many-body problem can then be viewed as an effort to enforce this particular boundary condition in the many-body wave function. Two routes can be taken in principle. One is to reformulate this boundary condition as a pseudopotential between atoms with opposite spins in the zero-range limit. Another way is to deal with this boundary condition explicitly. We shall follow the second route in the following.

The above discussions, when formulated in terms of density matrices, tell us the following. First, in calculating any physical quantities of interest, knowledge of the two-body density matrix is sufficient. Secondly, the short range form of the eigenfunction $\tilde{\tilde{\chi}}_i(r)$ associated with the two-body density matrix defined before is determined by the two-body physics only, while in the region $l_{\mathrm{VdW}} \ll r \lesssim a_s, k_{\mathrm{F}}^{-1}$, it is given by $r\,\tilde{\tilde{\chi}}_i(r) \equiv C_i(\xi, T)\overline{\chi}(r)$, where

$$\overline{\chi}(r) = 1 - \frac{r}{a_s}, \quad l_{\mathrm{VdW}} \ll r \lesssim a_s, k_{\mathrm{F}}^{-1} \tag{2.14}$$

and $C_i(\xi, T)$ is the normalization constant, which in principle depends on ξ as well as temperature T. Note that according to the classification used before, for classes (B) and (C), $C_i(\xi, T)$ is of the form $l^{-1/2}$, where l is some microscopic length scale (to be identified later), while for class (A), $C_i(\xi, T)$ is normalized as $L^{-1/2}$, where L is the linear size of the system. We emphasize that $\overline{\chi}(r)$ is of this particular form and common to all $\tilde{\tilde{\chi}}_i(r)$ only for the region indicated; its short-range form is the same as that of $\tilde{\tilde{\chi}}_i(r)$, except for the normalization $C_i(\xi, T)$. From a many-body point of view, the complicated short-range physics is not interesting and furthermore, as the discussion above has made clear, can be computed without reference to the many-body state (except the normalizations $C_i(\xi, T)$ which we shall take care of explicitly). It is thus desirable to separate the short-range dependence in any physical quantity that we might be interested in computing. The hope is that, once this is done, the part that remains would be insensitive to the short-range complications and hence be universal.

To do this, let us introduce an arbitrary short-range ($\sim l_{\mathrm{VdW}}$) function $s(\mathbf{r})$ that operates only between the opposite spin states and consider the following integral:

$$A \equiv \int d\mathbf{r}_1 d\mathbf{r}_2 s(\mathbf{r}_1 - \mathbf{r}_2) \left\langle \psi_1^{\dagger}(\mathbf{r}_1)\psi_2^{\dagger}(\mathbf{r}_2)\psi_2(\mathbf{r}_2)\psi_1(\mathbf{r}_1) \right\rangle. \tag{2.15}$$

Using Eqs. 2.2 and 2.5, we can write the above expression as

$$\sum_i n_i \int d\mathbf{r}\, s(\mathbf{r}) \left| \tilde{\tilde{\chi}}_i(r) \right|^2 \tag{2.16}$$

with the eigenfunction $\tilde{\tilde{\chi}}_i(r)$ appearing in the sum corresponding to the singlet spin wave function $\zeta(S = 0, m = 0)$. Now using Eq. 2.14 above, we find

$$A \equiv \sum_i n_i |C_i(\xi, T)|^2 \int dr s(r) |\overline{\chi}(r)|^2$$

$$\equiv h(\xi, T) k_{\mathrm{F}} N \int dr s(r) |\overline{\chi}(r)|^2. \tag{2.17}$$

Here, we have defined a positive definite universal function

$$h(\xi, T) \equiv \sum_i \frac{n_i}{N k_{\mathrm{F}}} |C_i(\xi, T)|^2 > 0 \tag{2.18}$$

and inserted a factor k_{F}^{-1} to make $h(\xi, T)$ dimensionless. N is the total number of atoms. The structure of $h(\xi, T)$ is clear. Apart from the constant $(N k_{\mathrm{F}})^{-1}$, it is a weighted sum of the eigenvalues of the two-body density matrix. We emphasize again that all the n_i's appearing in the sum correspond to singlet eigenfunctions. According to the discussion before, if we have a simple BEC, where only one n_i, say n_0, is of order of N, then this term will make the largest contribution $\sim O(1)$, while all the other terms contribute $\sim O(1/N)$. Note that the sum of the latter might still be larger than the contribution from n_0. Typically, as in the theory of superconductivity, n_0 is associated with the eigenfunction χ_0 that is bound in space, namely $C_0(\xi, T) \sim l^{-1/2}$, where l in the case of superconductivity turns out to be given by the zero temperature Ginzburg-Landau coherence length ξ_{GL}. This conclusion is also valid in the BCS limit of the crossover, while in the BEC limit $C_0(\xi, T) \sim a_s^{-1/2}$ and around unitarity, $C_0(\xi, T) \sim k_{\mathrm{F}}^{1/2}$ (see below).

We further note that the integral in Eq. 2.17 is a purely two-body quantity and as such does not depend on the many-body parameters of the system, namely, temperature T and Fermi energy ε_{F}. Depending on the form of $s(r)$, it might depend on the scattering length a_s in some complicated way, but as its normalization has made clear, it displays no singularity as one approaches unitarity, $a_s = \pm \infty$. Thus, to all intents and purposes, it can be regarded as a known parameter. The function $h(\xi, T)$, on the other hand, incorporates only the many-body physics and thus one expects it to be universal and independent of the particular alkali element under consideration. The physical significance of $h(\xi, T)$ lies in the fact that as far as the short-range physics is concerned, the many-body system looks just like a two-body problem except that one has to normalize the corresponding two-body wave function in the region $l_{\mathrm{VdW}} \ll r \lesssim a_s, k_{\mathrm{F}}^{-1}$ by a value determined by $h(\xi, T)$ [see Eq. 2.17]. Once this is recognized, it is easy to see that $h(\xi, T)$ determines the momentum distribution of the many-body system in the region $k_{\mathrm{F}}, a_s^{-1} \ll k \ll l_{\mathrm{VdW}}^{-1}$, $n_k = 4\pi k_{\mathrm{F}} n h(\xi, T)/k^4$, where $n = N/V$ is the average density. In the literature, the combination $C = 4\pi k_{\mathrm{F}} n h(\xi, T)$ is referred to as the "Contact" [24].

In the following, we consider two representative physical quantities in which the universal function $h(\xi, T)$ plays a central role. Common to those physical quantities is that they can be cast in the form of a short-range function, convoluted with the two-body density matrix. Physically, this means that these physical quantities are sensitive to short-range physics and the many-body physics only enters in the determination of the overall amplitude. For more details, see ref. [25].

As we have discussed before, once we eliminate the closed channel from the problem, the open channel potential $V(r)$ acquires an additional magnetic field dependence, which by appropriate rescaling, can be written in terms of a dimensionless parameter λ and hence $V(r; \lambda)$. Now, if we consider a process in which λ changes adiabatically, then according to general arguments of thermodynamics

$$\left.\frac{\partial E}{\partial \lambda}\right|_S = \left\langle \frac{\partial H}{\partial \lambda} \right\rangle = \left\langle \frac{\partial V(r; \lambda)}{\partial \lambda} \right\rangle, \tag{2.19}$$

where E and S are the total energy and entropy of the system, respectively. The average includes both quantum mechanical and statistical ones. In the last step, we have used the fact that only the interaction term in the Hamiltonian depends on λ. Note that $\frac{\partial V(r;\lambda)}{\partial \lambda}$ is a short-range function and we can use the decomposition established before. Furthermore, by using a relation between the variation of the scattering length a_s and that of the interaction potential (see ref. [21], p. 158),

$$\delta a_s^{-1} = -\frac{m}{\hbar^2} \left[\int_0^\infty dr \frac{\partial V(r; \lambda)}{\lambda} |\overline{\chi}(r)|^2 \right] \delta\lambda, \tag{2.20}$$

we find, for fixed density,

$$\left.\frac{\partial E}{\partial \xi}\right|_S = 2\varepsilon_F N h(\xi, T). \tag{2.21}$$

The above relation can be conveniently written, using the theorem of small increments (see ref. [26], p. 50), in terms of the free energy F of the system

$$\left.\frac{\partial F}{\partial \xi}\right|_T = 2\varepsilon_F N h(\xi, T). \tag{2.22}$$

Several conclusions can be drawn immediately. Firstly, since $h(\xi, T)$ is positive definite, the free energy F is a strictly increasing function of ξ. Secondly, if we expand F around $\xi = 0$, taking note that $h(\xi = 0, T)$ is a well-defined quantity, we find that in the vicinity of $\xi = 0$, F increases linearly with ξ. By using other thermodynamic relations, one can write the specific heat, entropy and pressure of the system in terms of the universal function $h(\xi, T)$. For more details, see ref. [25].

A second quantity we consider is the interaction energy of the system. For this we simply replace $s(r)$ by the interaction potential $V(r)$ and we find that interaction energy per particle is given by

$$\frac{\langle V \rangle}{N} = C_V(a_s) k_F h(\xi, T), \tag{2.23}$$

where $C_V(a_s) = \int dr V(r)|\overline{\chi}(r)|^2$ is the extracted two-body factor. Note that at unitarity, the interaction energy scales with k_F, rather than ε_F (as a naïve dimension

analysis would suggest). The reason for this lies in the fact that interaction energy is sensitive to short-range physics and is not universal. A rough understanding of the k_F scaling might go as follows. Let us look at the many-body wave function $\Psi_N^{(n)}(\mathbf{r}_1\sigma_1, \mathbf{r}_2\sigma_2, \ldots, \mathbf{r}_N\sigma_N)$ and ask what can possibly set the scale for the normalization in the region $l_{\mathrm{VdW}} \ll |\mathbf{r}_i - \mathbf{r}_j| \lesssim a_s, k_F^{-1}, \sigma_i \neq \sigma_j$. At unitarity, the only scale that is relevant in the region indicated is k_F^{-1} and since the radial wave function has dimension $[L]^{-1/2}$, we conclude

$$\lim_{l_{\mathrm{VdW}} \ll |\mathbf{r}_i - \mathbf{r}_j| \lesssim k_F^{-1}} |\mathbf{r}_i - \mathbf{r}_j| \, \Psi_N^{(n)}(\mathbf{r}_1\sigma_1, \mathbf{r}_2\sigma_2, \ldots, \mathbf{r}_N\sigma_N) \propto k_F^{1/2}. \tag{2.24}$$

The interaction energy, which depends on the modulus square amplitude of the wave function, turns out to depend linearly on k_F, as obtained above. We note that the same reasoning leads to the conclusion that the average radio-frequency shift and the population of closed channel molecules also scale with k_F at unitarity. For more details concerning the later two quantities, see Refs. [25, 27].

The realization of the existence of the universal function in the many-body physics was first made by Tan based on an analysis of the many-body wave function and some of his results were later re-derived by Braaten and Platter using the operator product expansion, which is the ideal tool to explore the short-range physics in a field theory context [28, 24]. Recently, Combescot et al. [29] have extended the same consideration to two dimensions.

An important consequence of the considerations given above is that it should be possible to check the mutual consistency of experimental results obtained on different physical quantities. This should be particularly useful at unitarity, where the dependence of such quantities on the details of the trap used should disappear.

References

1. Ogg, R.A.: Phys. Rev. **69**, 243 (1946)
2. Schafroth, M.R.: Phys. Rev. **96**, 1442 (1954)
3. Schafroth, M.R., Butler, S.T., Blatt, J.M.: Helv. Phys. Acta. **30**, 93 (1957)
4. Bardeen, J., Cooper, L.N., Schrieffer, J.R.: Phys. Rev. **108**, 1175 (1957)
5. Blatt, J.M.: Theory of Superconductivity. Academic, New York (1964)
6. Yang, C.N.: Revs. Mod. Phys. **34**, 694 (1962)
7. Penrose, O., Onsager, L.: Phys. Rev. **104**, 576 (1956)
8. Moskalenko, S.A.: Fiz. Tverd. Tela. **4**, 276 (1962) [Sov. Phys.-Solid State **4**, 276 (1962)]
9. Blatt, J.M., Boer, K.W., Brandt, W.: Phys. Rev. **126**, 1691 (1962)
10. Keldysh, L.V., Kopaev, Yu.V.: Fiz. Tverd. Tela. **6**, 2791 (1964) [Sov. Phys. Solid State **6**, 2219 (1965)]
11. des Cloizeaux, J.: J. Phys. Chem. Solids **26**, 259 (1965)
12. Keldysh, L.V., Kozlov, A.N.: Zh. Eksp. Teor. Fiz. **54**, 978 (1968) [Sov. Phys. JETP **27**, 521 (1968)]

13. Bardeen, J., Schrieffer, J.R.: "Recent Developments in Superconductivity". In: Gorter, C.J. (eds.) Progress in Low Temperature Physics, vol 3, pp. 170–228. North-Holland Publishing Company, Amsterdam (1961)
14. Eagles, D.M.: Phys. Rev. **186**, 456 (1969)
15. Leggett, A.J.: In: Pekalski, A., Przystawa, J. (eds.) Modern Trends in the Theory of Condensed Matter., pp. 13. Springer, New York (1980)
16. Leggett, A.J.: J. Phys. (Paris) **42**, C7 (1980)
17. Modawi, A.G.K.: Thesis, University of Sussex (1980) (unpublished)
18. Modawi, A.G.K., Leggett, A.J.: J. Low Temp. Phys. **109**, 625 (1997)
19. Nozières, P., Schmitt-Rink, S.: J. Low Temp. Phys. **59**, 195 (1985)
20. Randeria, M.: Crossover from BCS theory to Bose-Einstein condensation. In: Griffin, A., Snoke, D., Stringari, S. (eds.) Bose-Einstein Condensation, pp. 355–392. Cambridge University, Cambridge (1995)
21. Leggett, A.J.: Quantum Liquids: Bose Condensation and Cooper Pairing in Condensed Matter Systems. Oxford University Press, Oxford (2006)
22. Petrov, D.S., Salamon, C., Shlyapinikov, G.V.: Phys. Rev. Lett. **93**, 090404 (2004)
23. Gor'kov, L.P., Melik-Barkhudarov, T.K.: JETP **13**, 1081 (1961)
24. Braaten, E., Platter, L.: Phys. Rev. Lett. **100**, 205301 (2008)
25. Zhang, S., Leggett, A.J.: Phys. Rev. A **79**, 023601 (2009)
26. Landau, L.D., Lifshitz, E.M.: Statistical Physics. Butterworth-Heinemann, Oxford (2002)
27. Werner, F., Tarruell, L., Castin, Y.: Eur. Phys. J. B **68**, 401 (2009)
28. Tan, S.: Ann. Phys. (NY) **323**, 2952 (2008)
29. Combescot, R., Alzetto, F., Leyronas, X.: Phys. Rev. A **79**, 053640 (2009)

Chapter 3
Crossovers in Unitary Fermi Systems

Henning Heiselberg

Abstract Universality and crossover is described for attractive and repulsive inter-
actions where, respectively, the BCS–BEC and crossover takes place and a ferromag-
netic phase transition is claimed. Crossovers are also described for optical lattices and
multicomponent systems. The crossovers, universal parameters and phase transitions
are described within the Leggett and NSR models and calculated in detail within the
Jastrow-Slater approximation. The physics of ultracold Fermi atoms is applied to
neutron, nuclear and quark matter, nuclei and electrons in solids whenever possible.
Specifically, the differences between optical lattices and cuprates is discussed w.r.t.
antiferromagnetic, d-wave superfluid phases and phase separation.

3.1 Introduction and the Bertsch Problem

A decade ago at the 10th Manybody Conference G. Bertsch posed the problem
(see [1] for full text):

> How does a system of Fermi particles with infinite s-wave scattering length but
> vanishing interaction range behave?

This seemingly innocent question turned out to be rather fundamental and trig-
gered an explosion of interest and number of papers on physics now referred to
as *universal physics, the unitarity limit, BCS–BEC crossover*, and strongly inter-
acting and correlated systems in general. His question was partly motivated from
nuclear physics and the physics of neutron stars where dilute gases of neutrons exist

H. Heiselberg (✉)
Applied Research, DALO,
Lautrupbjerg 1-5, DK-2750 Ballerup,
Denmark
e-mail: heiselberg@mil.dk

in the inner crust. The neutron-neutron $^1S_0$ scattering length $a \simeq -18.5\,\text{fm}$ is long (and negative) compared to the order of magnitude smaller interaction range $R \sim 1\,\text{fm}$, because two neutrons almost have a bound state. Admittably, Bertsch was also motivated by expectations that cold gases of Fermi atoms might be created like the BEC a few years earlier, and that it might be possible to tune interactions near Feshbach resonances between two hyperfine states in order to make the scattering length truly go to $\pm\infty$. Both were rapidly and successfully accomplished in a number of remarkable experiments where also the BCS–BEC crossover, multicomponent systems, optical lattices, etc. have been studied.

The solution to the Bertsch problem for two-component systems is as simple as it is fundamental [2, 3]:

Since $R \rightarrow 0$ and $a \rightarrow \pm\infty$ both parameters must vanish from the problem leaving only one remaining length scale: the interparticle distance or equivalently the inverse of the Fermi wavenumber k_F^{-1}. All thermodynamic quantities become *universal*.

The proof is a dimensional argument which will be described in detail below. As an example, the energy per particle is an *universal* constant times the energy of a non-interacting Fermi gas $(3/5)E_F = 3\hbar^2 k_F^2/10\,m$. The $a \rightarrow \pm\infty$ limit is referred to as the universal or *unitarity* limit and the gas as a *unitary* gas. The name comes from scattering theory where e.g. the s-wave scattering cross section at relative momentum k is limited by $\sigma_0 \le 4\pi/k^2$ due to unitarity of the scattering matrix. For weak interactions $\sigma_0 = 4\pi a^2$ which would diverge like the energy per particle (see Eq. 3.3)—if extrapolated to $a \rightarrow \pm\infty$. In the unitary gas the cross section and the thermodynamic quantities are instead limited by unitarity and universality respectively.

In the neutron gas |a| is long but fixed and the unitarity limit is defined as $|a| \gg r_0 \gg R$, where $r_0 = (3n/4\pi)^{-1/3} \sim k_F^{-1}$ is the interparticle distance, k_F the Fermi wavenumber at density $n = k_F^3/3\pi^2$ for two components/spin states. Thus the unitarity limit ranges from nuclear saturation density $n_{NM} \simeq 3/4\pi R^3 \simeq 0.15\,\text{fm}^{-3}$, and more than three orders of magnitude down in density to $\sim |a|^{-3}$. In this region, e.g. the energy per particle scales as an universal constant times E_F. The unitarity limit became easily accessible experimentally as it became possible to tune atomic interaction strengths near Feshbach resonances [4], where $a \rightarrow \pm\infty$ corresponding to two-atom bound states at threshold. The scattering length could also be extended to positive values corresponding to bound molecular states and for strongly bound states $a \rightarrow 0_+$ even a molecular BEC.

The Bertsch problem described above was originally intended for two component system as spin 1/2 neutrons or ultracold atoms in two hyperfine states but it is also relevant for a nucleon gas, since the neutron and a proton have the weakly bound state of deuterium and therefore a large positive scattering length $a \simeq +20\,\text{fm}$. Isospin symmetric nuclear matter, however, has two spin and two isospin states i.e. four

components and does not have a unitarity limit. It is in fact unstable at subnuclear matter densities where a liquid gas phase transition occurs. This was successfully described in [3] where estimates showed that as Pauli blocking between same spins is effectively reduced as the number of spin states increases, the Pauli pressure can no longer overcome the unitary attraction. Only two component systems are stable and provides a unitary gas. Three component systems are marginal and four and higher component systems are unstable. Such multicomponent systems are now studied, e.g. ^{6}Li with three hyperfine states [5–7], ^{137}Yb with six nuclear spin states [8], and heteronuclear mixtures of ^{40}K and ^{6}Li [9, 10]. Multi-component systems have intriguing similarities with neutron, nuclear and quark matter. In the latter color superconductivity between the 2 spin, 8 color and 2–3 flavor states may occur [11].

When the interactions are varied, e.g. near a Feshbach resonance, the thermo-dynamic quantities depend on the dimensionless parameter ak_F. All the thermo-dynamic quantities become universal functions of the crossover parameter ak_F or equivalently $x = 1/ak_F$ in the sense that they do not depend on the system whether a gas of atoms, neutrons, or any other Fermi particle as long as $R \ll |a|, r_0$. The universality argument is intimately connected to the smooth approach to the unitarity limit and crossover. At finite temperatures the universal thermodynamic functions depend on T/E_F as well. A decade earlier pairing models [12–15] had already described the crossover from BCS to the BEC limit and calculated pairing gaps, transition temperatures and chemical potentials.

In these lecture notes universality, crossover and correlations will be described. Not only the BCS–BEC crossover in uniform system but also the repulsive "ferro-magnetic" crossover, in multicomponent systems, traps and lattices. Mostly Fermi atoms are discussed but applications to neutron, nuclear and quark matter, nuclei and electrons in solids are made wherever possible.

3.2 Universality and Crossover

Universality is usually understood as the universal scaling in the unitarity (Bertsch) limit where the interaction range ($R \to 0$) and scattering length ($a \to \pm\infty$) are suffi-ciently short and large respectively that the thermodynamic quantities are independent of either or any other details of the interaction (such as effective ranges, etc.) and only given by universal constants.

When only the interaction range is negligible ($R \to 0$) but the scattering length varies, as it is possible in ultracold atomic systems around Feshbach resonances, there is another dimensionless parameter in the problem usually taken as ak_F or $x = 1/ak_F$. The thermodynamic quantities are thus universal functions of this *crossover* para-meter varying from weakly interacting $x \to -\infty$ over the unitarity limit $x = 0$ to the strongly interacting molecular limit $x \to +\infty$. In pairing models [13–15] these limits are named the BCS and BEC limits respectively and the crossover as BCS–BEC crossover. When finite temperatures are considered the thermodynamic quantities are universal functions of both x and T/E_F [16].

Fig. 3.1 Sketch of
correlations in a
two-component gas. *Top row*
shows the gradual pairing of
different components (spin
states) with increasing
attraction, i.e. the crossover
from BCS via unitary gas to
the molecular BEC. *Bottom
row* shows the crossover for
repulsive interactions from
the dilute gas to either a hard
sphere (Gutzwiller) or a
ferromagnetic phase
(see text)
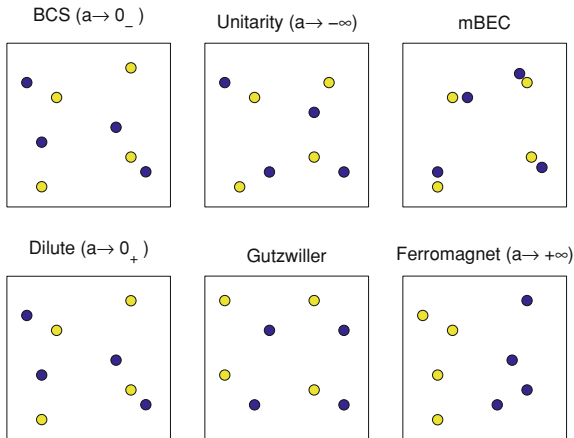
It should be emphasized that there are *several crossovers* (see Fig. 3.1). The most common one is that for increasingly attractive scattering lengths also known from pairing models [13–15] and referred to as the BCS–BEC crossover. Here the cold atoms start out in the weakly attractive limit with BCS pairing i.e. $x = 1/ak_F \to -\infty$ and goes over the unitarity limit $x = 0$ to the strongly attractive limit $x \to +\infty$, where a molecular BEC forms. Another crossover starts out with weak repulsive interactions, i.e. a small positive scattering length, and increasing it towards $ak_F \to +\infty$. A recent experiment claims to observe a phase transition in a ^{6}Li gas to a ferromagnetic state for $ak_F \gtrsim 2$ [17]. These two crossover are different because the latter has a node in the short range correlation function [18]. In principle there are a novel crossover for each number of nodes, however, they become increasingly short lived due to three-body losses. The different crossovers have different universal thermodynamic functions, universal parameters and quite different superfluid and ferromagnetic phases.

We will in the following subsections describe universality and crossover mainly for the BCS–BEC crossover and briefly for the "ferromagnetic" crossover. A number of thermodynamic functions are described which are calculated within the Jastrow-Slater approximation for the many-body wave function.

3.2.1 Universality in the Unitarity Limit

The dimensional argument implies that any thermodynamic function, for example the energy per particle in units of the Fermi energy, can at zero temperature only depend on one dimensionless scale such as x

$$\frac{E}{N} = \frac{3}{5} E_F (1 + \beta(x)). \tag{3.1}$$

Here, the ratio between the interaction and kinetic energy $\beta(x)$ is a "universal" many-body function in sense that it and all other thermodynamic functions are independent of the system, e.g. dilute neutron matter, helium gases, atomic gases, etc. Earlier definitions are $\eta = (3/5)(1 + \beta)$ [19–21] and $\nu = (5/3)\beta$ [3].

The universality and crossover hypothesis implicitly assumes that the transition to the unitarity limit and the crossover is smooth, i.e. the derivatives of $\beta(x)$ are finite. Taking the derivative with respect to density gives

$$\frac{\partial E/N}{\partial n} = \frac{3}{5}(1 + \beta(x))\frac{\partial E_G}{\partial n} - \frac{E_F}{5n} x\beta'(x) \qquad (3.2)$$

where $\beta'(x) = \partial\beta(x)/\partial x$. We observe that derivatives of β w.r.t. densities or k_F: $k_F\partial/\partial k_F = -x\partial/\partial x$, always brings a factor x or $1/a$. In the unitarity limit $x = 0$, such terms as the second term in Eq. 3.2 therefore vanishes and only the universal parameter $\beta(0)$ remains. By repeating the argument all density derivatives of the energy such as chemical potential, pressure, first sound speed, compressibility, etc. depend only on this one universal parameter $\beta(0)$. Other thermodynamic variables than density derivatives of E/N can, however, depend on higher derivatives $\beta^{(n)}(0)$ as we shall see below.

The first estimates based on Pade' approximants and Galitskii resummation gave $\beta(0) \simeq -0.67$ [2, 3] in the unitary limit whereas the Jastrow-Slater approximation yielded $\beta(0) \simeq -0.54$. The Leggett pairing model, which will be described in detail in a later section, predicts $\beta(0) \simeq -0.40$. Ground state energies have been calculated more accurately numerically by Monte Carlo for systems with a finite number of Fermions in a box. The earliest actually use the Jastrow-Slater as trial wave functions for Green's function [19–21] and diffusion [22] Monte Carlo. Since pairing becomes important at crossover a more general BCS wave function based on the Jastrow wave function was also employed. Extrapolating to a large number of particles they obtained $\beta(0) = -0.56 \pm 0.01$ and $\beta(0) = -0.58 \pm 0.01$ respectively in the unitary limit.

Recent measurements [4, 23–33] of $\beta(0)$ confirm the unitarity limit near Feshbach resonances. Several experiments with trapped Fermi atoms have recently measured energies in the strongly interacting or dense limit near Feshbach resonances. The energy in the trap (excluding that from the harmonic oscillator potential) is $E/N = (3/8)E_F\sqrt{1 + \beta(0)}$ where $E_F = (3N)^{1/3}\hbar\omega$ is the Fermi energy in a trapped non-interacting gas. The first measurements by the Duke group [4] measured the energy of ^{6}Li Fermi atoms near a Feshbach resonance from expansion energies. These early measurements were later corrected for thermal energies and find $\beta(0) = -0.4 \pm 0.1$. [4, 28, 29]. With the discovery of a molecular BEC the Innsbruck group [32, 33] has been able to measure the size of the atomic cloud, which scales with $(1 + \beta)^{1/4}$, around the Feshbach resonance at very low temperatures, and find $\beta(0) = -0.68 \pm 0.1$. Recent accurate measurements find $\beta(0) = -0.49 \pm 0.02$ [34].

Other thermodynamic variables may in the unitarity limit depend on other universal parameters. For example, the number of closed channel molecules is proportional to $\beta'(x)$ [35–37] and one obtains $\beta'(0) \simeq -0.5$. From the slope of collective

modes near the unitarity limit $\beta'(0) \simeq -1.0$ [4, 28, 29]. Generally, the universal function $\beta(x)$ is given by a Taylor expansion in terms of an infinite number number of derivatives $\beta^{(n)}(0)$, which all are universal parameters that determine all the universal thermodynamic functions.

Unlike neutrons, ultracold atoms can have many internal bound states and corresponding Feshbach resonances as the background magnetic field is increased. Thus solutions are multivalued for a given scattering length where the gas is in a metastable state. For example, starting from a non-interacting gas ($a = 0$) and increasing the scattering length $a > 0$ we also approach an unitarity limit $a \to +\infty$ [38], which differs from that in the BCS–BEC crossover when the scattering length is decreased $a < 0$. This unitarity limit is similar to that for bosons as $a \to +\infty$ [18], where the scattering length must be positive in order for the system to be stable. As will be described in detail the two-body wave function has a node and therefore the universal functions differs from those in the BCS–BEC crossover. In principle a new universal limit and crossover exist for each number of nodes, $n = 1, 2, 3, \ldots$, in the two-body correlation function. These will, however, be increasingly unstable towards three-body losses. The $n = 1$ has been observed for bosons in the atomic-molecular transition in a ^{85}Rb BEC [39–43] and is in agreement with the predicted value from JS with $\kappa_1 = 2.80$. For fermions the predicted value is calculated below within the Jastrow-Slater approximations $\beta_1(0) \simeq 2.93$ which is compatible with a recent experiment [17]. This value is about six times $|\beta(0)|$ demonstrating that these two universal limits are very different.

3.2.2 Thermodynamic Crossover Functions

As argued above any thermodynamic function can only depend on one dimensionless scale such as x at zero temperature when the range of interaction is sufficiently small. For example, the energy per particle in units of the Fermi energy is given in Eq. 3.1 in terms of the universal many-body crossover function $\beta(x) = E_{int}/E_{kin}$. It is well known in the dilute limit for Fermions [44, 45]

$$\frac{E}{N} = \frac{3}{5} E_F + \frac{\pi \hbar^2}{m} an + \cdots \tag{3.3}$$

to leading orders, whereas for molecular bosons

$$\frac{E}{N} = -\frac{\hbar^2}{2ma^2} + \frac{\pi \hbar^2}{2m} a_M n + \cdots, \tag{3.4}$$

where the molecular scattering length is $a_M \simeq 0.6a$ [23–27, 46]. Thus we obtain

$$\beta(x) = \begin{cases} 10/(9\pi x) + 4(11 - 2\ln 2)/(21\pi^2 x^2) + \cdots & x \to -\infty \\ \beta(0) + \beta'(0)x + \cdots & x \simeq 0 \\ -5x^2/3 - 1 + (a_M/a)5/(18\pi x) + \cdots & x \to +\infty \end{cases}. \tag{3.5}$$

Fig. 3.2 The universal
functions $\beta(x)$ and $\beta_1(x)$
within JS. Also shown are
the BCS limit of Eq. 3.5 and
the chemical potential in the
Leggett crossover model
(see text). On the BEC side
$(x > 0)$ the molecular
energy been subtracted
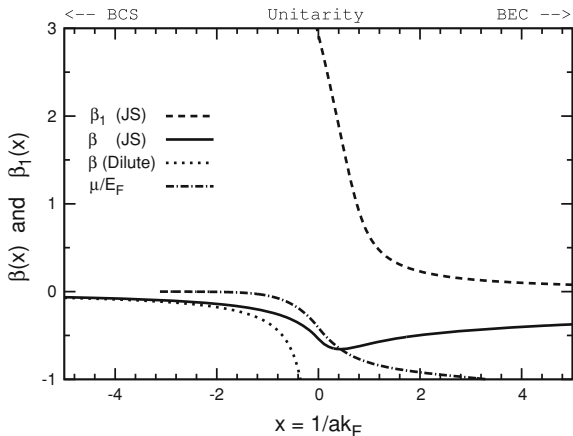
In Fig. 3.2 various model calculations of the universal function $\beta(x)$ are shown.
The chemical potential is in terms of the universal function

$$\mu(x) = \left(\frac{\partial E}{\partial N}\right)_{V,S} = E_F\left(1 + \beta - \frac{1}{5}x\beta'\right). \tag{3.6}$$

In both the hydrodynamic limit and for a superfluid gas the first sound is given
by the adiabatic sound speed

$$c_S^2(x) = \frac{n}{m}\left(\frac{\partial\mu}{\partial n}\right)_{V,S} = \frac{1}{3}v_F^2\left[1 + \beta - \frac{3}{5}x\beta' + \frac{1}{10}x^2\beta''\right], \tag{3.7}$$

where $v_F = \hbar k_F/m$.
The compressibility $\kappa = n^{-2}(\partial n/\partial\mu)$ is related to first sound as

$$\kappa^{-1} = n^2\left(\frac{\partial\mu}{\partial n}\right)_{V,S} = mnc_S^2. \tag{3.8}$$

The pressure $P = n(\mu - E/N) = n^2\, dE/dV$ is

$$P(x) = \frac{2}{5}E_Fn[1 + \beta - x\beta'/2]. \tag{3.9}$$

The polytropic index $P \propto n^{\gamma+1}$ is defined as the logarithmic derivative of the
pressure

$$\gamma(x) \equiv \frac{n}{P}\frac{dP}{dn} - 1 = \frac{\frac{2}{3}(1 + \beta) - x\beta'/2 + x^2\beta''/6}{1 + \beta - x\beta'/2}. \tag{3.10}$$

γ approaches 2/3 in both the dilute and unitarity limit whereas it approaches $\gamma = 1$
in the molecular limit. This index determines the frequency of collective modes in
traps [47].

We notice that all the above thermodynamic derivatives w.r.t. density only depend on one universal parameter $\beta(0)$ in the unitarity limit $x = 0$ as argued above. Most thermodynamic quantities behave in the unitary gas as in a free Fermi gas except for the universal scaling factor $(1 + \beta(0))$. This factor, however, cancels in the polytropic index and therefore $\gamma = 2/3$ in both the unitarity and BCS limit and the collective modes are the same as has been verified experimentally [4].

3.2.3 Finite Temperature

At finite temperature the thermodynamic functions also depend on the parameter T/E_F (see, e.g., [3, 16, 48, 49]). Using $(\partial(E/N)/\partial T)_{V,N} = T(\partial s/\partial T)_{V,N} = c_V$, where $s = S/N$ is the entropy and c_V the specific heat per particle, we obtain from Eq. 3.1

$$\beta(x, T/E_F) = \beta(x, 0) + \frac{5}{3} \int_0^T c_V \left(x, \frac{T'}{E_F} \right) \frac{dT'}{E_F}. \tag{3.11}$$

The entropy is at temperatures well below the superfluid transition temperature $T \ll T_c$ given by phonon fluctuations

$$s = \frac{2\pi^2}{45n} \left(\frac{T}{c_S} \right)^3. \tag{3.12}$$

Inserting in Eq. 3.11 gives at low temperatures.

$$\beta(x, T/E_F) = \beta(x, 0) + 5 \frac{T}{E_F} s. \tag{3.13}$$

The temperature corrections scales as $\sim (T/T_F)^4$ and since $T \ll T_c \simeq 0.19 E_F$, the temperature dependence is almost flat as also observed in [34].

In a Fermi liquid $s = (\pi^2 m^*/2m)T/E_F$, where m^* is the effective mass, and thus

$$\beta(x, T/E_F) \simeq \beta(x, T_c/E_F) + \frac{5\pi^2}{6} \frac{m^*}{m} \frac{T^2 - T_c^2}{E_F^2}, \tag{3.14}$$

when $T_c < T \ll E_F$. Recent accurate measurements find $\beta(0, 0) = -0.49 \pm 0.01$ and $m^*/m = 1.13 \pm 0.03$ [34] in the unitarity limit. These allow us to extract the Landau parameters at zero temperature $F_0^s = (1 + \beta(0, 0))m^*/m - 1 \simeq -0.42$ and $F_1^s = 3(m^*/m - 1) \simeq 0.39$. In the BCS limit $m^*/m = 1 + [8(7\ln 2 - 1)/15\pi^2]a^2 k_F^2$ and $F_0 = 1 + (10/9\pi)ak_F$.

As the temperature decreases towards the critical temperature the change in $\beta(T)$ from a Fermi liquid Eq. 3.14 towards a superfluid Eq. 3.13 allowed determination of $T_c/E_F = 0.19 \pm 0.02$ [34].

At temperatures below $T < T_c$ the normal and superfluid components lead to two (first and second) sound modes in the collisional limit. In the BCS and BEC limit these are also referred to as the compressional and thermal sound modes. Their velocities u_1 and u_2 are given by the positive and negative solutions respectively of [50, 51]

$$u^2 = \frac{c_S^2 + c_2^2}{2} \pm \sqrt{\left(\frac{c_S^2 + c_2^2}{2}\right)^2 - c_T^2 c_2^2}. \tag{3.15}$$

The thermodynamic quantities entering are the adiabatic $c_S^2 = (\partial P/\partial n)_S$ and the isothermal $c_T^2 = (\partial P/\partial n)_T$ compressional sound speed squared. The "thermal" sound wave $c_2^2 = n_s s^2 T/n_n c_V$ acts as a coupling or mixing term and is small in the two limits. Here, $n = n_n + n_s$ is the total, n_n the normal and n_s the superfluid density. The difference between the adiabatic and isothermal sound speed squared can also be expressed as

$$c_S^2 - c_T^2 = \left(\frac{\partial s}{\partial n}\right)_T^2 \frac{n^2 T}{c_V}. \tag{3.16}$$

The mixing of the compressional and thermal sound modes is particular interesting at crossover where they mix and couple strongly. They undergo avoided crossing, i.e. the compressional change smoothly into a thermal sound mode and visa versa around the unitarity limit [48].

3.2.4 Jastrow-Slater Approximation

The Jastrow and Jastrow-Slater (JS) approximation was among the earliest models applied to the unitarity limit and crossover [3]. It has the advantage that it provides analytical results for the universal parameters that are easy to understand and has proven to be quite accurate when compared to experiment. It gives an ansatz for the strongly correlated wavefunctions which is also the starting point as trial wavefunctions in Monte Carlo calculations [22]. Finally, JS can be generalized to describe both bosons and fermions with any number of spin states as well as other universal limits.

The Jastrow and the JS approximation methods were developed for strongly interacting and correlated Bose and Fermi fluids respectively such as ^{4}He, ^{3}He and nuclear matter in [52–55] and has more recently been applied to kaon condensation [56], cold atomic Fermi [38] and Bose [18] gases. As explained in these references the JS wave function

$$\Psi_{JS}(\mathbf{r}_1, \ldots, \mathbf{r}_N) = \Phi_S \prod_{i,j'} \phi(\mathbf{r}_i - \mathbf{r}_{j'}), \tag{3.17}$$

incorporates essential two-body correlations in the Jastrow function $\phi(r)$. The anti-symmetric Slater wave function Φ_S for free fermions Φ_S insures that same spins are spatially anti-symmetric. The Jastrow wave function only applies to particles with different spins (indicated by the primes). The pair correlation function $\phi(r)$ can be determined variationally by minimizing the expectation value of the energy, $E/N = \langle \Psi|H|\Psi\rangle / \langle\Psi|\Psi\rangle$, which may be calculated by Monte Carlo methods that are fairly well approximated by including only two-body clusters. The basic idea of this method is that at short distances $r \ll r_0$ the Jastrow function $\phi(r)$ obeys the Schrödinger equation for a pair of particles interacting through a potential $U(r)$

$$\left[-\frac{\hbar^2}{m}\frac{d^2}{dr^2} + U(r)\right] r\phi(r) = \varepsilon_M r\phi(r), \tag{3.18}$$

where the eigenvalue energy of two atoms $\varepsilon_M = 2E_{int}/N$. Many-body effects become important, when r is comparable to r_0, but are found to be small in lowest order constrained variation (LOCV [3, 38, 52–56]). Here the boundary conditions that $\phi(r > d)$ is constant and $\phi'(r = d) = 0$ are imposed at the healing distance d, which is determined self consistently from number conservation (see [38] for details)

$$\frac{\nu-1}{\nu}n\int_0^d \frac{\phi^2(r)}{\phi^2(d)}4\pi r^2\, dr = 1 \tag{3.19}$$

Note that a given component only interact and correlate with the $(\nu - 1)$ other components which explains the prefactor. In the dilute limit $\phi(r) \simeq 1$ and so $d = (\nu/(\nu - 1))^{1/3}r_0$. In the unitary limit $a \to \pm\infty$ the healing length now approaches $d = r_0(2\nu/(\nu - 1)3)^{1/3} = (3\pi/(\nu - 1))^{1/3}k_F^{-1}$. Generally $d \simeq r_0$. The boundary condition at short distances is given by the scattering length $(r\phi)'/r\phi = -1/a$ at $r = 0$.

3.2.4.1 Attractive Crossover

For negative scattering lengths or negative energies $\varepsilon_M < 0$ the solution to the Schrödinger equation gives a wave-function $r\phi(r) \propto \sinh[k(r - b)]$ for weak interactions which change to $r\phi(r) \propto \cosh[k(r - b)])$ for stronger interactions (see Fig. 3.4). The boundary conditions and number conservation determine the phase kb, the energy and the healing length d. For small scattering lengths $b = a$ whereas $b = 0$ in the unitarity limit. The interaction energy $E_{int}/N = -\hbar^2 k^2/2m$ is given by [57]

$$\frac{a}{d} = \frac{\kappa^{-1}\tanh\kappa - 1}{1 - \kappa\tanh\kappa}, \tag{3.20}$$

with $\kappa = kd$. In the BCS limit Eq. 3.20 gives the correct interaction energy per particle, Eq. 3.3. In contrast the negative energy solution to Eq. 3.20 reduces in the

unitarity limit to $\kappa \tanh \kappa = 1$ with solution $\kappa_0 = 1.1997\ldots$ As the scattering length cross over from $-\infty$ to $+\infty$ the negative energy state is analytically continued towards the molecular bound state with $E/N = -\hbar^2/2ma^2$ as $a \to +0$.

In addition to the interaction energy $E_{int} = \kappa^2/2md^2$ as calculated above a kinetic energy $(3/5)E_F$ appears due to the Slater ground state. The total energy becomes

$$\frac{E}{N} = \frac{3}{5}E_F - \frac{\hbar^2 \kappa^2}{2m\,\mathrm{d}^2}. \tag{3.21}$$

From the definition Eq. 3.5 we obtain the universal function

$$\beta = -\frac{5}{3}\left(\frac{\kappa}{\mathrm{d}\,k_F}\right)^2. \tag{3.22}$$

In the unitarity limit $\kappa = \kappa_0 = 1.1997$ and $\mathrm{d}\,k_F = (3\pi/(\nu - 1))^{1/3}$ and the universal parameter is for a general number of spin states

$$\beta(0) = -\frac{5}{3}\left(\frac{\nu - 1}{3\pi}\right)^{2/3}\kappa_0^2. \tag{3.23}$$

Thus in a two-component system $\beta(0) = -0.54$ which lies between Monte Carlo results $\beta(0) \simeq -0.56$ [22] and recent experimental data $\beta(0) \simeq -0.49$ [34].

The universal function $\beta(x)$ is shown in Fig. 3.2 for the JS approximation. Also shown is the chemical potential within the Leggett crossover model which will be discussed below in connection with pairing. The JS model includes self energies and is therefore a better approximation on the BCS side $(x < 0)$. On the BEC side $(x > 0)$ both models approach the molecular energy (subtracted in Fig. 3.2) but to next orders both model overestimates the energy: the JS model by the Slater energy and the Leggett model by overestimating the molecular scattering length a_M by a factor ~ 3.

The dependence on the scattering length is given by Eq. 3.20. By taking the derivative on both sides w.r.t. x we obtain

$$\beta'(0) = -\frac{10}{3}\frac{1 - \kappa_0^{-2}}{(3\pi)^{1/3}} \simeq -0.48. \tag{3.24}$$

This JS prediction is somewhat lower than that of Monte Carlo: $\beta'(0) = -1.0 \pm 0.1$ [19–22]. The slopes of the axial and longitudinal collective frequencies of trapped unitary Fermi gases are directly proportional to $\beta'(0)$ and measurements also give $\beta'(0) \simeq -1.0$ [4, 28, 29]. Analysis of the number of closed channel molecules indicates $\beta'(0) \simeq -0.5$ [35–37]. In the Leggett pairing model $\beta'(0) \simeq -1.0$.

The universal parameter $\beta'(0)$ will be related to short range correlations in Sect. 3.2.5.

3.2.4.2 Repulsive Crossover

Starting from a positive scattering length and positive interaction energy the solution to the Schrödinger equation gives a wave-function $r\phi(r) \propto \sin[k(r-b)]$ (see Fig. 3.4). The boundary conditions and number conservation gives [18]

$$\frac{a}{d} = \frac{\kappa^{-1}\tan\kappa - 1}{1 + \kappa\tan\kappa}. \tag{3.25}$$

As in the BCS limit Eq. 3.25 gives the correct interaction energy per particle in the dilute limit, Eq. 3.3. In the unitarity limit $a \to +\infty$, the positive energy solution reduces to $\kappa\tan\kappa = -1$ with multiple solutions $\kappa_1 = 2.798386\ldots$, $\kappa_2 = 6.1212\ldots$, etc., and asymptotically $\kappa_n = n\pi$ for integer n. Generally, $n = 0, 1, 2, \ldots$ is the number of nodes in the JS wavefunction and each determines a new universal limit with universal parameters depending on the number of nodes. The phase in the wave function is $kb = \pi(n-1/2)$ whenever the unitarity limit of n nodes is encountered.

The resulting energy is

$$\frac{E}{N} = \frac{3}{5}E_F + \frac{\hbar^2\kappa^2}{2md^2}, \tag{3.26}$$

and we obtain from Eq. 3.1

$$\beta(x) = \frac{5}{3}\left(\frac{\kappa}{dk_F}\right)^2. \tag{3.27}$$

Because Eq. 3.25 have a string of solutions for given a, κ and β are multivalued functions for a given scattering length or x, which we distinguish by an index β_n referring to the number of nodes $n = 0, 1, 2, \ldots$. The attractive case discussed above is the $n = 0$ case, i.e. universal function in the BCS–BEC crossover is also $\beta = \beta_0$. $n = 1$ is the first weakly repulsive crossover where a ferromagnetic phase transition may occur and is also shown in Figs. 3.2 and 3.3

The universal parameter in this repulsive unitarity limit is

$$\beta_1(x=0) = +\frac{5}{3}\left(\frac{\nu-1}{3\pi}\right)^{2/3}\kappa_1^2 \simeq 2.93(\nu-1)^{2/3}. \tag{3.28}$$

The index denotes that this universal parameter is for the wave function with one node. It has recently been measured in a ^{6}Li gas in two spin states [17]. The chemical potential in the optical trap almost doubles going from the non-interacting to the unitarity limit. As shown below it scales as $\mu \propto \sqrt{1 + \beta_1(0)}$ giving $\beta_1(0) \sim 3$ compatible with JS. However, the experiments also indicate a phase transition in repulsive unitarity limit from a paramagnetic to a ferromagnetic phase. This phase transition is supported by the JS models as will be shown in Sect. 3.2.7.

Fig. 3.3 κ^2 vs. scattering length in the JS model in units of interparticle distance r_0
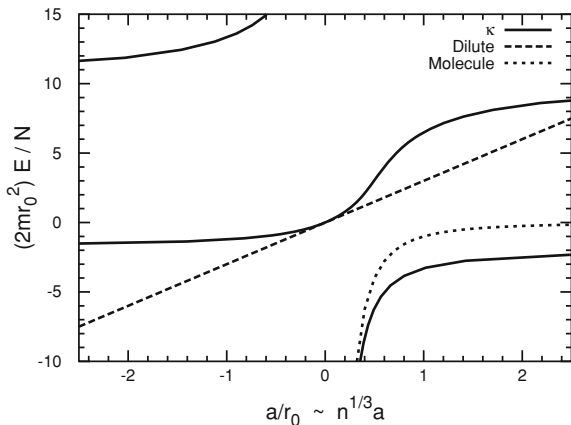
As for the attractive crossover we calculate within JS the derivative from Eq. 3.25

$$\beta_1'(0) = -\frac{10}{3}\frac{(1-\kappa_1^{-2})}{(3\pi)^{1/3}} \simeq -1.38. \tag{3.29}$$

3.2.5 Short Range Correlations

The short range two-body correlations are connected to thermodynamic quantities of the system [58]. We shall here derive one important example at zero temperature and use the Jastrow-Slater results above to actually calculate a new universal number. We refer to [49, 59] for finite temperature extensions.

Following [49] we scale the two-body potential by a factor λ and obtain from Feynmann-Hellmann

$$\frac{\partial E/V}{\partial \lambda} = \frac{1}{V}\left\langle \frac{\partial H}{\partial \lambda}\right\rangle = \int d^3r\, U(r)\langle \psi_1^\dagger(\mathbf{r})\psi_2^\dagger(0)\psi_2(0)\psi_1(\mathbf{r})\rangle_\lambda. \tag{3.30}$$

Here the correlation function at short ranges is

$$\langle \psi_1^\dagger(\mathbf{r})\psi_2^\dagger(0)\psi_2(0)\psi_1(\mathbf{r})\rangle_\lambda = \phi_\lambda^2(r) = C\left(\frac{1}{r}-\frac{1}{a_\lambda}\right)^2, \tag{3.31}$$

where ϕ_λ is the solution to the two-body Schrödinger equation (3.18) but with potential $\lambda U(r)$. C is a normalization factor such that $(1/V)\int d^3r\,\phi_\lambda^2(r) = (n/2)^2$, and will later be interpreted as the correlation strength.

Taking the derivative of the Schrödinger equation w.r.t. λ, multiplying by $r\phi_\lambda$, and integrating over r we obtain

$$\int\limits_0^{r_c} \mathrm{d}r\, U(r)(r\phi_\lambda(r))^2 = -\frac{C}{m}\frac{\partial a^{-1}}{\partial \lambda},$$ (3.32)

where r_c is any range between $R \ll r_c \ll r_0$. Combining Eqs. 3.30 and 3.32 gives

$$\frac{\partial E/V}{\partial a^{-1}} = -\frac{4\pi C}{m}.$$ (3.33)

From Eq. 3.1 we can relate the correlation strength to the derivative of the universal functions $\beta_n(x)$ as

$$C_n = -\frac{k_F^4}{40\pi^3}\beta_n'(x),$$ (3.34)

where the node index n distinguishes the various universal functions as discussed above. In the unitarity limits we can determine $C_n(x=0)$ by inserting $\beta_0'(0) = -0.54$ or $\beta_1'(0) = -1.38$ from JS Eqs. 3.24 and 3.29, etc. $C_n(x)$ can also be obtained directly from the JS wave-function, normalization and Eq. 3.31.

The Fourier transform of the wave-function at large momenta is determined by the short range correlations $\phi(k) = \int d^3 r e^{i\mathbf{k}\cdot\mathbf{r}}\phi(r) \simeq 4\pi\sqrt{C}/k^2$. Therefore the momentum distribution for a spin state has the tail

$$n_\sigma(k) = \phi^2(k) = (4\pi)^2 C/k^4,$$ (3.35)

at large momenta as is well known for Fermi liquids [44, 45]. The correlation strength is directly measured in the number of closed channel molecules [35, 36]

$$N_M = \frac{\partial E}{\partial a^{-1}}\frac{\partial a^{-1}}{\partial B}\frac{1}{\mu_M},$$ (3.36)

where μ_M is twice the magnetic moment of the atom. The scattering length depends on the applied magnetic field as $a \simeq a_{bg}[1 - \Delta B/(B - B_0)]$ near a Feshbach resonance at B_0. Experiments find for the BCS–BEC crossover [35, 36] $\beta_0'(0) \simeq -0.5$ which agrees well with that of JS and is compatible with model estimates [37].

3.2.6 Instability in Multicomponent Systems

The original Bersch problem was intended for two-component systems as neutron matter or spin-balanced ultracold atoms in two hyperfine states. Early extrapolations of the dilute energy of Eq. 3.3 to $a \to -\infty$ led to the belief that the unitarity limit was unstable towards collapse [60] as a nuclear gas whereas in fact the two-component system is the only stable unitary gas. The predicted scaling for the neutron gas at subnuclear density as given by the unitary gas of Eq. 3.1 triggered the memory of Vijay Pandharipande [61], who had the impression that Bethe and Brueckner were

aware of this scaling when they looked at low density neutron matter in neutron star context back in the '50s [52, 62, 63].[1] Calculations by Carlson et al. [19–21] have later confirmed this scaling in neutron gases.

Multicomponent systems are now studied, e.g. ^{6}Li with three hyperfine states [5–7], ^{137}Yb with six nuclear spin states [8], and heteronuclear mixtures of ^{40}K and ^{6}Li [9, 10]. Such multi-component systems have intriguing similarities with neutron, nuclear and quark matter where color superconductivity between the 2 spin, 8 color and 2–3 flavor states may occur [11].

For the gas to be stable towards collapse in the unitarity limit the energy must be positive, i.e., $1 + \beta(0) > 0$. In the JS approximation we obtain in the unitary limit from Eq. 3.23 $\beta(0) = 0, -0.54, -0.85, -1.12, \ldots,$ for $\nu = 1, 2, 3, 4, \ldots$ spin states respectively. Therefore the JS approximation predicts that up to $\nu \leq 3$ spin states are stable in the unitary limit whereas in the Galitskii approximation only $\nu = 1, 2$ are stable [3]. Pauli blocking is effectively reduced in many component system and can only stabilize one, two and perhaps three component Fermi systems in the unitary limit. The stability of two spin states towards collapse has been confirmed for a ^{6}Li and ^{40}K gases near Feshbach resonances. The marginal case $\nu = 3$ has been studied with ^{6}Li atoms, which have three spin states with broad and close lying Feshbach resonances, and although the loss rate of atoms is large near Feshbach and Efimov resonances [5–7] the gas is sufficiently long lived for measurements and does not collapse. It has long been known that neutron star matter [64–67] with two spin states likewise has positive energy at all densities whereas for symmetric nuclear matter with two spin and two isospin states, i.e. $\nu = 4$, the energy per particle is negative. Nuclear matter is therefore unstable towards collapse and subsequent implosion, spinodal decomposition and fragmentation at subnuclear densities [68]. Above nuclear saturation densities, $k_F R \gtrsim 1$, short range repulsion stabilizes matter up to maximum masses of neutron stars $\sim 2.2 \, \mathrm{M_\odot}$, where gravitation makes such heavy neutron stars unstable towards collapse [64]. The conjecture is therefore that the $\nu > 3$ Fermi systems are unstable and non-universal in the unitarity limit $a \to -\infty$. Bose atoms corresponds to $\nu = \infty$, since no Pauli blocking applies, and are unstable for negative scattering lengths.

The $\nu = 3$ system is relevant for several reasons. Traps with ultracold ^{6}Li atoms with three hyperfine states are sufficiently stable and long lived [5–7] to be studied in detail. The three Feshbach resonances are, however, separate in magnetic field so that the unitarity limit is not simultaneous for the three components. The three body system has interesting Efimov states which are non-universal [69–71], i.e. besides the scattering length the system depends on an additional potential parameter such as the effective range. This non-universality persists for three bosons confined in a trap [72] and non-universality is therefore expected for a gas with three state Fermi atoms as experiments for the ^{6}Li system also indicates [5–7]. Therefore three component systems do not have an universal limit and are only marginally stable, i.e. stable towards collapse but suffer three-body losses.

---

[1] However, no written reference has been found in the works of Bethe, Brueckner or Pandharipande so far.

In spin polarized systems or systems with different densities of the spin components the stability conditions depends on the various component densities. Also the system may undergo phase separation into a more symmetric phase and an asymmetric phase as, e.g., nuclei and a neutron gas in the inner crust of neutron stars. Similarly, spin polarized atoms at low temperature in traps may for strong attractive interactions separate into a paired spin balanced phase in the centre with a mantle of excess spin atoms. Likewise phase separation of strongly repulsive fermions may separate into domains of ferromagnetic phases in the centre with a paramagnetic mantle around.

3.2.7 Repulsive Interactions and Itinerant Ferromagnetism

For a small positive scattering length the Fermi gas is a paramagnet (PM). For stronger repulsion Stoner [73] predicted a phase transition to a ferromagnet (FM) which a recent experiment claim to have observed [17]. Stoner's argument was based on the dilute equation of state of Eq. 3.3 which generally for a spin polarized two-component system of total density $n = n_\downarrow + n_\uparrow$ and polarization $\eta = (n_\downarrow - n_\uparrow)/n$ is

$$E/N = \frac{3}{10} E_F \left[(1+\eta)^{5/3} + (1-\eta)^{5/3} + \frac{20}{9\pi}(1+\eta)(1-\eta)k_F a \right]. \quad (3.37)$$

Expanding for small polarization gives an equation of the Ginzburg–Landau type

$$E/NE_F \simeq \frac{3}{5} + \frac{2}{3\pi} ak_F + \frac{1}{3}\left(1 - \frac{2}{\pi} ak_F\right)\eta^2 + 3^{-4}\eta^4 + \mathcal{O}(\eta^6). \quad (3.38)$$

It predicts a second order phase transition at $ak_F = \pi/2$ from a PM to a FM with polarization $\eta = \pm\sqrt{27(2ak_F - 1/\pi)}$. Due to the small fourth order coefficient it quickly leads to a locally fully polarized system $\eta = \pm 1$.

Unfortunately the predicted transition occurs close to the unitarity limit where the dilute equation of state is not valid. Higher orders may be important as exemplified by including the next order correction of order a^2. It changes the transition from second to first order [74] at low temperatures up to a tri-critical point at $T_c \simeq 0.2T_F$, where the transition becomes second order again. However, the dilute expansion remains invalid in the unitarity limit.

The Jastrow-Slater approximation extends to the unitarity limit also for positive scattering lengths as discussed above. Number conservation of the various spin densities is automatically included in the healing length, see e.g. Eq. 3.19. As result the energy is

$$\frac{E}{N} = \frac{3}{10} E_F \left[(1+\eta)^{5/3} + (1-\eta)^{5/3} + \beta_1(1+\eta)(1-\eta)^{2/3} \right.$$
$$\left. + \beta_1(1+\eta)^{2/3}(1-\eta) \right] + \mathcal{O}(\eta^6). \quad (3.39)$$

$\beta_1(x, \eta)$ is now also a function of polarization but for simplicity we shall ignore this dependency as we expect it to be minor. Expanding for small polarization we find

$$E/NE_F \simeq \frac{3}{5}(1 + \beta_1) + \frac{1}{3}\left(1 - \frac{7}{5}\beta_1\right)\eta^2 + 3^{-4}(1 - \beta_1)\eta^4. \qquad (3.40)$$

Truncating to order η^4 would (erroneously) predict a second order phase transition from a PM to a FM at $\beta_1(x) = 5/7 \simeq 0.71$. The fourth order term is even smaller than the dilute prediction of Eq. 3.38, and it is therefore necessary to include higher orders. By equating the energy of the unpolarized gas, $\sim(1 + \beta_1)$ with that of a fully polarized gas, $\sim 2^{2/3}$, we find a first order transition at $\beta_1 = 2^{2/3} - 1 \simeq 0.59$, since this value is smaller than 5/7. In view of the approximations made in this model calculation and the proximity of the two β_1 values for the first and second order transitions, we can not reliably determine whether the order of the PM-FM transition is first or second. However, since the repulsive interaction energy in the unitarity limit $\beta_1(0) \simeq \kappa_1^2/(3\pi)^{2/3} \simeq 2.93$ is much larger than the critical value $\beta_1 \simeq 0.59$ we can safely conclude that the transition to a FM does take place at a value corresponding to $ak_F \simeq 0.85$.

In a recent experiment the transition is observed around $ak_F^0 \simeq 2.2$ at temperatures $T/T_F = 0.12$ and $ak_F^0 \simeq 4.2$ at $T/T_F = 0.22$ [17]. Presumably, the critical value for ak_F^0 is smaller at zero temperature. Also the Fermi wavenumber k_F^0 is the central value for a non-interacting gas which is larger than the average value over the trap of the gas that is further expanded due to repulsive interactions. More experiments will determine $\beta_1(x)$, a possible ferromagnetic phase and critical value for ak_F.

When the number of atoms in the two spin states is balanced the ferromagnetic domains of $\eta = \pm 1$ coexist. Their domain sizes may be to small to observe in present experiments [17]. The densities of the two components will, however, have interesting distributions for unbalanced two-component systems in traps, where the minority component will be suppressed in the centre and both phase separation and ferromagnetism can occur. In three component systems, when there are more than one Feshbach resonance as in ^{6}Li, with Feshbach magnetic field such that two resonances a_{12} and a_{13} are large but a_{23} small, the atoms will separate between a FM phase of 1 and a mixed FM phase of $2+3$ with different densities.

It should be emphasized that for positive scattering lengths the wave function and thus the correlations function between fermions of unlike spin and bosons $\chi = r\phi \sim \sin(kr - b)$ has a node somewhere within the interparticle distance $[0; r_0]$ (see [18] and Fig. 3.4). It does not vanish as $r \to 0$ as does the wave function for a short range repulsive potential as in hard sphere scattering, where $a \simeq R$. Therefore the Gutzwiller approximation discussed in [75] applies to hard sphere gases, strongly correlated nuclear fluids and liquid helium but not to the repulsive unitarity limit of ultracold gases (see Fig. 3.1).

Fig. 3.4 The JS wave function $r\phi(r)/d\phi(d)$ in the dilute limit ($\kappa = 0$), the attractive unitarity limit (κ_0), towards the mBEC ($\kappa = 2$), the repulsive unitarity limit with one (κ_1) and two nodes (κ_2)
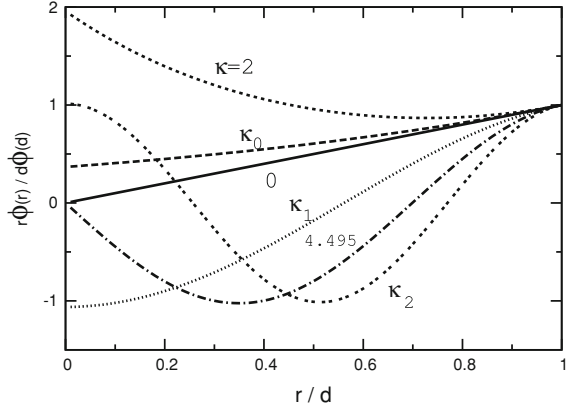
3.3 Pairing in Uniform Systems and the BCS–BEC Crossover

Experiments on superfluid Fermi gases have recenty confirmed the BCS to BEC crossover models [12–15, 76, 77] for pairing that was developed after the invention of BCS theory. The development of BCS–BEC crossover will be described historically with increasing level of complexity.

3.3.1 BCS Limit

Bardeen, Cooper and Schriffer (BCS) first wrote down the famous gap equation [78] for an attractive two-body interaction $U(r) < 0$

$$\Delta_{\mathbf{p}} = -\frac{1}{V}\sum_{\mathbf{p}'} U(\mathbf{p}', \mathbf{p})\frac{1 - 2f(E_{\mathbf{p}}')}{2E_{\mathbf{p}'}}\Delta_{\mathbf{p}'}, \qquad (3.41)$$

which can be elegantly derived via the Bogoliubov transformation [79]. Here, $f(\varepsilon) = (\exp(\varepsilon - \mu)/T) + 1)^{-1}$ is the Fermi distribution function, $E_{\mathbf{k}} = \sqrt{(\varepsilon_{\mathbf{k}} - \mu)^2 + \Delta_0^2}$ the quasi-particle energy and $\varepsilon_{\mathbf{k}} = \hbar^2 k^2/2m$ the free particle energy. In the BCS limit number conservation insures that $\mu = E_F$. $U(\mathbf{p}, \mathbf{p}') = U(\mathbf{p} - \mathbf{p}')$ is the Fourier transform of $U(\mathbf{r})$. In metals phonons provide a small residual attractive interaction $U(\mathbf{p}', \mathbf{p}) \simeq -V_{ph}$ with a cutoff of order the Debye frequency ω_D. As result we obtain from Eq. 3.41 the BCS s-wave gap $\Delta_0 = 2\hbar\omega_D e^{-1/N(0)V_{ph}}$ at zero temperature.

In the years immediately after BCS was developed the gap equation was generalized in terms of scattering lengths [80, 81]. When the interaction U(r) is short range, its Fourier transform $U(\mathbf{p} - \mathbf{p}')$ is long range in momentum. It is then convenient to replace the interaction by its scattering matrix $T = U + UG_0T$, where $G_0 = 1/(2\varepsilon_{\mathbf{k}} - i\delta)$, is the vacuum propagator for two particles. At low momenta

the scattering matrix is given by the s-wave scattering length $T = 4\pi\hbar^2 a/m \equiv U_0$. Eliminating U in the gap equation 3.1 gives

$$1 = \frac{U_0}{2V} \sum_{\mathbf{k}} \left[\frac{1}{\varepsilon_{\mathbf{k}}} - \frac{1 - 2f(E_{\mathbf{k}})}{E_{\mathbf{k}}} \right]. \qquad (3.42)$$

Note that the difference between the vacuum and in medium Green's functions automatically cuts off the high momenta, which are now included in the scattering length. Solving this gap equation at zero temperature for a Fermi gas interacting through an attractive scattering length $a < 0$ gave a pairing gap in the dilute limit, $|a|k_F \ll 1$, [80, 81]

$$\Delta_0 = \frac{8}{e^2} E_F \exp\left[\frac{\pi}{2ak_F}\right]. \qquad (3.43)$$

3.3.2 Induced Interactions

Gorkov[2] pointed out that many-body effects (induced interactions) lead to the next order correction in the interaction [82–86]

$$U_{ind}(\mathbf{p}', \mathbf{p}) = -\frac{U_{12}^2}{M} \sum_{\mathbf{q}} \frac{f(\xi_1(\mathbf{k}' + \mathbf{q})) - f(\xi_1(\mathbf{q}))}{\xi_1(\mathbf{k}' + \mathbf{q}) - \xi_1(\mathbf{q})}$$
$$+ \sum_{j,\mathbf{q}} \frac{U_{1j}U_{2j}}{M} \frac{f(\xi_3(\mathbf{k} + \mathbf{q})) - f(\xi_3(\mathbf{q}))}{\xi_3(\mathbf{k} + \mathbf{q}) - \xi_3(\mathbf{q})}. \qquad (3.44)$$

f is the Fermi distribution of $\xi_j(\mathbf{q}) = \varepsilon_{\mathbf{q}} - \mu_j$, $\mathbf{k}' = \mathbf{p} + \mathbf{p}'$ and $\mathbf{k} = \mathbf{p} - \mathbf{p}'$, where $\mathbf{p}_i$ are the momenta of the two pairing spin states. Induced interactions due to particle-hole loop diagrams from $j = 3, ..., \nu$ spin states are responsible for the second sum in Eq. 3.44 and has opposite sign. For two components, however, it is absent.

In the two-component spin-balanced system the induced interactions effectively leads to a second order correction to the scattering length $a \rightarrow a + (2/3\pi) \ln(4e)k_F a^2$ [82, 83], where $a = a_{12}$ and $U_{12} = U_0 = 4\pi\hbar^2 a/m$. Including this correction in Eq. 3.43 reduces the gap by a factor $(4e)^{1/3} \simeq 2.2$

$$\Delta = \left(\frac{2}{e}\right)^{7/3} E_F \exp\left[\frac{\pi}{2ak_F}\right]. \qquad (3.45)$$

The induced interactions consists of a repulsive direct part and an attractive part due a loop diagram which is therefore proportional to the number of components ν.

---

[2] Inquiring into details about their calculation some 40 years later Gorkov only remembered "...that it was a particular difficult calculation!"

The induced interactions therefore scale as $(3 - \nu)$ in a system of ν spin balanced multi-components with the same scattering length. The corresponding gap is

$$\Delta = (4e)^{\nu/3-1}\Delta_0. \tag{3.46}$$

For spin polarized systems or for the ^{6}Li systems with three different scattering lengths the pairing gap is described in Ref. [84]. Adding bosons enhance pairing [83].

In the unitary limit $k_F|a| \gtrsim 1$ the gap is of order the Fermi energy [13]. Extrapolating (3.2) to $ak_F \rightarrow \pm \infty$ [3] gives a number $\Delta = 0.49E_F$ close to that found from odd-even staggering binding energies $\Delta = 0.54E_F$ calculated by Monte Carlo [19–21]. The crossover model of Leggett described below gives a somewhat larger gap $\Delta^{Leggett}/E_F = 0.69$. Such values of order the Fermi energy are one or two orders of magnitude larger those found in metals and high temperature superconductivity and was met by disbelief among condensed matter physicist and the crossover was considered academic. Only after the realization and confirmation of the BCS–BEC crossover in experiments with ultracold atoms was its significance acknowledged.

It also follows from the BCS gap equation that the gap and thus superfluidity and superconductivity all vanish at a critical temperature

$$T_c = \frac{e^{C_E}}{\pi}\Delta \simeq 0.567\Delta, \tag{3.47}$$

for any weak interaction ($C_E = 0.577...$ is Euler's constant). In the unitarity and BEC limits the critical temperature is no longer proportional to the gap.

3.3.3 Leggett's BCS–BEC Crossover

Eagles and Leggett made the important step of connecting BCS pairing to a BEC of molecular bosons via crossover. Eagles gave an early treatment of the crossover from BCS superconductivity to a BEC in the context of systems with low carrier concentrations [12]. For pedagogical reasons we will follow Leggett who solved the gap equation of Eq. 3.42 and number conservation

$$N = \sum_{\mathbf{k}} \left[1 - \frac{\varepsilon_{\mathbf{k}} - \mu}{E_{\mathbf{k}}} \right], \tag{3.48}$$

self consistently in the crossover. The beauty of Leggett's crossover model Eqs. 3.42 and 3.48 is that it describes the crossover continuously as function of the parameter $x = 1/ak_F$ from the BCS limit ($x \rightarrow -\infty$) over the unitarity limit ($x = 0$) to the BEC limit ($x \rightarrow +\infty$). It is important to include (pairing) interactions in the chemical potential through number conservation as it changes the chemical potential dramatically.

In the dilute (BCS) limit the gap equation leads to the standard BCS gap of Eq. 3.43—not including the Gorkov correction. The chemical potential is $\mu = E_F$ and does not include the standard mean field Hartree-Fock correction of a dilute gas.

In the BEC limit the pairing gap approaches

$$\Delta = 4E_F/\sqrt{3\pi a k_F}. \tag{3.49}$$

The chemical potential approaches half of the molecular binding energy $\varepsilon_M = -\hbar^2/ma^2$,

$$\mu = -\frac{\hbar^2}{2ma^2} + \frac{\pi\hbar^2 na}{m}, \tag{3.50}$$

plus the BEC mean field corresponding to a molecular scattering length of $a_M = 2a$. Four-body [46], Monte Carlo calculations [22] and experiments [23] do, however, indicate that $a_M \simeq 0.6a$.

On the BCS side the minimum quasiparticle energy is Δ and occur when $k = k_F$. On the BEC side the chemical potential is negative and the minimum quasiparticle excitation energy is the quasiparticle energy for $\mathbf{k} = 0$

$$E_{qp} = \sqrt{\mu^2 + \Delta^2}. \tag{3.51}$$

The quasiparticle energy is observed in the spin excitation response function [77, 87, 88].

In the Leggett model the gap vanishes in the BEC limit at a critical temperature $T_c^{\text{dissoc}} = |\varepsilon_M|/\ln(|\varepsilon_M|/E_F)^{3/2}$, which is smaller than the quasi-particle excitation energy. It is not the on-set temperature for superfluidity but rather a molecular pair dissociation temperature [14, 15]. The onset of superfluidity occurs at a lower critical temperature for a molecular BEC, T_c^{BEC}.

The Leggett model fails in the BEC limit because of the basic assumption that only opposite momenta fermions (zero total momentum pairs) can pair. Pairs with non-zero momenta are thermal excitations of molecular bosons and including such degrees of freedom lowers the critical temperatures increasingly towards the (molecular) BEC limit.

3.3.4 NSR

The model of Noziéres & Schmit-Rink (NSR) [14, 15] extends the Leggett model so that it correctly describes the critical temperature in the molecular BEC limit. We will therefore give a brief outline of NSR with emphasis on how pair motion is included and how it corrects the Leggett model in the BEC limit. Also, the NSR approach is formulated such that it applies to optical lattices discussed in Sect. 3.5 with few but crucial differences.

In the NSR model the (molecular) pair momentum $\mathbf{q}$ is included in the two-particle correlation function. To lowest order it is given by the propagator for two free atoms

$$
\begin{aligned}
\Pi(\mathbf{q}, \omega_\nu) &= \frac{T}{V} \sum_{\mathbf{k}, \omega_m} G_0(\mathbf{k}, i\omega_m) G_0(\mathbf{q} - \mathbf{k}, i\omega_\nu - i\omega_m) \\
&= \frac{1}{V} \sum_{\mathbf{k}} \frac{1 - f(\varepsilon_{\mathbf{q}/2+\mathbf{k}}) - f(\varepsilon_{\mathbf{q}/2-\mathbf{k}})}{\omega_\nu + 2\mu - \varepsilon_{\mathbf{q}/2+\mathbf{k}} - \varepsilon_{\mathbf{q}/2-\mathbf{k}}},
\end{aligned}
\tag{3.52}
$$

In Eq. 3.52 the Matsubara frequencies $\omega_m = m 2\pi T i$ have been summed over integers m.

We now scale the potential by λ and sum up interactions energies $(U\Pi)^n$ from $n = 1, 2, \ldots$ ladders. We obtain for the expectation value of the interaction energy in state λ gives

$$
\langle \lambda U \rangle = -T \sum_{\mathbf{q}, \omega_\nu} \frac{\lambda U \Pi(\mathbf{q}, \omega_\nu)}{1 - \lambda U \Pi(\mathbf{q}, \omega_\nu)}.
\tag{3.53}
$$

From the Hellmann-Feynmann theorem we now obtain the interaction part of the free energy

$$
\mathbf{\Omega}_{int} = \int_0^1 \frac{dx}{\lambda} \langle \lambda U \rangle = T \sum_{\mathbf{q}, \omega_\nu} \ln[1 - U\Pi(\mathbf{q}, \omega_\nu)].
\tag{3.54}
$$

As in the gap equation (3.42) large momenta contributions are removed by replacing $U\Pi$ by $U_0\Pi_r$, where the renormalized propagator is

$$
\Pi_r(\mathbf{q}, \omega_\nu) = \Pi(\mathbf{q}, \omega_\nu) + \frac{1}{V} \sum_{\mathbf{k}} \frac{1}{2\varepsilon_{\mathbf{k}}}.
\tag{3.55}
$$

Inserting into Eq. 3.54 gives the thermodynamic potential

$$
\mathbf{\Omega} = \mathbf{\Omega}_0 + T \sum_{\mathbf{q}, \omega_\nu} \ln[1 - U_0 \Pi_r(\mathbf{q}, \omega_\nu)],
\tag{3.56}
$$

where $\mathbf{\Omega}_0 = -2T \sum_{\mathbf{q}} \ln[1 + e^{(\varepsilon_q - \mu)/T}]$ is the free energy for non-interacting Fermions. The frequency sum in Eq. 3.56 can, using the residue theorem, be converted to an ω-integral of the Bose distribution function $(\exp(\omega/T) - 1)^{-1}$ around the real axis, where the logarithm in Eq. 3.56 has a cut.

In the BEC limit, where μ is large and negative, it follows from Eq. 3.52 that $1 - U_0 \Pi_r(\mathbf{q}, \omega)$ is proportional to $\omega - \varepsilon_M(q) + 2\mu$, where

$$
\varepsilon_M(q) = -\frac{\hbar^2}{ma^2} + \frac{\hbar^2 q^2}{4m},
\tag{3.57}
$$

Fig. 3.5 Superfluid transition temperatures from the Leggett crossover, Gorkov and NSR
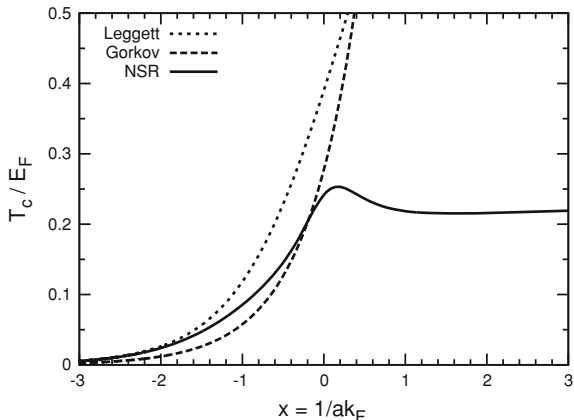
is the molecular binding and kinetic energy of a pair with mass 2m and momentum $\mathbf{q}$. Therefore the derivative of $\ln[1 - U_0 \Pi_r(\mathbf{q}, \omega_\nu)]$ with respect to μ has a pole at $\omega = \varepsilon_M(q) - 2\mu$ with residue 2. Using the residue theorem again we obtain the number equation

$$N \simeq -\frac{d\,\Omega}{d\,\mu} \simeq 2\sum_{\mathbf{q}} \frac{1}{e^{(\varepsilon_M(q)-2\mu)/T} - 1}. \tag{3.58}$$

Here we have ignored the contribution to the thermodynamic potential Ω_0 from free Fermions which is negligible in the BEC limit. The number equation is simply that of a free Bose gas as opposed to that of a Fermi gas Eq. 3.48 in the BCS limit.

Whereas the number equation changes qualitatively from free Fermi atoms to free Bose molecules in the crossover, the gap equation is unchanged and given by Eq. 3.42. In the BEC limit the gap equation simply yields that the chemical potential is half the molecular binding energy, $\mu = -\hbar^2/2ma^2$. The number equation now gives

$$T_c = \frac{\pi}{[2\zeta(3/2)]^{2/3}} \frac{\hbar^2 n^{2/3}}{m} \simeq 0.218 E_F, \tag{3.59}$$

i.e., the critical temperature is independent of the pairing interaction and given by T_c^{BEC} for the molecular BEC. At T_c^{BEC} all bosons are thermally excited with none remaining at zero momentum.

In general the gap equation (3.58) and number conservation $N = d\,\Omega/d\mu$ with $\Omega = \Omega_0 + \Omega_{int}$ from Eq. 3.54 have to be solved self-consistently for the critical temperature and the chemical potential in the BCS–BEC crossover. The result for T_c is shown in Fig. 3.5. One notices that NSR predicts a maximum near the unitarity limit. Recent experiments find $T_c/E_F = 0.19 \pm 0.02$ [34] whereas earlier found $T_c/E_F = 0.29 \pm 0.03$ [4]. This is compatible with the gap $\Delta = 0.44 E_F$ found in [89].

Fig. 3.6 Shells in a 3D
harmonic oscillator trap
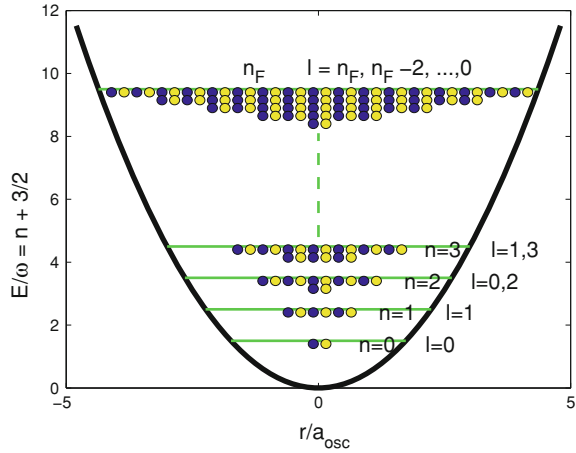
Although the NSR model is a qualitative improvement of the Leggett model by
correctly describing T_c in the BEC limit, it still omits a number of effects such as
particle-hole contributions, selfenergies and induced interactions from the medium.
Consequently, the Hartree field and Gorkov corrections are not included, and in the
BEC limit the molecule-molecule scattering length 2a implied by Eq. 3.50 is a factor
~ 3 too large [46]. More elaborate models [76, 77, 90] include some of these effects
and do not find a maximum for T_c/E_F around the unitarity limit (Fig. 3.6).

3.4 Atomic Traps and Nuclei

Traps are necessary for confining the atoms and creates a density distribution that is
maximal at central density and decrease towards the cloud size R where it vanishes.
Thus all densities are present at once which can be difficult to separate experimentally
in order to extract the (n,T) phase diagram.

From a nuclear point of view harmonic oscillator (HO) traps are wonderful toy
systems since they provide confined systems, which are a first approximation to the
nuclear mean field potential. Additionally we can tune the interactions and therefore
the level splitting and pairing. Also millions of Fermi atoms can be confined and not
just the $\lesssim 250$ neutron and protons in nuclei limited by fission. Therefore one can
study the crossover from few to infinite number of particles which is necessary in
order to e.g. link pairing in nuclei to that in neutron and nuclear matter. Similarities
between the (prolate) nuclear mean field and cigar shaped optical traps can also be
exploited in studies of shell structures, pairing and collective modes.

3.4.1 Scaling in Atomic Traps

In a noninteracting two spin balanced Fermi gas in a spherically symmetric HO potential at zero temperature the particles fill HO shells of energy $n\hbar\omega$, $n = 1, 2, \ldots, n_F$ up to the Fermi shell $n_F = (3N)^{1/3}$ with Fermi energy $E_F = n_F\hbar\omega$. For a sufficiently large number N of particles confined in a (shallow) trap the system size R is so long that density variations and the extent of possible phase transition interfaces can be ignored and one can apply the local density and the Thomas-Fermi approximation. Here the total chemical potential is given by the sum of the harmonic oscillator (HO) trap potential and the local chemical potential $\mu_i = dE/dN_i$

$$\mu_i(r) + \frac{1}{2}m\omega^2 r^2 = \frac{1}{2}m\omega^2 R_i^2, \qquad (3.60)$$

which must be constant over the lattice for all components $i = 1, 2, \ldots$. It can therefore be set to its value at the its edge R_i, which gives the r.h.s. in Eq. 3.60. We shall mainly discuss spin balanced two component systems where the chemical potential and radii are equal. The equation of state determines $\mu(n)$ in terms of the universal function of Eq. 3.60.

In the dilute limit and in the unitarity limits $\mu = \xi\hbar^2 k_F^2/2m$, where $\xi = 1$ and $\xi = 1 + \beta(0)$ respectively. In both cases Eq. 3.60 gives $n(r) = k_F^3(r)/3\pi^2 = n_0 (1 - r^2/R^2)^{3/2}$, where $n_0 = \xi^{-3/4}(2n_F)^{3/2}/3\pi^2 a_{osc}^3$ is the central density and $R = \xi^{1/4}\sqrt{2n_F}a_{osc}$ the cloud size; $a_{osc} = \sqrt{\hbar/m\omega}$ is the oscillator length. The attraction contracts the gas to a higher central density such that $R \propto k_F^{-1}(0) \propto \xi^{1/4}$. The total energy of the trapped gas is $E/N = (3/8)\xi^{1/2}n_F\hbar\omega$.

For a more general equation of state $P \propto n^{\gamma+1}$ or $\mu \propto n^\gamma$ with polytropic index γ the equilibrium density is $n_{eq} = n_0(1 - r^2/R^2)^{1/\gamma}$, where $R^2 = 2(\gamma + 1) P_0/\gamma n_0 m\omega^2$. P_0 and n_0 are the pressure and density in the centre of the trap. In both the non-interacting and the unitary limit $\gamma = 2/3$ whereas $\gamma = 1$ in the BEC limit and for a bose gas.

As suggested in [16] it is convenient to measure the density along the axial axis integrated over transverse cross section $n(z) = \int n(r)\, dx\, dy$. From the Gibbs-Duhem equation $(dP/d\mu)_T = n$ using Eq. 3.60 we obtain the pressure in the centre along the axial axis by integrating over transverse coordinates

$$P(z) = \frac{m\omega_\perp}{2\pi}n(z). \qquad (3.61)$$

At the same time the chemical potential $\mu(z) = m\omega_z(R_z^2 - z^2)$ is known by measuring the size $R(z)$ of the cloud along the z-axis. Thus $P(\mu)$ can be measured and the equation of state extracted at any temperature.

In a Fermi liquid we obtain from Eqs. 3.9 and 3.14 that the pressure w.r.t. that in a free Fermi gas is

$$P(x, T)/P_{FG} = 1 + \beta(x) + \frac{5\pi^2}{8}\frac{m^*}{m}\frac{T^2}{E_F^2}. \qquad (3.62)$$

Detailed measurements of the intensive variables (T, P, μ) gives $\beta(0) = -0.49(2)$ and $m^*/m = 1.13(3)$ [34].

3.4.2 Collective Modes

Tickling the trapped atoms sets them into oscillations at certain eigen-frequencies called collective modes. Such giant dipole and quadrupole modes have been important for studying nuclei [91]. The collective modes can be calculated from the equation of state and the Euler equation

$$mn\frac{\partial \mathbf{v}}{\partial t} = -\nabla\left(P + nm\sum_i \omega_i^2 r_i^2\right), \tag{3.63}$$

where $\mathbf{v} = \partial \mathbf{r}/\partial t$ is the local velocity. The last term is the gradient of a generally deformed HO potential. The Euler equation can be solved analytically for polytropic equation of states. For spherical symmetric 3D traps one finds collective modes at eigen frequencies $\omega_{\eta l}$ for a mode with $\eta = 0, 1, 2, \ldots$ nodes and angular momentum l given by [47]

$$\frac{\omega_{\eta l}^2}{\omega_0^2} = l + 2\eta[\gamma(\eta + l + 1/2) + 1]. \tag{3.64}$$

Similar expressions exist for modes in deformed traps [92] which have been measured in detail [4, 28].

For attractive interactions the system is superfluid at zero temperature and therefore irrotational with a quenched moment of inertia. As the temperature is increased above T_c the moment of inertia increase to rigid value and hereby the critical temperature $T_c = 0.19(1)E_F$ is found [93]. Deformed system can be rotated but has a quenched moment of inertia $I = \delta^2 I_{rigid}$ [94].

3.4.3 Shell Structure and Pairing in Atomic Traps

The pairing gap generally increase with the level degeneracy or density of states [91]. For pairing in a single level of angular momentum l or shell n_F the pairing gap scales with the number of degenerate states $(2l + 1)$ or $(n_F + 1)(n_F + 2)$ respectively. If levels are split or distributed the gap depends on the density of levels around the Fermi level as in the uniform case of Eq. 3.43.

For very weak interactions the level splitting of single particle levels $l = n_F, n_F - 2, \ldots, 1$ or 0 in the HO shell n_F is smaller than the pairing gap when there are sufficiently few ($n_F \lesssim 10$) atoms in a HO potential. The pairing occurs between all states in the shell leading to the supergap [95, 96]
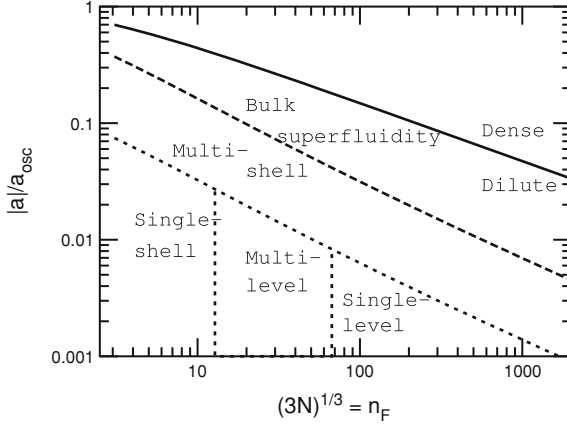
Fig. 3.7 Diagram displaying the regimes for the various pairing mechanisms (see text) at zero temperature in HO traps vs. the number of particles $N = n_F^3/3$ and the interaction strength a. The dotted lines indicate the transitions between single-shell pairing $\Delta = G$, multi-level, single-level, and multi-shell pairing. At the dashed line determined by $2G \ln(\gamma n_F) = \hbar\omega$ the pairing gap is $\Delta \simeq \hbar\omega$, and it marks the transition from multi-shell pairing to bulk superfluidity Eq. 3.45. The pairing gap is $\Delta = 0.54 E_F$ above the full line $\rho|a|^3 \geq 1$, which separates the dilute from the dense gas (From [95, 96])

$$G = \frac{32\sqrt{2n_F + 3}}{15\pi^2} \frac{|a|}{a_{osc}} \hbar\omega. \qquad (3.65)$$

For more particles or stronger interactions the situation becomes more complicated depending on the gap size with respect to the level splitting as shown in Fig. 3.7. Increasing the number of particles cause level splitting so that pairing is reduced to multi-level and eventually single level pairing. Increasing the interaction strength increase pairing to nearby shells [95, 96] referred to as multi-shell pairing in Fig. 3.7. The general case can be solved within the Bogoliubov-deGennes equations [57, 95, 96]. For stronger interactions and many particles the pairing approaches that in a uniform or bulk system, and eventually dense system with $|a|k_F > 1$ and the unitarity limit is reached.

The various pairing mechanisms and phases of Fig. 3.7 can be studied at low temperatures is which hopefully will be reached in the near future.

3.4.4 Pairing in Nuclei

We can exploit some interesting similarities between pairing in nuclei [91, 97] and that of Fermi atoms in traps [57, 95, 96]. To a first approximation the nuclear mean field is often taken as harmonic oscillator (HO) potential just as the optical traps. Secondly, the residual pairing interaction between nucleons is taken as a short range (delta function) interaction as for cold atoms.

Before these result can be applied to nuclei there are, however, a number of differences that must be taken into account. Large nuclei have approximately constant central density $\rho_0 \simeq 0.14\,\text{fm}^{-3}$ and Fermi energy E_F in bulk. Therefore the HO frequency, which is fitted to the nuclear mean field, decreases with the number of nucleons $A = N + Z$, where N now is the number of neutrons and Z the number of protons in the nucleus, as $\hbar\omega \simeq E_F/n_F \simeq 41\text{MeV}/A^{1/3}$. In the valley of β-stability the number of protons is $Z \simeq A/(2 + 0.0155A^{2/3})$. Therefore in medium and large nuclei the difference between the Fermi energies of protons and neutrons exceeds the pairing gap so that pairing between protons and neutrons does not occur.

Secondly, the nuclear mean field deviates from a HO potential by being almost constant inside the nucleus and vanish outside. The resulting net anharmonic nuclear field is *stronger* and *opposite* in sign to the corresponding (anharmonic) mean field in atomic traps. Therefore, the level splitting is larger and the ordering of the l-levels is reversed. In addition, a strong spin-orbit force splits the single particle states of total angular momentum $j = l \pm 1/2$, such that the $j = n_F + 1/2$ is lowered down to the shell $(n_F - 1)$ below. The level splitting can be parametrized by a single parameter taken from analyses of nuclear spectra. It increases with shell number up to $n_F \simeq 6$ for heavy nuclei. Due to the strong spin-orbit force the $j = l \pm 1/2$ states are split and the $j = n_F + 1/2$ is lowered down to the shell below. The magic numbers become $N, Z = 8, 14, 28, 50, 82, 126, 184, \ldots$, etc. rather than the h.o. filled shell particle numbers $N, Z = 2, 8, 20, 40, 70, 112, 168, 240, \ldots$, etc.

The pairing gaps and quasi-particle energies can now be calculated by solving the Bogoliubov-deGennes gap equation [95, 96] which are shown in Fig. 3.8 for neutrons. The strong level splitting in nuclei has the effect that pairing is strongest when the shell is half filled and weak near closed shells simply because there are fewer states available for pairing, i.e., the level density is smaller. Averaging over several shells, however, the mean gap is well approximated by the supergap because the reduction in pairing due to level splitting is compensated by additional pairing to nearby shells. Since $\hbar\omega$ scale as $\sim A^{-1/3}$ and $a_{osc} \propto n_F^{1/2}$ the single-shell pairing gap also scales as $G \sim A^{-1/3}$. Therefore, the pairing gaps in light and medium mass nuclei scale approximately as [57]

$$\Delta \simeq G \simeq \frac{|a|}{0.41\,\text{fm}} \frac{5.5\text{MeV}}{A^{1/3}}. \tag{3.66}$$

As shown in Fig. 3.8 the supergap does not depend on the level-splitting and is therefore a robust prediction for the average magnitude and mass scaling of pairing gaps in nuclei.

The data on neutron and proton pairing is obtained from the odd-even staggering of nuclear binding energies $B(N, Z)$. It has been shown that mean field contributions can be removed [100] by using the three-point filter $\Delta^{(3)}(N) = (-1)^N[B(N - 1, Z)/2 + B(N + 1, Z)/2 - B(N, Z)]$. We compare in Fig. 3.8 to the experimental $\Delta^{(3)}(N)$ averaged over isotopes with the calculated gaps. The analogous for protons $\Delta^{(3)}(Z)$ averaged over isotones compare similarly to Bogolibov-deGennes calculations
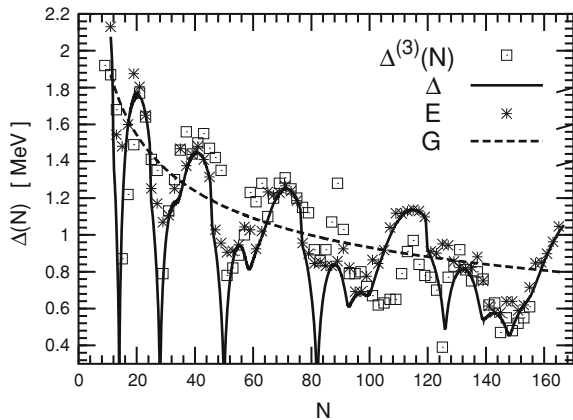
Fig. 3.8 Neutron pairing energies versus the number of neutrons. The experimental odd-even staggering energies $\Delta^{(3)}(N)$ are averaged over isotopes [98–100]. The calculated gaps Δ and quasiparticle energies E are obtained from the gap equation (see text) with effective coupling strength $a = -0.41$ fm. The supergap G is shown with dashed line. See [57] for details and corresponding plot for protons

[57, 95, 96]. In the calculations the effective coupling is the only adjustable parameter which is fitted to the experimental data. For both neutrons and protons we extract $a \simeq -0.41$ fm.

Considering the simplicity of the model it describes a large number of experimental gaps fairly well on average. In a number of cases, however, the calculated pairing gaps differ significantly from the measured neutron gaps. Some of these deviations can be attributed to the crude single particle level spectra assumed.

The pairing in nuclear matter can now be estimated once the effective interaction has been determined using Eq. 3.43. Note that the effective interaction includes induced interactions. Inserting $a = -0.41$ fm and $k_F = 1.3$ fm^{-1} at nuclear saturation density, $\rho_0 = 0.15$ fm^{-3}, we obtain the proton and neutron pairing gaps

$$\Delta \simeq 1.1 \text{MeV}, \tag{3.67}$$

in the bulk of very large nuclei and in symmetric nuclear matter at nuclear saturation density. This number is compatible with earlier calculations [64–67] of the $^1S_0$ pairing gap in nuclear and neutron star matter around normal nuclear matter densities.

Neutron star matter has a wide range of densities and is asymmetric, $Z/A \sim 0.1$, above normal nuclear matter densities. One can attempt to estimate of the pairing gaps as function of density from the gap in bulk, Eq. 3.43, with $a \simeq -0.41$ fm and the neutron or proton Fermi wave numbers $k_F^{N,Z} = (3\pi^2 \rho_{N,Z})^{1/3}$ as function of densities. However, the effective interaction a is density dependent. At higher densities we expect that the effective interaction becomes repulsive as is the case for the nuclear mean field at a few times nuclear saturation density. At lower densities the

effective scattering length should approach that in vacuum which for neutron-neutron scattering is $a(^1S_0) \simeq -18$ fm.

In spite of several simplifying approximations in this atomic trap model for nuclear pairing it provides at least a qualitative description of pairing in most nuclei. The effective interaction $a = -0.41$ fm is the same for both neutrons and protons which reflects that both are close to forming bound states. At central densities $x = 1/ak_F \simeq -1.9$, i.e. on the BCS side of the unitarity limit.

3.4.5 Quark and Gluon Matter

The Coulomb and QCD interactions $\sim g^2/r$ or their Fourier transform $\sim g^2/q^2$ are long range and therefore contrary to the short range interactions underlying universality. The long range QED and QCD interactions requires screening of infrared divergences [101] whereas in unitary gases ultraviolet cutoffs are provided by renormalizing the short range interaction in terms of the scattering length. Never the less a number of similarities have appeared.

Confinement is caused by strong color fields between quarks and gluons which forms bound state hadrons at temperatures below $T \lesssim T_{QGP} \simeq 160$ MeV and densities below a few times normal nuclear matter density, $\rho_0 = 0.15$ fm^{-1}. These may again form a nuclear liquid at temperatures below the nucleon gas critical temperature $T \lesssim T_{NG} \simeq 15$ MeV for a four component nuclear system as discussed above. In the hadron gas the interparticle distance is larger than the confinement interaction range, and the quark molecules can therefore be viewed as a molecular gas. However, color neutrality requires either Fermi molecules of three quarks (baryons) or quark-antiquark Bose pairs (mesons). Of the two phase transitions in the molecular gas of hadrons only the neutron gas can be viewed as a BCS–BEC crossover as discussed in Sect. 3.2.6. The instability and first order transition of a four-component nuclear gas was discussed in Sect. 3.2.6 can be viewed as multi-component crossover. Here the effective scattering length is that between neutrons and protons $a \sim 20$ fm, i.e. on the molecular BEC side, and the nuclear matter is in the unitarity limit in the sense that $x = 1/ak_F \sim 0_+$ although they now are kept in place by short range repulsive forces. The transition from nuclear to quark matter or a hadron gas to a quark-gluon plasma is quite different because the interaction range is always of order the interparticle distance. The strong short range repulsive forces between nucleons leads to a strongly correlated wavefunction as in hard sphere scattering and the strongly correlated nuclear fluid. In this case the Gutzwiller approximation of Ref. [75] is valid and the matter does not undergo a ferromagnetic transition separating the unlike components (see Fig. 3.1). As seen from the quark-gluon side one can define a "crossover parameter" $x \sim \Lambda_{QCD}/k_F$ which at high densities is in the unitarity limit. With decreasing densities the running coupling constant Λ_{QCD} diverges when the quark-gluon plasma undergoes a first order transition to a hadron gas with $x \gtrsim 1$.

Quark pairing also have similarities to pairing in nuclear and multi-component atomic gases. Color superconductivity between the 2 spin, 8 color and 2–3 flavor

states is very sensitive to flavor imbalance [11]. If the strange quark mass is small the up, down and strange quark Fermi levels are close. If pairing is sufficiently strong such that the gap exceeds the Fermi level splitting all flavors can pair. It is amazing that properties of pairing in quark matter, which may exist in unaccessible cores of neutron stars, can be studied in tabletop experiments with ultracold multicomponent spin-imbalanced Fermi atomic gases.

Another interesting similarity is elliptic flow. The overlap zone in semi-central high energy nuclear collisions is prolate (cigar shaped) as are optical traps. In subsequent expansion the hydrodynamics forces stronger expansion in the direction where systems is narrowest initially. This makes the momentum distribution azimuthally asymmetric—referred to as elliptic flow. Results indicate that both "liquids", the QGP/hadronic and ultracold unitary atomic gas, expand as almost perfect fluids initially i.e. their viscosities are record breaking low [102–104].

Correlations can reveal the quantum phase structure. Originally Hanbury-Brown & Twiss measured the Bose-Einstein correlations between stellar photons and determined the diameters of nearby stars. Similar correlations between mesons in high energy nuclear collisions have been exploited to determine the freezeout size of the collision zones [105, 106]. Also Fermi anticorrelations have been observed between baryons. In ultracold atomic systems analogous "noise" correlations have been found near the BCS–BEC crossover due to pairing [23–26]. Bragg peaks have been observed for bosons in 3D [107] and 2D [108] lattices, and dips for 3D fermions in [109].

3.5 Optical Lattices

A standing wave can be generated by shining lasers onto traps which generates a 3D cubic or 2D square lattice potential with spacing $\lambda = 2\pi/k$, which is half the laser wavelength. The lattice height V_0 varies with laser intensity and the scattering length. In the tight binding approximation the onsite coupling

$$U = E_R a k \sqrt{8/\pi}\, \xi^3 \tag{3.68}$$

and hopping parameter

$$t = E_R (2/\sqrt{\pi})\xi^3 e^{-2\xi^2}, \tag{3.69}$$

where $E_R = \hbar^2 k^2/2m$ is the recoil energy and $\xi = (V_0/E_R)^{1/4}$. Varying V_0 and the scattering length a near Feshbach resonances allows us to tune the Hubbard parameters U and t (Fig. 3.9).

The lattice constant λ introduces another lengths scale so that the thermodynamic quantities generally depend on both density and interaction strength. Therefore universality is broken except for low filling which corresponds to dilute Fermi gases.

The Hubbard Hamiltonian on a D-dimensional lattice describes optical lattices that are sufficiently deep for a one-band model to apply,
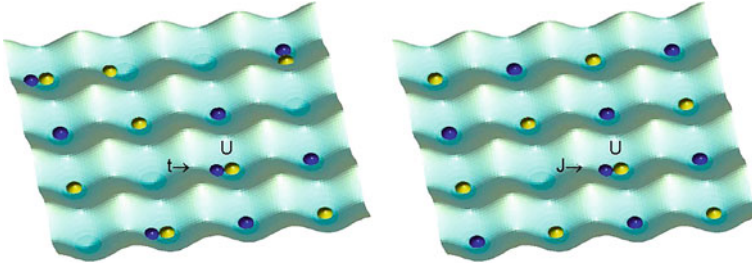
Fig. 3.9 2D optical lattices loaded with fermions in two spin states (*yellow and blue*) at half filling. For onsite attraction ($U < 0$, *left*) opposite spins tend to pair. For onsite repulsion ($U > 0$, *right*) the ground state is an AF with virtual hopping $J = 4t^2/U$

$$H = \sum_{i,\sigma<\sigma'} U_{\sigma,\sigma'}\hat{n}_{i\sigma}\hat{n}_{i\sigma'} - t \sum_{\langle ij\rangle,\sigma} \hat{a}_{i\sigma}^{\dagger}\hat{a}_{j\sigma}. \tag{3.70}$$

Here $\hat{a}_{i\sigma}^{\dagger}$ is the Fermi creation operator of the hyperspin states $\sigma = 1, 2, \ldots, \nu$, $n_{i\sigma} = \hat{a}_{i\sigma}^{\dagger}\hat{a}_{i\sigma}$ the density and $\langle ij\rangle$ denotes nearest neighbours with hopping parameter t. Due to particle-hole symmetry results for a given site filling n also applies to $2 - n$.

The Hubbard model is of fundamental importance in condensed matter physics where it explains properties of Mott insulators, antiferromagnets, d-wave superconductivity, etc. The Hubbard model can only be solved in 1D for fermions but a number of models and numerical calculations have given insight in the various phases and order parameters. Optical lattices may tell us the answers in a few years.

3.5.1 On-Site Attraction and Pairing

We start by investigating s-wave pairing between to spin balanced states due to an attractive on-site interaction $U < 0$. The mean field gap equation for singlet superfluidity at zero temperature is [110, 111]

$$\Delta_{\mathbf{p}'} = -\frac{1}{M}\sum_{\mathbf{p}} U(\mathbf{p}',\mathbf{p})\Delta_{\mathbf{p}}\frac{\tanh(E_{\mathbf{p}}/2T)}{2E_{\mathbf{p}}}, \tag{3.71}$$

where M is the number of lattice points and $E_{\mathbf{p}} = \sqrt{(\varepsilon_{\mathbf{p}} - \mu)^2 + \Delta_{\mathbf{p}}^2}$ with $\varepsilon_{\mathbf{p}} = 2t\sum_{i=1,D}(1 - \cos p_i)$.

The density $n = 1 - \sum_{\mathbf{p}}(\varepsilon_{\mathbf{p}}/E_{\mathbf{p}})\tanh(E_{\mathbf{p}}/2T)/M$, is also the filling fraction in units where the lattice constant is unity. Momenta are in the first Brillouin zone only $|p_i| \leq \pi$ taking $\lambda = 1$ for convenience.

Due to particle-hole symmetry results also apply replacing the density by $(2 - n)$ and chemical potentials by $(4Dt - \mu)$, where $4Dt$ is the bandwidth in D dimensions. At low filling $\varepsilon_p = tp^2$ and results also apply to uniform systems replacing $t = 1/2m$.

3.5.1.1 Pairing in the Dilute Limit

We first calculate the zero temperature gaps for weak attraction $|U| \ll t$ excluding induced interactions. The s-wave gap $\Delta_{\mathbf{p}'} = \Delta_0$ is then momentum-independent because the interaction U is. The gap equation 3.71 reduces to: $1 = -(U_0/M) \sum_{\mathbf{p}} 1/2 E_{\mathbf{p}}$, from which the gap can be calculated analytically at low and half filling to leading orders in 3D and 2D (for 1D see, e.g. [112]).

The 3D lattice has a critical coupling [87, 88]

$$U_c = -M \bigg/ \left(\sum_{\mathbf{q}} 1/2\varepsilon_{\mathbf{q}} \right) = -8\sqrt{2}t \bigg/ \left[\sum_{l=0}^{\infty} P_{2l}(\sqrt{9/8})(2l-1)!!/2^{2l}l! \right] \simeq -7.913t, \tag{3.72}$$

where a two-body bound state can be formed at zero density ($\mu = 0$). This threshold corresponds to the unitarity limit of infinite scattering length in the uniform system and naturally enters the sum in the gap equation. The dilute gap becomes to leading orders

$$\Delta_0^{3D} = \frac{8}{e^2} \mu \, \exp\left[\frac{4\pi^2 t}{k_F} \left(\frac{1}{U} - \frac{1}{U_c} \right) \right], n \ll 1, \tag{3.73}$$

at low densities where $\mu = t k_F^2 \ll t$. The level density at the Fermi surface $N(\mu) = k_F/(4\pi^2 t)$ enters in the exponent as in standard BCS theory. U_c acts as a cutoff in the one-band Hubbard model which in the uniform (continuum) limit is absorbed into the scattering length a. Thus Eq. 3.73 is the finite lattice equivalent of the gap in the uniform system $\Delta_0^{3D} = (8/e^2)\mu \, \exp(\pi/2k_F a)$, with $U^{-1} - U_c^{-1} = U_0^{-1}$, where $U_0 = 4\pi a/m$ as in the uniform case, such that threshold $U = U_c$ corresponds to $|a| = \infty$.

Near half filling the level density is surprisingly constant $N(\mu) \simeq 0.143/t$ in a wide range $4t \leq \mu \leq 8t$ around half filling. To leading orders the gap becomes [110, 111]

$$\Delta_0^{3D} = \alpha \, t \, \exp\left[\frac{1}{N(\mu)U} \right], n \simeq 1, \tag{3.74}$$

where the prefactor $\alpha \simeq 6.544$ can be calculated numerically.

The 2D lattice has a superfluid s-wave gap that be calculated from the gap equation [113]

$$\Delta_0^{2D} = \sqrt{8\pi\mu t} \, \exp\left[\frac{4\pi t}{U} \right], n \ll 1, \tag{3.75}$$

when the density $n = k_F^2 / 2\pi$ is small. The 2D level density is $N(\mu) = 1/(4\pi t)$. Eq. 3.75 assumes that the on-site coupling and the gap are small such that $\Delta_0^{2D} \lesssim \mu$. This is not fulfilled at sufficiently low densities where instead $\Delta_0^{2D} = 4\pi t$ $\exp(8\pi t/U)$, which also is the two-body binding energy in 2D at zero density. There is always a two-body bound state in 2D with purely attractive interaction and therefore U_c vanishes. In 3D a similar pair condensate (a molecular BEC) appears when $a > 0$ corresponding to $U < U_c$.

For intermediate fillings the pairing is more complicated in 2D. Near half filling $n \simeq 1$ the level density $N(\varepsilon) = \ln(16t/|\varepsilon - 4t|)/(2\pi^2 t)$ has a logarithmic singularity due to the van Hove singularity. Calculating the r.h.s. of the gap equation therefore gives a double log: $1 = |U|/(4\pi^2) \ln^2(32t/\Delta_0^{2D})$, to leading logarithmic orders, resulting in the gap when $n \simeq 1$ [113]

$$\Delta_0^{2D} = 32t \exp(-2\pi\sqrt{t/|U|}). \tag{3.76}$$

In the strong coupling limit $\Delta = |U|/2$.

3.5.1.2 Induced Interactions on the Lattice

In 3D the induced interactions are at low densities $n \ll 1$ the same as in the uniform case Eq. 3.44 and reduce gaps and T_c by a factor $(4e)^{1/3} \simeq 2.2$. Near half filling the reduction factor is ~ 3.9 for weak interactions. For stronger interactions the induced interactions are enhanced [84] leading to a reduction of the gap by a factor ~ 25 when $U = -3t$.

In 2D the induced interactions suppress the gap by a factor e in the dilute limit [114] but are divergent at half filling due to the singular level density [84]. The induced interactions have been calculated for general spin polarization and number of components in 3D and 2D optical lattices [85].

3.5.1.3 Crossover and the BEC Limit

As the interactions become stronger the Fermi gas gradually undergoes crossover to a molecular BEC. On the lattice, however, the finite bandwidth automatically provides a cutoff which affects the crossover and changes the BEC limit on the lattice qualitatively from the uniform case. We shall describe this crossover employing the NSR model as above for the uniform case but with a finite bandwidth. Our starting point is again the two-particle correlation function of Eq. 3.52. In the BEC limit (large negative chemical potential) we find from Eq. 3.52 that $1 - U\Pi(\mathbf{q}, \omega)$ is proportional to $\omega - \varepsilon_M(q) + 2\mu$ as in NSR, where now the molecular boson energy is

$$\varepsilon_M(\mathbf{q}) = -U + J \sum_{i=1,3} [1 - \cos(q_i)] \tag{3.77}$$

Fig. 3.10 Superfluid transition temperatures in a 3D lattice at half filling for the NSR model, the Heisenberg model within (Weiss) mean field $T_c = 1.5J$ and Monte Carlo. "Gorkov" is the weakly attractive limit of Eq. 3.74 reduced by a factor 3.9 due to induced interactions
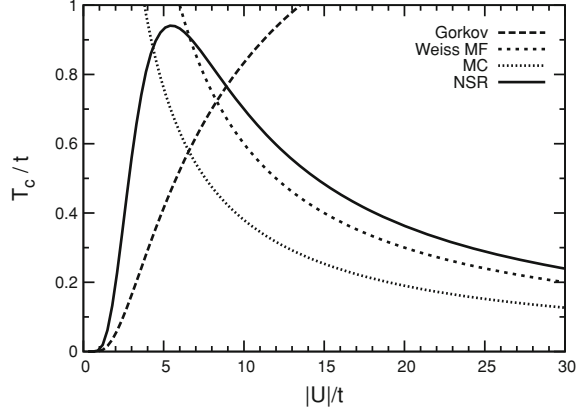
with $J = 4t^2/U$. Therefore the number equation reduces to the condition for BEC in an ideal Bose gas as Eq. 3.58

$$N \simeq -\frac{d\Omega_{int}}{d\mu} \simeq 2 \sum_{\mathbf{q}} \frac{1}{e^{(\varepsilon_M(\mathbf{q})-2\mu)/T} - 1}, \qquad (3.78)$$

but with the molecular boson energy of Eq. 3.77 in stead of 3.57. The gap equation at T_c yields a chemical potential $\mu = -U/2$ in the BEC limit, and inserting this in the number equation gives a critical temperature

$$T_c = \frac{2\pi}{[2\zeta(3/2)]^{2/3}} n^{2/3} J \simeq 2.09 n^{2/3} J, \qquad (3.79)$$

when $n \ll 1$. For n = 1 we obtain $T_c = 1.71J$.

The crossover in optical lattices is shown in Fig. 3.10 at half filling. The critical temperature decreases with interaction strength in the BEC limit and thus differs from uniform systems where it approaches a constant T_c^{BEC}.

The Hubbard model can in the BEC limit be mapped onto the Heisenberg spin model in a magnetic field for which accurate calculations exist, which allows us to check the NSR and other models [115]. Half filling corresponds precisely to zero magnetic field, i.e.,

$$H = J \sum_{\langle ij \rangle} \mathbf{S}_i \cdot \mathbf{S}_j, \qquad (3.80)$$

and the Néel temperature corresponds to $T_N = T_c$ in the BEC limit. In (Weiss molecular) mean field theory $T_N = 1.5J$, quantum Monte Carlo $T_N = 0.95J$, high temperature expansions $T_N = 0.90J$, as compared to $T_c = 1.71J$ in NSR. Extending the NSR model with charge and spin density fluctuations gives a smaller value $T_c \simeq 0.4J$ because molecular repulsion is overestimated [115].

3.5.2 On-Site Repulsion

On-site repulsive interactions $U > 0$ generally disfavours doubly occupied sites and lead to a Mott gap at half filling of order $\sim U/2$ at very low temperatures. Mott insulator (MI) transitions are observed for bosons in traps at fillings $n = 1, 2, 3, 4, 5, \ldots$ [23–27]. For fermions the phase diagram is more complex, an antiferromagnet (AF) at and near half filling, a paramagnet (PM) otherwise and possible a ferromagnet for very strong repulsion [116]. Furthermore the AF phase may be unstable towards phase separation to two coexisting phases: an AF at half filling and a PM at filling slightly below or above half filling. The co-existing phase may also be unstable towards stripes. In 2D these phase also compete with d-wave superfluidity.

3.5.2.1 Antiferromagnetism

At half filling fermions are known to form a MI in 1D [117] whereas in two and higher dimensions an antiferromagnetic (AF) insulator is found in Monte-Carlo calculations. The AF alternating spin order on the lattice is driven by the simple fact that hopping can occur to a neighbouring site only if it is occupied by an opposite spin, which generates a super-exchange coupling.

We will here study the AF phase and its transition to a paramagnet at the Néel temperature T_N. Remarkably, it undergoes a crossover very similar to the critical temperature described above for attractive interactions, i.e. $T_N \sim T_c$. For weak repulsion T_N can be determined from the mean field gap equation

$$1 = \frac{U}{M} \sum_{\mathbf{p}} \frac{\tanh(\varepsilon_{\mathbf{p}}/2T_N)}{2\varepsilon_{\mathbf{p}}}, \qquad (3.81)$$

which is identical to that for T_c of Eq. 3.71 except for the sign of U. Therefore $T_N = T_c$ within mean field. Induced interactions can be included as for T_c as described above and therefore reduce T_N by a factor ~ 3.7 at half filling [118, 119] which is very similar to the reduction of T_c by induced interactions as discussed above.

For stronger coupling fluctuations reduce the mean field gap and T_N as for the NSR model of T_c. At very strong coupling the repulsive Hubbard model can at half filling also be mapped onto the Heisenberg model with coupling J. Therefore T_N is also in this limit given by T_c as function of $|U|$, and the details of the crossover [120, 121] are quite similar to the BCS–BEC crossover.

The AF phase transition masks a possible MI phase. By frustrating the system one can, however, remove the AF order and observe the MI transition by a vanishing conductivity or compressibility. Another way to suppress the AF order is to include multi-components which naturally upsets the alternating spin up/down order in a two-component AF. The limit of many components actually correspond to a Bose system where MI transitions are found at every integer filling.

3.5.2.2 Phase Separation

Mean field theory provides a first impression of the phases competing for the ground state and has the advantage that it is computationally simple as compared to more complicated theories. The MF equations for the Hubbard model are standard and we refer to, e.g., Refs. [110, 111, 122]. The energy densities can be calculated within the Hartree-Fock approximation for the paramagnetic (PM), ferromagnetic (FM), antiferromagnetic (AF) and phase separation (PS).

At low density $n \ll 1$ the ground state is that of a dilute paramagnetic (PM) gas with energy

$$\varepsilon_{PM} = -4tn + \left[\frac{\pi}{2}t + \frac{1}{4}U\right]n^2 + \mathcal{O}(n^3). \qquad (3.82)$$

In units where the lattice spacing is unity ($\lambda = 1$) this energy per site is also the energy density, and the density is the site filling fraction.

Near half filling $\varepsilon_{PM} = -(4/\pi)^2 t + U/4$, which becomes positive when the repulsive interaction exceeds $U/t \geq 64/\pi^2 \simeq 6.5$. The PM phase is then no longer the ground state. In a state with only one spin the antisymmetry of the wavefunction automatically removes double occupancy and the repulsive term $Un^2/4$ in Eq. 3.82 disappears. Such a ferromagnetic (FM) state always has negative energy $\varepsilon_{FM} \leq 0$ for $n \leq 1$ and is a candidate for the ground state. AF, linear AF [123] and stripe phases are other competing candidates. Furthermore phase separation (PS) and mixed phases can occur near half filling. When $U \lesssim 7t$ the ground state of the 2D MF Hubbard model undergoes transitions from an AF at half filling to a mixed AF + PM phase for doping $\delta = 1 - n$ up to a finite (U dependent) value $|\delta| \leq \delta_s$ where after a pure PM phase takes over [122]. For larger U the phase diagram is more complicated with a pure as well as mixed FM phases between the AF and PM phases. A finite next neighbour hopping term t' makes the phase diagram asymmetric around half filling, extends the AF phase and changes the phase diagram considerably.

At half filling $n = 1$ the ground state is an AF. Near half filling $0 \leq |\delta| \ll 1$ the MF equations and AF energy can be expanded as

$$\varepsilon_{AF} = -J\left[1 + \frac{3}{2}\delta + 2\delta^2 + \cdots\right]. \qquad (3.83)$$

The concave dependence on δ signals phase separation into a mixed phase of AF and PM by the Maxwell construction. The PS extends from the AF phase with density $n = 1$ to a PM phase. Dynamical mean field theory [116] find that for particle or hole doping $\delta = 1 - n$, phase separation occurs between an AF at half filling and a paramagnet at a critical filling δ_s depending on the coupling. It has a maximum $\delta_s \simeq 0.14$ around the coupling $U \simeq 9t$ where also T_N is maximal. PS is not observed in cuprates. It may be inhibited by long range Coulomb repulsion between electrons in cuprates as will be discussed later.

3.5.2.3 d-Wave Superfluidity in 2D

d-wave or $d_{x^2-y^2}$ pairing is particular favoured on a square lattice with on-site repulsion (which disfavours s-wave pairing) and nearest neighbour attraction as e.g. provided by the super-exchange coupling in the Hubbard and Heisenberg models with two spin components. The discussion below emphasizes how 2D and also 3D optical lattices can resolve important issues as the existence of phase separation, stripe phases and dSF.

Repulsive onsite interactions $U > 0$ inhibit s-wave pairing unless a longer range attraction is added such as a nearest neighbour interaction $V \sum_{\langle ij \rangle} n_i n_j$. Super-exchange in the Hubbard model generates a similar nearest neighbour (spin-spin) interaction with coupling $J = 4t^2/U$, which is believed to be responsible for high temperature superconductivity [124]. In the limit $U \to \infty$ extended s-wave pairing can occur but requires a strong nearest neighbour attraction $V < -\pi^2 t/2$ [110, 125], whereas d-wave pairing occurs naturally in 2D for even weak nearest neighbour attraction. The d-wave mean field gap equation is (see, e.g., [110, 125])

$$1 = -\frac{V}{4} \sum_{\mathbf{q}} \frac{\eta_{\mathbf{q}}^2}{2E_{\mathbf{q}}}, \tag{3.84}$$

where now $E_{\mathbf{q}} = \sqrt{\varepsilon_{\mathbf{q}}^2 + \Delta_d^2 \eta_{\mathbf{q}}^2}$ and $\eta_{\mathbf{q}} = 2[\cos q_x - \cos q_y]$. At low filling the d-wave gap can be calculated within mean field to leading orders in the density [126]

$$\Delta_d = \frac{t}{\sqrt{n}} \exp\left[\frac{4}{\pi n^2}\left(\frac{t}{V} + c_0 + c_1 n + c_2 n^2\right)\right], \quad n \ll 1, \tag{3.85}$$

The higher order corrections in density are: $c_0 = 4/\pi - 1 \simeq 0.27$, $c_1 = \pi/2 - 1 \simeq 0.57$ and $c_2 \simeq 0.09$.

At half filling we can calculate the d-wave gap within mean field as above if correlations can be ignored, which requires that the on-site interaction is small. To leading logarithmic orders the d-wave pairing gap is

$$\Delta_d = \frac{8}{e^2} t \, \exp\left[-\pi \sqrt{t/|V|}\right], \quad n = 1. \tag{3.86}$$

where again the singular level density leads to a gap similar to Eq. 3.75. It is a coincidence that the prefactor $8/e^2$ is the same as in Eq. 3.73. Correlations are, however, expected to suppress the d-wave mean field gap of Eq. 3.86 near half filling when the on-site repulsion is strong.

T_c can in 3D be calculated from the gap equation 3.71 whereas in 2D a Berezinskii–Kosterlitz–Thouless transition occurs [127] at a lower temperature T_{BKT}. At low density the transition temperature is in 3D generally proportional to the gap with the same prefactor $T_c/\Delta = e^{C_E}/\pi \simeq 0.567$ for both s- and d-wave superfluidity with and without induced interactions [51]. In 2D a mean field critical temperature $T_{MF} > T_{BKT}$ [127], can be calculated from the gap equation as above and we find that

Fig. 3.11 Order parameters for dSF (Δ_{SC}), AF (m) and double occupancy (d) vs. doping $\delta = 1 - n$ for $J/t = 4t/U = 1/3$ in RMFT for the 2D t-J-U model. From [126]
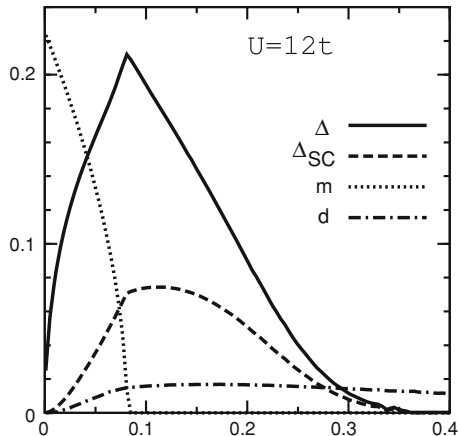
the same ratio applies even near half filling where logarithmic singularities appear. This implies that induced interactions change the mean field critical temperatures by the same factor as the gap of Eq. (3.46).

3.5.2.4 t-J-U Model Predictions

The various competing phases can be studied in the 2D t-J-U model within the Gutzwiller projection method and renormalized mean field theory (RMFT) [126]. This method approximates the strong correlations and generally agrees well with full variational Monte Carlo calculations [128–131]. RMFT predicts phase separation near half filling between an antiferromagnetic (AF) Neél order and a d-wave superfluid (dSF) phase for sufficiently strong onsite repulsion.

The t-J-U model was employed by Laughlin, Zhang and coworkers [129–131] to study AF, HTc and "gossamer superconductivity" in cuprates and organic superconductors. Both the Hubbard and t-J models are included in the t-J-U Hamiltonian $H = H_U + H_t + H_s$ or

$$H = U \sum_i \hat{n}_{i\uparrow} \hat{n}_{i\downarrow} - t \sum_{\langle ij \rangle \sigma} \hat{a}_{i\sigma}^\dagger \hat{a}_{j\sigma} + J \sum_{\langle ij \rangle} \mathbf{S_i S_j}, \qquad (3.87)$$

where $\hat{a}_{i\sigma}$ is the usual Fermi creation operator, $\sigma = (\uparrow, \downarrow)$ is the two hyperfine states $\left(\text{e.g.} \left(-\frac{9}{2}, -\frac{7}{2}\right) \text{ for } {}^{40}\text{K}\right)$, $n_{i\sigma} = \hat{a}_{i\sigma}^\dagger \hat{a}_{i\sigma}$ the density, $\mathbf{S}_i = \sum_{\sigma\sigma'} \hat{a}_{i\sigma}^\dagger \boldsymbol{\sigma}_{\sigma\sigma'} \hat{a}_{i\sigma'}$ and $\langle ij \rangle$ denotes nearest neighbours. U is the on-site repulsive interaction, t the nearest-neighbour hopping parameter and J the spin-spin or super-exchange coupling.

The t-J-U model allows for doubly occupied sites and thereby also MI transitions. As both are observed in optical lattices the t-J-U model is more useful as opposed to the t-J model which allows neither. For large U/t the t-J-U and Hubbard models reduce to the t-J model with spin-spin coupling $J = 4t^2/U$ due to virtual hopping.
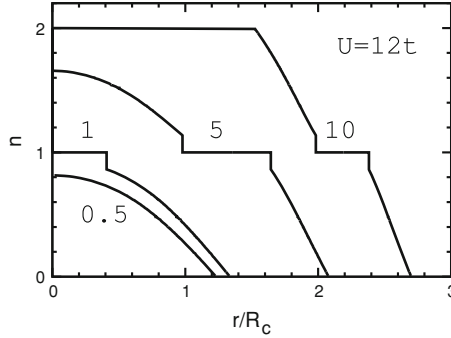
Fig. 3.12 Density distributions of Fermi atoms in a zero temperature 2D optical lattice confined by a harmonic trap for $U = 12t$ ($J = t/3$) filled with the number of particles $N/N_c = 0.5, 1, 5,$ and 10. The density discontinuities from $n \simeq 1.14$ and $n \simeq 0.86$ to the antiferromagnetic insulator at $n = 1$ due to PS between dSF and AF are absent for stripe phases (see text). Thus the density distribution changes to a *Capitol* form rather than the usual *wedding cake* form for Mott insulators

At finite J and U the t-J-U model is to some extent double counting with respect to the Hubbard model with $J = 0$. However, when RMFT is applied the virtual hopping and resulting spin-spin interaction vanishes in the Hubbard (t-U) model, i.e. $J = 0$, which justifies the explicit inclusion of the spin Hamiltonian as done in the t-J-U model.

The AF phase dominates near half filling suppressing the superfluid order parameter. The AF order parameter is $m = (\sqrt{3}/2)\sqrt{1 - T/T_N}$ at temperatures just below the critical Néel temperature $T_N = 2J$. The d-wave superfluid gap depends sensitively on coupling, magnetization and double occupancy as seen in Fig. 3.11. It competes with the AF order parameter and dominates slightly away from half filling as seen in Fig. 3.11.

However, near half filling phase separation is found between an AF phase at half filling coexisting with a dSC phase at a density $|x| \lesssim 0.12$ as determined by the Maxwell construction. The PS is found to terminate at coupling $J \simeq 0.55t$ ($U \simeq 7.3t$) where the double occupancy undergoes a first order transion from zero to a finite value. The PS has a curious effect on the density distribution in a trap as shown in Fig. 3.12. The trap size is of order $R_c = \sqrt{8t/\hbar\omega}a_{osc}$, and the number of trapped particles $N = 2\pi \int_0^R n(r)r\,dr$ is of order $N_c = \pi R_c^2$ in 2D.

The density distributions and MI plateaus have been measured experimentally for Bose atoms in optical lattices by, e.g., differentiating between singly and doubly occupied sites [107]. Recently Schneider et al. [132] have measured column densities for Fermi atoms in optical lattices and find evidence for incompressible Mott and band insulator phases. Even lower temperatures are required for observing the AF and dSF phases and the density discontinuities due to PS.

Spin and charge density waves in form of stripes are not included in the above RMFT calculations. Stripes are observed in several cuprates [133] whereas numerical calculations are model dependent. Long range Coulomb frustration can explain why

Fig. 3.13 Typical phase diagram of high temperature superconductors. Neél temperatures (T_N) and critical temperatures for d-wave superconductivity (T_c) are plotted vs. particle ($\delta < 0$) and hole ($\delta > 0$) doping. T^* is the pseudogap (see text)
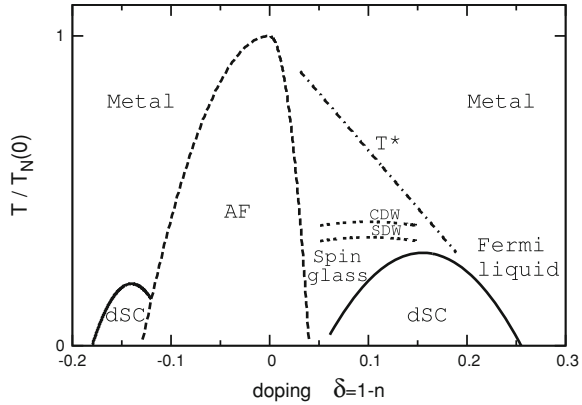
PS is replaced by stripes and an AF phase at very low doping [126] as observed in cuprates.

3.5.3 High Temperature Superconductivity in Optical Lattices

After Kamerlingh Onnes discovered superconductivity in 1911 it took nearly half a century before Bardeen, Cooper and Schriefer (BCS) in 1957 understood the physics behind the manybody pairing mechanism. In comparison half the time has passed since Bednorz & Müller in 1986 discovered high temperature superconductivity (HTc). Although important progress has been made on the mechanisms behind this important phenomenon, a full understanding is still lacking. Most agree that HTc is d-wave and can probably be described by the one band Hubbard model on a two-dimensional (2D) lattice with strong repulsive on-site interaction $U \sim 3t$, but no consensus has been reached on the origins and influence of the pseudogap, charge and spin gaps, stripes, etc.

A sketch of a typical phase diagrams of HTc cuprates is shown in Fig. 3.13. The antiferromagnetic phase extends around half filling and is asymmetric due to next neighbour hopping terms t'. The Neél temperature drops rapidly from its maximal value $T_N(\delta = 0)$ - somewhat lower than the Fermi temperature. The maximal $T_c \lesssim$ 100K are collected in the "Uemura" plot [134]. It is typically between one and two orders of magnitude lower than the Fermi energy which again is several orders of magnitude larger than conventional superconductors as Nb, Sn, Al, Zn.

Optical lattices hold great promises for solving the HTc problem [135, 136] since densities, temperatures, interactions, spins, etc. can be varied in a controlled manner and studied in experiments, where the sub nanometer lattice constants in solids are upscaled to micrometers in optical lattices. One serious experimental hindrance remains, namely the extremely low temperatures required, but we have hopes that

the experimentalists can overcome this problem rapidly as in so many other cases with cold atoms—and it certainly does not hinder theoretical studies.

3.5.3.1 Stripes

Stripes have been discovered in low-energy magnetic neutron scattering in doped cuprates at incommensurate longitudinal and horizontal charge and spin wave numbers [133], e.g. $\mathbf{Q}_c = (2\pi/\lambda)(0, \pm \delta/\delta_s)$ and $\mathbf{Q}_s = (\pi/\lambda)(1, 1 \pm \delta/\delta_s)$ for the longitudinal charge and spin wave numbers respectively. Here, the average doping or holes are all in the stripes with hole filling δ_s embedded in an AF with filling no holes (half filled) such that the average hole density is $\delta = 1 - n$. The stripes are half filled $\delta_s = 1/2$ for low average dopings $\delta \leq 1/8$ but at larger doping it increases linearly to filled stripes $\delta_s = 1$ such that $\delta/\delta_s = 1/4$ remains constant. Therefore the charge (spin) density stripes appear with periodic distance d *(2d)* depending on doping as $d = \lambda\delta_s/\delta$. The stripe distance decreases with increasing doping until $\delta \geq 1/8$, where after the stripes remain at a distance $d = 4\lambda$. The stripes act as anti-phase domain walls and the spin density wave therefore has periodicity twice the length of the charge-density wave. When $1/8 \leq \delta \leq 1/4$ the 2D spin orientation therefore looks like

$$\cdots \downarrow\uparrow\downarrow \circ \uparrow\downarrow\uparrow \circ \downarrow\uparrow\downarrow \circ \uparrow\downarrow\uparrow \circ \cdots$$
$$\cdots \uparrow\downarrow\uparrow \circ \downarrow\uparrow\downarrow \circ \uparrow\downarrow\uparrow \circ \downarrow\uparrow\downarrow \circ \cdots$$
$$\cdots \downarrow\uparrow\downarrow \circ \uparrow\downarrow\uparrow \circ \downarrow\uparrow\downarrow \circ \uparrow\downarrow\uparrow \circ \cdots$$

etc., in case of vertical stripes $\circ$. They are spin-balanced at filling $1 - \delta_s$ and occur with periodicity $d = 4\lambda$.

Diagonal, horizontal/vertical, checkerboard stripe solutions have been found in a number of models. In MF models Zaanen and Gunnarson [137–140] found stripes of hole density $\delta_s = 1$ that are vertical or horizontal for $U/t \lesssim 3 - 4$ and diagonal otherwise. In DMRG calculations [141, 142] stripes with hole density $\delta_s = 1/2$ are found in agreement with experiments [133]. Stripes appear at temperatures above HTc but below the pseudogap T^* [143, 144] and there are some evidence that charge density waves appear at slightly higher temperatures than spin density waves.

The stripe phase is a specific ordered mixed AF and PM phase and is a continuous transition between the two pure phases as function of density. Similar mixed phase solutions are believed to occur in neutron star crusts between nuclear matter and a neutron gas and possibly also between quark and nuclear matter [145, 146]. In both cases Coulomb energies add complexity to the mixed phases by ordering them into structured crystallic phases.

The various MI, AF, stripe, d- and s-wave superfluid phases have distinct density and momentum correlation functions [23–27, 107–109, 126, 147, 148].

3.5.3.2 Coulomb Frustration

Long range Coulomb interactions prevent phase separation into two bulk phases of different charge density but may not inhibit the formation of localized holes, pairs and stripes. The phase diagrams of cuprates with such Coulomb frustration and optical lattices without may therefore be very different. Coulomb frustration in cuprates has been discussed in connection with stripes (see e.g. [149–151]).

In the following we shall consider the stripes as rods with charge less than the surrounding phase and calculate the additional Coulomb energy of such structures. Coulomb energy densities have been calculated for structures of various dimensionality D and volume filling fraction f [145, 146]

$$\varepsilon_C = \frac{2\pi}{D+2}\Delta\rho^2 R^2 f\left[\frac{2}{D-2}\left(1-\frac{D}{2}f^{1-2/D}\right)+f\right]. \qquad (3.88)$$

Here, the charge density difference between the two phases is $\Delta\rho = e\delta_s/\lambda^3$ for the stripes and the volume filling fraction is $f = \delta/\delta_s = \lambda/d$. The dimensionality is $D = 3$ for spherical droplets or bubbles, $D = 2$ for rods and tubes and $D = 1$ for plate-like structures. The diameter of the spheres, rods or the thickness of the plates is of order the distance between layers $2R \sim \lambda \sim 4$ Å. The stripes are rods in a 2D plane but are embedded in a 3D layered structure. For $D = 2$ the expression in the square bracket of Eq. 3.88 reduces to $[\ln(1/f) - 1 + f]$. The logarithm originates from the Coulomb integral $\int^l dz/z$ along the rod length z, which is cutoff by other rods at a length scale $l \sim \lambda\sqrt{f}$. For the cuprates we furthermore reduce the Coulomb field by a dielectric constant of order $\varepsilon_D \sim 5$. The resulting Coulomb energy of stripe or rod-like structures $D = 2$ is

$$\varepsilon_C \simeq \frac{\pi}{8}\frac{\delta_s e^2}{\lambda^4 \varepsilon_D} f\left[\ln(1/f) - 1 + f\right]. \qquad (3.89)$$

Energy costs associated with the interface structures are usually added. Such surface energies are difficult to calculate for the stripes because their extent is only a single lattice constant. In principle they are already included in the stripe models. We will therefore just add the Coulomb energies given above. However, the Coulomb energies and the energy of the systems as a whole, may be reduced by screening and hole hopping into the AF whereby R increases but $\Delta\rho$ and f are reduced.

Inserting numbers $e^2/\hbar c = 1/137$, $\varepsilon_D = 5$, $\delta_s = 1/2$, $\lambda = 4$Å, we find that $\varepsilon_c \simeq 150\text{meV}(\delta/\lambda^3)[\ln(1/f) - 1 + f]$. In comparison the energy gain by changing phase from an AF to a stripe or PM phase increases with doping as $\sim J\delta/\lambda^3$, where $J \simeq (0.1 - 0.2)t \simeq 50 - 100\text{meV}$ in the cuprates. The Coulomb energy of Eq. 3.89 thus dominates at small doping due to the logarithmic singularity and therefore the AF phase of density $n \lesssim 1$ is preferred.

The AF phase is the ground state as long as the Coulomb energy of Eq. 3.89 exceeds Jx/λ^3 corresponding to doping less than

$$\delta_{AF} \simeq \delta_s \exp\left[-\frac{8}{\pi}\frac{J\lambda\varepsilon_D}{\delta_s e^2} - 1\right]. \qquad (3.90)$$

Inserting the above numbers we find $\delta_{AF} \simeq 0.1$ which is within range of the observed $|\delta_{AF}| \simeq 0.03$ for hole doped and $\delta_{AF} \simeq 0.15$ for particle doped cuprates. In MF the particle-hole asymmetry arises from the next-nearest neighbour hopping $t' \simeq -0.3t$ and leads to an AF phase extending from half filling up to a particle doped density $n > 1$ [122].

In the above picture the incommensurate stripe phases at small doping arise due to Coulomb frustration when $t' = 0$. At larger doping the stripes approach each other and will eventually affect each other. Experimentally the stripes undergo a transition from an incommensurate to a commensurate phase at $\delta \simeq 1/8$ corresponding to a stripe periodicity of four lattice spacings.

The Mermin-Wagner theorem states that a continuous symmetry cannot be spontaneously broken at finite temperature in two and lower dimensional systems for sufficiently short range interactions [152, 153], and as a consequence there can be no phase transition at finite temperature. In stead a Berezinskii-Kosterlitz-Thouless transition can occur as found in the 2D Hubbard model [127]. This is incompatible with the phase diagram of HTc cuprates where AF, dSC and stripe phase transitions are observed. These paradoxial transitions and the origin of the phases are still unresolved problems which are largely avoided in the literature. Some suggest that inter-planar couplings effectively increase the dimension above two. Others that correlations lengths are so long that they effectively looks like real transitions. Another suggestion in line with the Coulomb frustration discussed above is that Coulomb interactions are responsible for the phase transitions to stripes and d-wave superconductivity. The long range Coulomb interactions are not comprised in the Mermin-Wagner theorem, which only applies to sufficiently short range interactions $U(r) \propto r^{-\alpha}$ with $\alpha \geq D + 2$ [152, 153].

3.6 Summary and Outlook

In the last decade the physics of cold atoms has brought important understanding of the unitarity limit, universality, the BCS–BEC crossover, and many other properties of cold Fermi atomic systems as describe above and elsewhere in this volume. Presently a number of other interesting phenomena are investigated such as the three component system of ^{6}Li and other multicomponent systems, the ferromagnetic transition at large positive (repulsive) scattering lengths, spin polarized systems, phases in optical lattices, etc.

In these lecture notes the main topic has been universality in crossover. Not only the BCS–BEC crossover in uniform system but also in the repulsive "ferromagnetic" crossover, in multicomponent systems, traps and lattices. The Fermi particles have mostly been atoms but applications to neutron, nuclear and quark matter, nuclei and electrons in solids have been made wherever possible.

In view on the important impact that the question Bertsch posed a decade ago made, we may attempt to ask new relevant questions:

> What are the universal thermodynamic functions and parameters for positive scattering lengths and is there a ferromagnetic phase transition as $a \to +\infty$?

– in both uniform systems and traps. One opinion is given above but a dispute is ongoing [16, 17].

A most promising direction is optical lattices where we may ask:

> What are the phase diagrams of the two and three dimensional Hubbard models as realized in optical lattices?

Attractive interactions will lead to a superfluid state with critical temperatures that have been calculated in detail by Monte Carlo. For repulsive interactions the phase diagram is not very well known in 2D or 3D even for the single band t-U or t-J model. The antiferromagnetic phase may extend to densities near half filling before undergoing a transition to a paramagnet but it is competing with phase separation, stripe phases and a ferromagnetic phase for very strong repulsion. In 2D it also competes with d-wave superconductivity.

A related question, which is particular relevant for HTc, is:

> Does the 2D Hubbard model (as realized in optical lattices) exhibit high temperature superconductivity (as seen in cuprates)?

Because the electrons in HTc have charge they cannot undergo phase separation in bulk, which in turn may be responsible for stripe formation in cuprates in the region of densities and temperatures where also d-wave superconductivity appears. Ultracold Fermi atoms are neutral and can therefore undergo phase separation near half filling as is predicted in some models, e.g. the t-J-U model with Gutzwiller projections discussed above. If so, the region of densities near half filling with antiferromagnetic and d-wave superconductivity do not exist in optical lattices. Cuprates may also have multiband coupling and certainly has next nearest neighbour hoppings, which cause asymmetries in the phase diagrams around half filling for both the AF and dSC phases. In any case, the differences between the phase diagram of the cuprates and the Hubbard model as realized in optical lattices will reveal the important driving mechanisms and possible additional ingredients present in the phenomenon of HTc. 2D optical lattices may also resolve the Mermin-Wagner paradox.

In summary, we have good reasons to believe that ultracold Fermi atoms in traps and optical lattices will in few years bring deeper understanding of strongly correlated systems, its para-, ferro- and antiferromagnetic phases, Mott insulators, stripes, s- and d-wave superfluidity, and high temperature superconductivity.

References

1. Bishop, R.F., Gernoth, K.A., Walet, N.R., Xian, Y. (Eds.): Proc. of 10th Conf. on Recent Progress in Many-Body Theories, *World Sci.* (1999)
2. Baker, G.A.: Int. J. Mod. Phys. B **15**, 1314 (2001)
3. Heiselberg, H.: Phys. Rev. A **63**, 043606 (2001)
4. O'Hara, K.M., Hemmer, S.L., Gehm, M.E., Granade, S.R., Thomas, J.E.: Science **298**, 2179 (2002)
5. Jochim, S., et al.: Phys. Rev. Lett. **91**, 240402 (2003)
6. Bartenstein, M., et al.: ibid. **92**, 120401 (2004)
7. Ottenstein, T.B., Lompe, T., Kohnen, M., Wenz, A.N., Jochim, S.: Phys. Rev. Lett **101**, 203202 (2008)
8. Kitagawa, M. et al.: Phys. Rev. A **77**, 012719 (2008)
9. Spiegelhalder, F.M., et al.: arXiv:0908.1101
10. Wille, E., et al.: Phys. Rev. Lett. **100**, 053201 (2008)
11. Alford, M.G., Rajagopal, K., Schaefer, T., Schmitt, A.: Rev. Mod. Phys **80**, 1455 (2008)
12. Eagles, D.M.: Phys. Rev. **186**, 456 (1969)
13. Leggett A.J.: (1980) in Modern Trends in the Theory of Condensed Matter, Pekalski A., Przystawa R., (ed.) Lect. Notes in Physics 115, (Springer-Verlag) 13
14. Nozières, P., Schmidt-Rink, S., Low, J.: Temp. Phys. **59**, 195 (1982)
15. Sá de Melo, C.A.R., Randeria, M., Engelbrecht, J.R.: Phys. Rev. Lett. **71**, 3202 (1993)
16. Ho, T.-L.: Phys. Rev. Lett. **92**, 090402 (2004)
17. Jo, G-B. et al.: Science **325**, 1521–1524 (2009)
18. Cowell, S., Heiselberg, H., Mazets, I.E., Morales, J., Pandharipande, V.R., Pethick, C.J.: Phys. Rev. Lett. **88**, 210403 (2002)
19. Carlson, J., Chang, S-Y., Pandharipande, V.R., Schmidt, K.E.: Phys. Rev. Lett. **91**, 50401 (2003)
20. Chang, S-Y., et al.: Phys. Rev. A **70**, 043602 (2004)
21. Chang, S-Y., et al.: Nucl. Phys. A **746**, 215 (2004)
22. Astrakharchik, G.E., Boronat, J., Casulleras, J., Giorgini, S.: Phys. Rev. Lett. **93**, 200 (2004)
23. Hadzibabic, Z., Gupta, S., Stan, C.A., Schunck, C.H., Zwierlein, M.W., Dieckmann, K., Ketterle, W.: Phys. Rev. Lett. **91**, 160401 (2003)
24. Zwierlein, M.W., et al.: Phys. Rev. Lett. **91**, 250401 (2003)
25. Zwierlein, M.W., et al.: ibid. **92**, 120403 (2004)
26. Gupta, S., et al.: Science **300**, 47 (2003)
27. Chin, J.K., et al.: Nature **443**, 961 (2006)
28. Bourdel, T., et al.: Phys. Rev. Lett. **91**, 020402 (2003); cond-mat/0403091
29. Cubizolles, J., et al.: cond-mat/0308018
30. Regal, C.A., Jin, D.S.: Phys. Rev. Lett. **90**, 230404 (2003)
31. Regal, C.A., Ticknor, C., Bohn, J.L., Jin, D.S.: cond-mat/0305028
32. Chin, C., Bartenstein, M., Altmeyer, A., Riedl, S., Jochim, S., Hecker Denschlag, J., Grimm, R.: Science **305**, 1128 (2004)
33. Bartenstein, M., et al.: Phys. Rev. Lett. **92**, 203201 (2004)
34. Nascimbene, S., Navon, N., Jiang, K.J., Cevy, F., Salomon, C.: Nature **463**, 1057 (2011)
35. Strecker, K.E., Partridge, G.B., Hulet, R.G.: Phys. Rev. Lett. **91**, 080406 (2003)
36. Partridge, G.B., et al.: Phys. Rev. Lett. **95**, 020404 (2005)
37. Werner, F., Tarruell, L., Castin, Y.: Eur. Phys. J. **B68**, 401 (2009)
38. Heiselberg, H.: J. Phys. B: At. Mol. Opt. Phys. **37**, 1–13 (2004)
39. Holland, M.J., DeMarco, B., Jin, D.S.: Science **285**, 1703 (1999)
40. DeMarco, B., Papp, S.B., Jin, D.S.: Phys. Rev. Lett. **86**, 5409 (2001)
41. Truscott, S.G., et al.: Science **291**, 2570 (2001)
42. Schreck, F., et al.: Phys. Rev. A **64**, 011402 (2001)
43. O'Hara, K.M., et al.: Phys. Rev. Lett. **85**, 2092 (2000)

44. Lee, T.D., Yang, C.N.: Phys. Rev. **105**, 1119 (1957)
45. Belyakov, V.A.: Sov. Phys. JETP **13**, 850 (1961)
46. Petrov, D.S., Salomon, C., Shlyapnikov, G.: Phys. Rev. Lett. **93**, 090404 (2004)
47. Heiselberg, H.: Phys. Rev. Lett. **93**, 040402 (2004)
48. Heiselberg, H.: Phys. Rev. A **73**, 013607 (2006)
49. Yu, Z., Bruun, G.M., Baym, G.: Phys. Rev. A **80**, 023615 (2009)
50. Griffin, A., Zaremba, E.: Phys. Rev. A **956**, 4839 (1997)
51. Pethick, C.J., Smith, H.: Bose-Einstein Condensation in Dilute Gases. Cambridge University Press, Cambridge (2002)
52. Pandharipande, V.R.: Nucl. Phys. A **174**, 641 (1971)
53. Pandharipande, V.R.: Nucl. Phys. A **178**, 123 (1971)
54. Pandharipande, V.R., Bethe, H.A.: Phys. Rev. C **7**, 1312 (1973)
55. Pandharipande, V.R., Schmidt, K.E.: Phys. Rev. A **15**, 2486 (1977)
56. Carlson, J., Heiselberg, H., Pandharipande, V.R.: Phys. Rev. C **63**, 017603 (2001)
57. Heiselberg, H.: Phys. Rev. A **68**, 053616 (2003)
58. Fisher, M.: Phil. Mag. **7**, 1731 (1962)
59. Tan, S.: Ann. Phys. **323**, 2971–2986 (2008)
60. Houbiers, M. et al.: Phys. Rev. A **56**, 4846 (1997)
61. Pandharipande, V.R.: Private Communication, Nordita (1999)
62. Brueckner, K.A., Levinson, C.A., Mahmoud, H.M.: Phys. Rev. **103**, 1353 (1956)
63. Bethe, H.A., Goldstone, J.: Proc. Roy. Soc. (London), **A238**, 551 (1957)
64. Baym, G., Pethick, C.J.: Ann. Rev. Astr. Astrophys. **17**, 415 (1979)
65. Pandharipande, V.R.: Int. J. of Mod. Phys. **B13**, 543 (1999)
66. Heiselberg, H., Pandharipande, V.R.: Ann. Rev. Nucl. Part. Sci. **50**, 481–524 (2000)
67. Heiselberg, H., Hjorth-Jensen, M.: Phys. Rep. **50**, 481–524 (2000)
68. Heiselberg, H., Pethick, C.J., Ravenhall, D.G.: Phys. Rev. Letts. **61**, 818 (1988)
69. Efimov, V.: Phys. Lett. B **33**, 563 (1970)
70. Braaten, E., et al.: Phys. Rev. Lett. **87**, 160407 (2001)
71. Braaten, E., et al.: Phys. Rev. A **63**, 063609 (2001)
72. Jonsell, S., Heiselberg, H., Pethick, C.J.: Phys. Rev. Lett. **88**, 50401 (2002)
73. Stoner, E.: Phil. Mag. **15**, 1018 (1933)
74. Conduit, G.J., Simons, B.D.: arXiv: 0907.372
75. Zhai, H.: arXiv: 0909.4917
76. Pieri, P., Pisani, L., Strinati, G.C.: Phys. Rev. B **70**, 094508 (2004)
77. Bloch, I., Dalibard, J., Zwerger, W.: Rev. Mod. Phys. **80**, 885 (2008)
78. Bardeen, J., Cooper, L.N., Schrieffer, J.R.: Phys. Rev. **108**, 1175 (1957)
79. Bogoliubov, N.N.: Sov. Phys. JETP **7**, 41 (1958)
80. van Hove, L.: Phys. **25**, 849 (1959)
81. Emery, V.J.: Nucl. Phys. **19**, 154 (1960)
82. Gorkov, L.P., Melik-Barkhudarov, T.K.: JETP **13**, 1018 (1961)
83. Heiselberg, H., Pethick, C.J., Smith, H., Viverit, L.: Phys. Rev. Letts. **85**, 2418 (2000)
84. Martikainen, J.-P., Kinnunen, J., Törma, P., Pethick, C.J.: Phys. Rev. Lett. **103**, 260403 (2009)
85. Kim, D.-H., Törma, P., Martikainen, J.-P.: Phys. Rev. Lett. **102**, 245301 (2009)
86. Heiselberg, H.: arXiv:0905.2107
87. Burovski, E., Prokofev, N., Svistunov, B., Troyer, M.: Phys. Rev. Lett. **96**, 160402 (2006)
88. Burovski, E., Kozik, E., Prokof'ev, N., Svistunov, B., Troyer, M.: Phys. Rev. Lett. **101**, 090402 (2008)
89. Schirotzek, A., Shin, Y., Schunck, C.H., Ketterle, W.: arXiv:0808.0026
90. Haussmann, R., Rantner, W., Cerrito, S., Zwerger, W.: Phys. Rev. A **75**, 023610 (2007)
91. Bohr, A., Mottelson, B.R.: Nuclear Structure I+II. Benjamin, New York (1969)
92. Cozzini, M., Stringari, S.: Phys. Rev. A **67**, 041602(R) (2003)
93. Riedl S., et al.: arXiv:0907.3814
94. Clancy, B., Luo, L., Thomas, J.E.: arXiv:0705.2782

95. Heiselberg H., Mottelson B.R.: Phys. Rev. Lett. **88**, 190401 (2002)
96. Bruun, G.M., Heiselberg, H.: Phys. Rev. A **65**, 053407 (2002)
97. Bohr, A., Mottelson, B.R., Pines, D.: Phys. Rev. **110**, 936 (1958)
98. Audi, G., Wapstra, A.H.: Nucl. Phys. **A595**, 409 (1995)
99. Dobaczewski, J., et al.: Phys. Rev. **C63**, 024308 (2001)
100. Dobaczewski, J. et al.: Phys.Rev. C **63**, 024308 (2001)
101. Baym, G., Heiselberg, H.: Phys.Rev. D **56**, 5254–5259 (1997)
102. Thomas, J.E.: Proc. of Quark Matter 09
103. Gelman, B.A., Shuryak, E.V., Zahed, I.: Phys. Rev. A **72**, 043601 (2005)
104. Schaefer, T., Teaney, D.: Rept. Prog. Phys. **72**, 126001 (2009)
105. Baym, G.: Acta. Phys. Polon. B29, 1839–1884 (1998)
106. Heiselberg, H.: Phys. Rev. Lett. **82**, 2052–2055 (1999)
107. Fölling, S. et al.: Nature **434**, 481 (2005)
108. Spielman, I.B., Phillips, W.D., Porto, J.V.: Phys. Rev. Lett. **98**, 080404 (2007)
109. Rom, T., Best, Th., van Oosten, D., Schneider, U., Fölling, S., Paredes, B., Bloch, I.: Nature **444**, 733 (2006)
110. Micnas, R., Ranninger, J., Robaszkiewicz, S., Tabor, S.: Phys. Rev. B **37**, 9410 (1988)
111. Micnas, R., Ranninger, J., Robaszkiewicz, S., Tabor, S.: Rev. Mod. Phys. **67**, 117 (1998)
112. Marsiglio, F.: Phys. Rev. B **55**, 575 (1997)
113. Dupuis, N., Phys. Rev. B **70**, 134502 (2004). Note that the approximate level density used leads to a gap reduced by a factor $2/\pi$ in the dilute limit.
114. Nishida, Y., Son, D.T.: Phys. Rev. A **75**, 063617 (2007)
115. Tamaki, H., Ohashi, Y., Miyake, K.: arXiv:0803.2084
116. Pruschke, T., Zitzler, R.: J. Phys.: Condens. Matter **15**, 7867 (2003)
117. Lieb, E.H., Wu, F.Y.: Phys. Rev. Lett. **20**, 1445 (1968)
118. van Dongen, P.G.J.: Phys. Rev. Lett. **67**, 757 (1991)
119. van Dongen, P.G.J.: Phys. Rev. B **50**, 14016 (1994)
120. Staudt, R., Dzierzawa, M., Muramatsu, A.: Eur. Phys. J. B **17**, 411 (2000)
121. Georges, A.: arXiv:cond-mat/0702122
122. Langmann, E., Wallin, M.: cond-mat/0406608
123. Kusko, C., Markiewicz, R.S.: cond-mat/0102440
124. Anderson, P.W.: Sci. **235**, 1196 (1987)
125. Pistolesi, F., Nozieres, Ph.: Phys. Rev. B **66**, 054501 (2002)
126. Heiselberg, H.: Phys. Rev. A **79**, 063611 (2009)
127. Paiva, T., Scalettar, R., Randeria, M., Trivedi, N.: arXiv:0906.2141
128. See e.g., Edegger, B., Muthukumar, V.N., Gros, C.: Advances in Physics **56**, 927 (2007), and References therein
129. Laughlin, R.B.: arXiv:cond-mat/0209269
130. Zhang, F.C.: Phys. Rev. Lett. **90**, 207002 (2003)
131. Gan, J.Y., Zhang, F.C., Su, Z.B.: Phys. Rev. B **71**, 014508 (2005)
132. Schneider, U. et al.: Sci. **322**, 1520 (2008)
133. Tranquada, J.M. et al.: Phys. Rev. B **54**, 7489 (1996)
134. Uemura, Y.J.: Physica C **282**, 194 (1997)
135. Hofstetter, W., Cirac, J.I., Zoller, P., Demler, E., Lukin, M.D.: Phys. Rev. Lett. **89**, 220407 (2002)
136. Chen, Q., et al.: Phys. Rep. **412**, 1 (2005)
137. Zaanen, J., Gunnarsson, O.L.: Phys. Rev. B **40**, 7391 (1989)
138. Poilblanc, D., Rice, T.M.: Phys. Rev. B **39**, 9749 (1989)
139. Schulz, H.J.: J. Physiq. 50, 2833 (1989)
140. Machida, K.: Physica C **158**, 192 (1989)
141. Scalapino, D.J.: Physics Reports **250**, 329 (1995); and cond-mat/0610710, to appear as Chapter 13 in "Handbook of High Temperature Superconductivity", Schrieffer, J.R. (ed.) Springer, 2006

142. White, S.R., Scalapino, D.J.: Phys. Rev. Lett. **81**, 3227 (1998)
143. Berg, E., Fradkin, E., Kivelson, S.A., Tranquada, J.: New J. Phys. **11**, 115004 (2009)
144. Vojta, M., Adv. Phys. **58**, 699 (2009)
145. Pethick, C.J., Ravenhall, G.R.: Ann. NY Acad. Sci. **647**, 503 (1991)
146. Heiselberg, H., Pethick, C.J., Staubo, E.F.: Phys. Rev. Lett. **70**, 1355 (1993)
147. Köhl, M., Moritz, H., Stöferle, T., Gunter, K., Esslinger, T.: Phys. Rev. Lett. **94**, 080403 (2005)
148. Andersen, B.M., Bruun, G.M.: Phys. Rev. A **76**, 041602(R) (2007)
149. Seibold, G., Castellani, C., Di Castro, C., Grilli, M.: cond-mat/9803184
150. Lorenzana, J., Castellani, C., Di Castro, C.: Phys. Rev. B **64**, 235128 (2001)
151. Arrigoni, E., Fradkin, E., Kivelson, S.A.: Phys. Rev. B **69**, 214519 (2004)
152. Bogoliubov, N.N.: Sowjetunion **6**, 1 (1962)
153. Mermin, N.D., Wagner, H.: Phys. Rev. Lett. **17**, 1133 (1966)

Chapter 4
Pairing Fluctuations Approach to the BCS–BEC Crossover

G. C. Strinati

Abstract This paper gives a survey of a diagrammatic approach for fermionic pairing fluctuations, which are relevant to the BCS–BEC crossover realized with ultracold Fermi gases. Emphasis will be given to the physical intuition about the relevant physical processes that can be associated with this approach. Specific results will be presented for thermodynamic and dynamical quantities, where a critical comparison with alternative diagrammatic approaches will also be attempted.

4.1 Introduction

The BCS–BEC crossover has been of considerably interest over the last several years, especially after its experimental realization with ultracold Fermi (^{6}Li and ^{40}K) gases (for recent reviews about ultracold Fermi gases, see: [1, 2]). By this approach, a *continuous evolution* is sought from a BCS-like situation whereby Cooper pairs are highly overlapping, to a BEC-like situation where composite bosons form out of fermion pairs and condense at sufficiently low temperature. Here, reference to composite bosons stems from the fact that the temperatures of formation and condensation are in this case comparable with each other, in contrast with more conventional point-like bosons for which the two temperatures are quite different (reflecting the fact that their internal structure has no relevance to problems related to condensation). Accordingly, a theoretical description of composite bosons should take into account not only their overall bosonic structure associated with the center-of-mass motion, but also their composite nature in terms of the degrees of freedom of the constituent fermions.

G. C. Strinati (✉)
Dipartimento di Fisica, Università di Camerino,
62032 Camerino, Italy
e-mail: giancarlo.strinati@unicam.it

Fig. 4.1 Scattering length for ^{6}Li atoms versus magnetic field. The *inset* amplifies the behavior of the narrow resonance (adapted from Fig. 2 of Ref. [8])
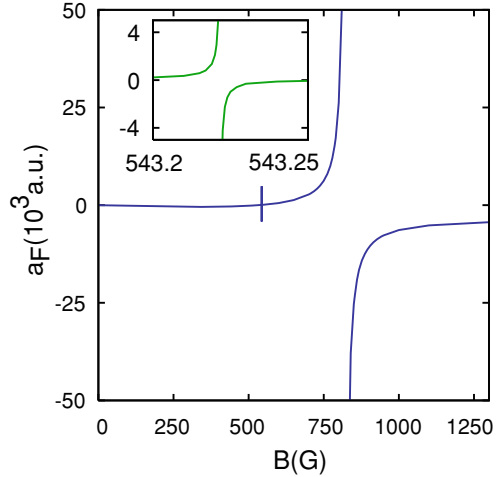
The key feature of ultracold Fermi atoms that has allowed the realization of the BCS–BEC crossover is the possibility of varying essentially at will the strength of the attractive interaction between fermions of different species [3], attraction which results in the formation of Cooper pairs in a medium, on the one hand, and of composite bosons in vacuum, on the other hand, out of the two fermion species. (In the case of ultracold atoms, the spin of an electron is replaced by an analogous quantum number associated with the atomic hyperfine levels.) Owing to this unique possibility, ultracold atoms should be regarded as prototype systems, with respect to others in Nature for which this possibility is hindered. Specifically, in ultracold atomic gases the attractive interaction is varied through the use of the so-called *Fano-Feshbach resonances*, which are characterized by a resonant coupling between the scattering state of two atoms with near-zero energy and a bound state in a close channel [4–6]. Changing (through the variation of a static magnetic field B) the position of the bound state with respect to threshold in a suitable way, one can modify the value of the (fermionic) *scattering length a_F* from negative values before the formation of the bound state in the two-body problem to positive values once the bound state is formed [7]. As an example, Fig. 4.1 shows the scattering length for the collision of two ^{6}Li atoms versus B.

In this context, the dimensionless parameter $(k_F a_F)^{-1}$ acquires a special role for the corresponding many-body system at finite density. Here, the Fermi wave vector k_F of the non-interacting system (which is defined as $k_F = \sqrt{2mE_F}$ both for a homogeneous and a trapped system—see below) is a measure of the (inverse of the) interparticle distance, m being the fermion mass and E_F the Fermi energy of non-interacting fermions (we set $\hbar = 1$ throughout). When the Fano-Feshbach resonance is sufficiently "broad" (like for ^{6}Li and ^{40}K atoms used in experiments thus far), in fact, the many-body fermion problem can be described in a simplified way by a single-channel Hamiltonian with an instantaneous short-range

interaction [8]. The strength of this interaction, in turn, can be parametrized in terms of the above scattering length a_F of the two-body (molecular) problem, which shares the same ultraviolet divergency associated with the short-range character of the two-body potential [9, 10]. In this way one ends up with all physical quantities of interest for the many-body system depending on the interaction only through the parameter $(k_F a_F)^{-1}$.

In terms of this parameter, one finds that for most physical quantities the crossover between the BCS and BEC regimes is exhausted, in practice, within a range ≈ 1 about the unitary limit at $(k_F a_F)^{-1} = 0$ where a_F diverges. Outside this limited range, the BCS and BEC regimes (whereby $(k_F a_F)^{-1} \lesssim -1$ and $1 \lesssim (k_F a_F)^{-1}$, in the order) are characterized by the product $k_F |a_F|$ being quite smaller than unity (corresponding to a diluteness condition), so that theoretical approaches can in principle be controlled in terms of this small quantity in these two separate regimes. No such small parameter evidently exists, however, in the unitary regime about $(k_F a_F)^{-1} = 0$, whose theoretical description consequently constitutes a formidable task.

It is then clear that theoretical treatments of the BCS–BEC crossover should provide as accurate as possible descriptions of the two regimes where the above diluteness condition applies, either in terms of the constituent fermions (BCS regime) or of the composite bosons (BEC regime). Specifically, this has to occur via a *single* fermionic theory that bridges across these two limiting representations, by recovering controlled approximations on both sides of the crossover and providing at the same time a continuous evolution between them, thereby spanning also the unitary regime where use of the theory could a priori not be justified.

The prototype of this kind of approach is represented by the BCS theory itself at *zero temperature*. As remarked originally by Leggett [11] (see also Ref. [12]), the BCS wave function is quite more general than originally thought, in the sense that it contains as an appropriate limit the coherent state associated with a Bose–Einstein condensate of composite bosons made up of opposite-spin fermions. This limit is reached when the occupation numbers of all possible fermionic single-particle states are much less than unity, so that the Fermi surface is completely washed out.

The argument can be made more quantitative by solving the coupled gap and density equations provided by the BCS theory [13, 14] for a homogeneous system at $T = 0$ (for which an analytic solution exists in terms of elliptic integrals [15]), to obtain the gap (order) parameter Δ_0 and fermionic chemical potential μ_0 as functions of $(k_F a_F)^{-1}$ as shown in Fig. 4.2. Note that the chemical potential crosses over as expected, from the value E_F of the Fermi energy of non-interacting fermions in the BCS limit, to (half the value of) the binding energy $\varepsilon_0 = (m a_F^2)^{-1}$ of the two-body (molecular) problem within the single-channel model in the BEC limit. In both limits, $\Delta_0 / |\mu_0| \ll 1$ albeit for different physical reasons.

The BCS theory is a mean-field approximation which relies on the Cooper pairs being highly overlapping in real space [13], so that their effects can be dealt with "on the average". As such, it is expected to be a valid approximation even *at finite temperature* whenever this condition is satisfied. It should accordingly apply to the BCS limit of the BCS–BEC crossover, but not to the unitary or BEC regimes where the typical length scale for correlation between two fermions with different
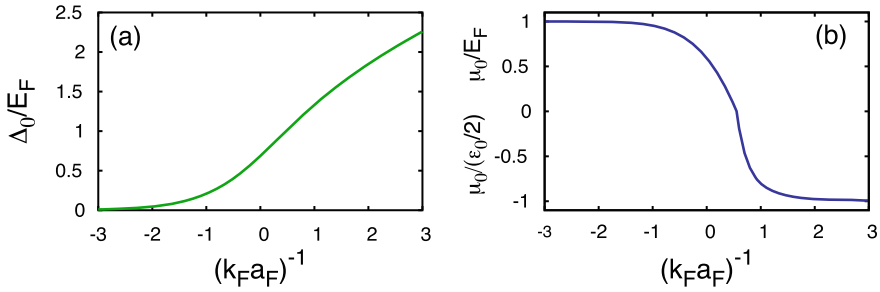
Fig. 4.2 a Gap parameter Δ_0 and **b** chemical potential μ_0 for a homogeneous system at zero temperature versus the coupling parameter $(k_F a_F)^{-1}$, evaluated across the BCS–BEC crossover within mean field

Fig. 4.3 Pair coherence length ξ_{pair} (*dashed line*) and phase coherence (healing) length ξ_{phase} (*full line*) versus $(k_F a_F)^{-1}$, evaluated at zero temperature as in Ref. [15] according to their definitions given in Refs. [16, 17], respectively
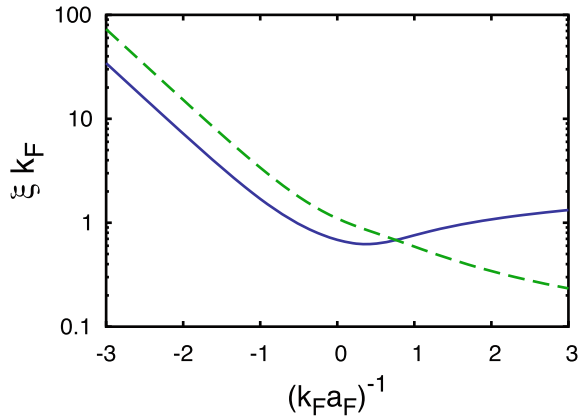
spins becomes comparable with the interparticle spacing k_F^{-1}. This is shown in Fig. 4.3 where the (zero-temperature) *intra-pair* coherence length ξ_{pair} is plotted versus $(k_F a_F)^{-1}$.

It is then evident that, away from the BCS limit, inclusion of *fluctuation corrections* beyond mean field becomes essential to account for the relevant physical properties of the system. An equivalent way of stating the problem is that, away from the BCS limit, the intra- and *inter-pair* coherence lengths are expected to differ considerably from each other. This is also shown in Fig. 4.3 where the inter-pair coherence length ξ_{phase} is reported for comparison. [In the BCS limit the two lengths differ by an irrelevant numerical factor ($\xi_{\text{pair}} \simeq (3/\sqrt{2})\xi_{\text{phase}}$) owing to their independent definitions, so that the two curves in Fig. 4.3 are parallel to each other in this coupling regime.] In particular, in the BEC regime ξ_{pair} corresponds to the size of a composite boson while ξ_{phase} represents the healing length associated with spatial fluctuations of the center-of-mass wave function of composite bosons.

It was indeed within this framework that the BCS–BEC crossover attracted attention also for high-temperature (cuprate) superconductors [18, 19], for which the product $k_F \xi_{pair}$ was estimated to be about $5 \div 10$ in contrast with more conventional superconductors for which it is of the order $10^3 \div 10^5$. Several theoretical works were then put forward on the BCS–BEC crossover in this context [16, 20–24], with the limitations, however, that the origin and characteristics of the attractive interaction at the basis of this crossover were not known for cuprate superconductors. These limitations have eventually been fully removed with the advent of ultracold Fermi atoms, to which we shall limit our considerations in the following.

One related reason to invoke the inclusion of fluctuation corrections beyond mean field stems from the values obtained within BCS theory for the critical temperature at which the order parameter vanishes. Only a numerical solution of the coupled gap and density equations is amenable for generic values of $(k_F a_F)^{-1}$, but analytic results can still be obtained in the BCS and BEC limits. One gets [9]:

$$k_B T_c \simeq \frac{8 E_F e^\gamma}{\pi e^2} \exp\{\pi/(2 a_F k_F)\} \tag{4.1}$$

in the BCS limit (where k_B is Boltzmann constant and γ Euler constant with $e^\gamma/\pi \simeq 0.567$), and

$$k_B T_c \simeq \frac{\varepsilon_0}{2 \ln (\varepsilon_0/E_F)^{3/2}} \tag{4.2}$$

in the BEC limit, respectively. While the result (4.1) corresponds to what is familiar from BCS theory for weak coupling [13], the result (4.2) does *not* coincide with what one would expect in the BEC limit, namely, the expression of the Bose–Einstein condensation temperature $k_B T_{BEC} = 3.31 n_B^{2/3}/(2m)$ where $n_B = n/2$ is the density of composite bosons in terms of the density n of the constituent fermions. On the contrary, the expression (4.2) increases without bound when approaching the BEC limit for $1 \ll (k_F a_F)^{-1}$.

The points is that the critical temperature obtained from the solution of the mean-field equations corresponds to the process of pair formation and not of pair condensation. The two temperatures coincide only in the BCS (weak-coupling) limit (in the weak-coupling limit, the diagrammatic corrections introduced by [25] modify the expression (4.1) for T_c, reducing its prefactor by about 2.2.), where pairs form and condense at the same time. In the BEC (strong-coupling) limit, on the other hand, pairs form at a higher temperature than that at which they eventually condense owing to quantum effects. Accordingly, the expression (4.2) signals the phenomenon of pair dissociation, and as such it must be regarded as a "crossover" temperature T^* which does not correspond to a true phase transition. The complete plot of T^* obtained by solving numerically the mean-field gap and density equations throughout the BCS–BEC crossover is shown for the homogeneous (h) and trapped (t) cases in Fig. 4.4, where it corresponds to the upper dashed and full lines, respectively (the remaining two curves labeled by T_c result instead beyond mean field and will be discussed in Sect. 4.2).
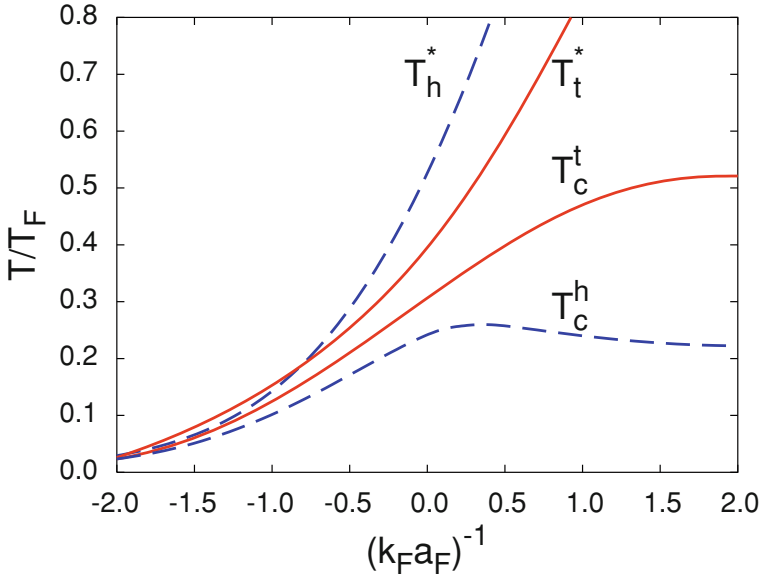
Fig. 4.4 Temperature versus coupling diagram for the trapped (*full lines*) and homogeneous (*dashed lines*) system, where the critical temperature T_c and pair-breaking temperature T^* are shown. Each temperature is normalized to the respective Fermi temperature T_F (adapted from Fig. 1 of Ref. [26])

It is thus evident from the above discussion that the main limitation of the mean-field description we have considered thus far is that it includes only the degrees of freedom internal to the pairs which are associated with pair-breaking, but omits completely the translational ones. The latter are responsible for the collective sound mode, which represents the main source of elementary excitations in the BEC regime [27]. To overcome this severe limitation for a sensible description of the BCS–BEC crossover in terms of a fermionic theory, it is then necessary to go beyond mean field and include *pair-fluctuation* effects as discussed in the next section.

4.2 Inclusion of Pairing Fluctuations

A diagrammatic approach for fermionic pairing fluctuations was first considered by Galitskii [28] for a dilute Fermi gas with strong short-range repulsion [29]. There it was shown that the relevant fermionic self-energy can be taken of the form depicted in Fig. 4.5, where Γ^0 is the pair propagator describing the repeated scattering in the medium between two fermions of opposite spins.

The short-range nature of the potential requires one to introduce at the outset a regularization procedure that eliminates the ultraviolet divergences. This is done by exploiting the two-fermion problem in vacuum, which shares the same sort of
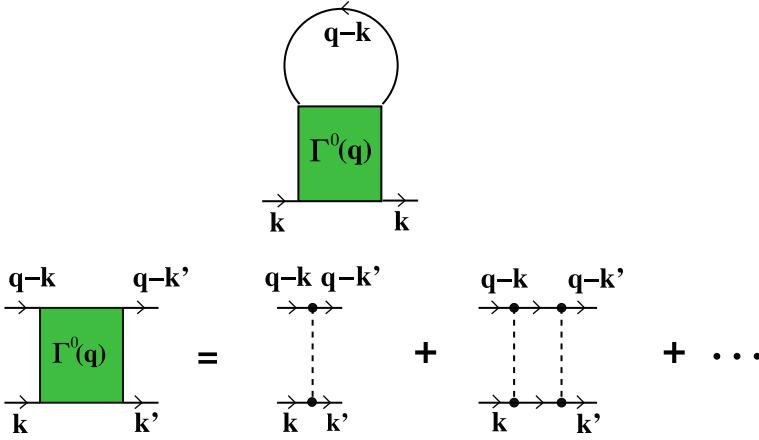
Fig. 4.5 Single-particle fermionic self-energy in the normal phase (*upper panel*) expressed in terms of the pair (*ladder*) propagator Γ^0 between two fermions of opposite spins (*lower panel*). *Full* and *dashed lines* represent the fermionic propagator and interaction potential, respectively, while the labels k (k') and q correspond to fermionic and bosonic four-vectors, in the order

divergences and for which the (positive) strength v_0 of the repulsive interaction can be related to the ultraviolet cutoff k_0 in wave-vector space through the following equation for the two-body t-matrix in the low-energy limit [30]:

$$\frac{m}{4\pi a_F} = \frac{1}{v_0} + \int^{k_0} \frac{d\mathbf{k}}{(2\pi)^3} \frac{m}{\mathbf{k}^2}. \tag{4.3}$$

This relation defines the (fermionic) scattering length a_F, which is positive in this case and remains smaller than the range $\pi/(2k_0)$ of the potential if its strength v_0 is kept finite.

To the leading order in a_F, this self-energy results in a repulsive "mean-field shift" $(4\pi a_F/m)n/2$ of the chemical potential, where n is the total fermion density for both spin components. This is because, to the leading order in a_F, $\Gamma^0(q) \simeq (-4\pi a_F/m)$ and the loop in the upper panel of Fig. 4.5 gives half the fermionic density n (we consider throughout the case of equal populations of spin up and down fermions). Terms up to the second order in a_F were also obtained by the Galitskii original approach [28].

The above choice of the self-energy emphasizes *pair-fluctuation effects* via the repeated scattering of two (opposite spin) fermions in the medium. As such, it has been considered physically relevant *also* to the case of an attractive short-range potential with a negative v_0 [20, 31, 32], for which a_F has the typical resonant behavior of Fig. 4.1 associated with the BCS–BEC crossover. By this extrapolation, the formal structure of the Galitskii self-energy is carried over to the domain of strong coupling, and even further to the repulsive side of the resonance where a molecular state forms (a firm basis for this extrapolation has recently been provided by [33]).

Let's write down explicitly the analytic expressions corresponding to the diagrams depicted in Fig. 4.5, for the simplest case when all fermionic propagators appearing therein are "bare" ones [31]. One has:

$$\Sigma(\mathbf{k}, \omega_n) = -k_B T \sum_\nu \int \frac{d\mathbf{q}}{(2\pi)^3} \Gamma^0(\mathbf{q}, \Omega_\nu) G_0(\mathbf{q} - \mathbf{k}, \Omega_\nu - \omega_n) \qquad (4.4)$$

for the fermionic self-energy, and

$$\frac{(-1)}{\Gamma^0(\mathbf{q}, \Omega_\nu)} = \frac{m}{4\pi a_F} + \int \frac{d\mathbf{k}}{(2\pi)^3} \left[k_B T \sum_n G_0(\mathbf{k}, \omega_n) G_0(\mathbf{q} - \mathbf{k}, \Omega_\nu - \omega_n) - \frac{m}{|\mathbf{k}|^2} \right] \qquad (4.5)$$

for the (inverse of the) pair propagator. Here, $G_0(\mathbf{k}, \omega_n) = [i\omega_n - \xi(\mathbf{k})]^{-1}$ is the bare fermion propagator ($\xi(\mathbf{k}) = \mathbf{k}^2/(2m) - \mu$ being the free-particle dispersion measured with respect to the chemical potential μ), while $\omega_n = \pi k_B T(2n + 1)$ (n integer) and $\Omega_\nu = 2\pi k_B T \nu$ (ν integer) are fermionic and bosonic Matsubara frequencies at temperature T, in the order. Note how the strength v_0 of the attractive interparticle potential has been eliminated in the expression (4.5) in favor of the scattering length a_F via the relation (4.3), which now admits also negative value for a_F consistently with the behavior shown in Fig. 4.1.

With the self-energy (4.4) one dresses the bare fermion propagator to obtain the full propagator

$$G(\mathbf{k}, \omega_n) = \frac{1}{G_0(\mathbf{k}, \omega_n)^{-1} - \Sigma(\mathbf{k}, \omega_n)}, \qquad (4.6)$$

in terms of which the chemical potential can be eventually eliminated in favor of the density via the expression ($\eta = 0^+$):

$$n = 2k_B T \sum_n e^{i\omega_n \eta} \int \frac{d\mathbf{k}}{(2\pi)^3} G(\mathbf{k}, \omega_n). \qquad (4.7)$$

On physical grounds, the relevance of the expressions (4.4) and (4.5) to the BCS–BEC crossover can be appreciated from the following considerations. While in the BCS weak-coupling limit (where $a_F < 0$ and $(k_F a_F)^{-1} \ll -1$) the pair propagator maintains formally the same expression $\Gamma^0(q) \simeq -4\pi a_F/m$ of the repulsive case, in the BEC strong-coupling limit (where $0 < a_F$ and $1 \ll (k_F a_F)^{-1}$) it acquires the polar structure of a free-boson propagator [10, 21]:

$$\Gamma^0(\mathbf{q}, \Omega_\nu) = -\frac{8\pi}{m^2 a_F} \frac{1}{i\Omega_\nu - \mathbf{q}^2/(4m) + \mu_B} \qquad (4.8)$$

where the bosonic chemical potential μ_B reduces to $2\mu + \varepsilon_0$ in this limit when the composite bosons have size $\approx a_F$. In this limit, we may expand the fermionic propagator (4.6) to the lowest order in Σ

$$G(\mathbf{k}, \omega_n) \simeq G_0(\mathbf{k}, \omega_n) + G_0(\mathbf{k}, \omega_n)\Sigma(\mathbf{k}, \omega_n)G_0(\mathbf{k}, \omega_n), \qquad (4.9)$$

and consistently approximate the self-energy (4.4) in the form:

$$\Sigma(\mathbf{k}, \omega_n) \simeq -G_0(-\mathbf{k}, -\omega_n)k_B T \sum_{\nu} e^{i\Omega_\nu \eta} \int \frac{d\mathbf{q}}{(2\pi)^3} \Gamma^0(\mathbf{q}, \Omega_\nu). \qquad (4.10)$$

In this way, we obtain for the density (4.7):

$$n \simeq 2 \int \frac{d\mathbf{k}}{(2\pi)^3} \frac{1}{e^{\xi(\mathbf{k})/(k_B T)} + 1} - 2 \int \frac{d\mathbf{q}}{(2\pi)^3} k_B T \sum_{\nu} \frac{e^{i\Omega_\nu \eta}}{i\Omega_\nu - \mathbf{q}^2/(4m) + \mu_B} \qquad (4.11)$$

where use has been made of the result

$$\int \frac{d\mathbf{k}}{(2\pi)^3} k_B T \sum_{n} G_0(\mathbf{k}, \omega_n)^2 G_0(-\mathbf{k}, -\omega_n) \simeq -\frac{m^2 a_F}{8\pi} \qquad (4.12)$$

which is valid when $\mu \simeq -\varepsilon_0/2$ is the largest energy scale in the problem. Under these circumstances, the first term on the right-hand side of Eq. 4.11 is strongly suppressed by the smallness of the fugacity $e^{\mu/(k_B T)}$, while the second term therein represents the density n_B of a non-interacting system of (composite) bosons with chemical potential μ_B, yielding eventually $n \simeq 2n_B$. With the inclusion of pairing fluctuations, the density equation (4.7) thus reproduces the standard result for the Bose–Einstein condensation temperature $k_B T_{\text{BEC}} = 3.31 n_B^{2/3}/m_B$ where $m_B = 2m$ is the mass of a composite boson.

Note further that, if only the first term on the right-hand side of Eq. 4.11 were retained, one would get for the chemical potential:

$$\frac{\mu}{k_B T} \simeq \ln\left[\frac{n}{2}\left(\frac{2\pi}{mk_B T}\right)^{3/2}\right] \qquad (4.13)$$

which coincides with the classical expression at temperature T [29]. Setting in this expression $\mu \simeq -\varepsilon_0/2$ and $T = T_c$, the value (4.2) for the critical temperature T_c is readily recovered.

Quite generally at any coupling across the BCS–BEC crossover, the critical temperature is obtained from the normal phase by enforcing in Eq. 4.5 the instability condition $1/\Gamma^0(\mathbf{q} = 0, \Omega_\nu = 0) = 0$, in conjunction with the density equation (4.7). The resulting values for T_c are plotted for the homogeneous (h) and trapped (t) cases in Fig. 4.4, where they correspond the lower dashed and full lines, respectively. In both cases, in the temperature window between T_c and T^* composite bosons are formed but not yet condensed.

In the context of the BCS–BEC crossover, pairing fluctuations in the normal phase were first considered by Nozières and Schmitt-Rink (NSR) [34], with the purpose of obtaining a sensible extrapolation of the critical temperature from the BCS to the BEC limit (in Ref. [34] the density equation was obtained by an alternative procedure

via the thermodynamic potential). It was later remarked in Ref. [35] that the NSR procedure corresponds to a t-matrix theory in which one keeps only the lowest-order terms of Eq. 4.9 for all couplings and not just in the BEC limit. In practice, differences between the numerical results, obtained alternatively by the NSR procedure or by the approach based on Eqs. 4.4–4.7 where the expansion (4.9) is avoided, remain sufficiently small even in the unitary region.

The approach for the normal phase based on Eqs. 4.4–4.7 was considered in Ref. [31] to study fermionic single-particle properties above T_c in the homogeneous case, and later extended to consider the effects of a trap. Owing to the presence of two bare fermion propagator G_0 in the particle–particle bubble of Eq. 4.5, this approach is sometimes referred to as the "G_0–G_0 t-matrix". This is to distinguish it from alternative t-matrix approaches, notably: (i) the "G–G_0 t-matrix" approach [36] where one bare G_0 and one self-consistent G enter the particle–particle bubble defining the pair propagator, while a bare G_0 is kept in the definition of the fermionic self-energy (cf. Eq. 4.4); (ii) the "G–G t-matrix" approach [37] where all single-particle Green's functions are self-consistent ones. These alternative approaches were both utilized recently to study the fermionic single-particle spectral function in the normal phase [38, 39]. (It should be mentioned in this context that a t-matrix approach formally similar to the G_0–G_0 one was proposed in Ref. [40], where the bare value of the chemical potential for the non-interacting Fermi gas was inserted in the self-energy in the spirit of a $1/N$ expansion.)

While the G–G_0 and G–G t-matrix approaches have been implemented according to their strict definitions, the pairing-fluctuation approach of Eqs. 4.4–4.7 can be allowed to retain the original flexibility of the diagrammatic fermionic structure which is "modular" in nature. In this sense, it can be progressively improved by including additional self-energy corrections which are regarded important, especially in the BCS and BEC regimes where the approximations can be controlled. This implies, in particular, that the pair propagator in the expression (4.4) can be dressed via "bosonic" self-energy insertions, which lead, for instance, to the Gorkov and Melik-Barkudarov corrections [25] on the BCS side and to the Popov theory for composite bosons [41] on the BEC side. Consideration of the latter is expected to be especially important on physical grounds, since it effectively introduces a repulsive interaction among the composite bosons which ensures, in particular, the stability of the system under compression.

One major shortcoming of the pairing-fluctuation approach of Eqs. 4.4–4.7 is, in fact, that it leads to a diverging compressibility when the temperature is lowered down to T_c from the normal phase. This behavior is shown in Fig. 4.6 at unitarity, and can be ascribed to the fact that the pair propagator (4.5) corresponds to *non-interacting* composite bosons.

The price one has to pay, for setting up theoretical improvements over and above the pairing-fluctuation approach discussed in the present section, is the unavoidable increase of their numerical complexity when calculating physical quantities. Some of these improvements will be discussed in the next section.

The above pairing-fluctuation approach can, in addition, be extended to the super-fluid phase below T_c, whereby the pair propagator acquires a matrix structure that
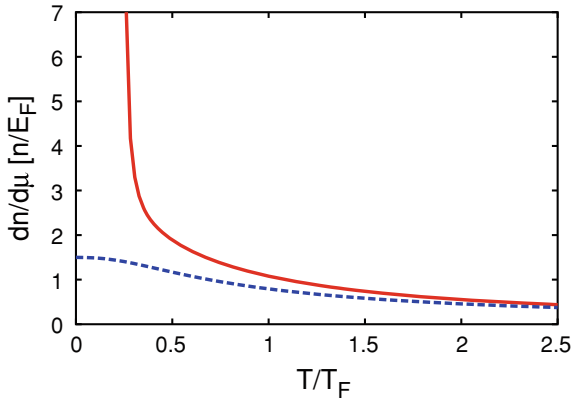
maps onto the bosonic normal and anomalous propagators within the Bogoliubov theory [42, 43]. This extension (together with its Popov refinement [41]) will also be considered in the next section.

4.3 Bogoliubov and Popov Approaches, and the Boson–Boson Residual Interaction

A pairing-fluctuation approach was implemented on physical grounds below T_c in Refs. [42, 43], by adopting a fermionic self-energy in the broken-symmetry phase that represents fermions coupled to superconducting fluctuations in weak coupling and to bosons described by the Bogoliubov theory in strong coupling. This approach has allowed for a systematic study of the BCS–BEC crossover in the temperature range $0 < T < T_c$.

A diagrammatic theory for the BCS–BEC crossover below T_c was actually first proposed by Haussmann [21], by extending the self-consistent t-matrix approximation to the broken-symmetry phase. While the ensuing coupled equations for the chemical potential and order parameter were initially solved at T_c only, an improved version of this self-consistent theory was recently implemented for the whole thermodynamics of the BCS–BEC crossover [37]. We postpone an explicit comparison with this alternative approach to Sect. 4.4, where a selection of numerical results will be presented.

By the approach of Refs. [42, 43], the pair propagator in the broken-symmetry phase has the following matrix structure:

$$\begin{pmatrix} \Gamma_{11}(q) & \Gamma_{12}(q) \\ \Gamma_{21}(q) & \Gamma_{22}(q) \end{pmatrix} = \frac{\begin{pmatrix} A(-q) & B(q) \\ B(q) & A(q) \end{pmatrix}}{A(q)A(-q) - B(q)^2} \tag{4.14}$$

where

$$-A(q) = \frac{m}{4\pi a_F} + \int \frac{d\mathbf{k}}{(2\pi)^3} \left[k_B T \sum_n \mathcal{G}_{11}(k+q)\mathcal{G}_{11}(-k) - \frac{m}{|\mathbf{k}|^2} \right] \quad (4.15)$$

$$B(q) = \int \frac{d\mathbf{k}}{(2\pi)^3} k_B T \sum_n \mathcal{G}_{12}(k+q)\mathcal{G}_{21}(-k). \quad (4.16)$$

This structure is represented diagrammatically in Fig. 4.7a, where only combinations with $\ell_L = \ell'_L$ and $\ell_R = \ell'_R$ survive the regularization we have adopted for the potential (cf. Eq. 4.3). It represents an approximation to the Bethe–Salpeter equation for the fermionic two-particle Green's function in the particle–particle channel. In the above expressions, $q = (\mathbf{q}, \Omega_\nu)$ and $k = (\mathbf{k}, \omega_n)$ are four-vectors, and

$$\mathcal{G}_{11}(\mathbf{k}, \omega_n) = -\frac{\xi(\mathbf{k}) + i\omega_n}{E(\mathbf{k})^2 + \omega_n^2} = -\mathcal{G}_{22}(-\mathbf{k}, -\omega_n)$$

$$\mathcal{G}_{12}(\mathbf{k}, \omega_n) = \frac{\Delta}{E(\mathbf{k})^2 + \omega_n^2} = \mathcal{G}_{21}(\mathbf{k}, \omega_n) \quad (4.17)$$

are the BCS single-particle Green's functions in Nambu notation [14], with $E(\mathbf{k}) = \sqrt{\xi(\mathbf{k})^2 + \Delta^2}$ for an isotropic (s-wave) order parameter Δ (which we take to be real without loss of generality).

In analogy to what was done for obtaining the expression (4.8) in the strong-coupling limit, one can show that the pair propagator (4.14) reduces in the same limit to the following expressions:

$$\Gamma_{11}(q) = \Gamma_{22}(-q) \simeq \frac{8\pi}{m^2 a_F} \frac{\mu_B + i\Omega_\nu + \mathbf{q}^2/(4m)}{E_B(\mathbf{q})^2 - (i\Omega_\nu)^2} \quad (4.18)$$

and

$$\Gamma_{12}(q) = \Gamma_{21}(q) \simeq \frac{8\pi}{m^2 a_F} \frac{\mu_B}{E_B(\mathbf{q})^2 - (i\Omega_\nu)^2}, \quad (4.19)$$

where

$$E_B(\mathbf{q}) = \sqrt{\left(\frac{\mathbf{q}^2}{2m_B} + \mu_B\right)^2 - \mu_B^2} \quad (4.20)$$

has the form of the Bogoliubov dispersion relation [29], $\mu_B = \Delta^2/(4|\mu|) = 2\mu + \varepsilon_0$ being the corresponding value of the bosonic chemical potential. Apart from the overall factor $-8\pi/(m^2 a_F)$ (and a sign difference in the off-diagonal component [42]), the expressions (4.18) and (4.19) coincide, respectively, with the normal and anomalous non-condensate bosonic propagators within the Bogoliubov approximation [29].
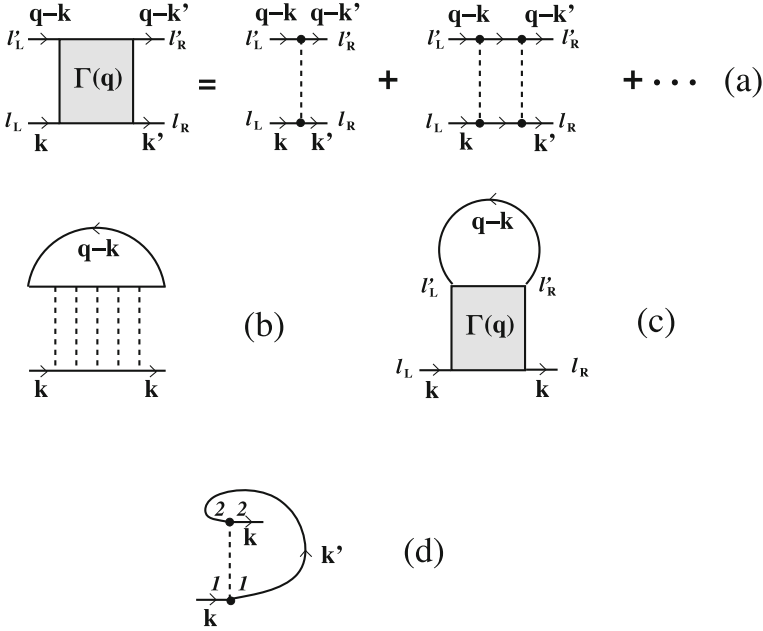
Fig. 4.7 Single-particle fermionic self-energy for the broken-symmetry phase (panel **c**), expressed in terms of the pair propagator Γ with Nambu structure (panel **a**). The BCS contribution to the self-energy is shown in panel **d**, and the corresponding self-energy for the normal-phase of Fig. 4.5 is also reported in panel **b** for comparison (reproduced from Fig. 1 of Ref. [43])

For any coupling, in Ref. [43] the corresponding fermionic self-energy was taken of the form:

$$\Sigma_{11}(k) = -\Sigma_{22}(-k) = -k_B T \sum_\nu \int \frac{d\mathbf{q}}{(2\pi)^3} \Gamma_{11}(\mathbf{q}, \Omega_\nu) \mathcal{G}_{11}(\mathbf{q} - \mathbf{k}, \Omega_\nu - \omega_n)$$

$$\Sigma_{12}(k) = \Sigma_{21}(k) = -\Delta \tag{4.21}$$

where Σ_{11} is shown diagrammatically in Fig. 4.7c (with $\ell_L = \ell'_L = \ell_R = \ell'_R = 1$) and Σ_{12} in Fig. 4.7d.

With this choice of the self-energy, the fermionic propagator is then obtained by solving Dyson's equation in matrix form:

$$\begin{pmatrix} G_{11}^{-1}(k) & G_{12}^{-1}(k) \\ G_{21}^{-1}(k) & G_{22}^{-1}(k) \end{pmatrix} = \begin{pmatrix} G_0(k)^{-1} & 0 \\ 0 & -G_0(-k)^{-1} \end{pmatrix} - \begin{pmatrix} \Sigma_{11}(k) & \Sigma_{12}(k) \\ \Sigma_{21}(k) & \Sigma_{22}(k) \end{pmatrix}. \tag{4.22}$$

Note that the BCS expressions (4.17) for the single-particle Green's functions result by neglecting in Eq. 4.22 the diagonal self-energy terms associated with pairing fluctuations.

By the approach of Ref. [43], the "normal" propagator G_{11} is inserted in the density equation

$$n = 2k_B T \sum_n e^{i\omega_n \eta} \int \frac{d\mathbf{k}}{(2\pi)^3} G_{11}(\mathbf{k}, \omega_n) \tag{4.23}$$

which replaces Eq. 4.7 below T_c, while in the gap equation

$$\Delta = - v_0 k_B T \sum_n \int \frac{d\mathbf{k}}{(2\pi)^3} \mathcal{G}_{12}(\mathbf{k}, \omega_n) \tag{4.24}$$

the BCS "anomalous" propagator (4.17) is maintained (albeit with modified numerical values of the chemical potential and order parameter that result from the simultaneous solution of Eqs. 4.23 and 4.24). This ensures that the bosonic propagators (4.14) remain *gapless*.

It is instructive to consider once more the BEC limit, whereby the diagonal part of the self-energy acquires the following approximate form [43]:

$$\Sigma_{11}(\mathbf{k}, \omega_n) \simeq \frac{8\pi}{m^2 a_F} \frac{1}{i\omega_n + \xi(\mathbf{k})} n'_B(T). \tag{4.25}$$

Here,

$$n'_B(T) = \int \frac{d\mathbf{q}}{(2\pi)^3} \left[u_B^2(\mathbf{q}) b(E_B(\mathbf{q})) - v_B^2(\mathbf{q}) b(-E_B(\mathbf{q})) \right] \tag{4.26}$$

represents the bosonic *noncondensate density*, with the Bose distribution $b(x) = \{\exp[x/(k_B T)] - 1\}^{-1}$ and the standard bosonic factors of the Bogoliubov transformation [29]:

$$v_B^2(\mathbf{q}) = u_B^2(\mathbf{q}) - 1 = \frac{\frac{\mathbf{q}^2}{2m_B} + \mu_B - E_B(\mathbf{q})}{2E_B(\mathbf{q})}. \tag{4.27}$$

In this case, solution of the Dyson's equation (4.22) yields:

$$G_{11}(\mathbf{k}, \omega_n) \simeq \frac{1}{i\omega_n - \xi(\mathbf{k}) - \frac{\Delta^2 + \Delta_{pg}^2}{i\omega_n + \xi(\mathbf{k})}} \tag{4.28}$$

with the notation $\Delta_{pg}^2 = 8\pi n'_B(T)/(m^2 a_F)$. When inserted into the density equation (4.23) the above expression gives:

$$n \simeq \frac{m^2 a_F}{4\pi} \left(\Delta^2 + \Delta_{pg}^2 \right) = 2 \left(n_0(T) + n'_B(T) \right) \tag{4.29}$$

where the *condensate density* $n_0(T)$ is identified via $\Delta^2 = 8\pi n_0(T)/(m^2 a_F)$.

It is relevant to comment at this point on the value of the scattering length a_B, which results in the BEC limit of the above approach from the residual interaction between composite bosons. This value is obtained, for instance, by manipulating the gap equation (4.24) in this limit, yielding:

Fig. 4.8 a Effective boson–boson interaction $\bar{u}_2$. **b** Additional terms associated with the t-matrix $\bar{t}_B$ for composite bosons. *Light lines* stand for free-fermion propagator and *broken lines* for fermionic interaction potential. Spin labels are not shown explicitly (reproduced from Fig. 2 of Ref. [41])
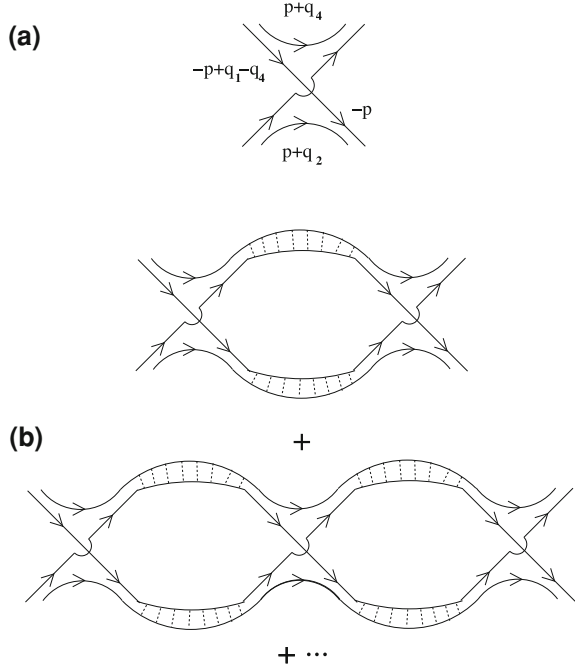
$$\frac{\Delta^2}{4|\mu|} \simeq 2\left(\sqrt{2|\mu|\varepsilon_0} - 2|\mu|\right) \simeq \mu_B. \qquad (4.30)$$

With the relation between Δ^2 and n_0 utilized in Eq. 4.29 and the asymptotic result $|\mu| \simeq (2ma_F^2)^{-1}$, the expression (4.30) can be cast in the form $\mu_B = 4\pi a_B n_0/m_B$ that corresponds to the value of the Bogoliubov theory with $a_B = 2a_F$.

This result can also be interpreted diagrammatically as being associated with the lowest-order (Born approximation) value for the effective boson–boson interaction [10]. This is represented in Fig. 4.8a and can be obtained from the following expression where all bosonic four-momenta q_i $(i = 1, \ldots, 4)$ vanish:

$$\bar{u}_2(0, 0, 0, 0) = k_B T \sum_n \int \frac{d\mathbf{p}}{(2\pi)^3} G_0(p)^2 G_0(-p)^2$$

$$\simeq \int \frac{d\mathbf{p}}{(2\pi)^3} \frac{1}{4\xi(\mathbf{p})^3} \simeq \left(\frac{m^2 a_F}{8\pi}\right)^2 \left(\frac{4\pi a_F}{m}\right) \qquad (4.31)$$

with the last line holding in the BEC limit. Apart from the overall factor $(m^2 a_F/(8\pi))^2$ (that compensates for the presence of the factor $-8\pi/(m^2 a_F)$ in the expression (4.8) of the free-boson propagator), the result (4.31) is indeed consistent with a residual bosonic interaction corresponding to $a_B = 2a_F$.

The correct value for a_B (=0.6a_F), which includes all possible scattering processes between two composite bosons in isolation, was originally determined in Ref. [44]

from the exact solution of the Schrödinger equation for dimer–dimer elastic scattering, and later confirmed in Ref. [45] through a completely diagrammatic treatment at zero density. In this context, even before this exact result was available, it was shown in Ref. [10] that the scattering processes corresponding to the t-matrix diagrams for composite bosons (the lowest ones of which are depicted in Fig. 4.8b) lead by themselves to a considerable reduction of the value of $a_B (\simeq 0.75 a_F)$ starting from the value $a_B = 2a_F$ of the Born approximation. As a matter of fact, the complete diagrammatic treatment of Ref. [45] (that yields the exact value $a_B = 0.6 a_F$) adds to the diagram of Fig. 4.8a all other additional (zero density) processes which are irreducible with respect to the propagation of two composite bosons, and then uses the result in the place of the diagram of Fig. 4.8a as the new kernel of the integral equation depicted in Fig. 4.8b.

The above considerations suggest us a way to improve on the Bogoliubov approximation for composite bosons, in order to include the diagrammatic contributions leading to a refined value of a_B with respect to the Born approximation (in the following, we shall limit ourselves to recovering the value $a_B \simeq 0.75 a_F$ in the BEC limit). To this end, we first approximately obtain the pair propagators $\mathbf{\Gamma}_B$ for any value of the fermionic coupling, by adopting the following Dyson's type equation in matrix form [41] in the place of the expressions (4.14):

$$\mathbf{\Gamma}_B(q) = \mathbf{\Gamma}_B^0(q) + \mathbf{\Gamma}_B^0(q) \mathbf{\Sigma}_B(q) \mathbf{\Gamma}_B(q). \tag{4.32}$$

Here, $\mathbf{\Gamma}_B^0(q)$ is the free-boson propagator with inverse

$$\mathbf{\Gamma}_B^0(q)^{-1} = \begin{pmatrix} \Gamma^0(q)^{-1} & 0 \\ 0 & \Gamma^0(-q)^{-1} \end{pmatrix} \tag{4.33}$$

where $\Gamma^0(q)^{-1}$ is given by Eq. 4.5, and

$$\mathbf{\Sigma}_B(q) = \Delta^2 \begin{pmatrix} -2\bar{u}_2(0, q, 0, q) & \bar{u}_2(0, 0, -q, q) \\ \bar{u}_2(0, 0, -q, q) & -2\bar{u}_2(0, q, 0, q) \end{pmatrix} \tag{4.34}$$

is the bosonic self-energy within the Bogoliubov approximation, which contains two degenerate forms of the effective boson–boson interaction (cf. Fig. 4.8a):

$$\bar{u}_2(q_1, q_2, q_3, q_4) = k_B T \sum_n \int \frac{d\mathbf{p}}{(2\pi)^3} G_0(-p) G_0(p + q_2) G_0(-p + q_1 - q_4) G_0(p + q_4). \tag{4.35}$$

To guarantee the ladder propagators $\mathbf{\Gamma}_B(q)$ of Eq. 4.32 to be gapless when $q = 0$ for any value of the fermionic coupling, we impose the condition:

$$\Gamma^0(q = 0)^{-1} - \Sigma_B^{11}(q = 0) - \Sigma_B^{12}(q = 0) = 0 \tag{4.36}$$

which plays the role in the present context of the Hugenholtz–Pines theorem for point-like bosons [29]. The Bogoliubov approximation for the composite bosons in the BEC limit with an improved value of a_B then results [10], by replacing in Eq. 4.34

Fig. 4.9 Graphical representation of the Popov self-energy for composite bosons, that results upon dressing the *upper fermionic line* in the particle–particle channel. An analogous dressing done for the lower fermionic line accounts for the factor of two in Eq. 4.38 (reproduced from Fig. 4 of Ref. [41])
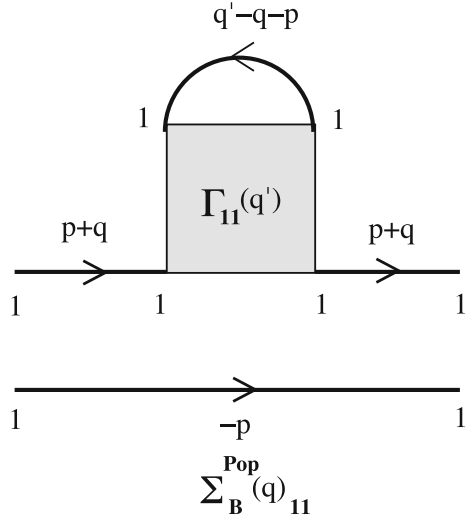
the boson–boson interaction $\bar{u}_2$ with the following expression of the t-matrix for composite bosons (cf. Fig. 4.8b):

$$\bar{t}_B(q_1, q_2, q_3, q_4) = \bar{u}_2(q_1, q_2, q_3, q_4) - k_B T \sum_{\nu_5} \int \frac{d\mathbf{q}_5}{(2\pi)^3}$$

$$\times \bar{u}_2(q_1, q_2, q_5, q_1 + q_2 - q_5)\Gamma^0(q_5)\Gamma^0(q_1 + q_2 - q_5)\bar{t}_B(q_1 + q_2 - q_5, q_5, q_3, q_4).$$
(4.37)

Further improvements can be implemented by replacing the pair propagators (4.14) with more refined descriptions of composite bosons in the BEC limit, and then using these improved descriptions throughout the BCS–BEC crossover to modify the fermionic single-particle self-energy accordingly. An example is the so-called Popov approximation for composite bosons [41], whereby the bosonic self-energy represented diagrammatically in Fig. 4.9 is employed to modify the original Bogoliubov propagators (4.14). In the broken-symmetry phase, this bosonic self-energy has the form:

$$\Sigma_B^{\text{Pop}}(q)_{11} = -2k_B T \sum_n \int \frac{d\mathbf{p}}{(2\pi)^3} k_B T \sum_{\nu'} \int \frac{d\mathbf{q}'}{(2\pi)^3}$$

$$\times G_{11}(p+q)^2 G_{11}(-p)G_{11}(q'-q-p)\Gamma_{11}(q').$$
(4.38)

The Popov propagators for composite bosons are then obtained as follows, in terms of the corresponding Bogoliubov propagators (4.14):

$$
\begin{pmatrix} \Gamma_{11}^{\mathrm{Pop}}(q) \ \Gamma_{12}^{\mathrm{Pop}}(q) \\ \Gamma_{21}^{\mathrm{Pop}}(q) \ \Gamma_{22}^{\mathrm{Pop}}(q) \end{pmatrix} = \frac{\begin{pmatrix} A(-q) - \Sigma_B^{\mathrm{Pop}}(-q)_{11} & B(q) \\ B(q) & A(q) - \Sigma_B^{\mathrm{Pop}}(q)_{11} \end{pmatrix}}{[A(q) - \Sigma_B^{\mathrm{Pop}}(q)_{11}][A(-q) - \Sigma_B^{\mathrm{Pop}}(-q)_{11}] - B(q)^2}
$$
(4.39)

where $A(q)$ and $B(q)$ are given by Eqs. 4.15 and 4.16, in the order. The propagators (4.39) are gapless provided

$$
A(q=0) - \Sigma_B^{\mathrm{Pop}}(q=0)_{11} - B(q=0) = 0.
$$
(4.40)

This generalizes to the present context the condition $A(q=0) - B(q=0) = 0$ for gapless Bogoliubov propagators, and effectively replaces the gap equation (4.24) for all practical purposes.

In addition, the same treatment that was made above to improve on the relation $a_B = 2a_F$ in the BEC limit can be applied here, by first rewriting the expression (4.38) in terms of the bare boson–boson interaction (4.35)

$$
\Sigma_B^{\mathrm{Pop}}(q)_{11} \simeq -2k_B T \sum_{\nu'} \int \frac{d\mathbf{q}'}{(2\pi)^3} \bar{u}_2(q', q, q', q) \Gamma_{11}(q'),
$$
(4.41)

and then replacing $\bar{u}_2$ by the t-matrix $\bar{t}_B$ for composite bosons of Eq. 4.37.

The final form of the fermionic self-energy is eventually obtained by reconsidering the expressions (4.21), where now the Popov propagator $\Gamma_{11}^{\mathrm{Pop}}$ of Eq. 4.39 takes the place of Γ_{11} while Δ satisfies the condition (4.40) in the place of the original gap equation.

From a physical point of view, the relevance of the Popov approximation results because it introduces *an effective repulsion* among the composite bosons through the presence of their noncondensate density. The importance of this repulsion should be especially evident in the normal phase, when the Bogoliubov propagators (4.14) reduce to free-boson propagator (4.5) and miss accordingly this residual bosonic interaction. While commenting on Fig. 4.6 we have already pointed out that this is the reason for a diverging compressibility at T_c when only "bare" pairing fluctuations are considered.

In the next section we shall discuss a number of thermodynamic as well as dynamical results obtained by implementing the Popov approximation *in the normal phase* throughout the BCS–BEC crossover (the unitary limit will specifically be considered). In this case, the (inverse of the) Popov propagator for composite bosons is obtained from the relation $\Gamma^{\mathrm{Pop}}(q)^{-1} = \Gamma^0(q)^{-1} - \Sigma_B^{\mathrm{Pop}}(q)$, where Σ_B^{Pop} is given by Eq. 4.41 with Γ^0 replacing Γ_{11}. In addition, to improve on the description of the boson–boson scattering, we shall replace the bare $\bar{u}_2$ in Eq. 4.41 by the t-matrix $\bar{t}_B$ for composite bosons given by Eq. 4.37. In this way, the 2-boson scattering will be dealt with beyond the Born approximation.

In this context, it will be relevant to compare the results obtained by the above approach in the normal phase for thermodynamic and dynamical quantities (F. Palestini et al., unpublished), with those obtained by an alternative approach based on a

self-consistent t-matrix approximation, as described in Ref. [37] for the thermodynamics and in Ref. [39] for the dynamics of the BCS–BEC crossover, respectively. (Results for a homogeneous system will only be presented.) Interest in this comparison is also justified on physical grounds, by considering the different treatments of the effective boson–boson interaction which result from the two approaches. As remarked already, the Popov approach with $\bar{t}_B$ replacing $\bar{u}_2$ concentrates on 2-boson scattering beyond the lowest order (Born) approximation, while the self-consistent t-matrix approach includes a sequence of $3, 4, \ldots$, n-boson scattering processes, where each process is dealt with at the lowest order. Although these alternative sets of processes (namely, improved 2-boson versus n-boson scattering) can be clearly identified by a diagrammatic analysis in the (BEC) strong-coupling limit [10], the question of how the relevance of these processes extends to the unitarity limit remains open and can be addressed only via numerical calculations. This question will be partially addressed in the next section.

4.4 Results for Thermodynamic and Dynamical Quantities

Physical quantities that can be considered for a quantum many-body system are conveniently organized as single- and two-particle properties, and are correspondingly obtained in terms of single- and two-particles Green's functions. In addition, these properties may refer to the equilibrium state of the system or to excitations over and above this state. In the first case they can be conveniently obtained within the Matsubara formalism with discrete imaginary frequencies, while in the second case a (sometimes nontrivial) analytic continuation to the real frequency axis is required [29]. In the present context of a pairing-fluctuation diagrammatic approach to the BCS–BEC crossover, we shall limit ourselves to considering the chemical potential and the total energy per particle as examples of thermodynamic properties, and the single-particle spectral function as an example of dynamical properties, for which consideration of pairing fluctuations appears especially relevant.

This relevance is most evident in the *normal phase*, because the occurrence of pairing fluctuations acts to extend above T_c characteristic effects of pairing (notably, what is referred to as the "pseudogap physics" associated with the noncondensate density like in Eq. 4.28), effects which would otherwise be peculiar of the broken-symmetry phase below T_c only.

4.4.1 Thermodynamic Properties

For a homogeneous Fermi gas in the normal phase, the fermionic chemical potential μ can be obtained from the density equation (4.7) and the total energy per particle from the following expression [29]:

$$\frac{E}{N} = \frac{1}{n} k_B T \sum_n e^{i\omega_n \eta} \int \frac{d\mathbf{k}}{(2\pi)^3} \left(\frac{\mathbf{k}^2}{2m} + \mu + i\omega_n \right) G(\mathbf{k}, \omega_n) \qquad (4.42)$$

where N is the total particle number. In Eqs. 4.7 and 4.42, different approximations are embodied in different forms of the fermionic single-particle Green's function G. In particular, we shall consider approximate forms of G obtained within: (i) the t-matrix approach given by Eqs. 4.4–4.6; (ii) its further simplification (sometimes referred to as the Nozières-Schmitt-Rink (NSR) approximation) whereby the fermionic propagator is expanded like in Eq. 4.9 for any coupling (and not just in the BEC limit); (iii) the Popov approach with an improved description of the boson–boson scattering as discussed in Sect. 4.3; (iv) the fully self-consistent (sc) t-matrix approach of Ref. [37] that was mentioned in Sect. 4.2.

At unitarity, the results of these diagrammatic approaches for μ and E/N can also be compared with Quantum Monte Carlo (QMC) calculations, which are available over a wide temperature range. This comparison is shown in Fig. 4.10. Several features are here apparent. At high enough temperatures, all data progressively merge to the t-matrix approach, which is known to become exact in this limit where it reduces to the virial expansion of Beth and Uhlenbeck [46]. While only minor differences appear between the t-matrix and the NSR approaches (with independent NRS calculations yielding comparable results [47]), the Popov approach is seen to a add positive contribution both to μ and E/N. This is in line with the expectation that the Popov approach takes into account the residual (repulsive) interaction among composite bosons [41], which is missed by the t-matrix approach. In addition, the fully self-consistent t-matrix approach, which at high enough temperature should also asymptotically reduce to the t-matrix approach without self-consistency, shows deviations from the t-matrix and Popov approaches that are more marked in μ than in E/N. No compelling conclusions can, therefore, apparently be drawn by comparing self-consistent versus non-self-consistent pairing-fluctuation approaches as far as the thermodynamic quantities are concerned. Quite generally, it can be stated that good overall agreement results by comparing QMC calculations with diagrammatic pairing-fluctuation approaches, signifying that the latter are able to capture the relevant physical processes. Note finally from Fig. 4.10 that the progressively increasing differences between the t-matrix and Popov approaches when lowering the temperature reflects the fact that the divergence of the compressibility resulting from the t-matrix approach (shown in Fig. 4.6) is suitably cut off by the Popov approach, which yields a finite value for this quantity at T_c (F. Palestini et al., unpublished).

Alternative theoretical approaches yield different values of the critical temperature T_c, as shown in Table 4.1. These values can be compared with the corresponding ones that are extracted from experiments, as reported in Table 4.2. Although for this quantity the self-consistent t-matrix approach seems to perform better than the non-self-consistent one(s), one should be aware of the fact that additional corrections to the pair propagator Γ^0, like those introduced in Gor'kov and Melik-Barkhudarov [25] in the weak-coupling (BCS) limit to represent the medium polarization and shown to have a sizable effect on T_c in that limit, might still act to reduce somewhat further the value of T_c even at unitarity. Definite comparison with

Fig. 4.10 **a** Chemical potential and **b** energy per particle (in units of E_F) versus the temperature (in units of T_F), as obtained: In F. Palestini et al. (unpublished) by the t-matrix approach (*dashed lines*), the NSR approximation (*dashed-dotted lines*), and the Popov approach (*thick full lines*). In Ref. [37] by the fully self-consistent t-matrix approach (*dotted lines*). In Ref. [48] (*full squares*) and in Ref. [49] (*full circles*) by QMC calculations. Results obtained by the modified virial expansion of Ref. [50] (*thin full lines*) are also shown for comparison
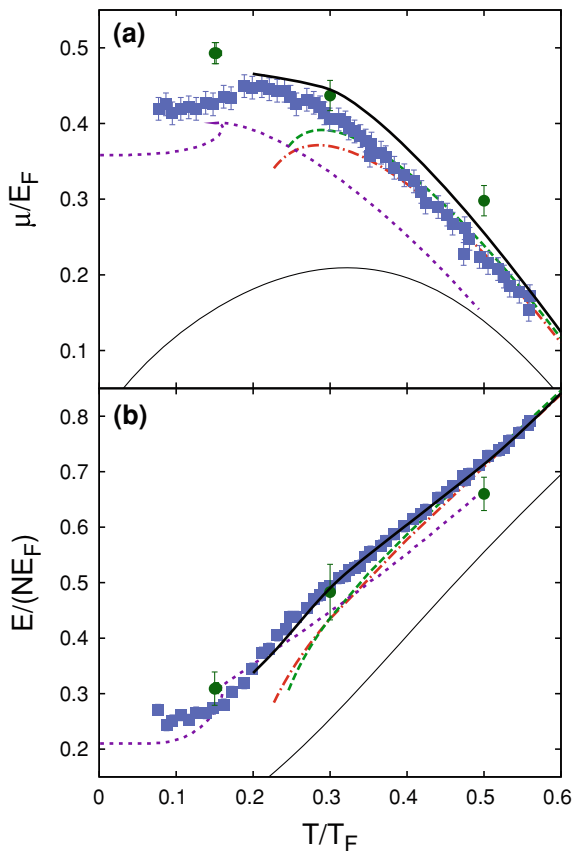
the experimental values of T_c reported in Table 4.2 should then await for a proper inclusion of these additional corrections. To elicit a more quantitative comparison among theoretical and experimental thermodynamic quantities, Tables 4.1 and 4.2 list, in addition, the values of μ and E/N that are available both at zero temperature and T_c.

The sizable effects that pairing fluctuations have on the thermodynamic quantities of Fig. 4.10 over and above the free-Fermi gas behavior can be appreciated by sketching therein the plots of μ and E/N for the non-interacting Fermi gas (recall, in particular, that $\mu_{\mathrm{ni}}(T=0)/E_F = 1$, $E_{\mathrm{ni}}(T=0)/(NE_F) = 0.6$, $\mu_{\mathrm{ni}}(T=0.6T_F)/E_F = 0.625$, and $E_{\mathrm{ni}}(T=0.6T_F)/(NE_F) = 1.15$). The effects of pairing fluctuations in these quantities are thus seen to extend over a wide temperature range up to several times T_F, being related to the *high-energy scale* Δ_∞ introduced in Ref. [58] in terms of the trace of the pair propagator Γ^0.

There exists, however, an additional energy scale (usually referred to as the *pseudogap*) which is also related to pairing fluctuations but is instead characteristic of the *low-energy* physics about T_c. This energy scale is most evident when

Table 4.1 Thermodynamic quantities obtained theoretically for a homogeneous Fermi system at unitarity by alternative pairing-fluctuation approaches and QMC calculations (relevant references are specified)

	t-Matrix	NSR	Popov	sc t-Matrix	QMC I	QMC II
β	−0.57 (F. Palestini et al., unpublished)	−0.599 [47]		−0.64 [37]	−0.63(5) [51]	
$\mu(T=0)$	0.455 [52]	0.401 [47]		0.36 [37]	∼0.42 [48]	
T_c	0.243 (F. Palestini et al., unpublished)	0.225 (F. Palestini et al., unpublished)	0.199 (F. Palestini et al., unpublished)	0.160 [37]	< 0.15 [51]	0.152(7) [49]
$\mu(T_c)$	0.365 (F. Palestini et al., unpublished)	0.336 (F. Palestini et al., unpublished)	0.464 (F. Palestini et al., unpublished)	0.394 [37]	0.43(1) [51]	0.493(14) [49]
$E(T_c)/N$	0.296 (F. Palestini et al., unpublished)	0.278 (F. Palestini et al., unpublished)	0.337 (F. Palestini et al., unpublished)	0.304 [37]	0.270(6) [51]	0.31(1) [49]

Energies are in units of E_F and temperatures of T_F. Here, the dimensionless parameter β results from the relation $1 + \beta = E(T=0)/E_{ni}(T=0)$ that holds at unitarity, where E_{ni} is the energy of the corresponding non-interacting system

Table 4.2 Thermodynamic quantities obtained experimentally for a homogeneous Fermi system at unitarity (references are specified)

	Exp. [53]	Exp. [54]	Exp. [55]	Exp. [50]	Exp. [56]	Exp. [57]
β	$-0.62(2)$	$-0.68^{+0.13}_{-0.10}$	$-0.54^{+0.05}_{-0.12}$	$-0.58(1)$	$-0.54(5)$	
$\mu(T=0)$	$0.38(2)$	$0.32^{+0.13}_{-0.10}$	$0.46^{+0.05}_{-0.12}$	$0.42(1)$	$0.46(5)$	
T_c				$0.157(15)$		~ 0.15
$\mu(T_c)$				$0.49(2)$		

Energies are in units of E_F and temperatures of T_F. The chemical potential at $T=0$ is here obtained via the relation $\mu(T=0)/E_F = 1+\beta$ that holds at unitarity, the parameter β being directly measured. (Experimental data for $E(T_c)/N$ are not available for comparison with the theoretical values reported in Table 4.1)

looking at the properties of the single-particle spectral function, to be considered next.

4.4.2 Dynamical Properties

The spectral function $A(\mathbf{k}, \omega)$ for single-particle fermionic excitations results after analytic continuation of the fermion propagator $G(\mathbf{k}, \omega_n)$ from the Matsubara (ω_n) to the real (ω) frequency axis, via the relation $A(\mathbf{k}, \omega) = -\operatorname{Im} G^R(\mathbf{k}, \omega)/\pi$ where $G^R(\mathbf{k}, \omega)$ is the retarded fermion propagator. Through a related analytic continuation of the fermionic self-energy Σ, $A(\mathbf{k}, \omega)$ can be eventually cast in the form:

$$A(\mathbf{k}, \omega) = -\frac{1}{\pi} \frac{\operatorname{Im} \Sigma(\mathbf{k}, \omega)}{[\omega - \xi_{\mathbf{k}} - \operatorname{Re} \Sigma(\mathbf{k}, \omega)]^2 + [\operatorname{Im} \Sigma(\mathbf{k}, \omega)]^2} \tag{4.43}$$

where again $\xi(\mathbf{k}) = \mathbf{k}^2/(2m) - \mu$. For any given wave vector $\mathbf{k}$, the frequency structure of the real and imaginary parts of $\Sigma(\mathbf{k}, \omega)$ thus determines the positions and widths of the peaks in $A(\mathbf{k}, \omega)$.

The archetype of a pairing-gap behavior for $A(\mathbf{k}, \omega)$ is embodied in the two-peak structure of the following expression (cf. Eq. 4.17):

$$A(\mathbf{k}, \omega) = u(\mathbf{k})^2 \delta(\omega - E(\mathbf{k})) + v(\mathbf{k})^2 \delta(\omega + E(\mathbf{k})) \tag{4.44}$$

where $E(\mathbf{k}) = \sqrt{\xi(\mathbf{k})^2 + \Delta^2}$ and $v(\mathbf{k})^2 = 1 - u(\mathbf{k})^2 = (1 - \xi(\mathbf{k})/E(\mathbf{k}))/2$, which holds at the mean-field level in the broken-symmetry phase. When pairing fluctuations beyond mean field are included [31], a two-peak structure still persists in the normal phase above T_c, although with broad and asymmetric peaks replacing the delta spikes of Eq. 4.44 while the total area remains unity. Even in this case, the positions of the two peaks in the spectral function follow quite closely the BCS-like dispersions $\pm\sqrt{\xi(\mathbf{k})^2 + \Delta_{\mathrm{pg}}^2}$, provided the value Δ_{pg} of the pseudogap is inserted in the place of the BCS gap Δ of Eq. 4.44. An example of this behavior is shown in Fig. 4.11 for weak coupling.

Fig. 4.11 Peak positions of
the spectral function at T_c for
negative (*lower branch*) and
positive (*upper branch*)
energies versus the wave
vector when $(k_F a_F)^{-1} =$
-0.72. The spectral function
is here obtained within the
t-matrix approach of [31].
Full lines represent a
BCS-like fit (adapted from
Fig. 15 of [31])
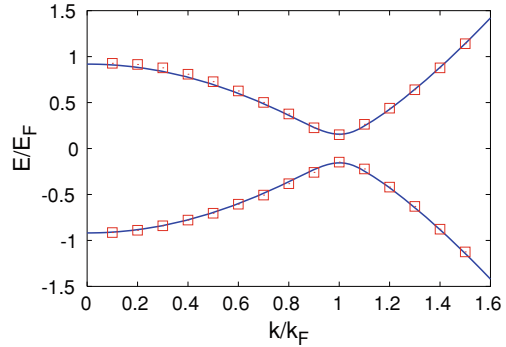
A systematic study of the single-particle spectral function in the normal phase
across the BCS–BEC crossover was originally performed in Ref. [31] within the
t-matrix approach given by Eq. 4.4–4.6. Interest in this study was recently revived by
the advent of a novel experimental technique for ultracold Fermi gases [59], whereby
the wave vector of photo-excited atoms is resolved in radio-frequency spectra taken
at different couplings and temperatures. One should mention in this context the
comparison made in Ref. [38] between theoretical results obtained by the t-matrix
and G–G_0 approaches, as well as the calculation performed in Ref. [39] within the
fully self-consistent t-matrix approach.

Similarly to what was done in Sect. 4.4.1 for thermodynamic properties, here we
compare the results for $A(\mathbf{k}, \omega)$ obtained alternatively by the t-matrix, the Popov,
and the fully self-consistent (sc) t-matrix approaches (while referring to F. Palestini
et al. (unpublished) for a more complete analysis of this comparison). We then show
in Fig. 4.12 the results obtained for $A(\mathbf{k}, \omega)$ at unitarity and $k = k_F$ by the three
approaches, at the respective values of the critical temperature. (Analytic continua-
tion from Matsubara to real frequencies has been performed in panel (a) by the direct
substitution $i\omega_n \rightarrow \omega + i\eta$, in panel (b) by the Padé approximants, and in panel (c)
by the maximum-entropy method.) Note how the two-peak structure that is evident in
panel (a) remains noticeable in panel (b), but has essentially disappeared in panel (c).
This is consistent with a general understanding [60] that non-self-consistent calcu-
lations favor pseudogap behavior while self-consistent calculations tend to suppress
it. As the other side of the medal, one would tend to attribute [39] to self-consistent
calculations a more precise description of thermodynamic properties with respect to
non-self-consistent approaches.

In this respect, it should be noticed that the Popov approach, while improving
considerably on the thermodynamic description with respect to the t-matrix approach
as discussed in Sect. 4.4.1, preserves also an evident pseudogap behavior in the single-
particle spectral function. This is made evident in Fig. 4.13, where the dispersion of
the two peaks of $A(\mathbf{k}, \omega)$ is reported at unitarity and $T = T_c$ for the t-matrix, the
Popov, and the sc t-matrix approaches. (Close to k_F, where the two peaks in $A(\mathbf{k}, \omega)$
are broad and overlap each other, the position of the less intense peak was determined

Fig. 4.12 Single-particle spectral function at unitarity when $T = T_c$ and $k = k_F$, as obtained by: **a** the t-matrix approach of Ref. [31], **b** the Popov approach of F. Palestini et al., (unpublished) **c** the sc t-matrix approach of Ref. [39]. (The plot of panel **c** has been extracted from Fig. 4 of Ref. [39])
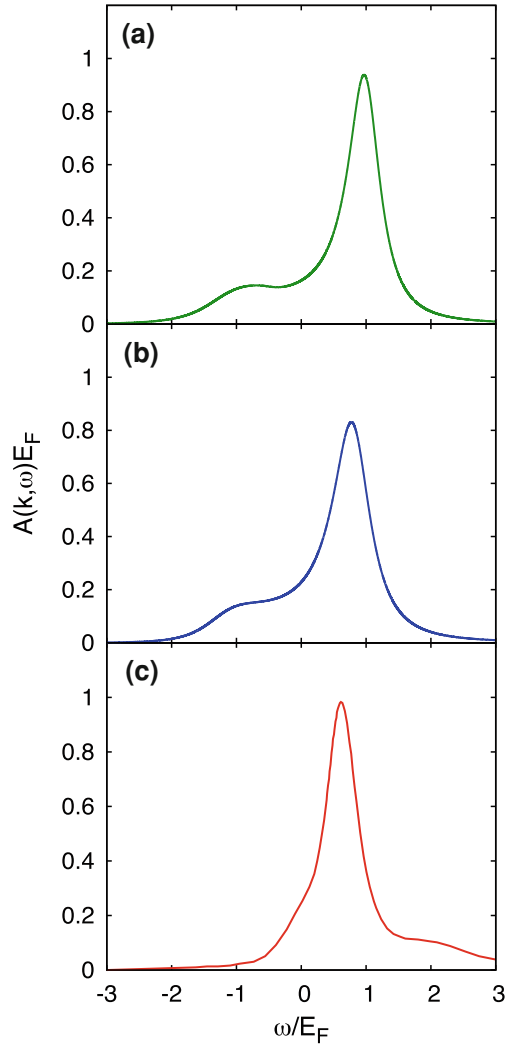
by subtracting from $A(\mathbf{k}, \omega)$ the profile of the most intense peak.) The value of the pseudogap, identified by (half) the minimum energy separation between the upper and lower branches, remains essentially unmodified when adding the Popov on top of t-matrix fluctuations, but it closes up when full self-consistency is included.

Stringent comparison with both experimental data and QMC calculations will eventually decide what version of pairing-fluctuation theories is able to provide the closest agreement for thermodynamic as well as for dynamical quantities, in systems like ultracold Fermi gases where only the mutual attractive interaction can be responsible for their physical behavior.

Fig. 4.13 Dispersion of the two peaks of the spectral function at unitarity and $T = T_c$ obtained by the t-matrix approach (*empty squares*), the Popov approach (*full dots*), and the sc t-matrix approach (*stars*). (Stars have been extracted from the curves in Fig. 4 of Ref. [39])
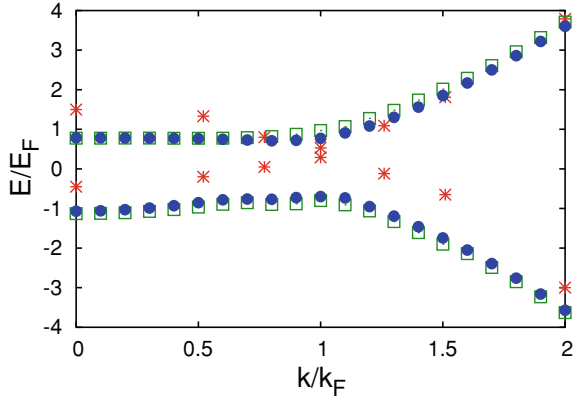
4.5 Concluding Remarks

A gas of ultracold Fermi atoms, whose mutual interaction is governed by a (broad) Fano-Feshbach resonance, represents a physical system of fermions containing only pairing degrees of freedom. This feature naturally conveys their theoretical description in terms of "pairing fluctuations" of several kinds in the particle–particle channel, which extend characteristic two-body processes to a finite-density situation. The difficulty here is that, at finite density, the relevant processes of the pairing type can be unambiguously identified only in the weak-coupling (BCS) regime where a fermion description is appropriate and in the strong-coupling (BEC) regime where a description in terms of composite bosons holds, because in both regimes the presence of the small parameter $k_F|a_F|$ guides the selection of the diagrammatic contributions for dilute systems. In additions, in these regimes useful analytic approximations can be quite generally derived from these diagrammatic contributions, which help considerably one's physical intuition in picturing the involved processes. This kind of physical intuition is hard to emerge from more numerically oriented approaches (like QMC calculations) or more abstract approaches (like the renormalization group methods [61]), thus making diagrammatic approaches to the BCS–BEC crossover more appealing in this respect. In principle, diagrammatic approaches may not be controlled in the unitary region, which is intermediate between the BCS and BEC regimes and where the diluteness condition does not apply owing to the divergence of $|a_F|$. Nevertheless, the good control of the approximations which can be achieved *separately* in the BCS and BEC regimes *and* the limited extension of the unitary region $(-1 \lesssim (k_F a_F)^{-1} \lesssim +1)$ enable one to formulate a single fermionic theory that bridges across the BCS and BEC regimes and is able to furnish a good description of the unitary region for most practical purposes. This is the spirit with which diagrammatic pairing-fluctuation approaches to the BCS–BEC crossover have been formulated and applied to a variety of problems, both in the normal and superfluid phases.

It is finally relevant to mention that the interest in the physics brought about by consideration of pairing fluctuations is not limited to a system of ultracold Fermi atoms. In particular, the issue of the possible occurrence of a pseudogap in single-particle excitations is of considerable interest both in condensed matter [62] and nuclear physics [63]. This gives to ultracold Fermi gases the role of prototype systems, in which issues of general interest can be conveniently addressed by exploiting the unprecedented flexibility that they provide in the control of their physical parameters.

References

1. Bloch, I., Dalibard, J., Zwerger, W.: Rev. Mod. Phys. **80**, 885 (2008)
2. Giorgini, S., Pitaevskii, L.P., Stringari, S.: Rev. Mod. Phys. **80**, 1215 (2008)
3. Inouye, S., Andrews, M.R., Stenger, J., Miesner, H.-J., Stamper-Kurn, D.M., Ketterle, W.: Nature **392**, 151 (1998)
4. Fano, U.: Nuovo Cimento **12**, 156 (1935)
5. Fano, U.: Phys. Rev. **124**, 1866 (1961)
6. Feshbach, H.: Ann. Phys. **19**, 287 (1962)
7. Fano, U., Rau, A.R.P.: Atomic Collisions and Spectra. Academic Press, New York (1986)
8. Simonucci, S., Pieri, P., Strinati, G.C.: Europhys. Lett. **69**, 713 (2005)
9. SádeMelo, C.A.R., Randeria, M., Engelbrecht, J.R: Phys. Rev. Lett. **71**, 3202 (1993)
10. Pieri, P., Strinati, G.C.: Phys. Rev. B **61**, 15370 (2000)
11. Leggett, A.J: In: Pekalski, A., Przystawa, R. (eds.) Modern Trends in the Theory of Condensed Matter. Lecture Notes in Physics, vol. 115, p. 13. Springer, Berlin (1980)
12. Eagles, D.M.: Phys. Rev. **186**, 456 (1969)
13. Bardeen, J., Cooper, L.N., Schrieffer, J.R.: Phys. Rev. **108**, 1175 (1957)
14. Schrieffer, J.R.: Theory of Superconductivity. Benjamin, New York (1964)
15. Marini, M., Pistolesi, F., Strinati, G.C.: Eur. Phys. J. B **1**, 151 (1998)
16. Pistolesi, F., Strinati, G.C.: Phys. Rev. B **49**, 6356 (1994)
17. Pistolesi, F., Strinati, G.C.: Phys. Rev. B **53**, 15168 (1996)
18. Uemura, Y.J., Le, L.P., Luke, G.M., Sternlieb, B.J., Wu, W.D., Brewer, J.H., Riseman, T.M., Seaman, C.L., Maple, M.B., Ishikawa, M., Hinks, D.G., Jorgensen, J.D., Saito, G., Yamochi, H.: Phys. Rev. Lett. **66**, 2665 (1991)
19. Uemura, Y.J., Keren, A., Le, L.P., Luke, G.M., Sternlieb, B.J., Wu, W.D., Brewer, J.H., Whetten, R.L., Huang, S.M., Lin, S., Kaner, R.B., Diederich, F., Donovan, S., Grüner, G., Holczer, K.: Nature **352**, 605 (1991)
20. Randeria, M., Duan, J.-M., Shieh, L.-Y.: Phys. Rev. B **41**, 327 (1990)
21. Haussmann, R.: Z. Phys. B: Condens. Matter **91**, 291 (1993)
22. Stintzing, S., Zwerger, W.: Phys. Rev. B **56**, 9004 (1997)
23. Jankó, B., Maly, J., Levin, K.: Phys. Rev. B **56**, 11407(R) (1997)
24. Chen, Q., Kosztin, I., Jankó, B., Levin, K.: Phys. Rev. Lett. **81**, 4708 (1998)
25. Gor'kov, L.P., Melik-Barkhudarov, T.K.: Sov. Phys. JETP **13**, 1018 (1961)
26. Perali, A., Pieri, P., Pisani, L., Strinati, G.C.: Phys. Rev. Lett. **92**, 220404 (2004)
27. Spuntarelli, A., Pieri, P., Strinati, G.C.: Phys. Rep. **488**, 111 (2010) and references quoted therein
28. Galitskii, V.M.: Sov. Phys. JETP **7**, 104 (1958). See also Ref. [29], Sect. 11.
29. Fetter, A.L., Walecka, J.D.: Quantum Theory of Many-Particle Systems. McGraw-Hill, New York (1971)

30. Rodberg, L.S., Thaler, R.M.: Introduction to the Quantum Theory of Scattering. Academic, New York (1967), Sect. 5.4
31. Perali, A., Pieri, P., Strinati, G.C., Castellani, C.: Phys. Rev. B **66**, 024510 (2002)
32. Combescot, R.: Phys. Rev. Lett. **91**, 120401 (2003)
33. Vagor, A., Schomerus, H., Shanenko, A.: Phys. Rev. B **76**, 214513 (2007)
34. Nozières, P., Schmitt-Rink, S.: J. Low. Temp. Phys. **59**, 195 (1985)
35. Serene, J.W.: Phys. Rev. B **40**, 10873 (1989)
36. Levin, K., Chen, Q., Chien, C.-C., He, Y.: Ann. Phys. **325**, 233 (2010)
37. Haussmann, R., Rantner, W., Cerrito, S., Zwerger, W.: Phys. Rev. A **75**, 023610 (2007)
38. Chien, C.-C., Guo, H., He, Y., Levin, K.: Phys. Rev. A **81**, 023622 (2010)
39. Haussmann, R., Punk, M., Zwerger, W.: Phys. Rev. A **80**, 063612 (2009)
40. Veillette, M., Moon, E.G., Lamacraft, A., Radzihovsky, L., Sachdev, S., Sheehy, D.E.: Phys. Rev. A **78**, 033614 (2008)
41. Pieri, P., Strinati, G.C.: Phys. Rev. B **71**, 094520 (2005)
42. Andrenacci, N., Pieri, P., Strinati, G.C.: Phys. Rev. B **68**, 144507 (2003)
43. Pieri, P., Pisani, L., Strinati, G.C.: Phys. Rev. B **70**, 094508 (2004)
44. Petrov, D.S., Salomon, C., Shlyapnikov, G.V.: Phys. Rev. Lett. **93**, 090404 (2004)
45. Brodsky, I.V., Kagan, M.Yu., Klaptsov, A.V., Combescot, R., Leyronas, X.: JETP Lett. **82**, 273 (2005)
46. Combescot, R., Leyronas, X., Kagan, M.Yu.: Phys. Rev. A **73**, 023618 (2006)
47. Hu, H., Liu, X.J., Drummond, P.D.: Europhys. Lett. **74**, 574 (2006)
48. Bulgac, A., Drut, J.E., Magierski, P.: Phys. Rev. Lett. **96**, 090404 (2006)
49. Burovski, E., Prokofev, N., Svistunov, B., Troyer, M.: Phys. Rev. Lett. **96**, 160402 (2006)
50. Nascimbène, S., Navon, N., Jiang, K., Chevy, F., Salomon, C.: Nature **463**, 1057 (2010)
51. Bulgac, A., Drut, J.E., Magierski, P.: Phys. Rev. A **78**, 023625 (2008)
52. Perali, A., Pieri, P., Strinati, G.C.: Phys. Rev. Lett. **93**, 100404 (2004)
53. Luo, L., Thomas, J.E.: J. Low Temp. Phys. **154**, 1 (2009)
54. Bartenstein, M., Altmeyer, A., Riedl, S., Jochim, S., Chin, C., Denschlag, J.H., Grimm, R.: Phys. Rev. Lett. **92**, 120401 (2004)
55. Stewart, J.T., Gaebler, J.P., Regal, C.A., Jin, D.S.: Phys. Rev. Lett. **97**, 220406 (2006)
56. Partridge, G.B., Li, W., Kamar, R.I., Liao, Y.-a., Hulet, R.G.: Science **311**, 503 (2006)
57. Shin, Y.I., Schunck, C.H., Schirotzek, A., Ketterle, W.: Nature **451**, 689 (2008)
58. Perali, A., Pieri, P., Strinati, G.C.: Nat. Phys. **5**, 736 (2009)
59. Stewart, J.T., Gaebler, J.P., Jin, D.S.: Nature **454**, 744 (2008)
60. Puig von Friesen, M., Verdozzi, C., Almbladh, C.-O.: Phys. Rev. Lett. **103**, 176404 (2009) and references quoted therein
61. Floerchinger, S., Scherer, M.M., Wetterich, C.: Phys. Rev. A **81**, 063619 (2010)
62. Damascelli, A., Shen, Z.-X., Hussain, Z.: Rev. Mod. Phys. **75**, 473 (2003)
63. Bożek, P.: Nucl. Phys. A **657**, 187 (1999)

Chapter 5
The Unitary Gas and its Symmetry Properties

Yvan Castin and Félix Werner

Abstract   The physics of atomic quantum gases is currently taking advantage of a powerful tool, the possibility to fully adjust the interaction strength between atoms using a magnetically controlled Feshbach resonance. For fermions with two internal states, formally two opposite spin states ↑ and ↓, this allows to prepare long lived strongly interacting three-dimensional gases and to study the BEC–BCS crossover. Of particular interest along the BEC–BCS crossover is the so-called unitary gas, where the atomic interaction potential between the opposite spin states has virtually an infinite scattering length and a zero range. This unitary gas is the main subject of the present chapter: it has fascinating symmetry properties, from a simple scaling invariance, to a more subtle dynamical symmetry in an isotropic harmonic trap, which is linked to a separability of the N-body problem in hyperspherical coordinates. Other analytical results, valid over the whole BEC–BCS crossover, are presented, establishing a connection between three recently measured quantities, the tail of the momentum distribution, the short range part of the pair distribution function and the mean number of closed channel molecules. The chapter is organized as follows. In Sect. 5.1, we introduce useful concepts, and we present a simple definition and basic properties of the unitary gas, related to its scale invariance. In Sect. 5.2, we describe various models that may be used to describe the BEC–BCS crossover, and in particular the unitary gas, each model having its own advantage and shedding some particular light on the unitary gas properties: scale invariance and a virial theorem hold within the zero-range model, relations between the derivative of the energy with respect to the inverse scattering length and the short range pair correlations or the

Y. Castin (✉)
Laboratoire Kastler Brossel, Ecole normale supérieure,
CNRS and UPMC, Paris, France
e-mail: yvan.castin@lkb.ens.fr

F. Werner
Department of Physics, University of Massachusetts,
Amherst, USA
e-mail: werner@lkb.ens.fr

tail of the momentum distribution are easily derived using the lattice model, and the same derivative is immediately related to the number of molecules in the closed channel (recently measured at Rice) using the two-channel model. In Sect. 5.3, we describe the dynamical symmetry properties of the unitary gas in a harmonic trap, and we extract their physical consequences for many-body and few-body problems.

5.1 Simple Facts About the Unitary Gas

5.1.1 What is the Unitary Gas?

First, the unitary gas is ... a gas. As opposed to a liquid, it is a dilute system with respect to the interaction range b: its mean number density ρ satisfies the constraint

$$\rho b^3 \ll 1. \tag{5.1}$$

For a rapidly decreasing interaction potential $V(r)$, b is the spatial width of $V(r)$. In atomic physics, where $V(r)$ may be viewed as a strongly repulsive core and a Van der Waals attractive tail $-C_6/r^6$, one usually assimilates b to the Van der Waals length $(mC_6/\hbar^2)^{1/4}$.

The intuitive picture of a gas is that the particles mainly experience binary scattering, the probability that more than two particles are within a volume b^3 being negligible. As a consequence, what should really matter is the knowledge of the scattering amplitude f_k of two particles, where k is the relative momentum, rather than the r dependence of the interaction potential $V(r)$. This expectation has guided essentially all many-body works on the BEC–BCS crossover: One uses convenient models for $V(r)$ that are very different from the true atomic interaction potential, but that reproduce correctly the momentum dependence of f_k at the relevant low values of k, such as the Fermi momentum or the inverse thermal de Broglie wavelength, these relevant low values of k having to satisfy $kb \ll 1$ for this modelization to be acceptable.

Second, the unitary gas is such that, for the relevant values of the relative momentum k, the modulus of f_k reaches the maximal value allowed by quantum mechanics, the so-called unitary limit [1]. Here, we consider s-wave scattering between two opposite-spin fermions, so that f_k depends only on the modulus of the relative momentum. The optical theorem, a consequence of the unitarity of the quantum evolution operator [1], then implies

$$\mathrm{Im}\, f_k = k|f_k|^2. \tag{5.2}$$

Dividing by $|f_k|^2$, and using $f_k/|f_k|^2 = 1/f_k^*$, one sees that this fixes the value of the imaginary part of $1/f_k$, so that it is strictly equivalent to the requirement that there exists a real function $u(k)$ such that

$$f_k = -\frac{1}{ik + u(k)} \tag{5.3}$$

for all values of k. We then obtain the upper bound $|f_k| \leq 1/k$. Ideally, the unitary gas saturates this inequality for all values of k:

$$f_k^{\text{unitary}} = -\frac{1}{ik}. \tag{5.4}$$

In reality, Eq. 5.4 cannot hold for all k. It is thus important to understand over which range of k Eq. 5.4 should hold to have a unitary gas, and to estimate the deviations from Eq. 5.4 in that range in a real experiment. To this end, we use the usual low-k expansion of the denominator of the scattering amplitude [1], under validity conditions specified in [2]:

$$u(k) = \frac{1}{a} - \frac{1}{2}r_e k^2 + \dots \tag{5.5}$$

The length a is the scattering length, the length r_e is the effective range of the interaction. Both a and r_e can be of arbitrary sign. Even for $1/a = 0$, even for an everywhere non-positive interaction potential, r_e can be of arbitrary sign. As this last property seems to contradict a statement in the solution of problem 1 in Sect. 131 of [3], we have constructed an explicit example depicted in Fig. 5.1, which even shows that the effective range may be very different in absolute value from the true potential range b, i.e. r_e/b for $a^{-1} = 0$ may be in principle an arbitrarily large and negative number. Let us assume that the ... in Eq. 5.5 are negligible if $kb \ll 1$, an assumption that will be revisited in Sect. 5.2.3.3. Noting k_{typ} a typical relative momentum in the gas, we thus see that the unitary gas is in practice obtained as a double limit, a *zero range* limit

$$k_{\text{typ}}b \ll 1, k_{\text{typ}}|r_e| \ll 1 \tag{5.6}$$

and an *infinite scattering length* limit:

$$k_{\text{typ}}|a| \gg 1. \tag{5.7}$$

At zero temperature, we assume that $k_{\text{typ}} = k_F$, where the Fermi momentum is conventionally defined in terms of the gas total density ρ as for the ideal spin-1/2 Fermi gas:

$$k_F = (3\pi^2 \rho)^{1/3}. \tag{5.8}$$

In a trap, ρ and thus k_F are position dependent. Condition (5.7) is well satisfied experimentally, thanks to the Feshbach resonance. The condition $k_F b \ll 1$ is also well satisfied at the per cent level, because $b \approx$ the Van der Waals length is in the nanometer range. Up to now, there is no experimental tuning of the effective range
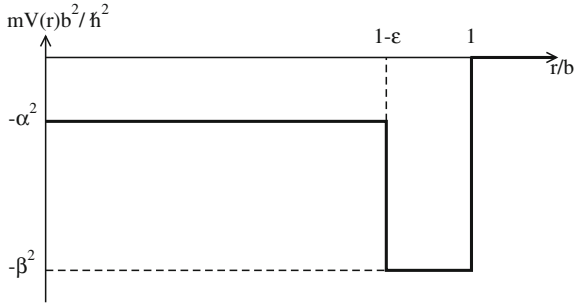
Fig. 5.1 A class of non-positive potentials (of compact support of radius b) that may lead to a negative effective range in the resonant case $a^{-1} = 0$. The resonant case is achieved when the three parameters α, β and ε satisfy $\tan[(1-\varepsilon)\alpha]\tan(\varepsilon\beta) = \alpha/\beta$. Then from Smorodinskii's formula, see Problem 1 in Sect. 131 of [3], one sees that $r_e/b \leq 2$. One also finds that $r_e/b \sim -\cos^2\theta/(\pi\varepsilon)^2 \to -\infty$ when $\varepsilon \to 0$ with $\alpha = \pi$, $\beta\varepsilon \to \theta$, where $\theta = 2.798386\ldots$ solves $1 + \theta\tan\theta = 0$

r_e, and there are cases where $k_F|r_e|$ is not small. However, to study the BEC–BCS crossover, one uses in practice the so-called broad Feshbach resonances, which do not require a too stringent control of the spatial homogeneity of the magnetic field, and where $|r_e| \sim b$; then Eq. 5.6 is also satisfied.

We note that the assumption $k_{\text{typ}} = k_F$, although quite intuitive, is not automatically correct. For example, for bosons, as shown by Efimov [4], an effective three-body attraction takes place, leading to the occurrence of the Efimov trimers; this attraction leads to the so-called problem of *fall to the center* [3], and one has $1/k_{\text{typ}}$ of the order of the largest of the two ranges b and $|r_e|$. Eq. 5.6 is then violated, and an extra length scale, the three-body parameter, has to be introduced, breaking the scale invariance of the unitary gas. Fortunately, for three fermions, there is no Efimov attraction, except for the case of different masses for the two spin components: if two fermions of mass $m_\uparrow$ interact with a lighter particle of mass $m_\downarrow$, the Efimov effect takes place for $m_\uparrow/m_\downarrow$ larger than $\simeq 13.607$ [5, 6]. If a third fermion of mass $m_\uparrow$ is added, a four-body Efimov effect appears at a slightly lower mass ratio $m_\uparrow/m_\downarrow \simeq 13.384$ [7]. In what follows we consider the case of equal masses, unless specified otherwise.

At non-zero temperature $T > 0$, another length scale appears in the unitary gas properties, the thermal de Broglie wavelength λ_{dB}, defined as

$$\lambda_{\text{dB}}^2 = \frac{2\pi\hbar^2}{mk_BT}. \tag{5.9}$$

At temperatures larger than the Fermi temperature $T_F = \hbar^2 k_F^2/(2mk_B)$, one has to take $k_{\text{typ}} \sim 1/\lambda_{\text{dB}}$ in the conditions Eq. 5.7. In practice, the most interesting regime is however the degenerate regime $T < T_F$, where the non-zero temperature does not bring new conditions for unitarity.

5.1.2 Some Simple Properties of the Unitary Gas

As is apparent in the expression of the two-body scattering amplitude Eq. 5.4, there is no parameter or length scales issuing from the interaction. As a consequence, for a gas in the trapping potential $U(\mathbf{r})$, the eigenenergies E_i of the N-body problem only depend on $\hbar^2/m$ and on the spatial dependence of $U(\mathbf{r})$: the length scale required to get an energy out of $\hbar^2/m$ is obtained from the shape of the container.

This is best formalized in terms of a spatial scale invariance. Qualitatively, if one changes the volume of the container, even if the gas becomes arbitrarily dilute, it remains at unitarity and strongly interacting. This is of course not true for a finite value of the scattering length a: If one reduces the gas density, $\rho^{1/3}a$ drops eventually to small values, and the gas becomes weakly interacting.

Quantitatively, if one applies to the container a similarity factor λ in all directions, which changes its volume from V to $\lambda^3 V$, we expect that each eigenenergy scales as

$$E_i \rightarrow \frac{E_i}{\lambda^2} \tag{5.10}$$

and each eigenwavefunction scales as

$$\psi_i(\mathbf{X}) \rightarrow \frac{\psi_i(\mathbf{X}/\lambda)}{\lambda^{3N/2}}. \tag{5.11}$$

Here $\mathbf{X} = (\mathbf{r}_1, \ldots, \mathbf{r}_N)$ is the set of all coordinates of the particles, and the λ-dependent factor ensures that the wavefunction remains normalized. The properties (5.10, 5.11), which are at the heart of what the unitary gas really is, will be put on mathematical grounds in Sect. 5.2 by replacing the interaction with contact conditions on ψ. Simple consequences may be obtained from these scaling properties, as we now discuss.

In a harmonic isotropic trap, where a single particle has an oscillation angular frequency ω, taking as the scaling factor the harmonic oscillator length $a_{\mathrm{ho}} = [\hbar/(m\omega)]^{1/2}$, one finds that

$$\frac{E_i}{\hbar\omega} = \mathscr{F}_i(N) \tag{5.12}$$

where the functions $\mathscr{F}_i$ are universal functions, ideally independent of the fact that one uses lithium 6 or potassium 40 atoms, and depending only on the particle number.

In free space, the unitary gas cannot have a N-body bound state (an eigenstate of negative energy), whatever the value of $N \geq 2$. If there was such a bound state, which corresponds to a square integrable eigenwavefunction of the relative (Jacobi) coordinates of the particles, one could generate a continuum of such square integrable eigenstates using Eqs. 5.10, 5.11. This would violate a fundamental property of self-adjoint Hamiltonians [8]. Another argument is that the energy of a discrete universal bound state would depend only on $\hbar$ and m, which is impossible by dimensional analysis.

At thermal equilibrium in the canonical ensemble in a box, say a cubic box of volume $V = L^3$ with periodic boundary conditions, several relations may be obtained if one takes the thermodynamic limit $N \to +\infty$, $L^3 \to +\infty$ with a fixed density ρ and temperature T, and if one assumes that the free energy F is an extensive quantity. Let us consider for simplicity the case of equal population of the two spin states, $N_\uparrow = N_\downarrow$. Then, in the thermodynamic limit, the free energy per particle $F/N \equiv f$ is a function of the density ρ and temperature T. If one applies a similarity of factor λ and if one change T to T/λ^2 so as to keep a constant ratio $E_i/(k_B T)$, that is a constant occupation probability for each eigenstate, one obtains from Eq. 5.10 that

$$f(\rho/\lambda^3, T/\lambda^2) = f(\rho, T)/\lambda^2. \tag{5.13}$$

At zero temperature, f reduces to the ground state energy per particle $e_0(\rho)$. From Eq. 5.13 it appears that $e_0(\rho)$ scales as $\rho^{2/3}$, exactly as the ground state energy of the ideal Fermi gas. One thus simply has

$$e_0(\rho) = \xi e_0^{\text{ideal}}(\rho) = \frac{3\xi}{5} \frac{\hbar^2 k_F^2}{2m} \tag{5.14}$$

where k_F is defined by Eq. 5.8 and ξ is a universal number. This is also a simple consequence of dimensional analysis [9]. Taking the derivative with respect to N or to the volume, this shows that the same type of relation holds for the zero temperature chemical potential, $\mu_0(\rho) = \xi \mu_0^{\text{ideal}}(\rho)$, and for the zero temperature total pressure, $P_0(\rho) = \xi P_0^{\text{ideal}}(\rho)$, so that

$$\mu_0(\rho) = \xi \frac{\hbar^2 k_F^2}{2m} \tag{5.15}$$

$$P_0(\rho) = \frac{2\xi}{5} \rho \frac{\hbar^2 k_F^2}{2m}. \tag{5.16}$$

At non-zero temperature, taking the derivative of Eq. 5.13 with respect to λ in $\lambda = 1$, and using $F = E - TS$, where E is the mean energy and $S = -\partial_T F$ is the entropy, as well as $\mu = \partial_N F$, one obtains

$$\frac{5}{3} E - \mu N = TS. \tag{5.17}$$

From the Gibbs-Duhem relation, the grand potential $\Omega = F - \mu N$ is equal to $-PV$, where P is the pressure of the gas. This gives finally the useful relation

$$PV = \frac{2}{3} E, \tag{5.18}$$

that can also be obtained from dimensional analysis [9], and that of course also holds at zero temperature (see above). All these properties actually also apply to the ideal

Fermi gas, which is obviously scaling invariant. The relation (5.18) for example was established for the ideal gas in [10].

Let us finally describe at a macroscopic level, i.e. in a hydrodynamic picture, the effect of the similarity Eq. 5.11 on the quantum state of a unitary gas, assuming that it was initially at thermal equilibrium in a trap. In the initial state of the gas, consider a small (but still macroscopic) element, enclosed in a volume dV around point $\mathbf{r}$. It is convenient to assume that dV is a fictitious cavity with periodic boundary conditions. In the hydrodynamic picture, this small element is assumed to be at local thermal equilibrium with a temperature T. Then one performs the spatial scaling transform Eq. 5.10 on each many-body eigenstate ψ of the thermal statistical mixture, which does not change the statistical weigths. How will the relevant physical quantities be transformed in the hydrodynamic approach?

The previously considered small element is now at position $\lambda \mathbf{r}$, and occupies a volume $\lambda^3 dV$, with the same number of particles. The hydrodynamic mean density profile after rescaling, ρ_λ, is thus related to the mean density profile ρ before scaling as

$$\rho_\lambda(\lambda \mathbf{r}) = \rho(\mathbf{r})/\lambda^3. \tag{5.19}$$

Second, is the small element still at (local) thermal equilibrium after scaling? Each eigenstate of energy E_{loc} of the locally homogeneous unitary gas within the initial cavity of volume dV is transformed by the scaling into an eigenstate within the cavity of volume $\lambda^3 dV$, with the eigenenergy E_{loc}/λ^2. Since the occupation probabilities of each local eigenstate are not changed, the local statistical mixture remains thermal provided that one rescales the temperature as

$$T_\lambda = T/\lambda^2. \tag{5.20}$$

A direct consequence is that the entropy of the small element of the gas is unchanged by the scaling, so that the local entropy *per particle s* in the hydrodynamic approach obeys

$$s_\lambda(\lambda \mathbf{r}) = s(\mathbf{r}). \tag{5.21}$$

Also, since the mean energy of the small element is reduced by the factor λ^2 due to the scaling, and the volume of the small element is multiplied by λ^3, the equilibrium relation Eq. 5.18 imposes that the local pressure is transformed by the scaling as

$$p_\lambda(\lambda \mathbf{r}) = p(\mathbf{r})/\lambda^5. \tag{5.22}$$

5.1.3 Application: Inequalities on ξ and Finite-Temperature Quantities

Using the previous constraints imposed by scale invariance of the unitary gas on thermodynamic quantities, in addition to standard thermodynamic inequalities, we

show that one can produce constraints involving both the zero-temperature quantity ξ and finite-temperature quantities of the gas.

Imagine that, at some temperature T, the energy E and the chemical potential μ of the non-polarized unitary Fermi gas have been obtained, in the thermodynamic limit. If one introduces the Fermi momentum Eq. 5.8 and the corresponding Fermi energy $E_F = \hbar^2 k_F^2/(2m)$, this means that on has at hand the two dimensionless quantities

$$A \equiv \frac{E}{N E_F} \tag{5.23}$$

$$B \equiv \frac{\mu}{E_F}. \tag{5.24}$$

As a consequence of Eq. 5.18, one also has access to the pressure P. We now show that the following inequalities hold at any temperature T:

$$\left(\frac{3}{5A}\right)^{2/3} B^{5/3} \leq \xi \leq \frac{5A}{3}. \tag{5.25}$$

In the canonical ensemble, the mean energy $E(N,T,V)$ is an increasing function of temperature for fixed volume V and atom number N. Indeed one has the well-known relation $k_B T^2 \partial_T E(N, T, V) = \mathrm{Var} H$, and the variance of the Hamiltonian is non-negative. As a consequence, for any temperature T:

$$E(N, T, V) \geq E(N, 0, V). \tag{5.26}$$

From Eq. 5.14 we then reach the upper bound on ξ given in Eq. 5.25.

In the grand canonical ensemble, the pressure $P(\mu, T)$ is an increasing function of temperature for a fixed chemical potential. This results from the Gibbs-Duhem relation $\Omega(\mu, T, V) = -V P(\mu, T)$ where Ω is the grand potential and V the volume, and from the differential relation $\partial_T \Omega(\mu, T) = -S$ where $S \geq 0$ is the entropy. As a consequence, for any temperature T:

$$P(\mu, T) \geq P(\mu, 0). \tag{5.27}$$

For the unitary gas, the left hand side can be expressed in terms of A using (5.18). Eliminating the density between Eq. 5.15 and 5.16 we obtain the zero temperature pressure

$$P(\mu, 0) = \frac{1}{15\pi^2 \xi^{3/2}} \frac{\hbar^2}{m} \left(\frac{2m\mu}{\hbar^2}\right)^{5/2}. \tag{5.28}$$

This leads to the lower bound on ξ given in Eq. 5.25.

Let us apply Eq. 5.25 to the Quantum Monte Carlo results of [11]: at the critical temperature $T = T_c$, $A = 0.310(10)$ and $B = 0.493(14)$, so that
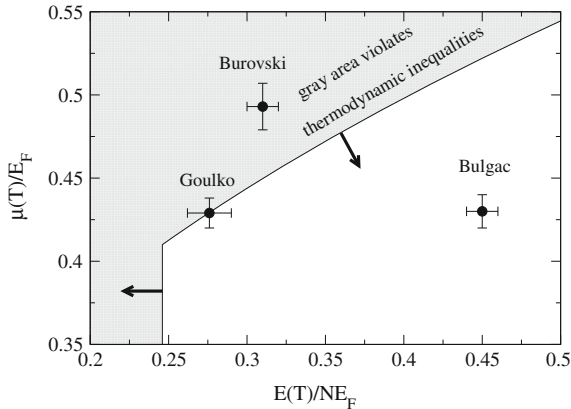
Fig. 5.2 For the spin balanced uniform unitary gas at thermal equilibrium: assuming $\xi = 0.41$ in Eq. 5.25 defines a zone (*shaded in gray*) in the plane energy–chemical potential that is forbidden at all temperatures. The black disks correspond to the unbiased Quantum Monte Carlo results of Burovski et al. [11], of Bulgac et al. [13], and of Goulko et al. [14] at the critical temperature. Taking the unknown exact value of ξ, which is below the fixed node upper bound 0.41 [12], will shift the forbidden zone boundaries as indicated by the arrows

$$0.48(3) \le \xi_{[11]} \le 0.52(2). \tag{5.29}$$

This deviates by two standard deviations from the fixed node result $\xi \le 0.40(1)$ [12]. The Quantum Monte Carlo results of [13], if one takes a temperature equal to the critical temperature of [11], give $A = 0.45(1)$ and $B = 0.43(1)$; these values, in clear disagreement with [11], lead to the non-restrictive bracketing $0.30(2) \le \xi_{[13]} \le 0.75(2)$. The more recent work [14] finds $k_B T_c/E_F = 0.171(5)$ and at this critical temperature, $A = 0.276(14)$ and $B = 0.429(9)$, leading to

$$0.41(3) \le \xi_{[14]} \le 0.46(2). \tag{5.30}$$

Another, more graphical application of our simple bounds is to assume some reasonable value of ξ, and then to use Eq. 5.25 to construct a zone in the energy-chemical potential plane that is forbidden at all temperatures. In Fig. 5.2 , we took $\xi = 0.41$, inspired by the fixed node upper bound on the exact value of ξ [12]: the shaded area is the resulting forbidden zone, and the filled disks with error bars represent the in principle exact Quantum Monte Carlo results of various groups at $T = T_c$. It is apparent that the prediction of [11] lies well within the forbidden zone and thus violates thermodynamic inequalities. The prediction of [13] is well within the allowed zone, whereas the most recent prediction of [14] is close to the boundary between the forbidden and the allowed zones. If one takes a smaller value for ξ, the boundaries of the forbidden zone will shift as indicated by the arrows on the figure. All this shows that simple reasonings may be useful to test and guide numerical studies of the unitary gas.

5.1.4 Is the Unitary Gas Attractive or Repulsive?

According to a common saying, a weakly interacting Fermi gas ($k_F|a| \ll 1$) experiences an effective repulsion for a positive scattering length $a > 0$, and an effective attraction for a negative scattering length $a < 0$. Another common fact is that, in the unitary limit $|a| \to +\infty$, the gas properties do not depend on the sign of a. As the unitary limit may be apparently equivalently obtained by taking the limit $a \to +\infty$ or the limit $a \to -\infty$, one reaches a paradox, considering the fact that the unitary gas does not have the same ground state energy than the ideal gas and cannot be at the same time an attractive and repulsive state of matter.

This paradox may be resolved by considering the case of two particles in an isotropic harmonic trap. After elimination of the center of mass motion, and restriction to a zero relative angular momentum to have s-wave interaction, one obtains the radial Schrödinger equation

$$-\frac{\hbar^2}{2\mu}\left[\psi''(r) + \frac{2}{r}\psi'(r)\right] + \frac{1}{2}\mu\omega^2 r^2 \psi(r) = E_{\mathrm{rel}}\psi(r), \qquad (5.31)$$

with the relative mass $\mu = m/2$. The interactions are included in the zero range limit by the $r = 0$ boundary conditions, the so-called Wigner-Bethe-Peierls contact conditions described in Sect. 5.2:

$$\psi(r) = A[r^{-1} - a^{-1}] + O(r) \qquad (5.32)$$

that correctly reproduce the free space scattering amplitude

$$f_k^{\mathrm{zero\,range}} = -\frac{1}{a^{-1} + ik}. \qquad (5.33)$$

The general solution of Eq. 5.31 may be expressed in terms of Whittaker M et W functions. For an energy E_{rel} not belonging to the non-interacting spectrum $\{(\frac{3}{2} + 2n)\hbar\omega, n \in \mathbb{N}\}$, the Whittaker function M diverges exponentially for large r and has to be disregarded. The small r behavior of the Whittaker function W, together with the Wigner-Bethe-Peierls contact condition, leads to the implicit equation for the relative energy, in accordance with [15]:

$$\frac{\Gamma\left(\frac{3}{4} - \frac{E_{\mathrm{rel}}}{2\hbar\omega}\right)}{\Gamma\left(\frac{1}{4} - \frac{E_{\mathrm{rel}}}{2\hbar\omega}\right)} = \frac{a_{\mathrm{ho}}^{\mathrm{rel}}}{2a} \qquad (5.34)$$

with the harmonic oscillator length of the relative motion, $a_{\mathrm{ho}}^{\mathrm{rel}} = [\hbar/(\mu\omega)]^{1/2}$.

The function $\Gamma(x)$ is different from zero $\forall x \in \mathbb{R}$ and diverges on each nonpositive integers. Thus Eq. 5.34 immediately leads in the unitary case to the spectrum $E_{\mathrm{rel}} \in \{(2n + 1/2)\hbar\omega, n \in \mathbb{N}\}$. This can be readily obtained by setting in Eq. 5.31 $\psi(r) = f(r)/r$, so that f obeys Schrödinger's equation for a 1D harmonic oscillator,
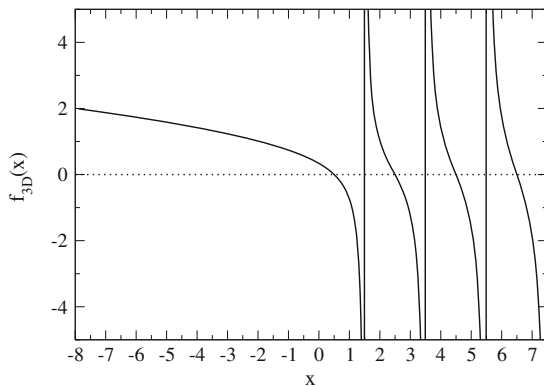
Fig. 5.3 For the graphical solution of Eq. 5.34, which gives the spectrum for two particles in a three-dimensional isotropic harmonic trap, plot of the function $f_{3D}(x) = \Gamma(\frac{3}{4} - \frac{x}{2})/\Gamma(\frac{1}{4} - \frac{x}{2})$, where x stands for $E_{\text{rel}}/(\hbar\omega)$

with the constraint issuing from Eq. 5.32 that $f(r = 0) \neq 0$, which selects the even 1D states.

The graphical solution of Eq. 5.34, see Fig. 5.3 , allows to resolve the paradox about the attractive or repulsive nature of the unitary gas. For example starting with the ground state wavefunction of the ideal gas case, of relative energy $E_{\text{rel}} = \frac{3}{2}\hbar\omega$, it appears that the two adiabatic followings (i) $a = 0^+ \to a = +\infty$ and (ii) $a = 0^- \to -\infty$ lead to *different* final eigenstates of the unitary case, to an excited state $E_{\text{rel}} = \frac{5}{2}\hbar\omega$ for the procedure (i), and to the ground state $E_{\text{rel}} = \frac{1}{2}\hbar\omega$ for procedure (ii).

The same explanation holds for the many-body case: the interacting gas has indeed several energy branches in the BEC–BCS crossover, as suggested by the toy model[1] of [16], see Fig. 5.4. Starting from the weakly attractive Fermi gas and ramping the scattering length down to $-\infty$ one explores a part of the ground energy branch, where the unitary gas is attractive; this ground branch continuously evolves into a weakly repulsive condensate of dimers [17] if $1/a$ further moves from 0^- to 0^+ and then to $+\infty$. The attractive nature of the unitary gas on the ground energy branch will become apparent in the lattice model of Sect. 5.2. On the other hand, starting from the weakly repulsive Fermi gas and ramping the scattering up to $+\infty$, one explores an effectively repulsive excited branch.

In the first experiments on the BEC–BCS crossover, the ground branch was explored by adiabatic variations of the scattering length and was found to be stable. The first excited energy branch was also investigated in the early work [18], and more recently in [19] looking for a Stoner demixing instability of the strongly repulsive two-component Fermi gas. A difficulty for the study of this excited branch

---

[1] This toy model replaces the many-body problem with the one of a matterwave interacting with a single scatterer in a hard wall cavity of radius $\propto 1/k_F$.

Fig. 5.4 In the toy model
of [16], for the homogeneous
two-component unpolarized
Fermi gas, energy per
particle on the ground branch
and the first excited branch
as a function of the inverse
scattering length. The Fermi
wavevector is defined in
Eq. 5.8, $E_F = \hbar^2 k_F^2/(2m)$ is
the Fermi energy, and a is
the scattering length
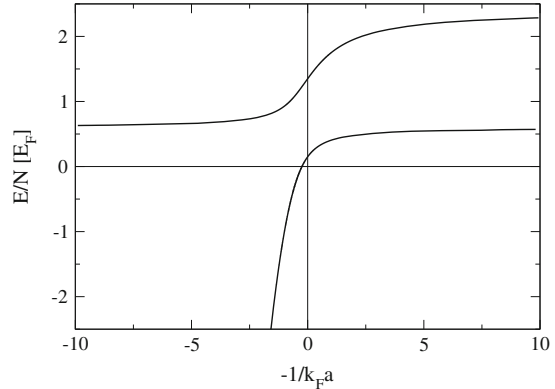
is its metastable character: Three-body collisions gradually transfer the gas to the
ground branch, leading e.g. to the formation of dimers if $0 < k_F a \lesssim 1$.

5.1.5 Other Partial Waves, Other Dimensions

We have previously considered the two-body scattering amplitude in the s-wave
channel. What happens for example in the p-wave channel? This channel is relevant
for the interaction between fermions in the same internal state, where a Feshbach
resonance technique is also available [20, 21]. Can one also reach the unitarity limit
Eq. 5.4 in the p-wave channel?

Actually the optical theorem shows that relation Eq. 5.3 also holds for the p-wave
scattering amplitude f_k. What differs is the low-k expansion of $u(k)$, that is now given
by

$$u(k) = \frac{1}{k^2 \mathcal{V}_s} + \alpha + \ldots, \qquad (5.35)$$

where $\mathcal{V}_s$ is the scattering volume (of arbitrary sign) and α has the dimension of the
inverse of a length. The unitary limit would require $u(k)$ negligible as compared to
k. One can in principle tune $\mathcal{V}_s$ to infinity with a Feshbach resonance. Can one then
have a small value of α at resonance? A theorem for a compact support interaction
potential of radius b shows however that [22, 23]

$$\lim_{|\mathcal{V}_s| \to +\infty} \alpha \geq 1/b. \qquad (5.36)$$

A similar conclusion holds using two-channel models of the Feshbach resonance
[23, 24]. α thus assumes a huge positive value on resonance, which breaks the scale
invariance and precludes the existence of a p-wave unitary gas. This does not prevent
however to reach the unitary limit in the *vicinity* of a particular value of k. For $\mathcal{V}_s$

large and negative, neglecting the . . . in Eq. 5.35 under the condition $kb \ll 1$, one indeed has $|u(k)| \ll k$, so that $f_k \simeq -1/(ik)$, in a vicinity of

$$k_0 = \frac{1}{(\alpha|\mathscr{V}_s|)^{1/2}}. \tag{5.37}$$

Turning back to the interaction in the s-wave channel, an interesting question is whether the unitary gas exists in reduced dimensions.

In a one-dimensional system the zero range interaction may be modeled by a Dirac potential $V(x) = g\delta(x)$. If g is finite, it introduces a length scale $\hbar^2/(mg)$ that breaks the scaling invariance. Two cases are thus scaling invariant, the ideal gas $g = 0$ and the impenetrable case $1/g = 0$. The impenetrable case however is mappable to an ideal gas in one dimension, it has in particular the same energy spectrum and thermodynamic properties [25].

In a two-dimensional system, the scattering amplitude for a zero range interaction potential is given by [26]

$$f_k^{2D} = \frac{1}{\gamma + \ln(ka_{2D}/2) - i\pi/2} \tag{5.38}$$

where $\gamma = 0.57721566\ldots$ is Euler's constant and a_{2D} is the scattering length. For a finite value of a_{2D}, there is no scale invariance. The case $a_{2D} \to 0$ corresponds to the ideal gas limit. At first sight, the opposite limit $a_{2D} \to +\infty$ is a good candidate for a two-dimensional unitary gas; however this limit also corresponds to an ideal gas. This appears in the 2D version of the lattice model of Sect. 5.2 [27]. This can also be checked for two particles in an isotropic harmonic trap. Separating out the center of mass motion, and taking a zero angular momentum state for the relative motion, to have interaction in the s-wave channel, one has to solve the radial Schrödinger equation:

$$-\frac{\hbar^2}{2\mu}\left[\psi''(r) + \frac{1}{r}\psi'(r)\right] + \frac{1}{2}\mu\omega^2 r^2 \psi(r) = E_{\text{rel}}\psi(r) \tag{5.39}$$

where $\mu = m/2$ is the reduced mass of the two particles, E_{rel} is an eigenenergy of the relative motion, and ω is the single particle angular oscillation frequency. The interactions are included by the boundary condition in $r = 0$:

$$\psi(r) = A\ln(r/a_{2D}) + O(r), \tag{5.40}$$

which is constructed to reproduce the expression of the scattering amplitude Eq. 5.38 for the free space problem.

The general solution of Eq. 5.39 may be expressed in terms of Whittaker functions M and W. Assuming that E_{rel} does not belong to the ideal gas spectrum $\{(2n + 1)\hbar\omega, n \in \mathbb{N}\}$, one finds that the M solution has to be disregarded because it diverges exponentially for $r \to +\infty$. From the small r behavior of the W solution, one obtains the implicit equation

Fig. 5.5 For the graphical
solution of Eq. 5.41, which
gives the spectrum for two
interacting particles in a
two-dimensional isotropic
harmonic trap, plot
of the function $f_{2D}(x) = \frac{1}{2}\psi[(1-x)/2] + \gamma$ where x
stands for $E_{\text{rel}}/(\hbar\omega)$ and the
special function ψ is the
logarithmic derivative of the
Γ function
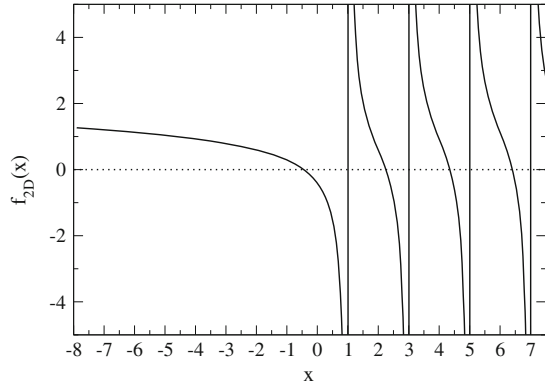
$$\frac{1}{2}\psi\left(\frac{\hbar\omega - E_{\text{rel}}}{2\hbar\omega}\right) + \gamma = -\ln(a_{2D}/a_{\text{ho}}^{\text{rel}}) \tag{5.41}$$

where the relative harmonic oscillator length is $a_{\text{ho}}^{\text{rel}} = [\hbar/(\mu\omega)]^{1/2}$ and the digamma
function ψ is the logarithmic derivative of the Γ function. If $a_{2D} \to +\infty$, one then
finds that E_{rel} tends to the ideal gas spectrum $\{(2n+1)\hbar\omega, n \in \mathbb{N}\}$ from below, see
Fig. 5.5, in agreement with the lattice model result that the 2D gas with a large and
finite a_{2D} is a weakly attractive gas.

5.2 Various Models and General Relations

There are basically two approaches to model the interaction between particles for
the unitary gas (and more generally for the BEC–BCS crossover).

In the first approach, see Sect. 5.2.1 and Sect. 5.2.3, one takes a model with a
finite range b and a fixed (e.g. infinite) scattering length a. This model may be in
continuous space or on a lattice, with one or several channels. Then one tries to
calculate the eigenenergies, the thermodynamic properties from the thermal density
operator $\propto \exp(-\beta H)$, etc, and the zero range limit $b \to 0$ should be taken at
the end of the calculation. Typically, this approach is followed in numerical many-
body methods, such as the approximate fixed node Monte Carlo method [12, 28, 29]
or unbiased Quantum Monte Carlo methods [11, 13, 30]. A non-trivial question
however is whether each eigenstate of the model is universal in the zero range limit,
that is if the eigenenergy E_i and the corresponding wavefunction ψ_i converge for
$b \to 0$. In short, the challenge is to prove that the ground state energy of the system
does not tend to $-\infty$ when $b \to 0$.

In the second approach, see Sect. 5.2.2 , one directly considers the zero range
limit, and one replaces the interaction by the so-called Wigner-Bethe-Peierls con-
tact conditions on the N-body wavefunction. This constitutes what we shall call the
zero-range model. The advantage is that only the scattering length appears in the

problem, without unnecessary details on the interaction, which simplifies the problem and allows to obtain analytical results. For example the scale invariance of the unitary gas becomes clear. A non-trivial question however is to know whether the zero-range model leads to a self-adjoint Hamiltonian, with a spectrum then necessarily bounded from below for the unitary gas (see Sect. 5.1.2), without having to add extra boundary conditions. For $N = 3$ bosons, due to the Efimov effect, the Wigner-Bethe-Peierls or zero-range model becomes self-adjoint only if one adds an extra three-body contact condition, involving a so-called three-body parameter. In an isotropic harmonic trap, at unitarity, there exists however a non-complete family of bosonic universal states, independent from the three-body parameter and to which the restriction of the Wigner-Bethe-Peierls model is hermitian [31, 32]. For equal mass two-component fermions, it is hoped in the physics literature that the zero-range model is self-adjoint for an arbitrary number of particles N. Surprisingly, there exist works in mathematical physics predicting that this is *not* the case when N is large enough [33, 34]; however the critical mass ratio for the appearance of an Efimov effect in the unequal-mass $3 + 1$ body problem given without proof in [34] was not confirmed by the numerical study[7], and the variational ansatz used in [33] to show that the energy is unbounded below does not have the proper fermionic exchange symmetry. This mathematical problem thus remains open.

5.2.1 Lattice Models and General Relations

5.2.1.1 The Lattice Models

The model that we consider here assumes that the spatial positions are discretized on a cubic lattice, of lattice constant that we call b as the interaction range. It is quite appealing in its simplicity and generality. It naturally allows to consider a contact interaction potential, opposite spin fermions interacting only when they are on the same lattice site. Formally, this constitutes a separable potential for the interaction (see Sect. 5.2.3 for a reminder), a feature known to simplify diagrammatic calculations [35]. Physically, it belongs to the same class as the Hubbard model, so that it may truly be realized with ultracold atoms in optical lattices [36], and it allows to recover the rich lattice physics of condensed matter physics and the corresponding theoretical tools such as Quantum Monte Carlo methods [11, 30].

The spatial coordinates **r** of the particles are thus discretized on a cubic grid of step b. As a consequence, the components of the wavevector of a particle have a meaning modulo $2\pi/b$ only, since the plane wave function $\mathbf{r} \to \exp(i\mathbf{k} \cdot \mathbf{r})$ defined on the grid is not changed if a component of $\mathbf{k}$ is shifted by an integer multiple of $2\pi/b$. We shall therefore restrict the wavevectors to the first Brillouin zone of the lattice:

$$\mathbf{k} \in \mathscr{D} \equiv \left[-\frac{\pi}{b}, \frac{\pi}{b}\right]^3. \tag{5.42}$$

This shows that the lattice structure in real space automatically provides a cut-off in momentum space. In the absence of interaction and of confining potential, eigen-modes of the system are plane waves with a dispersion relation $\mathbf{k} \to \varepsilon_{\mathbf{k}}$, supposed to be an even and non-negative function of $\mathbf{k}$. We assume that this dispersion relation is independent of the spin state, which is a natural choice since the $\uparrow$ and $\downarrow$ particles have the same mass. To recover the correct continuous space physics in the zero lattice spacing limit $b \to 0$, we further impose that it reproduces the free space dispersion relation in that limit, so that

$$\varepsilon_{\mathbf{k}} \sim \frac{\hbar^2 k^2}{2m} \quad \text{for } kb \to 0. \tag{5.43}$$

The interaction between opposite spin particles takes place when two particles are on the same lattice site, as in the Hubbard model. In first quantized form, it is represented by a discrete delta potential:

$$V = \frac{g_0}{b^3} \delta_{\mathbf{r}_1, \mathbf{r}_2}. \tag{5.44}$$

The factor $1/b^3$ is introduced because $b^{-3} \delta_{\mathbf{r}, \mathbf{0}}$ is equivalent to the Dirac distribution $\delta(\mathbf{r})$ in the continuous space limit. To summarize, the lattice Hamiltonian in second quantized form in the general trapped case is

$$
\begin{aligned}
H = {}& \sum_{\sigma=\uparrow,\downarrow} \int_{\mathscr{D}} \frac{d^3 k}{(2\pi)^3} \varepsilon_{\mathbf{k}} c_\sigma^\dagger(\mathbf{k}) c_\sigma(\mathbf{k}) + \sum_{\sigma=\uparrow,\downarrow} \sum_{\mathbf{r}} b^3 U(\mathbf{r}) (\psi_\sigma^\dagger \psi_\sigma)(\mathbf{r}) \\
& + g_0 \sum_{\mathbf{r}} b^3 (\psi_\uparrow^\dagger \psi_\downarrow^\dagger \psi_\downarrow \psi_\uparrow)(\mathbf{r}).
\end{aligned}
\tag{5.45}
$$

The plane wave annihilation operators $c_\sigma(\mathbf{k})$ in spin state σ obey the usual continuous space anticommutation relations $\{c_\sigma(\mathbf{k}), c_{\sigma'}^\dagger(\mathbf{k}')\} = (2\pi)^3 \delta(\mathbf{k} - \mathbf{k}') \delta_{\sigma\sigma'}$ if $\mathbf{k}$ and $\mathbf{k}'$ are in the first Brillouin zone,[2] and the field operators $\psi_\sigma(\mathbf{r})$ obey the usual discrete space anticommutation relations $\{\psi_\sigma(\mathbf{r}), \psi_{\sigma'}^\dagger(\mathbf{r}')\} = b^{-3} \delta_{\mathbf{r}\mathbf{r}'} \delta_{\sigma\sigma'}$. In the absence of trapping potential, in a cubic box with size L integer multiple of b, with periodic boundary conditions, the integral in the kinetic energy term is replaced by the sum $\sum_{\mathbf{k}\in\mathcal{D}} \varepsilon_{\mathbf{k}} \tilde{c}_{\mathbf{k}\sigma}^\dagger \tilde{c}_{\mathbf{k}\sigma}$ where the annihilation operators then obey the discrete anticommutation relations $\{\tilde{c}_{\mathbf{k}\sigma}, \tilde{c}_{\mathbf{k}'\sigma'}^\dagger\} = \delta_{\mathbf{k}\mathbf{k}'} \delta_{\sigma\sigma'}$ for $\mathbf{k}, \mathbf{k}' \in \mathscr{D}$.

The coupling constant g_0 is a function of the grid spacing b. It is adjusted to reproduce the scattering length of the true interaction. The scattering amplitude of two atoms on the lattice with vanishing total momentum, that is with incoming particles of opposite spin and opposite momenta $\pm \mathbf{k}_0$, reads

$$f_{k_0} = -\frac{m}{4\pi\hbar^2} \left[g_0^{-1} - \int_{\mathscr{D}} \frac{d^3 k}{(2\pi)^3} \frac{1}{E + i0^+ - 2\varepsilon_{\mathbf{k}}} \right]^{-1} \tag{5.46}$$

---

[2] In the general case, $\delta(\mathbf{k} - \mathbf{k}')$ has to be replaced with $\sum_{\mathbf{K}} \delta(\mathbf{k} - \mathbf{k}' - \mathbf{K})$ where $\mathbf{K} \in (2\pi/b)\mathbb{Z}^3$ is any vector in the reciprocal lattice.

as derived in details in [37] for a quadratic dispersion relation and in [38] for a general dispersion relation. Here the scattering state energy $E = 2\varepsilon_{\mathbf{k}_0}$ actually introduces a dependence of the scattering amplitude on the direction of $\mathbf{k}_0$ when the dispersion relation $\varepsilon_{\mathbf{k}}$ is not parabolic. If one is only interested in the expansion of $1/f_{k_0}$ up to second order in k_0, e.g. for an effective range calculation, one may conveniently use the isotropic approximation $E = \hbar^2 k_0^2/m$ thanks to (5.43). Adjusting g_0 to recover the correct scattering length gives from Eq. 5.46 for $k_0 \to 0$:

$$\frac{1}{g_0} = \frac{1}{g} - \int_{\mathscr{D}} \frac{d^3 k}{(2\pi)^3} \frac{1}{2\varepsilon_{\mathbf{k}}},\tag{5.47}$$

with $g = 4\pi\hbar^2 a/m$. The above formula Eq. 5.47 is reminiscent of the technique of renormalization of the coupling constant [39, 40]. A natural case to consider is the one of the usual parabolic dispersion relation,

$$\varepsilon_{\mathbf{k}} = \frac{\hbar^2 k^2}{2m}.\tag{5.48}$$

A more explicit form of Eq. 5.47 is then [41, 42]:

$$g_0 = \frac{4\pi\hbar^2 a/m}{1 - Ka/b}\tag{5.49}$$

with a numerical constant given by

$$K = \frac{12}{\pi} \int_0^{\pi/4} d\theta \ln(1 + 1/\cos^2\theta) = 2.442\,749\,607\,806\,335\ldots,\tag{5.50}$$

and that may be expressed analytically in terms of the dilog special function.

5.2.1.2 Simple Variational Upper Bounds

The relation Eq. 5.49 is quite instructive in the zero range limit $b \to 0$, for fixed non-zero scattering length a and atom numbers N_σ: In this limit, the lattice filling factor tends to zero, and the lattice model is expected to converge to the continuous space zero-range model, that is to the Wigner-Bethe-Peierls model described in Sect. 5.2.2. For each of the eigenenergies this means that

$$\lim_{b \to 0} E_i(b) = E_i,\tag{5.51}$$

where in the right hand side the set of E_i's are the energy spectrum of the zero range model. On the other hand, for a small enough value of b, the denominator in the right-hand side of Eq. 5.49 is dominated by the term $-Ka/b$, the lattice coupling constant g_0 is clearly negative, and the lattice model is attractive, as already pointed out in [43]. By the usual variational argument, this shows that the ground state energy of

the zero range interacting gas is below the one of the ideal gas, for the same trapping potential and atom numbers N_σ :

$$E_0 \le E_0^{\text{ideal}}. \tag{5.52}$$

Similarly, at thermal equilibrium in the canonical ensemble, the free energy of the interacting gas is below the one of the ideal gas:

$$F \le F^{\text{ideal}}. \tag{5.53}$$

As in [44] one indeed introduces the free-energy functional of the (here lattice model) interacting gas, $\mathcal{F}[\hat{\rho}] = \text{Tr}[H\hat{\rho}] + k_B T \text{Tr}[\hat{\rho} \ln \hat{\rho}]$, where $\hat{\rho}$ is any unit trace system density operator. Then

$$\mathcal{F}[\hat{\rho}_{\text{th}}^{\text{ideal}}] = F^{\text{ideal}}(b) + \text{Tr}[\hat{\rho}_{\text{th}}^{\text{ideal}} V], \tag{5.54}$$

where $\hat{\rho}_{\text{th}}^{\text{ideal}}$ is the thermal equilibrium density operator of the ideal gas in the lattice model, and V is the interaction contribution to the N-body Hamiltonian. Since the minimal value of $\mathcal{F}[\hat{\rho}]$ over $\hat{\rho}$ is equal to the interacting gas lattice model free energy $F(b)$, the left hand side of Eq. 5.5 is larger than $F(b)$. Since the operator V is negative for small b, because $g_0 < 0$, the right hand side of Eq. 5.53 is smaller than $F^{\text{ideal}}(b)$. Finally taking the limit $b \to 0$, one obtains the desired inequality. The same reasoning can be performed in the grand canonical ensemble, showing that the interacting gas grand potential is below the one of the ideal gas, for the same temperature and chemical potentials μ_σ:

$$\Omega \le \Omega^{\text{ideal}}. \tag{5.55}$$

In [45], for the unpolarized unitary gas, this last inequality was checked to be obeyed by the experimental results, but it was shown, surprisingly, to be violated by some of the Quantum Monte Carlo results of [11]. For the particular case of the spatially homogeneous unitary gas, the above reasonings imply that $\xi \le 1$ in Eq. 5.14, so that the unitary gas is attractive (in the ground branch, see Sect. 5.1.4). Using the BCS variational ansatz in the lattice model[3] [46] one obtains the more stringent upper bound [40]:

$$\xi \le \xi_{\text{BCS}} = 0.5906\ldots \tag{5.56}$$

5.2.1.3 Finite-Range Corrections

For the parabolic dispersion relation, the expectation Eq. 5.51 was checked analytically for two opposite spin particles: for $b \to 0$, in free space the scattering amplitude

---

[3] One may check, e.g. in the sector $N_\uparrow = N_\downarrow = 2$, that the BCS variational wavefunction, which is a condensate of pairs in some pair wavefunction, does not obey the Wigner-Bethe-Peierls boundary conditions even if the pair wavefunction does, so it looses its variational character in the zero-range model.

Fig. 5.6 Diamonds: the first low eigenenergies for three (↑↑↓) fermions in a cubic box with a lattice model, as functions of the lattice constant b [42]. The box size is L, with periodic boundary conditions, the scattering length is infinite, the dispersion relation is parabolic Eq. 5.48. The unit of energy is $E_0 = (2\pi\hbar)^2/2mL^2$. Straight lines: Linear fits performed on the data over the range $b/L \leq 1/15$, except for the energy branch $E \simeq 2.89 E_0$ which is linear on a smaller range. Stars in $b = 0$: Eigenenergies predicted by the zero-range model
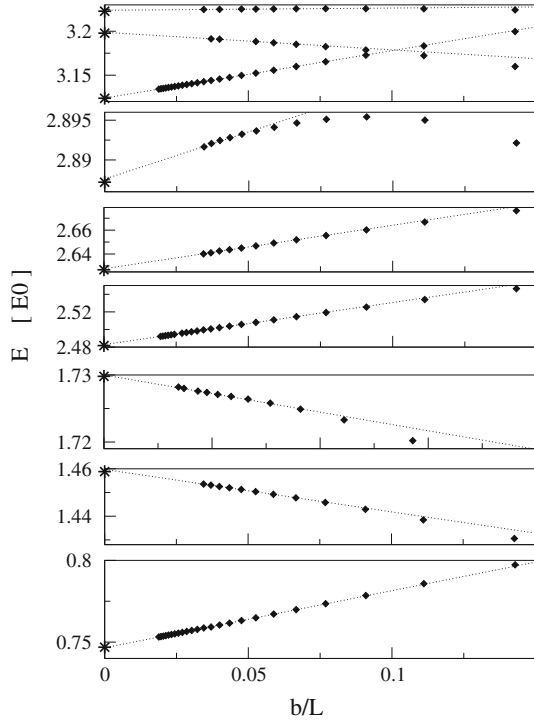
(5.46), and in a box the lattice energy spectrum, converge to the predictions of the zero-range model [42]. It was also checked numerically for $N = 3$ particles in a box, with two ↑ particles and one ↓ particle: as shown in Fig. 5.6, for the first low energy eigenstates with zero total momentum, a convergence of the lattice eigenenergies to the Wigner-Bethe-Peierls ones is observed, in a way that is eventually linear in b for small enough values of b. As discussed in [38], this asymptotic linear dependence in b is expected for Galilean invariant continuous space models, and the first order deviations of the eigenergies from their zero range values are linear in the effective range r_e of the interaction potential, as defined in Eq. 5.5, with model-independent coefficients:

$$\frac{dE_i}{dr_e}(b \to 0) \quad \text{is model-independent.} \tag{5.57}$$

However, for lattice models, Galilean invariance is broken and the scattering between two particles depends on their center-of-mass momentum; this leads to a breakdown of the universal relation (5.57), while preserving the linear dependence of the energy with b at low b [47].

A procedure to calculate r_e in the lattice model for a general dispersion relation $\varepsilon_{\mathbf{k}}$ in presented in Appendix 1. For the parabolic dispersion relation Eq. 5.47, its value was given in [46] in numerical form. With the technique exposed in Appendix 1, we

have now the analytical value:

$$r_e^{\text{parab}} = b\frac{12\sqrt{2}}{\pi^3}\arcsin\frac{1}{\sqrt{3}} = 0.336\,868\,47\ldots b. \tag{5.58}$$

The usual Hubbard model, whose rich many-body physics is reviewed in [48], was also considered in [46]: It is defined in terms of the tunneling amplitude between neighboring lattice sites, here $t = -\hbar^2/(2mb^2) < 0$, and of the on-site interaction $U = g_0/b^3$. The dispersion relation is then

$$\varepsilon_{\mathbf{k}} = \frac{\hbar^2}{mb^2}\sum_{\alpha=x,y,z}[1 - \cos(k_\alpha b)] \tag{5.59}$$

where the summation is over the three dimensions of space. It reproduces the free space dispersion relation only in a vicinity of $\mathbf{k} = \mathbf{0}$. The explicit version of Eq. 5.47 is obtained from Eq. 5.49 by replacing the numerical constant K by $K^{\text{Hub}} = 3.175911\ldots$. In the zero range limit this leads for $a \neq 0$ to $U/|t| \to -7.913552\ldots$, corresponding as expected to an *attractive* Hubbard model, lending itself to a Quantum Monte Carlo analysis for equal spin populations with no sign problem [11, 13]. The effective range of the Hubbard model, calculated as in Appendix 1, remarkably is negative [46]:

$$r_e^{\text{Hub}} \simeq -0.305718b. \tag{5.60}$$

It becomes thus apparent that an *ad hoc* tuning of the dispersion relation $\varepsilon_{\mathbf{k}}$ may lead to a lattice model with a zero effective range. As an example, we consider a dispersion relation

$$\varepsilon_{\mathbf{k}} = \frac{\hbar^2 k^2}{2m}[1 - C(kb/\pi)^2], \tag{5.61}$$

where C is a numerical constant less than $1/3$. From Appendix 1 we then find that

$$r_e = 0 \quad \text{for} \quad C = 0.2570224\ldots \tag{5.62}$$

The corresponding value of g_0 is given by Eq. 5.49 with $K = 2.899952\ldots$.

As pointed out in [47], additionally fine-tuning the dispersion relation to cancel not only r_e but also another coefficient (denoted by B in [47]) may have some practical interest for Quantum Monte Carlo calculations that are performed with a non-zero b, by canceling the undesired linear dependence of thermodynamical quantities and of the critical temperature T_c on b.

5.2.1.4 Energy Functional, Tail of the Momentum Distribution and Pair Correlation Function at Short Distances

A quite ubiquitous quantity in the short-range or large-momentum physics of gases with zero range interactions is the so-called "contact", which, restricting here for

simplicity to thermal equilibrium in the canonical ensemble, can be defined by

$$C \equiv \frac{4\pi m}{\hbar^2} \left(\frac{dE}{d(-1/a)} \right)_S = \frac{4\pi m}{\hbar^2} \left(\frac{dF}{d(-1/a)} \right)_T . \tag{5.63}$$

For zero-range interactions, this quantity C determines the large-k tail of the momentum distribution

$$n_\sigma(\mathbf{k}) \underset{k \to \infty}{\sim} \frac{C}{k^4} \tag{5.64}$$

as well as the short-distance behavior of the pair distribution function

$$\int d^3 R \, g_{\uparrow\downarrow}^{(2)} \left(\mathbf{R} + \frac{\mathbf{r}}{2}, \mathbf{R} - \frac{r}{2} \right) \underset{r \to 0}{\sim} \frac{C}{(4\pi r)^2} . \tag{5.65}$$

Here the spin-σ momentum distribution $n_\sigma(\mathbf{k})$ is normalised as $\int \frac{d^3 k}{(2\pi)^3} n_\sigma(\mathbf{k}) = N_\sigma$. The relations (5.63–5.65) were obtained in [49, 50]. Historically, analogous relations were first established for one-dimensional bosonic systems [51, 52] with techniques that may be straightforwardly extended to two dimensions and three dimensions [38]. Another relation derived in [49] for the zero-range model expresses the energy as a functional of the one-body density matrix:

$$E = \sum_{\sigma = \uparrow, \downarrow} \int \frac{d^3 k}{(2\pi)^3} \frac{\hbar^2 k^2}{2m} \left[n_\sigma(\mathbf{k}) - \frac{C}{k^4} \right] + \frac{\hbar^2 C}{4\pi m a} + \sum_{\sigma = \uparrow, \downarrow} \int d^3 r \, U(\mathbf{r}) \rho_\sigma(\mathbf{r}) \tag{5.66}$$

where $\rho_\sigma(\mathbf{r})$ is the spatial number density.

One usually uses (5.64) to define C, and then derives (5.63). Here we rather take (5.63) as the definition of C. This choice is convenient both for the two-channel model discussed in Sect. 5.2.3 and for the rederivation of (5.64–5.66) that we shall now present, where we use a lattice model before taking the zero-range limit.

From the Hellmann-Feynman theorem (that was already put forward in [51]), the interaction energy E_{int} is equal to $g_0 (dE/dg_0)_S$. Since we have $d(1/g_0)/d(1/g) = 1$ [see the relation (5.47) between g_0 and g], this can be rewritten as

$$E_{\mathrm{int}} = \frac{\hbar^4}{m^2} \frac{C}{g_0} . \tag{5.67}$$

Expressing $1/g_0$ in terms of $1/g$ using once again (5.47), adding the kinetic energy, and taking the zero-range limit, we immediately get the relation (5.66). For the integral over momentum to be convergent, (5.64) must hold (in the absence of mathematical pathologies).

To derive (5.65), we again use (5.67), which implies that the relation

$$\sum_{\mathbf{R}} b^3 g_{\uparrow\downarrow}^{(2)} (\mathbf{R} + \mathbf{r}/2, \mathbf{R} - \mathbf{r}/2) = \frac{C}{(4\pi)^2} |\phi(\mathbf{r})|^2 \tag{5.68}$$

holds for $\mathbf{r} = \mathbf{0}$, were $\phi(\mathbf{r})$ is the zero-energy two-body scattering wavefunction, normalised in such a way that

$$\phi(\mathbf{r}) \simeq \frac{1}{r} - \frac{1}{a} \text{ for } r \gg b \tag{5.69}$$

[see [38] for the straightforward calculation of $\phi(\mathbf{0})$]. Moreover, in the regime where r is much smaller than the typical interatomic distances and than the thermal de Broglie wavelength (but not necessarily smaller than b), it is generally expected that the $\mathbf{r}$-dependence of $g^{(2)}_{\uparrow\downarrow}(\mathbf{R} + \mathbf{r}/2, \mathbf{R} - \mathbf{r}/2)$ is proportional to $|\phi(\mathbf{r})|^2$, so that (5.68) remains asymptotically valid. Taking the limits $b \to 0$ and then $r \to 0$ gives the desired (5.65).

Alternatively, the link (5.64, 5.65) between short-range pair correlations and large-k tail of the momentum distribution can be directly deduced from the short-distance singularity of the wavefunction coming from the contact condition (5.75) and the corresponding tail in Fourier space [38], similarly to the original derivation in 1D [52]. Thus this link remains true for a generic out-of-equilibrium statistical mixture of states satisfying the contact condition [49, 38].

5.2.1.5 Absence of Simple Collapse

To conclude this section on lattice models, we try to address the question of the advantage of lattice models as compared to the standard continuous space model with a binary interaction potential $V(\mathbf{r})$ between opposite spin fermions. Apart from practical advantages, due to the separable nature of the interaction in analytical calculations, or to the absence of sign problem in the Quantum Monte Carlo methods, is there a true physical advantage in using lattice models?

One may argue for example that everywhere non-positive interaction potentials may be used in continuous space, such as a square well potential, with a range dependent depth $V_0(b)$ adjusted to have a fixed non-zero scattering and no two-body bound states. E.g. for a square well potential $V(\mathbf{r}) = -V_0\theta(b - r)$, where $\theta(x)$ is the Heaviside function, one simply has to take

$$V_0 = \frac{\hbar^2}{mb^2} \left(\frac{\pi}{2}\right)^2 \tag{5.70}$$

to have an infinite scattering length. For such an attractive interaction, it seems then that one can easily reproduce the reasonings leading to the bounds Eqs. 5.52, 5.53. It is known however that there exists a number of particles N, in the unpolarized case $N_\uparrow = N_\downarrow$, such that this model in free space has a N-body bound state, necessarily of energy $\propto -\hbar^2/(mb^2)$ [28, 53, 54]. In the thermodynamic limit, the unitary gas is thus not the ground phase of the system, it is at most a metastable phase, and this prevents a derivation of the bounds Eqs. 5.52, 5.53. This catastrophe is easy to predict variationally, taking as a trial wavefunction the ground state of the ideal Fermi gas enclosed in a fictitious cubic hard wall cavity of size $b/\sqrt{3}$ [55]. In the large N limit,

the kinetic energy in the trial wavefunction is then $(3N/5)\hbar^2 k_F^2/(2m)$, see Eq. 5.14, where the Fermi wavevector is given by Eq. 5.8 with a density $\rho = N/(b/\sqrt{3})^3$, so that

$$E_{\text{kin}} \propto N^{5/3} \frac{\hbar^2}{mb^2}. \tag{5.71}$$

Since all particles are separated by a distance less than b, the interaction energy is exactly

$$E_{\text{int}} = -V_0(N/2)^2 \tag{5.72}$$

and wins over the kinetic energy for N large enough, $2800 \lesssim N$ for the considered ansatz. Obviously, a similar reasoning leads to the same conclusion for an everywhere negative, non-necessarily square well interaction potential.[4] One could imagine to suppress this problem by introducing a hard core repulsion, in which case however the purely attractive nature of V would be lost, ruining our simple derivation of Eqs. 5.52, 5.53.

The lattice models are immune to this catastrophic variational argument, since one cannot put more than two spin 1/2 fermions "inside" the interaction potential, that is on the same lattice site. Still they preserve the purely attractive nature of the interaction. This does not prove however that their spectrum is bounded from below in the zero range limit, as pointed out in the introduction of this section.

5.2.2 Zero-Range Model, Scale Invariance and Virial Theorem

5.2.2.1 The Zero-Range Model

The interactions are here replaced with contact conditions on the N-body wavefunction. In the two-body case, the model, introduced already by Eq. 5.32, is discussed in details in the literature, see e.g. [56] in free space where the scattering amplitude f_k is calculated and the existence for $a > 0$ of a dimer of energy $-\hbar^2/(2\mu a^2)$ and wavefunction $\phi_0(r) = (4\pi a)^{-1/2}\exp(-r/a)/r$ is discussed, μ being the reduced mass of the two particles. The two-body trapped case, solved in [15], was already presented in Sect. 5.1.4. Here we present the model for an arbitrary value of N.

For simplicity, we consider in first quantized form the case of a fixed number $N_\uparrow$ of fermions in spin state $\uparrow$ and a fixed number $N_\downarrow$ of fermions in spin state $\downarrow$, assuming that the Hamiltonian cannot change the spin state. We project the N-body state vector $|\Psi\rangle$ onto the non-symmetrized spin state with the $N_\uparrow$ first particles in

---

[4] In fixed node calculations, an everywhere negative interaction potential is used [12, 28, 29]. It is unknown if N in these simulations exceeds the minimal value required to have a bound state. Note that the imposed nodal wavefunction in the fixed node method, usually the one of the Hartree-Fock or BCS state, would be however quite different from the one of the bound state.

spin state $\uparrow$ and the $N_\downarrow$ remaining particles in spin state $\downarrow$, to define a scalar N-body wavefunction:

$$\psi(\mathbf{X}) \equiv \left(\frac{N!}{N_\uparrow! N_\downarrow!}\right)^{1/2} \langle \uparrow, \mathbf{r}_1 | \otimes \dots \langle \uparrow, \mathbf{r}_{N_\uparrow} | \langle \downarrow, \mathbf{r}_{N_\uparrow+1} | \otimes \dots \langle \downarrow, \mathbf{r}_N | \Psi \rangle \quad (5.73)$$

where $\mathbf{X} = (\mathbf{r}_1, \dots, \mathbf{r}_N)$ is the set of all coordinates, and the normalization factor ensures that ψ is normalized to unity.[5] The fermionic symmetry of the state vector allows to express the wavefunction on another spin state (with any different order of $\uparrow$ and $\downarrow$ factors) in terms of ψ. For the considered spin state, this fermionic symmetry imposes that ψ is odd under any permutation of the first $N_\uparrow$ positions $\mathbf{r}_1, \dots, \mathbf{r}_{N_\uparrow}$, and also odd under any permutation of the last $N_\downarrow$ positions $\mathbf{r}_{N_\uparrow+1}, \dots, \mathbf{r}_N$.

In the Wigner-Bethe-Peierls model, that we also call zero-range model, the Hamiltonian for the wavefunction ψ is simply represented by the same partial differential operator as for the ideal gas case:

$$H = \sum_{i=1}^{N} \left[-\frac{\hbar^2}{2m} \Delta_{\mathbf{r}_i} + U(\mathbf{r}_i) \right], \quad (5.74)$$

where U is the external trapping potential supposed for simplicity to be spin state independent. As is however well emphasized in the mathematics of operators on Hilbert spaces [8], an operator is defined not only by a partial differential operator, but also by the choice of its so-called *domain D(H)*. A naive presentation of this concept of domain is given in the Appendix 2. Here the domain does not coincide with the ideal gas one. It includes the following Wigner-Bethe-Peierls contact conditions: for any pair of particles i,j, when $r_{ij} \equiv |\mathbf{r}_i - \mathbf{r}_j| \to 0$ for a fixed position of their centroid $\mathbf{R}_{ij} = (\mathbf{r}_i + \mathbf{r}_j)/2$, there exists a function A_{ij} such that

$$\psi(\mathbf{X}) = A_{ij}(\mathbf{R}_{ij}; (\mathbf{r}_k)_{k \neq i,j})(r_{ij}^{-1} - a^{-1}) + O(r_{ij}). \quad (5.75)$$

These conditions are imposed for all values of $\mathbf{R}_{ij}$ different from the positions of the other particles $\mathbf{r}_k$, k different from i and j. If the fermionic particles i and j are in the same spin state, the fermionic symmetry imposes $\psi(\dots, \mathbf{r}_i = \mathbf{r}_j, \dots) = 0$ and one has simply $A_{ij} \equiv 0$. For i and j in different spin states, the unknown functions A_{ij} have to be determined from Schrödinger's equation, e.g. together with the energy E from the eigenvalue problem

$$H\psi = E\psi. \quad (5.76)$$

Note that in Eq. 5.76 we have excluded the values of $\mathbf{X}$ where two particle positions coincide. Since $\Delta_{\mathbf{r}_i} r_{ij}^{-1} = -4\pi \delta(\mathbf{r}_i - \mathbf{r}_j)$, including these values would require

---

[5] The inverse formula giving the full state vector in terms of $\psi(\mathbf{X})$ is $|\Psi\rangle = \left(\frac{N!}{N_\uparrow! N_\downarrow!}\right)^{1/2} A |\uparrow \rangle^{N_\uparrow} |\downarrow\rangle^{N_\downarrow} |\psi\rangle$, where the projector A is the usual antisymmetrizing operator $A = (1/N!) \sum_{\sigma \in S_N} \varepsilon(\sigma) P_\sigma$.

a calculation with distributions rather than with functions, with regularized delta interaction pseudo-potential, which is a compact and sometimes useful reformulation of the Wigner-Bethe-Peierls contact conditions [6, 56, 57, 58].

As already pointed out below Eq. 5.75, $A_{ij} \equiv 0$ if i and j are fermions in the same spin state. One may wonder if solutions exist such that $A_{ij} \equiv 0$ even if i and j are in different spin states, in which case ψ would simply vanish when $r_{ij} \to 0$. These solutions would then be common eigenstates to the interacting gas and to the ideal gas. They would correspond in a real experiment to long lived eigenstates, protected from three-body losses by the fact that ψ vanishes when two particles or more approach each other. In a harmonic trap, one can easily construct such "non-interacting" solutions, as for example the famous Laughlin wavefunction of the Fractional Quantum Hall Effect. "Non-interacting" solutions also exists for spinless bosons. These non-interacting states actually dominate the ideal gas density of states at high energy [32, 55].

5.2.2.2 What is the Kinetic Energy?

The fact that the Hamiltonian is the same as the ideal gas, apart from the domain, may lead physically to some puzzles. E.g. the absence of interaction term may give the impression that the energy E is the sum of trapping potential energy and kinetic energy only. This is actually not so. The correct definition of the mean kinetic energy, valid for general boundary conditions on the wavefunction, is

$$E_{\text{kin}} = \int d^{3N}X \frac{\hbar^2}{2m} |\partial_{\mathbf{X}}\psi|^2. \tag{5.77}$$

This expression in particular guaranties that $E_{\text{kin}} \geq 0$. If $A_{ij} \neq 0$ in Eq. 5.75, one then sees that, although ψ is square integrable in a vicinity of $r_{ij} = 0$ thanks to the Jacobian $\propto r_{ij}^2$ coming from three-dimensional integration, the gradient of ψ diverges as $1/r_{ij}^2$ and cannot be square integrable. Within the zero-range model one then obtains an infinite kinetic energy

$$E_{\text{kin}}^{\text{WBP}} = +\infty. \tag{5.78}$$

Multiplying Eq. 5.76 by ψ and integrating over $\mathbf{X}$, one realizes that the total energy is split as the trapping potential energy,

$$E_{\text{trap}} = \int d^{3N}X |\psi(\mathbf{X})|^2 \sum_{i=1}^{N} U(\mathbf{r}_i) \tag{5.79}$$

and as the sum of kinetic plus interaction energy:

$$E_{\text{kin}} + E_{\text{int}} = -\int d^{3N}X \frac{\hbar^2}{2m} \psi^* \Delta_{\mathbf{X}}\psi. \tag{5.80}$$

This means that the interaction energy is $-\infty$ in the Wigner-Bethe-Peierls model. All this means is that, in reality, when the interaction has a non-zero range, both the kinetic energy and the interaction energy of interacting particles depend on the interaction range b, and diverge for $b \to 0$, in such a way however that the sum $E_{\mathrm{kin}} + E_{\mathrm{int}}$ has a finite limit given by the Wigner-Bethe-Peierls model. We have seen more precisely how this happens for lattice models in Sect. 5.2.1.4, see the expression (5.67) of E_{int} and the subsequent derivation of (5.66).[6]

5.2.2.3 Scale Invariance and Virial Theorem

In the case of the unitary gas, the scattering length is infinite, so that one sets $1/a = 0$ in Eq. 5.75. The domain of the Hamiltonian is then imposed to be invariant by any isotropic rescaling Eq. 5.11 of the particle positions. To be precise, we define for any scaling factor $\lambda > 0$:

$$\psi_\lambda(\mathbf{X}) \equiv \frac{\psi(\mathbf{X}/\lambda)}{\lambda^{3N/2}}, \qquad (5.81)$$

and we impose that $\psi_\lambda \in D(H)$ for all $\psi \in D(H)$. This is the precise mathematical definition of the scale invariance loosely introduced in Sect. 5.1.2. In particular, it is apparent in Eq. 5.75 that, for $1/a = 0$, ψ_λ obeys the Wigner-Bethe-Peierls contact conditions if ψ does. On the contrary, if ψ obeys the contact conditions for a finite scattering length a, ψ_λ obeys the contact condition for a different, fictitious scattering length $a_\lambda = \lambda a \neq a$ and $D(H)$ cannot be scaling invariant.

There are several consequences of the scale invariance of the domain of the Hamiltonian $D(H)$ for the unitary gas. Some of them were presented in Sect. 5.1.2, other ones will be derived in Sect. 5.3. Here we present another application, the derivation of a virial theorem for the unitary gas. This is a first step towards the introduction of a SO(2,1) Lie algebra in Sect. 5.3. To this end, we introduce the infinitesimal generator D of the scaling transform Eq. 5.81, such that[7]

$$\psi_\lambda(\mathbf{X}) = e^{-iD \ln \lambda} \psi(\mathbf{X}). \qquad (5.82)$$

Taking the derivative of Eq. 5.81 with respect to λ in $\lambda = 1$, one obtains the hermitian operator

$$D = \frac{1}{2i}(\mathbf{X} \cdot \partial_{\mathbf{X}} + \partial_{\mathbf{X}} \cdot \mathbf{X}) = \frac{3N}{2i} - i\mathbf{X} \cdot \partial_{\mathbf{X}}. \qquad (5.83)$$

---

[6] For a continuous-space model with an interaction potential $V(r)$, we have [76, 38] $E_{\mathrm{int}} = \frac{C}{(4\pi)^2} \int d^3r\, V(r)|\phi(r)|^2$ where C is still defined by (5.63) and $\phi(r)$ still denotes the zero-energy two-body scattering state normalised according to (5.69).

[7] The scaling transform (5.81) defines a unitary operator $T(\lambda)$ such that $\psi_\lambda = T(\lambda)\psi$. One has $T(\lambda_1)T(\lambda_2) = T(\lambda_1\lambda_2)$. To recover the usual additive structure as for the group of spatial translations, one sets $\lambda = \exp \theta$, so that $T(\theta_1)T(\theta_2) = T(\theta_1 + \theta_2)$ and $T(\theta) = \exp(-i\theta D)$ where D is the generator. This is why $\ln \lambda$ appears in Eq. 5.82.

The commutator of D with the Hamiltonian is readily obtained. From the relation $\Delta_{\mathbf{X}}\psi_\lambda(\mathbf{X}) = \lambda^{-2}(\Delta\psi)(\mathbf{X}/\lambda)$, one has

$$e^{iD\ln\lambda}(H - H_{\text{trap}})e^{-iD\ln\lambda} = \frac{1}{\lambda^2}(H - H_{\text{trap}}) \tag{5.84}$$

where $H_{\text{trap}} = \sum_{i=1}^{N} U(\mathbf{r}_i)$ is the trapping potential part of the Hamiltonian. It remains to take the derivative in $\lambda = 1$ to obtain

$$i[D, H - H_{\text{trap}}] = -2(H - H_{\text{trap}}). \tag{5.85}$$

The commutator of D with the trapping potential is evaluated directly from Eq. 5.83:

$$i[D, H_{\text{trap}}] = \sum_{i=1}^{N} \mathbf{r}_i \cdot \partial_{\mathbf{r}_i} U(\mathbf{r}_i). \tag{5.86}$$

This gives finally

$$i[D, H] = -2(H - H_{\text{trap}}) + \sum_{i=1}^{N} \mathbf{r}_i \cdot \partial_{\mathbf{r}_i} U(\mathbf{r}_i). \tag{5.87}$$

The standard way to derive the virial theorem in quantum mechanics [59], in a direct generalization of the one of classical mechanics, is then to take the expectation value of $[D, H]$ in an eigenstate ψ of H of eigenenergy E. This works here for the unitary gas because the domain $D(H)$ is preserved by the action of D. On one side, by having H acting on ψ from the right or from the left, one trivially has $\langle [D, H] \rangle_\psi = 0$. On the other side, one has Eq. 5.87, so that

$$E = \sum_{i=1}^{N} \left\langle U(\mathbf{r}_i) + \frac{1}{2}\mathbf{r}_i \cdot \partial_{\mathbf{r}_i} U(\mathbf{r}_i) \right\rangle_\psi. \tag{5.88}$$

This relation was obtained with alternative derivations in the literature (see [60] and references therein). One of its practical interests is that it gives access to the energy from the gas density distribution [61]. As already mentioned, the scale invariance of the domain of H is crucial to obtain this result. If $1/a$ is non zero, a generalization of the virial relation can however be obtained, that involves $dE/d(1/a)$, see [62, 63].

5.2.3 Two-Channel Model and Closed-Channel Fraction

5.2.3.1 The Two-Channel Model

The lattice models or the zero-range model are of course dramatic simplifications of the real interaction between two alkali atoms. At large interatomic distances, much larger than the radius of the electronic orbitals, one may hope to realistically represent this interaction by a function $V(r)$ of the interatomic distance, with a van der Waals

attractive tail $V(r) \simeq - C_6/r^6$, a simple formula that actually neglects retardation effects and long-range magnetic dipole–dipole interactions. As discussed below the gas phase condition Eq. 5.1, this allows to estimate b with the so-called van der Waals length, usually in the range of 1-10 nm.

At short interatomic distances, this simple picture of a scalar interaction potential $V(r)$ has to be abandoned. Following quantum chemistry or molecular physics methods, one has to introduce the various Born-Oppenheimer potential curves obtained from the solution of the electronic eigenvalue problem for fixed atomic nuclei positions. Restricting to one active electron of spin 1/2 per atom, one immediately gets two ground potential curves, the singlet one corresponding to the total spin $S = 0$, and the triplet one corresponding to the total spin $S = 1$. An external magnetic field B is applied to activate the Feshbach resonance. This magnetic field couples mainly to the total electronic spin and thus induces *different* Zeeman shifts for the singlet and triplet curves. In reality, the problem is further complicated by the existence of the nuclear spin and the hyperfine coupling, that couples the singlet channel to the triplet channel for nearby atoms, and that induces a hyperfine splitting within the ground electronic state for well separated atoms.

A detailed discussion is given in [64, 65]. Here we take the simplified view depicted in Fig. 5.7: the atoms interact *via* two potential curves, $V_{\mathrm{open}}(r)$ and $V_{\mathrm{closed}}(r)$. At large distances, $V_{\mathrm{open}}(r)$ conventionally tends to zero, whereas $V_{\mathrm{closed}}(r)$ tends to a positive value V_∞, one of the hyperfine energy level spacings for a single atom in the applied magnetic field. In the two-body scattering problem, the atoms come from $r = +\infty$ in the internal state corresponding to $V_{\mathrm{open}}(r)$, the so-called open channel, with a kinetic energy $E \ll V_\infty$. Due to a coupling between the two channels, the two interacting atoms can have access to the internal state corresponding to the curve $V_{\mathrm{closed}}(r)$, but only at short distances; at long distances, the external atomic wavefunction in this so-called closed channel is an evanescent wave that decays exponentially with r since $E < V_\infty$.

Now assume that, in the absence of coupling between the channels, the closed channel supports a bound state of energy E_b, called in what follows *the molecular state or the closed-channel molecule*. Assume also that, by applying a judicious magnetic field, one sets the energy of this molecular state close to zero, that is to the dissociation limit of the open channel. In this case one may expect that the scattering amplitude of two atoms is strongly affected, by a resonance effect, given the non-zero coupling between the two channels. This is in essence how the Feshbach resonance takes place.

The central postulate of the theory of quantum gases is that the short range details of the interaction are unimportant, only the low-momentum scattering amplitude f_k between two atoms is relevant. As a consequence, any simplified model for the interaction, leading to a different scattering amplitude f_k^{model}, is acceptable provided that

$$f_k^{\mathrm{model}} \simeq f_k \tag{5.89}$$
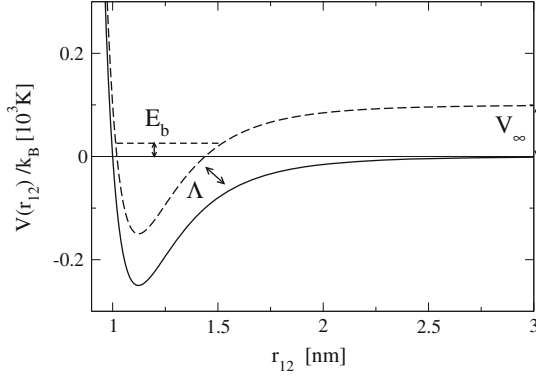
Fig. 5.7 Simple view of a Feshbach resonance. The atomic interaction is described by two curves (*solid line: open channel, dashed line: closed channel*). When one neglects the interchannel coupling Λ, the closed channel has a molecular state of energy E_b close to the dissociation limit of the open channel. The energy spacing V_∞ was greatly exaggerated, for clarity

for the relevant values of the relative momentum k populated in the gas. We insist here that we impose similar scattering amplitudes over some momentum range, not just equal scattering lengths a. For spin 1/2 fermions, typical values of k can be

$$k_{\text{typ}} \in \{a^{-1}, k_F, \lambda_{\text{dB}}^{-1}\} \tag{5.90}$$

where the Fermi momentum is defined in Eq. 5.8 and the thermal de Broglie wavelength in Eq. 5.9. The appropriate value of k_{typ} depends on the physical situation. The first choice $k_{\text{typ}} \sim a^{-1}$ is well suited to the case of a condensate of dimers ($a > 0$) since it is the relative momentum of two atoms forming the dimer. The second choice $k_{\text{typ}} \sim k_F$ is well suited to a degenerate Fermi gas of atoms (not dimers). The third choice $k_{\text{typ}} \sim \lambda^{-1}$ is relevant for a non-degenerate Fermi gas.

The strategy is thus to perform an accurate calculation of the "true" f_k, to identify the validity conditions of the simple models and of the unitary regime assumption Eq. 5.4. One needs a realistic, though analytically tractable, model of the Feshbach resonance. This is provided by the so-called *two-channel* models [65, 66, 67]. We use here the version presented in [68], which is a particular case of the one used in [64, 69] and Refs. therein: The open channel part consists of the original gas of spin 1/2 fermions that interact *via* a separable potential, that is in first quantized form for two opposite spin fermions, in position space:

$$\langle \mathbf{r}_1, \mathbf{r}_2 | V_{\text{sep}} | \mathbf{r}_1', \mathbf{r}_2' \rangle = \delta \left(\frac{\mathbf{r}_1 + \mathbf{r}_2}{2} - \frac{\mathbf{r}_1' + \mathbf{r}_2'}{2} \right) g_0 \chi(\mathbf{r}_2 - \mathbf{r}_1) \chi(\mathbf{r}_2' - \mathbf{r}_1'). \tag{5.91}$$

This potential does not affect the atomic center of mass, so it conserves total momentum and respects Galilean invariance. Its matrix element involves the product of a function of the relative position in the ket and of the same function of the relative position in the bra, hence the name *separable*. The separable potential is thus in

general non local. As we shall take a function χ of width $\approx b$ this is clearly not an issue. The coupling constant g_0 of the separable potential is well-defined by the normalization condition for χ, $\int d^3r \chi(\mathbf{r}) = 1$. In the presence of this open channel interaction only, the scattering length between fermions, the so-called background scattering length a_{bg}, is usually small, of the order of the potential range b, hence the necessity of the Feshbach resonance to reach the unitary limit.

In the closed channel part, a single two-particle state is kept, the one corresponding to the molecular state, of energy E_b and of spatial range $\lesssim b$. The atoms thus exist in that channel not in the form of spin $1/2$ fermions, but in the form of bosonic spinless molecules, of mass twice the atomic mass. The coupling between the two channels simply corresponds to the possibility for each boson to decay in a pair of opposite spin fermions, or the inverse process that two opposite spin fermions merge into a boson, in a way conserving the total momentum. This coherent Bose-Fermi conversion may take place only if the positions $\mathbf{r}_1$ and $\mathbf{r}_2$ of the two fermions are within a distance b, and is thus described by a relative position dependent amplitude $\Lambda \chi(\mathbf{r}_1 - \mathbf{r}_2)$, where for simplicity one takes the same cut-off function χ as in the separable potential. It is important to realize that the Bose–Fermi conversion effectively induces an interaction between the fermions, which becomes resonant for the right tuning of E_b and leads to the diverging total scattering length a.

The model is best summarized in second quantized form [68], introducing the fermionic field operators $\psi_\sigma(\mathbf{r})$, $\sigma = \uparrow, \downarrow$, obeying the usual fermionic anticommutation relations, and the bosonic field operator $\psi_b(\mathbf{r})$ obeying the usual bosonic commutation relations:

$$
\begin{aligned}
H = \int d^3r & \left[\sum_{\sigma=\uparrow,\downarrow} \psi_\sigma^\dagger \left(-\frac{\hbar^2}{2m}\Delta_{\mathbf{r}} + U \right)\psi_\sigma + \psi_b^\dagger \left(E_b - \frac{\hbar^2}{4m}\Delta_{\mathbf{r}} + U_b \right)\psi_b \right] \\
& + \Lambda \int d^3r_1 d^3r_2 \chi(\mathbf{r}_1 - \mathbf{r}_2) \left\{ \psi_b^\dagger[(\mathbf{r}_1 + \mathbf{r}_2)/2]\psi_\downarrow(\mathbf{r}_1)\psi_\uparrow(\mathbf{r}_2) + \text{h. c.} \right\} \\
& + g_0 \int d^3R d^3r d^3r' \chi(\mathbf{r})\chi(\mathbf{r}')\psi_\uparrow^\dagger(\mathbf{R} - \mathbf{r}/2)\psi_\downarrow^\dagger(\mathbf{R} + \mathbf{r}/2)\psi_\downarrow(\mathbf{R} + \mathbf{r}'/2)\psi_\uparrow(\mathbf{R} - \mathbf{r}'/2),
\end{aligned}
$$
$$(5.92)$$

where $U(\mathbf{r})$ and $U_b(\mathbf{r})$ are the trapping potentials for the fermions and the bosons, respectively.

5.2.3.2 Scattering Amplitude and Universal Regime

In free space, the scattering problem of two fermions is exactly solvable for a Gaussian cut-off function $\chi(\mathbf{r}) \propto \exp[-r^2/(2b^2)]$ [64, 68]. A variety of parameterizations are possible. To make contact with typical notations, we assume that the energy E_b of the molecule in the closed channel is an affine function of the magnetic field B, a reasonable assumption close to the Feshbach resonance:

$$
E_b(B) = E_b^0 + \mu_b(B - B_0) \tag{5.93}
$$

where B_0 is the magnetic field value right on resonance and μ_b is the effective magnetic moment of the molecule. Then the scattering length for the model Eq. 5.92 can be exactly written as the celebrated formula

$$a = a_{\text{bg}} \left(1 - \frac{\Delta B}{B - B_0} \right), \tag{5.94}$$

where ΔB, such that $E_b^0 + \mu_b \Delta B = \Lambda^2/g_0$, is the so-called width of the Feshbach resonance. As expected, for $|B - B_0| \gg |\Delta B|$, one finds that a tends to the background scattering length a_{bg} solely due to the open channel interaction. With ΔB one forms a length R_* [70] which is always non-negative:

$$R_* \equiv \frac{\hbar^2}{m a_{\text{bg}} \mu_b \Delta B} = \left(\frac{\Lambda}{2\pi b E_b^0} \right)^2, \tag{5.95}$$

where the factor 2π is specific to our choice of χ. Physically, the length R_* is also directly related to the effective range on resonance:

$$r_e^{\text{res}} = -2R_* + \frac{4b}{\sqrt{\pi}}, \tag{5.96}$$

where the numerical coefficient in the last term depends on the choice of χ. The final result for the scattering amplitude for the model Eq. 5.92 is

$$-\frac{1}{f_k} = ik + \frac{e^{k^2 b^2}}{a} \left[1 - \left(1 - \frac{a}{a_{\text{bg}}} \right) \frac{k^2}{k^2 - Q^2} \right] - ik \ \text{erf}(-ikb) \tag{5.97}$$

where erf is the error function, that vanishes linearly in zero, and the wavevector Q, such that

$$Q^2 \equiv \frac{m}{\hbar^2 g_0} \left(g_0 E_b - \Lambda^2 \right) = \frac{-1}{a_{\text{bg}} R_* (1 - a_{\text{bg}}/a)}, \tag{5.98}$$

may be real or purely imaginary.

The unitary limit assumption Eq. 5.4 implies that all the terms in the right hand side of Eq. 5.97 are negligible, except for the first one. We now discuss this assumption, restricting for simplicity to an infinite scattering length $a^{-1} = 0$ (i.e. a magnetic field sufficiently close to resonance) and a typical relative momentum $k_{\text{typ}} = k_F$ (i.e. a degenerate gas). To satisfy Eq. 5.89, with $f_k^{\text{model}} = -1/(ik)$, one should then have, in addition to the gas phase requirement $k_F b \ll 1$, that

$$\frac{k R_*}{|1 + k^2 a_{\text{bg}} R_*|} \ll 1 \ \forall k \in [0, k_F]. \tag{5.99}$$

Table 5.1 summarizes the corresponding conditions to reach the unitary limit.[8, 9] Remarkably, the condition $k_F |r_e^{\text{res}}| \ll 1$ obtained in Eq. 5.6 from the expansion of

---

[8] We discarded for simplicity the rather peculiar case where $k_F |a_{\text{bg}}| R_*$ is ≤ 1 but not $\ll 1$.

[9] An additional condition actually has to be imposed to have a universal gas, as we will see after Eq. 5.106.

Table 5.1 In the two-channel model, conditions deduced from Eq. 5.99 (supplementary to the gas phase condition $k_F b \ll 1$) to reach the unitary limit for a degenerate gas of spin 1/2 fermions of Fermi momentum k_F. It is assumed that the magnetic field is tuned right on resonance, so that the scattering length is infinite. The last column corresponds to narrow Feshbach resonances satisfying Eq. 5.100

	$k_F\sqrt{|a_{\mathrm{bg}}|R_*} \ll 1$	$k_F\sqrt{|a_{\mathrm{bg}}|R_*} > 1$
$a_{\mathrm{bg}} > 0$	$k_F R_* \ll 1$	$(R_*/a_{\mathrm{bg}})^{1/2} \ll 1$
$a_{\mathrm{bg}} < 0$	$k_F R_* \ll 1$	unreachable

$1/f_k$ to order k^2 is not the end of the story. In particular, if $a_{\mathrm{bg}} < 0$, $Q_{\mathrm{res}}^2 \equiv -1/(a_{\mathrm{bg}}R_*)$ is positive and $1/f_k$ diverges for $k = Q_{\mathrm{res}}$; if the location of this divergence is within the Fermi sea, the unitary limit is not reachable. This funny case however requires huge values of $R_* a_{\mathrm{bg}}$, that is extremely small values of the resonance width ΔB:

$$|\mu_b \Delta B| \lesssim \frac{\hbar^2 k_F^2}{2m}. \tag{5.100}$$

This corresponds to very narrow Feshbach resonances [71], whose experimental use requires a good control of the magnetic field homogeneity and is more delicate. Current experiments rather use broad Feshbach resonances such as on lithium 6, where $r_e^{\mathrm{res}} = 4.7$ nm [72], $a_{\mathrm{bg}} = -74$ nm, $R_* = 0.027$ nm [73], leading to $1/(|a_{\mathrm{bg}}|R_*)^{1/2} = 700 (\mu\mathrm{m})^{-1}$ much larger than $k_F \approx$ a few $(\mu\mathrm{m})^{-1}$, so that the unitary limit is indeed well reached.

5.2.3.3 Relation Between Number of Closed Channel Molecules and "Contact"

The fact that the two-channel model includes the underlying atomic physics of the Feshbach resonance allows to consider an observable that is simply absent from single channel models, namely the number of molecules in the closed channel, represented by the operator:

$$N_b \equiv \int d^3\mathbf{r}\, \psi_b^\dagger(\mathbf{r}) \psi_b(\mathbf{r}) \tag{5.101}$$

where ψ_b is the molecular field operator. The mean number $\langle N_b \rangle$ of closed channel molecules was recently measured by laser molecular excitation techniques [74].

This mean number can be calculated from a two-channel model by a direct application of the Hellmann–Feynman theorem [75, 68] (see also [76]). The key point is that the only quantity depending on the magnetic field in the Hamiltonian Eq. 5.92 is the internal energy $E_b(B)$ of a closed channel molecule. At thermal equilibrium in the canonical ensemble, we thus have

$$\left(\frac{dE}{dB}\right)_S = \langle N_b \rangle \frac{dE_b}{dB}. \tag{5.102}$$

Close to the Feshbach resonance, we may assume that E_b is an affine function of B, see Eq. 5.93, so that the scattering length a depends on the magnetic field as in Eq. 5.94. Parameterizing E in terms of the inverse scattering length rather than B, we can replace dE/dB by $dE/d(1/a)$ times $d(1/a)/dB$. The latter can be calculated explicitly from (5.94). Thus

$$\langle N_b \rangle = \frac{C}{4\pi} R_* \left(1 - \frac{a_{\mathrm{bg}}}{a}\right)^2, \tag{5.103}$$

where C is the contact defined in Eq. 5.63, and we introduced the length R_* defined in Eq. 5.95.

If the interacting gas is in the universal zero range regime, its energy E depends on the interactions only via the scattering length, independently of the microscopic details of the atomic interactions, and its dependence with $1/a$ may be calculated by any convenient model. Then, at zero temperature, for the unpolarized case $N_\uparrow = N_\downarrow$, the equation of state of the homogeneous gas can be expressed as

$$e_0 = e_0^{\mathrm{ideal}} f\left(\frac{1}{k_F a}\right), \tag{5.104}$$

where e_0 and e_0^{ideal} are the ground state energy per particle for the interacting gas and for the ideal gas with the same density, and the Fermi wavevector k_F was defined in Eq. 5.8. In particular, $f(0) = \xi$, where the number ξ was introduced in Eq. 5.14. Setting $\zeta \equiv -f'(0)$, we have for the homogeneous unitary gas

$$\frac{C^{\mathrm{hom}}}{V} = \zeta \frac{2}{5\pi} k_F^4, \tag{5.105}$$

so that

$$\frac{\langle N_b \rangle^{\mathrm{hom}}}{N} = \frac{3}{10} k_F R_* \zeta. \tag{5.106}$$

This expression is valid for a universal gas consisting mainly of fermionic atoms, which requires that $\langle N_b \rangle^{\mathrm{hom}}/N \ll 1$, i. e. $k_F R* \ll 1$. This condition was already obtained in Sect. 5.2.3.2 for the broad resonances of the left column of Table 5.1. In the more exotic case of the narrow resonances of the second column of Table 5.1, this condition has to be imposed in addition to the ones of Table 5.1.

5.2.3.4 Application of General Relations: Various Measurements of the Contact

The relation (5.103) allowed us to extract in [68] the contact C of the trapped gas [related to the derivative of the total energy of the trapped gas *via* Eq. 5.63] from
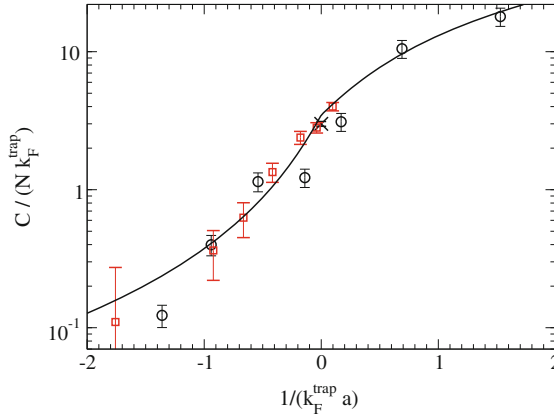
Fig. 5.8 The contact $C = \frac{dE}{d(-1/a)} \frac{4\pi m}{\hbar^2}$ of a trapped unpolarized Fermi gas. The circles are obtained from the measurements of $\langle N_b \rangle$ in [74], combined with the two channel model theory linking $\langle N_b \rangle$ to C [Eq. 5.103]. The cross was obtained in [78] by measuring the structure factor. The squares were obtained in [79] by measuring the momentum distribution. Solid line: zero-temperature theoretical prediction extracted from [29] as detailed in [68]. Here the Fermi wavevector k_F^{trap} of the trapped gas is defined by $\hbar^2 (k_F^{\text{trap}})^2 / (2m) = (3N)^{1/3} \hbar \bar{\omega}$, with $\bar{\omega}$ the geometric mean of the three oscillation frequencies ω_α and N the total atom number

the values of N_b measured in [74]. The result is shown in Fig. 5.8, together with a theoretical zero-temperature curve resulting from the local density approximation in the harmonically trapped case where $U(\mathbf{r}) = \frac{1}{2} m \sum_\alpha \omega_\alpha^2 x_\alpha^2$, the function f of (5.104) being obtained by interpolating between the fixed-node Monte-Carlo data of [29, 77] and the known asymptotic expressions in the BCS and BEC limits.[10]

While this is the first direct measurements of the contact in the BEC–BCS crossover, it has also been measured more recently:

- using Bragg scattering, *via* the large-momentum tail of the structure factor, directly related by Fourier transformation to the short-distance singularity Eq. 5.65 of the pair correlation function [78], see the cross at unitarity in Fig. 5.8
- *via* the tail of the momentum distribution Eq. 5.64 measured by abruptly turning off both trapping potential and interactions [79], see the squares in Fig. 5.8
- *via* (momentum resolved) radio-frequency spectroscopy [79, 80].

For the homogeneous unitary gas, the contact is conveniently expressed in terms of the dimensionless parameter ζ [see (5.105)]. The experimental value $\zeta = 0.91(5)$ was obtained by measuring the equation of state of the homogeneous gas with the technique proposed by [81] and taking the derivative of the energy with respect to the inverse scattering length [Eq. 5.63] (see [82] and the contribution of F. Chevy and C. Salomon in Chap. 11 of this volume). From the fixed-node Monte-Carlo calculations, one gets $\zeta \simeq 1$ by taking a derivative of the data of [29] for the function

---

[10] See [68] for details. The cusp at unitarity is of course an artefact of this interpolation procedure.

f, while the data of [77] for the pair correlation function together with the relation (65) give $\zeta \simeq 0.95$.[11],[12]

   In conclusion, the smallness of the interaction range leads to singularities; at first sight this may seem to complicate the problem as compared to other strongly interacting systems; however these singularities are well understood and have a useful consequence: the existence of exact relations resulting from the Hellmann-Feynman theorem [51] and from properties of the Fourier transform [52]. In particular this provides a "useful check on mutual consistency of various experiments", as foreseen in [83].

5.3 Dynamical Symmetry of the Unitary Gas

In this section, we present some remarkable properties of the unitary gas, derived from the zero-range model. The starting point is that the time evolution of the gas in a time dependent isotropic harmonic trap may be expressed exactly in terms of a gauge and scaling transform, see Sect. 5.3.1. This implies the existence of a SO(2,1) dynamical (or hidden) symmetry of the system, a formal property that we shall link to concrete consequences, such as the existence of an exactly decoupled bosonic degree of freedom (the breathing mode of the gas), see Sect. 5.3.2, or the separability of the *N*-body wavefunction in hyperspherical coordinates, see Sect. 5.3.3, which holds both in an isotropic harmonic trap and in free space and has several important consequences such as the analytical solution of the trapped three-body problem, see Sect. 5.3.4. In Sect. 5.3.5 we use the existence of the undamped breathing mode to rederive a remarkable property of the homogeneous unitary gas: its bulk viscosity vanishes. Section 5.3.6 concerns short-range scaling laws, which are related to the separability in hyperspherical coordinates, but hold for any scattering length and external potential.

5.3.1 Scaling Solution in a Time-Dependent Trap

In this section, we shall assume that the trapping potential $U(\mathbf{r})$ introduced in Eq. 5.74 is an isotropic harmonic potential. Whereas the hypothesis of harmonicity may be a good approximation in present experiments for small enough atomic clouds, the isotropy is not granted and requires some experimental tuning that, to our knowledge, remains to be done. On the other hand, we allow a general time dependence of the

---

[11] This value is also compatible with the data of [77] for the one-body density matrix, whose short-range singular part is related by Fourier transformation to the large-*k* tail of the momentum distribution [38].

[12] At unitarity, the local density approximation can be done analytically, yielding a relation between the contact *C* of the trapped gas and the one of the homogeneous gas: $\frac{C}{N k_F^{\text{trap}}} = \frac{512}{175} \frac{\zeta}{\xi^{1/4}}$ [68].

trap curvature, so that Schrödinger's equation for the *N*-body wavefunction defined in Eq. 5.73 is

$$i\hbar\partial_t \psi(\mathbf{X}, t) = \left[-\frac{\hbar^2}{2m}\Delta_{\mathbf{X}} + \frac{1}{2}m\omega^2(t)X^2 \right] \psi(\mathbf{X}, t), \qquad (5.107)$$

where we recall that $\mathbf{X}$ is the set of all particle coordinates, and $\omega(t)$ is the instantaneous angular oscillation frequency. The interaction between particles is described by the contact conditions Eq. 5.75, written here for the unitary gas, that is for $a^{-1} = 0$:

$$\psi(\mathbf{X}) = \frac{A_{ij}(\mathbf{R}_{ij}; (\mathbf{r}_k)_{k\neq i,j})}{r_{ij}} + O(r_{ij}). \qquad (5.108)$$

Let us consider the particular case, quite relevant experimentally, where the gas is initially at equilibrium in a static trap $\omega(t = 0) = \omega$. The gas is then in a statistical mixture of stationary states, so we can assume that the initial *N*-body wavefunction is an eigenstate of the Hamiltonian with energy E. At $t > 0$, the trap curvature is varied, which leads to an arbitrary time dependent $\omega(t)$. In typical experiments, one either sets abruptly $\omega(t)$ to zero, to perform a time of flight measurement, or one modulates $\omega(t)$ at some frequency to study the gas collective modes. Can we predict the evolution of the system? As shown in [58], the answer is yes, as we now explain.

In the absence of interactions, it is well known [84] that $\psi(\mathbf{X}, t)$ is deduced from the $t = 0$ wavefunction by a simple gauge plus scaling ansatz:

$$\psi(\mathbf{X}, t) = \frac{e^{i\theta(t)}}{\lambda^{3N/2}(t)}\exp\left[\frac{im\dot{\lambda}(t)}{2\hbar\lambda(t)}X^2 \right] \psi(\mathbf{X}/\lambda(t), 0), \qquad (5.109)$$

where $\dot{\lambda}(t) = d\lambda(t)/dt$. At time $t = 0$, one clearly has $\theta(0) = 0$,

$$\lambda(0) = 1 \quad \text{and} \quad \dot{\lambda}(0) = 0. \qquad (5.110)$$

Inserting this ansatz into Schrödinger's equation (5.107), we obtain a Newton like equation of motion for λ:

$$\ddot{\lambda}(t) = \frac{\omega^2}{\lambda^3(t)} - \omega^2(t)\lambda(t) \qquad (5.111)$$

to be solved with the initial conditions (5.110). We recall that ω stands for the *initial* angular oscillation frequency. The equation (5.111) is well studied in the literature, under the name of the Ermakov equation [85], and is in particular amenable to a linear form: one recognizes an equation for the distance to the origin for a two-dimensional harmonic oscillator of angular frequency $\omega(t)$, as obtained from Newton's equation and from the law of equal areas. In particular, if $\omega(t) = \omega_{\text{ct}}$ is a constant over some time interval, $\lambda(t)$ oscillates with a period π/ω_{ct} over that time interval.

The global phase $\theta(t)$ is given by

$$\theta(t) = -\frac{E}{\hbar} \int_0^t \frac{dt'}{\lambda^2(t')}. \qquad (5.112)$$

This suggests that θ still evolves at the stationary pace $-E/\hbar$ provided that one introduces a modified time, as done in [86] in a bosonic mean field context:

$$\tau(t) = \int_0^t \frac{dt'}{\lambda^2(t')}. \qquad (5.113)$$

We shall come back to this point below.

In presence of interactions, one has to check that the ansatz (5.109) obeys the contact conditions (5.108). First, the ansatz includes a scaling transform. As discussed in Sect. 5.2.2, this preserves the contact conditions and the domain of the Hamiltonian for the unitary gas. Second, the ansatz includes a quadratic gauge transform. Turning back to the definition of the contact conditions, we select an arbitrary pair of particles i and j and we take the limit $r_{ij} \to 0$ for a fixed centroid position $\mathbf{R}_{ij} = (\mathbf{r}_i + \mathbf{r}_j)/2$. In the gauge factor, the quantity $X^2 = \sum_{k=1}^N r_k^2$ appears. The positions $\mathbf{r}_k$ of the particles other than i and j are fixed. What matters is thus $r_i^2 + r_j^2$ that we rewrite as

$$r_i^2 + r_j^2 = 2R_{ij}^2 + \frac{1}{2}r_{ij}^2. \qquad (5.114)$$

R_{ij} is fixed. r_{ij} varies but it appears squared in the gauge transform, so that

$$\exp\left[\frac{im\dot{\lambda}(t)}{2\hbar\lambda(t)}r_{ij}^2/2\right]\left[\frac{1}{r_{ij}} + O(r_{ij})\right] = \frac{1}{r_{ij}} + O(r_{ij}) \qquad (5.115)$$

and the contact conditions are preserved by the gauge transform, even if the scattering length a was finite.

We thus conclude that the ansatz (5.109) gives the solution also for the unitary gas. This has interesting practical consequences. For measurements in position space, one has simple scaling relations, not only for the mean density $\rho_\sigma(\mathbf{r}, t)$ in each spin component σ:

$$\rho_\sigma(\mathbf{r}, t) = \frac{1}{\lambda^3(t)}\rho_\sigma(\mathbf{r}/\lambda(t), 0) \qquad (5.116)$$

but also for higher order density correlation functions: for example, the second order density correlation function defined in terms of the fermionic field operators as

$$g^{(2)}_{\sigma\sigma'}(\mathbf{r}, \mathbf{r}') \equiv \langle \psi_\sigma^\dagger(\mathbf{r})\psi_{\sigma'}^\dagger(\mathbf{r}')\psi_{\sigma'}(\mathbf{r}')\psi_\sigma(\mathbf{r})\rangle, \qquad (5.117)$$

evolves in time according to the scaling

$$g^{(2)}_{\sigma\sigma'}(\mathbf{r}, \mathbf{r}', t) = \frac{1}{\lambda^6(t)}g^{(2)}_{\sigma\sigma'}(\mathbf{r}/\lambda(t), \mathbf{r}'/\lambda(t), 0). \qquad (5.118)$$

As a consequence, if one abruptly switches off the trapping potential at $t = 0^+$, the gas experiences a ballistic expansion with a scaling factor

$$\lambda(t) = [1 + \omega^2 t^2]^{1/2}, \tag{5.119}$$

which acts as a perfect magnifying lens on the density distribution.

For non-diagonal observables in position space, some information is also obtained, with the gauge transform now contributing. For example the first order coherence function

$$g_{\sigma\sigma}^{(1)}(\mathbf{r}, \mathbf{r}') \equiv \langle \psi_\sigma^\dagger(\mathbf{r}') \psi_\sigma(\mathbf{r}) \rangle, \tag{5.120}$$

which is simply the matrix element of the one-body density operator between $\langle \mathbf{r}, \sigma |$ and $| \mathbf{r}', \sigma \rangle$, evolves according to

$$g_{\sigma\sigma}^{(1)}(\mathbf{r}, \mathbf{r}', t) = \frac{1}{\lambda^3(t)} \exp\left[\frac{im\dot{\lambda}(t)}{2\hbar\lambda(t)}(r^2 - r'^2) \right] g_{\sigma\sigma}^{(1)}(\mathbf{r}/\lambda(t), \mathbf{r}'/\lambda(t), 0). \tag{5.121}$$

The momentum distribution $n_\sigma(\mathbf{k})$ in the spin component σ is the Fourier transform over $\mathbf{r} - \mathbf{r}'$ and the integral over $(\mathbf{r} + \mathbf{r}')/2$ of the first order coherence function. For a ballistic expansion, directly transposing to three dimensions the result obtained in [87] from a time dependent scaling solution for the one-dimensional gas of impenetrable bosons, one has that the momentum distribution of the ballistically expanding unitary gas is asymptotically homothetic to the gas initial spatial density profile:

$$\lim_{t \to +\infty} n_\sigma(\mathbf{k}, t) = \left(\frac{2\pi\hbar}{m\omega} \right)^3 \rho_\sigma\left(\mathbf{r} = \frac{\hbar\mathbf{k}}{m\omega}, 0 \right). \tag{5.122}$$

We emphasize that the above results hold for an arbitrary gas polarization, that is for arbitrary numbers of particles in each of the two spin states $\sigma = \uparrow, \downarrow$. If the initial state is thermal, they hold whatever the value of the temperature, larger or smaller than the critical temperature T_c. These results however require the unitary limit (in particular $|a| = +\infty$) and a perfect isotropy of the harmonic trap. If the experimental goal is simply to have the ballistic expansion as a perfect magnifying lens, these two requirements remarkably may be removed, as shown in [88], if one is ready to impose an appropriate time dependence to the scattering length $a(t)$ and to the trap aspect ratio, in which case the ansatz (5.109) holds at all times. In the particular case of an isotropic trap, the procedure of [88] is straightforward to explain: If $\psi(t = 0)$ obeys the contact conditions with a finite scattering length a, the ansatz (5.109) obeys the contact conditions for a scattering length $\lambda(t)a$ so one simply has to adjust the actual scattering length in a time dependent way:

$$a(t) = \lambda(t)a \tag{5.123}$$

where λ evolves according to Eq. 5.111. As shown in the next section, the time dependent solution in the unitary case, apart from providing convenient scaling relations

on the density, is connected to several interesting intrinsic properties of the system, whereas the procedure of [88] does not imply such properties.

To be complete, we finally address the general case where the initial wavefunction of the unitary gas is not necessarily a stationary state but is arbitrary [89]. Then the observables of the gas have in general a non-trivial time dependence, even for a fixed trap curvature. If the trap curvature is time dependent, we modify the gauge plus scaling ansatz as follows:

$$\psi(\mathbf{X}, t) = \frac{1}{\lambda^{3N/2}(t)} \exp\left[\frac{im\dot{\lambda}(t)}{2\hbar\lambda(t)}X^2\right] \tilde{\psi}(\mathbf{X}/\lambda(t), \tau(t)), \qquad (5.124)$$

where $\tau(t)$ is the modified time introduced in Eq. 5.112, $\lambda(t)$ evolves according to Eq. 5.111 with the initial conditions (5.110), and the time-dependent wavefunction $\tilde{\psi}$ coincides with ψ at time $t = \tau = 0$ and obeys the unitary gas contact conditions. Then this ansatz obeys the contact conditions. When inserted in the time dependent Schrödinger equation (5.107), it leads to a Schrödinger equation for $\tilde{\psi}$ in the time independent external potential fixed to the $t = 0$ trap:

$$i\hbar\partial_\tau \tilde{\psi}(\mathbf{X}, \tau) = \left[-\frac{\hbar^2}{2m}\Delta_{\mathbf{X}} + \frac{1}{2}m\omega^2 X^2\right] \tilde{\psi}(\mathbf{X}, \tau). \qquad (5.125)$$

The gauge plus scaling transform, and the redefinition of time, have then totally cancelled the time dependence of the trap. If the initial wavefunction is an eigenstate of energy E, as was previously the case, one simple has $\tilde{\psi}(\tau) = \exp(-iE\tau/\hbar)\psi(t = 0)$ and one recovers the global phase factor in Eq. 5.109.

5.3.2 SO(2,1) Dynamical Symmetry and the Decoupled Breathing Mode

As shown in [90] for a two-dimensional Bose gas with $1/r^2$ interactions, the existence of a scaling solution such as Eq. 5.109 reflects a hidden symmetry of the Hamiltonian, the SO(2,1) dynamical symmetry. Following [89], we construct explicitly this dynamical symmetry for the unitary gas and we show that it has interesting consequences for the energy spectrum in a static isotropic harmonic trap.

Let us consider a gedankenexperiment: starting from the unitary gas is an energy eigenstate ψ, we modify in an infinitesimal way the trap curvature during the time interval $[0, t_f]$, and for $t > t_f$ we restore the initial trap curvature, $\omega(t) = \omega(0) = \omega$. Linearizing Eq. 5.111 around $\lambda = 1$ for $t > t_f$, we see that the resulting change in the scaling parameter λ is

$$\lambda(t) - 1 = \varepsilon e^{-2i\omega t} + \varepsilon^* e^{2i\omega t} + O(\varepsilon^2) \qquad (5.126)$$

where ε is proportional to the infinitesimal curvature change. Since λ oscillates indefinitely at frequency 2ω, this shows the existence of an undamped mode of frequency

2ω. This conclusion actually extends to excitations during $[0, t_f]$ of arbitrarily large amplitudes, as noted below Eq. 5.111 [90].

We calculate the resulting change in the N-body wavefunction, expanding Eq. 5.109 to first order in ε, putting in evidence the components that oscillate with Bohr frequencies $\pm 2\omega$:

$$\psi(\mathbf{X}, t) = e^{i\alpha} \left[e^{-iEt/\hbar} - \varepsilon e^{-i(E+2\hbar\omega)t/\hbar} L_+ + \varepsilon^* e^{-i(E-2\hbar\omega)t/\hbar} L_- \right] \\ \psi(\mathbf{X}, 0) + O(\varepsilon^2). \tag{5.127}$$

The time independent phase α depends on the details of the excitation procedure. We have introduced the operators

$$L_\pm = \pm i D + \frac{H}{\hbar\omega} - \frac{m\omega}{\hbar} X^2 \tag{5.128}$$

where D is the generator of the scaling transforms, as defined in Eq. 5.83, and $L_+ = L_-^\dagger$. We then read on Eq. 5.127 the remarkable property that the action of L_+ on an energy eigenstate ψ of energy E produces an energy eigenstate of energy $E + 2\hbar\omega$.[13] Similarly, the action of L_- on ψ produces an energy eigenstate of energy $E - 2\hbar\omega$, or eventually gives zero since the spectrum is bounded from below by $E \geq 0$ according to the virial theorem (5.88) applied to $U(\mathbf{r}) = \frac{1}{2} m\omega^2 r^2$. We see that the spectrum has thus a very simple structure, it is a collection of semi-infinite ladders, each ladder being made of equidistant energy levels separated by $2\hbar\omega$, see Fig. 5.9 , and $L_\pm$ acting respectively as a raising/lowering operator in that structure. Within each ladder, we call ψ_g the wavefunction corresponding to the ground step of that ladder, such that

$$L_- \psi_g = 0. \tag{5.129}$$

As shown in [90], this structure implies a dynamical SO(2,1) symmetry, meaning that the Hamiltonian H is part of the SO(2,1) Lie algebra. One starts with the commutation relations:

$$[H, L_\pm] = \pm 2\hbar\omega L_\pm \tag{5.130}$$

$$[L_+, L_-] = -4H/(\hbar\omega). \tag{5.131}$$

The first relation was expected from the raising/lowering nature of $L_\pm$. Both relations can be checked from the commutation relations Eqs. 5.85, 5.86 and from

$$\left[\frac{1}{2} X^2, -\frac{1}{2} \Delta_{\mathbf{X}} \right] = i D. \tag{5.132}$$

---

[13] As shown in [89], $L_+\psi$ cannot be zero.
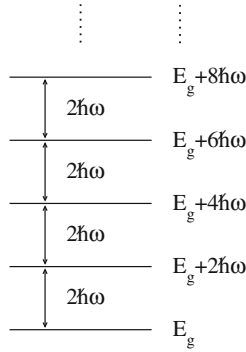
Fig. 5.9 The energy spectrum of the unitary gas in an isotropic harmonic trap is a collection of semi-infinite ladders such as the one depicted in the figure, with various ground step energies E_g. This structure is related to the existence of a decoupled bosonic mode, and holds whatever the numbers of fermions in each of the two spin components

We emphasize again the crucial point that the operators $L_\pm$ preserve the domain of the Hamiltonian in the present unitary case, since D and X^2 do. Obtaining the canonical commutation relations among the generators T_1, T_2 and T_3 of the SO(2,1) Lie algebra,

$$[T_1, T_2] \equiv -iT_3, \quad [T_2, T_3] \equiv iT_1, \quad [T_3, T_1] \equiv iT_2, \tag{5.133}$$

is then only a matter of rewriting:

$$T_1 \pm iT_2 \equiv \frac{1}{2}L_\pm \quad \text{and} \quad T_3 = \frac{H}{2\hbar\omega}. \tag{5.134}$$

Note the sign difference in the first commutator of Eq. 5.133 with respect to the other two commutators, and with respect to the more usual SO(3) or SU(2) Lie algebra.

Have we gained something in introducing the SO(2,1) Lie algebra, or is it simply a formal rewriting of the ladder structure already apparent in the simple minded approach Eq. 5.127, may ask a reader unfamiliar with dynamical symmetries. Well, an advantage is that we can immediately exhibit the so-called Casimir operator C,

$$C \equiv -4[T_1^2 + T_2^2 - T_3^2] = H^2 - \frac{1}{2}(\hbar\omega)^2(L_+L_- + L_-L_+), \tag{5.135}$$

guaranteed to commute with all the elements T_1, T_2 and T_3 of the algebra, so that C is necessarily a scalar within each ladder. Taking as a particularly simple case the expectation value of C within the ground step ψ_g of the ladder of energy E_g, and using Eq. 5.131 to evaluate $\langle\psi_g|L_-L_+|\psi_g\rangle$, we obtain $C|\psi_g\rangle = E_g(E_g - 2\hbar\omega)|\psi_g\rangle$. Inverting this relation thanks to the property $E_g \geq 3\hbar\omega/2$,[14] we can define the ground energy step operator H_g:

---

[14] To obtain this inequality, one uses a virial theorem after separation of the center of mass motion [89].

$$H_g = \hbar\omega + [C + (\hbar\omega)^2]^{1/2}, \tag{5.136}$$

which is scalar and equal to E_g within each ladder. A useful application of H_g is to rescale the raising and lowering operator $L_\pm$ to obtain simpler commutation relations: It appears that

$$b = [2(H + H_g)/(\hbar\omega)]^{-1/2}L_- \tag{5.137}$$

is a bosonic annihilation operator, which obeys the usual bosonic commutation relations, in particular with its hermitian conjugate

$$[b, b^\dagger] = 1. \tag{5.138}$$

$b^\dagger$ and b have the same raising/lowering properties as $L_\pm$, and commute with H_g. They have the usual simple matrix elements, e.g. $b^\dagger|n\rangle = (n + 1)^{1/2}|n + 1\rangle$ where $|n\rangle$ is the step number n of a ladder, n starting from 0. They allow an illuminating rewriting of the Hamiltonian:

$$H = H_g + 2\hbar\omega b^\dagger b \tag{5.139}$$

revealing that the unitary gas in a harmonic isotropic trap has a fully decoupled bosonic degree of freedom. This bosonic degree of freedom, physically, is simply the undamped breathing mode of the gas of frequency 2ω, identified for a different system in [90].

We now give two simple applications of the above formalism [89]. First, one can calculate the various moments of the trapping Hamiltonian $H_{trap} = \frac{1}{2}m\omega^2 X^2$, from the identity

$$H_{trap} = \frac{1}{2}H - \frac{\hbar\omega}{4}(L_+ + L_-) = \frac{\hbar\omega}{2}A^\dagger A \tag{5.140}$$

where $A = [b^\dagger b + H_g/(\hbar\omega)]^{1/2} - b$. Taking the expectation value of Eq. 5.140 within a given eigenstate of energy E, or within a statistical mixture of eigenstates, immediately gives

$$\langle H_{trap}\rangle = \frac{1}{2}\langle H\rangle, \tag{5.141}$$

a particular case of the virial theorem Eq. 5.88. Taking the expectation value of H_{trap}^2 for the thermal equilibrium density operator gives

$$4\langle H_{trap}^2\rangle = \langle H^2\rangle + \langle H\rangle\hbar\omega[2\langle b^\dagger b\rangle + 1] \tag{5.142}$$

where we used $\langle H_g b^\dagger b\rangle = \langle H_g\rangle\langle b^\dagger b\rangle$ for the thermal equilibrium. From the Bose formula, one has also $\langle b^\dagger b\rangle = [\exp(2\beta\hbar\omega) - 1]^{-1}$, with $\beta = 1/(k_B T)$ and T is the temperature.

The second, more impressive, application is to uncover a very interesting structure of the N-body wavefunction $\psi_g(\mathbf{X})$ of the ground energy step of an arbitrary ladder. We introduce hyperspherical coordinates $(X, \mathbf{n} = \mathbf{X}/X)$, where $\mathbf{n}$ is a unit vector is the space of $3N$ real coordinates. The innocent equation (5.129) becomes

$$\left[-\frac{3N}{2} - X\partial_X + \frac{E_g}{\hbar\omega} - \frac{m\omega}{\hbar}X^2 \right]\psi_g(\mathbf{X}) = 0. \tag{5.143}$$

This is readily integrated for a fixed hyperdirection $\mathbf{n}$:

$$\psi_g(\mathbf{X}) = e^{-m\omega X^2/(2\hbar)} X^{\frac{E_g}{\hbar\omega} - \frac{3N}{2}} f(\mathbf{n}) \tag{5.144}$$

where $f(\mathbf{n})$ is an unknown function of the hyperdirection. Eq. 5.144 has fascinating consequences.

First, it shows that ψ_g, being the product of a function of the modulus X and of a function of the hyperdirection, is *separable* in hyperspherical coordinates. The physical consequences of this separability, in particular for the few-body problem, are investigated in Sect. 5.3.4. Note that this separability holds for all the other steps of the ladder, since L_+ only acts on the hyperradius.

Second, we take the limit $\omega \to 0$ in Eq. 5.144: according to Eq. 5.12, $E_g/(\hbar\omega)$ is a constant, and $E_g \to 0$, whereas the Gaussian factor tends to unity. $\mathbf{n}$ is dimensionless, and we can take $f(\mathbf{n})$ to be ω independent if we do not normalize ψ_g to unity. We thus obtain in this limit a zero energy eigenstate of the free space problem,

$$\psi^{\text{free}}(\mathbf{X}) = X^{\frac{E_g}{\hbar\omega} - \frac{3N}{2}} f(\mathbf{n}) \tag{5.145}$$

which is independent of ω. This zero energy eigenstate is scaling invariant, in the sense that

$$\psi^{\text{free}}_\lambda(\mathbf{X}) = \frac{1}{\lambda^v}\psi^{\text{free}}(\mathbf{X}) \quad \forall \lambda > 0, \tag{5.146}$$

where ψ_λ is defined in Eq. 5.81 and

$$v = \frac{E_g}{\hbar\omega}. \tag{5.147}$$

In summary, starting from the wavefunction ψ_g of any ladder ground state of the trapped gas spectrum, one gets a scaling-invariant zero-energy free-space eigenstate $\psi^{\text{free}}_\lambda$, simply by removing the gaussian factor $e^{-m\omega X^2/(2\hbar)}$ in the expression (5.144) of ψ_g.

Remarkably, the reverse property is true. Let us imagine that we know a zero energy eigenstate ψ^{free} of the free space problem $H_{\text{free}} = -\frac{\hbar^2}{2m}\Delta_{\mathbf{X}}$,

$$\Delta_{\mathbf{X}}\psi^{\text{free}}(\mathbf{X}) = 0, \tag{5.148}$$

that of course also obeys the Wigner-Bethe-Peierls contact conditions for the unitary gas. Since H_{free} commutes with the generator D of the scaling transforms, we generally expect ψ^{free} to obey Eq. 5.146 with some exponent v, so that

$$i D \psi^{\text{free}} = v \psi^{\text{free}}. \tag{5.149}$$

Since ψ^{free} is not square integrable, the hermiticity of D does not imply that $v \in i\mathbb{R}$; on the contrary, we will see that $v \in \mathbb{R}$. Let us multiply ψ^{free} with a Gaussian factor:

$$\psi(\mathbf{X}) \equiv e^{-m\omega X^2/(2\hbar)} \psi^{\text{free}}(\mathbf{X}). \tag{5.150}$$

As we did for the gauge transform, see Eq. 5.115, we can show that ψ so defined obeys the Wigner-Bethe-Peierls contact conditions. Calculating the action on ψ of the Hamiltonian H of the trapped gas, and using Eq. 5.149, we directly obtain

$$H\psi = v\hbar\omega\psi, \tag{5.151}$$

i.e. ψ is indeed an eigenstate of the trapped gas with the eigenenergy $v\hbar\omega$. This ψ corresponds to the ground energy step of a ladder. Repeated action of L_+ will generate the other states of the ladder.

We have thus constructed a mapping between the trapped case and the zero energy free space case, for the unitary gas in an isotropic harmonic trap. A similar mapping (restricting to the ground state) was constructed by Tan in an unpublished work [91].

5.3.3 Separability in Internal Hyperspherical Coordinates

As shown in Sect. 5.3.2, the SO(2,1) dynamical symmetry of the unitary gas in an isotropic harmonic trap implies that the eigenstate wavefunctions $\psi(\mathbf{X})$ may be written as the product of a function of the modulus X and of a function of the direction $\mathbf{X}/X$. Here, following [89], we directly use this property at the level of the N-body Schrödinger equation, for $N > 2$, and we derive an effective Schrödinger equation for a hyperradial wavefunction, with interesting consequences discussed in Sect. 5.3.4. The derivation is restricted here to the case of particles of identical masses, as in the previous sections, but the separability in internal spherical coordinates may also hold for particles of different masses, as detailed in Appendix 3.

First, we introduce a refinement to the separability of Sect. 5.3.2: in a harmonic trap, the center of mass of the system is totally decoupled from the internal variables, that is from the relative coordinates $\mathbf{r}_i - \mathbf{r}_j$ of the particles. This is quite straightforward in Heisenberg picture, for an interaction modeled by a potential $V(|\mathbf{r}_i - \mathbf{r}_j|)$. The Heisenberg equations of motion for the center of mass position

$$\mathbf{C} \equiv \frac{1}{N} \sum_{i=1}^{N} \mathbf{r}_i \tag{5.152}$$

and the center of mass momentum $\mathbf{P} = \sum_{i=1}^{N} \mathbf{p}_i$ are indeed coupled only among themselves, due in particular to the fact that the interaction potential cannot change the total momentum $\mathbf{P}$ of the system:

$$\frac{d}{dt}\hat{\mathbf{P}}(t) = -Nm\omega^2\hat{\mathbf{C}}(t) \tag{5.153}$$

$$\frac{d}{dt}\hat{\mathbf{C}}(t) = \frac{\hat{\mathbf{P}}(t)}{Nm}. \tag{5.154}$$

The center of mass of the system thus behaves as a fictitious particle of mass Nm trapped in the harmonic potential $Nm\omega^2\mathbf{C}^2/2$, with a Hamiltonian

$$H_{\mathrm{CM}} = -\frac{\hbar^2}{2Nm}\Delta_{\mathbf{C}} + \frac{1}{2}Nm\omega^2 C^2. \tag{5.155}$$

The center of mass has of course the same angular oscillation frequency as the individual particles. This center of mass decoupling property clearly holds in the general harmonic *anisotropic* case. It persists in the zero range limit so it holds also for the zero-range model.

We can thus split the Hamiltonian Eq. 5.74 as the sum of the center of mass Hamiltonian H_{CM} and the internal Hamiltonian $H_{\mathrm{internal}} \equiv H - H_{\mathrm{CM}}$. As a consequence, we introduce as new spatial coordinates the center of mass position $\mathbf{C}$ and the set of internal coordinates

$$\mathbf{R} \equiv (\mathbf{r}_1 - \mathbf{C}, \ldots, \mathbf{r}_N - \mathbf{C}), \tag{5.156}$$

and we can seek eigenstates in the factorized form $\psi(\mathbf{X}) = \psi_{\mathrm{CM}}(\mathbf{C})\psi_{\mathrm{internal}}(\mathbf{R})$.

The crucial step is then to define *internal* hyperspherical coordinates, consisting in the hyperradius

$$R = \left[\sum_{i=1}^{N}(\mathbf{r}_i - \mathbf{C})^2\right]^{1/2} \tag{5.157}$$

and a convenient parameterization of the set of dimensionless internal coordinates $\mathbf{R}/R$. There is a technical subtlety due to the fact that the coordinates of $\mathbf{R}$ are not independent variables: Since the sum of the components of $\mathbf{R}$ along each spatial direction x, y and z is exactly zero, and since $\mathbf{R}/R$ is a unit vector, the vector $\mathbf{R}/R$ contains actually only $3N - 4$ independent dimensionless real variables. We then use the following result, that may be obtained with the appropriate Jacobi coordinates[15] [92]: There exists a parameterization of $\mathbf{R}/R$ by a set of $3N - 4$ internal hyperangles that we call Ω, such that the internal Hamiltonian takes the form

---

[15] For particles of equal masses one introduces the Jacobi coordinates $\mathbf{u}_i = (\frac{N-i}{N+1-i})^{1/2}\left[\mathbf{r}_i - (N-i)^{-1}\sum_{j=i+1}^{N}\mathbf{r}_j\right]$ for $1 \leq i \leq N - 1$. Then $\Delta_{\mathbf{X}} = N^{-1}\Delta_{\mathbf{C}} + \sum_{i=1}^{N-1}\Delta_{\mathbf{u}_i}$ and $R^2 = X^2 - NC^2 = \sum_{i=1}^{N-1}\mathbf{u}_i^2$. The general case of arbitrary masses is detailed in the Appendix 3.

$$H_{\text{internal}} = -\frac{\hbar^2}{2m}\left[\partial_R^2 + \frac{3N-4}{R}\partial_R + \frac{1}{R^2}\Delta_\Omega\right] + \frac{1}{2}m\omega^2 R^2, \qquad (5.158)$$

where Δ_Ω is the Laplacian on the unit sphere of dimension $3N - 4$. The expression between square brackets is the standard form for the usual Laplacian in dimension $d = 3N - 3$, written in hyperspherical coordinates, which justifies the name of "internal hyperspherical coordinates".

The separability in internal spherical coordinates means that the internal eigenstates in a trap can be written as products of a function of R and a function of Ω. This basically results from the reasoning below Eq. 5.148, with the little twist that one can further assume that the zero-energy free space eigenstate $\psi^{\text{free}}(\mathbf{X})$ has a zero total momentum, i. e. it is independent of the center of mass position.[16] The scale invariance Eq. 5.146 or equivalently Eq. 5.149 then implies

$$\psi^{\text{free}}(\mathbf{X}) = R^{s-(3N-5)/2}\phi(\Omega) \qquad (5.159)$$

with some exponent s shifted for convenience by $(3N - 5)/2$. The challenge is of course to determine the unknown function $\phi(\Omega)$ and the corresponding value of s. From Schrödinger's equation $\Delta_{\mathbf{X}}\psi^{\text{free}} = 0$ and the expression of the internal Laplacian in hyperspherical coordinates, see Eq. 5.158, one finds that s^2 solves the eigenvalue problem

$$\left[-\Delta_\Omega + \left(\frac{3N-5}{2}\right)^2\right]\phi(\Omega) = s^2\phi(\Omega), \qquad (5.160)$$

where $\phi(\Omega)$ has to obey the Wigner-Bethe-Peierls contact conditions Eq. 5.108 reformulated in hyperangular coordinates.[17] The merit of the shift $(3N - 5)/2$ is thus to reveal a symmetry $s \leftrightarrow -s$.

The generalization of the zero energy free space solution Eq. 5.159 to the finite energy trapped problem is simply provided by the ansatz:

$$\psi(\mathbf{X}) = \psi_{\text{CM}}(\mathbf{C})\phi(\Omega)R^{-(3N-5)/2}F(R). \qquad (5.161)$$

Here $\psi_{\text{CM}}(\mathbf{C})$ is any center of mass eigenstate wavefunction of energy E_{CM}, $\phi(\Omega)$ is any solution of the eigenvalue problem Eq. 5.160. Injecting the ansatz into Schrödinger's equation of eigenenergy E and using Eq. 5.158, one finds that

$$E = E_{\text{CM}} + E_{\text{internal}}, \qquad (5.162)$$

---

[16] The reasoning below Eq. 5.143 can also be adapted by putting the center of mass in its ground state $\psi_{\text{CM}}(\mathbf{C}) \propto \exp[-Nm\omega C^2/(2\hbar)]$ and by constructing purely internal raising and lowering operators of an internal SO(2,1) dynamical symmetry, that do not excite the center of mass motion contrarily to L_+ and L_- [89].

[17] These reformulated contact conditions are given explicitly in [55], Eq. 1.38.

where the hyperradial wavefunction $F(R)$ and the internal eigenenergy E_{internal} solve the eigenvalue problem:

$$-\frac{\hbar^2}{2m}\left[F''(R) + \frac{1}{R}F'(R)\right] + \left(\frac{\hbar^2 s^2}{2mR^2} + \frac{1}{2}m\omega^2 R^2\right)F(R) = E_{\text{internal}}F(R).$$
(5.163)

We note that, as detailed in the Appendix 3, this separability remarkably also holds in the case where the N particles have different masses [89], provided that they all have the same angular oscillation frequency ω in the trap, and that the Wigner-Bethe-Peierls model still defines a self-adjoint Hamiltonian for the considered mass ratios. The separability even holds when the Wigner-Bethe-Peierls model *supplemented with an additional boundary condition for $R \to 0$ and fixed Ω is self-adjoint, as is the case e.g. for $N = 3$ bosons, see below; indeed such a boundary condition only affects the hyperradial problem.

In practice the explicit calculation of s is possible for the few-body problem. The most natural approach in general is to try to calculate the functions A_{ij} in Eq. 5.108 in momentum space. From Eq. 5.108 it appears that A_{ij} is scaling invariant with an exponent $s + 1 - (3N - 5)/2$. Its Fourier transform[18] is then also scaling invariant, with an exponent given by a simple power-counting argument: Since A_{ij} is a function of $3(N - 2)$ variables, if one takes into account the fact that it does not depend on the center of mass position **C**, and since one has $[s + 1 - (3N - 5)/2] + 3(N - 2) = s + (3N - 5)/2$, its Fourier transform $\tilde{A}_{ij}$ scales as

$$\tilde{A}_{ij}(\mathbf{K}) = K^{-[s+(3N-5)/2]}f_{ij}(\mathbf{K}/K)$$
(5.164)

where **K** collects all the $3(N - 2)$ variables of $\tilde{A}_{ij}$ and f_{ij} denotes some functions to be determined. Remarkably it is the same quantity $(3N - 5)/2$ which appears in both Eqs. 5.159, 5.164.

This momentum space approach leads to integral equations. For $N = 3$, this integral equation was obtained in [93]; it was solved analytically in [94], the allowed values of s being the solutions of a transcendental equation. This transcendental equation was rederived from a direct analytical solution of (5.160) in position space in [4, 5], and generalised to arbitrary angular momenta, masses and statistics in [5]; for equal masses it is conveniently written in the form ([95] and refs. therein):

$$\frac{\Gamma\left(l + \frac{3}{2}\right)}{\Gamma\left(\frac{l+1+s}{2}\right)\Gamma\left(\frac{l+1-s}{2}\right)} = \frac{\eta}{\sqrt{3\pi}(-2)^l}\,{}_2F_1\left(\frac{l+1+s}{2}, \frac{l+1-s}{2}; l + \frac{3}{2}; \frac{1}{4}\right)$$
(5.165)

or alternatively [32]

---

[18] Since the Fourier transform $\tilde{A}_{ij}(\mathbf{K}) = \int d^{3(N-2)}Y e^{-i\mathbf{K}\cdot\mathbf{Y}}A_{ij}(\mathbf{Y})$ may lead to non-absolutely converging integrals at infinity, the calculation has to be performed using the language of distributions, with a regularizing factor $e^{-\eta Y}$, $\eta \to 0^+$.

$$\left[i^l \sum_{k=0}^{l} \frac{(-l)_k(l+1)_k}{k!} \frac{(1-s)_l}{(1-s)_k} \left(2^{-k}i(k-s)e^{is\frac{\pi}{2}} + \eta(-1)^l \frac{4}{\sqrt{3}} e^{i\frac{\pi}{6}(2k+s)}\right)\right]$$

$$-\left[(-i)^l \sum_{k=0}^{l} \frac{(-l)_k(l+1)_k}{k!} \frac{(1-s)_l}{(1-s)_k} \left(2^{-k}(-i)(k-s)e^{-is\frac{\pi}{2}} + \eta(-1)^l \frac{4}{\sqrt{3}} e^{-i\frac{\pi}{6}(2k+s)}\right)\right] = 0$$

$$(5.166)$$

where l is the total internal angular momentum quantum number, η is -1 for fermions ($N_\uparrow = 2$, $N_\downarrow = 1$) or $+2$ for spinless bosons, $_2F_1$ is a hypergeometric function, and $(x)_n \equiv x(x+1)\dots(x+n-1)$ with $(x)_0 \equiv 1$. The Eq. 5.165 has some spurious integer solutions ($l = 0, s = 2$ for fermions; $l = 0, s = 4$ and $l = 1, s = 3$ for bosons) which must be eliminated. For $N = 4$ there is no known analytical solution of the integral equation. Using the scale invariance of $\tilde{A}_{ij}(\mathbf{K})$ as in Eq. 5.164 and rotational symmetry however brings it to a numerically tractable integral equation involving the exponent s, that allowed to predict a four-body Efimov effect for three same-spin state fermions interacting with a lighter particle [7].

5.3.4 Physical Consequences of the Separability

As seen in the previous Sect. 5.3.3, the solution of the N-body problem ($N > 2$) for the unitary gas in a harmonic isotropic trap boils down to (i) the calculation of exponents s from zero-energy free space solutions, and (ii) the solution of the hyperradial eigenvalue problem Eq. 5.163. Whereas (i) is the most challenging part on a practical point of view, the step (ii) contains a rich physics that we now discuss.

Formally, the hyperradial problem Eq. 5.163 is Schrödinger's equation for one (fictitious) particle moving in two dimensions with zero angular momentum in the (effective) potential

$$U_{\text{eff}}(R) = \frac{\hbar^2}{2m} \frac{s^2}{R^2} + \frac{1}{2}m\omega^2 R^2. \qquad (5.167)$$

We will see that the nature of this problem is very different depending on the sign of s^2. The case $s^2 \geq 0$, i.e. s real, happens for $N = 3$ fermions ($N_\uparrow = 2$, $N_\downarrow = 1$), not only for equal masses, as can be tested numerically from (5.166) and even demonstrated analytically from the corresponding hyperangular eigenvalue problem [32] but also for unequal masses provided $m_\uparrow/m_\downarrow$ is below the critical value $13.60\dots$ where one of the s (in the angular momentum $l = 1$ channel) becomes imaginary [5]. For $N = 4$ fermions with ($N_\uparrow = 3$, $N_\downarrow = 1$,) the critical mass ratio above which one of the s (in the angular momentum $l = 1$ channel) becomes imaginary is slightly smaller, $m_\uparrow/m_\downarrow \simeq 13.384$ [7]. In the physics literature, s is believed to be real for fermions for any ($N_\uparrow, N_\downarrow$) for equal masses, this belief being supported by numerical and experimental evidence. For 3 identical bosons, it is well-known that one of the values of s (in the $l = 0$ channel) is imaginary [4], all other values being real.

5.3.4.1 Universal Case

In this section we assume that s is real and we can take the sign convention $s \geq 0$. We impose that the hyperradial wavefunction $F(R)$ is bounded for $R \to 0$; indeed, allowing $F(R)$ to diverge would physically correspond to a N-body resonance (see Appendix 6). The spectrum and the corresponding hyperradial wavefunctions then are [89]

$$E_{\text{internal}} = (s + 1 + 2q)\hbar\omega, \quad q \in \mathbb{N} \tag{5.168}$$

$$F(R) = \sqrt{\frac{2q!}{\Gamma(s + 1 + q)}} \frac{R^s}{(a_{ho})^{s+1}} e^{-\left(\frac{R}{2a_{ho}}\right)^2} L_q^{(s)}\left(\left(\frac{R}{a_{ho}}\right)^2\right) \tag{5.169}$$

where $L_q^{(s)}$ is a generalised Laguerre polynomial of order q, $a_{ho} \equiv \sqrt{\frac{\hbar}{m\omega}}$ is the harmonic oscillator length, and the normalisation is such that $\int_0^\infty dR\, R\, F(R)^2 = 1$. Eq. 5.168 generalises to excited states the result obtained for the ground state in [91].

We thus recover the $2\hbar\omega$ spacing of the spectrum discussed in Sect. 5.3.2. We can also reinterpret the scaling solution of Sect. 5.3.1 as a time-evolution of the hyperradial wavefunction with a time-independent hyperangular wavefunction; in particular, the undamped breathing mode corresponds to an oscillation of the fictitious particle in the effective potential (5.167).[19]

The expression (5.169) of $F(R)$ immediately yields the probability distribution $P(R)$ of the hyperradius via $P(R) = F(R)^2 R$. This analytical prediction is in good agreement with the numerical results obtained in [96] for up to 17 fermions.

In the large N limit (more precisely if $N_\uparrow$ and $N_\downarrow$ tend to infinity and their ratio goes to a constant), the ground state energy of the trapped unitary gas is expected to be given in an asymptotically exact way by hydrostatics (also called local density approximation). Amusingly, this allows to predict the large-N asymptotics of the smallest possible value of s. For $N_\uparrow = N_\downarrow = N/2 \to \infty$ this gives [91, 96]

$$s \sim \sqrt{\xi}\frac{(3N)^{4/3}}{4} \tag{5.170}$$

where ξ appears in the expression Eq. 5.14 for the ground state energy of the homogeneous unitary gas.

For spin-1/2 fermions, Eqs. 5.168, 5.169, combined with the transcendental equation (5.165) and the expression of the hyperangular wavefunctions [5], provide the complete solution of the unitary three-body problem in an isotropic harmonic trap

---

[19] Strictly speaking, such a time evolution of the wavefunction in *internal* hyperspherical coordinates corresponds to an internal scaling solution where the center of mass wavefunction is constant, whereas the scaling solution of Sect. 5.3.1 corresponds to a hyperradial motion in the hyperspherical coordinates $(X, \mathbf{n})$.

[32] (for completeness, one also has to include the eigenstates which are common to the unitary and the non-interacting problem [32], mentioned at the end of Sect. 5.2.2.1). This was first realised for the ground state in [91]. Remarkably, this 3-body spectrum in a trap allows to compute the third virial coefficient of the homogeneous unitary gas [97], whose value was confirmed experimentally (see [45] and the contribution of F. Chevy and C. Salomon in Chap. 11 of this volume).

For spinless bosons, the unitary three-body problem in an isotropic harmonic trap has two families of eigenstates (apart from the aforementioned common eigenstates with the non-interacting problem) [31, 32]: the states corresponding to real solutions s of the transcendental Equation 5.165, which we call universal states; and the states corresponding to the imaginary solution for s, which we call efimovian. Equations. 5.168, 5.169 apply to universal states. The efimovian states are discussed in the next section.

5.3.4.2 Efimovian Case

In this section we consider the case $s^2 < 0$, i.e. s is purely imaginary. In this case, all solutions of the Schrödinger-like equation 5.163 are bounded and oscillate more and more rapidly when $R \to 0$. In order to obtain a hermitian problem with a discrete spectrum, one has to impose the boundary condition [94, 55]:

$$\exists A / \ F(R) \sim A \ \mathrm{Im}\left[\left(\frac{R}{R_t}\right)^s\right] \quad \text{for } R \to 0, \tag{5.171}$$

where R_t is an additional three-body parameter. An equivalent form is:

$$\exists A'/F(R) \sim A'\sin\left[|s|\ln\left(\frac{R}{R_t}\right)\right] \quad \text{for } R \to 0. \tag{5.172}$$

The corresponding hyperradial wavefunctions are

$$F(R) = R^{-1}W_{E/2,s/2}(R^2/a_{ho}^2) \tag{5.173}$$

where W is a Whittaker function, and the spectrum is given by the implicit equation

$$\mathrm{arg}\Gamma\left[\frac{1 + s - E/(\hbar\omega)}{2}\right] = -|s|\ln(R_t/a_{ho}) + \mathrm{arg}\,\Gamma(1 + s)\,\mathrm{mod}\,\pi \tag{5.174}$$

obtained in [31], whose solutions form a discrete series, which is unbounded from below, and can be labeled by a quantum number $q \in \mathbb{Z}$.

In free space ($\omega = 0$,) there is a geometric series of bound states

$$E_q = -\frac{2\hbar^2}{mR_t^2}\exp\left(-q\frac{2\pi}{|s|} + \frac{2}{|s|}\mathrm{arg}\Gamma(1 + s)\right), \quad q \in \mathbb{Z} \tag{5.175}$$

$$F(R) = K_s \left(R\sqrt{2m|E|/\hbar^2} \right) \tag{5.176}$$

where K is a Bessel function. For three particles this corresponds to the well-known series of Efimov three-body bound states [4, 5]. This also applies to the four-body bound states in the aforementioned case of $(3 + 1)$ fermions with $m_\uparrow/m_\downarrow$ between $\simeq 13.384$ and $13.607\dots$ [7]. As expected, in the limit $E \to -\infty$, the spectrum of the efimovian states in the trap (5.174) approaches the free space spectrum (5.175). The unboundedness of the spectrum in the zero-range limit is a natural consequence of the Thomas effect and of the limit cycle behavior [55].

5.3.5 Vanishing Bulk Viscosity

In this section, we give a simple rederivation of the fact that the bulk viscosity of the unitary gas in the normal phase is zero. This result was obtained in [98] (see also [99]). It helps analysing e.g. the ongoing experimental studies of the shear viscosity, whose value is of fundamental importance ([100] and refs. therein). Although the superfluid regime was also treated in [98], we omit it here for simplicity. In our rederivation we shall use the scaling solution and the existence of the undamped breathing mode.[20]

In the hydrodynamic theory for a normal compressible viscous fluid [101, 98], the (coarse-grained) evolution of the gas in a trapping potential $U(\mathbf{r}, t)$ is described by the atom number density $\rho(\mathbf{r}, t)$, the velocity vector field $\mathbf{v}(\mathbf{r}, t)$, and the entropy per particle (in units of k_B) $s(\mathbf{r}, t)$. These 5 scalar functions solve five equations which are given for completeness in Appendix 4 although we will not directly use them here. We will only need the equation for the increase of the total entropy $S = \int \rho s d^3 r$ of the gas

$$\frac{dS}{dt} = \int \frac{\kappa \|\nabla T\|^2}{T^2} d^3 r + \int \frac{\eta}{2T} \sum_{ik} \left(\frac{\partial v_i}{\partial x_k} + \frac{\partial v_k}{\partial x_i} - \frac{2}{3}\delta_{ik}\nabla \cdot \mathbf{v} \right)^2 d^3 r + \int \frac{\zeta}{T} \|\nabla \cdot \mathbf{v}\|^2 d^3 r \tag{5.177}$$

which follows from the hydrodynamic equations (5.217, 5.215); note that the thermal conductivity κ, the shear viscosity η and the bulk viscosity ζ have to be ≥ 0 so that $dS/dt \geq 0$ [101]. The hydrodynamic theory is expected to become exact in the limit where the length (resp. time) scales on which the above functions vary are much larger than microscopic length (resp. time) scales such as $1/k_F$ (resp. $\hbar/E_F$).

We consider the following gedankenexperiment: starting with the gas at thermal equilibrium in a trap of frequency ω, we suddenly switch the trapping frequency at

---

[20] In article [98], the vanishing of the bulk viscosity was deduced from the so-called general coordinate and conformal invariance, the scaling solution being unknown to its author at the time of writing (although it had been obtained in [58]). The scaling solution was recently rederived using this general coordinate and conformal invariance [99]. Several other results presented in Sects. 5.3.2–5.3.4 were also rederived using this field theoretical formalism ([99] and refs. therein).

$t = 0$ to a different value ω_+. As we have seen in Sect. 5.3.1 and at the beginning of Sect. 5.3.2, this excites an *undamped* breathing mode: For $t > 0$, the size of the gas oscillates *indefinitely*. This rigorously periodic evolution of the system implies that the total entropy $S(t)$ is periodic, and since it cannot decrease, it has to be constant. Thus each of the terms in the right-hand-side of (5.177), and in particular the last term, has to vanish. Thus $\zeta(\mathbf{r}, t) \| \nabla \cdot \mathbf{v}(\mathbf{r}, t) \|^2 \equiv 0$. This implies that ζ is identically zero, as we now check. From the scaling evolution (5.109) of each many-body eigenstate, one can deduce (using the quantum-mechanical expression for the particle flux) that

$$\mathbf{v}(\mathbf{r}, t) = \frac{\dot{\lambda}}{\lambda} \mathbf{r}, \tag{5.178}$$

so that $\nabla \cdot \mathbf{v} = 3\dot{\lambda}/\lambda$. For t approaching 0 from above, we have $\dot{\lambda}(t) \neq 0$, as is intuitively clear and can be checked from Eqs. 5.110, 5.111; thus $\zeta(\mathbf{r}, t) = 0$ and by continuity $\zeta(\mathbf{r}, t = 0) = 0$. Since the central density and temperature in the initial equilibrium state of the gas are arbitrary, we conclude that $\zeta(\rho, T) = 0$ for all ρ and T. An alternative derivation of this result is presented in Appendix 5.

5.3.6 Short-Range Scaling Laws

As opposed to the previous sections, we now consider an arbitrary scattering length and an arbitrary external potential, possibly with periodic boundary conditions. Of all the particles $1, \ldots, N$, let us consider a subset $J \subset \{1, \ldots, N\}$ containing $n_\uparrow$ particles of spin $\uparrow$ and $n_\downarrow$ particles of spin $\downarrow$. From the particle positions $(\mathbf{r}_i)_{i \in J}$, we can define a hyperradius R_J and hyperangles Ω_J, and a center of mass position $\mathbf{C}_J$. The positions of all particles that do not belong to J are denoted by $\mathscr{R}_J = (\mathbf{r}_i)_{i \notin J}$. In the absence of a $(n_\uparrow + n_\downarrow)$-body resonance (see Appendix 6), one expects that, for any eigenstate, in the limit $R_J \to 0$ where all particles belonging to the subset J approach each other while $(\Omega_J, \mathbf{C}_J, \mathscr{R}_J)$ remain fixed, there exists a function A_J such that

$$\psi(\mathbf{r}_1, \ldots, \mathbf{r}_N) = R_J^\nu \phi(\mathbf{\Omega}_J) A_J(\mathbf{C}_j, \mathscr{R}_J) + o(R_J^\nu). \tag{5.179}$$

Here, $\nu = s_{\min}(n_\uparrow, n_\downarrow) - \frac{3(n_\uparrow + n_\downarrow) - 5}{2}$ with $s_{\min}(n_\uparrow, n_\downarrow)$ the smallest possible value of s for the problem of $n_\uparrow$ particles of spin $\uparrow$ and $n_\downarrow$ particles of spin $\downarrow$ (s being defined in Sect. 5.3.3) and $\phi(\Omega_J)$ is the corresponding hyperangular wavefunction (also defined in Sect. 5.3.3). This statement is essentially contained in [17, 91]. It comes from the intuition that, in the limit where the $n_\uparrow + n_\downarrow$ particles approach each other, the N-body wavefunction should be proportional to the $(n_\uparrow + n_\downarrow)$-body zero-energy free space wavefunction Eq. 5.159. This was used in [17] to predict that the formation rate of deeply bound molecules by three-body recombination, $\Gamma \equiv -\dot{N}/N$, behaves as $\hbar\Gamma/E_F \sim K \cdot (k_F b)^{2s_{\min}(2,1)}$ in the low-density limit, with b on the order of the van der Waals range and K a numerical prefactor which depends on short-range physics.

The analytical solution of the hyperangular three-body problem [Eq. 5.166] yields $s_{\min}(2, 1) = 1.772724\ldots$ (this value is reached in the angular momentum $l = 1$ channel). Experimentally, this scaling has not been checked, but the smallness of $\hbar\Gamma/E_F$ is one of the crucial in-gredients which allow to realise the unitary gas.

Appendix 1: Effective Range in a Lattice Model

To calculate the effective range r_e [defined by Eq. 5.5] for the lattice model of Sect. 5.2.1, it is convenient to perform in the expression (5.46) of the scattering amplitude an analytic continuation to purely imaginary incoming wavevectors k_0, setting $k_0 = iq_0$ with q_0 real and positive. Eliminating $1/g_0$ thanks to Eq. 5.47 we obtain the useful expression:

$$-\frac{1}{f_{k_0}} = \frac{1}{a} + 4\pi \int_{\mathscr{D}} \frac{d^3k}{(2\pi)^3} \left[\frac{1}{q_0^2 + 2m\varepsilon_{\mathbf{k}}/\hbar^2} - \frac{1}{2m\varepsilon_{\mathbf{k}}/\hbar^2} \right]. \qquad (5.180)$$

We first treat the case of the parabolic dispersion relation Eq. 5.48. A direct expansion of Eq. 5.180 in powers of q_0 leads to an infrared divergence. The trick is to use the fact that the integral over $\mathscr{D}$ in Eq. 5.180 can be written as the integral of the same integrand over the whole space minus the integral over the supplementary space $\mathbb{R}^3 \setminus \mathscr{D}$. The integral over the whole space may be performed exactly using

$$\int_{\mathbb{R}^3} \frac{d^3k}{(2\pi)^3} \left[\frac{1}{q_0^2 + k^2} - \frac{1}{k^2} \right] = -\frac{q_0}{4\pi}. \qquad (5.181)$$

This leads to the transparent expression, where the term corresponding to ik in Eq. 5.3, and which is non-analytic in the energy E, is now singled out:

$$-\frac{1}{f_{k_0}^{\text{parab}}} = \frac{1}{a} - q_0 - 4\pi \int_{\mathbb{R}^3 \setminus \mathscr{D}} \frac{d^3k}{(2\pi)^3} \left[\frac{1}{q_0^2 + k^2} - \frac{1}{k^2} \right]. \qquad (5.182)$$

This is now expandable in powers of q_0^2, leading to the effective range for the parabolic dispersion relation:

$$r_e^{\text{parab}} = \frac{1}{\pi^2} \int_{\mathbb{R}^3 \setminus \mathscr{D}} \frac{d^3k}{k^4}. \qquad (5.183)$$

We now turn back to the general case. The trick is to consider the difference between the inverse scattering amplitudes of the general case and the parabolic case with a common value of the scattering length:

$$\frac{1}{f_{k_0}^{\text{parab}}} - \frac{1}{f_{k_0}} = 4\pi \int_{\mathscr{D}} \frac{d^3k}{(2\pi)^3} \left[\frac{1}{q_0^2 + 2m\varepsilon_{\mathbf{k}}/\hbar^2} - \frac{1}{q_0^2 + k^2} - \frac{1}{2m\varepsilon_{\mathbf{k}}/\hbar^2} + \frac{1}{k^2} \right].$$
(5.184)

This is directly expandable to second order in q_0, leading to:

$$r_e - r_e^{\text{parab}} = 8\pi \int_{\mathscr{D}} \frac{d^3k}{(2\pi)^3} \left[\frac{1}{k^4} - \left(\frac{\hbar^2}{2m\varepsilon_{\mathbf{k}}} \right)^2 \right].$$
(5.185)

The numerical evaluation of this integral for the Hubbard dispersion relation Eq. 5.59 leads to the Hubbard model effective range Eq. 5.60.

Finally, we specialize the general formula to the parabolic plus quartic form Eq. 5.61. Setting $\mathbf{k} = (\pi/b)\mathbf{q}$ and using Eq. 5.183, we obtain

$$\frac{\pi^3 r_e^{\text{mix}}}{b} = \int_{\mathbb{R}^3 \setminus [-1,1]^3} \frac{d^3q}{q^4} + \int_{[-1,1]^3} \frac{d^3q}{q^4} \left[1 - \frac{1}{(1 - Cq^2)^2} \right].$$
(5.186)

The trick is to split the cube $[-1, 1]^3$ as the union of $B(0, 1)$, the sphere of center 0 and unit radius, and of the set $X = [-1, 1]^3 \setminus B(0, 1)$. One has also $\left(\mathbb{R}^3 \setminus [-1, 1]^3 \right) \cup X = \mathbb{R}^3 \setminus B(0, 1)$ so that

$$\frac{\pi^3 r_e^{\text{mix}}}{b} = \int_{\mathbb{R}^3 \setminus B(0,1)} \frac{d^3q}{q^4} + \int_{B(0,1)} \frac{d^3q}{q^4} \left[1 - \frac{1}{(1 - Cq^2)^2} \right] - \int_X \frac{d^3q}{q^4} \frac{1}{(1 - Cq^2)^2}.$$
(5.187)

One then moves to spherical coordinates of axis z. The first two terms in the right hand side may be calculated exactly. In particular, one introduces a primitive of $q^{-2}(1 - Cq^2)^{-2}$, given by $C^{1/2}\Phi(C^{1/2}q)$ with

$$\Phi(x) = \frac{x}{2(1 - x^2)} + \frac{3}{2}\text{arctanh}\, x - \frac{1}{x}.$$
(5.188)

In the last term of Eq. 5.187 one integrates over the modulus q of $\mathbf{q}$ for a fixed direction (θ, ϕ) where θ is the polar angle and ϕ the azimuthal angle. One then finds that q ranges from 1 to some maximal value $Q(\theta, \phi)$, and the integral over q provides the difference $\Phi(C^{1/2}Q) - \Phi(C^{1/2})$. Remarkably, the term $-\Phi(C^{1/2})$ cancels the contribution of the first two integrals in the right hand side of Eq. 5.187, so that

$$\frac{r_e^{\text{mix}}}{b} = -\frac{C^{1/2}}{\pi^3} \int_0^{2\pi} d\phi \int_{-1}^1 du\, \Phi[C^{1/2}Q(\theta, \phi)]$$
(5.189)

where as usual we have set $u = \cos\theta$. Using the symmetry under parity along each Cartesian axis, which adds a factor 8, and restricting to the face $q_x = 1$ of the cube, which adds a factor 3, the expression of $Q(\theta, \phi)$ is readily obtained, leading to

$$\frac{r_e^{\text{mix}}}{b} = -\frac{24C^{1/2}}{\pi^3} \int_0^{\pi/4} d\phi \int_0^{\frac{\cos\phi}{\sqrt{1 + \cos^2\phi}}} du\, \Phi\left(\frac{C^{1/2}}{\cos\phi\sqrt{1 - u^2}} \right).$$
(5.190)

In the limit $C \to 0$, $r_e^{\text{mix}} \to r_e^{\text{parab}}$, and Eq. 5.190 may be calculated analytically with $\Phi(x) \sim -1/x$ and with an exchange of the order of integration: This leads to Eq. 5.58. For a general value of $C \in [0, 1/3]$ we have calculated Eq. 5.190 numerically, and we have identified the magic value of C leading to a zero effective range, see Eq. 5.62. With the same technique, we can calculate the value of K appearing in Eq. 5.49 from the expression

$$K = \frac{12}{\pi C^{1/2}} \int_0^{\pi/4} d\phi \int_0^{\frac{\cos\phi}{\sqrt{1 + \cos^2\phi}}} du \ \text{arctanh} \ \frac{C^{1/2}}{\cos\phi \sqrt{1 - u^2}}. \tag{5.191}$$

Appendix 2: What is the Domain of a Hamiltonian?

Let us consider a Hamiltonian H represented by a differential operator also called H. A naive and practical definition of the domain $D(H)$ of H is that it is the set of wavefunctions over which the action of the Hamiltonian is indeed represented by the considered differential operator. In other words, if a wavefunction ψ_{bad} does not belong to $D(H)$, one should not calculate the action of H on ψ_{bad} directly using the differential operator H. If H if self-adjoint, one should rather expand ψ_{bad} on the Hilbert basis of eigenstates of H and calculate the action of H in this basis.

For example, for a single particle in one dimension in a box with infinite walls in $x = 0$ and $x = 1$, so that $0 \le x \le 1$, one has the Hamiltonian

$$H = -\frac{1}{2} \frac{d^2}{dx^2}, \tag{5.192}$$

with the boundary conditions on the wavefunction

$$\psi(0) = \psi(1) = 0 \tag{5.193}$$

representing the effect of the box. To be in the domain, a wavefunction $\psi(x)$ should be twice differentiable for $0 < x < 1$ and should obey the boundary conditions (5.193). An example of a wavefunction which is not in the domain is the constant wavefunction $\psi(x) = 1$. An example of wavefunction in the domain is

$$\psi(x) = 30^{1/2} x(1 - x). \tag{5.194}$$

If one is not careful, one may obtain wrong results. Let us calculate the mean energy and the second moment of the energy for ψ given by (5.194). By repeated action of H onto ψ, and calculation of elementary integrals, one obtains

$$\langle H \rangle_\psi = 5 \tag{5.195}$$

$$\langle H^2 \rangle_\psi = 0?! \tag{5.196}$$

Eq. 5.195 is correct, but Eq. 5.196 is wrong (it would lead to a negative variance of the energy) because $H\psi$ is not in $D(H)$ and the subsequent illicit action of H as the differential operator (5.192) gives zero.

How to calculate the right value of $\langle H^2 \rangle_\psi$? One introduces the orthonormal Hilbert basis of eigenstates of H,

$$\psi_n(x) = 2^{1/2}\sin[\pi(n+1)x], \quad n \in \mathbb{N}, \tag{5.197}$$

with the eigenenergy $\varepsilon_n = \frac{\pi^2}{2}(n+1)^2$. Then ψ of Eq. 5.194 may be expanded as $\sum_n c_n \psi_n(x)$, and the kth moment of the energy may be defined as

$$\langle H^k \rangle_\psi = \sum_{n\in\mathbb{N}} (\varepsilon_n)^k |c_n|^2. \tag{5.198}$$

Since $c_n = 4\sqrt{15}[1 + (-1)^n]/[\pi(n+1)]^3$, one recovers $\langle H \rangle_\psi = 5$ and one obtains the correct value $\langle H^2 \rangle_\psi = 30$, that leads to a positive energy variance as it should be. Also $\langle H^k \rangle_\psi = +\infty$ for $k \geq 3$.

The trick of expanding ψ in the eigenbasis of H is thus quite powerful, it allows to define the action of H on any wavefunction ψ in the Hilbert space (not belonging to the domain). It may be applied of course only if H is self-adjoint, as it is the case in our simple example.

Appendix 3: Separability and Jacobi Coordinates for Arbitrary Masses

We here consider $N \geq 2$ harmonically trapped particles interacting in the unitary limit, with possibly different masses m_i but with the same isotropic angular oscillation frequency ω. The Hamiltonian reads

$$H = \sum_{i=1}^{N} \left[-\frac{\hbar^2}{2m_i}\Delta_{\mathbf{r}_i} + \frac{1}{2}m_i\omega^2 r_i^2 \right] \tag{5.199}$$

and the unitary interaction is described by the Wigner-Bethe-Peierls contact conditions on the N-body wavefunction: For all pairs of particles (i,j), in the limit $r_{ij} = |\mathbf{r}_i - \mathbf{r}_j| \to 0$ with a *fixed* value of the centroid of the particles i and j, $\mathbf{R}_{ij} \equiv (m_i\mathbf{r}_i + m_j\mathbf{r}_j)/(m_i + m_j)$, that differs from the positions $\mathbf{r}_k$ of the other particles, $k \neq i, j$, there exists a function A_{ij} such that

$$\psi(\mathbf{r}_1, \ldots, \mathbf{r}_N) = \frac{A_{ij}(\mathbf{R}_{ij}; (\mathbf{r}_k)_{k\neq i,j})}{r_{ij}} + O(r_{ij}). \tag{5.200}$$

As is well known and as we will explain below, the internal Hamiltonian $H_{\text{internal}} = H - H_{\text{CM}}$, where $H_{\text{CM}} = -\frac{\hbar^2}{2M}\Delta_{\mathbf{C}} + \frac{1}{2}M\omega^2 C^2$, takes the form

$$H_{\text{internal}} = \sum_{i=1}^{N-1}\left[-\frac{\hbar^2}{2\bar{m}}\Delta_{\mathbf{u}_i} + \frac{1}{2}\bar{m}\omega^2 u_i^2\right] \tag{5.201}$$

in suitably defined Jacobi coordinates [see Eqs. 5.205, 5.214]. Here $\mathbf{C} = \sum_{i=1}^{N} m_i \mathbf{r}_i/M$ is the center of mass position, $M = \sum_{i=1}^{N} m_i$ is the total mass, and $\bar{m}$ is some arbitray mass reference, for example the mean mass M/N. Then it is straightforward to express Eq. 5.201 in hyperspherical coordinates, the vector $(\mathbf{u}_1, \ldots, \mathbf{u}_{N-1})$ with $3N - 3$ coordinates being expressed in terms of its modulus R and a set of $3N - 4$ hyperangles Ω, so that

$$H_{\text{internal}} = -\frac{\hbar^2}{2\bar{m}}\left[\partial_R^2 + \frac{3N-4}{R}\partial_R + \frac{1}{R^2}\Delta_{\Omega}\right] + \frac{1}{2}\bar{m}\omega^2 R^2 \tag{5.202}$$

where Δ_{Ω} is the Laplacian over the unit sphere of dimension $3N - 4$. As we shall see, the expression for the hyperradius is simply

$$R^2 \equiv \sum_{i=1}^{N-1} u_i^2 = \frac{1}{\bar{m}}\sum_{i=1}^{N} m_i(\mathbf{r}_i - \mathbf{C})^2. \tag{5.203}$$

This form of the Hamiltonian is then useful to show the separability of Schrödinger's equation for the unitary gas in hyperspherical coordinates [55, 89] for $N \geq 3$ and arbitrary masses. The separability Eq. 5.161 that was described for simplicity in the case of equal mass particles in Sect. 5.3.3 indeed still holds in the case of different masses, if the Wigner-Bethe-Peierls model defines a self-adjoint Hamiltonian.[21] We recall here the various arguments. First, for zero energy free space eigenstates, the form Eq. 5.159 is expected from scale invariance, if the Hamiltonian is self-adjoint [89]. Second, the form Eq. 5.161 for the general case, including non-zero energy and an isotropic harmonic trap, is expected because (i) the Hamiltonian (5.199), after separation of the center of mass, has the separable form (5.202) in hyperspherical coordinates, and (ii) Eq. 5.161 obeys the Wigner-Bethe-Peierls contact conditions if Eq. 5.159 does. This point (ii) results from the fact that the Wigner-Bethe-Peierls conditions are imposed, for each pair of particles *(i,j)*, for $r_{ij} \rightarrow 0$ with a *fixed* value of $\mathbf{R}_{ij}$ that differs from the positions $\mathbf{r}_k$ of the other particles, $k \neq i, j$. Using $\mathbf{r}_i = \mathbf{R}_{ij} + [m_j/(m_i + m_j)]\mathbf{r}_{ij}$ and $\mathbf{r}_j = \mathbf{R}_{ij} - [m_i/(m_i + m_j)]\mathbf{r}_{ij}$, with $\mathbf{r}_{ij} \equiv \mathbf{r}_i - \mathbf{r}_j$, we indeed find that

---

[21] Strictly speaking, it is sufficient that the Laplacian on the unit sphere together with the Wigner-Bethe-Peierls boundary conditions reexpressed in terms of hyperangles is self-adjoint, as extensively used in [7]. This is less restrictive than having the full Hamiltonian self-adjoint, since it allows for example to have a N-body Efimov effect while the $N - 1$ zero-range model is perfectly well-defined and does not experience any Efimov effect.

$$\bar{m}R^2 = \frac{m_i m_j}{m_i + m_j}r_{ij}^2 + (m_i + m_j)(\mathbf{R}_{ij} - \mathbf{C})^2 + \sum_{k \neq i,j} m_k(\mathbf{r}_k - \mathbf{C})^2. \quad (5.204)$$

For $N \geq 3$, we see that $\lim_{r_{ij} \to 0} R^2 > 0$, so that R varies only to second order in r_{ij} in that limit. Provided that the function $F(R)$ in Eq. 5.161 has no singularity at non-zero R, the Wigner-Bethe-Peierls contact conditions are preserved [similarly to the argument Eq. 5.115]. Third, bosonic or fermionic exchange symmetries imposed on the N-body wavefunction cannot break the separability in hyperspherical coordinates: Exchanging the positions of particles of same mass does not change the value of the hyperradius R, it only affects the hyperangles and thus the eigenvalues $[(3N - 5) /2]^2 - s^2$ of the Laplacian on the unit sphere.

To derive the form Eq. 5.201 of the internal Hamiltonian, we introduce the usual Jacobi coordinates given for example in [102]:

$$\mathbf{y}_i \equiv \mathbf{r}_i - \frac{\sum_{j=i+1}^{N} m_j \mathbf{r}_j}{\sum_{j=i+1}^{N} m_j} \quad \text{for } 1 \leq i \leq N - 1. \quad (5.205)$$

We note that $\mathbf{y}_i$ simply gives the relative coordinates of particle i with respect to the center of mass of the particles from $i + 1$ to N. To simplify notations, we also set $\mathbf{y}_N \equiv \mathbf{C}$. Here we derive Eq. 5.201 in a pedestrian way. Note that a more elegant derivation by recursion is given in page 63 of [55]. In compact form, the Jacobi change of variables corresponds to setting $\mathbf{y}_i = \sum_{j=1}^{N} M_{ij}\mathbf{r}_j$ for $1 \leq i \leq N$, where the non-symmetric matrix M is such that:

- In the case $1 \leq i < N$, one has: $M_{ij} = 0$ for $1 \leq j < i$, $M_{ij} = 1$ for $j = i$, and $M_{ij} = -m_j / \left(\sum_{k=i+1}^{N} m_k\right)$ for $i < j \leq N$.
- $M_{Nj} = m_j / \left(\sum_{k=1}^{N} m_k\right)$ for $1 \leq j \leq N$.

From the formula giving the derivative of a composite function, the kinetic energy operator writes

$$H_{\text{kin}} \equiv \sum_{i=1}^{N} -\frac{\hbar^2}{2m_i}\Delta_{\mathbf{r}_i} = -\frac{\hbar^2}{2}\sum_{j=1}^{N}\sum_{k=1}^{N} S_{jk}\text{grad}_{\mathbf{y}_j} \cdot \text{grad}_{\mathbf{y}_k}, \quad (5.206)$$

where the *symmetric* matrix S is defined as $S_{jk} = \sum_{i=1}^{N} M_{ji}M_{ki}/m_i$. The explicit calculation of the matrix elements S_{jk} is quite simple. Taking advantage of the fact that S is symmetric, one has to distinguish three cases, (i) $1 \leq j, k \leq N - 1$, with $j = k$ and $j < k$ as subcases, (ii) $j = k = N$, and (iii) $j < N, k = N$. One then finds that S is purely diagonal, with $S_{ii} = 1/\mu_i$ for $1 \leq i \leq N - 1$ and $S_{NN} = 1/M$. Here μ_i is the reduced mass for the particle i and for a fictitious particle of mass equal to the sum of the masses of the particles from $i + 1$ to N:

$$\frac{1}{\mu_i} = \frac{1}{m_i} + \frac{1}{\sum_{j=i+1}^{N} m_j} \quad \text{for } 1 \leq i \leq N - 1. \quad (5.207)$$

This results in the following form

$$H_{\text{kin}} = -\frac{\hbar^2}{2M}\Delta_{\mathbf{C}} - \sum_{i=1}^{N-1}\frac{\hbar^2}{2\mu_i}\Delta_{\mathbf{y}_i}. \tag{5.208}$$

The next step is to consider the trapping potential energy term. Inspired by Eq. 5.208 one may consider the guess

$$H_{\text{trap}} \equiv \sum_{i=1}^{N}\frac{1}{2}m_i\omega^2 r_i^2 \overset{?}{=} \frac{1}{2}M\omega^2 C^2 + \sum_{i=1}^{N-1}\frac{1}{2}\mu_i\omega^2 y_i^2. \tag{5.209}$$

Replacing each $\mathbf{y}_i$ by their expression in the guess gives

$$MC^2 + \sum_{i=1}^{N-1}\mu_i y_i^2 = \sum_{j=1}^{N}\sum_{k=1}^{N}Q_{jk}\mathbf{r}_j\cdot\mathbf{r}_k \tag{5.210}$$

where Q is uniquely defined once it is imposed to be a *symmetric* matrix. Setting $M_i = \sum_{j=i+1}^{N}m_j$ for $0 \leq i \leq N-1$, and $M_N = 0$, we find for the off-diagonal matrix elements

$$Q_{jk} = -\frac{\mu_{\min(j,k)}m_{\max(j,k)}}{M_{\min(j,k)}} + \frac{m_j m_k}{M} + m_j m_k \sum_{i=1}^{\min(j,k)-1}\frac{\mu_i}{M_i^2} \tag{5.211}$$

where $1 \leq j, k \leq N$, $\min(j,k)$ and $\max(j,k)$ respectively stand for the smallest and for the largest of the two indices j and k. The key relation is then that

$$\frac{\mu_i}{M_i^2} = \frac{1}{M_i} - \frac{1}{m_i + M_i} = \frac{1}{M_i} - \frac{1}{M_{i-1}} \tag{5.212}$$

since $M_i + m_i = M_{i-1}$ for $1 \leq i \leq N$. This allows to calculate the sum over i of μ_i/M_i^2, as all except the border terms compensate by pairs. E.g. for $j < k$:

$$\sum_{i=1}^{j-1}\frac{\mu_i}{M_i^2} = \frac{1}{M_{j-1}} - \frac{1}{M} \tag{5.213}$$

since $M_0 = M$. One then finds that the off-diagonal elements of the matrix Q vanish. The diagonal elements of Q may be calculated using the same tricks (5.212, 5.213), one finds $Q_{ii} = m_i$ for $1 \leq i \leq N$. As a consequence, the guess was correct and the question mark can be removed from Eq. 5.209.

The last step to obtain Eq. 5.201 is to appropriately rescale the usual Jacobi coordinates, setting

$$\mathbf{u}_i \equiv (\mu_i/\bar{m})^{1/2}\mathbf{y}_i \tag{5.214}$$

where $\bar{m}$ is an arbitrarily chosen mass. A useful identity is the expression for the square of the hyperradius, Eq. 5.203. Starting from the definition [first identity in Eq. 5.203] we see that $R^2 = \sum_{i=1}^{N-1}\frac{\mu_i}{\bar{m}}y_i^2$. Then the second identity in Eq. 5.203 results from the fact that the guess in Eq. 5.209 is correct.

Appendix 4: Hydrodynamic Equations

The hydrodynamic equations for a normal compressible viscous fluid are (see [98],[22] or Sect. 15 and Sect. 49 in [101]):

- the continuity equation

$$\frac{\partial \rho}{\partial t} + \nabla \cdot (\rho \mathbf{v}) = 0, \tag{5.215}$$

- the equation of motion

$$m\rho \left(\frac{\partial v_i}{\partial t} + \mathbf{v} \cdot \nabla v_i \right) = -\frac{\partial p}{\partial x_i} - \rho \frac{\partial U}{\partial x_i} + \sum_k \frac{\partial}{\partial x_k} \left[\eta \left(\frac{\partial v_i}{\partial x_k} + \frac{\partial v_k}{\partial x_i} - \frac{2}{3} \delta_{ik} \nabla \cdot \mathbf{v} \right) \right]$$

$$+ \frac{\partial}{\partial x_i} (\zeta \nabla \cdot \mathbf{v}) \tag{5.216}$$

where m is the atomic mass, η is the shear viscosity, ζ is the bulk viscosity, and the pressure $p(\mathbf{r}, t)$ [as well as the temperature $T(\mathbf{r}, t)$ appearing in the next equation] is as always expressible in terms of $\rho(\mathbf{r}, t)$ and $s(\mathbf{r}, t)$ *via* the equation of state,[23]

- the entropy-production equation

$$\rho T \left(\frac{\partial s}{\partial t} + \mathbf{v} \cdot \nabla s \right) = \nabla \cdot (\kappa \nabla T) + \frac{\eta}{2} \sum_{i,k} \left(\frac{\partial v_i}{\partial x_k} + \frac{\partial v_k}{\partial x_i} - \frac{2}{3} \delta_{ik} \nabla \cdot \mathbf{v} \right)^2 + \zeta \|\nabla \cdot \mathbf{v}\|^2 \tag{5.217}$$

where κ is the thermal conductivity.

Appendix 5: Alternative Derivation of the Vanishing Bulk Viscosity

Consider the particular case of a unitary gas initially prepared at thermal equilibrium in an isotropic harmonic trap at a temperature T above the critical temperature. When the harmonic trap becomes time dependent, $U(\mathbf{r}, t) = \frac{1}{2} m\omega^2(t) r^2$, each many-body eigenstate of the statistical mixture evolves under the combination Eq. 5.109 of a time dependent gauge transform and a time dependent scaling transform of scaling factor $\lambda(t)$. The effect of the gauge transform is to shift the momentum operator $\mathbf{p}_i$ of each particle i by the spatially slowly varying operator $m\mathbf{r}_i \dot{\lambda}/\lambda$. In

---

[22] There is a typo in Eq. 5.10 of [98]: $\nabla_i(\rho v^i \partial_i s)$ should be replaced by $\nabla_i(\rho v^i s)$.

[23] If we would neglect the position-dependence of η and ζ, (5.216) would reduce to the Navier-Stokes equation.

the hydrodynamic framework, this is fully included by the velocity field Eq. 5.178.[24] Using the macroscopic consequences of a spatial scaling Eqs. 5.19–5.22, one *a priori* obtains a time dependent solution of the hydrodynamic equations:

$$T(\mathbf{r}, t) = T(t = 0)/\lambda^2(t) \tag{5.218}$$

$$\rho(\mathbf{r}, t) = \rho(\mathbf{r}/\lambda, 0)/\lambda^3(t) \tag{5.219}$$

$$s(\mathbf{r}, t) = s(\mathbf{r}/\lambda, 0) \tag{5.220}$$

$$p(\mathbf{r}, t) = p(\mathbf{r}/\lambda, 0)/\lambda^5(t) \tag{5.221}$$

$$v_i(\mathbf{r}, t) = x_i \dot{\lambda}(t)/\lambda(t). \tag{5.222}$$

One then may *a posteriori* check that Eq. 5.215 is inconditionally satisfied, and that Eq. 5.217 is satisfied if $\zeta \equiv 0$. Setting $\zeta \equiv 0$ in Eq. 5.216, and using the hydrostatic condition $\nabla p = -\rho \nabla U$ at time $t = 0$, one finds that Eq. 5.216 holds provided that $\lambda(t)$ solves Eq. 5.111 as it should be.

Appendix 6: *n*-Body Resonances

Usually in quantum mechanics one takes the boundary condition that the wavefunction is bounded when two particles approach each other; in contrast, the Wigner-Bethe-Peierls boundary condition (5.75) expresses the existence of a two-body resonance. If the interaction potential is fine-tuned not only to be close to a two-body resonance (i.e. to have $|a| \gg b$) but also to be close to a n-body resonance (meaning that a real or virtual n-body bound state consisting of $n_\uparrow$ particles of spin $\uparrow$ and $n_\downarrow$ particles of spin $\downarrow$ is close to threshold), then one similarly expects that, in

---

[24] To formalize this statement, we consider a small but still macroscopic element of the equilibrium gas of volume dV around point $\bar{\mathbf{r}}$, with $k_F^{-1} \ll dV^{1/3} \ll R$ where k_F is the Fermi momentum and R the Thomas-Fermi radius of the gas. We can define the density operator $\hat{\rho}_{\text{elem}}$ of this element by taking the trace of the full N-body density operator over the spatial modes outside the element. Since the gauge transform in Eq. 5.109 is local in position space, $\hat{\rho}_{\text{elem}}$ experiences the same unitary gauge transform. It would be tempting to conclude from the general formula $dS = -k_B \text{Tr}[\hat{\rho}_{\text{elem}} \ln \hat{\rho}_{\text{elem}}]$ that the entropy dS of the element is not changed by the gauge transform. This is a valid conclusion however only if the gauge transform does not bring $\hat{\rho}_{\text{elem}}$ too far from local thermal equilibrium. To check this, we split the gauge transform for a single particle of position $\mathbf{r}$ as $mr^2\dot{\lambda}/(2\hbar\lambda) = m\dot{\lambda}/(2\hbar\lambda)[\bar{r}^2 + 2\bar{\mathbf{r}} \cdot (\mathbf{r} - \bar{\mathbf{r}}) + (\mathbf{r} - \bar{\mathbf{r}})^2]$. The first term is an innocuous uniform phase shift. The second term performs a uniform shift in momentum space by the announced value $m\mathbf{v}(\bar{\mathbf{r}}, t)$. Due to Galilean invariance, this has no effect on the thermodynamic quantities of the small element, such as its temperature, its pressure, its density, its entropy. With the estimate $\dot{\lambda}/\lambda \sim \omega$, $\bar{r} \sim R$, $m\omega R \sim \hbar k_F$, this second term is of order $k_F dV^{1/3} \gg 1$, not negligible. The third term is of order $m\omega dV^{2/3}/\hbar \sim N^{-1/3}k_F^2 dV^{2/3}$, negligible in the thermodynamic limit.

the zero-range limit, the interaction potential can be replaced by the Wigner-Bethe-Peierls boundary condition, *together with an additional boundary condition in the limit where any subset of $n_\uparrow$ particles of spin $\uparrow$ and $n_\downarrow$ particles of spin $\downarrow$ particles approach each other*. Using the notations of Sect. 5.3.6, this additional boundary condition reads [55, 70, 89, 103]:

$$\psi(\mathbf{r}_1, \ldots, \mathbf{r}_N) = \left(R_J^{-s} - \frac{\varepsilon}{l^{2s}} R_J^s \right) R_J^{-\frac{3n-5}{2}} \phi(\Omega_J) A_J(\mathbf{C}_j, \mathscr{R}_J) + o(R_J^v) \quad (5.223)$$

where $s = s_{\min}(n_\uparrow, n_\downarrow)$, while $l > 0$ and $\varepsilon = \pm 1$ are parameters of the model playing a role analogous to the absolute value and the sign of the two-body scattering length. This approach is only possible if the wavefunction remains square integrable, i.e. if $0 \le s < 1$, which we assume in what follows. This condition is satisfied e.g. for $n_\uparrow = 2, n_\downarrow = 1$ for a mass ratio $m_\uparrow/m_\downarrow \in [8.62\ldots; 13.6\ldots]$ [5]. Moreover we are assuming for simplicity that $s \ne 0$.

Let us now consider the particular case where the two-body scattering length is infinite, and the external potential is either harmonic isotropic, or absent. Then the separability in internal hyperspherical coordinates of Sect. 5.3.3 still holds for $n = N$. Indeed, Eq. 5.223 then translates into the boundary condition on the hyperradial wavefunction

$$\exists A \in \mathbb{R} / F(R) \underset{R \to 0}{=} A \cdot \left(R^{-s} - \frac{\varepsilon}{l^{2s}} R^s \right) + O\left(R^{s+2} \right) \quad (5.224)$$

and does not affect the hyperangular problem. Consequently [55],

• For the *n*-body bound state, which exists if $\varepsilon = +1$:

$$E = -\frac{2\hbar^2}{m\,l^2} \left[\frac{\Gamma(1+s)}{\Gamma(1-s)} \right]^{\frac{1}{s}}, \quad (5.225)$$

$$F(R) = K_s \left(R\sqrt{-2E\frac{m}{\hbar^2}} \right). \quad (5.226)$$

• For the eigenstates in a trap:

$$E \text{ solves: } -\varepsilon \cdot \left(\frac{\hbar}{m\omega l^2} \right)^s = \frac{\Gamma\left(\frac{1+s-E/(\hbar\omega)}{2} \right) \Gamma(-s)}{\Gamma\left(\frac{1-s-E/(\hbar\omega)}{2} \right) \Gamma(s)}, \quad (5.227)$$

$$F(R) = \frac{1}{R} W_{\frac{E}{2\hbar\omega}, \frac{s}{2}} \left(R^2 \frac{m\omega}{\hbar} \right). \quad (5.228)$$

In particular, for $l = \infty$, we are exactly at the *n*-body resonance, since the energy of the *n*-body bound state vanishes. The spectrum in a trap then is $E = (-s+1+2q)\hbar\omega$ with $q \in \mathbb{N}$.

Note that, most often, $s \ge 1$, in which case one would have to use an approach similar to the one developed by Pricoupenko for the case of two-body resonances in non-zero angular momentum channels, and to introduce a modified scalar product [22, 104].

References

1. Newton, R.G.: Scattering theory of waves and particles, 2nd edn. Springer, Berlin (1982)
2. Khuri, N.N., Martin, A., Richard, J.-M., Wu, T.T.: J. Math. Phys. **50**, 072105 (2009)
3. Landau, L.D., Lifshitz, E.M.: Quantum mechanics: non-relativistic theory. Elsevier Science, Oxford (2003)
4. Efimov, V.N., Yad, F.: **12**, 1080 (1970) [Sov. J. Nucl. Phys. **12**, 589 (1971)]
5. Efimov, V.: Nucl. Phys. A **210**, 157 (1973)
6. Petrov, D.S.: Phys. Rev. A **67**, 010703 (2003)
7. Castin, Y., Mora, C., Pricoupenko, L.: Phys. Rev. Lett. **105**, 223201 (2010)
8. Read, M., Berry, S.: Methods of modern mathematical physics 1: functional analysis. Academic Press (1980)
9. Ho, T-L.: Phys. Rev. Lett. **92**, 090402 (2004)
10. Uhlenbeck, G.E., Uehling, E.A.: Phys. Rev. **39**, 1014 (1932)
11. Burovski, E., Prokof'ev, N., Svistunov, B., Troyer, M.: Phys. Rev. Lett. **96**, 160402 (2006)
12. Gezerlis, A., Gandolfi, S., Schmidt, K.E., Carlson, J.: Phys. Rev. Lett. **103**, 060403 (2009)
13. Bulgac, A., Drut, J.E., Magierski, P.: Phys. Rev. A **78**, 023625 (2008)
14. Goulko, O., Wingate, M.: Phys. Rev. A **82**, 053621 (2010)
15. Busch, T., Englert, B.G., Rzazewski, K., Wilkens, M.: Found. Phys. **28**, 549 (1998)
16. Pricoupenko, L., Castin, Y.: Phys. Rev. A **69**, 051601 (2004)
17. Petrov, D.S., Salomon, C., Shlyapnikov, G.V.: Phys. Rev. Lett. **93**, 090404 (2004)
18. Bourdel, T., Cubizolles, J., Khaykovich, L., Magalhães, K.M.F., Kokkelmans, S.J.J.M.F., Shlyapnikov, G.V., Salomon, C.: Phys. Rev. Lett. **91**, 020402 (2003)
19. Jo, G.-B., Lee, Y.-R., Choi, J.-H., Christensen, C.A., Kim, T.H., Thywissen, J.H., Pritchard, D.E., Ketterle, W.: Science **325**, 1521 (2009)
20. Zhang, J., Van Kempen, E.G.M., Bourdel, T., Khaykovich, L., Cubizolles, J., Chevy, F., Teichmann, M., Tarruell, L., Kokkelmans, S.J.J.M.F., Salomon, C.: Phys. Rev. A **70**, 030702(R) (2004)
21. Gaebler, J.P., Stewart, J.T., Bohn, J.L., Jin, D.S.: Phys. Rev. Lett. **98**, 200403 (2007)
22. Pricoupenko, L.: Phys. Rev. Lett. **96**, 050401 (2006)
23. Jona-Lasinio, M., Pricoupenko, L., Castin, Y.: Phys. Rev. A **77**, 043611 (2008)
24. Chevy, F., van Kempen, E.G.M., Bourdel, T., Zhang, J., Khaykovich, L., Teichmann, M., Tarruell, L., Kokkelmans, S.J.J.M.F., Salomon, C.: Phys. Rev. A **71**, 062710 (2005)
25. Gaudin, M.: *La fonction d'onde de Bethe*. Masson, Paris (1983)
26. Pricoupenko, L., Olshanii, M.: J. Phys. B **40**, 2065 (2007)
27. Tonini, G., Werner, F., Castin, Y.: Eur. Phys. J. D **39**, 283 (2006)
28. Chang, S.Y., Pandharipande, V.R., Carlson, J., Schmidt, K.E.: Phys. Rev. A **70**, 043602 (2004)
29. Astrakharchik, G.E., Boronat, J., Casulleras, J., Giorgini, S.: Phys. Rev. Lett. **93**, 200404 (2004)
30. Juillet, O.: New J. Phys. **9**, 163 (2007)
31. Jonsell, S., Heiselberg, H., Pethick, C.J.: Phys. Rev. Lett. **89**, 250401 (2002)
32. Werner, F., Castin, Y.: Phys. Rev. Lett. **97**, 150401 (2006)
33. Dell'Antonio, G.F., Figari, R., Teta, A.: Ann. Inst. Henri Poincaré **60**, 253 (1994)
34. Minlos, R.: On pointlike interaction between *n* fermions and another particle. In: Dell'Antonio G.F., Figari R., Teta A., SISSA (Trieste) (eds.) Proceedings of the Workshop on Singular Schrödinger Operators, Trieste, 29 September–1 October 1994 (1995)
35. Nozières, P., Schmitt-Rink, S.: J. Low Temp. Phys. **59**, 195 (1985)
36. Greiner, M., Mandel, O., Esslinger, T., Hänsch, T.W., Bloch, I.: Nature **415**, 39 (2002)
37. Castin Y.: Simple theoretical tools for low dimension Bose gases. In: Olshanii M., Perrin H., Pricoupenko L. (eds.) Lecture notes of the 2003 Les Houches Spring School, *Quantum Gases in Low Dimensions*, J. Phys. IV France, vol. 116, p. 89 (2004)
38. Werner, F., Castin, Y.: Phys. Rev. A (2010, submitted)

39. Randeria, M.: Bose-Einstein Condensation. In: Griffin, A., Snoke, D.W., Stringari, S. (eds.) p. 355. Cambridge University Press, Cambridge (1995)
40. Engelbrecht, J.R., Randeria, M., Sá de Melo, C.: Phys. Rev. B **55**, 15153 (1997)
41. Mora, C., Castin, Y.: Phys. Rev. A **67**, 053615 (2003)
42. Pricoupenko, L., Castin, Y.: J. Phys. A **40**, 12863 (2007)
43. Castin, Y.: Talk at KITP (UCSB), 2004. http://online.itp.ucsb.edu/online/gases04/castin (2004)
44. Blaizot, J.-P., Ripka, G.: *Quantum theory of finite systems*. The MIT Press, Cambridge (1986)
45. Nascimbène, S., Navon, N., Jiang, K.J., Chevy, F., Salomon, C.: Nature **463**, 1057 (2010)
46. Castin, Y.: Basic tools for degenerate Fermi gases. In: Inguscio M., Ketterle W., Salomon C. (eds.) Lecture notes of the 2006 Varenna Enrico Fermi School on Fermi gases, SIF (2007)
47. Burovski, E., Prokof'ev, N., Svistunov, B., Troyer, M.: New J. Phys. **8**, 153 (2006)
48. Georges, A.: Condensed-matter physics with light and atoms: strongly correlated cold fermions in optical lattices. In: Inguscio M., Ketterle W., Salomon C. (eds.) Lecture notes of the 2006 Varenna Enrico Fermi School on Fermi gases, SIF (2007)
49. Tan, S.: Ann. Phys. **323**, 2952 (2008)
50. Tan, S.: Ann. Phys. **323**, 2971 (2008)
51. Lieb, E., Liniger, W.: Phys. Rev. **130**, 1605 (1963)
52. Olshanii, M., Dunjko, V.: Phys. Rev. Lett. **91**, 090401 (2003)
53. Blatt, J.M., Weisskopf, V.F.: *Theoretical nuclear physics*. Wiley, New York (1952)
54. Fregoso, B.M., Baym, G.: Phys. Rev. A **73**, 043616 (2006)
55. Werner, F.: Ph.D. thesis of the University Pierre et Marie Curie, Paris. http://tel.archives-ouvertes.fr/tel-00285587 (2008)
56. Castin, Y.: *Coherent atomic matter waves*. In: Kaiser R., Westbrook C., David F. (eds.) Lecture notes of Les Houches summer school, pp. 1–136. EDP Sciences and Springer (2001)
57. Huang, K.: Statistical mechanics. Wiley, New York (1963)
58. Castin, Y.: Comptes Rendus Physique **5**, 407 (2004)
59. Mayer, I.: *Simple theorems, proofs, and derivations in quantum chemistry*, p. 32. Kluwer, New York (2003)
60. Thomas, J.E.: Phys. Rev. A **78**, 013630 (2008)
61. Thomas, J.E., Kinast, J., Turlapov, A.: Phys. Rev. Lett. **95**, 120402 (2005)
62. Tan, S.: Ann. Phys. **323**, 2987 (2008)
63. Werner, F.: Phys. Rev. A **78**, 025601 (2008)
64. Köhler, T., Góral, K., Julienne, P.S.: Rev. Mod. Phys. **78**, 1311 (2006)
65. Timmermans, E., Tommasini, P., Hussein, M., Kerman, A.: Phys. Rep. **315**, 199 (1999)
66. Holland, M., Kokkelmans, S.J.J.M.F., Chiofalo, M.L., Walser, R.: Phys. Rev. Lett. **87**, 120406 (2001)
67. Milstein, J.N., Kokkelmans, S.J.J.M.F., Holland, M.J.: Phys. Rev. A **66**, 043604 (2002)
68. Werner, F., Tarruell, L., Castin, Y.: Eur. Phys. J. B **68**, 401 (2009)
69. Szymańska, M.H., Góral, K., Köhler, T., Burnett, K.: Phys. Rev. A **72**, 013610 (2005)
70. Petrov, D.S.: Phys. Rev. Lett. **93**, 143201 (2004)
71. Gurarie, V., Radzihovsky, L.: Ann. Phys. **322**, 2 (2007)
72. Simonucci, S., Pieri, P., Strinati, G.C.: Europhys. Lett. **69**, 713 (2005)
73. Bartenstein, M., Altmeyer, A., Riedl, S., Geursen, R., Jochim, S., Chin, C., Hecker, Denschlag, J., Grimm, R., Simoni, A., Tiesinga, E., Williams, C.J., Julienne, P.S.: Phys. Rev. Lett. **94**, 103201 (2005)
74. Partridge, G.B., Strecker, K.E., Kamar, R.I., Jack, M.W., Hulet, R.G.: Phys. Rev. Lett. **95**, 020404 (2005)
75. Braaten, E., Kang, D., Platter, L.: Phys. Rev. A **78**, 053606 (2008)
76. Zhang, S., Leggett, A.J.: Phys. Rev. A **79**, 023601 (2009)
77. Lobo, C., Carusotto, I., Giorgini, S., Recati, A., Stringari, S.: Phys. Rev. Lett. **97**, 100405 (2006)

78. Kuhnle, E.D., Hu, H., Liu, X.-J., Dyke, P., Mark, M., Drummond, P.D., Hannaford, P., Vale, C.J.: Phys. Rev. Lett. **105**, 070402 (2010)
79. Stewart, J.T., Gaebler, J.P., Drake, T.E., Jin, D.S.: Phys. Rev. Lett. **104**, 235301 (2010)
80. Contribution of E. Braaten in Chapter 6 of this volume, also available at arXiv:1008.2922
81. Ho, T.-L., Zhou, Q.: Nature Phys. **6**, 131 (2010)
82. Navon, N., Nascimbène, S., Chevy, F., Salomon, C.: Science **328**, 729 (2010)
83. Leggett, A.J.: Lecture 2 at the International Quantum Gases Workshop, Institut Henri Poincaré, Paris. http://www.phys.ens.fr/˜castin/files_pdf.html (2007)
84. Lewis, H.R.: J. Math. Phys. **9**, 1976 (1968)
85. Ermakov, V.P.: Univ. Izv. Kiev. **20**, 1 (1880)
86. Kagan, Yu., Surkov, E.L., Shlyapnikov, G.V.: Phys. Rev. A **54**, R1753 (1996)
87. Minguzzi, A., Gangardt, D.M.: Phys. Rev. Lett. **94**, 240404 (2005)
88. Lobo, C., Gensemer, S.D.: Phys. Rev. A **78**, 023618 (2008)
89. Werner, F., Castin, Y.: Phys. Rev. A **74**, 053604 (2006)
90. Pitaevskii, L.P., Rosch, A.: Phys. Rev. A **55**, R853 (1997)
91. Tan, S.: arXiv:cond-mat/0412764
92. Faddeev, L.D., Merkuriev, S.P.: *Quantum scattering theory for several particle systems*, Section 1.3.1. In: Flato M. (ed.) Kluwers Academic Publishers, Dordrecht (1993)
93. Skorniakov, G.V., Ter-Martirosian, K.A.: Sov. Phys. JETP **4**, 648 (1957)
94. Danilov, G.S.: Sov. Phys. JETP **13**, 349 (1961)
95. Birse, M.C.: J. Phys. A **39**, L49 (2006)
96. Blume, D., von Stecher, J., Greene, C.H.: Phys. Rev. Lett. **99**, 233201 (2007)
97. Liu, X.-J., Hu, H., Drummond, P.D.: Phys. Rev. Lett. **102**, 160401 (2009)
98. Son, D.T.: Phys. Rev. Lett. **98**, 020604 (2007)
99. Contribution by Y. Nishida and D. T. Son in Chapter 7 of this volume, also available at arXiv:1004.3597
100. Schäfer, T.: arXiv:1008:3876
101. Landau, L.D., Lifshitz, E.M.: Fluid mechanics. Pergamon, New York (1987)
102. Caldirola, P., Cirelli, R., Prosperi, G.: *Introduzione alla fisica teorica*, p. 534. Utet, Torino (1982)
103. Nishida, Y., Son, D.T., Tan, S.: Phys. Rev. Lett. **100**, 090405 (2008)
104. Pricoupenko, L.: Phys. Rev. A **73**, 012701 (2006)

Chapter 6
Universal Relations for Fermions with Large Scattering Length

Eric Braaten

6.1 Introduction

Particles with short-range interactions that produce a large scattering length have universal properties that depend only on the scattering length [1]. A system consisting of such particles is strongly interacting in the sense that there are effects of the interactions that must be treated nonperturbatively. These strong interactions give rise to strong correlations among the particless. Many theoretical methods, even if they are nonperturbative, are inadequate for dealing with such strong correlations. However, such a system is also governed by *universal relations* that follow from the short-distance and short-time dynamics associated with the large scattering length. These universal relations provide powerful constraints on the behavior of the system. They hold for any state of the system: few-body or many-body, ground state or nonzero temperature, homogeneous or in a trapping potential, normal state or superfluid, balanced in the two spin states or imbalanced. They connect various properties of the system, ranging from thermodynamic variables to large-momentum and high-frequency tails of correlation functions.

The systems for which the universal relations have been most extensively studied are those consisting of fermions with two spin states. The universal relations that have been derived thus far all involve a property of the system called the *contact*, which measures the number of pairs of fermions in the two spin states with small separations. Many of these relation were first derived by Shina Tan, and they are known as the *Tan relations* [2–4]. Tan derived these relations by exploiting the fact that the large scattering length can be taken into account through boundary conditions on the many-body Schrödinger wavefunction for otherwise noninteracting particles. The universal relations can also be derived concisely within a quantum field theory framework [5], where they follow from renormalization and from the operator

E. Braaten (✉)
Department of Physics, The Ohio State University,
Columbus, OH 43210, USA
e-mail: braaten@mps.ohio-state.edu

product expansion. Such a framework facilitates the derivation of additional universal relations and the systematic inclusion of corrections associated with the nonzero range of the interactions.

In this review, we summarize the current theoretical and experimental status of universal relations for systems consisting of fermions with two spin states and a large scattering length. We begin in Sect. 6.2 by presenting the Tan relations. In Sect. 6.3, we discuss the physical interpretation of the contact and we provide some illustrative examples. In Sect. 6.4, we present other universal relations that have been derived more recently. In Sect. 6.5, we describe exciting recent developments in the field of ultracold atoms involving measurements of the contact and experimental tests of the universal relations. In Sect. 6.6, we discuss the derivation of the universal relations, with an emphasis on quantum field theory methods.

6.2 The Tan Relations

The Tan relations were derived by Shina Tan in a series of three papers [2–4]. The first two of these papers were written in 2005, but they were not published until 2008, when all three papers were published back-to-back in Annals of Physics.

The Tan relations apply to systems consisting of fermions with two spin states whose scattering length a is large compared to the range r_0 of their interactions. We will refer to the fermions as atoms and label the two spin states by an index σ with values 1 and 2. In a many-body system, the number densities n_σ and the temperature T must also be small enough that the corresponding length scales are large compared to the range: $n_\sigma^{-1/3} \gg r_0$ and $\lambda_T \gg r_0$, where $\lambda_T = (2\pi\hbar^2/mk_BT)^{1/2}$. If the system is in an external trapping potential $V(\mathbf{r}) = \frac{1}{2}m\omega^2 r^2$, the length scale associated with the trap should also be large compared to the range: $(\hbar/m\omega)^{1/2} \gg r_0$.

The Tan relations involve an extensive quantity, the *contact C*, which is the integral over space of a local quantity, the *contact density* $\mathcal{C}(\mathbf{R})$:

$$C = \int d^3 R \, \mathcal{C}(\mathbf{R}). \qquad (6.1)$$

We proceed to present the Tan relations in chronological order.

6.2.1 Tails of Distributions

In the first of Tan's two 2005 papers, he derived three universal relations [2]. The first was for the tails of the momentum distributions $n_\sigma(\mathbf{k})$ for the two spin states $\sigma = 1, 2$:

Tail of the momentum distribution. The distributions of the wavevector $\mathbf{k}$ have power-law tails at large k:

$$n_\sigma(\boldsymbol{k}) \longrightarrow \frac{C}{k^4}. \tag{6.2}$$

The coefficient C is the contact and it is the same for both spin states.

The asymptotic behavior in (6.2) actually applies only in the scaling region $|a|^{-1} \ll k \ll r_0^{-1}$. The wavenumber must also be larger than the scales associated with the system, such as $n^{1/3}$, λ_T^{-1}, and $(m\omega/\hbar)^{1/2}$. The momentum distributions in Eq. 6.2 have been normalized so that the total number of atoms in the spin state σ is

$$N_\sigma = \int \frac{d^3k}{(2\pi)^3} n_\sigma(\boldsymbol{k}). \tag{6.3}$$

The universal relation in Eq. 6.2 implies that the contact is positive definite and has dimension $(\text{length})^{-1}$. Thus the contact density has dimensions $(\text{length})^{-4}$.

The total energy E of the system is the sum of the kinetic energy T, the interaction energy U, and the energy V associated with an external potential:

$$E = T + U + V. \tag{6.4}$$

The kinetic energy T (which should not be confused with the temperature) can be expressed as an integral over the momentum distribution:

$$T \equiv \sum_\sigma \int \frac{d^3k}{(2\pi)^3} \left(\frac{\hbar^2 k^2}{2m}\right) n_\sigma(\boldsymbol{k}). \tag{6.5}$$

The asymptotic behavior of the momentum distribution in Eq. 6.2 implies that T is ultraviolet divergent. This divergence actually occurs only in the zero-range limit $r_0 \to 0$. For interactions with a finite range, the integral in Eq. 6.5 is cut off by the range and therefore has a contribution that behaves like $1/r_0$ as $r_0 \to 0$. Thus the physical interpretation of the ultraviolet divergence is that T is sensitive to the range. The second Tan relation in Ref. [2] implies that the sensitivity of the kinetic energy to the range is cancelled by the interaction energy:

Energy relation. The sum of the kinetic and interaction energies is ultraviolet finite and it is completely determined by the momentum distributions $n_\sigma(\boldsymbol{k})$ and the contact C:

$$T + U = \sum_\sigma \int \frac{d^3k}{(2\pi)^3} \frac{\hbar^2 k^2}{2m} \left(n_\sigma(\boldsymbol{k}) - \frac{C}{k^4}\right) + \frac{\hbar^2}{4\pi m a} C. \tag{6.6}$$

In the integral on the right side, the subtraction term cancels the tail of the momentum distribution and makes the integral convergent in the ultraviolet. The sum of the two terms in Eq. 6.6 proportional to the contact C is the interaction energy. The first of those two terms is ultraviolet divergent. Thus the interaction energy is sensitive to the range, but that sensitivity is exactly cancelled by the kinetic energy. The last

term in Eq. 6.6 is the interaction energy that remains after subtracting the divergent term. Remarkably, it is also proportional to the contact.

The third Tan relation in Ref. [2] gives the asymptotic behavior of the correlation function for the densities of the two spin states at short distances:

Density–density correlator at short distances. The correlation between the number densities for the two spin states at points separated by a small distance r diverges as $1/r^2$ and the coefficient of the divergence is proportional to the contact density:

$$\left\langle n_1 \left(R + \frac{1}{2}r \right) n_2 \left(R - \frac{1}{2}r \right) \right\rangle \longrightarrow \frac{1}{16\pi^2} \left(\frac{1}{r^2} - \frac{2}{ar} \right) \mathcal{C}(R). \qquad (6.7)$$

Tan also pointed out that the contact density appears in the short-distance expansion for the correlator of the quantum field operators that create and annihilate the atoms. This expansion will be discussed in Sect. 6.6.4.4.

6.2.2 Changes in the Scattering Length

From the three universal relations described above, one might conclude that the contact is an esoteric property of the system that has only to do with tails of distributions. In the second of Tan's 2005 papers [3], he derived another universal relation that makes it clear that the contact is an absolutely central property of the system:

Adiabatic relation. The rate of change of the energy due to a small change in the inverse scattering length is proportional to the contact:

$$\left(\frac{\mathrm{d}E}{\mathrm{d}a^{-1}} \right)_S = -\frac{\hbar^2}{4\pi m} C. \qquad (6.8)$$

The derivative is evaluated with the entropy S held fixed. The particle numbers N_1 and N_2 are also implicitly held fixed.

In the simplest case, E is just an energy eigenvalue. The adiabatic relation also holds for any statistical mixture of eigenstates if the derivative is evaluated with the occupation numbers held fixed. By the adiabatic theorem of quantum mechanics, if the scattering length changes sufficiently slowly with time, the occupation numbers remain constant. Thus if the contact C is known as a function of a, the adiabatic relation in Eq. 6.8 can be integrated to obtain the accumulated change in E.

The adiabatic relation can also be expressed in terms of the derivative of the free energy $F = E - TS$ with the temperature T held fixed:

$$\left(\frac{\mathrm{d}F}{\mathrm{d}a^{-1}} \right)_T = -\frac{\hbar^2}{4\pi m} C. \qquad (6.9)$$

As pointed out by Tan, this implies that the contact determines the thermodynamics of the system. Given the contact of a system as a function of the scattering length a and other variables, such as N_1, N_2, and T, the free energy F can be obtained by

integrating Eq. 6.9 with respect to a. A convenient boundary condition is provided by the limit $a \to 0^-$, in which the atoms are noninteracting. From F, one can determine all the other thermodynamic functions.

If one uses Eq. 6.2 to define the contact in terms of the tail of the momentum distribution, this appears to be a case of the tail wagging the dog. The thermodynamic behavior of the system seems to be determined by the tail of the momentum distribution. However the proper interpretation is that the contact is a central property of the system that determines both the thermodynamics and the tail of the momentum distribution.

The adiabatic relation in Eq. 6.8 determines the change in the total energy when the scattering length changes very slowly. Tan also considered the opposite limit in which the scattering length changes very rapidly [3]:

Sudden change in the scattering length. If the scattering length is changed suddenly from a to a', the change in the total energy is proportional to the contact:

$$\Delta E = -\frac{\hbar^2}{4\pi m}\left(\frac{1}{a'} - \frac{1}{a}\right) C, \tag{6.10}$$

where C is the initial value of the contact.

This result requires the time scale for the sudden change in scattering length to be much slower than the time scale $mr_0^2/\hbar$ associated with the range. Tan also presented a more general result for the change in the energy due to a rapid change in the scattering length, which will be described in Sect. 6.4.5.

6.2.3 Additional Tan Relations

In Tan's 2008 paper, he derived two additional universal relations that apply for specific forms of the external potential [4].

Virial theorem. For a system in a harmonic trapping potential, the components of the energy E in Eq. 6.4 satisfy

$$T + U - V = -\frac{\hbar^2}{8\pi ma} C. \tag{6.11}$$

The virial theorem for the unitary limit $a = \pm\infty$ was first derived and also verified experimentally by Thomas, Kinast, and Turlapov [6]. The virial theorem in Eq. 6.11 is the generalization to finite scattering length.

Pressure relation. For a homogeneous system, the pressure and the energy density are related by

$$\mathcal{P} = \frac{2}{3}\mathcal{E} + \frac{\hbar^2}{12\pi ma} C. \tag{6.12}$$

The pressure relation was actually first derived in Ref. [3] for the special case of a balanced gas in which the two spin states have equal populations. The derivation was extended to the general case in Ref. [4].

If there are inelastic two-body scattering processes with a large energy release, they will result in a decrease in the number of low-energy atoms. Tan realized that the rate at which the number density of low-energy atoms decreases is proportional to the contact density $\mathcal{C}$ (Tan S, private communication). The proportionality constant was first given in Ref. [5]. If there are inelastic two-body scattering channels, the scattering length a has a negative imaginary part. The proportionality constant in the universal relation can be expressed in terms of that complex scattering length:

Inelastic two-body losses. If there are inelastic two-body scattering processes with a large energy release, the number density of low-energy atoms decreases at a rate that is proportional to the contact density:

$$\frac{d}{dt} n_\sigma(\boldsymbol{R}) = -\frac{\hbar(-\mathrm{Im}\, a)}{2\pi m |a|^2}\, \mathcal{C}(\boldsymbol{R}).$$ (6.13)

6.3 What is the Contact?

Given the Tan relations described in Sect. 6.2, it is evident that the contact is a central property of the system. But what is it? In this section, we provide an intuitive interpretation of the contact. We also provide additional insights into the contact by giving analytic expressions in some simple cases.

6.3.1 Intuitive Interpretation

An intuitive interpretation of the contact density can be derived from the universal relation for the density–density correlator in Eq. 6.7. That relation can be expressed in the form

$$\langle n_1(\boldsymbol{R} + \boldsymbol{r}_1)\, n_2(\boldsymbol{R} + \boldsymbol{r}_2)\rangle \longrightarrow \frac{1}{16\pi^2 |\boldsymbol{r}_1 - \boldsymbol{r}_2|^2} \mathcal{C}(\boldsymbol{R}).$$ (6.14)

If we integrate both $\boldsymbol{r}_1$ and $\boldsymbol{r}_2$ over a ball of radius s, we obtain

$$N_{\mathrm{pair}}(\boldsymbol{R}, s) \longrightarrow \frac{s^4}{4} \mathcal{C}(\boldsymbol{R}).$$ (6.15)

The left side simply counts the number of pairs inside that ball, which is the product $N_1 N_2$ of the number of atoms in the two spin states. The volume of that ball is $V = \frac{4}{3}\pi s^3$. One might naively expect the number of pairs to scale as V^2 as $V \to 0$. However, according to Eq. 6.15, it scales instead as $V^{4/3}$. That scaling

behavior applies only for s smaller than $|a|$ and also smaller than the length scales associated with the system, such as $n^{-1/3}$, λ_T, and $(\hbar/m\omega)^{1/2}$. The scaling behavior extends down to s of order the range r_0.

A naive definition of the density of pairs is the limit as $V \to 0$ of $N_1 N_2/V^2$, where N_1 and N_2 are the numbers of atoms in the volume V. This quantity has dimensions $(\text{length})^{-6}$. The result in Eq. 6.15 implies that the combination with a nontrivial small-volume limit is $N_1 N_2/V^{4/3}$, which has dimensions $(\text{length})^{-4}$. Thus a more appropriate definition of the local pair density is the small-volume limit of $N_1 N_2/V^{4/3}$, up to a normalization constant that can be chosen by convention. The unusual dimensions of $(\text{length})^{-4}$ for this local pair density can be expressed concisely by saying that this quantity has *scaling dimension* 4. The difference -2 between the scaling dimension and the naive dimension 6 is called the *anomalous dimension*. This anomalous dimension comes from the strong correlations associated with the large scattering length. This anomalous scaling behavior implies that the number of pairs in a very small volume is much larger than one would naively expect by extrapolating from larger volumes. The contact density is a measure of the local pair density that takes into account this anomalous scaling behavior.

Further intuition for the contact can be gleaned from the universal relation for the tail of the momentum distribution in Eq. 6.2. It implies that the number of atoms in either spin state whose wavenumber $\boldsymbol{k}$ is larger than K is

$$N_\sigma(|\boldsymbol{k}| > K) = \frac{1}{2\pi^2 K} C, \tag{6.16}$$

provided K is in the scaling region $1/|a| \ll K \ll 1/r_0$ and is larger than the wavenumber scales set by the system. Thus the contact is a measure of the number of atoms with large momentum.

When interpreting the contact density as a measure of the local pair density, one should not confuse those pairs with Cooper pairs, which are pairs with a specific momentum correlation. Under conditions in which Cooper pairs are well defined, the typical separation of the atoms in a Cooper pair is much larger than the interparticle spacing. The number of Cooper pairs in a volume V that is comparable to or smaller than the volume per particle is not well defined. It certainly does not have the anomalous scaling behavior $V^{-4/3}$ of the total number of pairs.

6.3.2 Few-Body Systems

The adiabatic relation in Eq. 6.8 can be used as an operational definition of the contact. If the energy of a system is known as a function of the scattering length, we can simply differentiate to get an expression for the contact. A simple example in the case $a > 0$ is the weakly-bound diatomic molecule, or *shallow dimer*, consisting of two atoms with spins 1 and 2. The universal result for its binding energy is $\hbar^2/ma^2$. Its energy is therefore

$$E_{\text{dimer}} = -\frac{\hbar^2}{ma^2}. \tag{6.17}$$

Using the adiabatic relation in Eq. 6.8, we find that the contact for the dimer is

$$C_{\text{dimer}} = \frac{8\pi}{a}. \tag{6.18}$$

Blume and Daily have calculated the contact numerically for the ground state of 4 fermions, 2 in each spin state, trapped in a harmonic potential and interacting through a potential with a large adjustable scattering length a [7]. They determined the contact as a function of a using four different universal relations: the tail of the momentum distribution in Eq. 6.2, the density-density correlator at short distances in Eq. 6.7, the adiabatic relation in Eq. 6.8, and the virial theorem in Eq. 6.11. The small differences between the four determinations of the contact were compatible with systematic errors associated with the nonzero range of the potential.

6.3.3 Balanced Homogeneous Gas

The contact density C for the homogeneous gas can be obtained by using the adiabatic relation in Eq. 6.8 as an operational definition. Dividing both sides of the equation by the volume, the relation can be expressed in the form

$$C = \frac{4\pi ma^2}{\hbar^2} \frac{d\mathcal{E}}{da}. \tag{6.19}$$

Analytic results for the energy density ε are available in various limits, and they can be used to obtain analytic expressions for the contact density.

We first consider the case of a balanced gas, in which the two spin states are equally populated, at zero temperature. The total number density $n = 2n_1 = 2n_2$ determines the Fermi momentum: $k_F = (3\pi^2 n)^{1/3}$. The ground state is determined by the dimensionless interaction variable $1/k_F a$. As this variable changes from $-\infty$ to 0 to $+\infty$, the ground state changes smoothly from a mixture of two weakly-interacting Fermi gases to a Bose-Einstein condensate of diatomic molecules. The ground state is always a superfluid. The mechanism for superfluidity evolves smoothly from the BCS mechanism, which is the Cooper pairing of atoms in the two spin states, to the BEC mechanism, which is the Bose-Einstein condensation of dimers.

In the *BCS limit* $a \to 0^-$, the energy density can be expanded in powers of $k_F a$:

$$\mathcal{E} = \frac{\hbar^2 k_F^5}{10\pi^2 m} \left(1 + \frac{10}{9\pi} k_F a + \cdots \right). \tag{6.20}$$

Using Eq. 6.19, we find that the contact density in the BCS limit is

$$C \longrightarrow 4\pi^2 n^2 a^2. \tag{6.21}$$

This is proportional to the low-energy cross section $4\pi a^2$ and to the product $(n/2)^2$ of the number densities of the two spin states. The contact density decreases to 0 as $a \to 0^-$, but it decreases only as a^2. This result emphasizes that the contact density is not closely related to the density of Cooper pairs, which decreases exponentially as $\exp(-\pi/k_F|a|)$ as $a \to 0^-$.

In the *unitary limit* $a \to \pm\infty$, the energy density can be expanded in powers of $1/k_F a$:

$$\mathcal{E} = \frac{\hbar^2 k_F^5}{10\pi^2 m} \left(\xi - \frac{\zeta}{k_F a} + \cdots \right), \tag{6.22}$$

where ξ and ζ are numerical constants. Using Eq. 6.19, we find that the contact density in the unitary limit is

$$\mathcal{C} \longrightarrow \frac{2\zeta}{5\pi} (3\pi^2 n)^{4/3}. \tag{6.23}$$

Since the interaction provides no length scale in the unitary limit, the contact density must be proportional to k_F^4 by dimensional analysis. An estimate $\zeta \approx 1$ for the numerical constant in Eq. 6.23 can be obtained from numerical calculations of the energy density near the unitary limit using quantum Monte Carlo methods [8, 9]. A more precise value can be obtained from numerical calculations of the density-density correlator in the unitary limit using the fixed-node diffusion Monte Carlo method [10]. Using the Tan relation for the density-density correlator in Eq. 6.7, we obtain the value

$$\zeta \approx 0.95. \tag{6.24}$$

In the *BEC limit* $a \to 0^+$, the energy density can be expanded in powers of $(k_F a)^{3/2}$:

$$\mathcal{E} = -\frac{\hbar^2 n}{2ma^2} + \frac{\pi \hbar^2 n^2 a_{dd}}{4m} \left(1 + \frac{128}{15} \sqrt{n a_{dd}^3/2\pi} + \cdots \right), \tag{6.25}$$

where $a_{dd} \approx 0.60a$ is the dimer-dimer scattering length [11]. The leading term is the total binding energy density for dimers with number density $n/2$ and binding energy given by Eq. 6.17. The second term is the mean-field energy of a Bose-Einstein condensate of dimers with dimer-dimer scattering length a_{dd}. Using Eq. 6.19, we find that the contact density in the BEC limit is

$$\mathcal{C} \longrightarrow \frac{4\pi n}{a}. \tag{6.26}$$

This is equal to the contact $8\pi/a$ for a dimer, which is given in Eq. 6.18, multiplied by the dimer number density $n/2$. The contact density diverges as $1/a$ as $a \to 0^+$. The first correction to the leading term in Eq. 6.26 is suppressed by a factor of $(k_F a)^3$.

Fig. 6.1 The dimensionless
contact density $s = \mathcal{C}/k_F^4$ for
the balanced homogeneous
gas as a function of the
dimensionless coupling
strength $1/k_F a$, from
Ref. [12]. The left *dashed
line* is the leading
contribution in the BCS limit
given by Eq. 6.21. The right
dashed line is the leading
contribution in the BEC limit
given by Eq. 6.26. The
contact density in the unitary
limit may be underpredicted
by about 16%

$$v = 1/k_F a$$
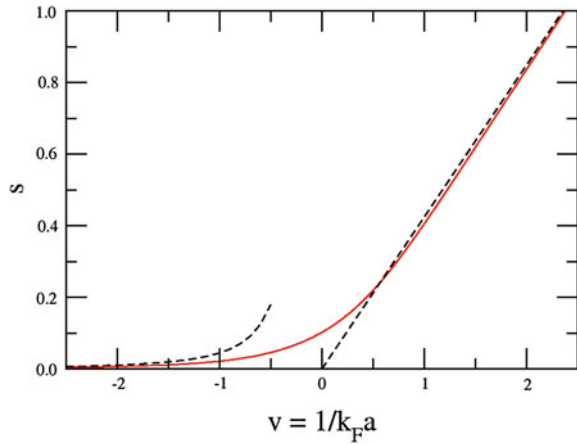
The contact density $\mathcal{C}$ for the ground state of the balanced homogeneous gas can be expressed as k_F^4 multiplied by a monotonically-increasing dimensionless function of $1/k_F a$. Haussmann, Punk, and Zwerger have calculated this function numerically [12]. They used the Luttinger–Ward self-consistent formalism to calculate the single particle spectral functions. The contact density was determined using the Tan relation in Eq. 6.2 for the tail of the momentum distribution. Their result for the contact density as a function of $1/k_F a$ is shown in Fig. 6.1. It interpolates smoothly between the BCS limit in Eq. 6.21 and the BEC limit in Eq. 6.26. Their result in the unitary limit corresponds to a value $\zeta \approx 0.80$ for the constant in Eq. 6.23. This is about 16% smaller than the value in Eq. 6.24 that was obtained from a fixed-node diffusion Monte Carlo calculation. This difference reflects a systematic theoretical error in the calculational method of either Ref. [10] or Ref. [12] or both.

The dependence of the contact density on the temperature has been determined analytically in various limits by Yu, Bruun, and Baym [13]. In the low-temperature limit, the leading thermal contribution to the contact density comes from phonons. The leading thermal correction at small T increases like T^4 [13]. It becomes significant when T is comparable to the Fermi temperature: $k_B T_F = \hbar^2 k_F^2/2m$. In the BCS limit and in the unitary limit, the thermal contribution differs from the contact at $T = 0$ by a factor of $(T/T_F)^4$ multiplied by a numerical constant. In the BEC limit, the thermal contribution is suppressed by a factor of $(T/T_F)^4$ and by a further factor of $(k_F a)^{1/2}$.

The contact density at high temperature can be calculated using the virial expansion. The high-temperature limit[1] was determined by Yu, Bruun, and Baym [13]:

---

[1] In Ref. [13], the contact density was denoted by $16\pi^2\hbar^2 C$ and the total number density was denoted by $2n$ instead of n.

$$\mathcal{C} \longrightarrow \frac{8\pi^2 \hbar^2 n^2}{m k_B T}. \tag{6.27}$$

Since the contact density increases as T^4 at small T and decreases as $1/T$ at sufficiently large T, it must achieve a maximum somewhere in between. The maximum occurs for T of order T_F. The maximum is pronounced only when a is near the unitary limit [13].

Palestini, Perali, Pieri, and Strinati have calculated the contact density for the balanced homogeneous gas at nonzero temperature using a diagrammatic t-matrix approximation [14]. They determined the contact from the high-momentum tail of the momentum distribution in Eq. 6.2 and from the high-frequency tail of the radio-frequency transition rate (which is discussed in Sect. 6.4.1).

Thus far, the calculational methods that have been used to calculate the contact density numerically involve uncontrolled approximations. While they may be accurate in certain limits, there may also be regions of $k_F a$ and T/T_F in which the systematic theoretical errors are not negligible.

6.3.4 Strongly-Imbalanced Homogeneous Gas

We now consider the strongly-imbalanced gas, in which a tiny population of minority atoms in state 2 is immersed in a system of atoms in state 1. The minority atoms can be considered as a dilute gas of impurities in the Fermi sea of majority atoms. In the homogeneous gas with number densities n_1 and n_2, the ground state is determined by the dimensionless interaction variable $1/k_{F1}a$, where $k_{F1} = (6\pi^2 n_1)^{1/3}$ is the Fermi wavenumber for the majority atoms. In the BCS limit $a \to 0^-$, the impurity particle is an atom in state 2. In the BEC limit $a \to 0^+$, the impurity particle is the dimer whose binding energy is given by Eq. 6.17. Using a diagrammatic Monte Carlo method, Prokof'ev and Svistunov have shown that there is a phase transition at a critical value a_c of the scattering length given by $1/k_{F1}a_c = 0.90 \pm 0.02$ [15]. As $1/k_{F1}a$ increases through this critical value, the impurity changes from a quasiparticle associated with the atom in state 2, which is called a *polaron*, to a dimer quasiparticle.

Analytic expressions for the contact density for the ground state of the strongly-imbalanced homogeneous gas can be obtained from the energy density using Eq. 6.19. In the *BCS limit* $a \to 0^-$, the contact density is

$$\mathcal{C} \longrightarrow 16\pi^2 n_1 n_2 a^2. \tag{6.28}$$

This is proportional to the low-energy cross section $4\pi a^2$ and to the product $n_1 n_2$ of the two number densities. The contact density is an increasing function of $1/a$ that is smooth except for a discontinuity at the phase transition at $a = a_c$. In the *BEC limit* $a \to 0^+$, the contact density is
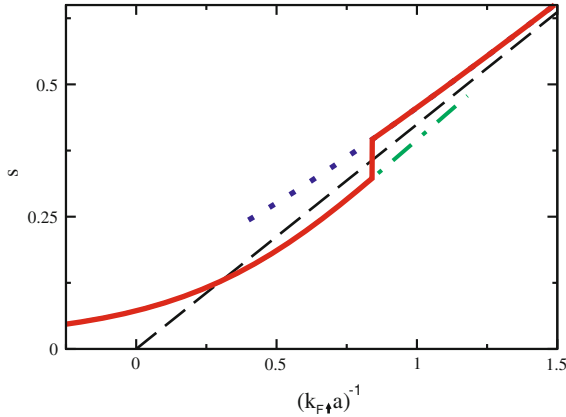
Fig. 6.2 The dimensionless contact density $s = \mathcal{C}/(6\pi^2 k_{F1} n_2)$ for the strongly-imbalanced homogeneous gas as a function of the dimensionless coupling strength $1/k_{F1}a$, from Ref. [16]. The *dashed line* is the leading contribution in the BEC limit given by Eq. 6.29. The *dotted* and *dash–dotted lines* are continuations of the *solid line* past the phase transition into metastable regions. The position of the phase transition may be underpredicted by about 7%

$$\mathcal{C} \longrightarrow \frac{8\pi n_2}{a}. \tag{6.29}$$

This is equal to the contact $8\pi/a$ for the dimer, which is given in Eq. 6.18, multiplied by the dimer number density n_2.

The contact density $\mathcal{C}$ for the ground state of the strongly-imbalanced homogeneous gas can be expressed as $k_{F1} n_2$ multiplied by a monotonically-increasing dimensionless function of $1/k_{F1}a$. This function has been calculated numerically by Punk, Dumitrescu, and Zwerger [16]. They used the adiabatic relation in Eq. 6.19 to obtain the contact from the ground state energy density, which they calculated using a variational method that gives a fairly good approximation to the results from the diagrammatic Monte Carlo method [15]. The results of Ref. [16] for the contact density as a function of $1/k_{F1}a$ are shown in Fig. 6.2. For large negative values of $1/k_{F1}a$, the contact density can be approximated by the BCS limit in Eq. 6.28. It is predicted to increase to about $5k_{F1}n_2$ in the unitary limit a to $\pm\infty$ and then to about $20k_{F1}n_2$ at the phase transition a_c, where it is predicted to have a discontinuity of about 20%. The prediction of the variational method for the position of the phase transition is $(k_{F1}a_c)^{-1} \approx 0.84$, which is about 7% smaller than the diagrammatic Monte Carlo result 0.90 ± 0.02. This difference reflects a systematic theoretical error in the variational method of Ref. [12]. For large positive values of $1/k_{F1}a$, the contact density can be approximated by the BEC limit in Eq. 6.29.

6.4 Other Universal Relations

Many new universal relations involving the contact have been discovered in recent years. They reveal that the contact plays a central role in many of the most important probes for ultracold atoms.

6.4.1 RF Spectroscopy

Given a system of atoms in spin states 1 and 2, a radio-frequency (rf) signal that is tuned to near the transition frequency between an atom in state 2 and an atom in a third spin state 3 can transform the atoms in state 2 coherently into linear combinations of atoms in states 2 and 3. These atoms can be subsequently transformed by decohering processes into a mixture of atoms in states 2 and 3. The net effect is a transfer of atoms from the state 2 to the state 3. The transition rate $\Gamma(\omega)$ for this process depends on the frequency ω of the rf signal. It is convenient to choose the offset for ω to be the transition frequency for a single atom. The transition rate for an extremely dilute sample of N_2 atoms is then a delta function at $\omega = 0$:

$$\Gamma(\omega) \longrightarrow \pi \Omega^2 \delta(\omega) N_2, \tag{6.30}$$

where Ω is the Rabi frequency associated with the transition. In a many-body system consisting of atoms in states 1 and 2, $\Gamma(\omega)$ can be modified by initial-state interactions between atoms in states 1 and 2 and by final-state interactions between atoms in state 3 and atoms in states 1 or 2. However the effects of these interactions are constrained by a sum rule [17, 18]:

$$\int\limits_{-\infty}^{\infty} d\omega \Gamma(\omega) = \pi \Omega^2 N_2. \tag{6.31}$$

If the atoms interact through large pair scattering lengths $a_{12} \equiv a$, a_{13}, and a_{23}, there are universal relations that govern the rf transition rate $\Gamma(\omega)$. One of these universal relations is a sum rule derived by Punk and Zwerger [19] and by Baym, Pethick, Yu, and Zwierlein [20]:

$$\int\limits_{-\infty}^{\infty} d\omega\, \omega \Gamma(\omega) = \frac{\hbar \Omega^2}{4m} \left(\frac{1}{a_{12}} - \frac{1}{a_{13}} \right) C_{12}, \tag{6.32}$$

where $C_{12} \equiv C$ is the contact for atoms in states 1 and 2. The term proportional to $1/a_{13}$ comes from final-state interactions between atoms in states 1 and 3. If we divide the sum rule in Eq. 6.32 by the sum rule in Eq. 6.31, we get an expression for the frequency shift $\langle \omega \rangle$ averaged over the system. This frequency shift is called the

clock shift. The universal relation for the clock shift has several interesting features. If $a_{13} = a_{12}$, the clock shift vanishes because of a symmetry relating atoms 2 and 3. The clock shift has smooth behavior in the unitary limit $a_{12} \to \pm\infty$. This behavior was first observed in experiments on rf spectroscopy in ^{6}Li atoms [21]. If we take the limit $a_{13} \to 0$ in Eq. 6.32, the sum rule diverges. This implies that if the scattering length a_{13} is not large, the clock shift is sensitive to the range.

Another universal relation for rf spectroscopy is that the high-frequency tail of $\Gamma(\omega)$ is proportional to the contact. The general result for large scattering lengths a_{12} and a_{13} was derived in Ref. [22]:

$$\Gamma(\omega) \longrightarrow \frac{\Omega^2 (a_{13}^{-1} - a_{12}^{-1})^2}{4\pi \omega (m\omega/\hbar)^{1/2}(a_{13}^{-2} + m\omega/\hbar)} C_{12}. \tag{6.33}$$

The asymptotic behavior in Eq. 6.33 holds when ω is much larger than the many-body frequency scales $\hbar k_F^2/m$ and $k_B T/\hbar$, but still much smaller than the frequency scale $\hbar/m r_0^2$ associated with the range. If $\omega \gg \hbar/m a_{13}^2$, the high-frequency tail decreases as $\omega^{-5/2}$. The result if the scattering length a_{13} is not large can be obtained by taking the limit $a_{13} \to 0$ in Eq. 6.33:

$$\Gamma(\omega) \longrightarrow \frac{\Omega^2}{4\pi \omega (m\omega/\hbar)^{1/2}} C_{12}. \tag{6.34}$$

In this case, the high-frequency tail decreases as $\omega^{-3/2}$. This scaling behavior was derived in Ref. [23] and the coefficient was first calculated correctly by Schneider and Randeria [24]. The scaling behavior was also pointed out in Ref. [25]. If $\Gamma(\omega)$ decreases asymptotically as $\omega^{-3/2}$, the sum rule in Eq. 6.32 diverges. Thus it is the high-frequency tail in Eq. 6.34 that makes this sum rule sensitive to the range in the case of a_{13} that is not large.

6.4.2 Photoassociation

Photoassociation uses a laser to transfer pairs of low-energy atoms into an excited molecular state with very high energy. The wavefunction of the molecule has support only over very short distances much smaller than the range r_0, so the pair of atoms must be very close together to have a reasonable probability of making the transition. If there is a closed-channel molecule near the two-atom threshold that can be excited by the laser, it can dominate the photoassociation rate. The rate is then proportional to the number N_{mol} of closed-channel molecules:

$$\Gamma = \frac{\Omega^2}{\gamma} N_{\text{mol}}, \tag{6.35}$$

where Ω is the Rabi frequency of the laser and γ is the line width of the excited molecule.

Werner, Tarruel, and Castin [27] and Zhang and Leggett [28] pointed out that if the large scattering length a comes from the tuning of the magnetic field B to near a Feshbach resonance associated with this closed-channel molecule, then N_{mol} is proportional to the contact. If the zero of energy is chosen to coincide with the threshold for the atoms, the rate of change of the energy of the system with respect to the magnetic field can be expressed as

$$\frac{\mathrm{d}E}{\mathrm{d}B} = -\mu_{\text{mol}} N_{\text{mol}}, \tag{6.36}$$

where μ_{mol} is the difference between the magnetic moment of the closed-channel molecule and twice the magnetic moment of an atom in the open channel. The scattering length $a(B)$ near a Feshbach resonance at B_0 can be parametrized by

$$a(B) = a_{\text{bg}} \left(1 - \frac{\Delta}{B - B_0} \right). \tag{6.37}$$

Combining Eqs. 6.36 and 6.37 and using the adiabatic relation in Eq. 6.8, we obtain an expression for the number of closed-channel molecules that is proportional to the contact [27]:

$$N_{\text{mol}} = \frac{R_* \Delta^2}{4\pi [\Delta - (B - B_0)]^2} C, \tag{6.38}$$

where R_* is a positive length that characterizes the width of the Feshbach resonance:

$$R_* = -\frac{\hbar^2}{m \mu_{\text{mol}} a_{\text{bg}} \Delta}. \tag{6.39}$$

That length can also be expressed as $R_* = -\frac{1}{2} r_s$, where r_s is the effective range at the center of the resonance $B = B_0$.

The universal relation between the number of closed-channel molecules and the contact was previously derived formally by Braaten, Kang and Platter [29], but they did not make the connection to photoassociation.

6.4.3 Structure Factors

Structure factors encode information about density-density correlations in a system. For a many-body system of fermions with two spin states, the correlations between the densities of the two spin states are particularly important. The corresponding static structure factor $S_{12}(q)$ for a homogeneous system is the Fourier transform in the separation vector $\boldsymbol{r}_1 - \boldsymbol{r}_2$ of the correlator $\langle n_1(\boldsymbol{r}_1) n_2(\boldsymbol{r}_2) \rangle$ of the two densities. The dynamic structure factor $S_{12}(q, \omega)$ is the Fourier transform in the separation

vector and the time interval between the two densities. It encodes information about the degrees of freedom that can be excited by density fluctuations. The static structure factor can be obtained by integrating $S_{12}(q, \omega)$ over ω.

If the scattering length is large, the static structure factor $S_{12}(q)$ has a high-momentum tail that decreases like $1/q$ [30]. Hu, Liu, and Drummond have pointed out that this tail is proportional to the contact density [31]:

$$S_{12}(q) \longrightarrow \frac{1}{8} \left(\frac{1}{q} - \frac{4}{\pi a q^2} \right) \mathcal{C}. \tag{6.40}$$

The normalization of $S_{12}(q)$ in Ref. [31] differs from that in Eq. 6.40 by a factor of $2/N$, where $N = N_1 + N_2$ is the total number of atoms. The universal relation in Eq. 6.40 follows simply by taking the Fourier transform of the Tan relation in Eq. 6.7 for the density-density correlation at short distances.

Son and Thompson have studied the dynamic structure factor $S_{12}(q, \omega)$ in the unitary limit [32]. They showed that the leading contribution in the scaling limit $\omega \to \infty$ and $q \to \infty$ with $x = \hbar q^2 / 2m\omega$ fixed is proportional to the contact density. The coefficient of $\mathcal{C}$ is $(m\omega^3/\hbar)^{-1/2}$ multiplied by a complicated function of the dimensionless scaling variable x, which they calculated analytically. For small x, their result reduces to

$$S_{12}(q, \omega) \longrightarrow \frac{4q^4}{45\pi^2 \omega (m\omega/\hbar)^{5/2}} \, \mathcal{C}. \tag{6.41}$$

Taylor and Randeria have also determined the high-frequency tail of the dynamic structure factor [33]. Their result for the limits $q \to 0$ followed by $\omega \to \infty$ differs from that in Eq. 6.41 by a factor of 3/2.

6.4.4 Viscosity Spectral Functions

Taylor and Randeria have derived universal relations for the viscosity spectral functions of a homogeneous gas [33]. They found that the shear viscosity spectral function $\eta(\omega)$ has a high-frequency tail that is proportional to the contact density. An error in the coefficient was corrected by Enss, Haussmann, and Zwerger [34]:

$$\eta(\omega) \longrightarrow \frac{\hbar^2}{15\pi (m\omega/\hbar)^{1/2}} \, \mathcal{C}. \tag{6.42}$$

Taylor and Randeria also derived a sum rule for $\eta(\omega)$:

$$\int_0^\infty d\omega \left(\eta(\omega) - \frac{\hbar^2 \mathcal{C}}{15\pi (m\omega/\hbar)^{1/2}} \right) = \frac{\pi \hbar}{3} \left(\mathcal{E} - \frac{3\hbar^2}{15\pi ma} \, \mathcal{C} \right), \tag{6.43}$$

where $\mathcal{E}$ is the energy density. Given the high-frequency tail of $\eta(\omega)$ in Eq. 6.42, the subtraction term on the left side of Eq. 6.43 is necessary to make the integral convergent.

Taylor and Randeria have also derived a sum rule for the bulk viscosity spectral function $\zeta(\omega)$ [33]:

$$\int_0^\infty d\omega \zeta(\omega) = \frac{\hbar^3}{72ma^2} \left(\frac{d\mathcal{C}}{da^{-1}} \right)_{S/N}, \tag{6.44}$$

where the derivative is taken with the entropy per particle held fixed. Since the spectral function $\zeta(\omega)$ is positive definite, the sum rule in Eq. 6.44 implies that the contact density $\mathcal{C}$ is a strictly increasing function of a^{-1}.

6.4.5 Rapid Change in the Scattering Length

In Ref. [3], Tan showed that if the scattering length $a(t)$ is time dependent, the total energy of the system changes at a rate that is proportional to the contact:

$$\frac{d}{dt} E(t) = -\frac{\hbar^2}{4\pi m} C(t)\dot{b}(t), \tag{6.45}$$

where $b(t) = 1/a(t)$ and $C(t)$ is the instantaneous contact at time t. If the external potential $V(\mathbf{r})$ is also changing with time, there is an additional term proportional to $\dot{V}(\mathbf{r})$ on the right side of Eq. 6.45. Tan referred to that equation as the *dynamic sweep theorem*.

The simplest case of a time-dependent scattering length is a sudden change in a, for which the change in the energy is given in Eq. 6.10. Tan also presented a more general result for a scattering length $a(t)$ that changes rapidly enough that the contact does not have time to evolve significantly from its original value. If the scattering length $a(t)$ changes over a short time interval T from an initial value $a(0)$ to a final value $a(T)$, the change in the total energy is

$$\Delta E = -\frac{\hbar^2}{4\pi m} \left(\frac{1}{a(T)} - \frac{1}{a(0)} + \sqrt{\frac{8\hbar}{\pi m}} \int_0^T dt \int_0^t dt' \sqrt{t - t'} \dot{b}(t)\dot{b}(t') \right) C, \tag{6.46}$$

where C is the contact at the initial time $t = 0$. The time interval T must be short compared to the time scales for the evolution of the system. It must also be long compared to the time scale $mr_0^2/\hbar$ set by the range.

Son and Thompson have also considered rapid changes in the scattering length for a system that is initially in the unitary limit [32]. The simplest case is a small-amplitude oscillation of the inverse scattering length about the unitary limit: $a(t)^{-1} =$

$\gamma_0 \cos(\omega t)$. If ω is large compared to the Fermi frequency $\hbar k_F^2/2m$, the energy density increases at a rate that is proportional to the contact density:

$$\frac{\mathrm{d}}{\mathrm{d}t}\mathcal{E} = \frac{\gamma_0^2 \hbar^2}{8\pi m}\sqrt{\frac{\hbar\omega}{m}}\,\mathcal{C}. \qquad (6.47)$$

The frequency ω must also be small compared to the frequency scale $\hbar/mr_0^2$ set by the range.

Another case of a rapidly varying scattering length considered in Ref. [32] is a pulse $a(t)^{-1}$ that differs from zero only during a short time interval. The change in the total energy is proportional to the contact:

$$\Delta E = \frac{\hbar^{5/2}}{4\pi^2 m^{3/2}}\left(\int\limits_0^\infty \mathrm{d}\omega\,\sqrt{\omega}\,|\tilde{\gamma}(\omega)|^2\right)C, \qquad (6.48)$$

where $\tilde{\gamma}(\omega)$ is the Fourier transform of the pulse: $\tilde{\gamma}(\omega) = \int_0^T \mathrm{d}t\,\exp(i\omega t)a(t)^{-1}$. This is consistent with the more general result in Eq. 6.46, which does not require the unitary limit before and after the pulse.

6.5 Making Contact with Experiment

There are some exciting recent developments in the study of the universal relations using experiments with ultracold atoms. They involve various measurements of the contact and the experimental verification of some of the universal relations.

6.5.1 Photoassociation

The Hulet group at Rice University in Houston has measured the photoassociation rate of a balanced mixture of ^{6}Li atoms in the lowest two hyperfine spin states [35]. The scattering length was controlled by using the Feshbach resonance near 834 G. They measured the photoassociation rate at various values of the scattering length, with $1/k_F a$ ranging from about -1.4 to about $+5.4$. The photoassociation laser can excite the closed-channel molecule that is responsible for the Feshbach resonance. The photoassociation rate can therefore be interpreted as a measurement of the number of closed-channel molecules. According to the universal relation in Eq. 6.38, this is proportional to the contact. However, at the time of the experiment, the concept of the contact was still unfamiliar. The number of closed-channel molecules was expected to be proportional to the square of the order parameter $|\Delta|^2$ [35]. In the BEC limit, $|\Delta|^2 \propto k_F/a$, which has the same dependence on a as the contact in Eq. 6.26. In the BCS limit, the order parameter decreases exponentially with
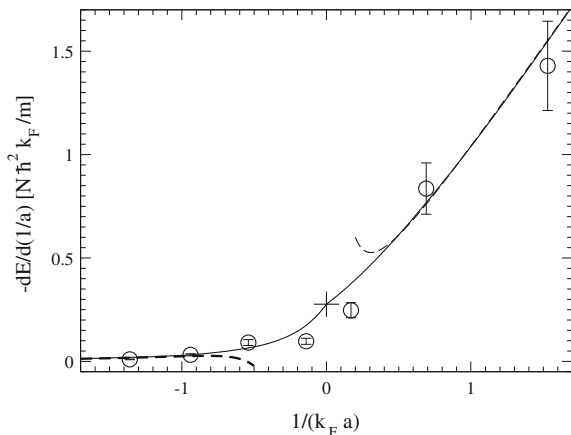
Fig. 6.3 The derivative of the energy E with respect to $1/a$ determined from measurements of the photoassociation rate of a trapped gas of ^{6}Li atoms, from Ref. [27]. The data come from measurements of the number of closed-channel molecules in Ref. [35]. The *solid line* is a theoretical prediction using the local density approximation, with the contact density for the homogeneous system obtained by interpolating between the BCS, unitary, and BEC limits. The symbol $+$ indicates the prediction for the contact in the unitary limit. The *dashed lines* are extrapolations from the BCS and BEC limits

$1/|a| : |\Delta|^2 \propto k_F^2 \exp(-\pi/(k_F|a|))$. This behavior is dramatically different from the contact in Eq. 6.21, which decreases like a^2 as $a \to 0^-$. Nevertheless, the measurements of the photoassociation rate were compatible with the assumption that it was proportional to $|\Delta|^2$, even for negative values of $1/k_F a$ as large as -1.4.

The first analysis of the data from Ref. [35] in terms of the contact was carried out by Werner, Tarruell, and Castin [27]. Their results are shown in Fig. 6.3. The contact extracted from the measured number of closed-channel molecules was in reasonable agreement with a theoretical prediction using the local density approximation, with the contact density for the homogeneous system obtained by interpolating between the BCS, unitary, and BEC limits.

6.5.2 Static Structure Factor

The static and dynamic structure factors for systems consisting of ultracold atoms can be probed by using Bragg spectroscopy. Bragg scattering is a two-photon process in which an atom absorbs a photon from one laser beam and emits a photon into a second laser beam. The net effect is the transfer of a selected momentum $\hbar\boldsymbol{k}$ and a selected energy $\hbar\omega$ to the atom, where $\boldsymbol{k}$ is the difference between the wavevectors of the two lasers and ω is the difference between their frequencies.
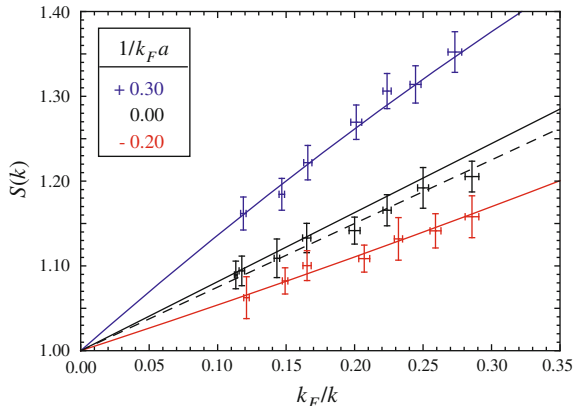
Fig. 6.4 The structure factor $S(k)$ for a trapped gas of ^{6}Li atoms as a function of k_F/k for three values of $1/k_F a$, from Ref. [37]. The *solid lines* are the universal predictions from Eq. 6.40 using the contact obtained from a theoretical calculation. The *dashed line* is a linear fit to the data for $1/k_F a = 0$

The Vale group at Swinburne University of Technology in Melbourne has used Bragg spectroscopy to study the static structure factor $S_{12}(k)$ [36]. They used a balanced mixture of ^{6}Li atoms in the lowest two hyperfine spin states. The scattering length was controlled by using the Feshbach resonance near 834 G. In Ref. [37], they reported measurements of the static structure factor $S_{12}(k)$ as a function of a for $k = 4.8 k_F$. These measurements are in good agreement with the universal relation for the large-momentum tail in Eq. 6.40, with the contact density for the homogeneous sytem obtained by interpolating between the BCS, unitary, and BEC limits. In Ref. [37], they also reported measurements of $S_{12}(k)$ as a function of k for $1/k_F a = -0.2$, 0, and $+0.3$, which are shown in Fig. 6.4. The measurements are linear in k_F/k, as predicted by the universal relation in Eq. 6.40. The slope is predicted to be proportional to the contact C. The contact for their trapped system at zero temperature was calculated in Ref. [37] using the local density approximation and a below-threshold Gaussian fluctuation theory for the homogeneous system. For $1/k_F a = -0.2$ and $+0.3$, the slope agrees well the universal relation. In the unitary limit $1/k_F a = 0$, the slope is smaller than predicted. The discrepancy could be attributed to the effects of nonzero temperature.

6.5.3 Comparing Measurements of the Contact

The Jin group at JILA in Boulder has measured the contact C for a trapped gas of atoms using three independent methods [38]. They used a balanced mixture of ^{40}K atoms in the two lowest hyperfine spin states at a temperature of about $0.1 T_F$. The scattering length was controlled by using the Feshbach resonance near 201 G.

The first method for measuring C used the Tan relation in Eq. 6.2 for the high-momentum tail of the momentum distribution $n_2(k)$. The interactions between the trapped atoms were turned off by changing the magnetic field to 209 G where the scattering length vanishes. The trapping potential was then turned off, and the momentum distribution was measured from the ballistic expansion of the cloud of atoms. The contact C is the large-momentum limit of $k^4 n_2(k)$. It was measured for values of $1/k_F a$ ranging from about -2.7 to about $+0.2$.

The second method for measuring the contact used the universal relation in Eq. 6.34 for the high-frequency tail of the radio-frequency (rf) transition rate. The rf signal was used to transfer atoms from state 2 into a third spin state 3 for which the pair scattering length a_{13} is not large. The rf transition rate $\Gamma(\omega)$ was determined by measuring the number of atoms transferred. The contact was then determined from the behavior of $\Gamma(\omega)$ at large ω. It was measured for values of $1/k_F a$ ranging from about-1.7 to about $+0.2$.

The third method for measuring C also used the Tan relation in Eq. 6.2, but the tail of the momentum distribution was determined by photoemission spectroscopy (PES). This involves using momentum-resolved rf spectroscopy to measure the distribution $n_2(k, \omega)$ of the momentum and energy of atoms in state 2, and then integrating over ω to determine the momentum distribution $n_2(k)$. The contact C is the large-momentum limit of $k^4 n_2(k)$. It was measured for the same values of $1/k_F a$ as the second method.

The three sets of measurements of the contact by the Jin group [38] are shown in Fig. 6.5. The results from the three methods are all consistent. They lie close to the theoretical prediction of Ref. [27], which was based on the local density approximation, with the contact density for the homogeneous system obtained by interpolating between the BEC, unitary, and BCS limits. These results provide direct experimental verification of the role of the contact in large-momentum and high-frequency tails for a many-body system of fermions with a large scattering length.

6.5.4 Tests of the Thermodynamic Tan Relations

The adiabatic relation in Eq. 6.8 and the virial theorem in Eq. 6.11 relate different contributions to the total energy E to the contact C. The adiabatic relation expresses a derivative of $(T + U) + V$ in terms of the contact. The virial theorem expresses the combination $(T + U) - V$ in terms of the contact. Thus measurements of $T + U$, V, and C provide two nontrivial tests of the Tan relations for the thermodynamic properties of the system.

The Jin group at JILA in Boulder has tested these Tan relations by measuring $T + U$ and V for the same system of ^{40}K atoms for which they measured the contact C [38], as described in Sect. 6.5.3. They measured the external potential energy V by imaging the spatial distribution of the cloud of atoms, which was trapped in a harmonic potential. They measured the combination $T + U$, which can be called
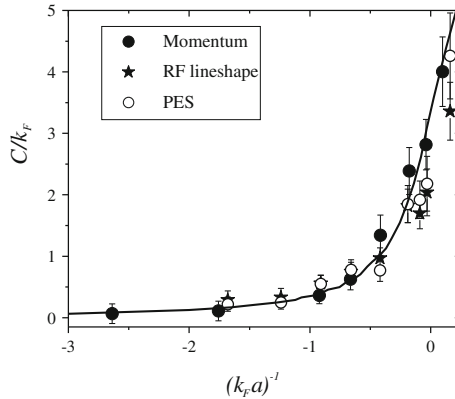
Fig. 6.5 Three measurements of the dimensionless contact C/k_F for a trapped gas of ^{40}K atoms as a function of $1/k_F a$, from Ref. [38]. The Fermi wavenumber k_F is defined by the Fermi energy for the trapped system: $E_F = \hbar^2 k_F^2/2m$. Two of the data sets are from the tail of the momentum distribution measured directly by ballistic expansion (*solid dots*) and indirectly by photoemission spectrometry (*open dots*). The third data set is from the high-frequency tail of the rf lineshape (*stars*)

the release energy, by turning off the trapping potential and observing the resulting expansion of the cloud. They measured $T + U$ and V at values of $1/k_F a$ ranging from about -3 to about $+0.3$. For the contact C, they used their measurements from photoemission spectroscopy described in Sect. 6.5.3. They found good agreement between the two sides of the adiabatic relation in Eq. 6.8 as shown in Fig. 6.6. They also found that the two sides of the virial theorem in Eq. 6.11 agreed to within the errors, which were roughly 1% of the Fermi energy. These results provide direct experimental verification of the role of the contact in the thermodynamics of a many-body system of fermions with a large scattering length.

6.5.5 Contact Density Near Unitarity

The contact density for the homogeneous gas has been determined by the Salomon group at École Normale Supérieure in Paris [39]. They used an imbalanced mixture of ^{6}Li atoms in the lowest two hyperfine spin states at a magnetic field near 834 G. They determined the equation of state for the homogeneous gas by measuring the number densities of the two spin states in a harmonic trapping potential integrated over the two tranverse dimensions. Their result for the numerical constant in Eq. 6.23 was $\zeta = 0.93(5)$. This is consistent with the value in Eq. 6.24 obtained from diffusion Monte Carlo calculations of the density–density correlator.
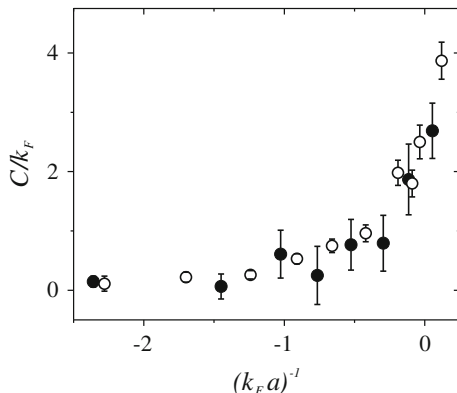
Fig. 6.6 Test of the adiabatic relation in a trapped gas of ^{40}K atoms, from Ref. [38]. The dimensionless contact C/k_F as a function of $1/k_F a$ determined from the derivative of the energy E with respect to $1/a$ (*solid dots*) is compared to the measurements using photoemission spectrometry (*open dots*). The Fermi wavenumber k_F is defined by the Fermi energy for the trapped system: $E_F = \hbar^2 k_F^2 / 2m$

6.6 Derivations of Universal Relations

In this section, we give an overview of various derivations of the universal relations. We begin by describing briefly the novel methods used in the original derivations of the Tan relations. We then describe briefly various other approaches that have been used to rederive the Tan relations. Finally, we describe in more detail how universal relations can be derived using quantum field theory methods involving renormalization and the operator product expansion.

6.6.1 Preliminaries

The scattering amplitude for S-wave atom–atom scattering can be written as

$$f(k) = \frac{1}{k \cot \delta_0(k) - ik},\tag{6.49}$$

where k is the relative wavenumber and $\delta_0(k)$ is the S-wave phase shift. If the interactions have a finite range, the low-energy expansion of the phase shift can be expressed as a power series in k^2:

$$k \cot \delta_0(k) = -1/a + \frac{1}{2} r_s k^2 + \cdots,\tag{6.50}$$

where r_s is the effective range. The coefficient of $(k^2)^n$ has dimensions $(\text{length})^{2n-1}$. Generically, all these coefficients are comparable to the range raised to the appropriate power. By fine tuning the interactions, the scattering length can be made much larger than the range. This fine-tuning leads to universal properties that depend on the interactions only through the scattering length.

The universality for large scattering length reflects a well-behaved *zero-range limit*, in which all the terms on the right side of Eq. 6.50 go to zero except the leading term. The phase shift reduces in this limit to

$$k \cot \delta_0(k) = -1/a. \tag{6.51}$$

The model in which the phase shift has this simple form up to arbitrarily large momentum is called the *Zero-Range Model*. The universal properties of a general model with large scattering length are realized in the Zero-Range Model in a particularly simple form, because a is the only length scale that arises from interactions. The price that must be paid is that the zero-range limit leads to divergences in some observables. It also leads to singularities in intermediate steps of the derivations of universal relations. An illustration is provided by the energy relation in Eq. 6.6. The kinetic energy T and the interaction energy U are separately ultraviolet divergent, but the divergences cancel in the sum $T + U$. The singularities associated with the zero-range limit can be regularized by backing off from the zero-range limit or by some equivalent device.

One way to represent the Zero-Range Model is in terms of the Schrödinger equation for noninteracting particles with peculiar boundary conditions. The Schrödinger wavefunction for N_1 fermions in state 1 and N_2 fermions in state 2 is a complex function $\Psi(\boldsymbol{r}_1, \ldots, \boldsymbol{r}_{N_1}; \boldsymbol{r}'_1, \ldots, \boldsymbol{r}'_{N_1})$ that is totally antisymmetric in the first N_1 positions and totally antisymmetric in the last N_2 positions. The proper normalization of the wavefunction is

$$\frac{1}{N_1! N_2!} \int d^3 r_1 \ldots \int d^3 r_{N_1} \int d^3 r'_1 \ldots \int d^3 r'_{N_2} \left| \Psi(\boldsymbol{r}_1, \ldots, \boldsymbol{r}_{N_1}; \boldsymbol{r}'_1, \ldots, \boldsymbol{r}'_{N_2}) \right|^2 = 1. \tag{6.52}$$

In the zero-range limit, this wavefunction diverges when the positions $\boldsymbol{r}_i$ and $\boldsymbol{r}'_j$ of any pair of fermions with different spins coincide. Its behavior when $\boldsymbol{r}_1$ and $\boldsymbol{r}'_1$ are nearly equal is

$$\Psi(\boldsymbol{R} + \tfrac{1}{2}\boldsymbol{r}, \boldsymbol{r}_2, \ldots, \boldsymbol{r}_{N_1}; \ \boldsymbol{R} - \tfrac{1}{2}\boldsymbol{r}, \boldsymbol{r}'_2, \ldots, \boldsymbol{r}'_{N_2})$$
$$\longrightarrow \phi(r)\Phi(\boldsymbol{r}_2, \ldots, \boldsymbol{r}_{N_1}; \ \boldsymbol{r}'_2, \ldots, \boldsymbol{r}'_{N_2}; \ \boldsymbol{R}), \tag{6.53}$$

where Φ is a smooth function of $\boldsymbol{R}$ and $\phi(r)$ is the zero-energy scattering wavefunction for two particles interacting through a large scattering length:

$$\phi(r) = \frac{1}{r} - \frac{1}{a}. \tag{6.54}$$

The Fourier transform of this wavefunction is

$$\tilde{\phi}(k) = \frac{4\pi}{k^2} - \frac{(2\pi)^3}{a}\delta^3(\mathbf{k}). \tag{6.55}$$

The Schrödinger equation for interacting particles with a large scattering length reduces in the zero-range limit to the Schrödinger equation for non-interacting particles with the wavefunction constrained to satisfy the Bethe–Peierls boundary conditions in Eq. 6.53.

6.6.2 Tan's Derivations

Tan derived many of his universal relations by using generalized functions, or distributions, to deal with the singularities associated with the zero-range limit [2, 3]. He introduced distributions $\Lambda(\mathbf{k})$ and $L(\mathbf{k})$ whose values at finite $\mathbf{k}$ are

$$\Lambda(\mathbf{k}) = 1, \qquad |\mathbf{k}| < \infty, \tag{6.56a}$$

$$L(\mathbf{k}) = 0, \qquad |\mathbf{k}| < \infty, \tag{6.56b}$$

and which have the following integrals over all $\mathbf{k}$:

$$\int \frac{d^3k}{(2\pi)^3} \frac{1}{k^2} \Lambda(\mathbf{k}) = 0 \tag{6.57a}$$

$$\int \frac{d^3k}{(2\pi)^3} \frac{1}{k^2} L(\mathbf{k}) = 1. \tag{6.57b}$$

Using these properties, it is easy to verify that the Fourier transform of the zero-energy scattering wavefunction in Eq. 6.55 satisfies

$$\int \frac{d^3k}{(2\pi)^3} \left[\Lambda(\mathbf{k}) + \frac{1}{4\pi a} L(\mathbf{k}) \right] \tilde{\phi}(\mathbf{k}) = 0. \tag{6.58}$$

This property allows the Bethe–Peierls boundary condition in Eq. 6.53 to be expressed as an equality rather than as a limit:

$$\int \frac{d^3k}{(2\pi)^3} \left[\Lambda(\mathbf{k}) + \frac{1}{4\pi a} L(\mathbf{k}) \right] \int d^3r e^{-i\mathbf{k}\cdot\mathbf{r}}$$
$$\times \Psi\left(\mathbf{R} + \frac{1}{2}\mathbf{r}, \mathbf{r}_2, \ldots, \mathbf{r}_{N_1}; \mathbf{R} - \frac{1}{2}\mathbf{r}, \mathbf{r}'_2, \ldots, \mathbf{r}'_{N_2} \right) = 0. \tag{6.59}$$

In addition to using $\Lambda(\mathbf{k})$ and $L(\mathbf{k})$ to impose the Bethe-Peierls boundary conditions, Tan used the distribution $\Lambda(\mathbf{k})$ to regularize the interaction term in the

Hamiltonian. He derived many of his universal relations by simple manipulations involving these distributions. They lead to an expression for the contact of the form

$$C = \frac{1}{2} \sum_\sigma \int \frac{d^3k}{(2\pi)^3} L(\mathbf{k}) k^2 n_\sigma(\mathbf{k}).$$ (6.60)

By the properties of the distribution $L(\mathbf{k})$ in Eqs. 6.56b and 6.57b, the integral extracts the coefficient of $1/k^4$ in the high-momentum tail of $n_\sigma(\mathbf{k})$.

6.6.3 Other Derivations

6.6.3.1 Braaten, Kang, and Platter

Braaten and Platter [5] used quantum field theory methods to rederive all the Tan relations in Sect. 6.2 except for the relation in Eq. 6.10 for the sudden change in the scattering length. They used the formulation of the Zero-Range Model as a local quantum field theory, as described later in Sect. 6.6.4.1. The singularities associated with the zero-range limit were regularized by imposing an ultraviolet cutoff on the momenta of virtual particles. The contact density was identified as the expectation value of a local operator. The universal relations were derived using renormalization, as described in Sect. 6.6.4.2, and the operator product expansion, as described in Sects. 6.6.4.4 and 6.6.4.5.

Braaten, Kang, and Platter [29] used quantum field theory methods to derive universal relations for the *Resonance Model*, in which the S-wave scattering phase shift is given by

$$k \cot \delta_0(k) = -\left(\lambda + \frac{g^2}{k^2 - \nu}\right)^{-1}.$$ (6.61)

The Resonance Model is a two-channel model, in which the states in the two-atom sector consist of a point-like molecule as well as the usual two-atom scattering states. It provides a natural model for a Feshbach resonance. The scattering length $a = \lambda - g^2/\nu$ agrees with the expression in Eq. 6.37 if we set $\lambda = a_{\rm bg}$, $\nu = -m\mu_{\rm mol}(B - B_0)/\hbar^2$, and $g^2 = 1/R_*$, where R_* is given in Eq. 6.39. Braaten, Kang, and Platter found that in the various universal relations that correspond to the Tan relations, the contact density is replaced by various linear combinations of the expectation values of three local operators. If the expression for $k \cot \delta_0(k)$ in Eq. 6.61 is well-approximated by $-1/a$ for all wavenumbers from 0 up to the scale set by the system, the expectation values of the three local operators must coincide in order for the universal relations to reduce to those of the Zero-Range Model. For a broad Feshbach resonance, which is defined by $|a_{\rm bg}| \gg R_*$, this requires only that $|a| \gg r_0$ and $kr_0 \ll 1$, where r_0 is the range of interactions in the absence of the Feshbach

resonance. For a narrow Feshbach resonance, which is defined by $|a_{bg}| \ll R_*$, this requires also that $k R_* \ll 1$.

6.6.3.2 Werner, Tarruell, and Castin

Werner [26] derived the virial theorem in Eq. 6.11 independently. The right side of Eq. 6.11 was expressed not in terms of the contact C but in terms of the derivative of the energy that appears in the adiabatic relation in Eq. 6.8.

Werner, Tarruell, and Castin [27] rederived the tail of the momentum distribution in Eq. 6.2, the adiabatic relation, and the density-density correlator at short distances in Eq. 6.7. The singularities associated with the zero-range limit were regularized by using a lattice model in which the fermions occupy the sites of a three-dimensional cubic lattice whose spacing b approaches 0. Werner, Tarruell and Castin also used a two-channel model to derive the universal relation for the number of closed-channel molecules in Eq. 6.38.

Werner and Castin [40] subsequently presented a much more thorough treatment of the universal relations for the Zero-Range Model and for the lattice model. In addition to the tail of the momentum distribution, the adiabatic relation, and the density-density correlator at short distances, they rederived the energy relation in Eq. 6.6 and the adiabatic sweep theorem, which is the generalization of Eq. 6.45 that allows for a time-dependent external potential. They showed that for a system in thermal equilibrium (which includes the ground state as a limiting case), the contact is an increasing function of $1/a$:

$$\frac{dC}{da^{-1}} > 0. \tag{6.62}$$

This inequality holds whether the derivative is evaluated at fixed entropy or at fixed temperature. The monotonic increase of the contact density with $1/a$ is illustrated in Figs. 6.1 and 6.2 for the cases of a homogeneous gas at zero temperature that is balanced and strongly imbalanced, respectively. Because the inequality in Eq. 6.62 does not hold in general, it should not be regarded as a universal relation.

Werner and Castin also generalized the universal relations to various other systems [40]. They considered the effects of a nonzero range for the interaction potential. They derived the generalizations of the universal relations to two spatial dimensions, which had been considered previously by Tan [41]. They also derived universal relations for two types of fermions with unequal masses $m_1 < m_2$, for identical bosons, and for mixtures of fermions and bosons with various masses. In some cases, including identical bosons and two types of fermions whose mass ratio m_2/m_1 exceeds the critical value 13.7, the universal relations are complicated by the Efimov effect [40].

6.6.3.3 Zhang and Leggett

Zhang and Leggett [28] rederived the adiabatic relation in Eq. 6.8 and the pressure relation in Eq. 6.12. They used a nonlocal quantum field theory with field operators $\psi_1(\mathbf{r})$ and $\psi_2(\mathbf{r})$ and with a short-range interaction potential $U(\mathbf{r})$. They restricted their attention to a homogeneous many-body system in equilibrium. The equal-time two-particle correlation function was expressed as a sum over eigenstates of the operator $\psi_2(\mathbf{r}_2)\psi_1(\mathbf{r}_1)$:

$$\langle \psi_1^\dagger(\mathbf{r}_1)\psi_2^\dagger(\mathbf{r}_2)\psi_2(\mathbf{r}_2)\psi_1(\mathbf{r}_1)\rangle = \sum_i \nu_i \phi^{(i)}(\mathbf{r}_1, \mathbf{r}_2)^* \phi^{(i)}(\mathbf{r}_1, \mathbf{r}_2), \qquad (6.63)$$

where ν_i is the average number of pairs with different spins in the eigenstate i and the eigenfunctions $\phi^{(i)}(\mathbf{r}_1, \mathbf{r}_2)$ are normalized accordingly in a large volume V. The Bethe–Peierls boundary conditions together with translation invariance imply that the limiting behavior of these eigenfunctions as the separation $r = |\mathbf{r}_1 - \mathbf{r}_2|$ goes to zero is

$$\phi^{(i)}\left(\mathbf{R}+\frac{1}{2}\mathbf{r}, \mathbf{R}-\frac{1}{2}\mathbf{r}\right) \longrightarrow C^{(i)}e^{i\mathbf{P}^{(i)}\cdot\mathbf{R}}\phi(r), \qquad (6.64)$$

where the normalization constant $C^{(i)}$ and the momentum vector $\mathbf{P}^{(i)}$ depend on the eigenstate i and $\phi(r)$ is the zero-energy scattering wavefunction defined in Eq. 6.54. The integral of the correlation function weighted by an arbitrary short-distance function $s(|\mathbf{r}_1 - \mathbf{r}_2|)$ therefore reduces to:

$$\int \mathrm{d}^3 r_1 \int \mathrm{d}^3 r_2 \, s(|\mathbf{r}_1 - \mathbf{r}_2|)\langle \psi_1^\dagger(\mathbf{r}_1)\psi_2^\dagger(\mathbf{r}_2)\psi_2(\mathbf{r}_2)\psi_1(\mathbf{r}_1)\rangle$$
$$= \frac{1}{4\pi}V\mathcal{C}\int_0^\infty \mathrm{d}r r^2 s(r)|\phi(r)|^2, \qquad (6.65)$$

where $\mathcal{C}$ is the contact density, which is given by

$$\mathcal{C} = 16\pi^2 \sum_i \nu_i |C^{(i)}|^2. \qquad (6.66)$$

Zhang and Leggett emphasized that the thermodynamics is universal and is completely determined by the contact density $\mathcal{C}$. Zhang and Leggett also used a two-channel model to derive a universal relation for the number of closed-channel molecules that can be reduced to Eq. 6.38 [28].

Zhang and Leggett derived a factorization formula for the interaction energy density [28] that separates the dependence on a and thermodynamic variables, such as the temperature and number densities, from the dependence on the short-distance parameters that determine the shape of the interaction potential $U(r)$. The interaction

energy is the special case of Eq. 6.65 in which the short-range function $s(r)$ is the interaction potential $U(r)$. The interaction energy density can be expressed as

$$\mathcal{U} = \frac{1}{4\pi} \, \mathcal{C} \int\limits_{0}^{\infty} \mathrm{d}r \, r^2 U(r) |\phi(r)|^2. \tag{6.67}$$

All the dependence on the thermodynamic variables and on the large scattering length a resides in the contact density $\mathcal{C}$.

6.6.3.4 Combescot, Alzetto, and Leyronas

Combescot, Alzetto, and Leyronas [42] rederived the tail of the momentum distribution in Eq. 6.2 and the energy relation in Eq. 6.6. They used the Schrödinger formalism in the coordinate representation to describe a system consisting of $N_1 + N_2$ fermions. The singularities associated with the zero-range limit were regularized by imposing a cutoff $|\mathbf{r}_i - \mathbf{r}'_j| > r_0$ on the separations of the two types of fermions. They expressed the contact in terms of the Fourier transform of the function Φ defined by the Bethe-Peierls boundary conditions in Eq. 6.53. By reverting to the coordinate representation, the contact density can be expressed as

$$\mathcal{C}(\mathbf{R}) = \frac{16\pi^2}{(N_1 - 1)!(N_2 - 1)!} \int \mathrm{d}^3 r_2 \dots \int \mathrm{d}^3 r_{N_1} \int \mathrm{d}^3 r'_2 \dots \int \mathrm{d}^3 r'_{N_2}$$
$$\times \left| \Phi(\mathbf{r}_2, \dots, \mathbf{r}_{N_1}; \mathbf{r}'_2, \dots, \mathbf{r}'_{N_2}; \mathbf{R}) \right|^2, \tag{6.68}$$

provided the wavefunction Ψ is properly normalized as in Eq. 6.52. This expression for the contact density was originally derived by Tan [2].

Combescot, Alzetto, and Leyronas generalized the tail of the momentum distribution and the energy relation to various other systems [42]. They generalized them to two spatial dimensions, which had been considered previously by Tan [41]. They generalized them to two types of fermions with different masses $m_1 < m_2$. They did not however consider the complications associated with the Efimov effect when the mass ratio m_2/m_1 exceeds the critical value 13.7 [40].

6.6.4 Quantum Field Theory Derivations

We proceed to explain how universal relations can be derived concisely using the methods of quantum field theory.

6.6.4.1 Zero-Range Model

A quantum field theory that describe atoms with two spin states must have fundamental quantum fields $\psi_\sigma(\mathbf{r})$, $\sigma = 1, 2$. The Hamiltonian operator for a local quantum field theory can be expressed as the integral over space of a Hamiltonian density operator: $H = \int d^3 R\, \mathcal{H}$. If the atoms are in an external potential $V(\mathbf{r})$, the Hamiltonian density operator is the sum of a kinetic term $\mathcal{T}$, an interaction term $\mathcal{U}$, and an external potential term $\mathcal{V}$:

$$\mathcal{H} = \mathcal{T} + \mathcal{U} + \mathcal{V}. \tag{6.69}$$

In the quantum field theory formulation of the Zero-Range Model, the three terms in the Hamiltonian density operator are

$$\mathcal{T} = \sum_\sigma \frac{1}{2m} \nabla \psi_\sigma^\dagger \cdot \nabla \psi_\sigma^{(\Lambda)}(\mathbf{R}), \tag{6.70a}$$

$$\mathcal{U} = \frac{g_0(\Lambda)}{m} \psi_1^\dagger \psi_2^\dagger \psi_2 \psi_1^{(\Lambda)}(\mathbf{R}), \tag{6.70b}$$

$$\mathcal{V} = V(\mathbf{R}) \sum_\sigma \psi_\sigma^\dagger \psi_\sigma(\mathbf{R}). \tag{6.70c}$$

For simplicity, we have set $\hbar = 1$. The superscripts (Λ) on the operators in Eqs. 6.70a and 6.70b indicate that their matrix elements are ultraviolet divergent and an ultraviolet cutoff is required to make them well defined. For the ultraviolet cutoff, we impose an upper limit $|\mathbf{k}| < \Lambda$ on the momenta of virtual particles. In the limit $\Lambda \to \infty$, the Hamiltonian density in Eq. 6.69 describes atoms with the phase shift given by Eq. 6.51 provided we take the bare coupling constant to be

$$g_0(\Lambda) = \frac{4\pi a}{1 - 2a\Lambda/\pi}. \tag{6.71}$$

In Ref. [5], Braaten and Platter identified the operator that measures the contact density in the quantum field theory formulation of the Zero-Range Model. It is convenient to introduce the diatom field operator Φ defined by

$$\Phi(\mathbf{R}) = g_0(\Lambda) \psi_2 \psi_1^{(\Lambda)}(\mathbf{R}). \tag{6.72}$$

This operator annihilates a pair of atoms at the point $\mathbf{R}$. The superscript (Λ) on the operator $\psi_1 \psi_2$ indicates that its matrix elements are ultraviolet divergent. Their dependence on Λ is exactly compensated by the prefactor $g_0(\Lambda)$, so Φ is an ultraviolet finite operator. The contact density operator is $\Phi^\dagger \Phi$ [5]. This is just the interaction energy density operator multiplied by a constant that depends on the

ultraviolet cutoff: $\Phi^\dagger \Phi = m g_0 \mathcal{U}$. The contact is obtained by taking the expectation value of the contact density operator and integrating over space:

$$C = \int d^3 R \langle \Phi^\dagger \Phi(\boldsymbol{R}) \rangle. \tag{6.73}$$

6.6.4.2 Renormalization

Several of the Tan relations follow very simply from the renormalization of the Zero-Range Model [5]. The renormalization condition in Eq. 6.71 implies that the bare coupling constant $g_0(\Lambda)$ satisfies

$$g_0(\Lambda) = \left(\frac{1}{4\pi a} - \frac{\Lambda}{2\pi^2} \right) g_0^2(\Lambda). \tag{6.74}$$

Its derivative with respect to a is

$$\frac{d}{da} g_0(\Lambda) = \frac{1}{4\pi a^2} g_0^2(\Lambda). \tag{6.75}$$

The energy relation in Eq. 6.6 and the adiabatic relation in Eq. 6.8 follow simply from these properties of the bare coupling constant:

Energy relation. The kinetic and interaction terms $\mathcal{T}$ and $\mathcal{U}$ in the Hamiltonian density operator are given in Eqs. 6.70a and 6.70b. After inserting the expression in Eq. 6.74 for the bare coupling constant g_0 into $\mathcal{U}$, the sum of $\mathcal{T}$ and $\mathcal{U}$ can be expressed as the sum of two finite operators:

$$\mathcal{T} + \mathcal{U} = \left(\sum_\sigma \frac{1}{2m} \nabla \psi_\sigma^\dagger \cdot \nabla \psi_\sigma^{(\Lambda)} - \frac{\Lambda}{2\pi^2 m} \Phi^\dagger \Phi \right) + \frac{1}{4\pi m a} \Phi^\dagger \Phi. \tag{6.76}$$

By taking the expectation value of both sides of Eq. 6.76, integrating over space, and using the expression for C in Eq. 6.73. we obtain the energy relation in Eq. 6.6.

Adiabatic relation. According to the Feynman-Hellman theorem, the rate of change in the energy due to a change in the scattering length can be expressed in the form

$$\left(\frac{dE}{da} \right)_S = \int d^3 R \left\langle \frac{\partial \mathcal{H}}{\partial a} \right\rangle. \tag{6.77}$$

The Hamiltonian density $\mathcal{H}$ depends on a only through the factor of g_0 in $\mathcal{U}$. Using the derivative of the bare coupling constant in Eq. 6.75, we obtain the derivative of the Hamiltonian density:

$$\frac{\partial \mathcal{H}}{\partial a} = \frac{1}{4\pi m a^2} \Phi^\dagger \Phi. \tag{6.78}$$

By inserting this into Eq. 6.77 and using the expression for C in Eq. 6.73, we obtain the adiabatic relation in Eq. 6.8.

The virial theorem in Eq. 6.73 and the pressure relation in Eq. 6.73 can be derived by combining renormalization with dimensional analysis. For the purposes of dimensional analysis, we can regard $\hbar = 1$ and m simply as conversion constants that allow any dimensionful quantity to be expressed as a length raised to an appropriate power.

Virial theorem. For a system in a harmonic trapping potential, the only parameters that an energy eigenvalue can depend on are the scattering length a and the angular frequency ω. The combinations with dimensions of length are a and $(m\omega)^{-1/2}$. Since an energy eigenvalue E has dimensions $1/(m\ \text{length}^2)$, the constraint of dimensional analysis can be expressed as the requirement that a differential operator that counts the factors of length gives -2 when acting on $E = \int d^3 R \langle \mathcal{H} \rangle$:

$$\left(a \frac{\partial}{\partial a} - 2\omega \frac{\partial}{\partial \omega} \right) \int d^3 R \langle \mathcal{H} \rangle = -2E. \tag{6.79}$$

Using the Feynman-Hellman theorem, this equation can be written

$$\int d^3 R \left(\frac{1}{4\pi ma} \langle \Phi^\dagger \Phi \rangle - 4 \langle \mathcal{V} \rangle \right) = -2E. \tag{6.80}$$

Using the expression for C in Eq. 6.73, we obtain the virial theorem in Eq. 6.11.

Pressure relation. For a homogeneous system, the only variables that the free energy density $\mathcal{F} = \mathcal{E} - T\mathcal{S}$ can depend on are the scattering length a, the temperature T, and the number densities n_i. The combinations with dimensions of length are a, $(mk_B T)^{-1/2}$, and $n_i^{-1/3}$. Since $\mathcal{F}$ has dimensions $1/(m\ \text{length}^5)$, the constraint of dimensional analysis can be expressed as the requirement that a differential operator that counts the factors of length gives -5 when acting on $\mathcal{F}$:

$$\left(a \frac{\partial}{\partial a} - 2T \frac{\partial}{\partial T} - 3n_1 \frac{\partial}{\partial n_1} - 3n_2 \frac{\partial}{\partial n_2} \right) \mathcal{F} = -5\mathcal{F}. \tag{6.81}$$

Using the adiabatic relation in Eq. 6.8, this can be written

$$\frac{1}{4\pi ma} C + 2T\mathcal{S} - 3\mu_1 n_1 - 3\mu_2 n_2 = -5\mathcal{F}, \tag{6.82}$$

where μ_i is the chemical potential for the spin state i. The pressure relation in Eq. 6.12 then follows from the thermodynamic identity $\mathcal{F} = -\mathcal{P} + \mu_1 n_1 + \mu_2 n_2$.

6.6.4.3 The Operator Product Expansion

Many universal relations are most concisely derived using the *operator product expansion* (OPE) of quantum field theory. The OPE was invented independently

in 1969 by three giants of theoretical physics: Leo Kadanoff [43], Alexander Polyakov [44], and Ken Wilson [45]. It is an expansion for the product of local operators at nearby points in terms of local operators at the same point:

$$O_A \left(\boldsymbol{R} + \frac{1}{2}\boldsymbol{r} \right) \ O_B \left(\boldsymbol{R} - \frac{1}{2}\boldsymbol{r} \right) = \sum_C f_{A,B}^C(\boldsymbol{r}) \ O_C(\boldsymbol{R}). \qquad (6.83)$$

The *Wilson coefficients* $f_{A,B}^C(\boldsymbol{r})$ are ordinary functions of the separation vector $\boldsymbol{r}$. The local operators $O_C(\boldsymbol{R})$ include some that can be obtained by Taylor-expanding the operators on the left side in powers of $\boldsymbol{r}$, but they also include additional operators that take into account effects from quantum fluctuations. The Wilson coefficients for these operators are not necessarily analytic functions of the vector $\boldsymbol{r}$, and they can even diverge as $\boldsymbol{r} \to 0$. One particularly simple local operator is the unit operator I, whose expectation value in any state is 1. The sum over C in Eq. 6.83 can be extended to include all local operators if we allow Wilson coefficients that are 0.

The OPE is a natural tool for generating universal relations, because it is an operator identity. By taking the expectation value of both sides of the OPE in Eq. 6.83 in some state of the system, we get an expression for the correlator of the operators O_A and O_B in terms of the expectation values of local operators in that state. Since this expansion holds for any state of the system, it is a universal relation.

A local operator $O_C(\boldsymbol{R})$ is assigned the *scaling dimension d_C* if the correlation function of O_C and its hermitian conjugate at points separated by r decreases asymptotically as $1/r^{2d_C}$ at small r. The unit operator I is assigned scaling dimension 0. In a weakly-interacting theory, the scaling dimensions can be obtained simply by dimensional analysis. In a strongly-interacting theory, they can be significantly different. The difference between the scaling dimension and its value in the corresponding non-interacting theory is called the *anomalous dimension*. At very small $\boldsymbol{r}$, the leading behavior of a nontrivial Wilson coefficient is determined by the scaling dimensions of the operators:

$$f_{A,B}^C(\boldsymbol{r}) \sim r^{d_C - d_A - d_B}. \qquad (6.84)$$

In the OPE in Eq. 6.83, the Wilson coefficients of higher dimension operators go to 0 more rapidly as $r \to 0$. A Wilson coefficient can be suppressed by a further power of r is there is an explicitly broken symmetry which, if exact, would require $f_{A,B}^C(\boldsymbol{r})$ to vanish. The extra suppression factor is the dimensionless combination of r and the symmetry breaking parameter.

The technical assumptions required to prove the OPE have been discussed by Wilson and Zimmerman [46]. The OPE can be expressed more precisely as an asymptotic expansion in the separation $r = |\boldsymbol{r}|$. The OPE in Eq. 6.83 can be organized into an expansion in powers of r by expanding the Wilson coefficients as Laurent series in r. The OPE is an asymptotic expansion if for any power p, there are only finitely many terms that go to zero more slowly than r^p. The scaling behavior of the Wilson coefficients in Eq. 6.84 guarantees that the OPE is an asymptotic expansion provided

every local operator $O_C(\mathbf{R})$ has a positive scaling dimension $d_C > 0$ and there are only finitely many local operators with scaling dimension $d_C < d$ for any positive number d. These conditions are satisfied in the Zero-Range Model, the Resonance Model, and other renormalizable local quantum field theories that are relevant to cold atoms.

An illustration of the operator product expansion with anomalous dimensions is provided by the Ising Model in 2 dimensions. The exact solution by Lars Onsager in 1944 [47] implies that correlation functions in the continuum limit have scaling behavior with anomalous dimensions. For example, the leading term in the correlation function for two spin operators σ as their separation $\mathbf{r}$ goes to 0 has the form

$$\left\langle \sigma\left(\mathbf{R} + \frac{1}{2}\mathbf{r}\right)\sigma\left(\mathbf{R} - \frac{1}{2}\mathbf{r}\right)\right\rangle \longrightarrow \frac{A}{|\mathbf{r}|^{1/4}}, \tag{6.85}$$

where A is a constant that does not depend on the state of the system. This correlator is singular as $r \to 0$. The power law behavior suggests that the system becomes scale invariant at short distances. The fractional power of r indicates that the spin operator has an anomalous dimension.

Kadanoff generalized the result for the correlator in Eq. 6.85 to an operator relation [43]:

$$\sigma\left(\mathbf{R} + \frac{1}{2}\mathbf{r}\right)\sigma\left(\mathbf{R} - \frac{1}{2}\mathbf{r}\right) = \frac{A}{|\mathbf{r}|^{1/4}}I + B|\mathbf{r}|^{3/4}\varepsilon(\mathbf{R}) + \cdots, \tag{6.86}$$

where I is the identity operator, $\varepsilon(\mathbf{R})$ is the energy fluctuation operator, and B is another constant. The infinitely many terms that are not shown explicitly in Eq. 6.86 go to 0 more rapidly than $r^{3/4}$ as $r \to 0$. The short-distance tail of the correlator in Eq. 6.85 can be obtained simply by taking the expectation value of Eq. 6.86. Kadanoff showed that the critical exponents of the Ising model, such as the exponent $\frac{1}{4}$ of $1/|\mathbf{r}|$ in Eq. 6.85, could be deduced simply from the knowledge of which operator products have singular Wilson coefficients. From the OPE in Eq. 6.86, we can deduce that the spin operator has scaling dimension $\frac{1}{8}$ and the energy fluctuation operator has scaling dimension 1.

The OPE in Eq. 6.83 can be described more precisely as a *short-distance operator product expansion*, because it involves operators at the same time with small spatial separation. It can be generalized to a *short-time operator product expansion*, in which the operators also have a small separation in time:

$$\mathcal{O}_A\left(\mathbf{R} + \frac{1}{2}\mathbf{r}, T + \frac{1}{2}t\right)\mathcal{O}_B\left(\mathbf{R} - \frac{1}{2}\mathbf{r}, T - \frac{1}{2}t\right) = \sum_C f_{A,B}^C(\mathbf{r}, t)\,\mathcal{O}_C(\mathbf{R}, T). \tag{6.87}$$

The Wilson coefficients $f_{A,B}^C(\mathbf{r}, t)$ are functions of the separation vector $\mathbf{r}$ and the time interval t. The short-time OPE is more subtle than the short-distance OPE because of the possibility that a correlator can have oscillatory behavior in t as $t \to 0$ [46]. The possibility of oscillatory behavior is avoided in the Euclidean version of the quantum field theory that corresponds to analytic continuation of

the time t to Euclidean time: $t \rightarrow -i\tau$. Thus the short-time OPE in Eq. 6.87 can be expressed most rigorously as an asymptotic expansion in $(\boldsymbol{r}, -i\tau)$, where τ is the Euclidean time separation obtained by the analytic continuation $t \rightarrow -i\tau$. In a Galilean-invariant theory, the appropriate scaling of $(\boldsymbol{r}, -i\tau)$ is such that τ scales in the same way as $|\boldsymbol{r}|^2$.

6.6.4.4 Short-Distance Operator Product Expansion

Universal relations for fermions with large scattering length can be derived from operator product expansions in the Zero-Range Model defined in Sect. 6.6.4.1. In this model, the scattering length a is the only length scale that arises from interactions. At distances much smaller than $|a|$, the model is scale invariant with nontrivial scaling dimensions. In the unitary limit $a \rightarrow \pm\infty$, the model is not only scale invariant at all distances but also conformally invariant [48]. If a is finite, we can regard $1/a$ as the symmetry-breaking parameter associated with the broken conformal symmetry.

The fundamental field operators ψ_1 and ψ_2 of the Zero-Range Model have the same scaling dimensions as in a noninteracting theory. However there are composite operators with anomalous scaling dimensions. The scaling dimension of an operator $\mathcal{O}_C$ can be deduced from its propagator at large momentum $\boldsymbol{k}$, which in a Galilean-invariant theory scales as $k^{2d_C - 5}$. Since the propagator for ψ_1 or ψ_2 is simply $(\omega - k^2/2m)^{-1}$, these fields have scaling dimensions $\frac{3}{2}$. The scaling dimension of the number density operator $\psi_\sigma^\dagger \psi_\sigma$ is twice that of ψ_σ, which is 3. If there were no interactions, the scaling dimension of the composite operator $\psi_1 \psi_2$, or equivalently the diatom field operator Φ defined in Eq. 6.72, would also be 3. However the propagator for Φ is

$$\int dt\, e^{i\omega t} \int d^3 r\, e^{-i\boldsymbol{k}\cdot\boldsymbol{r}} \langle \Phi(\boldsymbol{r}, t) \Phi^\dagger(\boldsymbol{0}, 0) \rangle = \frac{-i4\pi m}{-1/a + \sqrt{-m(\omega - k^2/4m)}}. \quad (6.88)$$

We have dropped an additive constant that is independent of ω and $\boldsymbol{k}$, which could be removed by renormalization. Since the propagator in Eq. 6.88 scales as k^{-1} at large k, Φ has scaling dimension 2 and therefore anomalous dimension -1. The scaling dimension of the contact density operator $\Phi^\dagger \Phi$ is twice that of Φ, which is 4.

The short-distance OPE can be used to derive the Tan relation for the tail of the momentum distribution in Eq. 6.2. The momentum distribution $n_\sigma(\boldsymbol{k})$ for atoms in the spin state σ can be expressed as

$$n_\sigma(\boldsymbol{k}) = \int d^3 R \int d^3 r\, e^{-i\boldsymbol{k}\cdot\boldsymbol{r}} \left\langle \psi_\sigma^\dagger \left(\boldsymbol{R} - \frac{1}{2}\boldsymbol{r} \right) \psi_\sigma \left(\boldsymbol{R} + \frac{1}{2}\boldsymbol{r} \right) \right\rangle. \quad (6.89)$$

The behavior at large $\boldsymbol{k}$ is dominated by the small-$\boldsymbol{r}$ region of the integral. We can therefore apply the OPE to the product of the operators $\psi_\sigma^\dagger$ and ψ_σ. As shown in Ref. [5], the leading terms in the OPE are

$$\psi_\sigma^\dagger \left(R - \frac{1}{2}r \right) \psi_\sigma \left(R + \frac{1}{2}r \right)$$

$$= \psi_\sigma^\dagger \psi_\sigma (R) + \frac{1}{2} r \cdot \left[\psi_\sigma^\dagger \nabla \psi_\sigma (R) - \nabla \psi_\sigma^\dagger \psi_\sigma (R) \right] - \frac{r}{8\pi} \Phi^\dagger \Phi (R) + \cdots . \quad (6.90)$$

We have written explicitly all terms whose Wilson coefficients go to zero more slowly than r^2 as $r \to 0$. The first two terms on the right side of the OPE in Eq. 6.90 can be obtained by multiplying the Taylor expansions of the two operators. The third term arises from quantum fluctuations involving pairs of atoms with small separations. That its Wilson coefficient is proportional to r can be predicted from the scaling dimensions of the operators using Eq. 6.84. The coefficient of r can be calculated using diagrammatic methods described in Ref. [29]. Note that this Wilson coefficient is not an analytic function of the vector $r = (x, y, z)$ at $r = 0$, because it is proportional to $r = \sqrt{x^2 + y^2 + z^2}$. The expectation value of the OPE in Eq. 6.90 can be expressed as

$$\left\langle \psi_\sigma^\dagger \left(R - \frac{1}{2}r \right) \psi_\sigma \left(R + \frac{1}{2}r \right) \right\rangle = n_\sigma (R) + i r \cdot \mathcal{P}_\sigma (R) - \frac{r}{8\pi} C(R) + \cdots , \quad (6.91)$$

where $\mathcal{P}_\sigma$ is the momentum density of atoms in the state σ. This form of the OPE was first written down by Tan [2].

Upon inserting the OPE in Eq. 6.90 into Eq. 6.89, the first two terms give a delta function in k and the gradient of such a delta function. They correspond to contributions to $n_\sigma (k)$ that decrease at large k faster than any power of k. In the third term, the Fourier transform of the Wilson coefficient at nonzero values of k can be obtained from the identity

$$\int d^3r e^{-i k \cdot r} r = -\frac{8\pi}{k^4}, \quad (6.92)$$

which can be derived by differentiating the Fourier transform of a $1/r$ potential. This term gives a power-law tail in the momentum distribution:

$$n_\sigma (k) \longrightarrow \frac{1}{k^4} \int d^3 R \langle \Phi^\dagger \Phi (R) \rangle . \quad (6.93)$$

Comparing with Eq. 6.2, we obtain the expression in Eq. 6.73 for the contact C in the Zero-Range Model. This verifies that the contact density operator is $\Phi^\dagger \Phi$, where Φ is the diatom field operator defined in Eq. 6.72.

The short-distance OPE can be used to derive the Tan relation in Eq. 6.7 for the density-density correlator at short distances [5]. The OPE for the number density operators $\psi_1^\dagger \psi_1$ and $\psi_2^\dagger \psi_2$ includes a term whose Wilson coefficient is singular as $r \to 0$:

$$\psi_1^\dagger \psi_1 \left(R + \frac{1}{2}r \right) \psi_2^\dagger \psi_2 \left(R - \frac{1}{2}r \right) = \frac{1}{16\pi^2} \left(\frac{1}{r^2} - \frac{2}{ar} \right) \Phi^\dagger \Phi (R) + \cdots . \quad (6.94)$$

All the other terms in the OPE are regular at $r = 0$. Taking the expectation value of both sides, we get the Tan relation in Eq. 6.7.

The OPE in Eq. 6.94 can also be used to derive the universal relation for the static structure factor $S_{12}(q)$ in Eq. 6.40. That structure factor can be expressed as

$$S_{12}(q) = \int d^3R \int d^3r\, e^{-i\boldsymbol{q}\cdot\boldsymbol{r}} \langle \psi_1^\dagger \psi_1 \left(\boldsymbol{R} - \frac{1}{2}\boldsymbol{r}\right) \psi_2^\dagger \psi_2 \left(\boldsymbol{R} + \frac{1}{2}\boldsymbol{r}\right) \rangle. \qquad (6.95)$$

According to the universal relation in Eq. 6.40, the high momentum tail has terms proportional to $1/q$ and $1/q^2$. They come from the singular terms proportional to $1/r^2$ and $1/r$ in the OPE in Eq. 6.94.

6.6.4.5 Short-Time operator product expansion

Other universal relations can be derived using the short-time operator product expansion in Eq. 6.87. We will illustrate the use of the short-time OPE by showing how it can be used to derive the universal relations for radio-frequency (rf) spectroscopy that were presented in Sect. 6.4.1.

The rf signal that causes a transition of an atom in spin state 2 into an atom in spin state 3 corresponds to the action of an operator $\psi_3^\dagger \psi_2(\boldsymbol{r}, t)$. The inclusive rate $\Gamma(\omega)$ for the production of atoms in state 3 can be expressed as

$$\Gamma(\omega) = \Omega^2 \text{Im}\, i \int dt\, e^{i(\omega + i\epsilon)t} \int d^3R \int d^3r\, \left\langle T\psi_2^\dagger \psi_3 \left(\boldsymbol{R} + \frac{1}{2}\boldsymbol{r}, t\right) \psi_3^\dagger \psi_2 \left(\boldsymbol{R} - \frac{1}{2}\boldsymbol{r}, 0\right) \right\rangle. \tag{6.96}$$

The symbol T in the matrix element implies that the product of operators is time ordered. For a large frequency ω, the integrals are dominated by small Euclidean time intervals $t = -i\tau$ and by small separations $\boldsymbol{r}$. We can therefore apply the short-time OPE in Eq. 6.87 to the product of operators $\psi_2^\dagger \psi_3$ and $\psi_3^\dagger \psi_2$. The Wilson coefficients of the leading one-body operator $\psi_2^\dagger \psi_2$ and the leading two-body operator $\Phi^\dagger \Phi$ were determined in Ref. [22]:

$$\int dt\, e^{i\omega t} \int d^3r\, \psi_2^\dagger \psi_3 \left(\boldsymbol{R} + \frac{1}{2}\boldsymbol{r}, t\right) \psi_3^\dagger \psi_2 \left(\boldsymbol{R} - \frac{1}{2}\boldsymbol{r}, 0\right)$$
$$= \frac{i}{\omega} \psi_2^\dagger \psi_2(\boldsymbol{R}) + \frac{i(a_{12}^{-1} - a_{13}^{-1})[a_{12}^{-1} - \sqrt{-m\omega}]}{4\pi m\omega^2 [a_{13}^{-1} - \sqrt{-m\omega}]} \Phi^\dagger \Phi(\boldsymbol{R}) + \cdots. \tag{6.97}$$

Upon inserting the OPE in Eq. 6.97 into Eq. 6.96, the $\psi_2^\dagger \psi_2$ term gives a delta function in ω. This corresponds to a contribution that decreases at large ω faster than any power. The leading contribution to the high-frequency tail comes from the $\Phi^\dagger \Phi$ term:

$$\Gamma(\omega) \longrightarrow \frac{\Omega^2 (a_{13}^{-1} - a_{12}^{-1})^2}{4\pi m\omega^2} \text{Im}\left(\frac{-1}{a_{13}^{-1} - \sqrt{-m(\omega + i\epsilon)}}\right) \int d^3R \langle \Phi^\dagger \Phi(\boldsymbol{R}) \rangle. \tag{6.98}$$

This reduces to the universal relation for the high-frequency tail in Eq. 6.33.

Sum rules for the rf transition rate $\Gamma(\omega)$, such as those in Eqs. 6.31 and 6.32, can be derived by expressing the integral along the real ω axis as a contour integral in the complex ω plane that wraps around the real axis. If we allow for a general weighting function $f(\omega)$, the sum rule becomes

$$\int\limits_{-\infty}^{\infty} d\omega f(\omega)\Gamma(\omega) = \Omega^2 \oint \frac{d\omega}{2\pi} f(\omega) \int dt e^{i\omega t} \int d^3R \int d^3r$$

$$\times \left\langle T\psi_2^\dagger \psi_3 \left(\boldsymbol{R}+\frac{1}{2}\boldsymbol{r}, t\right) \psi_3^\dagger \psi_2 (\boldsymbol{R}-\frac{1}{2}\boldsymbol{r}, 0) \right\rangle. \qquad (6.99)$$

If that contour is deformed into a circle whose radius approaches infinity, then ω has a large imaginary part along most of the contour. This justifies the use of the short-time OPE in Eq. 6.97. The sum rule can then be derived by evaluating the contour integral along the circle at infinity for each of the Wilson coefficients. For $f(\omega) = 1$, the only nonzero contribution is from the $\psi_2^\dagger \psi_2$ term and the sum rule reduces to Eq. 6.31. For $f(\omega) = \omega$, the only nonzero contribution is from the $\Phi^\dagger \Phi$ term and the sum rule reduces to Eq. 6.32. The weighting function $f(\omega)$ does not need to be a polynomial in ω. The Lorentzian function $f(\omega) = [(\omega - \omega_0)^2 + \gamma^2]^{-1}$ gives a family of sum rules with two adjustable parameters that is less sensitive to range corrections than that in Eq. 6.32 [22].

There are other universal relations that can be derived using the short-time OPE. One example is the high-frequency behavior of the structure factor $S_{12}(\omega, q)$, such as the universal relation in Eq. 6.41. It can be derived from the short-time OPE for the number density operators $\psi_1^\dagger \psi_1$ and $\psi_2^\dagger \psi_2$.

References

1. Braaten, E., Hammer, H.W.: Phys. Rept. **428**, 259 (2006). arXiv:cond-mat/0410417
2. Tan, S.: Ann. Phys. **323**, 2952 (2008). arXiv:cond-mat/0505200
3. Tan, S.: Ann. Phys. **323**, 2971 (2008). arXiv:cond-mat/0508320
4. Tan, S.: Ann. Phys. **323**, 2987 (2008). arXiv:0803.0841
5. Braaten, E., Platter, L.: Phys. Rev. Lett. **100**, 205301 (2008). arXiv:0803.1125
6. Thomas, J.E., Kinast, J., Turlapov, A.: Rev. Lett. **95**, 120402 (2005). arXiv:cond-mat/0503620
7. Blume, D., Daily, K.M.: Phys. Rev. A **80**, 053626 (2009). arXiv:0909.2701
8. Chang, S.Y., Pandharipande, V.R., Carlson, J., Schmidt, K.E.: Phys. Rev. A **70**, 043602 (2004). arXiv:physics/0404115
9. Astrakharchik, G.E., Boronat, J., Casulleras, J., Giorgini, S.: Phys. Rev. Lett. **93**, 200404 (2004). arXiv:cond-mat/0406113

10. Lobo, C., Carusotto, I., Giorgini, S., Recati, A., Stringari, S.: Phys. Rev. Lett. **97**, 100405 (2006). arXiv:cond-mat/0604282
11. Petrov, D.S., Salomon, C., Shlyapnikov, G.V.: Phys. Rev. Lett. **93**, 090404 (2004). arXiv:cond-mat/0309010
12. Haussmann, R., Punk, M., Zwerger, W.: Phys. Rev. A **80**, 063612 (2009). arXiv:0904.1333
13. Yu, Z., Bruun, G.M., Baym, G.: Phys. Rev. A **80**, 023615 (2009). arXiv:0905.1836
14. Palestini, F., Perali, A., Pieri, P., Strinati, G.C.: Phys. Rev. A **82**, 021605(R) (2010). arXiv:1005.1158
15. Prokof'ev, N., Svistunov, B.: Phys. Rev. B **77**, 020408(R) (2008). arXiv:0707.4259
16. Punk, M., Dumitrescu, P.T., Zwerger, W.: Phys. Rev. A **80**, 053605 (2009). arXiv:0908.1343
17. Yu, Z., Baym, G.: Phys. Rev. A **73**, 063601 (2006). arXiv:cond-mat/0510675
18. Zhang, S., Leggett, A.J.: Phys. Rev. A **77**, 033614 (2008)
19. Punk, M., Zwerger, W.: Phys. Rev. Lett. **99**, 170404 (2007). arXiv:0707.0792
20. Baym, G., Pethick, C.J., Yu, Z., Zwierlein, M.W.: Phys. Rev. Lett. **99**, 190407 (2007). arXiv:0707.0859
21. Zwierlein, M.W., Hadzibabic, Z,, Gupta, S., Ketterle, W.: Phys. Rev. Lett. **91**, 250404 (2003). arXiv:cond-mat/0306627
22. Braaten, E., Kang, D., Platter, L.: Phys. Rev. Lett. **104**, 223004 (2010). arXiv:1001.4518
23. Schneider, W., Shenoy, V.B., Randeria, M.: Theory of radio frequency spectroscopy of polarized Fermi gases. arXiv:0903.3006
24. Schneider, W., Randeria, M.: Phys. Rev. A **81**, 021601(R) (2010). arXiv:0910.2693
25. Pieri, P., Perali, A., Strinati, G.C.: Nat. Phys. **5**, 736 (2009). arXiv:0811.0770
26. Werner, F.: Phys. Rev. A **78**, 025601 (2008). arXiv:0803.3277
27. Werner, F., Tarruell, L., Castin, Y.: Phys. J. B **68**, 401 (2009). arXiv:0807.0078
28. Zhang, S., Leggett, A.J.: Phys. Rev. A **79**, 023601 (2009). arXiv:0809.1892
29. Braaten, E., Kang, D., Platter, L.: Phys. Rev. A **78**, 053606 (2008). arXiv:0806.2277
30. Combescot, R., Giorgini, S., Stringari, S.: Europhys. Lett. **75**, 695 (2006). arXiv:cond-mat/0512048
31. Hu, H., Liu, X.-J., Drummond, P.D.: Europhys. Lett. **91**, 20005 (2010). arXiv:1003.3511
32. Son, D.T., Thompson, E.G.: Phys. Rev. A **81**, 063634 (2010). arXiv:1002.0922
33. Taylor, E., Randeria, M.: Phys. Rev. A **81**, 053610 (2010). arXiv:1002.0869
34. Enss, T., Haussmann, R., Zwerger, W.: Ann. Phys. **326**, 770 (2011). arXiv:1008.0007
35. Partridge, G.B., Strecker, K.E., Kamar, R.I., Jack, M.W., Hulet, R.G.: Phys. Rev. Lett. **95**, 020404 (2005). arXiv:cond-mat/0505353
36. Kuhnle, E., Veeravalli, G., Dyke, P., Vale, C.J.: Phys. Rev. Lett. **101**, 250403 (2008). arXiv:0809.2145
37. Hu, H., Kuhnle, E,D., Liu, X.-J., Dyke, P., Mark, M., Drummond, P.D., Hannaford, P., Vale, C.J.: Phys. Rev. Lett. **105**, 070402 (2010). arXiv:1001.3200
38. Stewart, J.T., Gaebler, J.P., Drake, T.E., Jin, D.S.: Phys. Rev. Lett. **104**, 235301 (2010). arXiv:1002.1987
39. Navon, N., Nascimbène, S., Chevy, F., Salomon, C.: Science **328**, 729 (2010). arXiv:1004.1465
40. Werner, F., Castin ,Y.: Exact relations for quantum-mechanical few-body and many-body problems with short-range interactions in two and three dimensions. arXiv:1001.0774
41. Tan, S.: S-wave contact interaction problem: a simple description. arXiv:cond-mat/0505615
42. Combescot, R., Alzetto, F., Leyronas, X.: Phys. Rev. A **79**, 053640 (2009). arXiv:0901.4303
43. Kadanoff, L.P.: Phys. Rev. Lett. **23** 1430 (1969)
44. Wilson, K.G., Zimmermann, W.: Comm. Math. Phys. **24**, 87 (1972)
45. Onsager, L.: Phys. Rev. **65**, 117 (1944)
46. Son, D.T., Wingate, M.: Ann. Phys. **321**, 197 (2006). arXiv:cond-mat/0509786

Chapter 7
Unitary Fermi Gas, ϵ Expansion, and Nonrelativistic Conformal Field Theories

Yusuke Nishida and Dam Thanh Son

Abstract We review theoretical aspects of unitary Fermi gas (UFG), which has been realized in ultracold atom experiments. We first introduce the ϵ expansion technique based on a systematic expansion in terms of the dimensionality of space. We apply this technique to compute the thermodynamic quantities, the quasiparticle cum, and the criticl temperature of UFG. We then discuss consequences of the scale and conformal invariance of UFG. We prove a correspondence between primary operators in nonrelativistic conformal field theories and energy eigenstates in a harmonic potential. We use this correspondence to compute energies of fermions at unitarity in a harmonic potential. The scale and conformal invariance together with the general coordinate invariance constrains the properties of UFG. We show the vanishing bulk viscosities of UFG and derive the low-energy effective Lagrangian for the superfluid UFG. Finally we propose other systems exhibiting the nonrelativistic scaling and conformal symmetries that can be in principle realized in ultracold atom experiments.

7.1 Introduction

Interacting fermions appear in various subfields of physics. The Bardeen–Cooper–Schrieffer (BCS) mechanism shows that if the interaction is attractive, the Fermi surface is unstable toward the formation of Cooper pairs and the ground state of

Y. Nishida (✉)
Center for Theoretical Physics, Massachusetts Institute of Technology,
Cambridge, MA 02139, USA
e-mail: nishida@mit.edu

D. T. Son
Institute for Nuclear Theory, University of Washington,
Seattle, WA 98195, USA
e-mail: son@phys.washington.edu

the system exhibits superconductivity or superfluidity. Such phenomena have been observed in metallic superconductors, superfluid ^{3}He, and high-T_c superconductors. Possibilities of superfluid nuclear matter, color superconductivity of quarks, and neutrino superfluidity are also discussed in literatures; some of these states might be important to the physics of neutron stars.

In 2004, a new type of fermionic superfluid has been realized in ultracold atomic gases of ^{40}K and ^{6}Li in optical traps [1, 2]. Unlike the previous examples, these systems have a remarkable feature that the strength of the attraction between fermions can be arbitrarily tuned through magnetic field induced Feshbach resonances. The interatomic interaction at ultracold temperature is dominated by binary s-wave collisions, whose strength is characterized by the s-wave scattering length a. Across the Feshbach resonance, a^{-1} can, in principle, be tuned to any value from $-\infty$ to $+\infty$. Therefore, the ultracold atomic gases provide an ideal ground for studying quantum physics of interacting fermions from weak coupling to strong coupling.

In cold and dilute atomic gases, the interatomic potential is well approximated by a zero-range contact interaction: the potential range, $r_0 \sim 60a_0$ for ^{40}K and $r_0 \sim 30a_0$ for ^{6}Li, is negligible compared to the de Broglie wavelength and the mean interparticle distance ($n^{-1/3} \sim 5000$–$10000a_0$). The properties of such a system are *universal*, i.e., independent of details of the interaction potential. By regarding the two different hyperfine states of fermionic atoms as spin-↑ and spin-↓ fermions, the atomic gas reduces to a gas of spin-$\frac{1}{2}$ fermions interacting by the zero-range potential with the tunable scattering length a. The question we would like to understand is the phase diagram of such a system as a function of the dimensionless parameter $-\infty < (ak_F)^{-1} < \infty$, where $k_F \equiv (3\pi^2 n)^{1/3}$ is the Fermi momentum.

The qualitative understanding of the phase diagram is provided by picture of a BCS–BEC crossover [3–6] (the horizontal axis in Fig. 7.1). When the attraction between fermions is weak (BCS limit where $ak_F < 0$ and $|ak_F| \ll 1$), the system is a weakly interacting Fermi gas. Its ground state is superfluid by the BCS mechanism, where (loosely bound) Cooper pairs condense. On the other hand, when the attraction is strong (BEC limit where $0 < ak_F \ll 1$), two fermions form a bound molecule and the system becomes a weakly interacting Bose gas of such molecules. Its ground state again exhibits superfluidity, but by the Bose–Einstein condensation (BEC) of the tightly bound molecules. These two regimes are smoothly connected without phase transitions, which implies that the ground state of the system is a superfluid for any $(ak_F)^{-1}$. Both BCS and BEC limits can be understood quantitatively by using the standard perturbative expansion in terms of the small parameter $|ak_F| \ll 1$.

In contrast, a strongly interacting regime exists in the middle of the BCS–BEC crossover, where the scattering length is comparable to or exceeds the mean interparticle distance; $|ak_F| \gtrsim 1$. In particular, the limit of infinite scattering length $|ak_F| \to \infty$, which is often called the *unitarity* limit, has attracted intense attention by experimentalists and theorists alike. Beside being experimentally realizable in ultracold atomic gases using the Feshbach resonance, this regime is an idealization of the dilute nuclear matter, where the neutron–neutron scattering length $a_{nn} \simeq -18.5$ fm is larger than the typical range of the nuclear force $r_0 \simeq 1.4$ fm.
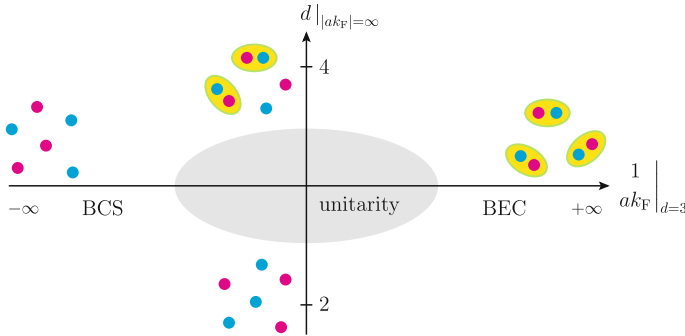
Fig. 7.1 Extended phase diagram of the BCS–BEC crossover in the plane of the inverse scattering length $(ak_F)^{-1}$ and the spatial dimension d. There are four limits where the system becomes noninteracting; $ak_F \to \pm 0$ and $d \to 4, 2$. The system is strongly interacting in the shaded region

Theoretical treatments of the Fermi gas in the unitary limit (unitary Fermi gas) suffer from the difficulty arising from the lack of a small expansion parameter: the standard perturbative expansion in terms of $|ak_F|$ is obviously of no use. Mean-field type approximations, with or without fluctuations, are often adopted to obtain a qualitative understanding of the BCS–BEC crossover, but they are not necessarily controlled near the unitarity limit. Therefore an important and challenging problem for theorists is to establish a *systematic* approach to investigate the unitary Fermi gas.

In Sect. 7.2 we describe one of such approaches. It is based on an expansion over a parameter which depends on the dimensionality of space [7–9]. In this approach, one extends the problem to arbitrary spatial dimension d, keeping the scattering length infinite $|ak_F| \to \infty$ (the vertical axis in Fig. 7.1). Then we can find two noninteracting limits on the d axis, which are $d = 4$ and $d = 2$. Accordingly, slightly below four or slightly above two spatial dimensions, the unitary Fermi gas becomes weakly interacting and thus a "perturbative expansion" is available. We show that the unitary Fermi gas near $d = 4$ is described by a weakly interacting gas of bosons and fermions, while near $d = 2$ it reduces to a weakly interacting Fermi gas. A small parameter for the perturbative expansion is $\epsilon \equiv 4 - d$ near four spatial dimensions or $\bar\epsilon \equiv d - 2$ near two spatial dimensions. After performing all calculations treating ϵ or $\bar\epsilon$ as a small expansion parameter, results for the physical case of $d = 3$ are obtained by extrapolating the series expansions to $\epsilon(\bar\epsilon) = 1$, or more appropriately, by matching the two series expansions. We apply this technique, the ϵ expansion, to compute the thermodynamic quantities [7, 8, 10, 11] (Sect. 7.2.3), the quasiparticle spectrum [7, 8] (Sect. 7.2.4), and the critical temperature [9] (Sect. 7.2.5). The main advantage of this method is that all calculations can be done analytically; its drawback is that interpolations to $d = 3$ are needed to achieve numerical accuracy.

Then in Sects. 7.3 and 7.4, we focus on consequences of another important characteristic of the unitary Fermi gas, namely, the scale and conformal invariance

[12–14]. We introduce the notion of nonrelativistic conformal field theories (NRCFTs) as theories describing nonrelativistic systems exhibiting the scaling and conformal symmetries. In Sect. 7.3.1, we describe a nonrelativistic analog of the conformal algebra, the so-called Schrödinger algebra [15, 16], and show in Sect. 7.3.2 that there is an operator-state correspondence [12]: a primary operator in NRCFT corresponds to an energy eigenstate of a few-particle system in a harmonic potential. The scaling dimension of the primary operator coincides with the energy eigenvalue of the corresponding state, divided by the oscillator frequency. We use the operator-state correspondence to compute the energies of two and three fermions at unitarity in a harmonic potential exactly (Sect. 7.3.3 with Appendix) and more fermions with the help of the ϵ expansion (Sect. 7.3.4).

The enlarged symmetries of the unitary Fermi gas also constrain its properties. By requiring the scale and conformal invariance and the general coordinate invariance of the hydrodynamic equations, we show that the unitary Fermi gas has the vanishing bulk viscosity in the normal phase [13] (Sect. 7.4.1). In the superfluid phase, two of the three bulk viscosities have to vanish while the third one is allowed to be nonzero. In Sect. 7.2, we derive the most general effective Lagrangian for the superfluid unitary Fermi gas that is consistent with the scale, conformal, and general coordinate invariance in the systematic momentum expansion [14]. To the leading and next-to-leading orders, there are three low-energy constants which can be computed using the ϵ expansion. We can express various physical quantities through these constants.

Finally in Sect. 7.5, we discuss other systems exhibiting the nonrelativistic scaling and conformal symmetries, to which a part of above results can be applied. Such systems include a mass-imbalanced Fermi gas with both two-body and three-body resonances [17] and Fermi gases in mixed dimensions [18]. These systems can be in principle realized in ultracold atom experiments.

7.2 ϵ Expansion for the Unitary Fermi Gas

In this section, we develop an analytical approach for the unitary Fermi gas based on a systematic expansion in terms of the dimensionality of space by using special features of four or two spatial dimensions for the zero-range and infinite scattering length interaction.

7.2.1 Why Four and Two Spatial Dimensions are Special?

7.2.1.1 Nussinovs' Intuitive Arguments

The special role of four and two spatial dimensions for the zero-range and infinite scattering length interaction has been first recognized by Nussinov and Nussinov [19]. At infinite scattering length, which corresponds to a resonance at zero energy,

the two-body wave function at a short distance $r \to 0$ behaves like

$$R(r) \propto \frac{1}{r^{d-2}} + O(r^{4-d}), \tag{7.1}$$

where r is the separation between two fermions with opposite spins. The first singular term $\sim 1/r^{d-2}$ is the spherically symmetric solution to the Laplace equation in d spatial dimensions. Accordingly the normalization integral of the wave function has the form

$$\int d\mathbf{r}\, R(r)^2 \propto \int\limits_0 dr \frac{1}{r^{d-3}}, \tag{7.2}$$

which diverges at the origin $r \to 0$ in higher dimensions $d \geq 4$. Therefore, in the limit $d \to 4$, the two-body wave function is concentrated at the origin and the fermion pair should behave like a point-like composite boson. This observation led Nussinov and Nussinov to conclude that the unitary Fermi gas at $d \to 4$ becomes a noninteracting Bose gas.

On the other hand, the singularity in the wave function (7.1) disappears in the limit $d \to 2$, which means that the interaction between the two fermions also disappears. This can be understood intuitively from the fact that in lower dimensions $d \leq 2$, any attractive potential possesses at least one bound state and thus the threshold of the appearance of the first bound state (infinite scattering length) corresponds to the vanishing potential. Therefore the unitary Fermi gas at $d \to 2$ should reduce to a noninteracting Fermi gas [19].

The physical case, $d = 3$, lies midway between these two limits $d = 2$ and $d = 4$. It seems natural to try to develop an expansion around these two limits and then extrapolate to $d = 3$. For this purpose, we need to employ a field theoretical approach.

7.2.1.2 Field Theoretical Approach

Spin-$\frac{1}{2}$ fermions interacting by the zero-range potential is described by the following Lagrangian density (here and below $\hbar = k_B = 1$):

$$\mathcal{L} = \sum_{\sigma = \uparrow, \downarrow} \psi_\sigma^\dagger \left(i\partial_t + \frac{\partial^2}{2m} + \mu \right) \psi_\sigma + c_0 \psi_\uparrow^\dagger \psi_\downarrow^\dagger \psi_\downarrow \psi_\uparrow. \tag{7.3}$$

In $d = 3$, the bare coupling c_0 is related to the physical parameter, the scattering length a, by

$$\frac{1}{c_0} = -\frac{m}{4\pi a} + \int \frac{d\mathbf{k}}{(2\pi)^d} \frac{1}{2\varepsilon_\mathbf{k}} \quad \left(\varepsilon_\mathbf{k} \equiv \frac{k^2}{2m} \right). \tag{7.4}$$

In dimensional regularization, used in this section, the second term vanishes and therefore the unitarity limit $a \to \infty$ corresponds to $c_0 \to \infty$.
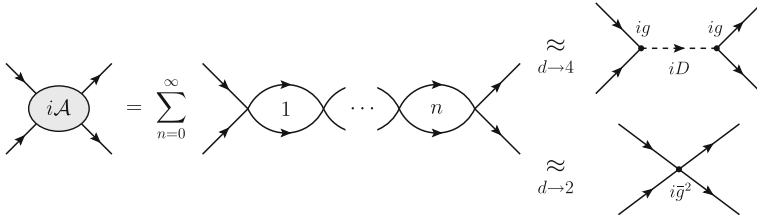
Fig. 7.2 Two-fermion scattering in vacuum in the unitarity limit. The scattering amplitude $i\mathcal{A}$ near $d=4$ is expressed by the propagation of a boson with the small effective coupling g, while it reduces to a contact interaction with the small effective coupling $\bar{g}^2$ near $d=2$

In order to understand the specialty of $d=4$ and $d=2$, we first study the scattering of two fermions in vacuum ($\mu=0$) in general d spatial dimensions. The two-body scattering amplitude $i\mathcal{A}$ is given by the geometric series of bubble diagrams depicted in Fig. 7.2. In the unitarity limit, we obtain

$$i\mathcal{A}(p_0, \boldsymbol{p}) = -i \frac{\left(\frac{4\pi}{m}\right)^{d/2}}{\Gamma\left(1 - \frac{d}{2}\right)\left(-p0 + \frac{\varepsilon_p}{2} - i0^+\right)^{d/2-1}}, \tag{7.5}$$

which vanishes when $d \to 4$ and $d \to 2$ because of the poles in $\Gamma\left(1 - \frac{d}{2}\right)$. This means that those dimensions correspond to the noninteracting limits and is consistent with the Nussinovs' arguments in Sect. 7.2.1.1.

Furthermore, by expanding $i\mathcal{A}$ in terms of $\epsilon = 4 - d \ll 1$, we can obtain further insight. The scattering amplitude to the leading order in ϵ becomes

$$i\mathcal{A}(p_0, \boldsymbol{p}) = -\frac{8\pi^2\epsilon}{m^2} \frac{i}{p_0 - \frac{\varepsilon_p}{2} + i0^+} + O(\epsilon^2)$$
$$\equiv (ig)^2 i D(p_0, \boldsymbol{p}) + O(\epsilon^2), \tag{7.6}$$

where we have defined $g^2 = \frac{8\pi^2\epsilon}{m^2}$ and $D(p_0, \boldsymbol{p}) = \left(p_0 - \frac{\varepsilon_p}{2} + i0^+\right)^{-1}$. The latter is the propagator of a particle of mass $2m$. This particle is a boson, which is the point-like composite of two fermions. Equation (7.6) states that the two-fermion scattering near $d=4$ can be thought of as occurring through the propagation of an intermediate boson, as depicted in Fig. 7.2. The effective coupling of the two fermions with the boson is $g \sim \epsilon^{1/2}$, which becomes small near $d=4$. This indicates the possibility to formulate a systematic perturbative expansion for the unitary Fermi gas around $d=4$ as a weakly interacting fermions and bosons.

Similarly, by expanding $i\mathcal{A}$ in $\bar{\epsilon} = d - 2 \ll 1$, the scattering amplitude becomes

$$i\mathcal{A}(p_0, \boldsymbol{p}) = i\frac{2\pi}{m}\bar{\epsilon} + O(\bar{\epsilon}^2) \equiv i\bar{g}^2 + O(\bar{\epsilon}^2), \tag{7.7}$$

where we have defined $\bar{g}^2 = \frac{2\pi}{m}\bar{\epsilon}$. Equation (7.7) shows that the two-fermion scattering near $d=2$ reduces to that caused by a contact interaction with the effective

coupling $\bar{g}^2$ (Fig. 7.2). Because $\bar{g}^2 \sim \bar{\epsilon}$ is small near $d = 2$, it will be possible to formulate another systematic perturbative expansion for the unitary Fermi gas around $d = 2$ as a weakly interacting fermions.

7.2.2 Feynman Rules and Power Counting of ϵ

The observations in Sect. 7.2.1.2 reveal how we should construct the systematic expansions for the unitary Fermi gas around $d = 4$ and $d = 2$. Here we provide their formulations and power counting rules of ϵ ($\bar{\epsilon}$). The detailed derivations of the power counting rules can be found in Ref. [8].

7.2.2.1 Around Four Spatial Dimensions

In order to organize a systematic expansion around $d = 4$, we make a Hubbard-Stratonovich transformation and rewrite the Lagrangian density (7.3) as

$$\mathcal{L} \rightarrow \sum_{\sigma=\uparrow,\downarrow} \psi_\sigma^\dagger \left(i\partial_t + \frac{\partial^2}{2m} + \mu \right) \psi_\sigma - \frac{1}{c_0} \phi^\dagger \phi + \psi_\uparrow^\dagger \psi_\downarrow^\dagger \phi + \phi^\dagger \psi_\downarrow \psi_\uparrow \qquad (7.8a)$$

$$= \Psi^\dagger \left(i\partial_t + \sigma_3 \frac{\partial^2}{2m} + \sigma_3 \mu \right) \Psi - \frac{1}{c_0} \phi^\dagger \phi + \Psi^\dagger \sigma_+ \Psi \phi + \phi^\dagger \Psi^\dagger \sigma_- \Psi, \qquad (7.8b)$$

where $\Psi \equiv (\psi_\uparrow, \psi_\downarrow^\dagger)^T$ is a two-component Nambu-Gor'kov field, $\sigma_\pm \equiv \frac{1}{2}(\sigma_1 \pm i\sigma_2)$, and $\sigma_{1,2,3}$ are the Pauli matrices. Because the ground state of the system at finite density is a superfluid, we expand ϕ around its vacuum expectation value $\phi_0 \equiv \langle\phi\rangle > 0$ as

$$\phi = \phi_0 + g\varphi \quad \text{with} \quad g \equiv \frac{(8\pi^2\epsilon)^{1/2}}{m} \left(\frac{m\phi_0}{2\pi} \right)^{\epsilon/4}. \qquad (7.9)$$

Here we introduced the effective coupling g and chose the extra factor $(m\phi_0/2\pi)^{\epsilon/4}$ so that φ has the same dimension as a nonrelativistic field.[1]

Because the Lagrangian density (7.8b) does not have the kinetic term for the boson field φ, we add and subtract its kinetic term by hand and rewrite the Lagrangian density as a sum of three parts, $\mathcal{L} = \mathcal{L}_0 + \mathcal{L}_1 + \mathcal{L}_2$, where

$$\mathcal{L}_0 = \Psi^\dagger \left(i\partial_t + \sigma_3 \frac{\partial^2}{2m} + \sigma_1 \phi_0 \right) \Psi + \varphi^\dagger \left(i\partial_t + \frac{\partial^2}{4m} \right) \varphi, \qquad (7.10a)$$

---

[1] The choice of the extra factor is arbitrary, if it has the correct dimension, and does not affect final results because the difference can be absorbed by the redefinition of φ. The particular choice of g in Eq. 7.9 [or $\bar{g}$ in Eq. 7.13] simplifies expressions for loop integrals in the intermediate steps.
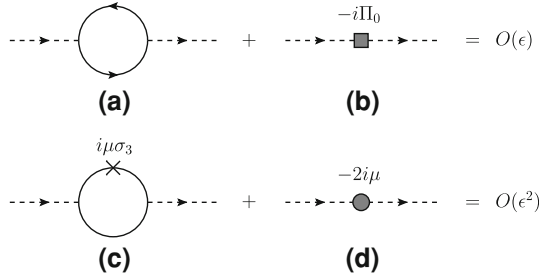
Fig. 7.3 Power counting rule of ϵ. The $1/\epsilon$ singularity in the boson self-energy diagram **a** or **c** can be canceled by combining it with the vertex from $\mathcal{L}_2$, **b** or **d**, to achieve the simple ϵ counting. *Solid* (*dotted*) *lines* are the fermion (boson) propagators iG (iD). The fermion loop in **c** goes around clockwise and counterclockwise and the *cross symbol* represents the μ insertion

$$\mathcal{L}_1 = g\Psi^\dagger \sigma_+ \Psi \varphi + g\varphi^\dagger \Psi^\dagger \sigma_- \Psi + \mu\Psi^\dagger \sigma_3 \Psi + 2\mu\varphi^\dagger \varphi, \tag{7.10b}$$

$$\mathcal{L}_2 = -\varphi^\dagger \left(i\partial_t + \frac{\partial^2}{4m} \right) \varphi - 2\mu\varphi^\dagger \varphi. \tag{7.10c}$$

Here we set $1/c_0 = 0$ in the unitarity limit. We treat $\mathcal{L}_0$ as the unperturbed part and $\mathcal{L}_1$ as a small perturbation. Note that the chemical potential μ is also treated as a perturbation because we will find it small, $\mu/\phi_0 \sim \epsilon$, by solving the gap equation. Physically, $\mathcal{L}_0 + \mathcal{L}_1$ is the Lagrangian density describing weakly interacting fermions Ψ and bosons φ with a small coupling $g \sim \epsilon^{1/2}$. $\mathcal{L}_2$ plays a role of counter terms that cancel $1/\epsilon$ singularities of loop integrals in certain types of diagrams (Fig. 7.3).

The unperturbed part $\mathcal{L}_0$ generates the fermion propagator,

$$G(p_0, \boldsymbol{p}) = \frac{1}{p_0^2 - E_{\boldsymbol{p}}^2 + i0^+} \begin{pmatrix} p_0 + \varepsilon_{\boldsymbol{p}} & -\phi_0 \\ -\phi_0 & p_0 - \varepsilon_{\boldsymbol{p}} \end{pmatrix}, \tag{7.11}$$

with $E_{\boldsymbol{p}} \equiv \sqrt{\varepsilon_{\boldsymbol{p}}^2 + \phi_0^2}$ and the boson propagator

$$D(p_0, \boldsymbol{p}) = \frac{1}{p_0 - \frac{\varepsilon_{\boldsymbol{p}}}{2} + i0^+}. \tag{7.12}$$

The first two terms in the perturbation part $\mathcal{L}_1$ generate the fermion–boson vertices whose coupling is g in Eq. 7.9. The third and fourth terms are the chemical potential insertions to the fermion and boson propagators. The two terms in $\mathcal{L}_2$ provide additional vertices, $-i\Pi_0$ and $-2i\mu$ in Fig. 7.3b, d, to the boson propagator, where $\Pi_0(p_0, \boldsymbol{p}) \equiv p_0 - \frac{\varepsilon_{\boldsymbol{p}}}{2}$.

The power counting rule of ϵ is simple and summarized as follows:

1. We regard ϕ_0 as $O(1)$ and hence $\mu \sim \epsilon\phi_0$ as $O(\epsilon)$.
2. We write down Feynman diagrams for the quantity of interest using the propagators from $\mathcal{L}_0$ and the vertices from $\mathcal{L}_1$.
3. If the written Feynman diagram includes any subdiagram of the type in Fig. 7.3a or c, we add the same Feynman diagram where the subdiagram is replaced by the vertex from $\mathcal{L}_2$ in Fig. 7.3b or d.
4. The power of ϵ for the given Feynman diagram is $O(\epsilon^{N_g/2+N_\mu})$, where N_g is the number of couplings g and N_μ is the number of chemical potential insertions.
5. The only exception is the one-loop vacuum diagram with one μ insertion (the second diagram in Fig. 7.5), which is $O(1)$ instead of $O(\epsilon)$ due to the $1/\epsilon$ singularity arising from the loop integral.

The same or similar power counting rule can be derived for the cases with unequal chemical potentials $\mu_\uparrow \neq \mu_\downarrow$ [8], unequal masses $m_\uparrow \neq m_\downarrow$ [20], at finite temperature $T \neq 0$ [9], and in the vicinity of the unitarity limit $c_0 \neq 0$ [8].

7.2.2.2 Around Two Spatial Dimensions

The systematic expansion around $d = 2$ in terms of $\bar{\epsilon}$ can be also organized in a similar way. Starting with the Lagrangian density (7.8b), we expand ϕ around its vacuum expectation value $\bar{\phi}_0 \equiv \langle\phi\rangle > 0$ as

$$\phi = \bar{\phi}_0 + \bar{g}\varphi \quad \text{with} \quad \bar{g} \equiv \left(\frac{2\pi\bar{\epsilon}}{m}\right)^{1/2} \left(\frac{m\mu}{2\pi}\right)^{-\bar{\epsilon}/4}. \tag{7.13}$$

Here we introduced the effective coupling $\bar{g}$ and chose the extra factor $(m\mu/2\pi)^{-\bar{\epsilon}/4}$ so that $\varphi^\dagger\varphi$ has the same dimension as the Lagrangian density.[2]

In the unitarity limit $1/c_0 = 0$, we rewrite the Lagrangian density as a sum of three parts, $\mathcal{L} = \bar{\mathcal{L}}_0 + \bar{\mathcal{L}}_1 + \bar{\mathcal{L}}_2$, where

$$\bar{\mathcal{L}}_0 = \Psi^\dagger \left(i\partial_t + \sigma_3 \frac{\partial^2}{2m} + \sigma_3\mu + \sigma_1\bar{\phi}_0\right)\Psi, \tag{7.14a}$$

$$\bar{\mathcal{L}}_1 = -\varphi^\dagger\varphi + \bar{g}\Psi^\dagger\sigma_+\Psi\varphi + \bar{g}\varphi^\dagger\Psi^\dagger\sigma_-\Psi, \tag{7.14b}$$

$$\bar{\mathcal{L}}_2 = \varphi^\dagger\varphi. \tag{7.14c}$$

We treat $\bar{\mathcal{L}}_0$ as the unperturbed part and $\bar{\mathcal{L}}_1$ as a small perturbation. Physically, $\bar{\mathcal{L}}_0 + \bar{\mathcal{L}}_1$ is the Lagrangian density describing weakly interacting fermions Ψ. Indeed, if we did not have $\bar{\mathcal{L}}_2$, we could integrate out the auxiliary fields φ and $\varphi^\dagger$,

---

[2] See the footnote after Eq. 7.9.
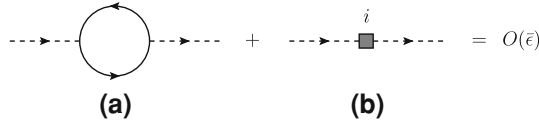
Fig. 7.4 Power counting rule of $\bar{\epsilon}$. The $1/\bar{\epsilon}$ singularity in the self-energy diagram of φ field (**a**) can be canceled by combining it with the vertex from $\bar{\mathcal{L}}_2$ (**b**) to achieve the simple $\bar{\epsilon}$ counting. *Solid* (*dotted*) *lines* are the fermion (auxiliary field) propagators $i\bar{G}$ ($i\bar{D}$)

$$\bar{\mathcal{L}}_1 \to \bar{g}^2 \Psi^\dagger \sigma_+ \Psi \Psi^\dagger \sigma_- \Psi = \bar{g}^2 \psi_\uparrow^\dagger \psi_\downarrow^\dagger \psi_\downarrow \psi_\uparrow, \tag{7.15}$$

which is the contact interaction between fermions with a small coupling $\bar{g}^2 \sim \bar{\epsilon}$. $\bar{\mathcal{L}}_2$ plays a role of a counter term that cancels $1/\bar{\epsilon}$ singularities of loop integrals in a certain type of diagrams (Fig. 7.4).

The unperturbed part $\bar{\mathcal{L}}_0$ generates the fermion propagator

$$\bar{G}(p_0, \boldsymbol{p}) = \frac{1}{p_0^2 - \bar{E}_{\boldsymbol{p}}^2 + i0^+} \begin{pmatrix} p_0 + \varepsilon_{\boldsymbol{p}} - \mu & -\bar{\phi}_0 \\ -\bar{\phi}_0 & p_0 - \varepsilon_{\boldsymbol{p}} + \mu \end{pmatrix} \tag{7.16}$$

with $\bar{E}_{\boldsymbol{p}} \equiv \sqrt{(\varepsilon_{\boldsymbol{p}} - \mu)^2 + \bar{\phi}_0^2}$. The first term in the perturbation part $\bar{\mathcal{L}}_1$ generates the propagator of φ field, $\bar{D}(p_0, \boldsymbol{p}) = -1$, and the last two terms generate the vertices between fermions and φ field with the coupling $\bar{g}$ in Eq. 7.13. $\bar{\mathcal{L}}_2$ provides an additional vertex i in Fig. 7.4b to the φ propagator.

The power counting rule of $\bar{\epsilon}$ is simple and summarized as follows:

1. We regard μ as $O(1)$.
2. We write down Feynman diagrams for the quantity of interest using the propagator from $\bar{\mathcal{L}}_0$ and the vertices from $\bar{\mathcal{L}}_1$.
3. If the written Feynman diagram includes any subdiagram of the type in Fig. 7.4a, we add the same Feynman diagram where the subdiagram is replaced by the vertex from $\bar{\mathcal{L}}_2$ in Fig. 7.4b.
4. The power of $\bar{\epsilon}$ for the given Feynman diagram is $O(\bar{\epsilon}^{N_{\bar{g}}/2})$, where $N_{\bar{g}}$ is the number of couplings $\bar{g}$.

7.2.3 Zero Temperature Thermodynamics

We now apply the developed ϵ expansion to compute various physical quantities of the unitary Fermi gas. Because of the absence of scales in the zero-range and infinite scattering interaction, the density n is the only scale of the unitary Fermi gas at zero temperature. Therefore all physical quantities are determined by simple dimensional analysis up to dimensionless constants of proportionality. Such dimensionless parameters are universal depending only on the dimensionality of space.

A representative example of the universal parameters is the ground state energy of the unitary Fermi gas normalized by that of a noninteracting Fermi gas with the same density:

$$\xi \equiv \frac{E_{\text{unitary}}}{E_{\text{free}}}. \tag{7.17}$$

ξ, sometimes called the Bertsch parameter, measures how much energy is gained due to the attractive interaction in the unitarity limit. In terms of ξ, the pressure P, the energy density $\mathcal{E}$, the chemical potential μ, and the sound velocity v_s of the unitary Fermi gas are given by

$$\frac{P}{\varepsilon_{\text{Fn}}} = \frac{2}{d+2}\xi \quad \frac{\mathcal{E}}{\varepsilon_{\text{Fn}}} = \frac{d}{d+2}\xi \quad \frac{\mu}{\varepsilon_F} = \xi \quad \frac{v_s}{v_F} = \sqrt{\frac{\xi}{d}}, \tag{7.18}$$

where $\varepsilon_F \equiv k_F^2/2m$ and $v_F \equiv k_F/m$ are the Fermi energy and velocity with $k_F \equiv \left[2^{d-1}\pi^{d/2}\Gamma\left(\frac{d}{2}+1\right)n\right]^{1/d}$ being the Fermi momentum in d spatial dimensions. ξ is thus a fundamental quantity characterizing the zero temperature thermodynamics of the unitary Fermi gas.

7.2.3.1 Next-to-Leading Orders

ξ can be determined systematically in the ϵ expansion by computing the effective potential $V_{\text{eff}}(\phi_0)$, whose minimum with respect to the order parameter ϕ_0 provides the pressure $P = -\min V_{\text{eff}}(\phi_0)$. To leading and next-to-leading orders in ϵ, the effective potential receives contributions from three vacuum diagrams depicted in Fig. 7.5. The third diagram, fermion loop with one boson exchange, results from the summation of fluctuations around the classical solution and is beyond the mean field approximation. Any other diagrams are suppressed near $d=4$ by further powers of ϵ. Performing the loop integrations, we obtain

$$V_{\text{eff}}(\phi_0) = \left[\frac{\phi_0}{3}\left\{1 + \frac{7 - 3(\gamma + \ln 2)}{6}\epsilon - 3C\epsilon\right\}\right.$$
$$\left. - \frac{\mu}{\epsilon}\left\{1 + \frac{1 - 2(\gamma - \ln 2)}{4}\epsilon\right\}\right]\left(\frac{m\phi_0}{2\pi}\right)^{d/2} + O(\epsilon^2), \tag{7.19}$$

where $C \approx 0.14424$ is a numerical constant. The minimization of $V_{\text{eff}}(\phi_0)$ with respect to ϕ_0 gives the gap equation, $\partial V_{\text{eff}}/\partial\phi_0 = 0$, which is solved by

$$\phi_0(\mu) = \frac{2\mu}{\epsilon}\left[1 + (3C - 1 + \ln 2)\epsilon + O(\epsilon^2)\right]. \tag{7.20}$$

The effective potential at its minimum provides the pressure $P(\mu) = -V_{\text{eff}}(\phi_0(\mu))$ as a function of μ. From Eq. 7.18 and $n = \partial P/\partial\mu$, we obtain ξ expanded in terms of ϵ:

$$V_{\text{eff}} = \bigcirc + \bigcirc + (\text{----}) + O(\epsilon^2)$$

$$O(1) \qquad O(1) \qquad O(\epsilon)$$
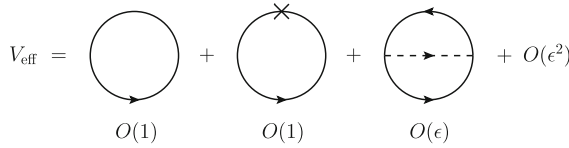
Fig. 7.5 Vacuum diagrams contributing to the effective potential near $d = 4$ to leading and next-to-leading orders in ϵ. The boson one-loop diagram vanishes at zero temperature

$$
\begin{aligned}
\xi|_{d \to 4} &= \frac{\epsilon^{3/2}}{2} \exp\left(\frac{\epsilon \ln \epsilon}{8 - 2\epsilon}\right)\left[1 - \left\{3C - \frac{5}{4}(1 - \ln 2)\right\}\epsilon + O(\epsilon^2)\right] \\
&= \frac{1}{2}\epsilon^{3/2} + \frac{1}{16}\epsilon^{5/2} \ln \epsilon - 0.0246\epsilon^{5/2} + O(\epsilon^{7/2}).
\end{aligned}
\tag{7.21}
$$

Although our formalism is based on the smallness of ϵ, we find that the next-to-leading-order correction is quite small compared to the leading term even at $\epsilon = 1$. The naive extrapolation to the physical dimension $d = 3$ gives

$$\xi \to 0.475 \qquad (\epsilon \to 1), \tag{7.22}$$

which is already close to the result from the Monte Carlo simulation $\xi \approx 0.40(1)$ (S. Zhang et al., Private communication). For comparison, the mean field approximation yields $\xi \approx 0.591$.

The above result can be further improved by incorporating the expansion around $d = 2$. Because we can find by solving the gap equation that the order parameter is exponentially small [8]

$$\bar{\phi}_0(\mu) = 2\mu e^{-1/\bar{\epsilon} - 1 + O(\bar{\epsilon})}, \tag{7.23}$$

its contribution to the pressure is negligible compared to any powers of $\bar{\epsilon}$. To leading and next-to-leading orders in $\bar{\epsilon}$, the effective potential receives contributions from two vacuum diagrams depicted in Fig. 7.6. Any other diagrams are suppressed near $d = 2$ by further powers of $\bar{\epsilon}$. From the pressure

$$P = -\bar{V}_{\text{eff}}(0) = \left[1 + \bar{\epsilon} + O(\bar{\epsilon}^2)\right]\frac{2\mu}{\Gamma\left(\frac{d}{2} + 2\right)}\left(\frac{m\mu}{2\pi}\right)^{d/2}, \tag{7.24}$$

we obtain ξ expanded in terms of $\bar{\epsilon}$:

$$\xi|_{d \to 2} = 1 - \bar{\epsilon} + O(\bar{\epsilon}^2). \tag{7.25}$$

The value of ξ in $d = 3$ can be extracted by interpolating the two expansions around $d = 4$ and $d = 2$. The simplest way to do so is to employ the Padé approximants. We write ξ in the form
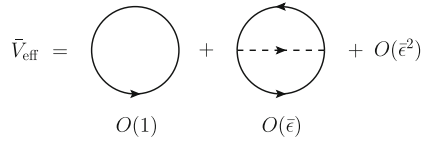
Fig. 7.6 Vacuum diagrams contributing to the effective potential near $d = 2$ to leading and next-to-leading orders in $\bar{\epsilon}$
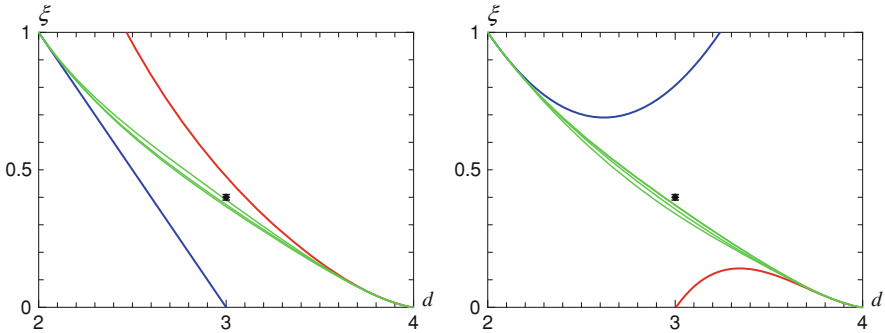
Fig. 7.7 ξ as a function of the spatial dimension d. *Left panel*: The *upper* (*lower*) *curve* is the extrapolation from the NLO expansion around $d = 4$ in Eq. 7.21 [$d = 2$ in Eq. 7.25]. The *middle three curves* show the Padé interpolations of the two NLO expansions. The *symbol* at $d = 3$ indicates the result $\xi \approx 0.40(1)$ from the Monte Carlo simulation (S. Zhang et al., Private communication). *Right panel*: The same as the *left panel* but including the NNLO corrections in Eq. 7.29 and Eq. 7.30

$$\xi = \frac{\epsilon^{3/2}}{2} \exp\left(\frac{\epsilon \ln \epsilon}{8 - 2\epsilon}\right) F(\epsilon), \qquad (7.26)$$

where $F(\epsilon)$ is an unknown function and the trivial nonanalytic dependence on ϵ was factored out.[3] We approximate $F(\epsilon)$ by ratios of two polynomials (Padé approximants) and determine their coefficients so that ξ in Eq. 7.26 has the correct next-to-leading-order (NLO) expansions both around $d = 4$ Eq. 7.21 and $d = 2$ Eq. 7.25. The left panel of Fig. 7.7 shows the behavior of ξ as a function of d. The middle three curves are the Padé interpolations of the two NLO expansions. In $d = 3$, these interpolations give

$$\xi \approx 0.391, \ 0.366, \ 0.373, \qquad (7.27)$$

which span a small interval $\xi \approx 0.377 \pm 0.014$.

---

[3] It has been shown that $F(\epsilon)$ has a nonanalytic term $-\frac{3}{8}\epsilon^3 \ln \epsilon$ to the next-to-next-to-next-to-leading order in ϵ [10]. Because we are working up to $O(\epsilon^2)$, we neglect such a nonanalytic contribution.

We can also employ different interpolation schemes, for example, by applying the Borel transformation to $F(\epsilon) = \frac{1}{\epsilon} \int_0^\infty dt e^{-t/\epsilon} G(t)$ and approximating the Borel transform $G(t)$ by the Padé approximants [8]. These Borel-Padé interpolations of the two NLO expansions give

$$\xi \approx 0.391, \ 0.364, \ 0.378 \tag{7.28}$$

in $d = 3$, which again span a small interval $\xi \approx 0.378 \pm 0.013$. Comparing the results in Eq. 7.27 and Eq. 7.28, we find that the interpolated values do not depend much on the choice of the Padé approximants and also on the employment of the Borel transformation.

7.2.3.2 Next-to-Next-to-Leading Orders

The systematic calculation of ξ has been carried out up to the next-to-next-to-leading-order (NNLO) corrections in terms of ϵ [10]:

$$\xi|_{d \to 4} = \frac{\epsilon^{3/2}}{2} \exp\left(\frac{\epsilon \ln \epsilon}{8 - 2\epsilon}\right) \left[1 - 0.04916\epsilon - 0.95961\epsilon^2 + O(\epsilon^3)\right] \tag{7.29}$$

and in terms of $\bar{\epsilon}$ [11, 20]:

$$\xi|_{d \to 2} = 1 - \bar{\epsilon} + 0.80685\bar{\epsilon}^2 + O(\bar{\epsilon}^3). \tag{7.30}$$

The middle four curves in the right panel of Fig. 7.7 are the Padé interpolations of the two NNLO expansions. In $d = 3$, these interpolations give

$$\xi \approx 0.340, \ 0.372, \ 0.370, \ 0.357, \tag{7.31}$$

which span an interval $\xi \approx 0.360 \pm 0.020$. [4] In spite of the large NNLO corrections both near $d = 4$ and $d = 2$, the interpolated values are roughly consistent with the previous interpolations of the NLO expansions (compare the two panels in Fig. 7.7). This indicates that the interpolated results are stable to inclusion of higher-order corrections and thus the ϵ expansion has a certain predictive power even in the absence of the knowledge on the higher-order corrections.

Finally we note that the limit $\xi|_{d \to 4} \to 0$ is consistent with the Nussinovs' picture of the unitary Fermi gas as a noninteracting Bose gas and $\xi|_{d \to 2} \to 1$ is consistent with the picture as a noninteracting Fermi gas in Sect. 7.2.1.1. It would be interesting to consider how ξ should be continued down to $d \to 1$. The unitary Fermi gas in $d = 3$ is analytically continued to spin-$\frac{1}{2}$ fermions with a hard-core repulsion in $d = 1$, which is equivalent for the thermodynamic quantities to free identical fermions with the same total density [21]. Therefore it is easy to find

---

[4] If we excluded the interpolation by the simple polynomial ($\xi \approx 0.340$) as was done in Ref. [10], we would obtain 0.367 ± 0.010, which is consistent with the Borel-Padé interpolations without the NNLO correction near $d = 2$ [10].

$$\xi|_{d \to 1} \to 4. \tag{7.32}$$

The incorporation of this constraint on the Padé interpolations of the two NNLO expansions yields $\xi \approx 0.365 \pm 0.010$ in $d = 3$.

7.2.4 Quasiparticle Spectrum

The ϵ expansion is also useful to compute other physical quantities of the unitary Fermi gas. Here we determine the spectrum of fermion quasiparticles in a superfluid. To leading order in ϵ, the dispersion relation $\omega(\boldsymbol{p})$ is given by the pole of the fermion propagator in Eq. 7.11; $\omega(\boldsymbol{p}) = E_{\boldsymbol{p}} = \sqrt{\varepsilon_{\boldsymbol{p}}^2 + \phi_0^2}$. It has a minimum at $|\boldsymbol{p}| = 0$ with the energy gap equal to $\Delta = \phi_0 = 2\mu/\epsilon$.

To the next-to-leading order in ϵ, the fermion propagator receives corrections from three self-energy diagrams depicted in Fig. 7.8. We can find that $\Sigma \sim O(\epsilon)$ is diagonal with the elements

$$\Sigma_{11}(p_0, \boldsymbol{p}) = -\frac{g^2}{2} \int \frac{d\boldsymbol{k}}{(2\pi)^d} \frac{E_{\boldsymbol{k}} - \varepsilon_{\boldsymbol{k}}}{E_{\boldsymbol{k}}(E_{\boldsymbol{k}} + \frac{\varepsilon_{\boldsymbol{k}-\boldsymbol{p}}}{2} - p_0 - i0^+)} \tag{7.33}$$

and $\Sigma_{22}(p_0, \boldsymbol{p}) = -\Sigma_{11}(-p_0, -\boldsymbol{p})$. From the pole of the fermion propagator, $\det\left[G^{-1}(\omega, \boldsymbol{p}) + \mu\sigma_3 - \Sigma(\omega, \boldsymbol{p})\right] = 0$, we obtain the dispersion relation

$$\omega(\boldsymbol{p}) = E_{\boldsymbol{p}} + \frac{\Sigma_{11} + \Sigma_{22}}{2} + \frac{\Sigma_{11} - \Sigma_{22} - 2\mu}{2E_{\boldsymbol{p}}} \varepsilon_{\boldsymbol{p}} + O(\epsilon^2), \tag{7.34}$$

where Σ_{11} and Σ_{22} are evaluated at $p_0 = E_{\boldsymbol{p}}$. The minimum of $\omega(\boldsymbol{p})$ will appear at small momentum $\varepsilon_{\boldsymbol{p}} \sim O(\epsilon)$. By expanding $\omega(\boldsymbol{p})$ with respect to $\varepsilon_{\boldsymbol{p}}$, we find that the dispersion relation around its minimum has the form

$$\omega(\boldsymbol{p}) \simeq \Delta + \frac{(\varepsilon_{\boldsymbol{p}} - \varepsilon_0)^2}{2\phi_0}. \tag{7.35}$$

Here Δ is the energy gap of the fermion quasiparticle given by

$$\begin{aligned}
\Delta|_{d \to 4} &= \phi_0 \left[1 - (8 \ln 3 - 12 \ln 2)\epsilon + O(\epsilon^2)\right] \\
&= \frac{2\mu}{\epsilon} \left[1 + (3C - 1 - 8 \ln 3 + 13 \ln 2)\epsilon + O(\epsilon^2)\right].
\end{aligned} \tag{7.36}$$

The minimum of the dispersion relation is located at $\varepsilon_{\boldsymbol{p}} = \varepsilon_0 > 0$ with

$$\varepsilon_0|_{d \to 4} = \mu + \frac{\epsilon\phi_0}{2} + O(\epsilon^2) = 2\mu + O(\epsilon^2), \tag{7.37}$$

where the solution of the gap equation (7.20) was substituted to ϕ_0.

Fig. 7.8 Fermion
self-energy diagrams near
$d = 4$ to the order $O(\epsilon)$

$$i\mu\sigma_3 = \quad \longrightarrow\!\!\times\!\!\longrightarrow$$

$$-i\Sigma = \quad \longrightarrow\!\!\!\!\frown\!\!\!\!\longrightarrow \quad + \quad \longrightarrow\!\!\!\!\frown\!\!\!\!\longrightarrow \quad + \ O(\epsilon^2)$$
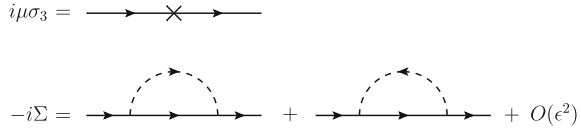
We can see that the next-to-leading-order correction is reasonably small compared to the leading term at least for $\Delta/\mu = 2/\epsilon\,(1 - 0.345\epsilon)$. The naive extrapolation to the physical dimension $d = 3$ gives

$$\frac{\Delta}{\mu} \to 1.31 \quad \text{and} \quad \frac{\varepsilon_0}{\mu} \to 2 \quad (\epsilon \to 1), \tag{7.38}$$

both of which are quite close to the results from the Monte Carlo simulation $\Delta/\mu \approx 1.2$ and $\varepsilon_0/\mu \approx 1.9$ [22]. For comparison, the mean field approximation yields $\Delta/\mu \approx 1.16$ and $\varepsilon_0/\mu \approx 1$.

Frequently Δ and ε_0 are normalized by the Fermi energy ε_F. By multiplying Eqs. 7.36 and 7.37 by $\mu/\varepsilon_F = \xi$ obtained previously in Eq. 7.21, we find

$$\frac{\Delta}{\varepsilon_F} \to 0.604 \quad \text{and} \quad \frac{\varepsilon_0}{\varepsilon_F} \to 1 \quad (\epsilon \to 1). \tag{7.39}$$

For comparison, the Monte Carlo simulation gives $\Delta/\varepsilon_F \approx 0.50$ and $\varepsilon_0/\varepsilon_F \approx 0.8$ [22] and the mean field approximation yields $\Delta/\varepsilon_F \approx 0.686$ and $\varepsilon_0/\varepsilon_F \approx 0.591$.

7.2.5 Critical Temperature

The formulation of the ϵ expansion can be extended to finite temperature $T \neq 0$ by using the imaginary time prescription [9]. Here we determine the critical temperature T_c for the superfluid phase transition of the unitary Fermi gas.

The leading contribution to T_c/ε_F in terms of ϵ can be obtained by the following simple argument. In the limit $d \to 4$, the unitary Fermi gas reduces to a noninteracting fermions and bosons with their chemical potentials μ and 2μ, respectively [see Eq. 7.10]. Because the boson's chemical potential vanishes at the BEC critical temperature, the density at $T = T_c$ is given by

$$
\begin{aligned}
n &= 2 \int \frac{d\boldsymbol{p}}{(2\pi)^4} \left[f_F(\varepsilon_{\boldsymbol{p}}) + f_B(\varepsilon_{\boldsymbol{p}}/2) \right] + O(\epsilon) \\
&= \left[\frac{\pi^2}{6} + \frac{8\pi^2}{6} \right] \left(\frac{mT_c}{2\pi} \right)^2 + O(\epsilon) = \frac{3\pi^2}{2} \left(\frac{mT_c}{2\pi} \right)^2 + O(\epsilon).
\end{aligned}
\tag{7.40}
$$

Comparing the contributions from Fermi and Bose distributions, we can see that only 8 of 9 fermion pairs form the composite bosons while 1 of 9 fermion pairs is dissociated. With the use of $\varepsilon_F \equiv \frac{2\pi}{m} \left[\Gamma\left(\frac{d}{2} + 1\right) \frac{n}{2} \right]^{2/d}$ at $d = 4$, we obtain

$$\left.\frac{T_{\rm c}}{\varepsilon_{\rm F}}\right|_{d\to 4}=\sqrt{\frac{2}{3\pi^2}}+O(\epsilon). \tag{7.41}$$

In order to compute the $O(\epsilon)$ correction to $T_{\rm c}/\varepsilon_{\rm F}$, we need to evaluate the effective potential $V_{\rm eff}(\phi_0)$ at finite temperature. The effective potential to leading order in ϵ is given by the fermion one-loop diagrams with and without one μ insertion and the boson one-loop diagram. Near $T\simeq T_{\rm c}$, we can expand $V_{\rm eff}(\phi_0)$ in ϕ_0/T and obtain

$$V_{\rm eff}(\phi)-V_{\rm eff}(0)\simeq\left[T\ \ln 2-\frac{\mu}{\epsilon}\right]\left(\frac{m\phi_0}{2\pi}\right)^2+\frac{\phi_0^2}{16T}\left(\frac{m\phi_0}{2\pi}\right)^2+\cdots. \tag{7.42}$$

The second order phase transition occurs when the coefficient of the quadratic term in ϕ_0 vanishes. Accordingly, at $T=T_{\rm c}$, the chemical potential is found to be

$$\mu=\epsilon T_{\rm c}\ln 2+O(\epsilon^2). \tag{7.43}$$

We then compute the $O(\epsilon)$ correction to the density $n=-\,\partial V_{\rm eff}/\partial\mu$ in Eq. 7.40 at $T=T_{\rm c}$ and hence $\phi_0=0$. For this purpose, we need to evaluate the fermion and boson one-loop diagrams with two μ insertions and the two-loop diagrams with one μ insertion to the fermion and boson propagators (Fig. 7.9). Performing the loop integrations and substituting Eq. 7.43, we can find

$$n=\left[\frac{3\pi^2}{2}-\left\{\frac{3\pi^2\ln 2+18\zeta'(2)}{4}+D-2(\ln 2)^2\right\}\epsilon\right]\left(\frac{mT_{\rm c}}{2\pi}\right)^{d/2}, \tag{7.44}$$

where $D\approx 1.92181$ is a numerical constant. From the definition $\varepsilon_{\rm F}\equiv\frac{2\pi}{m}\left[\Gamma\left(\frac{d}{2}+1\right)\frac{n}{2}\right]^{2/d}$, we obtain $T_{\rm c}/\varepsilon_{\rm F}$ up to the next-leading order in ϵ:

$$\left.\frac{T_{\rm c}}{\varepsilon_{\rm F}}\right|_{d\to 4}=0.260-0.0112\epsilon+O(\epsilon^2). \tag{7.45}$$

On the other hand, because the unitary Fermi gas near $d=2$ reduces to a weakly interacting Fermi gas, the critical temperature is provided by the usual BCS formula $T_{\rm c}=(e^\gamma/\pi)\,\Delta$, where Δ is the energy gap of the fermion quasiparticle at zero temperature. Because Δ in the expansion over $\bar{\epsilon}$ is already obtained by $\bar{\phi}_0=2\mu e^{-1/\bar{\epsilon}-1+O(\bar{\epsilon})}$ in Eq. 7.23, we easily find

$$\left.\frac{T_{\rm c}}{\varepsilon_{\rm F}}\right|_{d\to 2}=\frac{2e^\gamma}{\pi}e^{-1/\bar{\epsilon}-1+O(\bar{\epsilon})}, \tag{7.46}$$

where we used $\mu/\varepsilon_{\rm F}=\xi=1+O(\epsilon)$ Eq. 7.25. The exponential $e^{-1/\bar{\epsilon}}$ is equivalent to the mean field result while the correction e^{-1} corresponds to the Gor'kov–Melik-Barkhudarov correction in $d=3$.

Now the value of $T_{\rm c}/\varepsilon_{\rm F}$ in $d=3$ can be extracted by interpolating the two expansions around $d=4$ and $d=2$ just as has been done for ξ in Sect. 7.2.3.1. We write $T_{\rm c}/\varepsilon_{\rm F}$ in the form
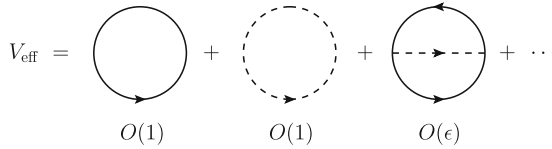
Fig. 7.9 Three types of diagrams contributing to the effective potential at finite temperature near $d = 4$ to leading and next-to-leading orders in ϵ. Each μ (2μ) insertion to the fermion (boson) line increases the power of ϵ by one. Note that at $T \geq T_\mathrm{c}$ where $\phi_0 = 0$, the μ insertion to the first diagram does not produce the $1/\epsilon$ singularity
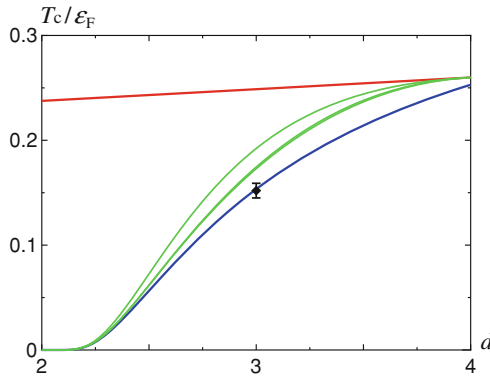
Fig. 7.10 Critical temperature T_c as a function of the spatial dimension d. The *upper* (*lower*) *curve* is the extrapolation from the NLO expansion around $d = 4$ in (7.45) [$d = 2$ in (7.46)]. The *middle three curves* show the Padé and Borel-Padé interpolations of the two NLO expansions. The *symbol* at $d = 3$ indicates the result $T_\mathrm{c}/\varepsilon_\mathrm{F} = 0.152(7)$ from the Monte Carlo simulation [23]

$$\frac{T_\mathrm{c}}{\varepsilon_\mathrm{F}} = \frac{2e^\gamma}{\pi} e^{-1/\bar{\epsilon}-1} F(\bar{\epsilon}), \tag{7.47}$$

where $F(\bar{\epsilon})$ is an unknown function and the nonanalytic dependence on $\bar{\epsilon}$ was factored out. We approximate $F(\bar{\epsilon})$ or its Borel transform $G(t)$ by ratios of two polynomials and determine their coefficients so that $T_\mathrm{c}/\varepsilon_\mathrm{F}$ in Eq. 7.47 has the correct NLO expansions both around $d = 4$ Eq. 7.45 and $d = 2$ Eq. 7.46. Figure 7.10 shows the behavior of $T_\mathrm{c}/\varepsilon_\mathrm{F}$ as a function of d. The middle three curves are the Padé and Borel-Padé interpolations of the two NLO expansions. In $d = 3$, these interpolations give

$$\frac{T_\mathrm{c}}{\varepsilon_\mathrm{F}} \approx 0.173, \ 0.175, \ 0.192, \tag{7.48}$$

which span an interval $T_\mathrm{c}/\varepsilon_\mathrm{F} \approx 0.180 \pm 0.012$. Our interpolated values are not too far from the result of the Monte Carlo simulation $T_\mathrm{c}/\varepsilon_\mathrm{F} = 0.152(7)$ [23]. For comparison, the mean field approximation yields $T_\mathrm{c}/\varepsilon_\mathrm{F} \approx 0.496$.

7.2.6 Phase Diagram of an Imbalanced Fermi Gas

The phase diagram of a density- and mass-imbalanced Fermi gas was studied using the ϵ expansion in Refs. [8, 20].

7.3 Aspects as a Nonrelativistic Conformal Field Theory

Because of the absence of scales in the zero-range and infinite scattering interaction, the theory describing fermions in the unitarity limit is a nonrelativistic conformal field theory (NRCFT). In this section, after deriving the Schrödinger algebra and the operator-state correspondence in NRCFTs, we compute the scaling dimensions of few-body composite operators exactly or with the help of the ϵ expansion, which provide the energies of a few fermions at unitarity in a harmonic potential.

7.3.1 Schrödinger Algebra

We start with a brief review of the Schrödinger algebra [15, 16]. For the latter application, we allow spin-$\uparrow$ and $\downarrow$ fermions to have different masses $m_\uparrow$ and $m_\downarrow$. We define the mass density:

$$\rho(\boldsymbol{x}) \equiv \sum_{\sigma\,=\,\uparrow,\downarrow} m_\sigma \psi_\sigma^\dagger(\boldsymbol{x})\psi_\sigma(\boldsymbol{x}) \tag{7.49}$$

and the momentum density:

$$j_i(\boldsymbol{x}) \equiv -\frac{i}{2} \sum_{\sigma\,=\,\uparrow,\downarrow} \left[\psi_\sigma^\dagger(\boldsymbol{x})\partial_i\psi_\sigma(\boldsymbol{x}) - \partial_i\psi_\sigma^\dagger(\boldsymbol{x})\psi_\sigma(\boldsymbol{x}) \right], \tag{7.50}$$

where $i = 1, \ldots, d$ and the arguments of time are suppressed. The Schrödinger algebra is formed by the following set of operators:

$$\text{mass}: \quad M \equiv \int d\boldsymbol{x}\,\rho(\boldsymbol{x}) \tag{7.51}$$

$$\text{momentum}: \quad P_i \equiv \int d\boldsymbol{x}\,j_i(\boldsymbol{x}) \tag{7.52}$$

$$\text{angular momentum}: \quad J_{ij} \equiv \int d\boldsymbol{x}\,\left[x_i j_j(\boldsymbol{x}) - x_j j_i(\boldsymbol{x}) \right] \tag{7.53}$$

$$\text{Galilean boost}: \quad K_i \equiv \int d\boldsymbol{x}\,x_i\,\rho(\boldsymbol{x}) \tag{7.54}$$

$$\text{dilatation}: \quad D \equiv \int d\mathbf{x}\, \mathbf{x} \cdot \mathbf{j}(\mathbf{x}) \tag{7.55}$$

$$\text{special conformal}: \quad C \equiv \int d\mathbf{x}\, \frac{\mathbf{x}^2}{2} \rho(\mathbf{x}) \tag{7.56}$$

and the Hamiltonian:

$$
\begin{aligned}
H = \sum_{\sigma=\uparrow,\downarrow} \int d\mathbf{x}\, \frac{\partial \psi_\sigma^\dagger(\mathbf{x}) \cdot \partial \psi_\sigma(\mathbf{x})}{2m_\sigma} \\
+ \int d\mathbf{x} \int d\mathbf{y}\, \psi_\uparrow^\dagger(\mathbf{x}) \psi_\downarrow^\dagger(\mathbf{y}) V(|\mathbf{x}-\mathbf{y}|) \psi_\downarrow(\mathbf{y}) \psi_\uparrow(\mathbf{x}).
\end{aligned}
\tag{7.57}
$$

D and C are the generators of the scale transformation ($\mathbf{x} \to e^\lambda \mathbf{x}$, $t \to e^{2\lambda} t$) and the special conformal transformation [$\mathbf{x} \to \mathbf{x}/(1+\lambda t)$, $t \to t/(1+\lambda t)$], respectively. In a scale invariant system such as fermions in the unitarity limit, these operators form a closed algebra.[5]

Commutation relations of the above operators are summarized in Table 7.1. The rest of the algebra is the commutators of M, which commutes with all other operators; $[M, \text{any}] = 0$. The commutation relations of J_{ij} with other operators are determined by their transformation properties under rotations:

$$[J_{ij}, N] = [J_{ij}, D] = [J_{ij}, C] = [J_{ij}, H] = 0, \tag{7.58a}$$

$$[J_{ij}, P_k] = i(\delta_{ik} P_j - \delta_{jk} P_i), \quad [J_{ij}, K_k] = i(\delta_{ik} K_j - \delta_{jk} K_i), \tag{7.58b}$$

$$[J_{ij}, J_{kl}] = i(\delta_{ik} J_{jl} + \delta_{jl} J_{ik} - \delta_{il} J_{jk} - \delta_{jk} J_{il}). \tag{7.58c}$$

These commutation relations can be verified by direct calculations, while only the commutator of $[D, H] = 2iH$ requires the scale invariance of the Hamiltonian in which the interaction potential has to satisfy $V(e^\lambda r) = e^{-2\lambda} V(r)$.

7.3.2 Operator-State Correspondence

7.3.2.1 Primary Operators

We then introduce local operators $\mathcal{O}(t, \mathbf{x})$ as operators that depend on the position in time and space $(t, \mathbf{x})$ so that

$$\mathcal{O}(t, \mathbf{x}) = e^{iHt - iP_i x_i} \mathcal{O}(0) e^{-iHt + iP_i x_i}. \tag{7.59}$$

---

[5] One potential that realizes the unitarity interaction is $V(r) = (\pi/2)^2 \lim_{r_0 \to 0} \theta(r_0 - r)/(2m_{\uparrow\downarrow} r_0^2)$, where $m_{\uparrow\downarrow} \equiv m_\uparrow m_\downarrow/(m_\uparrow + m_\downarrow)$ is the reduced mass.

Table 7.1 Part of the Schrödinger algebra (the values of [X, Y] are shown below)

$X \backslash Y$	P_j	K_j	D	C	H
P_i	0	$-i\delta_{ij}M$	$-iP_i$	$-iK_i$	0
K_i	$i\delta_{ij}M$	0	iK_i	0	iP_i
D	iP_j	$-iK_j$	0	$-2iC$	$2iH$
C	iK_j	0	$2iC$	0	iD
H	0	$-iP_j$	$-2iH$	$-iD$	0

A local operator $\mathcal{O}$ is said to have a scaling dimension $\Delta_{\mathcal{O}}$ and a mass $M_{\mathcal{O}}$ if it satisfies

$$[D, \mathcal{O}(0)] = i\Delta_{\mathcal{O}}\mathcal{O}(0) \quad \text{and} \quad [M, \mathcal{O}(0)] = M_{\mathcal{O}}\mathcal{O}(0). \tag{7.60}$$

With the use of the commutation relations in Table 7.1, we find that if a given local operator $\mathcal{O}$ has the scaling dimension $\Delta_{\mathcal{O}}$, then the scaling dimensions of new local operators $[P_i, \mathcal{O}]$, $[H, \mathcal{O}]$, $[K_i, \mathcal{O}]$, and $[C, \mathcal{O}]$ are given by $\Delta_{\mathcal{O}} + 1$, $\Delta_{\mathcal{O}} + 2$, $\Delta_{\mathcal{O}} - 1$, and $\Delta_{\mathcal{O}} - 2$, respectively. Therefore, by repeatedly taking the commutators with K_i and C, one can keep to lower the scaling dimensions. However, this procedure has to terminate because the scaling dimensions of local operators are bounded from below as we will show in Sect. 7.3.2.3. The last operator $\mathcal{O}_{\text{pri}}$ obtained in this way must have the property

$$[K_i, \mathcal{O}_{\text{pri}}(0)] = [C, \mathcal{O}_{\text{pri}}(0)] = 0. \tag{7.61}$$

Such operators that at $t = 0$ and $\boldsymbol{x} = \boldsymbol{0}$ commute with K_i and C will be called *primary operators*. Below the primary operator $\mathcal{O}_{\text{pri}}$ is simply denoted by $\mathcal{O}$.

Starting with an arbitrary primary operator $\mathcal{O}(t, \boldsymbol{x})$, one can build up a tower of local operators by taking its commutators with P_i and H, in other words, by taking its space and time derivatives (left tower in Fig. 7.11). For example, the operators with the scaling dimension $\Delta_{\mathcal{O}} + 1$ in the tower are $[P_i, \mathcal{O}] = i\partial_i\mathcal{O}$. At the next level with the scaling dimension $\Delta_{\mathcal{O}} + 2$, the following operators are possible; $[P_i, [P_j, \mathcal{O}]] = -\partial_i\partial_j\mathcal{O}$ and $[H, \mathcal{O}] = -i\partial_t\mathcal{O}$. Commuting those operators with K_i and C, we can get back the operators into the lower rungs of the tower. The task of finding the spectrum of scaling dimensions of all local operators thus reduces to finding the scaling dimensions of all primary operators.

It is worthwhile to note that two-point correlation functions of the primary operators are constrained by the scale and Galilean invariance up to an overall constant [24]. For example, the two-point correlation function of the primary operator $\mathcal{O}$ with its Hermitian conjugate is given by

$$\langle T\mathcal{O}(t, \boldsymbol{x})\mathcal{O}^\dagger(0)\rangle \propto \theta(t)t^{-\Delta_{\mathcal{O}}} \exp\left(iM_{\mathcal{O}^\dagger}\frac{|\boldsymbol{x}|^2}{2t}\right). \tag{7.62}$$
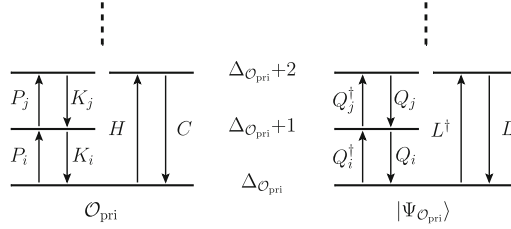
Fig. 7.11 Correspondence between the spectrum of scaling dimensions of local operators in NRCFT (*left tower*) and the energy spectrum of states in a harmonic potential (*right tower*). The *bottom* of each tower corresponds to the primary operator $\mathcal{O}_{\text{pri}}$ (primary state $|\Psi_{\mathcal{O}_{\text{pri}}}\rangle$)

This formula or its Fourier transform $\propto \left(-p_0 + \frac{p^2}{2M_{\mathcal{O}^\dagger}} - i0^+\right)^{\Delta_{\mathcal{O}} - d/2 - 1}$ will be useful to read off the scaling dimension $\Delta_{\mathcal{O}}$.

7.3.2.2 Correspondence to States in a Harmonic Potential

We now show that each primary operator corresponds to an energy eigenstate of the system in a harmonic potential. The Hamiltonian of the system in a harmonic potential is

$$H_\omega \equiv H + \omega^2 C, \tag{7.63}$$

where ω is the oscillator frequency. We consider a primary operator $\mathcal{O}(t, \mathbf{x})$ that is composed of annihilation operators in the quantum field theory so that $\mathcal{O}^\dagger(t, \mathbf{x})$ acts nontrivially on the vacuum: $\mathcal{O}^\dagger|0\rangle \neq 0$. We construct the following state using $\mathcal{O}^\dagger$ put at $t = 0$ and $\mathbf{x} = \mathbf{0}$:

$$|\Psi_{\mathcal{O}}\rangle \equiv e^{-H/\omega} \mathcal{O}^\dagger(0)|0\rangle. \tag{7.64}$$

If the mass of $\mathcal{O}^\dagger$ is $M_{\mathcal{O}^\dagger} > 0$, then $|\Psi_{\mathcal{O}}\rangle$ is a mass eigenstate with the mass eigenvalue $M_{\mathcal{O}^\dagger} : M|\Psi_{\mathcal{O}}\rangle = M_{\mathcal{O}^\dagger}|\Psi_{\mathcal{O}}\rangle$. Furthermore, with the use of the commutation relations in Table 7.1, it is straightforward to show that $|\Psi_{\mathcal{O}}\rangle$ is actually an energy eigenstate of the Hamiltonian H_ω with the energy eigenvalue $E = \Delta_{\mathcal{O}}\omega$:

$$\begin{aligned}
H_\omega|\Psi_{\mathcal{O}}\rangle &= \left(H + \omega^2 C\right) e^{-H/\omega} \mathcal{O}^\dagger(0)|0\rangle \\
&= e^{-H/\omega} \left(\omega^2 C - i\omega D\right) \mathcal{O}^\dagger(0)|0\rangle = \omega \Delta_{\mathcal{O}}|\Psi_{\mathcal{O}}\rangle,
\end{aligned} \tag{7.65}$$

where we used $[C, \mathcal{O}^\dagger(0)] = 0$ and $[D, \mathcal{O}^\dagger(0)] = i\Delta_{\mathcal{O}}$ and the fact that both C and D annihilate the vacuum.

Starting with the primary state $|\Psi_{\mathcal{O}}\rangle$, one can build up a tower of energy eigenstates of H_ω by acting the following raising operators (right tower in Fig. 7.11):

Table 7.2 Commutation relations of the Hamiltonian and the raising and lowering operators in the oscillator space (the values of [X, Y] are shown below)

$X\backslash Y$	$Q_j^\dagger$	Q_j	H_ω/ω	L	$L^\dagger$
$Q_i^\dagger$	0	$-\delta_{ij}M$	$-Q_i^\dagger$	$-Q_i$	0
Q_i	$\delta_{ij}M$	0	Q_i	0	$Q_i^\dagger$
H_ω/ω	$Q_j^\dagger$	$-Q_j$	0	-2L	$2L^\dagger$
L	Q_j	0	$2L$	0	H_ω/ω
$L^\dagger$	0	$-Q_j^\dagger$	$-2L^\dagger$	$-H_\omega/\omega$	0

$$Q_i^\dagger = \frac{P_i}{\sqrt{2\omega}} + i\sqrt{\frac{\omega}{2}}K_i \quad \text{and} \quad L^\dagger = \frac{H}{2\omega} - \frac{\omega}{2}C + \frac{i}{2}D. \qquad (7.66)$$

From the commutation relations $[H_\omega, Q_i^\dagger] = \omega Q_i^\dagger$ and $[H_\omega, L^\dagger] = 2\omega L^\dagger$, $Q_i^\dagger$ or $L^\dagger$ acting on $|\Psi_\mathcal{O}\rangle$ raise its energy eigenvalue by ω or 2ω. For example, the states $(Q_i^\dagger)^n|\Psi_\mathcal{O}\rangle$ with $n = 0, 1, 2, \ldots$ have their energy eigenvalues $E = (\Delta_\mathcal{O} + n)\omega$ and correspond to excitations of the center-of-mass motion in the i-direction, while $(L^\dagger)^n|\Psi_\mathcal{O}\rangle$ have $E = (\Delta_\mathcal{O} + 2n)\omega$ and correspond to excitations of the breathing mode [25, 26]. The primary state $|\Psi_\mathcal{O}\rangle$ is annihilated by the lowering operators Q_i and L:

$$Q_i|\Psi_\mathcal{O}\rangle = 0 \quad \text{and} \quad L|\Psi_\mathcal{O}\rangle = 0. \qquad (7.67)$$

Therefore $|\Psi_\mathcal{O}\rangle$ corresponds to the bottom of each semi-infinite tower of energy eigenstates, which is the ground state with respect to the center-of-mass and breathing mode excitations.

The commutation relations of the Hamiltonian and the raising and lowering operators in the oscillator space are summarized in Table 7.2. It is clear from the above arguments and also from Tables 7.1 and 7.2 that the roles of (P_i, K_i, D, C, H) in the free space is now played by $(Q_i^\dagger, Q_i, H_\omega, L, L^\dagger)$ in the oscillator space. Figure 7.11 illustrates the correspondence between the spectrum of scaling dimensions of local operators in NRCFT and the energy spectrum of states in a harmonic potential.

The operator-state correspondence elucidated here allows us to translate the problem of finding the energy eigenvalues of the system in a harmonic potential to another problem of finding the scaling dimensions of primary operators in NRCFT. In Sect. 7.3.3, we use this correspondence to compute the energies of fermions at unitarity in a harmonic potential. We note that the similar correspondence between quantities in a harmonic potential and in a free space has been discussed in the quantum-mechanical language in Refs. [25, 27].

7.3.2.3 Unitarity Bound of Scaling Dimensions

As we mentioned in Sect. 7.3.2.1, the scaling dimensions of local operators are bounded from below. The lower bound is equal to $d/2$, which can be seen from

the following intuitive physical argument. According to the operator-state correspondence, the scaling dimension of a primary operator is the energy eigenvalue of particles in a harmonic potential. The latter can be divided into the center of mass energy and the energy of the relative motion. The ground state energy of the center of mass motion is $(d/2)\,\omega$, while the energy of the relative motion has to be non-negative [25]. Thus, energy eigenvalues, and hence operator dimensions, are bounded from below by $d/2$.

More formally, the lower bound can be derived from the requirement of non-negative norms of states in our theory (Y. Tachikawa, Private communication). We consider the primary state $|\Psi_{\mathcal{O}}\rangle$ whose mass and energy eigenvalues are given by $M_{\mathcal{O}^{\dagger}}$ and $\Delta_{\mathcal{O}}\omega$:

$$M|\Psi_{\mathcal{O}}\rangle = M_{\mathcal{O}^{\dagger}}|\Psi_{\mathcal{O}},> \quad \text{and} \quad H_{\omega}|\Psi_{\mathcal{O}}\rangle = \Delta_{\mathcal{O}}\omega|\Psi_{\mathcal{O}}\rangle. \tag{7.68}$$

We then construct the following state:

$$|\Phi\rangle \equiv \left(L^{\dagger} - \sum_{i=1}^{d} \frac{Q_i^{\dagger} Q_i^{\dagger}}{2M_{\mathcal{O}^{\dagger}}}\right)|\Psi_{\mathcal{O}}\rangle, \tag{7.69}$$

and require that it has a non-negative norm $\langle\Phi|\Phi\rangle \geq 0$. With the use of the commutation relations in Table 7.2 and Eq. 7.67, the norm of $|\Phi\rangle$ can be computed as

$$\langle\Phi|\Phi\rangle = \left(\Delta_{\mathcal{O}} - \frac{d}{2}\right)\langle\Psi_{\mathcal{O}}|\Psi_{\mathcal{O}}\rangle \geq 0. \tag{7.70}$$

Therefore we find the lower bound on the scaling dimensions of arbitrary primary operators:

$$\Delta_{\mathcal{O}} \geq \frac{d}{2}. \tag{7.71}$$

The lower bound $d/2$ multiplied by ω coincides with the ground state energy of a single particle in a d-dimensional harmonic potential.

When the primary state $|\Psi_{\mathcal{O}}\rangle$ saturates the lower bound $\Delta_{\mathcal{O}} = d/2$, the vanishing norm of $\langle\Phi|\Phi\rangle = 0$ means that the state itself is identically zero; $|\Phi\rangle \equiv 0$. Accordingly, the state created by the corresponding primary operator $\mathcal{O}(t, \mathbf{x})$ obeys the free Schrödinger equation:

$$\left[i\partial_t - \frac{\partial^2}{2M_{\mathcal{O}^{\dagger}}}\right]\mathcal{O}^{\dagger}(t, \mathbf{x})|0\rangle = 0. \tag{7.72}$$

In addition to the trivial one-body operator ψ_{σ}, we will see nontrivial examples of primary operators that saturate the lower bound of the scaling dimensions.

If a theory contains an operator $\mathcal{O}$ with its scaling dimension between $d/2$ and $(d+2)/2$, then $\mathcal{O}^{\dagger}\mathcal{O}$ is a relevant deformation: $\Delta_{\mathcal{O}^{\dagger}\mathcal{O}} < d + 2$. Therefore, such a theory should contain a fine tuning in the $\mathcal{O}^{\dagger}\mathcal{O}$ channel. We will see this pattern explicitly below.

7.3.2.4 Nonuniversality of p-Wave Resonances

One consequence of the unitarity bound on operator dimensions is the impossibility of achieving universality in p-wave resonances in three spatial dimensions. This issue was raised in connection with the $\alpha - n$ scattering [28]. Theoretically, such a resonance would be described by the following Lagrangian density:

$$\mathcal{L} = \psi_\sigma^\dagger \left(i\partial_t + \frac{\partial^2}{2m} \right) \psi_\sigma + c_1 \phi_i^\dagger \left(i\partial_t + \frac{\partial^2}{4m} \right) \phi_i + c_2 \phi_i^\dagger \phi_i \qquad (7.73)$$

$$+ \left(\psi_\uparrow^\dagger \partial_i \psi_\downarrow^\dagger - \partial_i \psi_\uparrow^\dagger \psi_\downarrow^\dagger \right) \phi_i + \phi_i^\dagger \left(\psi_\downarrow \partial_i \psi_\uparrow - \partial_i \psi_\downarrow \psi_\uparrow \right), \qquad (7.74)$$

where c_1 and c_2 are bare couplings chosen to cancel out the divergences in the one-loop self-energy of ϕ_i. (In contrast to the s-wave resonance case, the loop integral is cubic divergent and requires two counter terms to regularize, corresponding to two simultaneous fine tunings of the scattering length and the effective range. In dimensional regularization, $c_1 = c_2 = 0$.) The field ϕ_i now has a finite propagator

$$\int dt d\mathbf{x} e^{ip_0 t - i\mathbf{p}\cdot\mathbf{x}} \langle T\phi_i(t, \mathbf{x})\phi_i^\dagger(0) \rangle \propto \left(-p_0 + \frac{\mathbf{p}^2}{4m} - i0^+ \right)^{-d/2}. \qquad (7.75)$$

Such a theory might appear healthy but the scaling dimension of ϕ_i, as one can see explicitly by comparing Eq. 7.75 with the Fourier transform of Eq. 7.62, is $\Delta_\phi = 1$ which is below the unitarity bound of $d/2$ in $d = 3$. (In a free theory $\Delta_\phi = d + 1$, but the fine tunings "reflect" Δ_ϕ with respect to $(d + 2)/2$ so that Δ_ϕ becomes 1.) Thus, p-wave resonances cannot be universal in three spatial dimensions. The proof given here is more general than that of Ref. [29, 30]. Other examples considered in Refs. [29] can also be analyzed from the light of the unitarity bound.

7.3.3 Scaling Dimensions of Composite Operators

All results derived in Sects. 7.3.1 and 7.3.2 can be applied to any NRCFTs. Here we concentrate on the specific system of spin-$\frac{1}{2}$ fermions in the unitarity limit and study various primary operators and their scaling dimensions. The simplest primary operator is the one-body operator $\psi_\sigma(\mathbf{x})$ whose scaling dimension is trivially given by

$$\Delta_{\psi_\sigma} = \frac{d}{2}. \qquad (7.76)$$

This value multiplied by ω indeed matches the ground state energy of one fermion in a d-dimensional harmonic potential.

7.3.3.1 Two-Body Operator

The first nontrivial primary operator is the two-body composite operator: $\phi(x) \equiv c_0 \psi_\downarrow \psi_\uparrow(x)$, which also appears as an auxiliary field of the Hubbard-Stratonovich transformation (7.8a). The presence of the prefactor $c_0 \sim \Lambda^{2-d}$ guarantees that matrix elements of $\phi(x)$ between two states in the Hilbert space are finite. Accordingly its scaling dimension becomes

$$\Delta_\phi = \Delta_{\psi_\uparrow} + \Delta_{\psi_\downarrow} + (2-d) = 2. \tag{7.77}$$

This result can be confirmed by computing the two-point correlation function of ϕ and comparing it with the Fourier transform of Eq. 7.62:

$$\int dt d\mathbf{x} e^{ip_0 t - i\mathbf{p}\cdot\mathbf{x}} \langle T\phi(t,\mathbf{x})\phi^\dagger(0)\rangle = \frac{\left(\frac{2\pi}{m_{\uparrow\downarrow}}\right)^{d/2}}{\Gamma\left(1-\frac{d}{2}\right)\left[-p_0 + \frac{\mathbf{p}^2}{2(m_\uparrow+m_\downarrow)} - i0^+\right]^{d/2-1}}. \tag{7.78}$$

According to the operator-state correspondence, the ground state energy of two fermions at unitarity in a harmonic potential is exactly 2ω for an arbitrary spatial dimension d. This result is consistent with our intuitive pictures of spin-$\uparrow$ and $\downarrow$ fermions in the unitarity limit as a single point-like composite boson in $d=4$, two noninteracting fermions in $d=2$, and two identical fermions in $d=1$ (see discussions in Sects. 7.2.1.1 and 7.2.3.2). Note that $\phi(x)$ in $d=4$ saturates the lower bound (7.71) and thus obeys the free Schrödinger equation (7.72) with mass $M_{\phi^\dagger} = m_\uparrow + m_\downarrow$. The same result in $d=3$ has been obtained by directly solving the two-body Schrödinger equation with a harmonic potential [31], which is consistent with the experimental measurement [32].

7.3.3.2 Three-Body Operators

We then consider three-body composite operators. The formula to compute their scaling dimensions for arbitrary mass ratio $m_\uparrow/m_\downarrow$, angular momentum l, and spatial dimension d is derived in Appendix. Here we discuss its physical consequences in $d=3$. Three-body operators composed of two spin-$\uparrow$ and one spin-$\downarrow$ fermions with orbital angular momentum $l=0$ and $l=1$ are

$$\mathcal{O}_{\uparrow\uparrow\downarrow}^{(l=0)}(\mathbf{x}) \equiv Z_0^{-1}\phi\psi_\uparrow(\mathbf{x}) \tag{7.79}$$

and

$$\mathcal{O}_{\uparrow\uparrow\downarrow}^{(l=1)}(\mathbf{x}) \equiv Z_1^{-1}\left[\left(m_\uparrow + m_\downarrow\right)\phi\partial_i\psi_\uparrow - m_\uparrow(\partial_i\phi)\psi_\uparrow\right](\mathbf{x}), \tag{7.80}$$

where $i=1,2,3$ and $Z_l \sim \Lambda^{-\gamma_l}$ is the renormalization factor. The mass factors in Eq. 7.80 are necessary so that the operator is primary; $[K_i, \mathcal{O}_{\uparrow\uparrow\downarrow}^{(l=1)}(0)] = 0$.
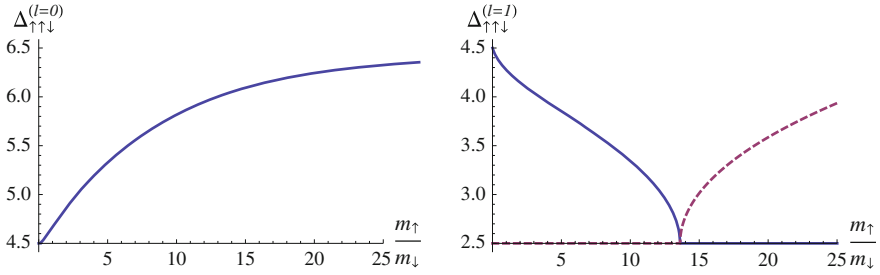
Fig. 7.12 Scaling dimensions of three-body composite operators $\mathcal{O}_{\uparrow\uparrow\downarrow}^{(l)}$ with angular momentum $l = 0$ (*left panel*) and $l = 1$ (*right panel*) as functions of the mass ratio $m_\uparrow/m_\downarrow$. In the *right panel*, the real part (*solid curve*) and the imaginary part shifted by $+2.5$ (*dashed curve*) are plotted

Their scaling dimensions $\Delta_{\uparrow\uparrow\downarrow}^{(l)} = \frac{7}{2} + l + \gamma_l$ obtained by solving Eq. 7.135 are plotted in Fig. 7.12 as functions of the mass ratio $m_\uparrow/m_\downarrow$. For $l = 0$ (left panel), $\Delta_{\uparrow\uparrow\downarrow}^{(l)}$ increases as $m_\uparrow/m_\downarrow$ is increased indicating the stronger effective repulsion in the *s*-wave channel. On the other hand, $\Delta_{\uparrow\uparrow\downarrow}^{(l)}$ for $l = 1$ (right panel) decreases with increasing $m_\uparrow/m_\downarrow$ and eventually, when the mass ratio exceeds the critical value $m_\uparrow/m_\downarrow > 13.607$, it becomes complex as $\Delta_{\uparrow\uparrow\downarrow}^{(l=1)} = \frac{5}{2} \pm i\,\mathrm{Im}(\gamma_1)$. [6] In this case, the Fourier transform of Eq. 7.62 implies that the two-point correlation function of $\mathcal{O}_{\uparrow\uparrow\downarrow}^{(l=1)}$ behaves as

$$\propto \sin\left[\mathrm{Im}(\gamma_1)\ln\left(\frac{\boldsymbol{p}^2 - (4m_\uparrow + 2m_\downarrow)p_0 - i0^+}{\Lambda^2}\right) + \theta\right]. \qquad (7.81)$$

Now the full scale invariance of the original NRCFT is broken down to a discrete scaling symmetry,

$$\boldsymbol{p} \to e^{n\pi/\mathrm{Im}(\gamma_1)}\boldsymbol{p} \quad \text{and} \quad p_0 \to e^{2n\pi/\mathrm{Im}(\gamma_1)}p_0, \qquad (7.82)$$

with n being an integer. This is a characteristic of the renormalization-group limit cycle and related to the existence of an infinite set of three-body bound states in the *p*-wave channel. Their energy eigenvalues form a geometric spectrum $E_{n+1}/E_n = e^{-2\pi/|\mathrm{Im}(\gamma_1)|}$, which is known as the Efimov effect [33, 34]. Because the system develops deep three-body bound states, the corresponding many-body system cannot be stable toward collapse.

We note that, in the range of the mass ratio $8.6186 < m_\uparrow/m_\downarrow < 13.607$, the scaling dimension of $\mathcal{O}_{\uparrow\uparrow\downarrow}^{(l=1)}$ satisfies $\frac{5}{2} < \Delta_{\uparrow\uparrow\downarrow}^{(l=1)} < \frac{7}{2}$. Accordingly the following three-body interaction term

$$\mathcal{L}_{\text{3-body}} = c_1 \mathcal{O}_{\uparrow\uparrow\downarrow}^{(1)\dagger}(t, \boldsymbol{x})\mathcal{O}_{\uparrow\uparrow\downarrow}^{(1)}(t, \boldsymbol{x}) \qquad (7.83)$$

---

[6] This situation illustrates a general feature: onsets of the Efimov effect occur when the ground state energy of the corresponding few-body system in a harmonic potential is equal to $\frac{d+2}{2}\omega$.

becomes renormalizable because now the coupling has the dimension $-2 < [c_1] < 0$. The Lagrangian density (7.8a) with $\mathcal{L}_{3\text{-body}}$ added defines a new renormalizable theory. In particular, when the coupling c_1 is tuned to its nontrivial fixed point ($c_1 \neq 0$) that describes a three-body resonance in the p-wave channel, the resulting theory provides a novel NRCFT. The corresponding system is that of spin-$\frac{1}{2}$ fermions with both two-body ($\uparrow\downarrow$) and three-body ($\uparrow\uparrow\downarrow$) resonances and its many-body physics was studied in Ref. [17].

7.3.4 Application of the ϵ Expansion

It would be difficult to determine exact scaling dimensions of composite operators with more than three fermions in $d = 3$. However, it is possible to estimate them with the help of the ϵ expansions around $d = 4$ and $d = 2$. The formulations developed in Sect. 7.2.2 can be used for the few-body problems as well just by setting $\mu = \phi_0 = 0$. Here we concentrate on the equal mass case $m_\uparrow = m_\downarrow$.

7.3.4.1 Scaling Dimensions Near Four Spatial Dimensions

The scaling dimensions of composite operators can be determined by studying their renormalizations. We start with the simplest three-body operator $\phi\psi_\uparrow$ near $d = 4$, which has zero orbital angular momentum $l = 0$. The leading-order diagram that renormalizes $\phi\psi_\uparrow$ is $O(\epsilon)$ and depicted in Fig. 7.13 (left). Performing the loop integration, we find that this diagram is logarithmically divergent at $d = 4$ and thus the renormalized operator differs from the bare one by the renormalization factor; $(\phi\psi_\uparrow)_{\text{ren}} = Z_{\phi\psi_\uparrow}^{-1} \phi\psi_\uparrow$, where $Z_{\phi\psi_\uparrow} = 1 - \frac{4}{3}\epsilon \ln \Lambda$. From the anomalous dimension $\gamma_{\phi\psi_\uparrow} = -\ln Z_{\phi\psi_\uparrow}/\ln \Lambda = \frac{4}{3}\epsilon$, we obtain the scaling dimension of the renormalized operator up to the next-to-leading order in ϵ:

$$\Delta_{\phi\psi_\uparrow} = \Delta_\phi + \Delta_{\psi_\uparrow} + \gamma_{\phi\psi_\uparrow} = 4 + \frac{5}{6}\epsilon + O(\epsilon^2). \tag{7.84}$$

According to the operator-state correspondence, there is a three-fermion state in a harmonic potential with $l = 0$ and energy equal to $E_3^{(0)} = \Delta_{\phi\psi_\uparrow}\omega$, which continues to the first excited state in $d = 3$. Even within the leading correction in ϵ, the naive extrapolation to $\epsilon \to 1$ yields $E_3^{(0)} \to 4.83\omega$, which is already close to the true first excited state energy 4.66622ω in $d = 3$ [27].

The ground state of three fermions in a harmonic potential has $l = 1$ in $d = 3$. The corresponding primary operator near $d = 4$ is $2\phi\partial\psi_\uparrow - (\partial\phi)\psi_\uparrow$, which is renormalized by the same diagram in Fig. 7.13 (left). From its anomalous dimension $\gamma = -\ln Z/\ln \Lambda = -\frac{1}{3}\epsilon$, we obtain the scaling dimension of the renormalized operator up to the next-to-leading order in ϵ:
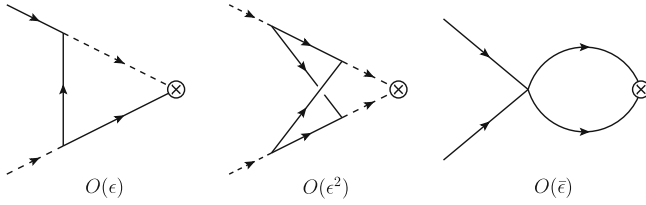
Fig. 7.13 Leading-order Feynman diagrams to renormalize the composite operators $\phi\psi_\uparrow$ (*left*) and $\phi\phi$ (*middle*) near $d = 4$ and $\psi_\uparrow\psi_\downarrow$ (*right*) near $d = 2$. These operators are inserted at $\otimes$

$$\Delta_{2\phi\partial\psi_\uparrow - (\partial\phi)\psi_\uparrow} = \Delta_\phi + \Delta_{\psi_\uparrow} + 1 + \gamma = 5 - \frac{5}{6}\epsilon + O(\epsilon^2). \qquad (7.85)$$

The operator-state correspondence tells us that the three-fermion state in a harmonic potential with $l = 1$ has the energy $E_3^{(1)} = \Delta_{2\phi\partial\psi_\uparrow - (\partial\phi)\psi_\uparrow}\omega$. The naive extrapolation to $\epsilon \to 1$ yields $E_3^{(1)} \to 4.17\omega$, which is already close to the true ground state energy 4.27272ω in $d = 3$ [27].

We now turn to the lowest four-body operator $\phi\phi$ with zero orbital angular momentum $l = 0$. The first nontrivial correction to its scaling dimension is $O(\epsilon^2)$ given by the diagram depicted in Fig. 7.13 (middle). The two-loop integral can be done analytically and we obtain the renormalization factor; $Z_{\phi\phi} = 1 - 8\epsilon^2 \ln \frac{27}{16} \ln \Lambda$. Therefore we find the scaling dimension of the renormalized operator $(\phi\phi)_{\mathrm{ren}} = Z_{\phi\phi}^{-1}\phi\phi$ to be

$$\Delta_{\phi\phi} = 2\Delta_\phi + \gamma_{\phi\phi} = 4 + 8\epsilon^2 \ln \frac{27}{16} + O(\epsilon^3). \qquad (7.86)$$

According to the operator-state correspondence, the ground state of four fermions in a harmonic potential has the energy $E_4^{(0)} = \Delta_{\phi\phi}\omega$. Because the $O(\epsilon^2)$ correction turns out to be large, we shall not directly extrapolate Eq. 7.86 to $\epsilon \to 1$ but will combine it with an expansion near $d = 2$.

The above results can be easily extended to a general number of fermions by evaluating the diagrams in Fig. 7.13 with more boson lines attached. The primary operators having N fermion number and orbital angular momentum l are summarized in Table 7.3 with their scaling dimensions computed in the ϵ expansion. The energy of the corresponding state in a harmonic potential is simply given by $E_N^{(l)} = \Delta_\mathcal{O}\omega$. The leading-order results [$E_N^{(0)} = N\omega$ for even N and $E_N^{(0)} = (N + 1)\omega$ and $E_N^{(1)} = (N + 2)\omega$ for odd N] can be intuitively understood by recalling that fermion pairs at unitarity in $d = 4$ form point-like bosons and they do not interact with each other or with extra fermions. Therefore the ground state of $N = 2n$ fermions consists of n free composite bosons occupying the same lowest energy state in a harmonic potential with the energy 2ω in $d = 4$. When $N = 2n+1$, the ground state has $l = 0$ and consists of n composite bosons and one extra fermion occupying the same lowest energy state again. In order to create an $l = 1$ state, one of the $n + 1$ particles has to be excited to the first excited state, which costs the additional energy 1ω. The leading correction to

Table 7.3 N-body composite operators with angular momentum l near $d = 4$ and their scaling dimensions in the ϵ expansion

N (l)	$\mathcal{O}_N^{(l)}$	$\Delta_\mathcal{O}$
$2n$ $(l=0)$	ϕ^n	$N + N(N-2)\epsilon^2 \ln \frac{27}{16} + O(\epsilon^3)$
$2n+1$ $(l=0)$	$\phi^n \phi_\uparrow$	$N + 1 + \frac{4N-7}{6}\epsilon + O(\epsilon^2)$
$2n+1$ $(l=1)$	$2\phi^n \partial \psi_\uparrow - \phi^{n-1}(\partial\phi)\psi_\uparrow$	$N + 2 + \frac{2N-21}{18}\epsilon + O(\epsilon^2)$

the energy, which is represented by the anomalous dimension in NRCFT, originates from the weak boson–fermion $[O(\epsilon)]$ or boson–boson $[O(\epsilon^2)]$ interaction. Finally we note that in $d = 4$, we can observe the odd–even staggering in the ground state energy; $E_N^{(0)} - \left(E_{N-1}^{(0)} + E_{N+1}^{(0)}\right)/2 = 1\omega$ for odd N.

7.3.4.2 Scaling Dimensions Near Two Spatial Dimensions

Similarly, we can determine the scaling dimensions of composite operators near $d = 2$ by studying their renormalizations. Here we consider the three-body operators $\psi_\uparrow \psi_\downarrow \partial_t \psi_\uparrow$ and $\psi_\uparrow \psi_\downarrow \partial \psi_\uparrow$, which are primary and have the orbital angular momentum $l = 0$ and $l = 1$, respectively. The leading-order diagrams that renormalize them are $O(\bar{\epsilon})$ and depicted in Fig. 7.13 (right) with one more fermion line attached. Performing the loop integrations, we find that these diagrams are logarithmically divergent at $d = 2$ and thus the renormalized operators differ from the bare ones by the renormalization factors; $Z_{\psi_\uparrow \psi_\downarrow \partial_t \psi_\uparrow} = 1 + \frac{3}{2}\bar{\epsilon} \ln \Lambda$ and $Z_{\psi_\uparrow \psi_\downarrow \partial \psi_\uparrow} = 1 + \frac{3}{2}\bar{\epsilon} \ln \Lambda$. From the anomalous dimensions $\gamma_\mathcal{O} = -\ln Z_\mathcal{O}/\ln \Lambda = -\frac{3}{2}\bar{\epsilon}$, we obtain the scaling dimensions of the renormalized operators up to the next-to-leading order in $\bar{\epsilon}$:

$$\Delta_{\psi_\uparrow \psi_\downarrow \partial_t \psi_\uparrow} = 3\Delta_{\psi_\sigma} + 2 + \gamma_{\psi_\uparrow \psi_\downarrow \partial_t \psi_\uparrow} = 5 + O(\bar{\epsilon}^2) \tag{7.87}$$

and

$$\Delta_{\psi_\uparrow \psi_\downarrow \partial \psi_\uparrow} = 3\Delta_{\psi_\sigma} + 1 + \gamma_{\psi_\uparrow \psi_\downarrow \partial \psi_\uparrow} = 4 + O(\bar{\epsilon}^2). \tag{7.88}$$

The operator-state correspondence tells us that the three-fermion states in a harmonic potential with $l = 0$ and $l = 1$ have the energies $E_3^{(0)} = \Delta_{\psi_\uparrow \psi_\downarrow \partial_t \psi_\uparrow}\omega$ and $E_3^{(1)} = \Delta_{\psi_\uparrow \psi_\downarrow \partial \psi_\uparrow}\omega$, respectively.

We can develop the same analysis for composite operators with more than three fermions by evaluating the diagram in Fig. 7.13 (right) with more fermion lines attached. The primary operators having $N \leq 6$ fermion number and orbital angular momentum l are summarized in Table 7.4 with their scaling dimensions computed in the $\bar{\epsilon}$ expansion. Note that composite operators having the same classical dimension can mix under the renormalization and thus the primary operator with the well-defined scaling dimension may have a complicated form such as for $N = 5$ and $l = 0$. The leading order results for the corresponding energies $E_N^{(l)} = \Delta_\mathcal{O}\omega$ in a harmonic potential can be easily understood by recalling that fermions at unitarity become

Table 7.4 N-body composite operators with angular momentum l near $d=2$ and their scaling dimensions in the $\bar{\epsilon}$ expansion

N (l)	$\mathcal{O}_N^{(l)}$	$\Delta_{\mathcal{O}}$	$E/\hbar\omega$ in $d=3$
2 ($l=0$)	$\psi_\uparrow\psi_\downarrow$	2	2 [31]
3 ($l=0$)	$\psi_\uparrow\psi_\downarrow(\partial_t\psi_\uparrow)$	$5+O(\bar{\epsilon}^2)$	4.66622 [27]
3 ($l=1$)	$\psi_\uparrow\psi_\downarrow(\partial\psi_\uparrow)$	$4+O(\bar{\epsilon}^2)$	4.27272 [27]
4 ($l=0$)	$\psi_\uparrow\psi_\downarrow(\partial\psi_\uparrow\cdot\partial\psi_\downarrow)$	$6-\bar{\epsilon}+(\bar{\epsilon}^2)$	≈ 5.028 [35]
5 ($l=0$)	$(*)$	$9-\frac{11\pm\sqrt{105}}{16}\bar{\epsilon}+O(\bar{\epsilon}^2)$	≈ 8.03 [35]
5 ($l=1$)	$\psi_\uparrow\psi_\downarrow(\partial\psi_\uparrow\cdot\partial\psi_\downarrow)\partial\psi_\uparrow$	$8-\bar{\epsilon}+O(\bar{\epsilon}^2)$	≈ 7.53 [35]
6 ($l=0$)	$\psi_\uparrow\psi_\downarrow(\partial\psi_\uparrow\cdot\partial\psi_\downarrow)^2$	$10-2\bar{\epsilon}+(\bar{\epsilon}^2)$	≈ 8.48 [35]

Known values for the energies of N fermions in a harmonic potential in $d=3$ are also shown in units of $\hbar\omega$ $(*)=a\psi_\uparrow\psi_\downarrow(\partial\psi_\uparrow\cdot\partial\psi_\downarrow)\partial^2\psi_\uparrow+b\psi_\uparrow\partial_i\psi_\downarrow(\partial\psi_\uparrow\cdot\partial\psi_\downarrow)\partial_i\psi_\uparrow+c\psi_\uparrow\psi_\downarrow((\partial_i\partial\psi_\uparrow)\cdot\partial\psi_\downarrow)\partial_i$ $\psi_\uparrow-d\psi_\uparrow\psi_\downarrow(\partial\psi_\uparrow\cdot\partial\psi_\downarrow)i\partial_t\psi_\uparrow$ with $(a,b,c,d)=(\pm 19\sqrt{3}-5\sqrt{35},\mp 16\sqrt{3},-6\sqrt{35}\mp 6\sqrt{3},$ $16\sqrt{35})$

noninteracting in $d=2$. Therefore the energy eigenvalue of each N-fermion state is just a sum of single particle energies in a harmonic potential in $d=2$, and obviously, the ground state energy shows the shell structure. The $O(\bar{\epsilon})$ correction to the energy, which is represented by the anomalous dimension in NRCFT, originates from the weak fermion–fermion interaction. We can see in Table 7.4 the rough agreement of the naive extrapolations of $\Delta_{\mathcal{O}}$ to $\bar{\epsilon}\to 1$ with the known values in $d=3$.

7.3.4.3 Interpolations of ϵ Expansions

We now extract the energy of N fermions in a harmonic potential in $d=3$ by interpolating the two expansions around $d=4$ and $d=2$ just as has been done for ξ in Sect. 7.2.3 and T_c/ε_F in Sect. 7.2.5. We approximate $E_N^{(l)}/\omega$ by ratios of two polynomials (Padé approximants) and determine their unknown coefficients so that the correct expansions both around $d=4$ (Table 7.3) and $d=2$ (Table 7.4) are reproduced.

Figure 7.14 shows the behaviors of the three-fermion energies $E_{N=3}^{(l)}$ with orbital angular momentum $l=0$ (left panel) and $l=1$ (right panel) as functions of d. The middle four curves are the Padé interpolations of the two NLO expansions. Because the exact results for arbitrary d can be obtained from Eq. 7.135 and 7.136, we can use this case as a benchmark test of our interpolation scheme. We find that the behaviors of the interpolated curves are quite consistent with the exact results even within the leading corrections in ϵ and $\bar{\epsilon}$. In $d=3$, these interpolations give

$$\frac{E_{N=3}^{(l=0)}}{\omega} \approx 4.71,\ 4.7,\ 4.72,\ 4.72 \tag{7.89}$$

and

$$\frac{E_{N=3}^{(l=1)}}{\omega} \approx 4.29,\ 4.3,\ 4.32,\ 4.29, \tag{7.90}$$
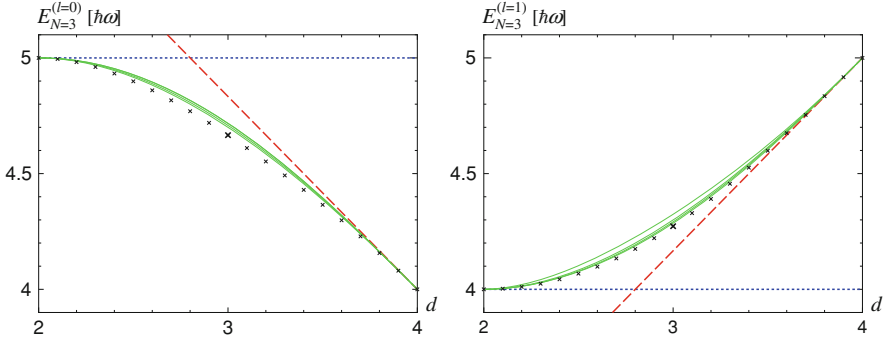
Fig. 7.14 Energies of three fermions in a harmonic potential in the *s*-wave channel $l = 0$ (*left panel*) and in the *p*-wave channel $l = 1$ (*right panel*) as functions of the spatial dimension *d*. The *dashed* (*dotted*) *lines* are the extrapolations from the NLO expansions around $d = 4$ in (7.84) and (7.85) [$d = 2$ in (7.87) and (7.88)]. The *four solid curves* show the Padé interpolations of the two NLO expansions. The *symbols* ($\times$) indicate the exact values for each *d* obtained from (7.135) and (7.136)

which span very small intervals $E_3^{(0)}/\omega \approx 4.71 \pm 0.01$ and $E_3^{(1)}/\omega \approx 4.30 \pm 0.02$. Our interpolated values are reasonably close to the exact results 4.66622ω and 4.27272ω in $d = 3$ [27].

Here we comment on the convergence of the ϵ expansions around $d = 4$ and $d = 2$. By performing the expansions up to $O(\epsilon^{50})$ with the use of the exact formula in (7.135) and studying their asymptotic behaviors, we can find that the ϵ expansions are convergent at least for these three-body problems. Their radii of convergence are estimated to be $|\epsilon| \lesssim 0.48$ and $|\bar{\epsilon}| \lesssim 1.0$ for the $l = 0$ case and $|\epsilon| \lesssim 1.4$ and $|\bar{\epsilon}| \lesssim 1.0$ for the $l = 1$ case.

The same analysis can be done for the energies of more than three fermions in a harmonic potential where exact results are not available. The Padé interpolations of the two NLO expansions for $N = 5$ yield

$$\frac{E_{N=5}^{(l=0)}}{\omega} \approx 7.71, \ 7.64, \ 7.66, \ 7.82 \tag{7.91}$$

and

$$\frac{E_{N=5}^{(l=1)}}{\omega} \approx 7.10, \ 7.16, \ 7.19, \ 7.09 \tag{7.92}$$

in $d = 3$, which span relatively small intervals $E_5^{(0)}/\omega \approx 7.73 \pm 0.09$ and $E_5^{(1)}/\omega \approx 7.14 \pm 0.05$. On the other hand, the Padé interpolations of the two NLO expansions for $N = 4, 6$ yield

$$\frac{E_{N=4}^{(l=0)}}{\omega} \approx 5.55, \ 4.94, \ 4.94, \ 4.90, \ 6.17 \tag{7.93}$$

and

$$\frac{E_{N=6}^{(l=0)}}{\omega} \approx 10.1, \ 7.92, \ 7.92, \ 7.80, \ 16.4 \tag{7.94}$$

in $d = 3$. The first and last values corresponding to the Padé approximants where all terms are distributed to the numerator or denominator are considerably off from the other three values. This would be because of the large NLO corrections near $d = 4$. If such two extreme cases are excluded, the other three values span rather small intervals $E_4^{(0)}/\omega \approx 4.92 \pm 0.02$ and $E_6^{(0)}/\omega \approx 7.86 \pm 0.06$. For comparison, the numerical results obtained by using a basis set expansion technique are shown in Table 7.4 [35].

7.4 General Coordinate and Conformal Invariance

Some nontrivial results can be obtained for the unitary Fermi gas using general symmetry arguments. For this end it is convenient to couple the unitary Fermi gas to an external gauge field A_μ ($\mu = 0, 1, 2, 3$) and to an external metric g_{ij}. Both A_μ and g_{ij} can be functions of time and space. Now the action of the unitary Fermi gas becomes

$$S = \int dt d\boldsymbol{x} \sqrt{g} \left(\frac{i}{2} \psi_\sigma^\dagger \ D_t \psi_\sigma - \frac{i}{2} D_t \psi_\sigma^\dagger \psi_\sigma - \frac{1}{2m} g^{ij} D_i \psi_\sigma^\dagger D_j \psi_\sigma + \psi_\uparrow^\dagger \psi_\downarrow^\dagger \phi + \phi^\dagger \psi_\downarrow \psi_\uparrow \right), \tag{7.95}$$

where $D_t = \partial_t - i A_0$ and $D_i = \partial_i - i A_i$ are covariant derivatives. We can see that A_0 plays the role of the external trapping potential. Recall that when the dimensional regularization is used, the term $\propto \phi^\dagger \phi$ is absent in the unitarity limit.

By direct calculations, one can verify that this action is invariant under the following transformations:

- Gauge transforms

$$\psi \to e^{i\alpha(t,\boldsymbol{x})} \psi, \quad \phi \to e^{2i\alpha(t,\boldsymbol{x})} \phi \tag{7.96a}$$

$$A_0 \to A_0 - \partial_t \alpha, \quad A_i \to A_i - \partial_i \alpha \tag{7.96b}$$

- General coordinate transformations

$$x^i \to x^{i'}, \quad x^i = x^i(t, x^{i'}) \tag{7.97a}$$

$$\psi(t, \boldsymbol{x}) \to \psi'(t, \boldsymbol{x}') = \psi(t, \boldsymbol{x}) \tag{7.97b}$$

$$\phi(t, \boldsymbol{x}) \to \phi'(t, \boldsymbol{x}') = \phi(t, \boldsymbol{x}) \tag{7.97c}$$

$$g_{ij}(t, \boldsymbol{x}) \to g_{i'j'}(t, \boldsymbol{x}') = \frac{\partial x^i}{\partial x^{i'}} \frac{\partial x^j}{\partial x^{j'}} g_{ij}(t, \boldsymbol{x}) \tag{7.97d}$$

$$A_0(t, \boldsymbol{x}) \rightarrow A_{0'}(t, \boldsymbol{x}') = A_0(t, \boldsymbol{x}) + \dot{x}^i A_i - \frac{1}{2} \dot{x}^i \dot{x}^j g_{ij} \qquad (7.97\text{e})$$

$$A_i(t, \boldsymbol{x}) \rightarrow A_{i'}(t, \boldsymbol{x}') = \frac{\partial x^i}{\partial x^{i'}} A_i(t, \boldsymbol{x}) - \frac{\partial x^i}{\partial x^{i'}} \dot{x}^j g_{ij}(t, \boldsymbol{x}) \qquad (7.97\text{f})$$

- Conformal transformations

$$t \rightarrow t', \quad t = t(t') \qquad (7.98\text{a})$$

$$\psi(t, \boldsymbol{x}) \rightarrow \psi'(t', \boldsymbol{x}) = \left(\frac{\partial t}{\partial t'}\right)^{3/4} \psi(t, \boldsymbol{x}) \qquad (7.98\text{b})$$

$$\phi(t, \boldsymbol{x}) \rightarrow \phi'(t', \boldsymbol{x}) = \left(\frac{\partial t}{\partial t'}\right) \phi(t, \boldsymbol{x}) \qquad (7.98\text{c})$$

$$A_0(t, \boldsymbol{x}) \rightarrow A_0'(t', \boldsymbol{x}) = \left(\frac{\partial t}{\partial t'}\right) A_0(t, \boldsymbol{x}) \qquad (7.98\text{d})$$

$$A_i(t, \boldsymbol{x}) \rightarrow A_i'(t', \boldsymbol{x}) = A_i(t, \boldsymbol{x}) \qquad (7.98\text{e})$$

$$g_{ij}(t, \boldsymbol{x}) \rightarrow g_{ij}'(t', \boldsymbol{x}) = \left(\frac{\partial t}{\partial t'}\right)^{-1} g_{ij}(t', \boldsymbol{x}). \qquad (7.98\text{f})$$

These symmetries allow one to transform the unitary Fermi gas in a free space into that in a harmonic potential with an arbitrary time-dependent frequency $\omega(t)$. This is done by a combination of a conformal transformation $t = f(t')$, a general coordinate transformation

$$x^i = \lambda^{-1}(t)x^{i'} \quad \text{with} \quad \lambda(t) = [f'(t)]^{-1/2}, \qquad (7.99)$$

and a gauge transformation with

$$\alpha = \frac{1}{2} \frac{\dot{\lambda}}{\lambda} x^2. \qquad (7.100)$$

If one starts with $A_\mu = 0$ and $g_{ij} = \delta_{ij}$, these three transformations leave the gauge vector potential A_i and the metric g_{ij} unchanged, but generate a scalar potential A_0:

$$A_0 = \frac{1}{2}\omega^2(t)x^2 \quad \text{with} \quad \omega^2(t) = -\frac{1}{2}\frac{\ddot{\lambda}}{\lambda}x^2. \qquad (7.101)$$

The transformed field operator is

$$\psi'(t, \boldsymbol{x}) = \exp\left(\frac{i}{2}\frac{\dot{\lambda}}{\lambda}x^2\right)\lambda^{-3/2}(t)\psi(f(t), \lambda^{-1}(t)\boldsymbol{x}). \tag{7.102}$$

This map between the unitary Fermi gas in the free space and that in the harmonic potential with the time-dependent frequency was previously found in Ref. [36].

In future applications, we only need the infinitesimal forms of the transformations. For reference, they are

$$\delta\psi = i\alpha\psi - \xi^k\partial_k\psi, \tag{7.103a}$$

$$\delta A_0 = -\dot{\alpha} - \xi^k\partial_k A_0 - A_k\dot{\xi}^k, \tag{7.103b}$$

$$\delta A_i = -\partial_i\alpha - \xi^k\partial_k A_i - A_k\partial_i\xi^k + mg_{ik}\dot{\xi}^k, \tag{7.103c}$$

$$\delta g_{ij} = -\xi^k\partial_k g_{ij} - g_{ik}\partial_j\xi^k - g_{kj}\partial_i\xi^k \tag{7.103d}$$

for the gauge and general coordinate transformations, and

$$\delta O = -\beta\dot{O} - \frac{1}{2}\Delta[O]\dot{\beta}O \tag{7.104}$$

for the conformal transformations, where $\Delta[O]$ is the dimension of a field O; $\Delta[\psi] = \frac{3}{2}$, $\Delta[\phi] = 2$, $\Delta[A_0] = 2$, $\Delta[A_i] = 0$, and $\delta[g_{ij}] = -2$.

7.4.1 Vanishing Bulk Viscosities

One consequence of the general coordinate and conformal invariance is the vanishing of the bulk viscosity of the unitarity Fermi gas in the normal phase, and the vanishing of two (out of three) bulk viscosities in the superfluid phase. These conclusions come from the requirement that hydrodynamic equations describing the motion of a fluid in the external gauge field and metric possess the same set of symmetries as the microscopic theory.

7.4.1.1 Normal Phase

In the normal phase, the hydrodynamic equations are written in term of the local mass density ρ, the local velocity v^i, and the local entropy per unit mass s. These equations are

$$\frac{1}{\sqrt{g}}\partial_t(\sqrt{g}\rho) + \nabla_i(\rho v^i) = 0, \tag{7.105}$$

$$\frac{1}{\sqrt{g}}\partial_t(\sqrt{g}\rho v_i) + \nabla_k \Pi_i^k = \frac{\rho}{m}(E_i - F_{ik}v^k), \tag{7.106}$$

$$\frac{1}{\sqrt{g}}\partial_t(\sqrt{g}\rho s) + \nabla_i\left(\rho v^i \partial_i s - \frac{\kappa}{T}\partial^i T\right) = \frac{2R}{T}, \tag{7.107}$$

where Π_{ik} is the stress tensor, κ is the thermal conductivity, and R is the dissipative function. Compared to the usual equations written for the flat metric and in the absence of the gauge field, we have replaced the derivatives ∂_i by the covariant derivatives ∇_i and added the force term in the momentum conservation equation (7.106), which comes from the electric force ($E_i = \partial_t A_i - \partial_i A_0$) and the magnetic Lorentz force ($F_{ik} = \partial_i A_k - \partial_k A_i$). The stress tensor can be written as

$$\Pi_{ik} = \rho v_i v_k + p g_{ik} - \sigma'_{ik}, \tag{7.108}$$

where p is the pressure and σ'_{ik} is the viscous stress tensor. The information about the kinetic coefficients is contained in σ'_{ik} and R.

In the dissipationless limit ($\sigma' = R = 0$), the hydrodynamic equations are invariant with respect to the general coordinate transformations, provided that ρ, s, and v^i transform as

$$\delta\rho = -\xi^k \partial_k \rho, \tag{7.109}$$

$$\delta s = -\xi^k \partial_k s, \tag{7.110}$$

$$\delta v^i = -\xi^k \partial_k v^i + v^k \partial_k \xi^i + \dot{\xi}^i. \tag{7.111}$$

Now consider the dissipative terms. To keep the equations consistent with the diffeomorphism invariance, one must require that σ'_{ij} and R transform as a two-index tensor and a scalar, respectively:

$$\delta\sigma'_{ij} = -\xi^k \partial_k \sigma'_{ij} - \sigma_{kj}\partial_i \xi^k - \sigma_{ik}\partial_j \xi^k, \tag{7.112}$$

$$\delta R = -\xi^k \partial_k R. \tag{7.113}$$

In a flat space the viscous stress tensor is given by

$$\sigma'_{ij} = \eta(\partial_i v_j + \partial_j v_i) + \left(\zeta - \tfrac{2}{3}\eta\right)\delta_{ij}\partial_k v^k, \tag{7.114}$$

where η and ζ are the shear and bulk viscosities. In the naive extension to the curved space where one simply covariantizes the spatial derivatives, σ'_{ij} is not a pure two-index tensor; its variation under the diffeomorphism contains extra terms proportional to $\dot{\xi}^k$. The correct extension is

$$\sigma'_{ij} = \eta(\nabla_i v_j + \nabla_j v_i + \dot{g}_{ij}) + \left(\zeta - \frac{2}{3}\eta\right) g_{ij} \left(\nabla_k v^k + \frac{\dot{g}}{2g}\right). \tag{7.115}$$

Similarly, the dissipative function R in the curved space becomes

$$2R = \frac{\eta}{2}\left(\nabla_i v_j + \nabla_j v_i - \frac{2}{3}g_{ij}\nabla_k v^k + \dot{g}_{ij} - \frac{1}{3}g_{ij}\frac{\dot{g}}{g}\right)^2$$

$$+ \zeta\left(\nabla_i v^i + \frac{\dot{g}}{2g}\right)^2 + \frac{\kappa}{T}\partial_i T \partial^i T. \tag{7.116}$$

We then turn to the conformal invariance. The dissipationless hydrodynamic equations are invariant under (7.104), if the dimensions of different fields are

$$\Delta[\rho] = 2\Delta[\psi] = 3, \quad \Delta[s] = 0, \quad \Delta[v^i] = 2. \tag{7.117}$$

Now let us consider the dissipation terms. From dimensional analysis, one finds that one has to set

$$\Delta[\eta] = \Delta[\zeta] = \Delta[\kappa] = \tfrac{3}{2} \tag{7.118}$$

for the hydrodynamic equations to be scale invariant. However, the conformal invariance is not preserved generically. The culprit is $\dot{g}_{ij}$ that transforms as

$$\delta \dot{g}_{ij} = -\beta \ddot{g}_{ij} + \ddot{\beta} g_{ij}, \tag{7.119}$$

which leads to σ'_{ij} and R not to conform to the pattern of (7.104), unless the bulk viscosity ζ vanishes. Thus the requirement of the conformal invariance of the hydrodynamic equations implies $\zeta = 0$.

7.4.1.2 Superfluid Phase

Similarly, we can repeat the argument for the superfluid case. The hydrodynamics of superfluids contains an additional degree of freedom, which is the condensate phase θ, whose gauge-covariant gradient is the superfluid velocity:

$$v_i^s = \frac{\hbar}{m}(\partial_i \theta + A_i). \tag{7.120}$$

It transforms in the same way as the normal velocity $v_i \equiv v_i^n$ under the general coordinate and conformal transformations. Its consequence is that the relative velocity between the superfluid and normal components $w^i = v_s^i - v^i$ transforms as a pure vector under the diffeomorphism:

$$\delta w^i = -\xi^k \partial_k w^i + w^k \partial_k \xi^i. \tag{7.121}$$

The $\dot{\xi}^i$ term in the variation cancels between δv_s and δv.

The diffeomorphism-invariant dissipative function in the curved space is

$$
\begin{aligned}
2R = \frac{\eta}{2} &\left(\nabla_i v_j + \nabla_j v_i - \frac{2}{3} g_{ij} \nabla_k v^k + \dot{g}_{ij} - \frac{1}{3} g_{ij} \frac{\dot{g}}{g} \right)^2 \\
&+ 2\zeta_1 \left(\nabla_i v^i + \frac{\dot{g}}{2g} \right) \nabla_j (\rho_s w^j) + \zeta_2 \left(\nabla_i v^i + \frac{\dot{g}}{2g} \right)^2 \\
&+ \zeta_3 [\nabla_i (\rho_s w^i)]^2 + \frac{\kappa}{T} \partial_i T \partial^i T.
\end{aligned}
\tag{7.122}
$$

Under the conformal transformations, R transforms as

$$
\delta R = -\beta \dot{R} - \frac{7}{2} \dot{\beta} R + \frac{3}{2} \zeta_1 \ddot{\beta} \nabla_i (\rho w^i) + \frac{3}{2} \zeta_2 \ddot{\beta} \left(\nabla_i v^i + \frac{\dot{g}}{2g} \right).
\tag{7.123}
$$

The requirement of the conformal invariance of the superfluid hydrodynamics implies that the $\ddot{\beta}$ terms must have vanishing coefficients, i.e., $\zeta_1 = \zeta_2 = 0$.

In conclusion, we find that in the unitary limit, the bulk viscosity vanishes in the normal phase. In the superfluid phase, two of the three bulk viscosities vanish.

7.4.2 Superfluid Effective Field Theory

At zero temperature, the long-distance dynamics of the unitary Fermi gas is described by an effective field theory, with some effective action S_{eff}. The effective theory should inherit the general coordinate invariance of the microscopic theory. This means that the effective action is invariant under the general coordinate transformations, which in its turn means that

$$
\delta \mathcal{L} = -\xi^k \partial_k \mathcal{L}.
\tag{7.124}
$$

The low-energy degree of freedom is the phase of the condensate θ. The time reversal symmetry means that the effective theory is invariant under

$$
t \to -t \quad \text{and} \quad \theta \to -\theta.
\tag{7.125}
$$

Since θ is a Nambu-Goldstone field, it should always appear with derivatives in the effective Lagrangian. Therefore, for power counting purposes, we can set $\dot{\theta}, \partial_i \theta \sim O(p^0)$. The leading-order effective Lagrangian should be

$$
\mathcal{L} = \mathcal{L}(\dot{\theta}, \partial_i \theta, A_0, A_i, g_{ij}).
\tag{7.126}
$$

The gauge invariance and the invariance with respect to three-dimensional general coordinate transformations (with time-independent ξ^i) limit the Lagrangian to be a function of two variables:

$$\mathcal{L} = \mathcal{L}\left(D_t\theta, \, g^{ij}D_i\theta D_j\theta\right), \tag{7.127}$$

where

$$D_t\theta = \dot{\theta} - A_0 \quad \text{and} \quad D_i\theta = \partial_i\theta - A_i. \tag{7.128}$$

The invariance of the effective theory with respect to general coordinate transformations requires

$$\mathcal{L} = P(X) \quad \text{with} \quad X = D_t\theta - \frac{g^{ij}}{2m}D_i\theta D_j\theta. \tag{7.129}$$

If we now set the metric to be flat and the external field to be zero, we find the most general form of the Lagrangian for superfluids:

$$\mathcal{L} = P\left(\dot{\theta} - \frac{(\partial_i\theta)^2}{2m}\right), \tag{7.130}$$

which was previously found by Greiter et al. [37] using a different line of arguments. Moreover, by studying the thermodynamics of the effective theory one finds that the function $P(X)$ is the same function that determines the dependence of the pressure on the chemical potential. To the next-to-leading order, the effective Lagrangian contains terms with two additional derivatives. The symmetries restrict the number of independent terms in the Lagrangian to two. This allows one to relate different physical quantities with each other [14].

7.5 Other Scale and Conformal Invariant Systems

We have discussed various theoretical aspects of the unitary Fermi gas. Finally we conclude this chapter by introducing other systems exhibiting the nonrelativistic scaling and conformal symmetries, to which a part of above results can be applied. One such system is a mass-imbalanced Fermi gas with both two-body and three-body resonances, which is already mentioned in Sect. 7.3.3.2. Its many-body physics is studied in Ref. [17].

The other systems are multi-species Fermi gases in mixed dimensions [18]. In all systems listed in Table 7.5, the coupling of the contact interaction term that involves all species has the dimension $[c_0] = -1$ and thus the theory with such an interaction term is renormalizable. In particular, when the coupling c_0 is tuned to its nontrivial fixed point ($c_0 \neq 0$) that describes an interspecies resonance, the resulting system becomes scale invariant. We can derive the reduced Schrödinger algebra and the operator-state correspondence for such a system [38]. The few-body and many-body physics of multi-species Fermi gases in mixed dimensions are studied in Refs. [18, 38–41]. Some of these systems can be in principle realized in ultracold atom experiments. Indeed the 2D–3D mixture has been recently realized using ^{41}K and ^{87}Rb and the interspecies scattering resonances were observed [42].

Table 7.5 Eight classes of scale invariant nonrelativistic systems proposed in Ref. [18]

# of species and dimensions	Spatial configurations	Symmetries +M, D, C, H
2 species in pure 3D	$x_A = x_B = (x, y, x)$	P_i, K_i, J_{ij} with $i, j = x, y, z$
2 species in 2D–3D mixture	$x_A = (x, y)$ $x_B = (x, y, z)$	P_i, K_i, J_{ij} with $i, j = x, y$
2 species in 1D–3D mixture	$x_A = (z)$ $x_B = (x, y, z)$	P_z, K_z, J_{xy}
2 species in 2D–2D mixture	$x_A = (x, z)$ $x_B = (y, z)$	P_z, K_z
2 species in 1D–2D mixture	$x_A = (z)$ $x_B = (x, y)$	J_{xy}
3 species in 1D–1D–1D mixture	$x_A = (x)$ $x_B = (y)$ $x_C = (z)$	None
3 species in 1D^2–2D mixture	$x_A = x_B = (x)$ $x_C = (x, y)$	P_x, K_x
4 species in pure 1D	$x_A = x_B = x_C = x_D = (x)$	P_x, K_x

In all cases, the coupling of the interspecies contact interaction term has the dimension $[c_0] = -1$ and can be tuned to the nontrivial fixed point describing an interspecies resonance

Appendix: Scaling Dimensions of Three-Body Operators

In this Appendix, we derive the formula to compute the scaling dimensions of three-body composite operators for arbitrary mass ratio $m_\uparrow/m_\downarrow$, angular momentum l, and spatial dimension d from a field theory perspective. We first consider a three-body operator composed of two spin-$\uparrow$ and one spin-$\downarrow$ fermions with zero orbital angular momentum $l = 0$:

$$\mathcal{O}_{\uparrow\uparrow\downarrow}^{(l=0)}(\boldsymbol{x}) \equiv Z_\Lambda^{-1} \phi \psi_\uparrow(\boldsymbol{x}), \tag{7.131}$$

where Z_Λ is a cutoff-dependent renormalization factor. We study the renormalization of the composite operator $\phi \psi_\uparrow$ by evaluating its matrix element $\langle 0 | \phi \psi_\uparrow(\boldsymbol{x}) | p, -p \rangle$. Feynman diagrams to renormalize $\phi \psi_\uparrow$ is depicted in Fig. 7.15. The vertex function $Z(p_0, \boldsymbol{p})$ in Fig. 7.15 satisfies the following integral equation:

$$\begin{aligned}
Z(p_0, \boldsymbol{p}) &= 1 - i \int \frac{dk_0 d\boldsymbol{k}}{(2\pi)^{d+1}} G_\uparrow(k) G_\downarrow(-p-k) D(-k) Z(k_0, \boldsymbol{k}) \\
&= 1 - \int \frac{d\boldsymbol{k}}{(2\pi)^d} G_\downarrow(-p-k) D(-k) Z(k_0, \boldsymbol{k}) \Big|_{k_0 = \frac{k^2}{2m_\uparrow}},
\end{aligned} \tag{7.132}$$

where we used the analyticity of $Z(k_0, \boldsymbol{k})$ on the lower half plane of k_0. $G_\sigma(p) \equiv \left(p_0 - \frac{p^2}{2m_\sigma} + 0^+ \right)^{-1}$ is the fermion propagator and $D(p)$ is the resumed propagator of ϕ field given in Eq. 7.78. If we set $p_0 = \frac{p^2}{2m_\uparrow}$, Eq. 7.132 reduces to the integral equation for $z(\boldsymbol{p}) \equiv Z\left(\frac{p^2}{2m_\uparrow}, \boldsymbol{p} \right)$.

Because of the scale and rotational invariance of the system, we can assume the form of $z(\boldsymbol{p})$ to be $z(\boldsymbol{p}) \propto \left(\frac{|\boldsymbol{p}|}{\Lambda} \right)^\gamma$, where Λ is a momentum cutoff. Accordingly the renormalization factor becomes $Z_\Lambda \propto \Lambda^{-\gamma}$ with $\gamma = -\partial \ln Z_\Lambda / \partial \ln \Lambda$ being the anomalous dimension of the composite operator $\phi \psi_\uparrow$. In terms of γ, the scaling dimension of the renormalized operator $\mathcal{O}_{\uparrow\uparrow\downarrow}^{(l=0)}$ is given by
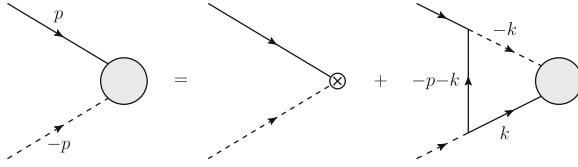
Fig. 7.15 Feynman diagrams to renormalize three-body composite operators. The *solid lines* are the propagators of $\psi_\uparrow$ and $\psi_\downarrow$ fields while the *dotted lines* are the resumed propagators of ϕ field. The *shaded bulbs* represent the vertex function $Z(p)$

$$\Delta_{\uparrow\uparrow\downarrow}^{(l=0)} = \Delta_\phi + \Delta_{\psi_\uparrow} + \gamma = 2 + \frac{d}{2} + \gamma. \tag{7.133}$$

Substituting the expression of $z(\boldsymbol{p})$ into Eq. 7.132 and performing the integration over $|\boldsymbol{k}|$ at $\Lambda \to \infty$, we obtain the following equation to determine γ:

$$1 = \frac{2\pi^{1/2} \left[\frac{m_\downarrow (2m_\uparrow + m_\downarrow)}{(m_\uparrow + m_\downarrow)^2} \right]^{1-d/2}}{\Gamma \left(1 - \frac{d}{2}\right) \Gamma \left(\frac{d-1}{2}\right) \sin[(\gamma+1)\pi]} \int_0^\pi d\theta \, \sin^{d-2}\theta \, \frac{\sin[(\gamma+1)\chi]}{\sin\chi} \tag{7.134}$$

with $\cos\chi \equiv \frac{m_\uparrow}{m_\uparrow + m_\downarrow} \cos\theta$. The integration over θ can be done analytically in $d = 3$, but otherwise, has to be done numerically.

Similarly, for general orbital angular momentum l, we can derive the equation satisfied by the anomalous dimension γ_l:

$$1 = \frac{2\pi^{1/2} \left[\frac{m_\downarrow (2m_\uparrow + m_\downarrow)}{(m_\uparrow + m_\downarrow)^2} \right]^{1-d/2}}{\Gamma \left(1 - \frac{d}{2}\right) \Gamma \left(\frac{d-1}{2}\right) \sin[(\gamma_l + l + 1)\pi]} \int_0^\pi d\theta \, \sin^{d-2}\theta \, \tilde{P}_l(\cos\theta) \frac{\sin[(\gamma_l + l + 1)\chi]}{\sin\chi}, \tag{7.135}$$

where $\tilde{P}_l(z)$ is a Legendre polynomial generalized to d spatial dimensions.[7] The scaling dimension of the renormalized operator $\mathcal{O}_{\uparrow\uparrow\downarrow}^{(l)}$ with orbital angular momentum l is now given by

$$\Delta_{\uparrow\uparrow\downarrow}^{(l)} = \Delta_\phi + \Delta_{\psi_\uparrow} + l + \gamma_l = 2 + \frac{d}{2} + l + \gamma_l. \tag{7.136}$$

$\Delta_{\uparrow\uparrow\downarrow}^{(l)}$ for $l = 0, 1$ in $d = 3$ are plotted as functions of the mass ratio $m_\uparrow/m_\downarrow$ in Fig. 7.12, while $\Delta_{\uparrow\uparrow\downarrow}^{(l)}$ for $l = 0, 1$ with equal masses $m_\uparrow = m_\downarrow$ are plotted in Fig. 7.14 as functions of the spatial dimension d.

---

[7] $\tilde{P}_0(z) = 1$, $\tilde{P}_1(z) = z$, ...

References

1. Regal, C.A., Greiner, M., Jin, D.S.: Phys. Rev. Lett. **92**, 040403 (2004) [arXiv:cond-mat/0401554]
2. Zwierlein, M.W., Stan, C.A., Schunck, C.H., Raupach, S.M.F., Kerman, A.J., Ketterle, W.: Phys. Rev. Lett. **92**, 120403 (2004) [arXiv:cond-mat/0403049]
3. Eagles, D.M.: Phys. Rev. **186**, 456 (1969)
4. Leggett, A.J.: Diatomic molecules and cooper Paris. In: Pekalski, A., Przystawa, R. (eds.) Modern Trends in the Theory of Condensed Matter. Springer, Berlin (1980)
5. Leggett, A.J.: J. Phys. (Paris) Colloq **41**, C7-19 (1980)
6. Nozières, P., Schmitt-Rink, S.: J. Low Temp. Phys. **59**, 195 (1985)
7. Nishida, Y., Son, D.T.: Phys. Rev. Lett. **97**, 050403 (2006) [arXiv:cond-mat/0604500]
8. Nishida, Y., Son, D.T.: Phys. Rev. A **75**, 063617 (2007) [arXiv:cond-mat/0607835]
9. Nishida, Y.: Phys. Rev. A **75**, 063618 (2007) [arXiv:cond-mat/0608321]
10. Arnold, P., Drut, J.E., Son, D.T.: Phys. Rev. A **75**, 043605 (2007) [arXiv:cond-mat/0608477]
11. Nishida, Y.: Phys. Rev. A **79**, 013627 (2009) [arXiv:0808.3826 [cond-mat.other]]
12. Nishida, Y., Son, D.T.: Phys. Rev. D **76**, 086004 (2007) [arXiv:0706.3746 [hep-th]]
13. Son, D.T.: Phys. Rev. Lett. **98**, 020604 (2007) [arXiv:cond-mat/0511721]
14. Son, D.T., Wingate, M.: Ann. Phys. **321**, 197 (2006) [arXiv:cond-mat/0509786]
15. Hagen, C.R.: Phys. Rev. D **5**, 377 (1972)
16. Niederer, U.: Helv. Phys. Acta **45**, 802 (1972)
17. Nishida, Y., Son, D.T., Tan, S.: Phys. Rev. Lett. **100**, 090405 (2008) [arXiv:0711.1562 [cond-mat.other]]
18. Nishida, Y., Tan, S.: Phys. Rev. Lett. **101**, 170401 (2008) [arXiv:0806.2668 [cond-mat.other]]
19. Nussinov, Z., Nussinov, S.: Phys. Rev. A **74**, 053622 (2006) [arXiv:cond-mat/0410597]
20. Nishida, Y.: Unitary Fermi gas in the ϵ expansion. Ph.D. Thesis, University of Tokyo (2007) [arXiv:cond-mat/0703465]
21. Nikolic, P., Sachdev, S.: Phys. Rev. A **75**, 033608 (2007) [arXiv:cond-mat/0609106]
22. Carlson, J., Reddy, S.: Phys. Rev. Lett. **95**, 060401 (2005) [arXiv:cond-mat/0503256]
23. Burovski, E., Prokof'ev, N., Svistunov, B., Troyer, M.: Phys. Rev. Lett. **96**, 160402 (2006) [arXiv:cond-mat/0602224]
24. Henkel, M.: J. Statist. Phys. **75**, 1023 (1994) [arXiv:hep-th/9310081]
25. Werner, F., Castin, Y.: Phys. Rev. Lett. **97**, 150401 (2006a) [arXiv:cond-mat/0507399]
26. Werner, F., Castin, Y.: Phys. Rev. A **74**, 053604 (2006b) [arXiv:cond-mat/0607821]
27. Tan, S.: Short range scaling laws of quantum gases with contact interactions. arXiv:cond-mat/0412764
28. Bertulani, C.A., Hammer, H.W., Van Kolck, U.: Nucl. Phys. A **712**, 37 (2002) [arXiv:nucl-th/0205063]
29. Hammer, H.W., Lee, D.: Phys. Lett. B **681**, 500 (2009) [arXiv:0907.1763 [nucl-th]]
30. Hammer, H.W., Lee, D.: Causality and the effective range expansion. arXiv:1002.4603 [nucl-th]
31. Busch, T., Englert, B.-G., Rzążewski, K., Wilkens, M.: Found. Phys. **28**, 549 (1998)
32. Stöferle, T., Moritz, H., Günter, K., Köhl, M., Esslinger, T.: Phys. Rev. Lett. **96**, 030401 (2006) [arXiv:cond-mat/0509211]
33. Efimov, V.: Sov. Phys. JETP Lett. **16**, 34 (1972)
34. Efimov, V.: Nucl. Phys. A **210**, 157 (1973)
35. Blume, D., von Stecher, J., Greene, C.H.: Phys. Rev. Lett. **99**, 233201 (2007) [arXiv:0708.2734 [cond-mat.other]]
36. Castin, Y.: Comptes Rendues Physique **5**, 407 (2004) [arXiv:cond-mat/0406020]
37. Greiter, M., Wilczek, F., Witten, E.: Mod. Phys. Lett. B **3**, 903 (1989)
38. Nishida, Y.: Ann. Phys. **324**, 897 (2009) [arXiv:0810.1321 [cond-mat.other]]

39. Nishida, Y., Tan, S.: Phys. Rev. A **79**, 060701 (2009) [arXiv:0903.3633 [cond-mat.other]]
40. Nishida, Y.: Phys. Rev. A **82**, 011605(R) (2010) [arXiv:0906.4584 [cond-mat.quant-gas]]
41. Nishida, Y., Son, D.T.: Phys. Rev. A **82**, 043606 (2010) [arXiv:0908.2159 [cond-mat.quant-gas]]
42. Lamporesi, G., Catani, J., Barontini, G., Nishida, Y., Inguscio, M., Minardi, F.: Phys. Rev. Lett. **104**, 153202 (2010) [arXiv:1002.0114 [cond-mat.quant-gas]]

Chapter 8
Dilute Fermi and Bose Gases

Subir Sachdev

Abstract We give a unified perspective on the properties of a variety of quantum liquids using the theory of quantum phase transitions. A central role is played by a zero density quantum critical point which is argued to control the properties of the dilute gas. An exact renormalization group analysis of such quantum critical points leads to a computation of the universal properties of the dilute Bose gas and the spinful Fermi gas near a Feshbach resonance.

8.1 Introduction

It is not conventional to think of dilute quantum liquids as being in the vicinity of a quantum phase transition. However, there is a simple sense in which they are, although there is often no broken symmetry or order parameter associated with this quantum phase transition. We shall show below that the perspective of such a quantum phase transition allows a unified and efficient description of the universal properties of quantum liquids.

Stated most generally, consider a quantum liquid with a global U(1) symmetry. We shall be particularly interested in the behavior of the conserved density, generically denoted by Q (usually the particle number), associated with this symmetry. The quantum phase transition is between two phases with a specific $T = 0$ behavior in the expectation value of Q. In one of the phases, $\langle Q \rangle$ is pinned precisely at a quantized value (often zero) and does not vary as microscopic parameters are varied. This

S. Sachdev (✉)
Department of Physics, Harvard University,
Cambridge, 02138 MA, USA
e-mail: sachdev@physics.harvard.edu

quantization ends at the quantum critical point with a discontinuity in the derivative of $\langle Q \rangle$ with respect to the tuning parameter (usually the chemical potential), and $\langle Q \rangle$ varies smoothly in the other phase; there is no discontinuity in the value of $\langle Q \rangle$, however.

The most familiar model exhibiting such a quantum phase transition is the dilute Bose gas. We express its coherent state partition function, Z_B, in terms of complex field $\Psi_B(x, \tau)$, where x is a d-dimensional spatial co-ordinate and τ is imaginary time:

$$Z_B = \int \mathscr{D}\Psi_B(x, \tau) \exp\left(-\int_0^{1/T} d\tau \int d^d x \mathscr{L}_B\right),$$

$$\mathscr{L}_B = \Psi_B^* \frac{\partial \Psi_B}{\partial \tau} + \frac{1}{2m}|\nabla \Psi_B|^2 - \mu|\Psi_B|^2 + \frac{u_0}{2}|\Psi_B|^4. \tag{8.1}$$

We can identify the charge Q with the boson density $\Psi_B^* \Psi_B$

$$\langle Q \rangle = -\frac{\partial \mathscr{F}_B}{\partial \mu} = \langle |\Psi_B|^2 \rangle, \tag{8.2}$$

with $\mathscr{F}_B = -(T/V) \ln Z_B$. The quantum critical point is precisely at $\mu = 0$ and $T = 0$, and there are *no* fluctuation corrections to this location from the terms in $\mathscr{L}_B$. So at $T = 0$, $\langle Q \rangle$ takes the quantized value $\langle Q \rangle = 0$ for $\mu < 0$, and $\langle Q \rangle > 0$ for $\mu > 0$; we will describe the nature of the onset at $\mu = 0$ and finite-T crossovers in its vicinity.

Actually, we will begin our analysis in Sect. 8.2 by a model simpler than Z_B, which displays a quantum phase transition with the same behavior in a conserved U(1) density $\langle Q \rangle$ and has many similarities in its physical properties. The model is exactly solvable and is expressed in terms of a continuum canonical spinless fermion field Ψ_F; its partition function is

$$Z_F = \int \mathscr{D}\Psi_F(x, \tau) \exp\left(-\int_0^{1/T} d\tau \int d^d x \mathscr{L}_F\right),$$

$$\mathscr{L}_F = \Psi_F^* \frac{\partial \Psi_F}{\partial \tau} + \frac{1}{2m}|\nabla \Psi_F|^2 - \mu|\Psi_F|^2. \tag{8.3}$$

$\mathscr{L}_F$ is just a free field theory. Like Z_B, Z_F has a quantum critical point at $\mu = 0$, $T = 0$ and we will discuss its properties; in particular, we will show that all possible fermionic nonlinearities are irrelevant near it. The reader should not be misled by the apparently trivial nature of the model in (8.3); using the theory of quantum phase transitions to understand free fermions might seem like technological overkill. We will see that Z_F exhibits crossovers that are quite similar to those near far more complicated quantum critical points, and observing them in this simple context leads to considerable insight.

In general spatial dimension, d, the continuum theories Z_B and Z_F have different, though closely related, universal properties. However, we will argue that the quantum critical points of these theories are *exactly* equivalent in $d = 1$. We will see that the bosonic theory Z_B is strongly coupled in $d = 1$, and will note compelling evidence that the solvable fermionic theory Z_F is its exactly universal solution in the vicinity of the $\mu = 0$, $T = 0$ quantum critical point. This equivalence extends to observable operators in both theories, and allows exact computation of a number of universal properties of Z_B in $d = 1$.

Our last main topic will be a discussion of the dilute spinful Fermi gas in Sect. 8.4. This generalizes Z_F to a spin $S = 1/2$ fermion $\Psi_{F\sigma}$, with $\sigma = \uparrow, \downarrow$. Now Fermi statistics do allow a contact quartic interaction, and so we have

$$Z_{Fs} = \int \mathscr{D}\Psi_{F\uparrow}(x, \tau)\mathscr{D}\Psi_{F\downarrow}(x, \tau) \exp\left(-\int\limits_0^{1/T} d\tau \int d^d x \mathscr{L}_{Fs}\right),$$

$$\mathscr{L}_{Fs} = \Psi_{F\sigma}^* \frac{\partial \Psi_{F\sigma}}{\partial \tau} + \frac{1}{2m}|\nabla\Psi_{F\sigma}|^2 - \mu|\Psi_{F\sigma}|^2 + u_0\Psi_{F\uparrow}^*\Psi_{F\downarrow}^*\Psi_{F\downarrow}\Psi_{F\uparrow}. \quad (8.4)$$

This theory conserves fermion number, and has a phase transition as a function of increasing μ from a state with fermion number 0 to a state with non-zero fermion density. However, unlike the above two cases of Z_B and Z_F, the transition is not always at $\mu = 0$. The problem defined in (8.4) has recently found remarkable experimental applications in the study of ultracold gases of fermionic atoms. These experiments are aslo able to tune the value of the interaction u_0 over a wide range of values, extended from repulsive to attractive. For the attractive case, the two-particle scattering amplitude has a Feshbach resonance where the scattering length diverges, and we obtain the unitarity limit. We will see that this Feshbach resonance plays a crucial role in the phase transition obtained by changing μ, and leads to a rich phase diagram of the so-called "unitary Fermi gas".

Our treatment of Z_{Fs} in the experimental important case of $d = 3$ will show that it defines a strongly coupled field theory in the vicinity of the Feshbach resonance for attractive interactions. It therefore pays to find alternative formulations of this regime of the unitary Fermi gas. One powerful approach is to promote the two fermion bound state to a separate canonical Bose field. This yields a model, Z_{FB} with both elementary fermions and bosons; i.e., it is a combination of Z_B and Z_{Fs} with interactions between the fermions and bosons. We will define Z_{FB} in Sect. 8.4, and use it to obtain a number of experimentally relevant results for the unitary Fermi gas.

Section 8.2 will present a thorough discussion of the universal properties of Z_F. This will be followed by an analysis of Z_B in Sect. 8.3, where we will use renormalization group methods to obtain perturbative predictions for universal properties. The spinful Fermi gas will be discussed in Sect. 8.4.

8.2 The Dilute Spinless Fermi Gas

This section will study the properties of Z_F in the vicinity of its $\mu = 0$, $T = 0$ quantum critical point. As Z_F is a simple free field theory, all results can be obtained exactly and are not particularly profound in themselves. Our main purpose is to show how the results are interpreted in a scaling perspective and to obtain general lessons on the nature of crossovers at $T > 0$.

First, let us review the basic nature of the quantum critical point at $T = 0$. A useful diagnostic for this is the conserved density Q, which in the present model we identify as $\Psi_F^\dagger \Psi_F$. As a function of the tuning parameter μ, this quantity has a critical singularity at $\mu = 0$:

$$\langle \Psi_F^\dagger \Psi_F \rangle = \begin{cases} (S_d/d)(2m\mu)^{d/2}, & \mu > 0, \\ 0, & \mu < 0, \end{cases} \tag{8.5}$$

where the phase space factor $S_d = 2/[\Gamma(d/2)(4\pi)^{d/2}]$.

We now proceed to a scaling analysis. Notice that at the quantum critical point $\mu = 0$, $T = 0$, the theory $\mathcal{L}_F$ is invariant under the scaling transformations:

$$\begin{aligned} x' &= xe^{-\ell}, \\ \tau' &= \tau e^{-z\ell}, \\ \Psi_F' &= \Psi_F e^{d\ell/2}, \end{aligned} \tag{8.6}$$

provided we make the choice of the dynamic exponent

$$z = 2. \tag{8.7}$$

The parameter m is assumed to remain invariant under the rescaling, and its role is simply to ensure that the relative physical dimensions of space and time are compatible. The transformation (8.6) also identifies the scaling dimension

$$\dim[\Psi_F] = d/2. \tag{8.8}$$

Now turning on a nonzero μ, it is easy to see that μ is a relevant perturbation with

$$\dim[\mu] = 2. \tag{8.9}$$

There will be no other relevant perturbations at this quantum critical point, and so we have for the correlation length exponent

$$\nu = 1/2. \tag{8.10}$$

We can now examine the consequences of adding interactions to $\mathcal{L}_F$. A contact interaction such as $\int dx (\Psi_F^\dagger(x)\Psi_F(x))^2$ vanishes because of the fermion anticommutation relation. (A contact interaction is however permitted for a spin-1/2 Fermi

gas and will be discussed in Sect. 8.4). The simplest allowed term for the spinless Fermi gas is

$$\mathscr{L}_1 = \lambda\big(\Psi_F^\dagger(x,\tau)\nabla\Psi_F^\dagger(x,\tau)\Psi_F(x,\tau)\nabla\Psi_F(x,\tau)\big), \tag{8.11}$$

where λ is a coupling constant measuring the strength of the interaction. However, a simple analysis shows that

$$\dim[\lambda] = -d. \tag{8.12}$$

This is negative and so λ is irrelevant and can be neglected in the computation of universal crossovers near the point $\mu = T = 0$. In particular, it will modify the result (8.5) only by contributions that are higher order in μ.

Turning to nonzero temperatures, we can write down scaling forms. Let us define the fermion Green's function

$$G_F(x,t) = \big\langle\Psi_F(x,t)\Psi_F^\dagger(0,0)\big\rangle; \tag{8.13}$$

then the scaling dimensions above imply that it satisfies

$$G_F(x,t) = (2mT)^{d/2}\,\Phi_{G_F}\left((2mT)^{1/2}x, Tt, \frac{\mu}{T}\right), \tag{8.14}$$

where Φ_{G_F} is a fully universal scaling function. For this particularly simple theory $\mathscr{L}_F$ we can of course obtain the result for G_F in closed form:

$$G_F(x,t) = \int \frac{d^dk}{(2\pi)^d}\frac{e^{ikx-i(k^2/(2m)-\mu)t}}{1+e^{-(k^2/(2m)-\mu)/T}}, \tag{8.15}$$

and it is easy to verify that this obeys the scaling form (8.14). Similarly the free energy $\mathscr{F}_F$ has scaling dimension $d + z$, and we have

$$\mathscr{F}_F = T^{d/2+1}\Phi_{\mathscr{F}_F}\left(\frac{\mu}{T}\right) \tag{8.16}$$

with $\Phi_{\mathscr{F}_F}$ a universal scaling function; the explicit result is, of course,

$$\mathscr{F}_F = -\int \frac{d^dk}{(2\pi)^d}\ln\big(1+e^{(\mu-k^2/(2m))/T}\big), \tag{8.17}$$

which clearly obeys (8.16). The crossover behavior of the fermion density

$$\langle Q\rangle = \big\langle\Psi_F^\dagger\Psi_F\big\rangle = -\frac{\partial\mathscr{F}_F}{\partial\mu} \tag{8.18}$$

follows by taking the appropriate derivative of the free energy. Examination of these results leads to the crossover phase diagram of Fig. 8.1. We will examine each of the regions of the phase diagram in turn, beginning with the two low-temperature regions.
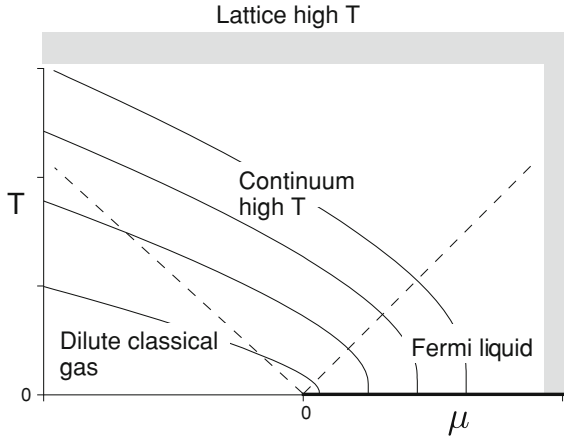
Fig. 8.1 Phase diagram of the dilute Fermi gas Z_F (Eq. 8.3) as a function of the chemical potential μ and the temperature T. The regions are separated by crossovers denoted by dashed lines, and their physical properties are discussed in the text. The full lines are contours of equal density, with higher densities above lower densities; the zero density line is $\mu < 0$, $T = 0$. The line $\mu > 0$, $T = 0$ is a line of $z = 1$ critical points that controls the longest scale properties of the low-T Fermi liquid region. The critical end point $\mu = 0$, $T = 0$ has $z = 2$ and controls global structure of the phase diagram. In $d = 1$, the Fermi liquid is more appropriately labeled a Tomonaga–Luttinger liquid. The shaded region marks the boundary of applicability of the continuum theory and occurs at $\mu, T \sim w$

8.2.1 Dilute Classical Gas, $k_B T \ll |\mu|$, $\mu < 0$

The ground state for $\mu < 0$ is the vacuum with no particles. Turning on a nonzero temperature produces particles with a small nonzero density $\sim e^{-|\mu|/T}$. The de Broglie wavelength of the particles is of order $T^{-1/2}$, which is significantly smaller than the mean spacing between the particles, which diverges as $e^{|\mu|/dT}$ as $T \to 0$. This implies that the particles behave semiclassically. To leading order from (8.15), the fermion Green's function is simply the Feynman propagator of a single particle

$$G_F(x, t) = \left(\frac{m}{2\pi i t}\right)^{d/2} \exp\left(-\frac{imx^2}{2t}\right), \qquad (8.19)$$

and the exclusion of states from the other particles has only an exponentially small effect. Notice that G_F is independent of μ and T and (8.19) is the exact result for $\mu = T = 0$. The free energy, from (8.16) and (8.17), is that of a classical Boltzmann gas

$$\mathscr{F}_F = -\left(\frac{mT}{2\pi}\right)^{d/2} e^{-|\mu|/T}. \qquad (8.20)$$

8.2.2 Fermi Liquid, $k_B T \ll \mu$, $\mu > 0$

The behavior in this regime is quite complex and rich. As we will see, and as noted in Fig. 8.1, the line $\mu > 0$, $T = 0$ is itself a line of quantum critical points. The interplay between these critical points and those of the $\mu = 0$, $T = 0$ critical end point is displayed quite instructively in the exact results for G_F and is worth examining in detail. It must be noted that the scaling dimensions and critical exponents of these two sets of critical points need not (and indeed will not) be the same. The behavior of the $\mu > 0$, $T = 0$ critical line emerges as a particular scaling limit of the global scaling functions of the $\mu = 0$, $T = 0$ critical end point. Thus the latter scaling functions are globally valid everywhere in Fig. 8.1, and describe the physics of all its regimes.

First it can be argued, for example, by studying asymptotics of the integral in (8.15), that for very short times or distances, the correlators do not notice the consequences of other particles present because of a nonzero T or μ and are therefore given by the single-particle propagator, which is the $T = \mu = 0$ result in (8.19). More precisely we have

$$G(x, t) \text{ is given by (8.19) for } |x| \ll (2m\mu)^{-1/2}, \quad |t| \ll \frac{1}{\mu}. \tag{8.21}$$

With increasing x or t, the restrictions in (8.21) are eventually violated and the consequences of the presence of other particles, resulting from a nonzero μ, become apparent. Notice that because μ is much larger than T, it is the first energy scale to be noticed, and as a first approximation to understand the behavior at larger x we may ignore the effects of T.

Let us therefore discuss the ground state for $\mu > 0$. It consists of a filled Fermi sea of particles (a Fermi liquid) with momenta $k < k_F = (2m\mu)^{1/2}$. An important property of the this state is that it permits excitations at arbitrarily low energies (i.e., it is *gapless*). These low energy excitations correspond to changes in occupation number of fermions arbitrarily close to k_F. As a consequence of these gapless excitations, the points $\mu > 0$ ($T = 0$) form a line of quantum critical points, as claimed earlier. We will now derive the continuum field theory associated with this line of critical points. We are interested here only in x and t values that violate the constraints in (8.21), and so in occupation of states with momenta near $\pm k_F$. So let us parameterize, in $d = 1$,

$$\Psi(x, \tau) = e^{ik_F x} \Psi_R(x, \tau) + e^{-ik_F x} \Psi_L(x, \tau), \tag{8.22}$$

where $\Psi_{R,L}$ describe right- and left-moving fermions and are fields that vary slowly on spatial scales $\sim 1/k_F = (1/2m\mu)^{1/2}$ and temporal scales $\sim 1/\mu$; most of the results discussed below hold, with small modifications, in all d. Inserting the above parameterization in $\mathscr{L}_F$, and keeping only terms lowest order in spatial gradients, we obtain the "effective" Lagrangean for the Fermi liquid region, $\mathscr{L}_{FL}$ in $d = 1$:

$$\mathscr{L}_{FL} = \Psi_R^\dagger \left(\frac{\partial}{\partial \tau} - i v_F \frac{\partial}{\partial x} \right) \Psi_R + \Psi_L^\dagger \left(\frac{\partial}{\partial \tau} + i v_F \frac{\partial}{\partial x} \right) \Psi_L, \tag{8.23}$$

where $v_F = k_F/m = (2\mu/m)^{1/2}$ is the Fermi velocity. Now notice that $\mathscr{L}_{FL}$ is invariant under a scaling transformation, which is rather different from (8.6) for the $\mu = 0$, $T = 0$ quantum critical point:

$$
\begin{aligned}
x' &= xe^{-\ell}, \\
\tau' &= \tau e^{-\ell}, \\
\Psi'_{R,L}(x',\tau') &= \Psi_{R,L}(x,\tau)e^{\ell/2}, \\
v'_F &= v_F.
\end{aligned} \tag{8.24}
$$

The above results imply

$$
z = 1, \tag{8.25}
$$

unlike $z = 2$ (Eq. 8.7) at the $\mu = 0$ critical point, and

$$
\dim[\Psi_{R,L}] = 1/2, \tag{8.26}
$$

which actually holds for all d and therefore differs from (8.8). Further notice that v_F, and therefore μ, are *invariant* under rescaling, unlike (8.9) at the $\mu = 0$ critical point. Thus v_F plays a role rather analogous to that of m at the $\mu = 0$ critical point: it is simply the physical units of spatial and length scales. The transformations (8.24) show that $\mathscr{L}_{LF}$ is scale invariant for each value of μ, and we therefore have a line of quantum critical points as claimed earlier. It should also be emphasized that the scaling dimension of interactions such as λ will also change; in particular not all interactions are irrelevant about the $\mu \neq 0$ critical points. These new interactions are, however, small in magnitude provided μ is small (i.e., provided we are within the domain of validity of the global scaling forms (8.14) and (8.16), and so we will neglect them here. Their main consequence is to change the scaling dimension of certain operators, but they preserve the relativistic and conformal invariance of $\mathscr{L}_{FL}$. This more general theory of $d = 1$ fermions is the Tomonaga–Luttinger liquid.

8.2.3 High-T Limit, $k_B T \gg |\mu|$

This is the last, and in many ways the most interesting, region of Fig. 8.1. Now T is the most important energy scale controlling the deviation from the $\mu = 0$, $T = 0$ quantum critical point, and the properties will therefore have some similarities to the "quantum critical region" of other strongly interacting models [17]. It should be emphasized that while the value of T is significantly larger than $|\mu|$, it cannot be so large that it exceeds the limits of applicability for the continuum action $\mathscr{L}_F$. If we imagine that $\mathscr{L}_F$ was obtained from a model of lattice fermions with bandwidth w, then we must have $T \ll w$.

We discuss first the behavior of the fermion density. In the high-T limit of the continuum theory $\mathscr{L}_F$, $|\mu| \ll T \ll w$, we have from (8.17) and (8.18) the universal

result

$$\langle \Psi_F^\dagger \Psi_F \rangle = (2mT)^{d/2} \int \frac{d^d y}{(2\pi)^d} \frac{1}{e^{y^2}+1} = (2mT)^{d/2} \zeta(d/2) \frac{(1-2^{d/2})}{(4\pi)^{d/2}}. \quad (8.27)$$

This density implies an interparticle spacing that is of order the de Broglie wavelength $= (1/2mT)^{1/2}$. Hence thermal and quantum effects are to be equally important, and neither dominate.

For completeness, let us also consider the fermion density for $T \gg w$ (the region above the shaded region in Fig. 8.1), to illustrate the limitations on the continuum description discussed above. Now the result depends upon the details of the nonuniversal fermion dispersion; on a hypercubic lattice with dispersion $\varepsilon_k - \mu$, we obtain

$$\langle \Psi_F^\dagger \Psi_F \rangle = \int_{-\pi/a}^{\pi/a} \frac{d^d k}{(2\pi)^d} \frac{1}{e^{(\varepsilon_k - \mu)/T} + 1}$$

$$= \frac{1}{2a^d} - \frac{1}{4T} \int_{-\pi/a}^{\pi/a} \frac{d^d k}{(2\pi)^d} (\varepsilon_k - \mu) + \mathcal{O}(1/T^2). \quad (8.28)$$

The limits on the integration, which extend from $-\pi/a$ to π/a for each momentum component, had previously been sent to infinity in the continuum limit $a \to 0$. In the presence of lattice cutoff, we are able to make a naive expansion of the integrand in powers of $1/T$, and the result therefore only contains negative integer powers of T. Contrast this with the universal continuum result (8.27) where we had noninteger powers of T dependent upon the scaling dimension of Ψ.

We return to the universal high-T region, $|\mu| \ll T \ll w$, and describe the behavior of the fermionic Green's function G_F, given in (8.15). At the shortest scales we again have the free quantum particle behavior of the $\mu = 0$, $T = 0$ critical point:

$$G_F(x, t) \text{ is given by (8.19) for } |x| \ll (2mT)^{-1/2}, \quad |t| \ll \frac{1}{T}. \quad (8.29)$$

Notice that the limits on x and t in (8.29) are different from those in (8.21), in that they are determined by T and not μ. At larger $|x|$ or t the presence of the other thermally excited particles becomes apparent, and G_F crosses over to a novel behavior characteristic of the high-T region. We illustrate this by looking at the large-x asymptotics of the equal-time G in $d = 1$ (other d are quite similar):

$$G_F(x, 0) = \int \frac{dk}{2\pi} \frac{e^{ikx}}{1 + e^{-k^2/2mT}}. \quad (8.30)$$

For large x this can be evaluated by a contour integration, which picks up contributions from the poles at which the denominator vanishes in the complex k plane.

The dominant contributions come from the poles closest to the real axis, and give the leading result

$$G_F(|x| \to \infty, 0) = - \left(\frac{\pi^2}{2mT} \right)^{1/2} \exp\left(-(1-i)\, (m\pi T)^{1/2}\, x \right). \qquad (8.31)$$

Thermal effects therefore lead to an exponential decay of equal-time correlations, with a correlation length $\xi = (m\pi T)^{-1/2}$. Notice that the T dependence is precisely that expected from the exponent $z = 2$ associated with the $\mu = 0$ quantum critical point and the general scaling relation $\xi \sim T^{-1/z}$. The additional oscillatory term in (8.31) is a reminder that quantum effects are still present at the scale ξ, which is clearly of order the de Broglie wavelength of the particles.

8.3 The Dilute Bose Gas

This section will study the universal properties quantum phase transition of the dilute Bose gas model Z_B in (8.1) in general dimensions. We will begin with a simple scaling analysis that will show that $d = 2$ is the upper-critical dimension. The first subsection will analyse the case $d < 2$ in some more detail, while the next subsection will consider the somewhat different properties in $d = 3$. Some of the results of this section were also obtained by Kolomeisky and Straley [9, 10].

We begin with the analog of the simple scaling considerations presented at the beginning of Sect. 8.2. At the coupling $u = 0$, the $\mu = 0$ quantum critical point of $\mathscr{L}_B$ is invariant under the transformations (8.6), after the replacement $\Psi_F \to \Psi_B$, and we have as before $z = 2$ and

$$\dim[\Psi_B] = d/2, \qquad \dim[\mu] = 2; \qquad (8.32)$$

these results will shortly be seen to be exact in all d. We can easily determine the scaling dimension of the quartic coupling u at the $u = 0$, $\mu = 0$ fixed point under the bosonic analog of the transformations (8.6); we find

$$\dim[u_0] = 2 - d. \qquad (8.33)$$

Thus the free-field fixed point is stable for $d > 2$, in which case it is suspected that a simple perturbative analysis of the consequences of u will be adequate. However, for $d < 2$, a more careful renormalization group–based resummation of the consequences of u is required. This identifies $d = 2$ as the upper-critical dimension of the present quantum critical point.

Our analysis of the case $d < 2$ for the dilute Bose gas quantum critical point will find, somewhat surprisingly, that all the renormalizations, and the associated flow equations, can be determined exactly in closed form. We begin by considering the one-loop renormalization of the quartic coupling u_0 at the $\mu = 0$, $T = 0$ quantum

Fig. 8.2 The ladder series of diagrams that contribute the renormalization of the coupling u in Z_B for $d < 2$
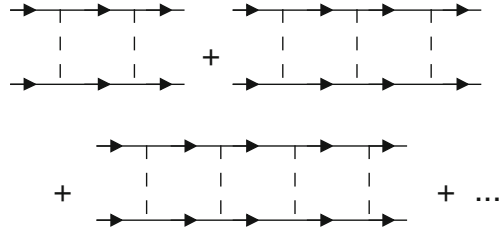
critical point. It turns out that only the ladder series of Feynman diagrams shown in Fig. 8.2 need be considered (the T matrix). Evaluating the first term of the series in Fig. 8.2 for the case of zero external frequency and momenta, we obtain the contribution

$$-u_0^2 \int \frac{d\omega}{2\pi} \int \frac{d^d k}{(2\pi)^d} \frac{1}{(-i\omega + k^2/(2m))} \frac{1}{(i\omega + k^2/(2m))} = -u_0^2 \int \frac{d^d k}{(2\pi)^d} \frac{m}{k^2} \tag{8.34}$$

(the remaining ladder diagrams are powers of (8.34) and form a simple geometric series). Notice the infrared singularity for $d < 2$, which is cured by moving away from the quantum critical point, or by external momenta.

We can proceed further by a simple application of the momentum shell RG. Note that we will apply cutoff Λ only in momentum space. The RG then proceeds by integrating *all* frequencies, and momentum modes in the shell between $\Lambda e^{-\ell}$ and Λ. The renormalization of the coupling u_0 is then given by the first diagram in Fig. 8.2, and after absorbing some phase space factors by a redefinition of interaction coupling

$$u_0 = \frac{\Lambda^{2-d}}{2m S_d} u, \tag{8.35}$$

we obtain [6, 7]

$$\frac{du}{d\ell} = \varepsilon u - \frac{u^2}{2}. \tag{8.36}$$

Here $S_d = 2/(\Gamma(d/2)(4\pi)^{d/2})$ is the usual phase space factor, and

$$\varepsilon = 2 - d. \tag{8.37}$$

Note that for $\varepsilon > 0$, there is a stable fixed point at

$$u^* = 2\varepsilon, \tag{8.38}$$

which will control all the universal properties of Z_B.

The flow equation (8.36), and the fixed point value (8.38) are *exact* to all orders in u or ε, and it is not necessary to consider u-dependent renormalizations to the

field scale of Ψ_B or any of the other couplings in Z_B. This result is ultimately a consequence of a very simple fact: The ground state of Z_B at the quantum critical point $\mu = 0$ is simply the empty vacuum with no particles. So any interactions that appear are entirely due to particles that have been created by the external fields. In particular, if we introduce the bosonic Green's function [the analog of (8.15)]

$$G_B(x, t) = \langle \Psi_B(x, t) \Psi_B^\dagger(0, 0) \rangle, \tag{8.39}$$

then for $\mu \leq 0$ and $T = 0$, its Fourier transform $G(k, \omega)$ is given exactly by the free field expression

$$G_B(k, \omega) = \frac{1}{-\omega + k^2/(2m) - \mu}. \tag{8.40}$$

The field $\Psi_B^\dagger$ creates a particle that travels freely until its annihilation at (x, t) by the field Ψ_B; there are no other particles present at $T = 0$, $\mu \leq 0$, and so the propagator is just the free field one. The simple result (8.40) implies that the scaling dimensions in (8.32) are exact. Turning to the renormalization of u, it is clear from the diagram in Fig. 8.2 that we are considering the interactions of just two particles. For these, the only nonzero diagrams are the one shown in Fig. 8.2, which involve repeated scattering of just these particles. Formally, it is possible to write down many other diagrams that could contribute to the renormalization of u; however, all of these vanish upon performing the integral over internal frequencies for there is always one integral that can be closed in one half of the frequency plane where the integrand has no poles. This absence of poles is of course just a more mathematical way of stating that there are no other particles around.

We will consider application of these renormalization group results separately for the cases below and above the upper-critical dimension of $d = 2$.

8.3.1 $d < 2$

First, let us note some important general implications of the theory controlled by the fixed point interaction (8.38). As we have already noted, the scaling dimensions of Ψ_B and μ are given precisely by their free field values in (8.32), and the dynamic exponent z also retains the tree-level value $z = 2$. All these scaling dimensions are identical to those obtained for the case of the spinless Fermi gas in Sect. 8.2. Further, the presence of a nonzero and universal interaction strength u^* in (8.38) implies that the bosonic system is stable for the case $\mu > 0$ because the repulsive interactions will prevent the condensation of infinite density of bosons (no such interaction was necessary for the fermion case, as the Pauli exclusion was already sufficient to stabilize the system). These two facts imply that the formal scaling structure of the bosonic fixed point being considered here is identical to that of the fermionic one considered in Sect. 8.2 and that the scaling forms of the two theories are *identical*. In particular, G_B will

obey a scaling form identical to that for G_F in (8.14) (with a corresponding scaling function Φ_{G_B}), while the free energy, and associated derivatives, obey (8.16) (with a scaling function $\Phi_{\mathscr{F}_B}$). The universal functions Φ_{G_B} and $\Phi_{\mathscr{F}_B}$ can be determined order by order in the present $\varepsilon = 2 - d$ expansion, and this will be illustrated shortly.

Although the fermionic and bosonic fixed points share the same scaling dimensions, they are distinct fixed points for general $d < 2$. However, these two fixed points are identical precisely in $d = 1$ [19]. Evidence for this was presented in Ref. [5], where the anomalous dimension of the composite operator Ψ_B^2 was computed exactly in the ε expansion and was found to be identical to that of the corresponding fermionic operator. Assuming the identity of the fixed points, we can then make a stronger statement about the universal scaling function: those for the free energy (and all its derivatives) are identical $\Phi_{\mathscr{F}_B} = \Phi_{\mathscr{F}_F}$ in $d = 1$. In particular, from (8.17) and (8.18) we conclude that the boson density is given by

$$\langle Q \rangle = \langle \Psi_B^\dagger \Psi_B \rangle = \int \frac{dk}{2\pi} \frac{1}{e^{(k^2/(2m)-\mu)/T} + 1} \tag{8.41}$$

in $d = 1$ only. The operators Ψ_B and Ψ_F are still distinct and so there is no reason for the scaling functions of their correlators to be the same. However, in $d = 1$, we can relate the universal scaling function of Ψ_B to those of Ψ_F via a continuum version of the Jordan-Wigner transformation

$$\Psi_B(x, t) = \exp\left(i\pi \int_{-\infty}^{x} dy\, \Psi_F^\dagger(y, t) \Psi_F(y, t) \right) \Psi_F(x, t). \tag{8.42}$$

This identity is applied to numerous exact results in Ref. [17]

As not all observables can be computed exactly in $d = 1$ by the mapping to the free fermions, we will now consider the $\varepsilon = 2 - d$ expansion. We will present a simple ε expansion calculation [18] for illustrative purposes. We focus on density of bosons at $T = 0$. Knowing that the free energy obeys the analog of (8.16), we can conclude that a relationship like (8.5) holds:

$$\langle \Psi_B^\dagger \Psi_B \rangle = \begin{cases} \mathscr{C}_d (2m\mu)^{d/2}, & \mu > 0, \\ 0, & \mu < 0, \end{cases} \tag{8.43}$$

at $T = 0$, with $\mathscr{C}_d$ a universal number. The identity of the bosonic and fermionic theories in $d = 1$ implies from (8.5) or from (8.41) that $\mathscr{C}_1 = S_1/1 = 1/\pi$. We will show how to compute $\mathscr{C}_d$ in the ε expansion; similar techniques can be used for almost any observable.

Even though the position of the fixed point is known exactly in (8.38), not all observables can be computed exactly because they have contributions to arbitrary order in u. However, universal results can be obtained order-by-order in u, which then become a power series in $\varepsilon = 2 - d$. As an example, let us examine the low order contributions to the boson density. To compute the boson density for $\mu > 0$, we anticipate that there is condensate of the boson field Ψ_B, and so we write

$$\Psi_B(x, \tau) = \Psi_0 + \Psi_1(x, t), \tag{8.44}$$

where Ψ_1 has no zero wavevector and frequency component. Inserting this into $\mathscr{L}_B$ in (8.1), and expanding to second order in Ψ_1, we get

$$\mathscr{L}_1 = -\mu|\Psi_0|^2 + \frac{u_0}{2}|\Psi_0|^4 - \Psi_1^* \frac{\partial \Psi_1}{\partial \tau} + \frac{1}{2m}|\nabla\Psi_1|^2$$
$$- \mu|\Psi_1|^2 + \frac{u_0}{2}\left(4|\Psi_0|^2|\Psi_1|^2 + \Psi_0^2\Psi_1^{*2} + \Psi_0^{*2}\Psi_1^2\right). \tag{8.45}$$

This is a simple quadratic theory in the canonical Bose field Ψ_1, and its spectrum and ground state energy can be determined by the familiar Bogoliubov transformation. Carrying out this step, we obtain the following formal expression for the free energy density $\mathscr{F}$ as a function of the condensate Ψ_0 at $T = 0$:

$$\mathscr{F}(\Psi_0) = -\mu|\Psi_0|^2 + \frac{u_0}{2}|\Psi_0|^4$$
$$+ \frac{1}{2}\int \frac{d^d k}{(2\pi)^d}\left[\left\{\left(\frac{k^2}{2m} - \mu + 2u_0|\Psi_0|^2\right)^2 - u_0^2|\Psi_0|^4\right\}^{1/2}\right.$$
$$\left. - \left(\frac{k^2}{2m} - \mu + 2u_0|\Psi_0|^2\right)\right]. \tag{8.46}$$

To obtain the physical free energy density, we have to minimize $\mathscr{F}$ with respect to variations in Ψ_0 and to substitute the result back into (8.46). Finally, we can take the derivative of the resulting expression with respect to μ and obtain the required expression for the boson density, correct to the first two orders in u_0:

$$\langle \Psi_B^\dagger \Psi_B \rangle = \frac{\mu}{u_0} + \frac{1}{2}\int \frac{d^d k}{(2\pi)^d}\left[1 - \frac{k^2}{\sqrt{k^2(k^2 + 4m\mu)}}\right]. \tag{8.47}$$

To convert (8.47) into a universal result, we need to evaluate it at the coupling appropriate to the fixed point (8.38). This is most easily done by the field-theoretic RG. So let us translate the RG equation (8.36) into this language. We introduce a momentum scale $\tilde{\mu}$ (the tilde is to prevent confusion with the chemical potential) and express u_0 in terms of a dimensionless coupling u_R by

$$u_0 = u_R \frac{(2m)\tilde{\mu}^\varepsilon}{S_d}\left(1 + \frac{u_R}{2\varepsilon}\right). \tag{8.48}$$

The motivation behind the choice of the renormalization factor in (8.48) is that the renormalized four-point coupling, when expressed in terms of u_R, and evaluated in $d = 2 - \varepsilon$, is free of poles in ε as can easily be explicitly checked using (8.34) and the associated geometric series. Then, we evaluate (8.47) at the fixed point value of u_R, compute any physical observable as a formal diagrammatic expansion in u_0, substitute u_0 in favor of u_R using (8.48), and expand the resulting expression in

powers of ε. All poles in ε should cancel, but the resulting expression will depend upon the arbitrary momentum scale $\tilde{\mu}$. At the fixed point value u_R^*, dependence upon $\tilde{\mu}$ then disappears and a universal answer remains. In this manner we obtain from (8.47) a universal expression in the form (8.43) with

$$\mathscr{C}_d = S_d \left[\frac{1}{2\varepsilon} + \frac{\ln 2 - 1}{4} + \mathscr{O}(\varepsilon) \right]. \tag{8.49}$$

8.3.2 $d = 3$

Now we briefly discuss $2 < d < 4$: details appear elsewhere [17]. In $d = 2$, the upper critical dimension, there are logarithmic corrections which were computed by Prokof'ev et al. [15]. Related results, obtained through somewhat different methods, are available in the literature [6, 13, 14, 19].

The quantum critical point at $\mu = 0$, $T = 0$ is above its upper-critical dimension, and we expect mean-field theory to apply. The analog of the mean-field result in the present context is the $T = 0$ relation for the density

$$\langle \Psi_B^\dagger \Psi_B \rangle = \begin{cases} \mu/u_0 + \cdots, & \mu > 0, \\ 0, & \mu < 0, \end{cases} \tag{8.50}$$

where the ellipses represents terms that vanish faster as $\mu \to 0$. Notice that this expression for the density is not universally dependent upon μ; rather it depends upon the strength of the two-body interaction u_0 (more precisely, it can be related to the s-wave scattering length a by $u_0 = 4\pi a/m$).The crossovers and phase transitions at $T > 0$ are sketched in Fig. 8.3. These are similar to those of the spinless Fermi gas, but now there can be a phase transition within one of the regions. Explicit expressions for the crossovers [17] have been presented by Rasolt et al. [16], Weichman et al. [29] and also addressed in earlier work [3, 22, 23].

8.4 The Dilute Spinful Fermi Gas: The Feshbach Resonance

This section turns to the case of the spinful Fermi gas with short-range interactions; as we noted in the introduction, this is a problem which has acquired renewed importance because of the new experiments on ultracold fermionic atoms.

The partition function of the theory examined in this section was displayed in (8.4). The renormalization group properties of this theory in the zero density limit are *identical* to those the dilute Bose gas considered in Sect. 8.3. The scaling dimensions of the couplings are the same, the scaling dimension of $\Psi_{F\sigma}$ is $d/2$ as for Ψ_B in (8.32), and the flow of the u is given by (8.36). Thus for $d < 2$, a spinful Fermi gas with repulsive interactions is described by the stable fixed point in (8.38).

However, for the case of spinful Fermi gas case, we can consider another regime of parameters which is of great experimental importance. We can also allow u to
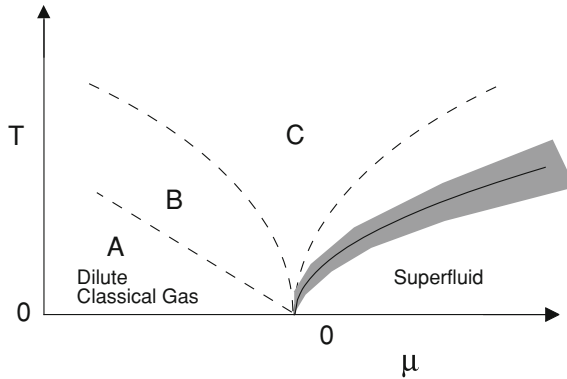
Fig. 8.3 Crossovers of the dilute Bose gas in $d=3$ as a function of the chemical potential μ and the temperature T. The regimes labeled A, B, C are described in Ref. [17]. The solid line is the finite-temperature phase transition where the superfluid order disappears; the shaded region is where there is an effective classical description of thermal fluctuations. The contours of constant density are similar to those in Fig. 8.1 and are not displayed
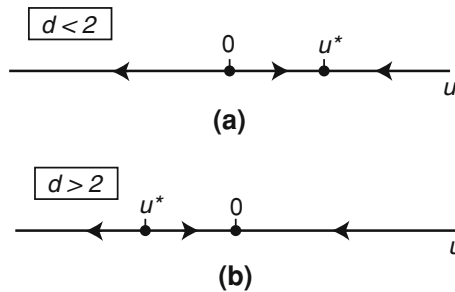
Fig. 8.4 The exact RG flow of (8.36). **a** For $d < 2$ ($\varepsilon > 0$), the infrared stable fixed point at $u = u^* > 0$ describes quantum liquids of either bosons or fermions with repulsive interactions which are generically universal in the low density limit. In $d=1$ this fixed point is described by the spinless free Fermi gas ('Tonks' gas), for all statistics and spin of the constituent particles. **b** For $d > 2$ ($\varepsilon < 0$) the infrared unstable fixed point at $u = u^* < 0$ describes the Feshbach resonance which obtains for the case of attractive interactions. The relevant perturbation $(u - u^*)$ corresponds to the the detuning from the resonant interaction

be attractive: unlike the Bose gas case, the $u < 0$ case is not immediately unstable, because the Pauli exclusion principle can stabilize a Fermi gas even with attractive interactions. Furthermore, at the same time we should also consider the physically important case with $d > 2$, when $\varepsilon < 0$. The distinct nature of the RG flows predicted by (8.36) for the two signs of ε are shown in Fig. 8.4.

Notice the *unstable* fixed point present for $d > 2$ and $u < 0$. Thus accessing the fixed point requires fine-tuning of the microscopic couplings. As discussed in [11, 12], this fixed point describes a Fermi gas at a *Feshbach resonance,* where the interaction between the fermions is universal. For $u < u^*$, the flow is to $u \to -\infty$:

this corresponds to a strong attractive interaction between the fermions, which then bind into tightly bound pairs of bosons, which then Bose condense; this corresponds to the so-called 'BEC' regime. On the other hand, for $u > u^*$, the flow is to $u \nearrow 0$, and the weakly interacting fermions then form the Bardeen-Cooper-Schrieffer (BCS) superconducting state.

Note that the fixed point at $u = u^*$ for Z_{Fs} has *two* relevant directions for $d > 2$. As in the other problems considered earlier, one corresponds to the chemical potential μ. The other corresponds to the deviation from the critical point $u - u^*$, and this [from (8.36)] has RG eigenvalue $-\varepsilon = d - 2 > 0$. This perturbation corresponds to the "detuning" from the Feshbach resonance, ν (not to be confused with the symbol for the correlation length exponent); we have $\nu \propto u - u^*$. Thus we have

$$\dim[\mu] = 2, \quad \dim[\nu] = d - 2. \tag{8.51}$$

These two relevant perturbations will have important consequences for the phase diagram, as we will see shortly.

For now, let us understand the physics of the Feshbach resonance better. For this, it is useful to compute the two body T matrix exactly by summing the graphs in Fig. 8.2, along with a direct interaction first order in u_0. The second order term was already evaluated for the bosonic case in (8.34) for zero external momentum and frequency, and has an identical value for the present fermionic case. Here, however, we want the off-shell T-matrix, for the case in which the incoming particles have momenta $k_{1,2}$, and frequencies $\omega_{1,2}$. Actual for the simple momentum-independent interaction u_0, the T matrix depends only upon the sums $k = k_1 + k_2$ and $\omega = \omega_1 + \omega_2$, and is independent of the final state of the particles, and the diagrams in Fig. 8.2 form a geometric series. In this manner we obtain

$$\frac{1}{T(k, i\omega)} = \frac{1}{u_0}$$

$$+ \int \frac{d\Omega}{2\pi} \int \frac{d^d p}{(2\pi)^d} \frac{1}{(-i(\Omega + \omega) + (p + k)^2/(2m))} \frac{1}{(i\Omega + p^2/(2m))}$$

$$= \frac{1}{u_0} + \int_0^\Lambda \frac{d^d p}{(2\pi)^d} \frac{m}{p^2} + \frac{\Gamma(1 - d/2)}{(4\pi)^{d/2}} m^{d/2} \left[-i\omega + \frac{k^2}{4m} \right]^{d/2 - 1}.$$

$$\tag{8.52}$$

In $d = 3$, the s-wave scattering amplitude of the two particles, f_0, is related to the T-matrix at zero center of mass momentum and frequency k^2/m by $f_0(k) = -mT(0, k^2/m)/(4\pi)$, and so we obtain

$$f_0(k) = \frac{1}{-1/a - ik} \tag{8.53}$$

where the scattering length, a, is given by

$$\frac{1}{a} = \frac{4\pi}{mu_0} + \int_0^\Lambda \frac{d^3 p}{(2\pi)^3} \frac{4\pi}{p^2}. \tag{8.54}$$
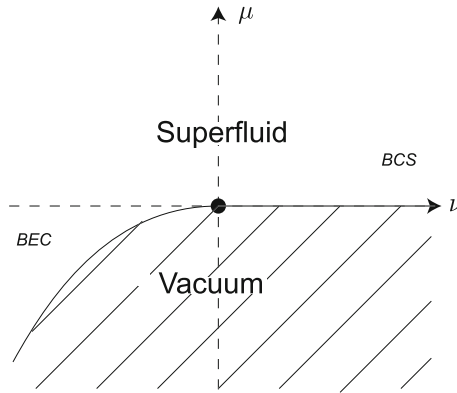
Fig. 8.5 Universal phase diagram at zero temperature for the spinful Fermi gas in $d = 3$ as a function of the chemical potential μ and the detuning ν. The vacuum state (shown hatched) has no particles. The position of the $\nu < 0$ phase boundary is determined by the energy of the two-fermion bound state in (8.56): $\mu = -\nu^2/(2m)$. The density of particles vanishes continuously at the second order quantum phase transition boundary of the superfluid phase, which is indicated by the thin continuous line. The quantum multicritical point at $\mu = \nu = 0$ (denoted by the filled circle) controls all the universal physics of the dilute spinful Fermi gas near a Feshbach resonance. The universal properties of the critical line $\mu = 0$, $\nu > 0$ map onto the theory of Sect. 8.2, while those of the critical line $\mu = -\nu^2/(2m)$, $\nu < 0$ map onto the theory of Sect. 8.3. This implies that the $T > 0$ crossovers in Fig. 8.1 apply for $\nu > 0$ (the "Fermi liquid" region of Fig. 8.1 now has BCS superconductivity at an exponentially small T), while those of Fig. 8.3 apply for $\nu < 0$

For $u_0 < 0$, we see from (8.54) that there is a critical value of u_0 where the scattering length diverges and changes sign: this is the Feshbach resonance. We identify this critical value with the fixed point $u = u^*$ of the RG flow (8.36). It is conventional to identify the deviation from the Feshbach resonance by the detuning ν

$$\nu \equiv -\frac{1}{a}. \tag{8.55}$$

Note that $\nu \propto u - u^*$, as claimed earlier. For $\nu > 0$, we have weak attractive interactions, and the scattering length is negative. For $\nu < 0$, we have strong attractive interactions, and a positive scattering length. Importantly, for $\nu < 0$, there is a two-particle bound state, whose energy can be deduced from the pole of the scattering amplitude; recalling that the reduced mass in the center of mass frame is $m/2$, we obtain the bound state energy, E_b

$$E_b = -\frac{\nu^2}{m}. \tag{8.56}$$

We can now draw the zero temperature phase diagram [11] of Z_{Fs} as a function of μ and ν, and the result is shown in Fig. 8.5.

For $\nu > 0$, there is no bound state, and so no fermions are present for $\mu < 0$. At $\mu = 0$, we have an onset of non-zero fermion density, just as in the other sections. These fermions experience a weak attractive interaction, and so experience the Cooper instability once there is a finite density of fermions for $\mu > 0$. So the ground state for $\mu > 0$ is a paired BCS superfluid, as indicated in Fig. 8.5. For small negative scattering lengths, the BCS state modifies the fermion state only near the Fermi level. Consequently as $\mu \searrow 0$ (specifically for $\mu < \nu^2/m$,) we can neglect the pairing in computing the fermion density. We therefore conclude that the universal critical properties of the line $\mu = 0$, $\nu > 0$ map precisely on to two copies (for the spin degeneracy) of the non-interacting fermion model Z_F studied in Sect. 8.2. In particular the $T > 0$ properties for $\nu > 0$ will map onto the crossovers in Fig. 8.1. The only change is that the BCS pairing instability will appear below an exponentially small T in the "Fermi liquid" regime. However, the scaling functions for the density as a function of μ/T will remain unchanged.

For $\nu < 0$, the situation changes dramatically. Because of the presence of the bound state (8.56), it will pay to introduce fermions even for $\mu < 0$. The chemical potential for a fermion pair is 2μ, and so the threshold for having a non-zero density of paired fermions is $\mu = E_b/2$. This leads to the phase boundary shown in Fig. 8.5 at $\mu = -\nu^2/(2m)$. Just above the phase boundary, the density of fermion pairs in small, and so these can be treated as canonical bosons. Computations of the interactions between these bosons [11] show that they are repulsive. Therefore we map their dynamics onto those of the dilute Bose gas studied in Sect. 8.3. Thus the universal properties of the critical line $\mu = -\nu^2/(2m)$ are equivalent to those of Z_B. Specifically, this means that the $T > 0$ properties across this critical line map onto those of Fig. 8.3.

Thus we reach the interesting conclusion that the Feshbach resonance at $\mu = \nu = 0$ is a multicritical point separating the density onset transitions of Z_F (Sect. 8.2) and Z_B (Sect. 8.3). This conclusion can be used to sketch the $T > 0$ extension of Fig. 8.5, on either side of the $\nu = 0$ line.

We now need a practical method of computing universal properties of Z_{Fs} near the $\mu = \nu = 0$ fixed point, including its crossovers into the regimes described by Z_F and Z_B. The fixed point (8.36) of Z_{Fs} provides an expansion of the critical theory in the powers of $\varepsilon = 2 - d$. However, observe from Fig. 8.4, the flow for $u < u^*$ is to $u \to -\infty$. The latter flow describes the crossover into the dilute Bose gas theory, Z_B, and so this cannot be controlled by the $2 - d$ expansion. The following subsections will propose two alternative analyses of the Feshbach resonant fixed point which will address this difficulty.

8.4.1 The Fermi-Bose Model

One successful approach is to promote the two fermion bound state in (8.56) to a canonical boson field Ψ_B. This boson should also be able to mix with the scattering states of two fermions. We are therefore led to consider the following model

$$Z_{FB} = \int \mathscr{D}\Psi_{F\uparrow}(x,\tau)\mathscr{D}\Psi_{F\downarrow}(x,\tau)\mathscr{D}\Psi_B(x,\tau)\exp\left(-\int d\tau d^dx \mathscr{L}_{FB}\right),$$

$$\mathscr{L}_{FB} = \Psi_{F\sigma}^* \frac{\partial\Psi_{F\sigma}}{\partial\tau} + \frac{1}{2m}|\nabla\Psi_{F\sigma}|^2 - \mu|\Psi_{F\sigma}|^2$$
$$+ \Psi_B^* \frac{\partial\Psi_B}{\partial\tau} + \frac{1}{4m}|\nabla\Psi_{F\sigma}|^2 + (\delta - 2\mu)|\Psi_B|^2$$
$$- \lambda_0\left(\Psi_B^*\Psi_{F\uparrow}\Psi_{F\downarrow} + \Psi_B\Psi_{F\downarrow}^*\Psi_{F\uparrow}^*\right). \tag{8.57}$$

Here we have taken the bosons to have mass $2m$, because that is the expected mass of the two-fermion bound state by Galilean invariance. We have omitted numerous possible quartic terms between the bosons and fermions above, and these will turn out to be irrelevant in the analysis below.

The conserved U(1) charge for Z_{FB} is

$$Q = \Psi_{F\uparrow}^*\Psi_{F\uparrow} + \Psi_{F\downarrow}^*\Psi_{F\downarrow} + 2\Psi_B^*\Psi_B, \tag{8.58}$$

and so Z_{FB} is in the class of models being studied here. The factor of 2 in (8.58) accounts for the 2μ chemical potential for the bosons in (8.57). For μ sufficiently negative it is clear that Z_{FB} will have neither fermions nor bosons present, and so $\langle Q \rangle = 0$. Conversely for positive μ, we expect $\langle Q \rangle \neq 0$, indicating a transition as a function of increasing μ. Furthermore, for δ large and positive, the Q density will be primarily fermions, while for δ negative the Q density will be mainly bosons; thus we expect a Feshbach resonance at intermediate values of δ, which then plays the role of detuning parameter.

We have thus argued that the phase diagram of Z_{FB} as a function of μ and δ is qualitatively similar to that in Fig. 8.5, with a Feshbach resonant multicritical point near the center. The main claim of this section is that the universal properties of Z_{FB} and Z_{Fs} are *identical* near this multicritical point [11, 12]. Thus, in a strong sense, the theories Z_{FB} and Z_{Fs} are equivalent. Unlike the equivalence between Z_B and Z_F, which held only in $d = 1$, the present equivalence applies for $d > 2$.

We will establish the equivalence by an exact RG analysis of the zero density critical theory. We scale the spacetime co-ordinates and the fermion field as in (8.6), but allow an anomalous dimension η_b for the boson field relative to (8.32):

$$x' = xe^{-\ell},$$
$$\tau' = \tau e^{-z\ell},$$
$$\Psi_{F\sigma}' = \Psi_{F\sigma}e^{d\ell/2}, \tag{8.59}$$
$$\Psi_B' = \Psi_B e^{(d+\eta_b)\ell/2}$$
$$\lambda_0' = \lambda_0 e^{(4-d-\eta_b)\ell/2}$$

where, as before, we have $z = 2$. At tree level, the theory Z_{FB} with $\mu = \delta = 0$ is invariant under the transformations in (8.59) with $\eta_b = 0$. At this level, we see that the coupling λ_0 is relevant for $d < 4$, and so we will have to consider the influence
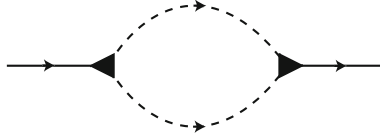
Fig. 8.6 Feynman diagram contributing to the RG. The dark triangle is the λ_0 vertex, the full line is the Ψ_B propagator, and the dashed line is the Ψ_F propagator

of λ_0. This also suggests that we may be able to obtain a controlled expansion in powers of $(4-d)$.

Upon considering corrections in powers of λ_0 in the critical theory, it is not difficult to show that there is a non-trivial contribution from only a single Feynman diagram: this is the self–energy diagram for Ψ_B which is shown in Fig. 8.6. All other diagrams vanish in the zero density theory, for reasons similar to those discussed for Z_B below (8.38). This diagram is closely related to the integrals in the T-matrix computation in (8.52), and leads to the following contribution to the boson self energy Σ_B:

$$\Sigma_B(k, i\omega)$$

$$= \lambda_0^2 \int \frac{d\Omega}{2\pi} \int\limits_{\Lambda e^{-\ell}}^{\Lambda} \frac{d^d p}{(2\pi)^d} \frac{1}{(-i(\Omega + \omega) + (p + k)^2/(2m))} \frac{1}{(i\Omega + p^2/(2m))}$$

$$= \lambda_0^2 \int\limits_{\Lambda e^{-\ell}}^{\Lambda} \frac{d^d p}{(2\pi)^d} \frac{1}{(-i\omega + (p + k)^2/(2m) + p^2/(2m))}$$

$$= \lambda_0^2 \int\limits_{\Lambda e^{-\ell}}^{\Lambda} \frac{d^d p}{(2\pi)^d} \frac{m}{p^2} - \lambda_0^2 \left(-i\omega + \frac{k^2}{4m}\left(2 - \frac{4}{d}\right)\right) \int\limits_{\Lambda e^{-\ell}}^{\Lambda} \frac{d^d p}{(2\pi)^d} \frac{m^2}{p^4}. \tag{8.60}$$

The first term is a constant that can absorbed into a redefinition of δ. For the first time, we see above a special role for the spatial dimension $d = 4$, where the momentum integral is logarithmic. Our computations below will turn to be an expansion in powers of $(4 - d)$, and so we will evaluate the numerical prefactors in (8.60) with $d = 4$. The result turns out to be correct to all orders in $(4-d)$, but to see this explicitly we need to use a proper Galilean-invariant cutoff in a field theoretic approach [11]. The simple momentum shell method being used here preserves Galilean invariance only in $d = 4$.

With the above reasoning, we see that the second term in the boson self-energy in (8.60) can be absorbed into a rescaling of the boson field under the RG. We therefore find a non-zero anomalous dimension

$$\eta_b = \lambda^2, \tag{8.61}$$

where we have absorbed phase space factors into the coupling λ by

Fig. 8.7 Feynman diagram for the mixing between the renormalization of the $\Psi_F^\dagger \Psi_F$ and $\Psi_B^\dagger \Psi_B$ operators. The filled circle is the $\Psi_F^\dagger \Psi_F$ source. Other notation is as in Fig. 8.6
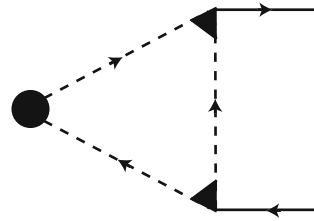
$$\lambda_0 = \frac{\Lambda^{2-d/2}}{m\sqrt{S_d}}\lambda. \tag{8.62}$$

With this anomalous dimension, we use (8.59) to obtain the exact RG equation for λ:

$$\frac{d\lambda}{d\ell} = \frac{(4-d)}{2}\lambda - \frac{\lambda^3}{2}. \tag{8.63}$$

For $d < 4$, this flow has a stable fixed point at $\lambda = \lambda^* = \sqrt{(4-d)}$. The central claim of this subsection is that the theory Z_{FB} at this fixed point is identical to the theory Z_{Fs} at the fixed point $u = u^*$ for $2 < d < 4$.

Before we establish this claim, note that at the fixed point, we obtain the exact result for the anomalous dimension of the the boson field

$$\eta_b = 4 - d. \tag{8.64}$$

Let us now consider the spectrum of relevant perturbations to the $\lambda = \lambda^*$ fixed point. As befits a Feshbach resonant fixed point, there are 2 relevant perturbations in Z_{FB}, the detuning parameter δ and the chemical potential μ. Apart from the tree level rescalings, at one loop we have the diagram shown in Fig. 8.7. This diagram has a $\Psi_{F\sigma}^\dagger \Psi_{F\sigma}$ source, and it renormalizes the co-efficient of $\Phi^\dagger\Phi$; it evaluates to

$$2\lambda_0^2 \int \frac{d\Omega}{2\pi} \int_{\Lambda e^{-\ell}}^{\Lambda} \frac{d^d p}{(2\pi)^d} \frac{1}{(-i\Omega + p^2/(2m))^2(i\Omega + p^2/(2m))}$$

$$= 2\lambda_0^2 \int_{\Lambda e^{-\ell}}^{\Lambda} \frac{d^d p}{(2\pi)^d} \frac{m^2}{p^4}. \tag{8.65}$$

Combining (8.65) with the tree-level rescalings, we obtain the RG flow equations

$$\frac{d\mu}{d\ell} = 2\mu$$

$$\frac{d}{d\ell}(\delta - 2\mu) = (2 - \eta_b)(\delta - 2\mu) - 2\lambda^2\mu, \tag{8.66}$$

where the last term arises from (8.65). With the value of η_b in (8.61), the second equation simplifies to

$$\frac{d\delta}{d\ell} = (2 - \lambda^2)\delta. \tag{8.67}$$

Thus we see that μ and δ are actually eigen-perturbations of the fixed point at $\lambda = \lambda^*$, and their scaling dimensions are

$$\dim[\mu] = 2, \quad \dim[\delta] = d - 2. \tag{8.68}$$

Note that these eigenvalues coincide with those of Z_{Fs} in (8.51), with δ identified as proportional to the detuning ν. This, along with the symmetries of Q conservation and Galilean invariance, establishes the equivalence of the fixed points of Z_{FB} and Z_{Fs}.

The utility of the present Z_{FB} formulation is that it can provide a description of universal properties of the unitary Fermi gas in $d = 3$ via an expansion in $(4 - d)$. Further details of explicit computations can be found in [12].

8.4.2 Large N Expansion

We now return to the model Z_{Fs} in (8.4), and examine it in the limit of a large number of spin components [11, 27]. We also use the structure of the large N perturbation theory to obtain exact results relating different experimental observable of the unitary Fermi gas.

The basic idea of the large N expansion is to endow the fermion with an additional flavor index $a = 1 \ldots N/2$, to the fermion field is $\Psi_{F\sigma a}$, where we continue to have $\sigma = \uparrow, \downarrow$. Then, we write Z_{Fs} as

$$Z_{Fs} = \int \mathcal{D}\Psi_{F\sigma a}(x, \tau) \exp\left(-\int_0^{1/T} d\tau \int d^d x \mathcal{L}_{Fs}\right),$$

$$\mathcal{L}_{Fs} = \Psi_{F\sigma a}^* \frac{\partial \Psi_{F\sigma a}}{\partial \tau} + \frac{1}{2m}|\nabla \Psi_{F\sigma a}|^2 - \mu|\Psi_{F\sigma a}|^2$$

$$+ \frac{2u_0}{N}\Psi_{F\uparrow a}^* \Psi_{F\downarrow a}^* \Psi_{F\downarrow b} \Psi_{F\uparrow b}. \tag{8.69}$$

where there is implied sum over $a, b = 1 \ldots N/2$. The case of interest has $N = 2$, but we will consider the limit of large even N, where the problem becomes tractable.

As written, there is an evident $O(N/2)$ symmetry in Z_{Fs} corresponding to rotations in flavor space. In addition, there is U(1) symmetry associated with Q conservation, and a SU(2) spin rotation symmetry. Actually, the spin and flavor symmetry combine to make the global symmetry U(1)$\times$ Sp(N), but we will not make much use of this interesting observation.

The large N expansion proceeds by decoupling the quartic term in (8.69) by a Hubbard-Stratonovich transformation. For this we introduce a complex bosonic field $\Psi_B(x, \tau)$ and write

$$Z_{Fs} = \int \mathscr{D}\Psi_{F\sigma a}(x, \tau)\mathscr{D}\Psi_B(x, \tau) \exp\left(-\int\limits_0^{1/T} d\tau \int d^d x \widetilde{\mathscr{L}}_{Fs}\right),$$

$$\widetilde{\mathscr{L}}_{Fs} = \Psi_{F\sigma a}^* \frac{\partial \Psi_{F\sigma a}}{\partial \tau} + \frac{1}{2m}|\nabla\Psi_{F\sigma a}|^2 - \mu|\Psi_{F\sigma a}|^2$$
$$+ \frac{N}{2|u_0|}|\Psi_B|^2 - \Psi_B\Psi_{F\uparrow a}^*\Psi_{F\downarrow a}^* - \Psi_B^*\Psi_{F\downarrow a}\Psi_{F\uparrow a}. \tag{8.70}$$

Here, and below, we assume $u_0 < 0$, which is necessary for being near the Feshbach resonance. Note that Ψ_B couples to the fermions just like the boson field in the Bose-Fermi model in (8.57), which is the reason for choosing this notation. If we perform the integral over Ψ_B in (8.70), we recover (8.69), as required. For the large N expansion, we have to integrate over $\Psi_{F\sigma a}$ first and obtain an effective action for Ψ_B. Because the action in (8.70) is Gaussian in the $\Psi_{F\sigma a}$, the integration over the fermion field involves evaluation of a functional determinant, and has the schematic form

$$\mathscr{Z}_{Fs} = \int \mathscr{D}\Psi_B(x, \tau) \exp\left(-N\mathscr{S}_{\text{eff}}[\Psi_B(x, \tau)]\right), \tag{8.71}$$

where $\mathscr{S}_{\text{eff}}$ is the logarithm of the fermion determinant of a single flavor. The key point is that the only N dependence is in the prefactor in (8.71), and so the theory of Ψ_B can controlled in powers of $1/N$.

We can expand $\mathscr{S}_{\text{eff}}$ in powers of Ψ_B: the p'th term has a fermion loop with p external Ψ_B insertions. Details can be found in [11, 27]. Here, we only note that the expansion to quadratic order at $\mu = \delta = T = 0$, in which case the co-efficient is precisely the inverse of the fermion T-matrix in (8.52):

$$\mathscr{S}_{\text{eff}}[\Psi_B(x, \tau)] = -\frac{1}{2}\int \frac{d\omega}{2\pi}\frac{d^d k}{(2\pi)^d}\frac{1}{T(k, i\omega)}|\Psi_B(k, \omega)|^2 + \dots \tag{8.72}$$

Given S_{eff}, we then have to find its saddle point with respect to Ψ_B. At $T = 0$, we will find the optimal saddle point at a $\Psi_B \neq 0$ in the region of Fig. 8.5 with a non-zero density: this means that the ground state is always a superfluid of fermion pairs. The traditional expansion about this saddle point yields the $1/N$ expansion, and many experimental observables have been computed in this manner [11, 27, 28].

We conclude our discussion of the unitary Fermi gas by deriving an exact relationship between the total energy, E, and the momentum distribution function, $n(k)$, of the fermions [25, 26]. We will do this using the structure of the large N expansion. However, we will drop the flavor index a below, and quote results directly for the physical case of $N = 2$. As usual, we define the momentum distribution function by

$$n(k) = \langle \Psi_{F\sigma}^\dagger (k, t) \Psi_{F\sigma}(k, t) \rangle, \tag{8.73}$$

with no implied sum over the spin label σ. The Hamiltonian of the system in (8.69) is the sum of kinetic and interaction energies: the kinetic energy is clearly an integral over $n(k)$ and so we can write

$$\begin{aligned}
E &= 2V \int \frac{d^d k}{(2\pi)^d} \frac{k^2}{2m} n(k) + u_0 V \langle \Psi_{F\uparrow}^\dagger \Psi_{F\downarrow}^\dagger \Psi_{F\downarrow} \Psi_{F\uparrow} \rangle \\
&= 2V \int \frac{d^d k}{(2\pi)^d} \frac{k^2}{2m} n(k) - u_0 \frac{\partial \ln Z_{Fs}}{\partial u_0}.
\end{aligned} \tag{8.74}$$

where V is the system volume, and all the Ψ_F fields are at the same x and t. Now let us evaluate the u_0 derivative using the expression for Z_{Fs} in (8.70); this leads to

$$\frac{E}{V} = 2 \int \frac{d^d k}{(2\pi)^d} \frac{k^2}{2m} n(k) + \frac{1}{u_0} \langle \Psi_B^*(x, t) \Psi_B(x, t) \rangle. \tag{8.75}$$

Now using the expression (8.54) relating u_0 to the scattering length a in $d = 3$, we can write this expression as

$$\frac{E}{V} = \frac{m}{4\pi a} \langle \Psi_B^* \Psi_B \rangle + 2 \int \frac{d^3 k}{(2\pi)^3} \frac{k^2}{2m} \left(n(k) - \frac{\langle \Psi_B^* \Psi_B \rangle m^2}{k^4} \right) \tag{8.76}$$

This is the needed universal expression for the energy, expressed in terms of $n(k)$ and the scattering length, and independent of the short distance structure of the interactions.

At this point, it is useful to introduce "Tan's constant" C, defined by [25, 26]

$$C = \lim_{k \to \infty} k^4 n(k). \tag{8.77}$$

The requirement that the momentum integral in (8.76) is convergent in the ultraviolet implies that the limit in (8.77) exists, and further specifies its value

$$C = m^2 \langle \Psi_B^* \Psi_B \rangle. \tag{8.78}$$

We now note that the relationship $n(k) \to m^2 \langle \Psi_B^* \Psi_B \rangle / k^4$ at large k is also as expected from a scaling perspective. We saw in Sect. 8.1 that the fermion field Ψ_F does not acquire any anomalous dimensions, and has scaling dimension $d/2$. Consequently $n(k)$ has scaling dimension zero. Next, note that the operator $\Psi_B^* \Psi_B$ is conjugate to the detuning from the Feshbach critical point; from (8.68) the detuning has scaling dimension $d - 2$, and so $\Psi_B^* \Psi_B$ has scaling dimension $d + z - (d - 2) = 4$. Combining these scaling dimensions, we explain the k^{-4} dependence of $n(k)$.

It now remains to establish the claimed exact relationship in (8.78) as a general property of a spinful Fermi gas near unitarity. As a start, we can examine the large k limit of $n(k)$ in the BCS mean field theory of the superfluid phase: the reader can

easily verify that the text-book BCS expressions for $n(k)$ do indeed satisfy (8.78). However, the claim of [1, 24] is that (8.78) is exact beyond mean field theory, and also holds in the non-superfluid states at non-zero temperatures. A general proof was given in [24], and relied on the operator product expansion (OPE) applied to the field theory (8.70). The OPE is a general method for describing the short distance and time (or large momentum and frequency) behavior of field theories. Typically, in the Feynman graph expansion of a correlator, the large momentum behavior is dominated by terms in which the external momenta flow in only a few propagators, and the internal momentum integrals can be evaluated after factoring out these favored propagators. For the present situation, let us consider the $1/N$ correction to the fermion Green's function given by the diagram in Fig. 8.8. Representing the bare fermion and boson Green's functions by G_F and G_B respectively, Fig. 8.8 evaluates to

$$G_F^2(k, \omega) \int \frac{d^d p}{(2\pi)^d} \frac{d\Omega}{2\pi} G_B(p, \Omega) G_F(-k + p, -\omega + \Omega). \qquad (8.79)$$

Here G_B is the propagator of the boson action $\mathscr{S}_{\text{eff}}$ specified by (8.72). In the limit of large k and ω, the internal p and Ω integrals are dominated by p and Ω much smaller than k and ω; so we can approximate (8.79) by

$$\begin{aligned} &G_F^2(k, \omega) G_F(-k, -\omega) \int \frac{d^d p}{(2\pi)^d} \frac{d\Omega}{2\pi} G_B(p, \Omega) \\ &= G_F^2(k, \omega) G_F(-k, -\omega) \langle \Psi_B^* \Psi_B \rangle. \end{aligned} \qquad (8.80)$$

This analysis can now be extended to all orders in $1/N$. Among these higher order contributions are terms which contribute self energy corrections to the boson propagator G_B in (8.80): it is clear that these can be summed to replace the bare G_B in (8.80) by the exact G_B. Then the value of $\langle |\Psi_B|^2 \rangle$ in (8.80) also becomes the exact value. All remaining contributions can be shown [24] to fall off faster at large k and ω than the terms in (8.80). So (8.80) is the exact leading contribution to the fermion Green's function in the limit of large k and ω after replacing $\langle |\Psi_B|^2 \rangle$ by its exact value. We can now integrate (8.80) over ω to obtain $n(k)$ at large k. Actually the ω integral is precisely that in (8.65), which immediately yields the needed relation (8.78).

Similar analyses can be applied to determine the the spectral functions of other observables [2, 4, 8, 20, 21, 24, 28].

Determining of the specific value of Tan's constant requires numerical computations in the *1/N* expansion of (8.71). From the scaling properties of the Feshbach resonant fixed point in $d=3$, we can deduce the result obeys a scaling form similar to (8.14):

$$C = (2mT)^2 \Phi_C \left(\frac{\mu}{T}, \frac{\nu}{\sqrt{2mT}} \right), \tag{8.81}$$

where Φ_C is a dimensionless universal function of its dimensionless arguments; note that the arguments represent the axes of Fig. 8.5. The methods of Ref. [11, 27] can now be applied to (8.78) to obtain numerical results for Φ_C in the $1/N$ expansion. We illustrate this method here by determining C to leading order in the $1/N$ expansion at $\mu = \nu = 0$. For this, we need to generalize the action (8.72) for Ψ_B to $T > 0$ and general N. Using (8.52) we can modify (8.72) to

$$\mathscr{S}_{\text{eff}} = NT \sum_{\omega_n} \int \frac{d^3k}{8\pi^3} \left[D_0(k, \omega_n) + D_1(k, \omega_n) \right] |\Psi_B(k, \omega_n)|^2, \tag{8.82}$$

where D_0 is the $T = 0$ contribution, and D_1 is the correction at $T > 0$:

$$D_0(k, \omega_n) = \frac{m^{3/2}}{16\pi} \sqrt{-i\omega_n + \frac{k^2}{4m}}$$

$$D_1(k, \omega_n) = \frac{1}{2} \int \frac{d^3p}{8\pi^3} \frac{1}{(e^{p^2/(2mT)} + 1)} \frac{1}{\left(-i\omega + p^2/(2m) + (p+k)^2/(2m) \right)}. \tag{8.83}$$

We now have to evaluate $\langle \Psi_B^* \Psi_B \rangle$ using the Gaussian action in (8.82). It is useful to do this by separating the D_0 contribution, which allows us to properly deal with the large frequency behavior. So we can write

$$\langle \Psi_B^* \Psi_B \rangle = \frac{1}{N} T \sum_{\omega_n} \int \frac{d^3k}{8\pi^3} \left[\frac{1}{D_0(k, \omega_n) + D_1(k, \omega_n)} - \frac{1}{D_0(k, \omega_n)} \right] + D_{00}. \tag{8.84}$$

In evaluating D_{00} we have to use the usual time-splitting method to ensure that the bosons are normal-ordered, and evaluate the frequency summation by analytically continuing to the real axis:

$$D_{00} = \frac{1}{N} \int \frac{d^3k}{8\pi^3} \lim_{\eta \to 0} T \sum_{\omega_n} \frac{e^{i\omega_n \eta}}{D_0(k, \omega_n)}$$

$$= \frac{16\pi}{Nm^{3/2}} \int \frac{d^3k}{8\pi^3} \int_{\frac{k^2}{4m}}^{\infty} \frac{d\Omega}{\pi} \frac{1}{(e^{\Omega/T} - 1)} \frac{1}{\sqrt{\Omega - k^2/(4m)}}.$$

$$= \frac{8.37758}{N} T^2 \tag{8.85}$$

The frequency summation in (8.84) can be evaluated directly on the imaginary frequency axis: the series is convergent at large ω_n, and is easily evaluated by a direct numerical summation. Numerical evaulation of (8.84) now yields

$$C = (2mT)^2 \left(\frac{0.67987}{N} + \mathscr{O}(1/N^2) \right) \tag{8.86}$$

at $\mu = \nu = 0$.

References

1. Braaten, E., Platter, L.: Phys. Rev. Lett. **100**, 205301 (2008)
2. Braaten, E., Kang, D., Platter, L.: Phys. Rev. Lett. **104**, 223004 (2010). arXiv:1001.4518
3. Combescot, R., Alzetto, F., Leyronas, X.: Phys. Rev. A **79**, 053640 (2009)
4. Creswick, R.J., Wiegel, F.W.: Phys. Rev. A **28**, 1579 (1983)
5. Damle, K., Sachdev, S.: Phys. Rev. Lett. **76**, 4412 (1996)
6. Fisher, D.S., Hohenberg, P.C.: Phys. Rev. B **37**, 4936 (1988)
7. Fisher, M.P.A., Weichman, P.B., Grinstein, G., Fisher, D.S.: Phys. Rev. B **40**, 546 (1989)
8. Haussmann, R., Punk, M., Zwerger, W.: Phys. Rev. A **80**, 063612 (2009)
9. Kolomeisky, E.B., Straley, J.P.: Phys. Rev. B **46**, 11749 (1992)
10. Kolomeisky, E.B., Straley, J.P.: Phys. Rev. B **46**, 13942 (1992)
11. Nikolic, P., Sachdev, S.: Phys. Rev. A **75**, 033608 (2007)
12. Nishida, Y., Son, D.T.: Phys. Rev. A **75**, 063617 (2007)
13. Popov, V.N.: Teor. Mat. Phys. **11**, 354 (1972)
14. Popov, V.N.: Functional Integrals in Quantum Field Theory and Statistical Physics. D. Reidel, Dordrecht (1983)
15. Prokof'ev, N., Ruebenacker, O., Svistunov, B.: Phys. Rev. Lett. **87**, 270402 (2001)
16. Rasolt, M., Stephen, M.J., Fisher, M.E., Weichman, P.B.: Phys. Rev. Lett. **53**, 798 (1984)
17. Sachdev, S.: Quantum Phase Transitions. Cambridge University Press, Cambridge (1999)
18. Sachdev, S., Senthil, T.: Annals. Phys. **251**, 76 (1996)
19. Sachdev, S., Senthil, T., Shankar, R.: Phys. Rev. B **50**, 258 (1994)
20. Schneider W., Shenoy V.B., Randeria M.: (2009). arXiv:0903.3006.
21. Schneider W., Randeria M.: Phys. Rev. A **81**, 021601(R) (2010). arXiv:0910.2693.
22. Singh, K.K.: Phys. Rev. B **12**, 2819 (1975)
23. Singh, K.K.: Phys. Rev. B **17**, 324 (1978)
24. Son D.T., Thompson E.G.: Phys. Rev. A **81**, 063634 (2010). arXiv:1002.0922.
25. Tan, S.: Annals. Phys. **323**, 2952 (2008)
26. Tan, S.: Annals. Phys. **323**, 2971 (2008)
27. Veillette, M.Y., Sheehy, D.E., Radzihovsky, L.: Phys. Rev. A **75**, 043614 (2007)
28. Veillette, M.Y., Moon, E.G., Lamacraft, A., Radzihovsky, L., Sachdev, S., Sheehy, D.E.: Phys. Rev. A **78**, 033614 (2008)
29. Weichman, P.B., Rasolt, M., Fisher, M.E., Stephen, M.J.: Phys. Rev. B **33**, 4632 (1986)

Chapter 9
The Unitary Fermi Gas: From Monte Carlo to Density Functionals

Aurel Bulgac, Michael McNeil Forbes and Piotr Magierski

Abstract In this chapter, we describe three related studies of the universal physics of two-component unitary Fermi gases with resonant short-ranged interactions. First we discuss an ab initio auxiliary field quantum Monte Carlo technique for calculating thermodynamic properties of the unitary gas from first principles. We then describe in detail a Density Functional Theory (DFT) fit to these thermodynamic properties: the Superfluid Local Density Approximation (SLDA) and its Asymmetric (ASLDA) generalization. We present several applications, including vortex structure, trapped systems, and a supersolid Larkin–Ovchinnikov (FFLO/LOFF) state. Finally, we discuss the time-dependent extension to the density functional (TDDFT) which can describe quantum dynamics in these systems, including non-adiabatic evolution, superfluid to normal transitions and other modes not accessible in traditional frameworks such as a Landau–Ginzburg, Gross–Pitaevskii, or quantum hydrodynamics.

9.1 Introduction

The question of how pairing correlations between two types of fermions develop with interaction strength has fascinated physicists for decades, beginning with the

A. Bulgac (✉)
Department of Physics, University of Washington, Seattle WA, USA
e-mail: bulgac@uw.edu

M. M. Forbes
Institute for Nuclear Theory and Department of Physics,
University of Washington, Seattle WA, USA
T-2, Los Alamos National Laboratory, Los Alamos NM, USA
e-mail: mforbes@uw.edu

P. Magierski
Faculty of Physics, Warsaw University of Technology, Warsaw, Poland
e-mail: Piotr.Magierski@if.pw.edu.pl

papers of Eagles [1] and Leggett [2], and followed by many others [3–6]. These initial studies focused on the inter-species pairing gap at various temperatures as the pairing interaction varied throughout the entire BCS–BEC crossover from weak to strong attraction.

Eagles and Leggett [1, 2] solved the Bardeen–Cooper–Schrieffer (BCS) mean-field equations only in the particle–particle (pairing) channel: The prevailing attitude (influenced by electronic systems) was that the pairing gap is much smaller than the self-energy (exponentially suppressed in weak-coupling), and that the presence or absence of pairing correlations was a tiny effect compared to the background density which determined the self-energy. Subsequent improvements to the theory focused only on a more accurate description of the pairing channel [3–11], neglecting the so called "Hartree–Fock" contributions to the total energy of such a system.

However, even in the weak coupling limit ($a < 0$ and $k_F|a| \ll 1$ where the Fermi energy $\varepsilon_F = p_F^2/2m$, the Fermi momentum $p_F = \hbar k_F = \hbar(3\pi^2 n)^{1/3}$, n is the total density, and a is the two-body s-wave scattering length)—which was rather thoroughly studied in the 1950s [12, 13]—it was evident that the "Hartree–Fock" and higher order particle-hole contributions dominate in the total energy. These contributions can be described perturbatively in terms of the small parameter $k_F a$ (in both BCS and BEC limits). In the BCS limit, for example, the leading contributions enter at linear order $\propto \varepsilon_F k_F a$ while the particle–particle pairing contributions are exponentially suppressed $\propto \varepsilon_F \exp(\pi/k_F a)$.

Despite neglecting the dominant particle-hole contributions, these mean-field studies correctly captured many of the *qualitative* features of the BCS–BEC crossover. This can be partially attributed to the fact that the particle–particle channel correctly accounts for the two-body bound state that dominates in the extreme BEC limit at strong attraction (however, higher order effects—describing the dimer–dimer interaction for example—are not correct [14–17]).

At unitarity, the majority of the interaction energy is due to the particle-hole channel: see [18] where the energy of the normal state at $T = 0$ was evaluated for the first time and the discussion in Sect. 9.2.6. In particular—above the critical temperature T_c, for example—the total energy of the normal phase exceeds the ground state energy by only about 20% or so [19]: This means that the condensation energy gained by the particle–particle pairing interaction is a relatively small contribution to the total interaction energy. A quantitative description of unitary physics must thus include these "Hartree–Fock" contributions and go beyond the simple mean-field models used initially to study the crossover.

In 1999, G.F. Bertsch [20] emphasized the special role played by the problem of a two-species Fermi gas at unitarity with large scattering length. In the crust of neutron stars one can find a situation where the scattering length a of the interaction is anomalously large compared to the other length scales, the average interparticle separation $n^{-1/3}$, and the range r_0 of the interaction: $r_0 \ll n^{-1/3} \ll |a|$. Since the Fermi momentum is small ($k_F r_0 \ll 1$), the neutrons effectively interact only in the relative s-partial wave, and the ground state energy should be some function of the physical parameters defining the system $E_{gs} = f(N, V, r_0, a, \hbar, m)$, where N is the particle number contained in a volume V of the system. In the formal limit of

$k_F r_0 \to 0$ and $1/k_F a \to 0$ this function simplifies:

$$E_{gs} = f(N, V, \hbar, m) = \frac{3}{5}\varepsilon_F N \xi, \qquad (9.1)$$

and all the non-perturbative effects are described by a single dimensionless constant: ξ (often referred to as the Bertsch parameter). At finite temperatures the total energy of the system becomes a slightly more complicated function, since now it depends also on the temperature T:

$$E(T) = f(N, V, T, \hbar, m) = \frac{3}{5}\varepsilon_F N \xi \left(\frac{T}{\varepsilon_F}\right). \qquad (9.2)$$

The Bertsch parameter (along with all other thermodynamic properties) becomes a "universal" function of the dimensionless variable T/ε_F [21].

In 1999 it was not yet clear whether this limit existed: One might expect such a system to collapse, since the naïve coupling constant $g = 4\pi\hbar^2 a/m$ is infinite at unitarity. Baker [22–24] provided the first clue that this system was actually stable. Carlson and collaborators [18] subsequently calculated the energy of this system, proving that it was stable, and showing that the superfluid paring gap was very large. Meanwhile, using a Feshbach resonance to induce an extremely large scattering length, J.E. Thomas and his collaborators [25] produce for the first time a quantum degenerate unitary gas of cold-atoms in a trap, thus providing experimental evidence that this system is indeed stable.

There has since been an explosion in both theoretical and experimental studies of resonant Fermi gases near the unitary regime (see for example the reviews [26–31]). On one hand, cold-atom experiments can simulate other systems of interest; for example, dilute superfluid neutron matter which can only exist in the crust of neutron stars, various condensed matter systems (the unitary gas exhibits a pseudogap that might shed light on the pseudogap in high-temperature superconductors), and quantum systems with extremely low viscosity similar to quark-gluon plasmas observed in ultra-relativistic heavy-ion collisions. On the other hand, the simplicity of the system provides an excellent vehicle through which the plethora of many-body techniques can be put to rigorous test, including both traditional approaches, as well as modern developments such as the ε-expansion and AdS/CFT correspondence [32, 33].

We shall not provide a cursory review of current theoretical techniques, but will instead focus on a couple of theoretical methods that have produced a large reliable set of information about the properties of unitary Fermi gases. The first approach is an ab initio Quantum Monte Carlo (QMC) method that has accurately evaluated many properties of these systems, and has been confirmed by experiments. The second approach is Density Functional Theory (DFT), which is in principle, an exact approach commonly used for describing "normal" systems (no superfluidity). We show how to extend the DFT to describe both superfluid systems and time-dependent phenomena, and how the DFT allows us to address phenomena that are essentially impossible to describe within a QMC approach.

9.2 The Quantum Monte Carlo Approach

9.2.1 From the Physical Problem to the Lattice Formulation

Atomic collisions in a trap occur at very low relative velocities (due to the diluteness of the gas) and this fact allows us to restrict the description to using the lowest partial waves only. In practice, the s-wave scattering phase shift fully determines the properties of a unitary Fermi gas, for which $r_0 \ll n^{-1/3} \ll |a|$. The detailed physics of the collision is more complicated since atoms are not point-like objects and can appear in various configurations. Roughly speaking, these can be associated with various valence electronic configurations. For example, atoms with a single valence electron (such as ^{6}Li) can form two possible electronic configurations in a binary system: a singlet and a triplet configuration. The inter-atomic potential describing a singlet configuration corresponds to the symmetric spatial wave function. It admits the existence of a bound state and corresponds to the closed (inaccessible) scattering channel. The triplet channel, on the other hand, is open and shallow: due to large (mainly electronic) magnetic moment, its energy can be easily tuned with respect to the closed singlet channel threshold by adjusting an external magnetic field. This allows experimentalists to use a Feshbach resonance to tune the effective interaction in the open channel to virtually any value: in particular, experiments with dilute clouds of cold atoms can directly probe the unitary regime.

A typical Hamiltonian describing the two channel atom-atom collision is of the form [34–38]:

$$H = \frac{p^2}{2M_r} + \sum_{i=1}^{2}(V_i^{hf} + V_i^Z) + V^c + V^d, \qquad (9.3)$$

where M_r is the reduced mass of two atoms, $V^{hf} = a_{hf}\mathbf{S}^e \cdot \mathbf{S}^n/\hbar^2$ is a hyperfine interaction term for each atom (with hyperfine constant a_{hf}), and $\mathbf{S}^e$ and $\mathbf{S}^n$ are the total electron spin and the total nuclear spin respectively. The Zeeman term $V^Z = (\gamma_e S_z^e + \gamma_n S_z^p)B$ describes the interaction with the external magnetic field B which is assumed to be parallel to the z-axis. The terms V^c and V^d denote the Coulomb interaction and dipole–dipole magnetic interaction, respectively. The dipole term contributes weakly to the interaction and can be neglected. The Coulomb term distinguishes singlet and triplet channels (due to different symmetry properties of electronic wave function) and produces different interaction potentials in both channels. Consequently, the continuum of the singlet channel lies above the continuum of the incident triplet channel. At very low collision energies, only the singlet channel is open. However the hyperfine interaction couples the singlet and triplet states and consequently, resonant scattering may occur due to the bound state of the singlet potential (see reviews [39–41] and references therein). An external magnetic field can thus be used as an experimental knob to control the resonance position, effectively

altering the atom-atom collision cross-section. In the limit of low collisional energy, the effective scattering length for two colliding atoms is well described by

$$a(B) = a_0 + \frac{C}{B - B_{\text{res}}}, \tag{9.4}$$

where a_0 is the triplet channel off-resonant background scattering length, and $C > 0$. The second term results from the coupling to the closed channel, and B_{res} is the value of the magnetic field where the Feshbach resonance occurs. In this way, experiments may realized the unitary Fermi gas by considering dilute systems ($r_0 \ll n^{-1/3}$) and tuning the scattering length (9.4) near the resonance ($n^{-1/3} \ll |a|$).

To determine the thermodynamic properties of an ensemble of fermionic atoms in a non-perturbative manner, we consider the system on a three dimensional (3D) cubic spatial lattice with periodic boundary conditions. The system consists of two species of fermions that we shall denote "a" and "b". In dilute neutron matter these would correspond to the two spin states of the neutrons, while in cold atom experiments these are the two populated hyperfine states. Although there are physical processes that can convert one species to another, for the purposes of the experiments we shall describe, these transitions are highly suppressed and one can consider each species to be independently conserved.

The lattice spacing l and size $L = N_s l$ introduce natural ultraviolet (UV) and infrared (IR) momentum cut-offs given by $\hbar k_c = \pi \hbar / l$ and $\hbar \Lambda_0 = 2\pi \hbar / L$, respectively. The momentum space has the shape of a cubic lattice, but in order to simplify the analysis, we place a spherically symmetric UV cut-off, including only momenta satisfying $k \leq k_c \leq \pi / l$. In order to minimize the discretization errors, the absolute value of scattering length must be much larger than the lattice spacing: $a \gg l$.

9.2.2 Effective Hamiltonian

As discussed in the introduction, it has by now been well established that the unitary regime exists and is stable. Hence, any sufficiently short-ranged interaction with large scattering length will exhibit the same universal physics. Here we use a contact (zero-range) interaction $V(\mathbf{r}_1 - \mathbf{r}_2) = -g\delta(\mathbf{r}_1 - \mathbf{r}_2)$ regularized by the lattice, which defines a momentum cut-off $\hbar k_c$. (We require all two-body matrix elements to vanish if the relative momentum of the incoming particles exceeds this cutoff.) The second quantized Hamiltonian of this system is

$$\hat{H} = \int d^3 r \left(-\sum_{\sigma = a,b} \hat{\psi}_\sigma^+(\mathbf{r}) \frac{\hbar^2 \nabla^2}{2m} \hat{\psi}_\sigma(\mathbf{r}) + g\hat{n}_a(\mathbf{r})\hat{n}_b(\mathbf{r}) \right), \tag{9.5}$$

where $\hat{n}_\sigma(\mathbf{r}) = \hat{\psi}_\sigma^+(\mathbf{r})\hat{\psi}_\sigma(\mathbf{r})$. Once the cutoff is imposed, the value of the bare coupling g can be tuned to fix the value of the renormalized physical coupling—in this case, the s-wave scattering length a. The relation between a and the coupling

constant g can be obtained from T matrix describing two-particle scattering induced by the interaction (9.5) with the s-wave phase shift:

$$k \cot \delta = -\frac{4\pi \hbar^2}{gm} - \frac{2}{\pi} k_c - \frac{k}{\pi} \ln \left| \frac{k_c - k}{k_c + k} \right|. \tag{9.6}$$

The low-momentum expansion of the scattering amplitude reads:

$$f(k) \approx \left[-\mathrm{i}k + \frac{4\pi \hbar^2}{gm} - \frac{2k_c}{\pi} + \frac{2k^2}{\pi k_c} + \mathrm{O}(k^3) \right]^{-1}. \tag{9.7}$$

At low momentum we have $f(k) = [-\mathrm{i}k - 1/a + r_{\mathrm{eff}} k^2/2 + O(k^3)]^{-1}$, which gives the relation between the bare coupling constant g and the scattering length a at a given momentum cutoff $\hbar k_c$:

$$\frac{1}{g} = \frac{m}{4\pi \hbar^2 a} - \frac{k_c m}{2\pi^2 \hbar^2} = \frac{m}{4\pi \hbar^2 a} \left(1 - \frac{2k_c a}{\pi} \right). \tag{9.8}$$

One has to remember, however, that the value of the coupling constant g has been determined for the two body system in its center of mass frame. On the other hand the Hamiltonian (9.5) is supposed to describe an ensemble of fermions in the box. Consequently, only a fraction of interacting pairs have their center of mass at rest with respect to the box. Most of the interaction processes will occur for pairs for which the center of mass velocity is nonzero. It implies that their mutual interaction will be characterized by a slightly different scattering length than (9.8). Consequently, the Hamiltonian will generate a systematic error in the description of interacting fermions. This error will scale as k_F/k_c and in order to minimize its influence one should keep the particle density as small as possible. Another source of systematic error is related to the nonzero effective range, which is generated by the interaction and is independent of the coupling constant $r_{\mathrm{eff}} = 4/(\pi k_c)$. Note however that the choice of k_c described above implies that $r_{\mathrm{eff}} < l$.

9.2.3 The Hubbard–Stratonovich Transformation

Since we are interested in the finite temperature thermodynamic properties of the system, it is natural to use the grand canonical ensemble to evaluate physical quantities. This is equivalent to considering a small portion of volume $V = L^3$ in thermal and chemical equilibrium with the larger system. Consequently we allow for energy and particle exchange between our subsystem and the larger system, fixing only the average values of these quantities in the box. The thermodynamic variables are thus the temperature T, the chemical potential μ, and the volume V. The partition function and average of an observable $\hat{O}$ are calculated according to

$$Z(\beta, \mu, V) = \text{Tr} \left\{ \exp[-\beta(\hat{H} - \mu \hat{N})] \right\},$$

$$O(\beta, \mu, V) = \frac{\text{Tr} \left\{ \hat{O} \exp[-\beta(\hat{H} - \mu \hat{N})] \right\}}{Z(\beta, \mu, V)}, \tag{9.9}$$

where $\beta = 1/T$ (in this work we will take Boltzmann's constant to be $k_B = 1$ so that temperature is expressed in units of energy). In order to be able to calculate these quantities we first factorize the statistical weight using the Trotter formula:

$$\exp[-\beta(\hat{H} - \mu \hat{N})] = \prod_{j=1}^{N_\tau} \exp[-\tau(\hat{H} - \mu \hat{N})] \tag{9.10}$$

where $\beta = N_\tau \tau$. The next step is to decompose the exponentials on the right hand side into exponentials that depend separately on the kinetic and potential energy operators. The second order expansion is (higher orders require more effort, see [42–45]):

$$\exp[-\tau(\hat{H} - \mu \hat{N})] = \exp\left[-\frac{\tau(\hat{K} - \mu \hat{N})}{2}\right] \exp(-\tau \hat{V}) \exp\left[-\frac{\tau(\hat{K} - \mu \hat{N})}{2}\right] + \text{O}(\tau^3), \tag{9.11}$$

where $\hat{K}$ is the kinetic energy operator, whose dispersion relation, for momenta smaller than the cut-off, is given by $\varepsilon_{\mathbf{k}} = \hbar^2 k^2/2m$. Since τ has the dimension of inverse energy, the above approximate representation makes sense only if $\tau_{\max}||\hat{V}|| \ll 1$ and $\tau_{\max}||\hat{K} - \mu \hat{N}|| \ll 1$. Since both the interaction and kinetic energies are extensive quantities, this restriction might appear as very strict. However, after performing a Hubbard–Stratonovich transformation (see below), this restriction is considerably eased and both the kinetic and the interaction energies in these inequalities are replaced by the corresponding intensive energies per particle. It is important to note that, because we have used the expansion up to O(τ^3), when calculating the partition function the error becomes O(τ^2). Indeed, the statistical weight involves a product of N_τ factors and is given by the following expression:

$$\exp[-\beta(\hat{H} - \mu \hat{N})]$$

$$= \exp\left[-\frac{\tau(\hat{K} - \mu \hat{N})}{2}\right] \times \left(\prod_{j=1}^{N_\tau} \exp[-\tau \hat{V}] \exp[-\tau(\hat{K} - \mu \hat{N})]\right)$$

$$\times \exp\left[+\frac{\tau(\hat{K} - \mu \hat{N})}{2}\right] + \text{O}(\tau^2) \tag{9.12}$$

Note also that this approach does not depend on the choice of dispersion relation in the kinetic energy term. However various choices of representation of derivatives on the lattice may lead to different discretization errors [46]. In our case we shall consider the kinetic energy operator in momentum space, $\varepsilon(k) = \hbar^2 k^2/2m$, which minimizes the discretization errors.

In order to efficiently evaluate the term containing the interaction, one has to replace it by the sum (or integral) of one body terms. This can be done with the Hubbard–Stratonovich transformation [47]. The transformation is not unique, and we take advantage of this freedom to ensure an efficient summation (or integration) scheme. In our case, due to the simplicity of the interaction term, a discrete Hubbard–Stratonovich transformation can be applied, similar to that in [48]:

$$
\exp[-g\tau \hat{n}_a(\mathbf{r})\hat{n}_b(\mathbf{r})] = \frac{1}{2} \sum_{\sigma(\mathbf{r},\tau_j)=\pm 1} [1 + A\sigma(\mathbf{r},\tau_j)\hat{n}_a(\mathbf{r})][1 + A\sigma(\mathbf{r},\tau_j)\hat{n}_b(\mathbf{r})],
$$

(9.13)

where $A = \sqrt{\exp(-g\tau) - 1}$, τ_j labels the location on the imaginary time axis, $j = 1, \ldots, N_\tau$, and $\sigma(\mathbf{r},\tau_j)$ is a field that can take values ± 1 at each point on the space-time lattice. This identity can be proved simply by evaluating both sides at $\hat{n}_{\{a,b\}}(\mathbf{r}) = 0, 1$. This discrete Hubbard–Stratonovich transformation is sensible only for $A < 1$, which means that the imaginary time step cannot exceed $|g|^{-1}\log 2$. The advantages of this transform is discussed, for example, in [46, 48].

Taking all this into account, the grand canonical partition function becomes

$$
Z(\beta, \mu, V) = \mathrm{Tr}\left\{\exp[-\beta(\hat{H} - \mu\hat{N})]\right\} = \int \prod_{\mathbf{r},\tau_j} \mathscr{D}\sigma(\mathbf{r},\tau_j)\mathbf{Tr}\,\hat{\mathscr{U}}(\{\sigma\}), \quad (9.14)
$$

where we define

$$
\hat{\mathscr{U}}(\{\sigma\}) = \prod_{j=1}^{N_\tau} \hat{\mathscr{W}}_j(\{\sigma\})
$$

(9.15)

and

$$
\hat{\mathscr{W}}_j(\{\sigma\}) = \exp\left[-\frac{\tau(\hat{K} - \mu\hat{N})}{2}\right] \times \left(\prod_{\mathbf{i}}[1 + A\sigma(\mathbf{r},\tau_j)\hat{n}_a(\mathbf{r})][1 + A\sigma(\mathbf{r},\tau_j)\hat{n}_b(\mathbf{r})]\right)
$$

$$
\times \exp\left[-\frac{\tau(\hat{K} - \mu\hat{N})}{2}\right].
$$

(9.16)

Since $\sigma(\mathbf{r},\tau)$ is discrete, the integration is in fact a summation:

$$
\int \prod_{\mathbf{r},\tau_j} \mathscr{D}\sigma(\mathbf{r},\tau_j) \equiv \sum_{\{\sigma\}} \frac{1}{2^{N_s^3 N_\tau}} \sum_{\{\sigma(\mathbf{r},\tau_1)\}=\pm 1} \sum_{\{\sigma(\mathbf{r},\tau_2)\}=\pm 1} \cdots \sum_{\{\sigma(\mathbf{r},\tau_{N_\tau})\}=\pm 1}, \quad (9.17)
$$

where

$$
\sum_{\{\sigma(\mathbf{r},\tau_j)\}=\pm 1} = \sum_{\sigma((1,0,0),\tau_j)=\pm 1} \sum_{\sigma((2,0,0),\tau_j)=\pm 1} \cdots \sum_{\sigma((N_s,N_s,N_s),\tau_j)=\pm 1}. \quad (9.18)
$$

In a shorthand notation we will write

$$\hat{\mathscr{U}}(\{\sigma\}) = \mathrm{T}_\tau \exp\left\{ -\int \mathrm{d}\tau[\hat{h}(\{\sigma\}) - \mu\hat{N}] \right\},$$

where T_τ stands for an imaginary time ordering operator and $\hat{h}(\{\sigma\})$ is a resulting σ-dependent one-body Hamiltonian. It is crucial to note that $\hat{\mathscr{U}}(\{\sigma\})$ can be expressed as a product of two operators which describe the imaginary time evolution of two species of fermions:

$$\hat{\mathscr{U}}(\{\sigma\}) = \hat{\mathscr{U}}_b(\{\sigma\})\hat{\mathscr{U}}_a(\{\sigma\}), \tag{9.19a}$$

$$\hat{\mathscr{U}}_b(\{\sigma\}) = \prod_{j=1}^{N_\tau} \hat{\mathscr{W}}_{jb}(\{\sigma\}), \qquad \hat{\mathscr{U}}_a(\{\sigma\}) = \prod_{j=1}^{N_\tau} \hat{\mathscr{W}}_{ja}(\{\sigma\}). \tag{9.19b}$$

As we only consider unpolarized systems, for which $\mu_a = \mu_b = \mu$, the operators for both species a and b are identical.

The expectation values of operators take the form:

$$O(\beta, \mu, V) = \frac{\mathrm{Tr}\left\{ \hat{O}\exp[-\beta(\hat{H} - \mu\hat{N})] \right\}}{Z(\beta, \mu, V)} = \int \frac{\prod_{\mathbf{i}j} \mathscr{D}\sigma(\mathbf{r}, \tau_j)\mathrm{Tr}\,\hat{\mathscr{U}}(\{\sigma\})}{Z(\beta, \mu, V)} \frac{\mathrm{Tr}\,\hat{O}\hat{\mathscr{U}}(\{\sigma\})}{\mathrm{Tr}\,\hat{\mathscr{U}}(\{\sigma\})}, \tag{9.20}$$

where we have introduced $\mathrm{Tr}\,\hat{\mathscr{U}}(\{\sigma\})$ for convenience: in the numerator it represents the probability measure used in our simulations (see below), and in the denominator it serves the purpose of moderating the variations of $\mathrm{Tr}\,\hat{O}\hat{\mathscr{U}}(\{\sigma\})$ as a function of the auxiliary field σ.

All of the above traces over Fock space acquire very simple forms [49, 50], and can be easily evaluated. In particular, $\mathrm{Tr}\,\hat{\mathscr{U}}(\{\sigma\})$ can be written as

$$\mathrm{Tr}\,\hat{\mathscr{U}}(\{\sigma\}) = \det[1 + \mathscr{U}(\{\sigma\})] = \det[1 + \mathscr{U}_b(\{\sigma\})]\det[1 + \mathscr{U}_a(\{\sigma\})], \tag{9.21}$$

where $\mathscr{U}$ (without the hat) is the representation of $\hat{\mathscr{U}}$ in the single-particle Hilbert space. The second equality is a result of the decomposition (9.19a, b) and is easy to prove by expanding both sides. For symmetric (unpolarized) systems the chemical potentials $\mu_a = \mu_b$ are the same for both species of fermion, so it follows that $\det[1 + \mathscr{U}_b(\{\sigma\})] = \det[1 + \mathscr{U}_a(\{\sigma\})]$. This implies that $\mathrm{Tr}\,\hat{\mathscr{U}}(\{\sigma\})$ is positive, i.e., that there is no fermion sign problem. Indeed, this allows to define a positive definite probability measure:

$$P(\{\sigma\}) = \frac{\mathrm{Tr}\,\hat{\mathscr{U}}(\{\sigma\})}{Z(\beta, \mu, V)} = \frac{\{\det[1 + \mathscr{U}_a(\{\sigma\})]\}^2}{Z(\beta, \mu, V)} = \frac{1}{Z(\beta, \mu, V)} \exp(2\,\mathrm{tr}\,(\log[1 + \mathscr{U}_a(\{\sigma\})])) \tag{9.22}$$

where the exponent in the last equation defines the negative of the so-called effective action. The positive definite probability measure is crucial for Monte Carlo (MC)

treatment, allowing for statistical sampling of the σ space. When considering the polarized system, the sign problem inevitably occurs, making the Monte Carlo procedure very difficult. The sign problem appears also when more complicated forms of interaction are applied. In such a case one can sometimes cure the problem by properly choosing the Hubbard–Stratonovich transformation [51].

The many-fermion problem is thus reduced to an Auxiliary Field Quantum Monte Carlo problem (AFQMC), to which the standard Metropolis algorithm can be applied, using (9.22) as a probability measure. Before moving on to the details of our Monte Carlo algorithm, we briefly discuss the expressions used to compute a few specific thermal averages.

Let us consider the one body operator

$$\hat{O} = \sum_{s,t=b,a} \int d^3\mathbf{r}_1 d^3\mathbf{r}_2 \hat{\psi}_s^+(\mathbf{r}_1) O_{st}(\mathbf{r}_1, \mathbf{r}_2) \hat{\psi}_t(\mathbf{r}_2) \tag{9.23}$$

From (9.20) it follows that

$$\langle \hat{O} \rangle = \sum_{\{\sigma\}} P(\{\sigma\}) \frac{\text{Tr}\hat{O}\hat{\mathscr{U}}(\{\sigma\})}{\text{Tr }\hat{\mathscr{U}}(\{\sigma\})} = \sum_{\{\sigma\}} P(\{\sigma\}) \frac{\text{Tr }\hat{O}\hat{\mathscr{U}}(\{\sigma\})}{\det[1 + \mathscr{U}(\{\sigma\})]}. \tag{9.24}$$

The calculation of the last term requires the evaluation of

$$\text{Tr}\left[\hat{\psi}_s^+(\mathbf{r}_1)\hat{\psi}_t(\mathbf{r}_2)\hat{\mathscr{U}}(\{\sigma\})\right] = \delta_{st} \det[1 + \mathscr{U}(\{\sigma\})]^2 n_s(\mathbf{r}_1, \mathbf{r}_2, \{\sigma\}) \tag{9.25}$$

where s and t run over both species (a or b), and

$$n_s(\mathbf{r}_1, \mathbf{r}_2, \{\sigma\}) = \sum_{\mathbf{k}_1, \mathbf{k}_2 \leq k_c} \varphi_{\mathbf{k}_1}(\mathbf{r}_1) \left[\frac{\mathscr{U}_s(\{\sigma\})}{1 + \mathscr{U}_s(\{\sigma\})}\right]_{\mathbf{k}_1, \mathbf{k}_2} \varphi_{\mathbf{k}_2}^*(\mathbf{r}_2) \tag{9.26}$$

Here $\varphi_{\mathbf{k}}(\mathbf{r}) = \exp(i\mathbf{k} \cdot \mathbf{r})/L^{3/2}$ are the single-particle orbitals on the lattice with periodic boundary conditions, and hence quantized momenta $\mathbf{k} = 2\pi\mathbf{n}/L$. This holds for any 1-body operator $\hat{O}$, if $\mathscr{U}$ is a product of exponentials of 1-body operators, as is the case once the Hubbard–Stratonovich transformation is performed. It is then obvious that the momentum representation of the one-body density matrix has the form

$$n_s(\mathbf{k}_1, \mathbf{k}_2, \{\sigma\}) = \left[\frac{\mathscr{U}_s(\{\sigma\})}{1 + \mathscr{U}_s(\{\sigma\})}\right]_{\mathbf{k}_1, \mathbf{k}_2} \tag{9.27}$$

which, for a non-interacting homogeneous Fermi gas, is diagonal and equal to the occupation number probability $1/(\exp[\beta(\varepsilon_{\mathbf{k}} - \mu)] + 1)$ of a state with the energy $\varepsilon_{\mathbf{k}} = \hbar^2 k^2/(2m)$.

Summarizing, the expectation value of any one-body operator may be calculated by summing over samples of the auxiliary field $\sigma(\mathbf{r}, \tau_j)$:

$$\langle \hat{O} \rangle = \int \prod_{\mathbf{r}, \tau_j} \mathscr{D}\sigma(\mathbf{r}, \tau_j) P(\{\sigma\}) \sum_{\mathbf{r}_1, \mathbf{r}_2} \sum_{s=a,b} O_{ss}(\mathbf{r}_1, \mathbf{r}_2) n_s(\mathbf{r}_1, \mathbf{r}_2, \{\sigma\}) \quad (9.28)$$

In particular, the kinetic energy can be calculated according to:

$$\langle \hat{K} \rangle = \int \frac{\prod_{\mathbf{r}, \tau_j} \mathscr{D}\sigma(\mathbf{r}, \tau_j) \mathrm{Tr} \mathscr{U}(\{\sigma\})}{Z(\beta, \mu, V)} \frac{\mathrm{Tr} \hat{K} \mathscr{U}(\{\sigma\})}{\mathrm{Tr} \, \mathscr{U}(\{\sigma\})}$$

$$= \int \prod_{\mathbf{r}, \tau_j} \mathscr{D}\sigma(\mathbf{r}, \tau_j) P(\{\sigma\}) \sum_{\mathbf{k}}^{k \leq k_c} \sum_{s=a,b} \left[n_s(\mathbf{k}, \mathbf{k}, \{\sigma\}) \frac{\hbar^2 \mathbf{k}^2}{2m} \right] \quad (9.29)$$

Analogously, for a generic two-body operator:

$$\hat{O} = \sum_{s,t,u,v=b,a} \int d^3 \mathbf{r}_1' d^3 \mathbf{r}_2' d^3 \mathbf{r}_1 d^3 \mathbf{r}_2 \hat{\psi}_s^+(\mathbf{r}_1') \hat{\psi}_t^+(\mathbf{r}_2') O_{stuv}(\mathbf{r}_1', \mathbf{r}_2', \mathbf{r}_1, \mathbf{r}_2) \hat{\psi}_v(\mathbf{r}_2) \hat{\psi}_u(\mathbf{r}_1).$$

$$(9.30)$$

In order to calculate $\langle \hat{O} \rangle$ one needs to evaluate the expression

$$\mathrm{Tr}\left[\hat{\psi}_s^+(\mathbf{r}_1') \hat{\psi}_t^+(\mathbf{r}_2') \hat{\psi}_v(\mathbf{r}_2) \hat{\psi}_u(\mathbf{r}_1) \hat{\mathscr{U}}(\{\sigma\}) \right]$$
$$= (\det[1 + \mathscr{U}(\{\sigma\})])^2 \left(\delta_{su} \delta_{tv} n_s(\mathbf{r}_1', \mathbf{r}_1, \{\sigma\}) n_t(\mathbf{r}_2', \mathbf{r}_2, \{\sigma\}) \right.$$
$$\left. - \delta_{sv} \delta_{tu} n_s(\mathbf{r}_1', \mathbf{r}_2, \{\sigma\}) n_t(\mathbf{r}_2', \mathbf{r}_1, \{\sigma\}) \right). \quad (9.31)$$

Hence, for the expectation value of the two body operator we get

$$\langle \hat{O} \rangle = \int \prod_{\mathbf{r}, \tau_j} \mathscr{D}\sigma(\mathbf{r}, \tau_j) P(\{\sigma\}) \times \sum_{\mathbf{r}_1', \mathbf{r}_2', \mathbf{r}_1, \mathbf{r}_2} \sum_{s,t=a,b}$$
$$\left[O_{stst}(\mathbf{r}_1', \mathbf{r}_2', \mathbf{r}_1, \mathbf{r}_2) n_s(\mathbf{r}_1', \mathbf{r}_1, \{\sigma\}) n_t(\mathbf{r}_2', \mathbf{r}_2, \{\sigma\}) \right.$$
$$\left. - O_{stts}(\mathbf{r}_1', \mathbf{r}_2', \mathbf{r}_1, \mathbf{r}_2) n_s(\mathbf{r}_1', \mathbf{r}_2, \{\sigma\}) n_t(\mathbf{r}_2', \mathbf{r}_1, \{\sigma\}) \right]. \quad (9.32)$$

In particular, the expectation value of the interaction energy reads:

$$\langle \hat{V} \rangle = -g \int \prod_{\mathbf{r}, \tau_j} \mathscr{D}\sigma(\mathbf{r}, \tau_j) P(\{\sigma\}) \sum_{\mathbf{r}} n_a(\mathbf{r}, \mathbf{r}, \{\sigma\}) n_b(\mathbf{r}, \mathbf{r}, \{\sigma\}) \quad (9.33)$$

It should be noted that in the symmetric system ($\mu_a = \mu_b$)

$$n_a(\mathbf{r}, \mathbf{r}', \{\sigma\}) = n_b(\mathbf{r}, \mathbf{r}', \{\sigma\}). \quad (9.34)$$

Hence,

$$\langle \hat{V} \rangle = -g \int \prod_{\mathbf{r}, \tau_j} \mathscr{D}\sigma(\mathbf{r}, \tau_j) P(\{\sigma\}) \sum_{\mathbf{r}} [n_a(\mathbf{r}, \mathbf{r}, \{\sigma\})]^2 \quad (9.35)$$

It is useful to introduce the correlation function

$$
\begin{aligned}
g_2(\mathbf{r}) &= \left(\frac{2}{N}\right)^2 \int d^3\mathbf{r}_1 d^3\mathbf{r}_2 \langle \psi_a^\dagger(\mathbf{r}_1 + \mathbf{r}) \psi_b^\dagger(\mathbf{r}_2 + \mathbf{r}) \psi_b(\mathbf{r}_2) \psi_a(\mathbf{r}_1) \rangle \\
&= \left(\frac{2}{N}\right)^2 \int \prod_{\mathbf{r},\tau_j} \mathscr{D}\sigma(\mathbf{r}, \tau_j) P(\{\sigma\}) \\
&\quad \times \int d^3\mathbf{r}_1 d^3\mathbf{r}_2 n_a(\mathbf{r}_1 + \mathbf{r}, \mathbf{r}_1, \{\sigma\}) n_b(\mathbf{r}_2 + \mathbf{r}, \mathbf{r}_2, \{\sigma\}),
\end{aligned}
\tag{9.36}
$$

(where N is the average particle number) which is normalized in such a way that for a non-interacting homogeneous Fermi gas $g_2(\mathbf{r}) = 3 j_1(k_F r)/(k_F r)$ and $g_2(0) = 1$.

9.2.4 Stabilization of the Algorithm for Small Temperatures

Once we have written the observables as in (9.20), the next step is to sum over all possible configurations of $\sigma(\mathbf{r}, \tau_j)$. This is still an impossible task, as for example, a lattice size $N_x^3 \times N_\tau$ (where typically $N_x = 8$ and $N_\tau \simeq 1000$), requires performing the sum over the $2^{N_x^3 \times N_\tau}$ points in configuration space. It is in these cases that a Monte Carlo approach becomes essential. By generating $\mathscr{N}$ independent samples of the field $\sigma(\mathbf{r}, \tau_j)$ with probability given by (9.22), and adding up the values of the integrand at those samples, one can estimate averages of observables with $O(1/\sqrt{\mathscr{N}})$ accuracy.

The standard Metropolis algorithm is used to generate the samples. Namely, at every MC step, the sign of σ is changed at random locations of the space-time lattice (see [19, 46, 52] for details). This procedure allows to probe the sigma space, in order to collect the set of statistically uncorrelated samples.

In order to compute the probability of a given σ configuration, it is necessary to find the matrix elements of $\mathscr{U}$, which entails applying it to a complete set of single-particle wave-functions. For the latter we chose plane waves (with momenta $\hbar k \le \hbar k_c$). This choice is particularly convenient because one can compute the overlap of any given function with the whole basis of plane waves by performing a single Fast Fourier Transform (FFT) on that function [46].

The procedure described above requires many matrix multiplications to calculate $\mathscr{U}$. In particular at low temperatures the number of matrix multiplications grows rapidly and the matrices have elements that vary over a large range of magnitudes. To avoid numerical instabilities it is necessary to separate the scales when multiplying the matrices, and a more costly but robust algorithm such as the Singular Value Decomposition (SVD) is required. In this section we follow the same approach developed in [49] to introduce the SVD to our calculations.

Let us write the matrix $\mathscr{U}(\{\sigma\})$ more explicitly:

$$\mathscr{U}(\{\sigma\}) = \prod_{j=1}^{N_\tau} \mathscr{W}_j(\{\sigma\}) = \mathscr{W}_{N_\tau} \mathscr{W}_{N_\tau-1} \cdots \mathscr{W}_2 \mathscr{W}_1, \tag{9.37}$$

where the $\mathscr{W}_k(\{\sigma\})$ are $N \times N$ matrices, for a single-particle basis of dimension N. Let us then define

$$\mathscr{U}_0 = 1$$
$$\mathscr{U}_1 = \mathscr{W}_1$$
$$\mathscr{U}_2 = \mathscr{W}_2 \mathscr{W}_1$$
$$\vdots$$
$$\mathscr{U}_n = \mathscr{W}_n \mathscr{W}_{n-1} \cdots \mathscr{W}_1 = \mathscr{W}_n \mathscr{U}_{n-1}. \tag{9.38}$$

To separate the scales one decomposes the matrix $\mathscr{U}_{n-1}$ before multiplying it by $\mathscr{W}_n$ to get $\mathscr{U}_n$. This process begins as follows

$$\mathscr{U}_0 = 1$$
$$\mathscr{U}_1 = \mathscr{W}_1 = \mathscr{S}_1 \mathscr{D}_1 \mathscr{V}_1$$
$$\mathscr{U}_2 = \mathscr{W}_2 \mathscr{W}_1 = (\mathscr{W}_2 \mathscr{S}_1 \mathscr{D}_1) \mathscr{V}_1 = \mathscr{S}_2 \mathscr{D}_2 \mathscr{V}_2 \mathscr{V}_1 \tag{9.39}$$

where $\mathscr{S}_1$ and $\mathscr{V}_1$ are orthogonal matrices (not necessarily inverses of each other), and $\mathscr{D}_1$ is a diagonal positive matrix containing the singular values of $\mathscr{U}_1$. The idea is that the actual multiplication should be done by first computing the factor in parenthesis in the last equation. This factor is then decomposed into $\mathscr{S}_2 \mathscr{D}_2 \mathscr{V}_2$, in preparation for the multiplication by $\mathscr{W}_3$, and so on. A generic step in this process looks like:

$$\mathscr{U}_n = \mathscr{W}_n \mathscr{U}_{n-1} = \mathscr{W}_n \mathscr{S}_{n-1} \mathscr{D}_{n-1} \mathscr{V}_{n-1} \mathscr{V}_{n-2} \cdots \mathscr{V}_1, \tag{9.40}$$

so that in the end

$$\mathscr{U}_{N_\tau} = \mathscr{U}(\{\sigma\}) = \mathscr{S}_{N_\tau} \mathscr{D}_{N_\tau} \mathscr{V}_{N_\tau} \mathscr{V}_{N_\tau-1} \cdots \mathscr{V}_1 = \mathscr{S} \mathscr{D} \mathscr{V}, \tag{9.41}$$

where we have decomposed the full product in the last step. Calculating the determinant, and therefore of the probability measure, is straightforward if we perform one final more SVD in the following chain of identities:

$$\det(1 + \mathscr{U}(\{\sigma\})) = \det(1 + \mathscr{S} \mathscr{D} \mathscr{V}) = \det(\mathscr{S}(\mathscr{S}^\dagger \mathscr{V}^\dagger + \mathscr{D})\mathscr{V})$$
$$= \det(\mathscr{S} \, \tilde{\mathscr{S}} \tilde{\mathscr{D}} \tilde{\mathscr{V}} \, \mathscr{V}) = \det(\mathscr{S} \, \tilde{\mathscr{S}}) \det(\tilde{\mathscr{D}}) \det(\tilde{\mathscr{V}} \mathscr{V}) \tag{9.42}$$

For equal densities (the symmetric case) we need this determinant squared, so we only care about the factor in the middle of the last expression: the other two factors have unit magnitude. Indeed, in that case we can write the probability measure as

$$P(\{\sigma\}) = \exp\left(\sum_{i=1}^{M} \log \tilde{d}_i\right) \tag{9.43}$$

where $\tilde{d}_i > 0$ are the elements in the diagonal of $\tilde{\mathscr{D}}$, and M is the dimension of the single particle Hilbert space. The number of SVD's required to stabilize the calculation grows as we increase β. In our calculations we have made limited use of the SVD, ranging from 2 decompositions at the highest T to 8 decompositions at low T's.

9.2.5 Finite Size Scaling

The Monte Carlo calculations are performed in a box of finite size with a finite average number of particles. We are interested, however, in the thermodynamic limit $N \to \infty$, $V \to \infty$ and $N/V = \text{const}$, so we need to consider the finite size scaling of the system so we can properly relate the values calculated in the box to their thermodynamic counterparts. This becomes particularly important in the vicinity of phase transitions where the correlation length ξ_{corr} characterizing the non-local degree of correlation of a system diverges:

$$\xi_{\text{corr}} \propto |t|^{-\nu}, \tag{9.44}$$

where $t = 1 - T/T_c$, T_c is the critical temperature, and ν is a universal critical exponent. For the $U(1)$ universality class, (which contains superfluid phase transitions), this exponent is well-known: $\nu = 0.671$.

When dealing with systems that have a finite size L^3, the theory of the renormalization group (RG) predicts a very specific behavior for the correlation functions close enough to the transition temperature (see e.g. [53]). In particular, the two-body density matrix $K(L,T)$ that gives the order parameter for off-diagonal long-range order, scales as

$$R(L, T) = L^{1+\eta} K(L, T) = f(x)(1 + cL^{-\omega} + \cdots), \tag{9.45}$$

where $\eta = 0.038$ is another universal critical exponent, $f(x)$ is a universal analytic function, $x = (L/\xi_{corr})^{1/\nu}$, and c is a non-universal constant, and $\omega \simeq 0.8$ is the critical exponent of the leading irrelevant field. One should keep in mind that typically one knows neither c nor T_c, but is interested in finding the latter.

In a typical Monte Carlo calculation $K(L,T)$ is computed for various lengths L_i and temperatures T. The procedure to locate the critical point (characterized by scale invariance) involves finding the "crossing" temperatures T_{ij}, for which $R(L_i, T_{ij}) = R(L_j, T_{ij})$ at two given lengths L_i and L_j. Assuming that one is close to the transition (so that the correlation length is large compared to any other scale), one can expand $f(x(|t|)) = f(0) + f'(0)L^{1/\nu}b|t|$ (where we set $\xi_{corr} = b|t|^{-\nu}$), and derive the relation

$$|T_c - T_{ij}| = \kappa g(L_i, L_j), \tag{9.46}$$

where

$$g(L_i, L_j) = L_j^{-(\omega+1/\nu)} \left[\frac{\left(\frac{L_j}{L_i}\right)^\omega - 1}{1 - \left(\frac{L_i}{L_j}\right)^{1/\nu}} \right] \tag{9.47}$$

and $\kappa = cT_c f(0)/bf'(0)$. If there were no non-universal corrections to scaling (i.e. if $c = 0$), then $\kappa = 0$ and $T_c = T_{ij}$, which means that, upon scaling by the appropriate factor (as above) all the curves $K(L, T)$ corresponding to different L's would cross exactly at T_c. In general these corrections are present, and it is therefore necessary to perform a linear fit of T_{ij} vs. $g(L_i, L_j)$ and extrapolate to infinite L in order to determine the true T_c [46].

9.2.6 Results: The Energy and the Entropy

The results of our Monte Carlo simulations are shown in Figs. 9.1 and 9.2 [19, 46, 52]. The Monte Carlo autocorrelation length was estimated (by computing the autocorrelation function of the total energy) to be approximately 200 Metropolis steps at $T \approx 0.2\varepsilon_F$. Therefore, the statistical errors are of the order of the size of the symbols in the figure. The chemical potential was chosen so as to have a total of about 45 particles for the 8^3 lattice. We have also performed calculations for particle numbers ranging from 30 to 80, for lattice sizes 8^3 and 10^3, and various temperatures: in all cases, the results agree to within the aforementioned errors.

According to the theory [54, 55] the asymptotic behavior in the limit of large momenta $n(k) \propto C(k_F/k)^n$ should at all temperatures be governed by the same exponent, namely $n = 4$. This is consistent with a value of the exponent $n = 4.5(5)$ extracted from the MC data. Both the energy 1 and the entropy 2 exhibit a definite transition between low and a high temperature regimes separated by a characteristic temperature T_0:

$$T_0 = 0.23(2)\varepsilon_F. \tag{9.48}$$

We shall discuss the relation between T_0, the superfluid critical temperature T_c, and the pair breaking temperature T^* in Sect. 9.2.8. First we focus on the low temperature limit.

At $T = 0$, several interesting quantities describe the symmetric unitary system: one is the energy as expressed through the Bertsch parameter $\xi = E_{SF}/E_{FG}$; related is the somewhat fictitious energy of the interacting normal state $\xi_N = E_N/E_{FG}$; finally, there is the pairing gap $\Delta = \eta\varepsilon_F$. The $T = 0$ value of these quantities have been obtained to high precision by other groups using the variational fixed-node Monte Carlo techniques [18, 56–58]. Unlike our approach, these $T = 0$ techniques

Fig. 9.1 The total energy
$E(T)$ with *open circles*, and
the chemical potential $\mu(T)$
with *squares*, both for the
case of an 8^3 lattice. The
combined
Bogoliubov-Anderson
phonon and fermion
quasiparticle contributions
$E_{\mathrm{ph+qp}}(T)$ (Eq. 9.50) is
shown as a *dashed line*. The
solid line represents the
energy of a free Fermi gas,
with an offset (see text).
From [46]
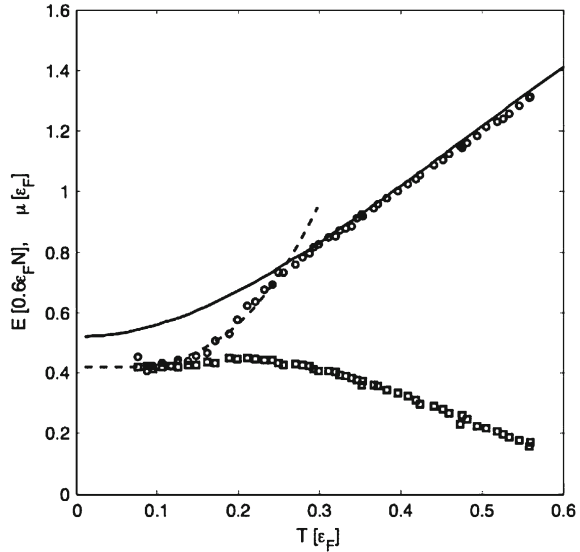
Fig. 9.2 The entropy per
particle with *circles* for 8^3
lattice, and with a *dashed
line* the entropy of a free
Fermi gas with a slight
vertical offset. The statistical
errors are the size of the
symbol or smaller. From [46]
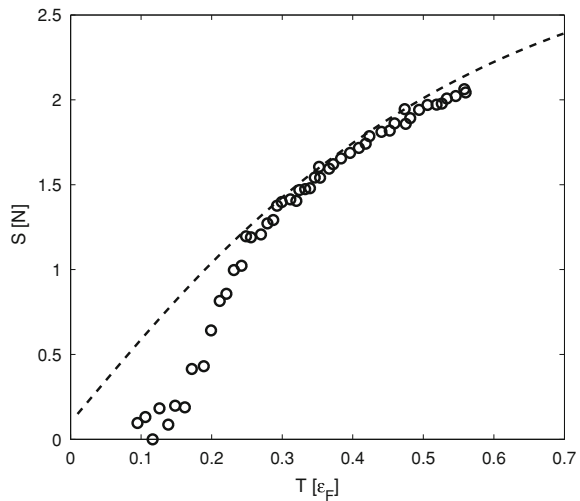
suffer from a sign problem that is overcome by using a fixed-node constraint: This
formally provides only an upper bound on the energy. Our result $\xi = 0.37(5)$ (see
Table 9.1 agrees with these variational bounds, $\xi = 0.44(1)$ [18, 56], $\xi = 0.42(1)$
[57, 58], and with more recently quoted AFQMC results $\xi = 0.40(1)$ [59]
(S. Zhang, K. E. Schmidt, J. Carlson. Private communication). Although not as
precise, our method is truly ab initio and hence provide a non-trivial validation of
these variational results.

Table 9.1 Results for the ground state energy, the characteristic temperature T_0, and the corresponding chemical potential and energy, from the caloric curves $E(T)$ and the upper bounds on the critical temperature T_c from finite size scaling and the corresponding chemical potentials and energies [46]

$1/k_F a$	$E(0)/E_F$	T_0	μ_0/ε_F	E_0/E_F	$T_c <$	μ_c/ε_F	E_c/E_F
-0.5	0.60(4)	0.14(1)	0.685(5)	0.77(2)	–	–	–
-0.4	0.59(4)	0.15(1)	0.65(1)	0.75(1)	–	–	–
-0.3	0.55(4)	0.165(10)	0.615(10)	0.735(10)	0.105(10)	0.61(1)	0.64(2)
-0.2	0.51(4)	0.19(1)	0.565(10)	0.725(10)	0.125(10)	0.56(1)	0.61(2)
-0.1	0.42(4)	0.21(2)	0.51(1)	0.71(2)	0.135(10)	0.50(1)	0.54(2)
0	0.37(5)	0.23(2)	0.42(2)	0.68(5)	0.15(1)	0.43(1)	0.45(1)
0.1	0.24(8)	0.26(3)	0.34(1)	0.56(8)	0.17(1)	0.35(1)	0.41(1)
0.2	0.06(8)	0.26(3)	0.22(1)	0.39(8)	0.19(1)	0.21(1)	0.25(1)

The quantity ξ_N for the normal state—though not precisely defined (since the normal state is not the ground state)—provides a useful description of the physics. For example, in the high temperature regime $T > T_0$, the energy is described well by the energy of a free Fermi gas shifted down by $1 - \xi_N$ (shown as a solid line in Fig. 9.1), where $\xi_N = \xi + \delta_\xi \approx 0.52$ can be found by determining what shift is necessary to make the solid curve coincide with the high temperature data (where the gas is expected to become normal).

Taking $\xi \approx 0.4$ this gives the condensation energy $\delta_\xi \approx 0.12$ which is roughly consistent with the estimate

$$\delta_\xi = \frac{\delta E}{\frac{3}{5}\varepsilon_F N} = \frac{5}{8}\left(\frac{\Delta}{\varepsilon_F}\right)^2 \simeq 0.15 \tag{9.49}$$

based on the BCS expression for $\delta E = \frac{3}{8}\frac{\Delta^2}{\varepsilon_F}N$ (see [60]) and the QMC value of the pairing gap where $\Delta \simeq 0.50\varepsilon_F$ [18, 58] and confirmed by us in [61] (which turns out to be very close to the weak-coupling prediction of Gorkov and Melik-Barkhudarov [13, 62]). Our estimate should also be compared with the results $\xi_N \approx 0.54$ of [18, 63] and $\xi_N \approx 0.56$ of [64] obtained by considering only normal state nodal constraints. Finally, a similar result $\xi_N \approx 0.57(2)$ (see Eq. 9.95e) arises from fitting the Superfluid Local Density Approximation (SLDA) density functional to be discussed in 'Symmetric Superfluid State $n_a = n_b$'.

At low temperatures, $T < T_0$, temperature dependence of the energy can be accounted for by the elementary excitations present in the superfluid phase: boson-like Bogoliubov-Anderson phonons and fermion-like gapped Bogoliubov quasiparticles. Their contributions are given by

$$E_{\text{ph+qp}}(T) = \frac{3}{5}\varepsilon_F N\left[\xi + \frac{\sqrt{3}\pi^4}{16\xi^{3/2}}\left(\frac{T}{\varepsilon_F}\right)^4 + \frac{5}{2}\sqrt{\frac{2\pi\Delta^3 T}{\varepsilon_F^4}}\exp\left(-\frac{\Delta}{T}\right)\right], \tag{9.50}$$

$$\Delta \approx \left(\frac{2}{e}\right)^{7/3} \varepsilon_F \exp\left(\frac{\pi}{2k_F a}\right), \tag{9.51}$$

The sum of the contributions from these excitations is plotted in Fig. 9.1 as a dashed line: Both of these contributions are comparable in magnitude over most of the temperature interval $(T_0/2, T_0)$. Since the above expressions are only approximate for $T \ll T_c$, the agreement with our numerical results may be coincidental.

At $T > T_c$ the system is expected to become normal. If T_0 and T_c are identified, then the fact that the specific heat is essentially that of a normal Fermi liquid $E_F(T)$ above T_0 is somewhat of a surprise: one would expect the presence of a large fraction of non-condensed but unbroken pairs. Indeed, the pair-breaking temperature has been estimated to be $T^* \simeq 0.55\varepsilon_F$, based on fluctuations around the mean-field, see [1–4, 6, 65, 66]. This implies that for $T_c < T < T^*$ there should be a noticeable fraction of non-condensed pairs. In the next sections we will show that this is indeed the case and that above the superfluid critical temperature, the fermionic spectrum still contains a gap, giving rise to the so-called pseudogap phase.

From the data for the energy E and chemical potential μ, one can compute the entropy S using the unitary relation $PV = \frac{2}{3}E$ (true of a free gas as well) which holds, where P is the pressure, V is the volume and E is the energy. It is straightforward to show that

$$\frac{S}{N} = \frac{E + PV - \mu N}{NT} = \frac{\xi(x) - \zeta(x)}{x}, \tag{9.52}$$

where $\zeta(x) = \mu/\varepsilon_F$ and $x = T/\varepsilon_F$ determines the entropy per particle in terms of quantities extracted from our simulation. As shown in Fig. 9.2, the entropy also departs from the free gas behavior below T_0.

This data can be used to calibrate the temperature scale at unitarity [19, 52]. Indeed, extending the suggestion of [67], from a known temperature in the BCS limit, the corresponding $S(T_{BCS})$ can be determined. Then, by adiabatically tuning the system to the unitary regime, one can uses $S(T_{BCS}) = S(T_{unitary})$ to determine T at unitarity. (In practice the experimental procedure goes in the opposite direction, namely measurements are performed at unitarity, and then the system is tuned to the deep BCS side, see [68]).

On the other hand, knowledge of the chemical potential as a function of temperature allows for the construction of density profiles by using of the Local Density Approximation (LDA) (see the next section). In turn, this makes it possible to determine $S(E)$ for the system in a trap, fixing the temperature scale via $\partial S/\partial E = 1/T$. Direct comparison with experiment shows remarkable agreement with our data (we discuss this later in Fig. 9.6)[69].

In the following we present a brief summary of our results near unitarity on both the BCS $a < 0$ and BEC $a > 0$ sides, (see Fig. 9.3 and Table 9.1). The coupling strength was varied in the range $-0.5 \leq 1/k_F a \leq 0.2$ (where $k_F = (3\pi^2 n)^{1/3}$), limited on the negative (BCS) side by the finite volume V (which becomes comparable to the size of the Cooper pairs), and on the positive (BEC) side by the finite lattice
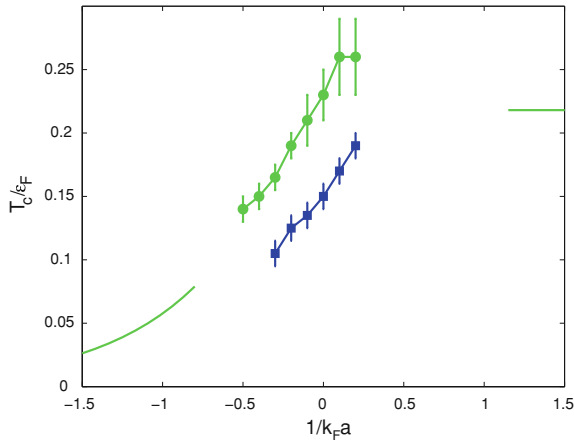
Fig. 9.3 The critical temperature T_c (*squares* either error bars) and the characteristic temperature T_0 (*circles* with error bars) around the unitary point determined in QMC and using finite size analysis. On the far left BCS side of the critical point we show (*solid green line*) the expected BCS critical temperature, including the corrections due to induced interactions [13, 62], and on the far right side of the BEC side of the unitary point we show (*solid green line*) the expect critical temperature in the BEC limit. For more details see [46]

spacing l (which becomes comparable to the size $a = O(l)$ of the localized dimers, manifesting as poor convergence of observables).

9.2.7 Response to External Probes and the Spectral Function

In order to get an insight into basic degrees of freedom which contribute to the low energy excitations of the system one has to investigate the response of the system to various external probes. Here we will present the simplest possible probe: adding a particle to the system and calculating the probability amplitude of finding it in a given single particle state. This requires calculating the one-body finite temperature (Matsubara) Green's function [70]:

$$\mathscr{G}(\mathbf{p}, \tau) = \frac{1}{Z} \mathrm{Tr}\{\exp[-(\beta - \tau)(H - \mu N)]\psi^\dagger(\mathbf{p}) \exp[-\tau(H - \mu N)\psi(\mathbf{p})]\}, \quad (9.53)$$

where $\beta = 1/T$ is the inverse temperature and $\tau > 0$. The trace is performed over the Fock space, and $Z = \mathrm{Tr}\{\exp[-\beta(H - \mu N)]\}$. The spectral weight function $A(\mathbf{p}, \omega)$ can be extracted from the finite temperature Green's function using the relation:

$$\mathscr{G}(\mathbf{p}, \tau) = -\frac{1}{2\pi} \int\limits_{-\infty}^{\infty} d\omega A(\mathbf{p}, \omega) \frac{\exp(-\omega\tau)}{1 + \exp(-\omega\beta)}. \quad (9.54)$$

By definition, $A(\mathbf{p}, \omega)$ fulfills the following constraints:

$$A(\mathbf{p}, \omega) \geq 0, \qquad \int_{-\infty}^{\infty} \frac{d\omega}{2\pi} A(\mathbf{p}, \omega) = 1. \tag{9.55}$$

Since our study focuses on the symmetric (unpolarized) system and the Hamiltonian is symmetric under $a \leftrightarrow b$, $\mathscr{G}(\mathbf{p}, \tau)$ is block diagonal and the species index is suppressed in all formulae. The numerical evaluation of the one-body temperature propagator (9.53) is performed as described above, using a Trotter expansion of $\exp[-\tau(H - \mu N)]$ followed by a Hubbard–Stratonovich transformation and Metropolis importance sampling. Details can be found in [61].

The numerical determination of $A(\mathbf{p}, \omega)$ by inverting (9.54) is an ill-posed problem that requires special methods. We have used two, based on completely different approaches. The first approach is the maximum entropy method [71–74], which is based on Bayes' theorem. QMC calculations provide us with a discrete set of values $\tilde{\mathscr{G}}(\mathbf{p}, \tau_i)$, where $i = 1, 2, \ldots, \mathscr{N}_\tau = 50$. We treat them as normally distributed random numbers around the true values $\mathscr{G}(\mathbf{p}, \tau_i)$. The Bayesian strategy consists in maximizing the *posterior probability*

$$P(A|\tilde{G}) \propto P(\tilde{G}|A)P(A) \tag{9.56}$$

of finding the right $A(\mathbf{p}, \omega)$ under the condition that $\tilde{\mathscr{G}}(\mathbf{p}, \tau_i)$ are known. Here,

$$P(\tilde{G}|A) \propto \exp\left(-\frac{1}{2}\chi^2\right) \tag{9.57}$$

is the *likelihood function*, where

$$\chi^2 = \sum_{i=1}^{\mathscr{N}_\tau} \left[\tilde{\mathscr{G}}(\mathbf{p}, \tau_i) - \mathscr{G}(\mathbf{p}, \tau_i)\right]^2 / \sigma^2. \tag{9.58}$$

The quantity $\mathscr{G}(\mathbf{p}, \tau_i)$ is determined by the spectral weight function in the discretized form of (9.54) at frequencies ω_k. The prior probability $P(A)$, describing our ignorance about the spectral weight function, is defined as $P(A) \propto \exp(\alpha S(\mathscr{M}))$, where $\alpha > 0$ and $S(\mathscr{M})$ is the relative information entropy with respect to the assumed model $\mathscr{M}$:

$$S(\mathscr{M}) = -\sum_k \Delta\omega \left[A(\mathbf{p}, \omega_k) - \mathscr{M}(\omega_k) - A(\mathbf{p}, \omega_k)\ln\left(\frac{A(\mathbf{p}, \omega_k)}{\mathscr{M}(\omega_k)}\right)\right]. \tag{9.59}$$

Hence the maximization of $P(A|\tilde{G})$ leads in practice to the minimization of the quantity $\frac{1}{2}\chi^2 - \alpha S(\mathscr{M})$ with respect to A [61].

The second approach is based on the SVD of the integral kernel $\mathscr{K}$ of (9.54), which can be rewritten in operator form as

$$\mathscr{G}(\mathbf{p}, \tau_i) = (\mathscr{K} A)(\mathbf{p}, \tau_i). \tag{9.60}$$

The operator $\mathscr{K}$ possesses a singular subspace

$$\mathscr{K} u_i = \lambda_i \mathbf{v}_i, \quad \mathscr{K}^* \mathbf{v}_i = \lambda_i u_i, \tag{9.61}$$

where $\mathscr{K}^*$ denotes the adjoint of $\mathscr{K}$, λ_i are the singular values, and u_i and $\mathbf{v}_i$ are right-singular functions and left-singular vectors respectively. The singular subspace forms a suitable basis for the expansion of the spectral weight function [75–77], which we can then write as

$$A(\mathbf{p}, \omega) = \sum_{i=1}^{r} b_i(\mathbf{p}) u_i(\omega), \qquad b_i(\mathbf{p}) = \frac{1}{\lambda_i} (\mathscr{G}(\mathbf{p}) \cdot \mathbf{v}_i), \tag{9.62}$$

where $(\_\cdot\_)$ is a scalar product and r is the rank of the operator $\mathscr{K} \mathscr{K}^*$. Since $\mathscr{G}(\mathbf{p}, \tau_i)$ is affected by Monte Carlo errors σ_i, the coefficients b_i carry some uncertainty Δb_i. Each set of expansion coefficients $\tilde{b}_i \in (b_i - \Delta b_i, b_i + \Delta b_i)$ reproduces $\mathscr{G}(\mathbf{p}, \tau_i)$ within its error bars. We use this flexibility of choosing the expansion coefficients to produce a solution satisfying constraints (9.55)[78]. The relative advantages of each method will be discussed elsewhere [79].

A sample of calculated spectral weight functions at unitarity are shown in Fig. 9.4. In order to characterize the quasiparticle excitation spectrum we have associated with the maximum of $A(\mathbf{p}, \omega)$ the quasiparticle energy $E(\mathbf{p})$:

$$E(\mathbf{p}) = \pm \sqrt{\left(\frac{p^2}{2m^*} + U - \mu \right)^2 + \Delta^2}, \tag{9.63}$$

where the effective mass m^*, the effective potential U, and the "pairing" gap Δ depend on temperature, and μ is an input parameter. In Fig. 9.5 we compare the spectrum of elementary fermionic excitations evaluated in [58], with the one extracted by us from our lowest temperature spectral weight function.

9.2.8 The Pairing Gap, Pseudogap, and Critical Temperature

In order to find the critical temperature for the superfluid-normal transition one has to perform the finite size analysis discussed in the previous section. Following this procedure, our data for the condensate fraction of the unitary Fermi gas indicates that $T_c \lesssim 0.15(1)\varepsilon_F$, considerably lower than the characteristic temperature $T_0 = 0.23(2)$ found by studying the behavior of the energy and the chemical potential (see Fig. 9.3 and Table 9.1). Even though this result for T_c is close to estimates by other groups (see e.g. [80–82]), it should be pointed out that the experimental data of [68] shows a distinctive feature in the energy versus entropy curve at a temperature close to T_0 (see [69]).

Fig. 9.4 Spectral weight function $A(\mathbf{p}, \omega)$ for three temperatures: $T = 0.15\varepsilon_F \approx T_c$ (*upper panel*), $T = 0.18\varepsilon_F \approx T_c$ (*middle panel*) and $T = 0.20\varepsilon_F$ (*lower panel*). The presence of a gap in clearly seen in the upper two panels. From [61]
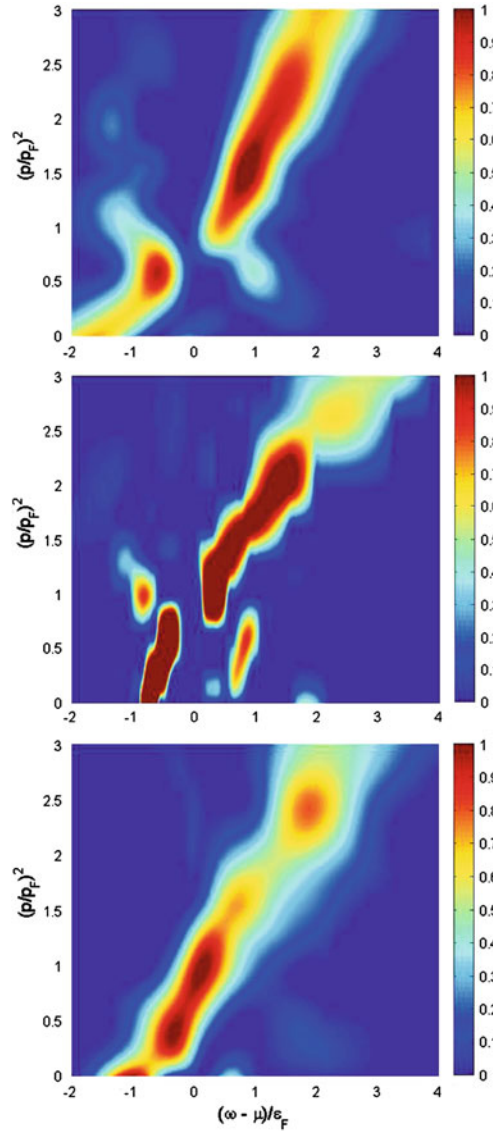
It is notable that both methods (the maximum entropy method and the SVD method) admit a "gapped" spectral function above the critical temperature T_c: a situation commonly called a pseudogap. It characterizes the range of temperatures where the system exists in an exotic state which is neither normal, nor superfluid, and defies a conventional BCS description. Therefore the onset of pairing and superfluidity can occur at different temperatures. On the other hand, the pseudogap is easy to understand in the BEC limit where stable dimers exist well above the critical temperature.
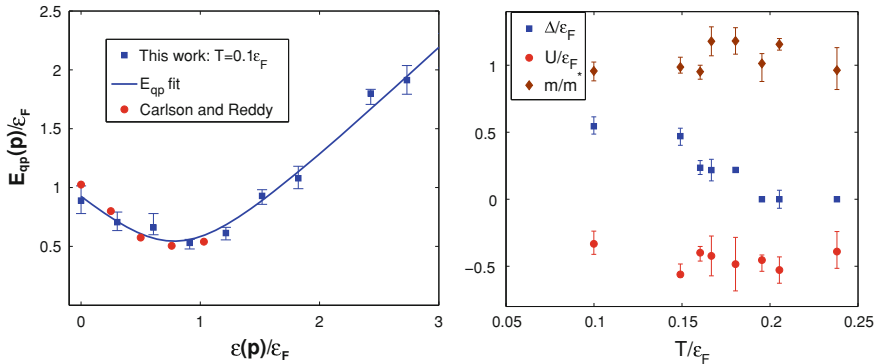
Fig. 9.5 Quantities extracted from the spectral weight function $A(\mathbf{p}, \omega)$ at $T = 0.1\varepsilon_F$ at unitarity (from [61]). Left: Quasiparticle energies $E(\mathbf{p})$ (*squares*). The line corresponds to the fit to (9.63). The circles are the results of Carlson and Reddy [58]. (See also Fig. 9.10 where the same data is used to fit the SLDA density functional.) Right: The single-particle parameters. One should note that while the effective mans and the self-energy show a very weak temperature dependence across the phase transition, the pairing gap halves in value at T_c and vanishes around T_0

This gives rise to a pseudogap phase, where the system share a BCS-like dispersion and a partially gapped density of states, but does not exhibit superfluidity. Several groups have been advocating various aspects of pseudogap physics in the unitary Fermi gas for the past few years [4, 66, 83–86].

There have been several experimental attempts to extract the pairing gap in ultra-cold dilute Fermi gases [87–89] and a theoretical explanation of these spectra was given in [90, 91]. It was later shown in [92–95] that these initial interpretations of the rf-spectra ignored the strong final state interaction effects. Recent experimental measurement of pair condensation in momentum space and a measurement of the single-particle spectral function using an analog to photo-emission spectroscopy, directly probed the pseudogap phase and revealed its existence for $1/(k_F a) \approx 0.15$ [96]. Although this lies on the BEC side, there are indications that the pseudogap persists well into the unitary regime [97, 98].

Our calculations show that the spectral function reveals the presence of a gap in the spectrum up to about $T^* \approx 0.20\varepsilon_F$ (see Fig. 9.5), and a two peak structure around the Fermi level at temperatures above T_c [61, 99]. We note that T^* is close to T_0 (not surprising in hindsight), the temperature at which the caloric curve $E(T)$ has a shoulder [19, 52] (called T_0 in [46]).

9.2.9 Describing Trapped Systems with Quantum Monte Carlo Results

The Monte Carlo calculations presented above assume that the system is uniform. In experiment, however, this condition is not fulfilled since atoms are trapped in

an external potential which induces inhomogeneity of density distribution. Most of the atomic trapping potentials used in these experiments can be approximated rather well with harmonic potential wells. Such potentials can be shown to satisfy the virial theorem at unitarity, namely $E(T, N) = 2N\langle U \rangle = 3m\omega_z^2\langle z^2 \rangle$ [100], and therefore simply measuring the spatial shape of the cloud allows for a unique determination of the unitary gas energy at any temperature. One of the main goals is therefore to provide a link between the results of experiment [68] and the available finite temperature QMC calculations.

At unitarity ($1/k_F a = 0$) the pressure of a homogeneous unitary gas is determined by a universal convex function $h_T(z)$:

$$\mathscr{P}(T, \mu) = \frac{2}{5}\beta\left[Th_T\left(\frac{\mu}{T}\right)\right]^{5/2}, \qquad \beta = \frac{1}{6\pi^2}\left(\frac{2m}{\hbar^2}\right)^{3/2}, \qquad (9.64)$$

where T and μ are the temperature and the chemical potential, respectively. $\mathscr{P}(T, \mu)$ is a convex function of its arguments (second law of thermodynamics) if and only if $h_T(z)$ is convex. One can show [101] that thermodynamic stability implies positivity $h_T(z) \geq 0$, monotonicity $h_T'(z) \geq 0$, and convexity $h_T''(z) \geq 0$. Remembering that the grand canonical potential is $\Omega(V, T, \mu) = -V\mathscr{P}(T, \mu)$ one can show that the energy of the system reads: $E = 3\mathscr{P}V/2$, where V is the volume of the system. As it was mentioned before, this relation between energy and pressure is identical in form to the one corresponding to non-interacting particles. In the high-temperature limit $\mu \to -\infty$ and $\mathscr{P}(T, \mu)$ tends from above to the free Fermi gas pressure. In the low-temperature limit $\mathscr{P}(T, \mu)$ tends from above to $\mathscr{P}(0, \xi\varepsilon_F) = 4\beta\varepsilon_F^{5/2}\xi/5$.

Standard manipulations show that all the thermodynamic potentials for the unitary Fermi gas can be expressed in terms of a single function of one variable, a property known as universality [19, 21, 52, 80, 81]. This property was incorporated in our interpolation. At high temperatures we notice that our results smoothly approach the corresponding free Fermi gas results with some offsets for the energy, chemical potential and entropy [19, 52].

At this point we assume that the LDA can be used to describe the properties of an atomic cloud in a trap. We will neglect the gradient corrections as one can show that for the mostly-harmonic traps used in typical experiments the role of the gradient corrections is relatively small [69], as the average interparticle distance, and thus the Fermi wave length, is much smaller than the harmonic oscillator length.

In this approach, the grand canonical thermodynamic potential for a unitary Fermi gas confined by an external potential $U(\mathbf{r})$ is a functional of the local density $n(\mathbf{r})$ given by

$$\Omega = \int d^3\mathbf{r}\left[\frac{3}{5}\varepsilon_F(\mathbf{r})\varphi(x)n(\mathbf{r}) + U(\mathbf{r})n(\mathbf{r}) - \lambda n(\mathbf{r})\right], \qquad (9.65)$$

where

$$x = \frac{T}{\varepsilon_F(\mathbf{r})}, \quad \varepsilon_F(\mathbf{r}) = \frac{\hbar^2}{2m}[3\pi^2 n(\mathbf{r})]^{2/3}, \qquad (9.66)$$

Fig. 9.6 Entropy as a function of energy for the unitary Fermi gas in the Duke trap [68]: experiment (*points with error bars*) and present work (*solid curve*), where $E_0 = N\varepsilon_F^{HO}$. Inset: log–log plot of $E(T)$ as results from our calculations and as derived from experimental data [68]. The temperature is units of the corresponding Fermi energy at the center of the trap: $\varepsilon_F(0)$. From [69]
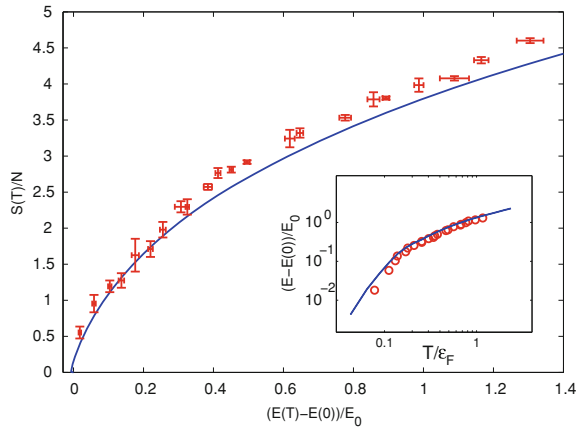
and we have used the universal form for the free energy per particle F/N in the unitary regime:

$$\frac{F}{N} = \frac{E - TS}{N} = \frac{3}{5}\varepsilon_F\varphi(x) = \frac{3}{5}\varepsilon_F[\xi(x) - x\sigma(x)], \qquad (9.67)$$

where for a homogeneous system $\xi(x) = 5E/3\varepsilon_F N$, $\sigma(x) = S/N$ is the entropy per particle and $x = T/\varepsilon_F$. The overall chemical potential λ and the temperature T are constant throughout the system. The density profile will depend on the shape of the trap as dictated by $\delta\Omega/\delta n(\mathbf{r}) = 0$, which results in:

$$\frac{\delta\Omega}{\delta n(\mathbf{r})} = \frac{\delta(F - \lambda N)}{\delta n(\mathbf{r})} = \mu(x(\mathbf{r})) + U(\mathbf{r}) - \lambda = 0. \qquad (9.68)$$

At a given T and λ, (9.66) and (9.68) completely determine the density profile $n(\mathbf{r})$ (and consequently both $E(T,N)$ and $S(T,N)$) in a given trap for a given total particle number. The only experimental input we have used is the particle number, the trapping potential and the scattering length at $B = 1,200$ G, taken from [68]. The potential was assumed to be an 'isotropic' Gaussian, as suggested by the experimental group [68], although it is not entirely clear to us to what extent this is accurate, especially in the axial direction. We have approximated the properties of the atomic cloud at $B = 840$ G with those at unitarity ($B = 834$ G), where we have MC data. For $B = 840$ G and for the parameters of the Duke experiment [68] one obtains $1/k_F a = -0.06$, using data of [102], if the Fermi momentum corresponds to the central density of the cloud at $T = 0$.

Our results for the entropy of the cloud and the density profiles for several temperatures, are shown in Figs. 9.6 and 9.7. In all the figures the temperature is measured in natural units of $\varepsilon_F(0)$, corresponding to the actual central density of the cloud at that specific temperature. In [68, 103] the temperature is expressed in units of the Fermi energy at $T = 0$ in a harmonic trap: $\varepsilon_F^{ho} = \hbar\Omega(3N)^{1/3}$. It is clear from Fig. 9.7 that the central density decreases with T and that the superfluid core disappears at $T_c = 0.23(2)\varepsilon_F(0)$, which translates into $T_c = 0.27(3)\varepsilon_F^{ho}$ to be compared
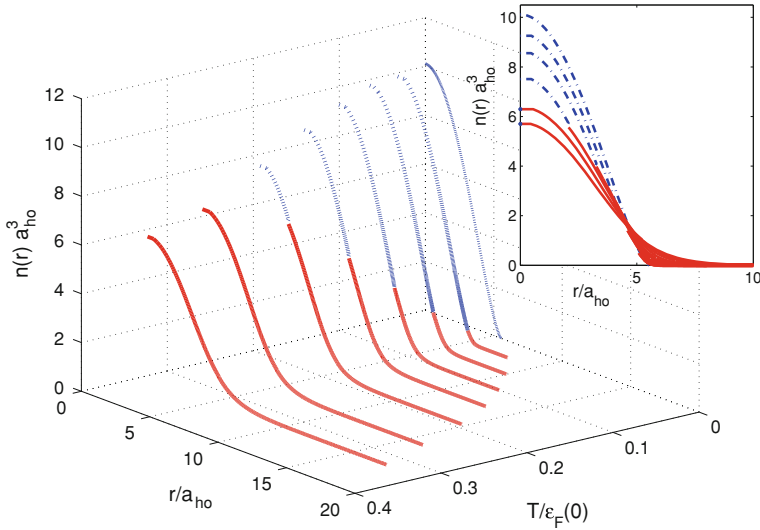
Fig. 9.7 The radial (along shortest axis) density profiles of the Duke cloud at various temperatures, as determined theoretically using the QMC results [19, 52]. The *dotted blue line* shows the superfluid part of the cloud, for which $x(\mathbf{r}) = T/\varepsilon_F(\mathbf{r}) \leq 0.23$. The *solid red line* shows the part of the system that is locally normal. Here $a_{ho}^2 = \hbar/m\omega_{max}$. From [69]

to $T_c = 0.29(2)\varepsilon_F^{ho}$ of [68]. There is a noticeable systematic difference between theory and experiment at high energies, see Fig. 9.6. This discrepancy can be attributed to the fact that the experiment was performed slightly off resonance, on the BCS side, where $1/k_F a = -0.06$.

Recently a couple of new experiments have been published, one by the Paris group [104] and another by the Tokyo group [105]. Using new techniques these groups were able to extract directly from cloud images the pressure as a function of the fugacity. While the Paris group has observed a very good agreement with our QMC results,
see Fig. 9.8, they have also noticed that the results of the Tokyo group show systematic differences [106].

One can summarize that so far the bulk of the theoretical predictions obtained in ab initio QMC have been confirmed experimentally with impressive accuracy in most cases, often at a level of a few percent, which is the accuracy of both theoretical calculations and of many experimental results as well. The emergence of a pseudogap in the unitary gas is a fascinating new feature, but still in its infancy both theoretically and experimentally.

9.3 Density Functional Theory for the Unitary Fermi Gas

The idea of DFT originated with Hohenberg and Kohn [107] and Kohn and Sham [108] (see the monographs [109, 110] for an overview) where they proved that the
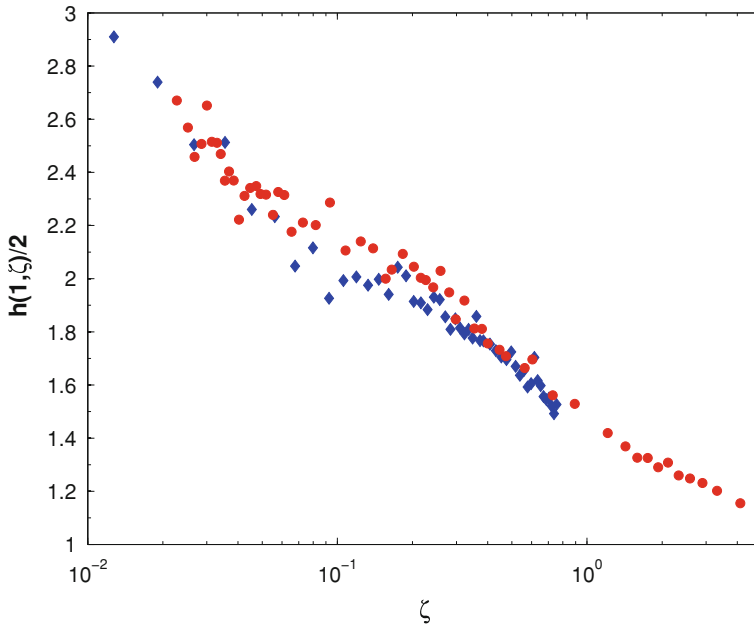
Fig. 9.8 The comparison between the ration of the pressure versus fugacity of a unitary Fermi gas and the pressure of a free Fermi gas: measured in [106] (*red filled circles*) and calculated in QMC in [69] (*blue filled diamonds*)

ground state energy and the density of a system of interacting fermions in an *arbitrary* external potential $V_{\text{ext}}(\mathbf{r})$ may be found by minimizing a functional

$$E[n(\mathbf{r})] + \int \mathrm{d}^3\mathbf{r} \; V_{\text{ext}}(\mathbf{r})n(\mathbf{r}). \tag{9.69}$$

The utility of this approach is that the functional $E[n(\mathbf{r})]$ depends only on the interactions of the system and is independent of the external potential. Thus, if we were able to deduce $E[n(\mathbf{r})]$ for the unitary Fermi gas, then by simply minimizing a single functional, we could determine the ground state in any external potential, including arbitrary trapping geometries and optical lattices.

The challenge is that the Hohenberg–Kohn theorem is an existence theorem. The exact form of the functional $E[n(\mathbf{r})]$ is unknown, and in general it may be extremely complicated and highly non-local. In problems that are under perturbative control, the functional can be formally derived (see [111]), but in highly non-perturbative problems such as the unitary gas, one must choose a physically motivated approximate functional and check its accuracy.

Our strategy is thus:

1. Postulate simple functional forms capturing the relevant physics with a small number of parameters.

2. Use ab initio results to fix these parameters.
3. Validate the functional with different ab initio and experimental results.
4. Make interesting and verifiable physical predictions.

The computational cost of minimizing the density functional is much less than solving for many-body wavefunctions, and one may consider substantially larger systems, untenable with ab initio methods. This allows one to make direct contact with typical mesoscopic experiments for example. In this way, one may view the density functional as a bridge between microscopic and mesoscopic physics.

As we have noted, although DFT is exact in principle, for non-trivial systems we must postulate a form for the functional. Nevertheless, it provides a substantial improvement to the ad hoc mean-field methods typically employed to study the properties of large non-perturbative many-body systems. Without a program for systematically correcting the functional, the DFT approach will not be the final word. However, judging from the success of the approach in quantum chemistry, and from the results presented here, we expect that without too much effort one should be able to obtain percent level accuracy for a wide range of systems, which should be sufficient for quite some time.

The qualitative success of the Eagles–Leggett [1, 2] mean-field model describing the BCS–BEC crossover suggests a functional description of the unitary Fermi gas in terms of quasi-particle fermionic states (see (9.76)). As discussed in Sect. 9.1, although the Bogoliubov de-Gennes (BdG) approximation is quite successful, it is quantitatively inaccurate as it describes *all* interaction effects through the condensation energy (pairing) alone, completely omitting the "Hartree–Fock" contribution which dominates the energetics. To see this, consider the typical local interaction $ga^\dagger b^\dagger ba$ between species a (spin up) and species b (spin down). The mean-field approximation retains the pairing term $g\langle a^\dagger b^\dagger\rangle\langle ba\rangle = g\nu^\dagger\nu$ and the Hartree term $g\langle a^\dagger a\rangle\langle b^\dagger b\rangle = gn_a n_b$. (The other quadratic Fock term $\langle a^\dagger b\rangle\langle b^\dagger a\rangle$ has zero expectation.) The problem arises upon renormalization: As discussed below, the anomalous density ν is formally divergent, and regularization requires taking the coupling $g \to 0$ to keep the gap parameter $\Delta = -g\nu$ finite. Since the densities remain finite, the Hartree contribution $gn_a n_b \to 0$ vanishes.

In weak coupling, one can carefully take the zero-range limit while summing ladders [12, 70], obtaining the well known form $an_a n_b$ of the Hartree interaction, which is clearly invalid in the unitary limit $|a| \to \infty$. In particular, for the symmetric phase $n_a = n_b = n$, there is no additional length scale, and so we must have a dependence $\sim n^{5/3}$ as dictated by dimensional analysis. This physics—the dominant contribution to the energetics (see the discussion below (9.49))—is completely missing from the BdG (mean-field) approach and is one of the main deficiencies we hope to overcome within an improved DFT description.

We shall first discuss an improved local DFT for symmetric systems $n_a = n_b = n$: the SLDA. This is a generalization of the Kohn-Sham LDA to includes pairing effects and subsumes the BdG form, adding an $n^{5/3}$ Hartree interaction term.

We subsequently extent the SLDA to study asymmetric systems $n_a \neq n_b$ through the use of the Asymmetric SLDA (ASLDA) functional that subsumes the SLDA.

The approach of both these approximations is to introduce as few parameters as possible that are consistent with the scaling and symmetries of the problem, then to determine the coefficients of these terms by matching to ab initio properties in the thermodynamic limit. The form of the functionals is described in Sect. 9.3.1, the fitting of the parameters is discussed in Sect. 9.3.2, and some physical applications are presented in Sect. 9.3.3.

9.3.1 The Energy Density Functional

We start with the most restrictive conditions of a cold ($T = 0$) symmetric ($n_a = n_b$, $m_a = m_b$) unitary ($|a| = \infty$) Fermi gas. As discussed in Sect. 9.1, the only dimensionful scale in the problem is the density n, so dimensional analysis provides significant constraints on the form of the functional and thermodynamic functions, allowing us to postulate a simple functional form characterized by only three dimensionless parameters. Relaxing any of these conditions will introduce additional dimensionless parameters. In particular, we consider the dimensionless polarization $p = (n_a - n_b)/(n_a + n_b)$ to formulate ASLDA [101, 112]. The generalized ASLDA functional promotes the dimensionless parameters to dimensionless functions of this asymmetry parameter p.

9.3.1.1 Local Density Approximation

In general, the energy functional might be a highly non-local and extremely complicated object. One major simplification is to assume that the functional is local and can be represented by a function of various types of densities. This amounts to introducing the energy density $\mathscr{E}$ which is a function (as opposed to a functional) of the local densities and their derivatives (referred to as gradient corrections):

$$E_{KS} = \int \mathrm{d}^3\mathbf{r}\, \mathscr{E}_{KS}[n(\mathbf{r}), \tau(\mathbf{r}), \nabla n(\mathbf{r}), \ldots] + U(\mathbf{r})n(\mathbf{r}) + \cdots, \qquad (9.70)$$

where $U(\mathbf{r})$ represents an external (trapping) potential. This LDA has met with remarkable success in quantum chemistry applications [109, 110, 113].

The simplest function contains a single term $E \propto n^{5/3}$. This—along with gradient corrections—has been explored in [114, 115], and, while it can model the energetics of the symmetric gas, it does not include information about pairing correlations. The extensions we describe here include both kinetic terms and an anomalous pairing density.

9.3.1.2 Densities and Currents

The first task is to construct the densities and currents. In the SLDA, we consider five types of densities: the standard particle densities $n_a(\mathbf{r}) \propto \langle a^\dagger(\mathbf{r})a(\mathbf{r})\rangle$

and $n_b(\mathbf{r}) \propto \langle b^\dagger(\mathbf{r})b(\mathbf{r})\rangle$, the kinetic densities $\tau_a(\mathbf{r}) \propto \langle a^\dagger(\mathbf{r})\Delta a(\mathbf{r})\rangle$ and $\tau_b(\mathbf{r}) \propto \langle b^\dagger(\mathbf{r})\Delta b(\mathbf{r})\rangle$, and an anomalous density $\nu(\mathbf{r}) \propto \langle a(\mathbf{r})b(\mathbf{r})\rangle$. When considering time dependence (Sect. 9.2.4), we must also include the currents $\mathbf{j}_a(\mathbf{r}) \propto \langle a^\dagger(\mathbf{r})\nabla a(\mathbf{r})\rangle$ and $\mathbf{j}_b(\mathbf{r}) \propto \langle b^\dagger(\mathbf{r})\nabla b(\mathbf{r})\rangle$ to restore Galilean invariance as discussed in Sect. 9.4.2. In principle, these densities may be non-local, but to simplify the functional we wish to consider only local quantities. The local form of the anomalous density ν leads to UV divergences that we must regularize as we discuss in Sect. 9.3.1.4.

The formal analysis proceeds with a four-component formalism discussed in 'Single Particle Hamiltonian', but the symmetries of the cold atom systems allow everything to be expressed in terms of two-component wavefunctions (see Appendix)

$$\Psi_n(\mathbf{r}) = \begin{pmatrix} u_n(\mathbf{r}) \\ v_n(\mathbf{r}) \end{pmatrix} \tag{9.71}$$

with energy E_n. The densities and currents are constructed from these as

$$n_a(\mathbf{r}) = \sum_n |u_n(\mathbf{r})|^2 f_\beta(E_n), \quad n_b(\mathbf{r}) = \sum_n |v_n(\mathbf{r})|^2 f_\beta(-E_n),$$
$$\tau_a(\mathbf{r}) = \sum_n |\nabla u_n(\mathbf{r})|^2 f_\beta(E_n), \quad \tau_b(\mathbf{r}) = \sum_n |\nabla v_n(\mathbf{r})|^2 f_\beta(-E_n), \tag{9.72a}$$

$$\nu(\mathbf{r}) = \frac{1}{2} \sum_n u_n(\mathbf{r}) v_n^*(\mathbf{r}) \left(f_\beta(-E_n) - f_\beta(E_n) \right),$$
$$\mathbf{j}_a(\mathbf{r}) = \frac{i}{2} \sum_n \left[u_n^*(\mathbf{r})\nabla u_n(\mathbf{r}) - u_n(\mathbf{r})\nabla u_n^*(\mathbf{r}) \right] f_\beta(E_n), \tag{9.72b}$$
$$\mathbf{j}_b(\mathbf{r}) = i2 \sum_n \left[v_n^*(\mathbf{r})\nabla v_n(\mathbf{r}) - v_n(\mathbf{r})\nabla v_n^*(\mathbf{r}) \right] f_\beta(-E_n),$$

where $f_\beta(E_n) = 1/(\exp(\beta E_n) + 1)$ is the Fermi distribution and $\beta = 1/T$ is the inverse temperature. Even though we shall only discuss the zero temperature limit of SLDA it is convenient for numerical purposes to introduce a very small temperature (much smaller than any other energy scale in the system) so that $\mathscr{E}(\mu)$ is a smooth function.

9.3.1.3 Functional Form

Our functionals generically include a kinetic term and a pairing term of the form

$$\mathscr{E} = \frac{\hbar^2}{m}\left(\frac{\tau_a + \tau_b}{2}\right) + g\nu^\dagger \nu + \cdots, \tag{9.73}$$

along with additional density dependent terms, where all of the densities and currents $n(\mathbf{r})$ etc. are functions of position but have no non-local structure. (Note that here

and in many of the following formulae we suppress the explicit dependence on position $\mathbf{r}$.) In the superfluid, this local approximation has formal difficulties since the anomalous density $\nu(\mathbf{r}, \mathbf{r}') \sim \sum u_n(\mathbf{r})v_n^*(\mathbf{r}') \sim |\mathbf{r} - \mathbf{r}'|^{-1}$ diverges for small $|\mathbf{r} - \mathbf{r}'|$ if the pairing field is taken to be a multiplicative operator $\Delta(\mathbf{r})$. The kinetic energy densities $\tau_{a,b}(\mathbf{r})$ diverge as well. A proper local formulation thus requires regularization [116] as discussed in Sect. 9.3.1.4. We introduce an energy cutoff E_c—$\nu_c(\mathbf{r}) \sim \sum_{|E|<E_c} u_n(\mathbf{r})v_n^*(\mathbf{r})$—and a cutoff dependent effective interaction g_{eff} such that

$$\Delta = -g\nu = -g_{\text{eff}}\nu_c \tag{9.74}$$

is finite and independent of the cutoff as $E_c \to \infty$. Once this is done, we can write the functional as

$$\mathscr{E} = \frac{\hbar^2}{m}\left(\frac{\tau_a + \tau_b}{2}\right) - \Delta^\dagger\nu + \cdots . \tag{9.75}$$

Note that ν is still formally divergent, but will cancel with a similar divergence in the kinetic piece such that the energy density is finite. The full forms of the local functionals considered here are thus:

Bogoliubov de-Gennes [117]:

$$\mathscr{E}_{\text{BdG}} = \frac{\hbar^2\tau_a}{2m_a} + \frac{\hbar^2\tau_b}{2m_b} + g\nu^\dagger\nu. \tag{9.76}$$

For homogeneous systems, this is equivalent to the Eagles–Leggett mean-field theory where the parameters here represent the bare parameters (elsewhere we shall only consider $m_a = m_b = m$) and the coupling constant is tuned to reproduce the vacuum two-body scattering length a. Note the absence of a self-energy: all of the interaction effects are modelled through the pairing interaction. One unphysical consequence is that the normal state is described as completely non-interacting in this model. While this may capture some qualitative features of the theory, and provides a rigorous variational bound on the energy, it cannot be trusted for quantitative results beyond the rather poor variational upper bound.

SLDA:

$$\mathscr{E}_{\text{SLDA}} = \frac{\hbar^2}{m}\left(\frac{\alpha}{2}(\tau_a + \tau_b) + \beta\frac{3}{10}(3\pi^2)^{2/3}(n_a + n_b)^{5/3}\right) + g\nu^\dagger\nu. \tag{9.77}$$

This may be thought of as the unitary generalization of the symmetric BdG functional for symmetric matter $n_a = n_b = n_+/2$ to include a self-energy term $n_+^{5/3}$ (whose form is fixed by simple dimensional analysis) and an effective mass $m_{\text{eff}} = m/\alpha$. The three parameters here α, β, and the pairing interaction g must be fixed by matching to experiments or ab initio calculations as discussed in

'Symmetric Superfluid State $n_a = n_b$'. Since g is formally zero in the large coupling limit, we characterize it with a dimensionless constant γ such that $g_{\text{eff}}^{-1} = (n_a + n_b)^{1/3}/\gamma - \Lambda$ where Λ is the cutoff discussed in Sect. 9.3.1.4.

ASLDA:

$$\mathscr{E}_{\text{ASLDA}} = \frac{\hbar^2}{m} \left(\alpha_a(n_a, n_b)\frac{\tau_a}{2} + \alpha_b(n_a, n_b)\frac{\tau_b}{2} + D(n_a, n_b) \right) + g\nu^\dagger \nu. \quad (9.78)$$

Here we allow for polarization $n_a \neq n_b$ and so we must generalize the parameters such as the effective masses and self-interaction to be functions of the local polarization $p = (n_a - n_b)/(n_a + n_b)$. Dimensional analysis restricts these $\alpha_{a,b}(\lambda n_a, \lambda n_b) = \alpha(n_a, n_b)$ and $D(\lambda n_a, \lambda n_b) = \lambda^{5/3}D(n_a, n_b)$ so that we need only to parametrize functions of the single variable p as discussed in Sect. 9.3.2.1.

To fully define these functionals, we must now regularize the pairing interaction g (Sect. 9.3.1.4) and then specify the values and functional forms of the parameters and parametric functions (Sect. 9.3.2).

9.3.1.4 Regularization

As formulated, the local theory is ultraviolet divergent due to the well known behaviour of the anomalous density:

$$\nu(\mathbf{r}, \mathbf{r}') \sim \sum_n u_n(\mathbf{r})v_n^*(\mathbf{r}') \propto \frac{1}{|\mathbf{r} - \mathbf{r}'|}. \quad (9.79)$$

There are many ways of dealing with this. For example, physical potentials are always non-local, and the non-locality naturally regulates the theory. However, in the unitary gas, the non-local (range of the interaction) is much smaller than any other length scale in the system and the stability of the system (see Sect. 9.1) indicates that the low-energy large-distance physics should be independent of the short-range details.

As a result, one can choose any sort of regularization scheme that is convenient and obtain the universal results with an appropriate limiting procedure. In the homogeneous case, one can use a variety of techniques: some interesting choices include dimensional regularization [118] and selective distribution functions [119]. The most straightforward is to use a momentum cutoff, but for inhomogeneous systems, momentum is not a good quantum number. Instead, an energy cutoff E_c suffices. All quantities—especially the divergent anomalous density—can be computed from states with energies below this cutoff:

$$\nu_c = \sum_{|E_n|<E_c} u_n v_n^* \frac{f_\beta(E_n) - f_\beta(-E_n)}{2}. \quad (9.80)$$

(To improve the behaviour, we actually use a smooth cutoff so that discontinuities are not introduced when levels cross in and out of the sum during the self-consistent iterations).

To better understand the nature of these divergences, consider the ultraviolet limit where the length scale is much smaller than any other scale in the system. In this limit, the semi-classical Thomas-Fermi approximation may be applied locally. The linear divergences in both the symmetric combination of the kinetic energy and in the anomalous density have the form

$$\tau_+(k) = \tau_a(k) + \tau_b(k) \rightarrow \frac{2(m^*)^2 \Delta^\dagger \Delta}{\hbar^4 k^2}, \qquad \nu(k) \rightarrow \frac{m^* \Delta}{\hbar^2 k^2}, \tag{9.81}$$

where the average effective mass $m^* = m/\alpha_+ = 2m/(\alpha_a + \alpha_b)$ enters explicitly through the equations of motion. From this it is clear that the combination

$$\frac{\hbar^2 \tau_+}{2m^*} - \Delta^\dagger \nu = \frac{\hbar^2}{m}\left(\frac{\alpha_a \tau_a}{2} + \frac{\alpha_b \tau_b}{2}\right) + g\nu^\dagger \nu$$

remains finite if we regularize the theory such that the gap parameter remains finite for all values of the cutoff

$$\Delta = -g_{\text{eff}} \nu_c. \tag{9.82}$$

When regularizing the BdG equations (9.76), we hold fixed the vacuum two-body scattering length,

$$\frac{m}{4\pi\hbar^2 a} = \frac{1}{g} + \frac{1}{2}\int - \frac{d^3\mathbf{k}}{(2\pi)^3} \frac{1}{\frac{\hbar^2 k^2}{2m} + i0^+} \tag{9.83}$$

where $\int -$ is the principal value integral. This may be easily derived from the pseudo-potential approach (see for example [120, 121] or for higher partial waves [122, 123]).

In the other DFTs (9.77) and (9.78), g does not represent the physical interaction, but is simply another parameter of the theory. Thus, we define a similar regularization scheme by introducing a finite function $\tilde{C}(n_a, n_b)$ that must be fit in order to characterize the pairing interaction and correlations.[1]

$$\tilde{C}(n_a, n_b) = -\frac{\alpha_+ \nu}{\Delta} + \frac{1}{2}\int - \frac{d^3\mathbf{k}}{(2\pi)^3} \frac{1}{\frac{\hbar^2 k^2}{2m} - \frac{\mu_+}{\alpha_+} + i0^+} = \frac{\alpha_+}{g_{\text{eff}}} + \Lambda. \tag{9.84}$$

This differs from (9.83) in two ways: (1) we have included a factor of the effective mass parameter α_+ to ensure that the divergences (9.81) cancel and, (2) we have shifted the pole of the integral by the average local chemical potential $\mu_+ = (\mu_a - \nu_a + \mu_b + \nu_b)/2$ to improve convergence. As pointed out in [116], the shift does not change the integral in the limit of infinite cutoff, but greatly improves the convergence if a cutoff is used. Given a fixed momentum cutoff $k < k_c$, the integral Λ in the second term can be performed exactly

---

[1] We have changed notations slightly from [124] using $\tilde{C}(n_a, n_b) = \alpha_+ C(n_a, n_b)$ which simplifies the equations because, in the limit of infinite cutoff, Λ is independent of any densities and functional parameters.

$$\Lambda = \frac{m}{\hbar^2} \frac{k_c}{2\pi^2} \left\{ 1 - \frac{k_0}{2k_c} \ln \frac{k_c + k_0}{k_c - k_0} \right\} \tag{9.85}$$

where $\hbar^2 k_0^2/(2m) = \mu_+/\alpha_+$ defines the location of the pole. In general, translational invariance is not preserved, and so we must use the fixed energy cutoff $|E(k)| < E_c$ that enters (9.80) rather than a momentum cutoff as the latter is not a good quantum number. To relate the two we used the local quasiparticle dispersion relationship:

$$\frac{\hbar^2}{2m} \alpha_+(\mathbf{r}) k_0^2(\mathbf{r}) - \mu_+(\mathbf{r}) = 0, \tag{9.86a}$$

$$\frac{\hbar^2}{2m} \alpha_+(\mathbf{r}) k_c^2(\mathbf{r}) - \mu_+(\mathbf{r}) = E_c. \tag{9.86b}$$

This defines a position-dependent momentum cutoff $k_c(\mathbf{r})$ and effective coupling constant $g(\mathbf{r})$ that can be used to regulate the anomalous density at any point in space:

$$\Lambda(\mathbf{r}) = \frac{m}{\hbar^2} \frac{k_c(\mathbf{r})}{2\pi^2} \left\{ 1 - \frac{k_0(\mathbf{r})}{2k_c(\mathbf{r})} \ln \frac{k_c(\mathbf{r}) + k_0(\mathbf{r})}{k_c(\mathbf{r}) - k_0(\mathbf{r})} \right\}, \tag{9.87a}$$

$$\frac{\alpha_+(\mathbf{r})}{g_{\text{eff}}(\mathbf{r})} = \tilde{C}\Big(n_a(\mathbf{r}), n_b(\mathbf{r})\Big) - \Lambda(\mathbf{r}), \tag{9.87b}$$

$$\Delta(\mathbf{r}) = -g_{\text{eff}}(\mathbf{r}) v_c(\mathbf{r}). \tag{9.87c}$$

Varying the functional with respect to the occupation numbers (see Appendix 'Formal Description of the DFT' for a formal description) allows us to derive the self-consistency conditions. Recall that the functional has the form

$$\alpha_-(n_a, n_b) \frac{\hbar^2 \tau_-}{2m} + \alpha_+(n_a, n_b) \left(\frac{\hbar^2 \tau_+}{2m} + \frac{g_{\text{eff}}}{\alpha_+} v_c^\dagger v_c \right) + \frac{\hbar^2}{m} D(n_a, n_b), \tag{9.88}$$

and that, in the limit of infinite cutoff, Λ has no dependence on the functional parameters so that[2]

$$d\tilde{C} = d\left(\frac{\alpha_+}{g_{\text{eff}}} \right) \quad \Rightarrow \quad d\left(\frac{g_{\text{eff}}}{\alpha_+} \right) = -\left(\frac{g_{\text{eff}}}{\alpha_+} \right)^2 d\tilde{C}. \tag{9.89}$$

Thus, we have the following equations:

$$\begin{pmatrix} K_a - \mu_a + v_a & \Delta^\dagger \\ \Delta & -K_b + \mu_b - v_b \end{pmatrix} \begin{pmatrix} u_n \\ v_n \end{pmatrix} = E_n \begin{pmatrix} u_n \\ v_n \end{pmatrix}$$

[2] There is a small correction due to the residual density dependence of Λ at finite cutoff but in practice this is insignificant.

where

$$K_a u = -\frac{\hbar^2}{2m} \nabla_i \left(\alpha_a(n_a, n_b) \nabla_i u \right)$$

$$K_b v = -\frac{\hbar^2}{2m} \nabla_i \left(\alpha_b(n_a, n_b) \nabla_i v \right)$$

$$v_a = \frac{\partial \alpha_-(n_a, n_b)}{\partial n_a} \frac{\hbar^2 \tau_-}{2m} + \frac{\partial \alpha_+(n_a, n_b)}{\partial n_a} \left(\frac{\hbar^2 \tau_+}{2m} - \frac{\Delta^\dagger v}{\alpha_+(n_a, n_b)} \right)$$

$$- \frac{\partial \tilde{C}(n_a, n_b)}{\partial n_a} \frac{\Delta^\dagger \Delta}{\alpha_+} + \frac{\hbar^2}{m} \frac{\partial D(n_a, n_b)}{\partial n_a} + U_a(\mathbf{r}),$$

$$\alpha_\pm(n_a, n_b) = \frac{1}{2} [\alpha_a(n_a, n_b) \pm \alpha_b(n_a, n_b)],$$

$$\tau_\pm = \tau_a \pm \tau_b.$$

and similarly with $a \leftrightarrow b$.

9.3.2 Determining the SLDA and ASLDA Energy Density Functionals

Unless one has perturbative control over the theory, one cannot in general determine the correct functional from first principles. Instead, the functional must be treated as a model incorporating the most relevant physics for the application at hand. As such, one must determine some parameters in order to make predictions about other properties of the system. Here we use properties of homogeneous matter in the thermodynamic limit to determine the parameters of our functional, and then use the functional to compute the properties of non-uniform systems such as trapped gases. Our hope is that the single particle states in the self-consistent approach will provide a good description of the finite size (shell) effects missing in the Thomas Fermi approximation.

Fortunately, the thermodynamic functions describing the unitary Fermi gas are tightly constrained [101], and have both calculational and experimental verification. We shall now describe how to use these constraints to determine the form of the dimensionless parameters describing the functional.

9.3.2.1 Homogeneous Matter

A simple Thomas-Fermi calculation can be employed to describe states of homogeneous matter by exploiting the translational invariance of the system. This allows us to fix all non-gradient terms in the functional. The only remaining term—the effective mass—must be fixed by other means and we use the quasiparticle properties to determine this coefficient.

Normal Phase

The energy-density for the normal phase of homogeneous matter has the form

$$\mathscr{E}[n_a, n_b] = \frac{\hbar^2}{m} \frac{\left(6\pi^2(n_a + n_b)\right)^{5/3}}{20\pi^2} G(p), \quad p = \frac{n_a - n_b}{n_a + n_b} \in [-1, 1]. \quad (9.90a)$$

where

$$G(p) = \alpha(p)\left(\frac{1+p}{2}\right)^{5/3} + \alpha(-p)\left(\frac{1-p}{2}\right)^{5/3} + 2^{-2/3}\beta(p) \quad (9.90b)$$

and $\beta(p)$ is defined through

$$D(n_a, n_b) = \frac{\left(6\pi^2(n_a + n_b)\right)^{5/3}}{20\pi^2} 2^{-2/3}\beta(p). \quad (9.90c)$$

The function $G(p)$ will be the main function that enters our numerical formulae.[3]

We shall define the dimensionless function $G(p)$ by fitting a simple even polynomial to the Monte-Carlo data tabulated for $f[p(x)]$.[4] From this, the function $D(n_a, n_b)$ may be directly expressed in terms of the inverse effective mass $\alpha(p)$, which may be independently parametrized:

$$D(n_a, n_b) = \frac{\left(6\pi^2(n_a + n_b)\right)^{5/3}}{20\pi^2}\left[G(p) - \alpha(p)\left(\frac{1+p}{2}\right)^{5/3} - \alpha(-p)\left(\frac{1-p}{2}\right)^{5/3}\right].$$

The function $G(p)$ describing the normal state has been well-constrained by Monte-Carlo data [64] (see Fig. 9.9). As shown in Fig. 9.9, the function $G(p)$ is very well parametrized by a simple quadratic polynomial:

$$G(p) = 0.357 + 0.642p^2. \quad (9.91)$$

---

[3] In our previous calculations [124, 125], we used a more complicated parametrization: the present form $G(p)$ is just as good and much simpler and we advocate its use instead.

[4] $G(p)$ is related to the other dimensionless functions $f(x)$ and $g(x)$ discussed in the literature as:

$$G(p) = \left(\frac{1+p}{2}g(p)\right)^{5/3} = \left(\frac{1+p}{2}\right)^{5/3} f(p), \quad x = \frac{n_b}{n_a} \in [0, \infty].$$

The function $g(x) = g[p(x)]$ introduced in [101] has the necessary and sufficient requirement of convexity to satisfy the second law of thermodynamics; and the function $f(x) = f[p(x)]$ was introduced in [126] and has been tabulated using Monte-Carlo methods [64].

$$G(p)$$

$$p = (n_a - n_b)/(n_a + n_b)$$

$$f(x) = g^{5/3}(x)$$

$$x = n_b/n_a$$
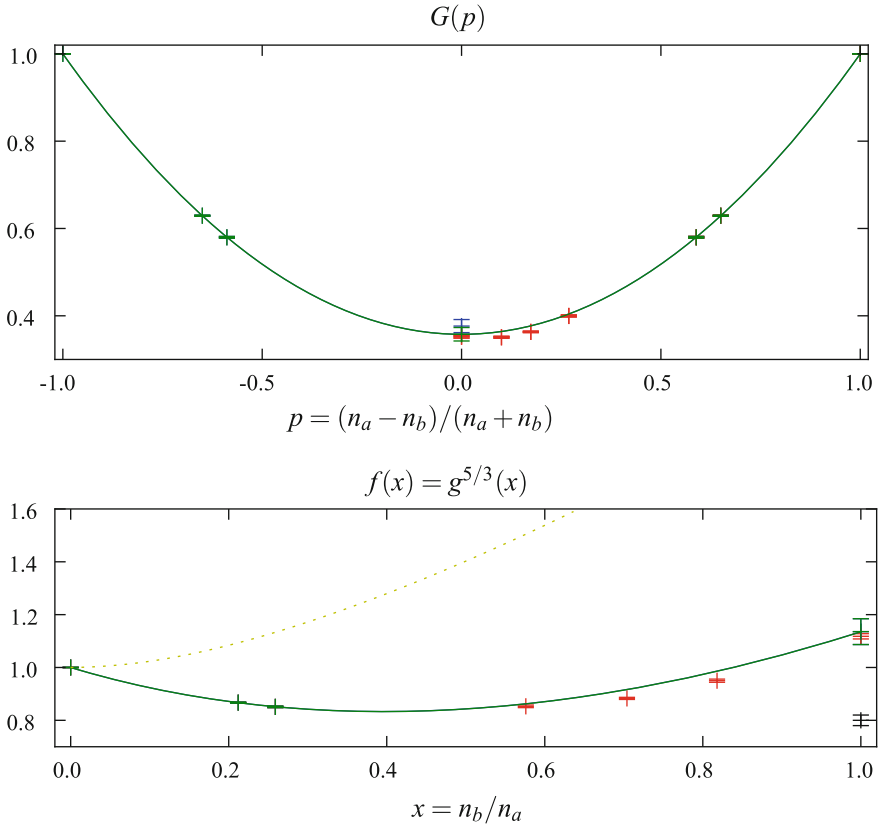
Fig. 9.9 Monte Carlo data used to fit the function $G(p)$ (*top*) and in its raw form $f(x) = g^{5/2}(x)$ (*bottom*) representing the energy of the normal state with respect to the energy of the free system. We excluded the red points from our fit because we suspect that they slightly contaminated by the superfluid state (and hence have a lower energy). Fitting these close to the superfluid state would require a double hump structure in $G(p)$ for which we do not yet see any physical motivation. To anchor the solution in the superfluid phase, we include a datum $\beta_{p=0}$ extracted from the symmetric state (9.95b). The value here depends slightly on whether or not we also extract an effective mass, or hold $\alpha = 1$ constant. Both fits are shown (but lie on top of each other). The present fit is the simple two-parameter quadratic given in (9.91). At the lower-right of the lower plot we have shown the values of $f_{x=1}$ for the superfluid state (*black point*). Finally, for comparison, we have included the function $f(x)$ obtained using the standard mean-field (Eagles–Leggett) approximation as a dotted yellow line to show that it bears little resemblance to the physical curves

Symmetric Superfluid State $n_a = n_b$

As suggested in [127], by considering the calculated properties of the fully paired symmetric superfluid, one may determine the values of the functions $\alpha(p)$, $\tilde{C}(n_a, n_b)$, and $D(n_a, n_b)$ at the point $p = 0$ where the energy density functional depends only on the symmetric combination of parameters $n_a = n_b$ and $\tau_a = \tau_b$.

For any value of the inverse effective mass $\alpha = \alpha_{p=0}$, one can uniquely determine the self-energy $\beta = \beta_{p=0}$ and pairing interaction γ by requiring that the energy and gap satisfy

$$\mathcal{E}_{SF} = \mathcal{E}(n, n) = \xi \mathcal{E}_{FG} = \xi \frac{\hbar^2}{m} \frac{(6\pi^2 n)^{5/3}}{10\pi^2}, \tag{9.92a}$$

$$\Delta = \eta \varepsilon_F = \eta \frac{\hbar^2}{m} \frac{(6\pi^2 n)^{2/3}}{2}. \tag{9.92b}$$

The parameters ξ and $\eta = \Delta/\varepsilon_F$ have been calculated using several Monte-Carlo techniques [18, 46, 58, 61] (S. Zhang, K. E. Schmidt, J. Carlson. Private communication). We take the following values in our estimates [58] (S. Zhang, K. E. Schmidt, J. Carlson. Private communication):

$$\xi = \frac{\mathcal{E}(n, n)}{\mathcal{E}_{FG}(n, n)} = 0.40(1), \qquad \eta = \frac{\Delta}{\varepsilon_F} = 0.504(24). \tag{9.93}$$

In order to determine the effective mass, we consider the quasiparticle dispersion relationship [58]. Within our density functional, this has the form

$$E_{qp}(k) = \sqrt{\left(\frac{\hbar^2 k^2}{2m_{\text{eff}}} - \mu_{\text{eff}} \right)^2 + \Delta^2} \tag{9.94}$$

where $n_a + n_b = k_F^3/3\pi^2$ is the Fermi wave-vector and μ_{eff} is the effective chemical potential. It turns out that μ_{eff} also depends on Δ/ε_F, so the quasiparticle dispersion relation is really a function of only two parameters: the effective mass and Δ/ε_F.

The fit to the Carlson–Reddy data [128] is shown in Fig. 9.10 and gives the following parameter values[5]:

$$\alpha_{p=0} = m_{\text{eff}}^{-1}/m^{-1} = 1.094(17), \tag{9.95a}$$

$$\beta_{p=0} = -0.526(18), \tag{9.95b}$$

$$\gamma^{-1} = -0.0907(77), \tag{9.95c}$$

$$\eta = \Delta/\varepsilon_F = 0.493(12), \tag{9.96d}$$

$$\xi_N = \alpha + \beta = 0.567(24). \tag{9.95e}$$

where $\xi_N \mathcal{E}_{FG}$ is the energy of the interacting normal state predicted by the functional. Note that this agrees very well with the value given by $G(p)$ in Fig. 9.9 (we have used this parameter as an additional point in the fitting of $G(p)$).

---

[5] We have performed a simple two-parameter non-linear least-squares fit which has a reduced $\chi^2_{\text{red}} = 1.1$, indicating a very good fit.
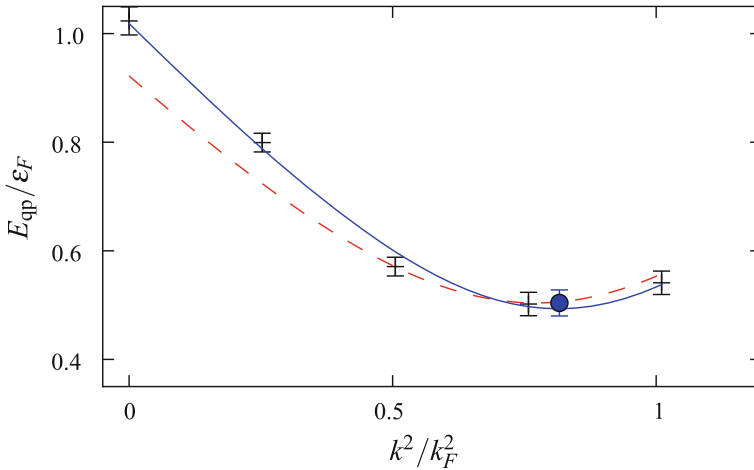
Fig. 9.10 Fit of the Monte-Carlo data for the quasiparticle dispersions from [58] with the BCS form (9.94). The solid blue curve is the full two-parameter fit including the mass as a parameter. This is used to determine the effective mass of the fully paired symmetric matter $m_{\mathrm{eff}} = 0.91(1)$. The *dashed red curve* is a one-parameter fit holding the mass fixed to $m = 1$

In principle, one should use some form of ab initio calculation or experimental measurement for polarized systems to determine the dependence of the parameters α, β, and γ on the polarization $p = n_b/n_a$. Unfortunately, the fermion sign problem has made this difficult and there is presently insufficient quality data to perform such a fit. Instead, we simply fix

$$\gamma(p) = \gamma_{p=0} = -11.11(94). \tag{9.96}$$

If high quality data about polarized superfluid states become available, one might consider promoting this parameter to a polarization dependent function similarly to $\alpha(p)$ and $G(p)$. This fixes the pairing interaction:

$$\tilde{C}(n_a, n_b) = \frac{m}{\hbar^2} \frac{\alpha_+(p)(n_a + n_b)^{1/3}}{\gamma(p)}. \tag{9.97}$$

Effective Mass Parametrization: $\alpha(n_a, n_b)$

As discussed above, the effective mass cannot be determined solely from the properties of homogeneous matter. It is also clear in DFT's developed perturbatively [129, 130] that the effective mass is arbitrary. In the ASLDA, however, the only gradient terms that enter the functional are the kinetic terms τ whose coefficients are the effective masses. To allay the need for additional gradient corrections, one must provide a parametrization of the effective mass. Fortunately, three values are well determined: In a fully polarized system, the effective mass of the majority species remains

Fig. 9.11 Inverse effective mass $\alpha(p) = m/m_{\mathrm{eff}}(p)$ as a function of the polarization $p = (n_a - n_b)/(n_a + n_b)$. The functional fit is the polynomial (9.98).
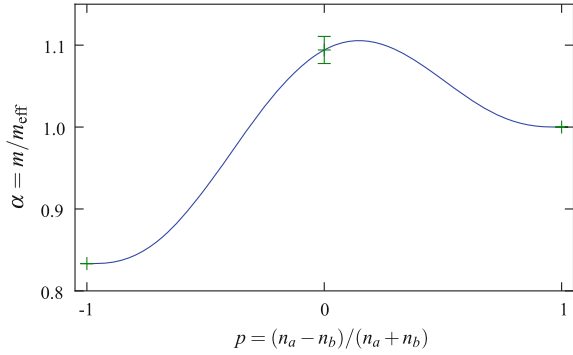
unchanged, $m_{p=1} = 1.0m$, while in the minority species, the effective "polaron" mass $m_{p=-1} = 1.20m$ [131]. We use this value, but note that there are other estimates: Monte Carlo calculations give $m_{-1} = 1.04(3)$ [64] and $m_{-1} = 1.09(2)$ [132], and experiments measure $m_{-1} = 1.06$ (no error given)[133] and $m_{-1} = 1.17(10)$ [134]. The third value for symmetric matter $m_0 = m/\alpha_{p=0}$ is determined in (9.95a).

We now have three data-points constraining the effective mass parametrization of $\alpha(p)$. For numerical reasons, in order to ensure that the effective potentials $v_{a,b}$ approach zero as the density falls to zero, we impose the additional constraint that the first and second derivatives of $\alpha(p)$ vanish at the end-points $p = \pm 1$. Taken together, this fixes a sixth order, two parameter polynomial approximation (Fig. 9.11) for $\alpha(p)$:

$$\alpha(p) = 1.094 + 0.156p(1 - 2p^2/3 + p^4/5) - 0.532p^2(1 - p^2 + p^4/3). \quad (9.98)$$

9.3.2.2 Summary

Here we summarize the complete definition of the ASLDA functional. The SLDA functional follows by setting the local polarization

$$p(\mathbf{r}) = \frac{n_a(\mathbf{r}) - n_b(\mathbf{r})}{n_a(\mathbf{r}) + n_b(\mathbf{r})} \quad (9.99)$$

to zero. First, fitting the quasiparticle dispersion relationships, gap and energy for the superfluid state gives the SLDA parameters at $p = 0$:

$$\alpha_{p=0} = 1.094(17), \quad \beta_{p=0} = -0.526(18), \quad \gamma_{p=0}^{-1} = -0.0907(77). \quad \text{(from (9.95))}$$

Using this derived effective mass, and the energy data for the normal state from Monte Carlo data we obtain the following polynomial fits defining the polarization dependence of the effective mass and self-energy:

$$\alpha(p) = 1.094 + 0.156p\left(1 - \frac{2p^2}{3} + \frac{p^4}{5}\right) - 0.532p^2\left(1 - p^2 + \frac{p^4}{3}\right), \quad \text{(from (9.98))}$$

$$G(p) = 0.357 + 0.642p^2, \quad \text{(from (9.91))}$$

$$\gamma(p) = \gamma_{p=0} = -11.11(94). \quad \text{(from (9.96))}$$

These fix the specification of the functional parameters

$$\alpha_a(n_a, n_b) = \alpha(p), \quad \alpha_b(n_a, n_b) = \alpha(-p), \quad \tilde{C}(n_a, n_b) = \frac{m}{\hbar^2} \frac{\alpha_+(p)(n_a + n_b)^{1/3}}{\gamma(p)},$$

$$D(n_a, n_b) = \frac{\left(6\pi^2(n_a + n_b)\right)^{5/3}}{20\pi^2} \left[G(p) - \alpha(p)\left(\frac{1+p}{2}\right)^{5/3} - \alpha(-p)\left(\frac{1-p}{2}\right)^{5/3} \right],$$

in terms of the densities

$$n_a(\mathbf{r}) = \sum_{|E_n| < E_c} |u_n(\mathbf{r})|^2 f_\beta(E_n), \quad n_b(\mathbf{r}) = \sum_{|E_n| < E_c} |v_n(\mathbf{r})|^2 f_\beta(-E_n),$$

$$\tau_a(\mathbf{r}) = \sum_{|E_n| < E_c} |\nabla u_n(\mathbf{r})|^2 f_\beta(E_n), \quad \tau_b(\mathbf{r}) = \sum_{|E_n| < E_c} |\nabla v_n(\mathbf{r})|^2 f_\beta(-E_n),$$

$$\nu(\mathbf{r}) = \frac{1}{2} \sum_{|E_n| < E_c} u_n(\mathbf{r}) v_n^*(\mathbf{r}) \left(f_\beta(-E_n) - f_\beta(E_n) \right),$$

$$\mathbf{j}_a(\mathbf{r}) = \frac{i}{2} \sum_{|E_n| < E_c} \left[u_n^*(\mathbf{r}) \nabla u_n(\mathbf{r}) - u_n(\mathbf{r}) \nabla u_n^*(\mathbf{r}) \right] f_\beta(E_n),$$

$$\mathbf{j}_b(\mathbf{r}) = \frac{i}{2} \sum_{|E_n| < E_c} \left[v_n^*(\mathbf{r}) \nabla v_n(\mathbf{r}) - v_n(\mathbf{r}) \nabla v_n^*(\mathbf{r}) \right] f_\beta(-E_n),$$

in the form

$$\mathscr{E}_{\text{ASLDA}} = \frac{\hbar^2}{m} \left(\alpha_a(n_a, n_b)\frac{\tau_a}{2} + \alpha_b(n_a, n_b)\frac{\tau_b}{2} + D(n_a, n_b) \right) + g_{\text{eff}} \nu^\dagger \nu$$

together with the renormalization conditions

$$\Delta(\mathbf{r}) = -g_{\text{eff}}(\mathbf{r}) \nu_c(\mathbf{r}), \quad \frac{\alpha_+(\mathbf{r})}{g_{\text{eff}}(\mathbf{r})} = \tilde{C}(\mathbf{r}) - \Lambda(\mathbf{r})$$

$$\Lambda(\mathbf{r}) = \frac{m}{\hbar^2} \frac{k_c(\mathbf{r})}{2\pi^2} \left\{ 1 - \frac{k_0(\mathbf{r})}{2k_c(\mathbf{r})} \ln \frac{k_c(\mathbf{r}) + k_0(\mathbf{r})}{k_c(\mathbf{r}) - k_0(\mathbf{r})} \right\},$$

$$\frac{\hbar^2}{2m}\alpha_+(\mathbf{r})k_0^2(\mathbf{r}) - \mu_+(\mathbf{r}) = 0, \quad \frac{\hbar^2}{2m}\alpha_+(\mathbf{r})k_c^2(\mathbf{r}) - \mu_+(\mathbf{r}) = E_c$$

where $\alpha_+ = (\alpha_a + \alpha_b)/2$ and $\mu_+ = (\mu_a - v_a + \mu_b + v_b)/2$ is the average chemical potential defined through the equations:

$$\begin{pmatrix} K_a - \mu_a + v_a & \Delta^\dagger \\ \Delta & -K_b + \mu_b - v_b \end{pmatrix} \begin{pmatrix} u_n \\ v_n \end{pmatrix} = E_n \begin{pmatrix} u_n \\ v_n \end{pmatrix}$$

where

$$K_a u = -\frac{\hbar^2}{2m} \nabla_i \big(\alpha_a(n_a, n_b) \nabla_i u \big)$$

$$K_b v = -\frac{\hbar^2}{2m} \nabla_i \big(\alpha_b(n_a, n_b) \nabla_i v \big)$$

$$v_a = \frac{\partial \alpha_-(n_a, n_b)}{\partial n_a} \frac{\hbar^2 \tau_-}{2m} + \frac{\partial \alpha_+(n_a, n_b)}{\partial n_a} \left(\frac{\hbar^2 \tau_+}{2m} - \frac{\Delta^\dagger v}{\alpha_+(n_a, n_b)} \right)$$

$$- \frac{\partial \tilde{C}(n_a, n_b)}{\partial n_a} \frac{\Delta^\dagger \Delta}{\alpha_+} + \frac{\hbar^2}{m} \partial D(n_a, n_b) \partial n_a + U_a(\mathbf{r}),$$

$$\alpha_\pm(n_a, n_b) = \frac{1}{2} [\alpha_a(n_a, n_b) \pm \alpha_b(n_a, n_b)],$$

$$\tau_\pm = \tau_a \pm \tau_b.$$

and similarly with $a \leftrightarrow b$.

9.3.3 Using the SLDA and ASLDA

Once the form of the DFT and its parameters have been fixed, the function needs to be tested and applied. Since we fit the parameters using QMC results for homogeneous matter, a non-trivial test is to compare it with ab initio results in inhomogeneous situations. This will asses the accuracy of the approximation we have made in neglecting gradient corrections beyond the kinetic term. In Sect. 9.3.3.1 we compare the predictions of the DFTs with QMC calculations of trapped systems. Next we show how the functionals can be used to explore mesoscopic physics inaccessible to QMC analysis techniques: we consider the structure of superfluid vortices in Sect. 9.3.3.2, and the prediction of a supersolid phase in the asymmetric case in Sect. 9.3.3.3.

9.3.3.1 Trapped Systems

The functional form of both the SLDA and ASLDA have been completely fixed by considering only homogeneous matter. Hence, a non-trivial test of the theory is to compare the energy of trapped systems with Monte Carlo calculations. This was first done for the SLDA in [127] and the results are shown in Fig. 9.12. Even for systems with only a few particles—which have large gradients—the agreement is within 10%. This rapidly improves to the percent level as one move to larger systems.

The agreement is somewhat remarkable. In particular, we have included no gradient corrections in the theory beyond the Kohn-Sham kinetic energy. These gradient corrections will contribute at some level, but in the present system the coefficients are extremely tiny (the leading gradient correction $\sim (\nabla n)^2/n$ should give corrections that scale as $E \propto N^{2/3}$ for which there is no evidence in the Monte Carlo data).

Fig. 9.12 The comparison between the GFMC [135], FN-DMC [136] and SLDA total energies $E(N)$. The clear odd–even staggering of the energies is due to the onset of the pairing correlations. The inset shows the discrepancy between the GFMC and FN-DMC and SLDA energies, $\delta E(N) = E_{MC}(N)/E_{SLDA}(N) - 1$, where $E_{MC}(N)$ stands for the energies obtained in GFMC or FN-DMC respectively
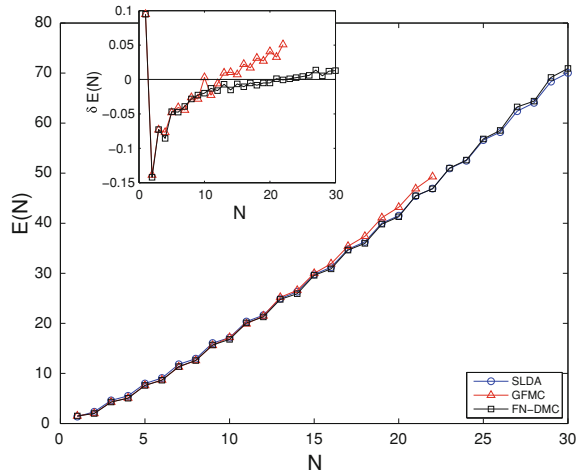
In any case, the agreement provides strong evidence that the SLDA captures the relevant energetics to provide a quantitative model of the unitary Fermi gas.

We should point out that the gradient terms in the SLDA are completely characterized by the kinetic terms. Thus, finite size effects are highly sensitive to the inverse effective mass parameter α. As mentioned in 'Symmetric Superfluid State $n_a = n_b$', the energy and gap can be fit with $\alpha = 1$, but the resulting parametrization demonstrates a marked systematic deviation from the trap energies shown in Fig. 9.12. It is reassuring that the agreement is restored when the effective mass is chosen (9.95a) to reproduce the quasiparticle spectrum.

We have validated the ASLDA in a similar manner for trapped systems in Table 9.2. Again, the agreement is at the few percent level in virtually all cases. In general, the formulation of the unitary DFT has a remarkable ability to capture the finite size effects in systems down to even a few particles [138], lending credence to the approximation of neglecting further gradients beyond the standard kinetic terms. This was somewhat anticipated since the kinetic terms completely describe finite size (shell) effects in the non-interacting system, but is non-trivial in the strongly interacting case of the unitary gas.

Note that the BdG and SLDA functionals have also been considered in larger trapped systems [139, 140].

9.3.3.2 Vortex Structure

The first use of the SLDA was to determine the structure of superfluid vortices [60]. In this work, two forms of SLDA (slightly different parameter values) were considered, and the solution for an axial symmetric vortex with unit circulation was found. The method of solution uses a technique that properly treats the

Table 9.2 Comparison between the ASLDA density functional as described in this section and the FN-DMC calculations [136, 137] for a harmonically trapped unitary gas at zero temperature

(N_a, N_b)	E_{FNDMC}	E_{ASLDA}	(error) (%)
Normal State			
(3,1)	6.6 ± 0.01	6.687	1.3
(4,1)	8.93 ± 0.01	8.962	0.36
(5,1)	12.1 ± 0.1	12.22	0.97
(5,2)	13.3 ± 0.1	13.54	1.8
(6,1)	15.8 ± 0.1	15.65	0.93
(7,2)	19.9 ± 0.1	20.11	1.1
(7,3)	20.8 ± 0.1	21.23	2.1
(7,4)	21.9 ± 0.1	22.42	2.4
(8,1)	22.5 ± 0.1	22.53	0.14
(9,1)	25.9 ± 0.1	25.97	0.27
(9,2)	26.6 ± 0.1	26.73	0.5
(9,3)	27.2 ± 0.1	27.55	1.3
(9,5)	30 ± 0.1	30.77	2.6
(10,1)	29.4 ± 0.1	29.41	0.034
(10,2)	29.9 ± 0.1	30.05	0.52
(10,6)	35 ± 0.1	35.93	2.7
(20,1)	73.78 ± 0.01	73.83	0.061
(20,4)	73.79 ± 0.01	74.01	0.3
(20,10)	81.7 ± 0.1	82.57	1.1
(20,20)	109.7 ± 0.1	113.8	3.7
(35,4)	154 ± 0.1	154.1	0.078
(35,10)	158.2 ± 0.1	158.6	0.27
(35,20)	178.6 ± 0.1	180.4	1
Superfluid State			
(1, 1)	2.002 ± 0	2.302	15
(2, 2)	5.051 ± 0.009	5.405	7
(3, 3)	8.639 ± 0.03	8.939	3.5
(4, 4)	12.573 ± 0.03	12.63	0.48
(5, 5)	16.806 ± 0.04	16.19	3.7
(6, 6)	21.278 ± 0.05	21.13	0.69
(7, 7)	25.923 ± 0.05	25.31	2.4
(8, 8)	30.876 ± 0.06	30.49	1.2
(9, 9)	35.971 ± 0.07	34.87	3.1
(10, 10)	41.302 ± 0.08	40.54	1.8
(11, 11)	46.889 ± 0.09	45	4
(12, 12)	52.624 ± 0.2	51.23	2.7
(13, 13)	58.545 ± 0.18	56.25	3.9
(14, 14)	64.388 ± 0.31	62.52	2.9
(15, 15)	70.927 ± 0.3	68.72	3.1
(1, 0)	1.5 ± 0.0	1.5	0
(2, 1)	4.281 ± 0.004	4.417	3.2
(3, 2)	7.61 ± 0.01	7.602	0.1
(4, 3)	11.362 ± 0.02	11.31	0.49
(7, 6)	24.787 ± 0.09	24.04	3
(11, 10)	45.474 ± 0.15	43.98	3.3
(15, 14)	69.126 ± 0.31	62.55	9.5

The normal state energies are obtained by fixing $\Delta = 0$ in the functional: In the FN-DMC calculations, this is obtained by choosing a nodal ansatz without any pairing. In the case of small asymmetry, the resulting "normal states" may be a somewhat artificial construct as there is no clear way of preparing a physical system in this "normal state" when the ground state is superfluid
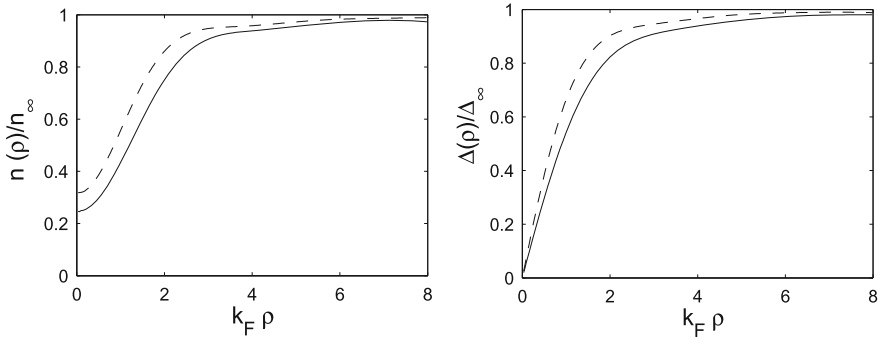
Fig. 9.13 Density profile (*left*) and gap parameter (*right*) from [60] for a superfluid vortex in the symmetric $n_a = n_b$ unitary Fermi gas with unit circulation. The solid curve corresponds to a parametrization of the SLDA with no self-energy $\beta = 0$ but including an effective mass correction. The dotted curve corresponds to a version with unit effective mass $\alpha = 1$. The other two parameters were fixed to reproduce the best approximation to energies of the normal and superfluid states known at the time: $\xi_N = 0.54$ and $\xi_{SF} = 0.44$. The current parameter set (9.95a, b, c, d, e) should be preferred, but gives similar results. Note: The solid curve does not have the required currents to restore Galilean invariance (see Sect. 9.4.2), but the effect should be small here. Since the dotted curve has no effective mass correction, Galilean corrections are not required

infinite boundary conditions without truncating the physical space and introducing finite-size artifacts (see [141, 142] for details). The profile for this vortex is shown in Fig. 9.13. In particular, it was predicted that the vortices should have a significant density depletion in the core—something that is not observed in the weak-coupling limit where pairing is exponentially suppressed. This predicted core depletion allows for the direct imaging of vortices in rotating trapped gasses [143], providing direct evidence for superfluidity in these systems.

9.3.3.3 FFLO/LOFF

The first application of the ASLDA was to consider the energetic stability of a Larkin–Ovchinnikov–Fulde-Ferrell (LOFF) [146–148] polarized superfluid state [125]. The density functional as constructed naturally supports a strong first-order phase transition between the fully paired superfluid state and the interacting normal state (dashed line in Fig. 9.14). We seed the functional with a periodic solution of the form shown in Fig. 9.15 with a node in the gap $\Delta(z)$. Allowing the system to relax to the optimal period L we find that this Larkin–Ovchinnikov type of solution has significantly lower energy than the competing pure and mixed phases over a large range of the phase diagram.

This is a qualitatively new prediction of the ASLDA: such states are only metastable in the BdG. The effect of the self-energy corrections is to reduce the energy of these states to favor them over the homogeneous phases. It is interesting to note that the density contrast of these states is comparable to the density contrast in vortices (see Fig. 9.13). Such states have yet to be observed in experiments: this may be
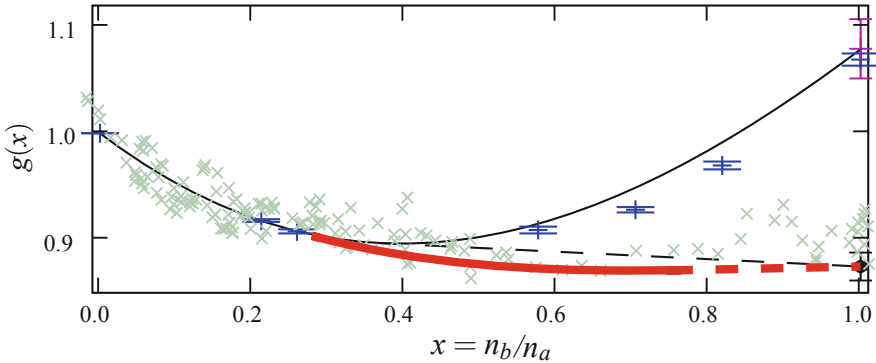
Fig. 9.14 The dimensionless convex function $g(x)$ [101] that defines the energy density $\mathcal{E}(n_a, n_b) = \frac{3}{5} \frac{\hbar^2}{2m} (6\pi^2)^{2/3} [n_a g(x)]^{5/3}$ as a function of the asymmetry $x = n_b/n_a$ (this plot is very similar to Fig. 9.9). The points with error-bars (*blue online*) are the Monte Carlo data from [64, 132, 144]. The fully-paired solution $g(1) = (2\xi)^{3/5}$ is indicated to the bottom right, and the recent MIT data [133] is shown (light ×) for comparison. The phase separation discussed in [64, 101, 132, 144] is shown by the Maxwell construction (*thin black dashed line*) of the first-order transition. The LO state (*thick red curve*) has *lower energy* than all pure states and phase separations previously discussed. The Maxwell construction of the weakly first-order transition between the superfluid and LOFF phase is shown by the *thick dashed line* (*red*)

because the physical region in which the LO state is favoured exists only in a thin shell. Also, the one-dimensional structure discussed here will be unstable at any finite temperature [149] (see also [150]) but might be stabilized in traps. The ground state will most likely be some sort of three-dimensional lattice structure (see for example [151]) which will likely require a fairly large physical volume to exists without significant frustration. The ideal situation would be a very flat trap tuned so that the LO region occupies a large physical space at the center of this trap, however, the construction of such traps presently poses some experimental difficulties that we hope will be overcome in the near future.

9.4 Time-Dependent Superfluid Local Density Approximation

9.4.1 Time-Dependent Equations for the Quasiparticle Wave Functions

The equations for the time-dependent quasiparticle wave functions $u_{n,\sigma}(\mathbf{r}, t)$, $v_{n,\sigma}(\mathbf{r}, t)$ have the time-dependent Bogoliubov-de Gennes form
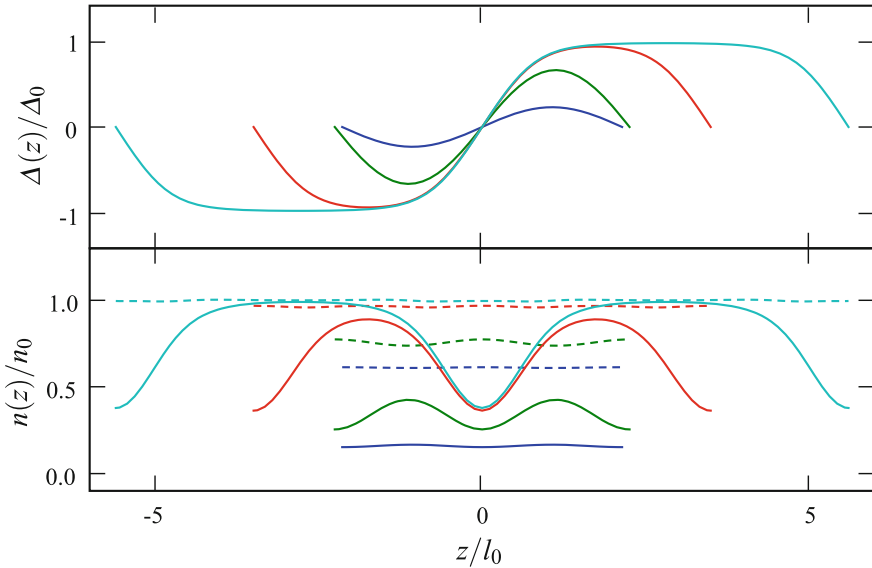
Fig. 9.15 A single LO period showing the spatial dependence of the pairing field $\Delta(z)$ (*top*) and the number densities of the majority (*dotted*) and minority (*solid*) species (*bottom*) at the values. Units are fixed so that $\mu_- = \mu_a - \mu_b$ is held fixed as it is for trapped systems. We normalize everything in terms of the density $n_0 = n_a = n_b$, interparticle spacing $l_0 = n_0^{-1/3}$, and superfluid pairing gap Δ_0 of the fully paired superfluid at the superfluid/LO transition point close to the center of the cloud. At the superfluid/LO transition, the character of the solution is that of widely spaced domain walls (see for example [145]). As one proceeds outward in the trap, the period and amplitude of the solution decreases until it is almost sinusoidal at the transition point to the interacting normal phase

$$
i\hbar \frac{\partial}{\partial t}
\begin{pmatrix} u_a \\ u_b \\ v_a \\ v_b \end{pmatrix}
=
\begin{pmatrix}
h_a + U_a & 0 & 0 & \Delta \\
0 & h_b + U_b & -\Delta & 0 \\
0 & -\Delta^* & -h_a^* - U_a & 0 \\
\Delta^* & 0 & 0 & -h_b^* - U_b
\end{pmatrix}
\begin{pmatrix} u_a \\ u_b \\ v_a \\ v_b \end{pmatrix}.
\qquad (9.100)
$$

For the sake of simplicity, we have dropped the arguments $(\mathbf{r}, t)$ for all functions in these equations. Note also that the external potentials $U_\sigma(\mathbf{r}, t)$ are real. The only difference with the static SLDA in the structure of $h_\sigma(\mathbf{r}, t)$ are the contributions arising from the variation of the current density correction to the kinetic energy density $\tilde{\tau}(\mathbf{r}, t)$ (104,110), which are required by Galilean invariance to be discussed in Sect. 9.4.2. The chemical potentials $\mu_{a,b}$, which can always be thought of as external constraints, are implicitly included in $U_\sigma(\mathbf{r}, t)$. The chemical potentials can also be removed by a simple gauge transformation of the quasi-particle wave functions. It is straightforward to show that these equations conserve the total particle number for arbitrary time-dependent external fields and also for arbitrary time variations of the coupling constant $g(t)$. As expected however, in the presence of an external pairing field, particle number is not conserved: particles can be exchanged with the coupled system implied by the source of the external pairing field.

9.4.2 Galilean Invariance

The functionals as expressed in Sect. 9.2.3 are not manifestly covariant under Galilean transformation (a subset of the general coordinate invariance discussed in [152] which restrict the form of higher-order gradient terms). To restore this covariance, the currents currents $\mathbf{j}_a(\mathbf{r})$ and $\mathbf{j}_b(\mathbf{r})$ described in (9.72a, b) must be included. These vanish in time-reversal invariant ground states, but are crucial for discussing states that break time reversal and for the general time-dependent analysis. In nuclear physics Galilean covariance have been considered for quite some time [153–156], and the contribution of these currents is often essential for describing the properties of excited states.

We start by expressing the Galilean invariance of the Lagrangian density for a single Fermi species (see [152] for a more general discussion)

$$\mathscr{L} = \psi^\dagger \left(i\hbar\partial_t - \frac{(-i\hbar\nabla)^2}{2m} \right) \psi. \tag{9.101}$$

This is invariant under the following Galilean transformation:

$$\psi(\mathbf{x}, t) \rightarrow \exp\left[-i\left(\tfrac{1}{2}m|\mathbf{v}|^2 t + m\mathbf{v}\cdot\mathbf{x} \right) \right] \psi(\mathbf{x} + \mathbf{v}t, t). \tag{9.102}$$

From this, we see that the currents and kinetic densities transform as

$$\mathbf{j} = \frac{i}{2}(\psi^\dagger \nabla\psi + \text{h.c.}) \rightarrow \mathbf{j} + m\mathbf{v}n, \tag{9.103a}$$

$$\tau = \frac{1}{2m}\nabla\psi^\dagger \nabla\psi \rightarrow \tau + \mathbf{v}\cdot\mathbf{j} + \tfrac{1}{2}m|\mathbf{v}|^2 n. \tag{9.103b}$$

It follows directly that for a two-component system, the following combinations are Galilean invariant:

$$\tilde{\tau}_\sigma = \tau_\sigma - \frac{|\mathbf{j}_\sigma|^2}{2m_\sigma n_\sigma}, \qquad \frac{\mathbf{j}_b}{m_b n_b} - \frac{\mathbf{j}_a}{m_a n_a}. \tag{9.104}$$

We would like to separate out the center of mass motion from the intrinsic functional, so we introduce the total mass current and density:

$$\mathbf{j}_+ = \mathbf{j}_a + \mathbf{j}_b, \qquad \rho_+ = m_a n_a + m_b n_b. \tag{9.105}$$

We may then write the functional in the following way:

$$\mathscr{E} = \frac{|\mathbf{j}_+|^2}{2\rho_+} + \tilde{\mathscr{E}}. \tag{9.106}$$

The first term captures the energy of the center of mass motion and $\tilde{\mathscr{E}}$ describes the remaining intrinsic energy of the system, and should be strictly Galilean invariant.

Excited states may be described by an extension of the DFT method commonly referred to as Time-Dependent Density Functional Theory (TDDFT) [157–160]. This theory describes the evolution of the one-body number density in the presence of an arbitrary one-body external field. As in the case of static DFT, one can prove an existence theorem [157–159]. This states that a functional exists from which one can determine the exact time-dependent number density for a given quantum system, and can be expressed in the form

$$
\mathscr{S} = \frac{i\hbar}{2} \int dt\, d^3 r \sum_{n,\sigma} \left\{ v_{n,\sigma}(\mathbf{r}, t) \frac{\partial v_{n,\sigma}^*(\mathbf{r}, t)}{\partial t} - v_{n,\sigma}^*(\mathbf{r}, t) \frac{\partial v_{n,\sigma}(\mathbf{r}, t)}{\partial t} \right\}
$$

$$
- \int dt\, d^3 r \left\{ \frac{\hbar^2}{2m} \sum_{\sigma} \tau_{\sigma}(\mathbf{r}, t) + \sum_{\sigma} U_{\sigma}(\mathbf{r}, t) n_{\sigma}(\mathbf{r}, t) \right.
$$

$$
\left. + \mathscr{E}\left[n_a(\mathbf{r}, t), \tilde{\tau}_a(\mathbf{r}, t), n_b(\mathbf{r}, t), \tilde{\tau}_b(\mathbf{r}, t), |v(\mathbf{r}, t)|^2, g(\mathbf{r}, t) \right] \right\}. \quad (9.107)
$$

Here $\sigma = a, b$ labels the two fermion species. The existence proof for superfluid systems is analogous to the proof for normal systems [157–159]. Here $U_{\sigma}(\mathbf{r}, t)$ are arbitrary time-dependent one-body external fields, which couple to the conserved number densities of the fermion species $n_{\sigma}(\mathbf{r}, t)$. These external fields can represent couplings to the laboratory environment, such as a trapping potential, which can be used to manipulate and study these systems.

The direct coupling of an external gauge field to the electric charge and magnetic moments of the particles can also be incorporated in a straightforward manner, by the usual process of converting the global particle number symmetry to a local symmetry by invoking the principle of gauge invariance. We can also couple an arbitrary time-dependent external pairing field as well to represent interactions with another superfluid system brought into the proximity of the system under study. As mentioned above, this will violate the conservation of particle number as particles are now able to be exchanged with the other system. Finally, the last argument $g(\mathbf{r}, t)$ of the interaction term $\mathscr{E}$ represents the possibility of varying the coupling constants in space and time. In particular, as discussed in Sect. 9.1, by means of a Feshbach resonance an external magnetic field can be used to directly control the scattering length, providing yet another handle to manipulate and study these systems.

In the functional $\mathscr{S}$ we have separated the kinetic energy $\hbar^2 \sum_{\sigma} \tau_a(\mathbf{r}, t)/2m$ from the interaction energy in order to disentangle the dependence on the reference frame. The interaction energy encoded in the functional $\mathscr{E}$ should be independent of the motion of the system as a whole. By default, the properties of the ground states of a physical system are typically discussed in the center of mass reference frame. When the system is excited by various external probes, inevitably currents appear. In the LDA it is natural to assume that the energy density separates into the kinetic energy of center of mass (which depends only on its local center of mass velocity and its corresponding mass) and the internal energy (which should not depend on the local center of mass velocity). The energy density $\mathscr{E}\left[n_a(\mathbf{r}, t), \tilde{\tau}_a(\mathbf{r}, t), n_b(\mathbf{r}, t), \tilde{\tau}_b(\mathbf{r}, t), |v(\mathbf{r}, t)|^2, g(\mathbf{r}, t) \right]$ is the same as in the

static SLDA, with the only difference that the dependence on the modified kinetic energy density $\tilde{\tau}_\sigma(\mathbf{r}, t)$ now includes the current densities (9.72b) to satisfy Galilean invariance

$$\mathbf{j}_\sigma(\mathbf{r}, t) = \frac{i\hbar}{2} \sum_n \left[\nabla v_{n,\sigma}(\mathbf{r}, t) v_{n,\sigma}^*(\mathbf{r}, t) - v_{n,\sigma}(\mathbf{r}, t) \nabla v_{n,\sigma}^*(\mathbf{r}, t) \right]. \qquad (9.108)$$

Here we will describe a slightly different philosophy in implementing the Galilean invariance than discussed at the beginning of this section, which leads to a somewhat different definition of the modified kinetic energy densities $\tilde{\tau}_\sigma(\mathbf{r}, t)$ than those introduced in (9.104) above. This ambiguity illustrates the freedom one has in introducing currents and using no other restriction except Galilean invariance.

Upon boosting the system to a frame with a velocity $\mathbf{V}$, the current density changes $\mathbf{j}_\sigma(\mathbf{r}, t) \rightarrow \mathbf{j}_\sigma(\mathbf{r}, t) + mn(\mathbf{r}, t)\mathbf{V}$. We introduce the velocity of the local center of mass frame ($m_a = m_b = m$)

$$\mathbf{V}(\mathbf{r}, t) = \frac{\mathbf{j}_+(\mathbf{r}, t)}{\rho_+(\mathbf{r}, t)}, \qquad (9.109)$$

where we have introduced the total current $\mathbf{j}_+$ and density ρ_+ from (9.105). Consequently, the following combination of the kinetic energy density, current density and number density

$$\tilde{\tau}_\sigma(\mathbf{r}, t) = \tau_\sigma(\mathbf{r}, t) - \mathbf{j}_\sigma(\mathbf{r}, t) \cdot \mathbf{V}(\mathbf{r}, t) + \frac{mn_\sigma(\mathbf{r}, t)\mathbf{V}^2(\mathbf{r}, t)}{2}, \qquad (9.110)$$

renders the energy density locally Galilean invariant [127]. $\tilde{\tau}_\sigma(\mathbf{r}, t)$ is therefore the internal kinetic energy density in the local center of mass frame, which is different from the form of modified kinetic energy introduced in (9.104). The difference between the two approaches to enforcing the Galilean invariance amounts to terms proportional to $|\mathbf{j}_b/m_b n_b - \mathbf{j}_a/m_a n_a|^2$, see (9.104).

It is worth noticing that because the Galilean invariance is built in, one of the famous relations in the Landau's Fermi liquid theory linking the effective mass of the quasiparticles with the p-wave interaction (denoted F_1) is automatically satisfied (see [12]).

Note also that if terms arise of the form $\mathbf{j}_a(\mathbf{r}, t) \cdot \mathbf{j}_b(\mathbf{r}, t)$, a new physical effect appears whereby the local velocity of one species depends also on the velocity of the other species. In other words, the inverse mass becomes a tensor in the spin ("isospin") space. By including terms of the form $|(\mathbf{j}_a(\mathbf{r}, t) \cdot \nabla n_\sigma(\mathbf{r}, t))|^2$, the effective mass becomes a tensor in real space. This was discussed in [161] in connection with the construction of the optimal local Schrödinger equation to represent a non-local equation. In particular, it seems that, in order to describe some rather subtle level orderings of the single-particle spectrum found in the a non-local Schrödinger equation, one needs a tensor effective mass in the local equations. This is also related to the discussion of superfluid mixtures, where it was observed long ago that one superfluid can drag the other one without any dissipation: the Andreev-Bashkin effect
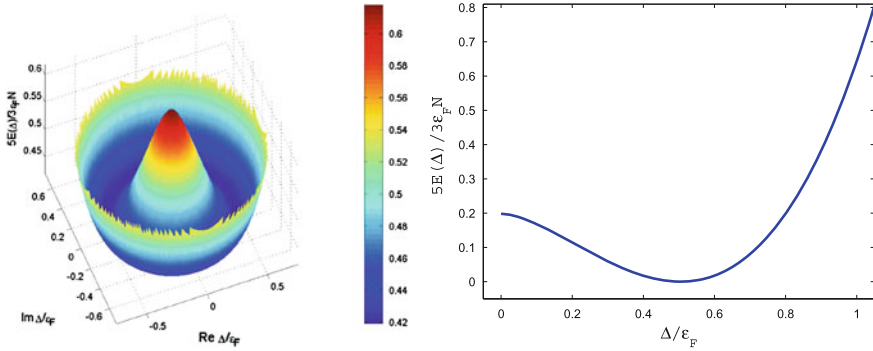
Fig. 9.16 The profile of the energy of a unitary Fermi gas as a function of the pairing gap with respect to the energy of the ground state. One would naïvely expect that this system if released from a point almost at the tip of the "Mexican hat" will roll down along the radial direction, past the equilibrium value $\Delta_0 = 0.5\varepsilon_F$ and oscillate indefinitely back and forth

[162, 163]. Similar effects arise when one considers the terms induced by Galilean invariance (9.110) or $\mathbf{j}_a(\mathbf{r}, t) \cdot \mathbf{j}_b(\mathbf{r}, t)$, when the presence of a current of one species induces a current of the other species.

9.4.3 The Excitation of the Pairing Higgs Mode

We shall illustrate the power of the Time-Dependence SLDA (TD-SLDA) by examining the response of a superfluid unitary gas to the time variation of the scattering length [164]. This problem has been studied extensively in the weak coupling regime when $k_F|a| \ll 1$ and $a < 0$, see [165–184]. The initial state of the system will be the ground state, and at subsequent times, the evolution will be adiabatic in the sense that no entropy production is allowed. To some extent this is a rather strong limitation of this time-dependent description of the quantum evolution, a restriction which can be lifted if one would consider a further extension of the formalism, the Stochastic TD-SLDA [185] which will not be discussed here.

Consider the following scenario [164]: start with a homogeneous unitary Fermi gas in its ground state. At first slowly reduce the coupling constant γ from its unitary value to a very small but still negative value. If this change is slow enough, then the system tracks the ground state into the ground state of the system with an exponentially small pairing gap. Now rapidly ramp the coupling γ back to its unitary value and let the system evolve. This essentially looks at the evolution of an almost normal system with the unitary DFT. The behavior we observe is rather surprising.

Many approaches have been developed to describe the dynamics of a fermionic superfluid at or near $T = 0$ including superfluid hydrodynamics, a Landau–Ginzburg or Gross–Pitaevskii (LG/GP) like description, and effective field theory, see [26, 32,
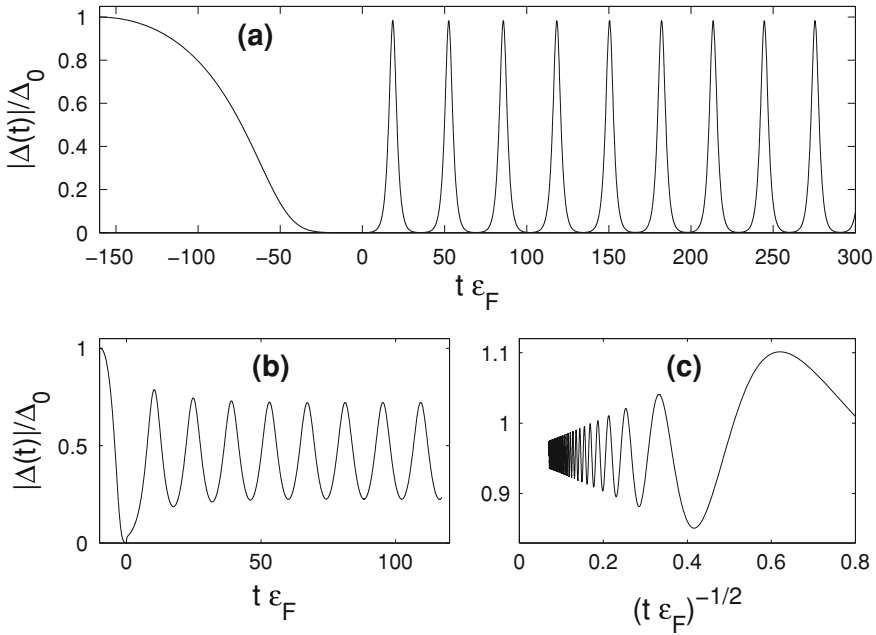
Fig. 9.17 The panels *a,b* and *c* display response of the homogeneous system to an initial switching time interval $t_0 \varepsilon_F = 160, 10$ and 160 and values of the gap corresponding to γ_s are $\gamma_s/\gamma = 0.005, 0.005$ and 0.5 respectively, where γ is the coupling constant controlling the magnitude of the pairing gap and $\Delta_0 \approx 0.5 \varepsilon_F$ is the gap equilibrium value, both at unitarity. The panels *a* and *b* show that when the system is released from the neighborhood of the tip of the "Mexican hat" potential the pairing gap oscillates back and forth, but never past the equilibrium value Δ_0. At the same time the system will rotate around the origin as the phase of the pairing field (not shown here) will monotonically evolve in time as well. However, when the system is released from an initial position closer to the minimum at Δ_0 the oscillation is damped, $\Delta(t) = \Delta_\infty + A \sin(2\Delta_\infty t + \phi)/\sqrt{\Delta_\infty t}$, with a mean frequency $2\Delta_\infty$ and around a value smaller than the equilibrium $\Delta_\infty < \Delta_0$, a behavior which was first studied in [165] in the BCS limit, when the coupling is weak

115, 152, 186–190]. The common thread in all these approaches is the desire to identify a significantly smaller set of relevant degrees of freedom, and achieve an accurate description of the phenomena within a reduced framework. As a rule, when reducing the number of the degrees of freedom, one assumes that the system evolves through states where local equilibrium is maintained. In this instance, one would naïvely expect that the system dynamics are governed by an effective "Mexican hat" potential, Fig. 9.16, representing the energy of the system as a function of the complex pairing field. The system is brought adiabatically from the minimum of the potential to almost the "tip of the Mexican hat", and released with zero initial "velocity". The naïve picture is that the system will "roll" down along the radial direction accelerating until it reaches the minimum of the potential, pass through the minimum, and oscillate back and forth along the "radial" direction without damping.

One might also inspect the LG/GP description of the dynamics of the system using the nonlinear Schrödinger equation

$$i\hbar\frac{\partial\Psi(\mathbf{r},t)}{\partial t} = -\frac{\hbar^2\Delta\Psi(\mathbf{r},t)}{4m} + \mathcal{U}(|\Psi(\mathbf{r},t)|^2)\Psi(\mathbf{r},t). \qquad (9.111)$$

Since there are no spatial gradients in this system (we have changed the coupling in a uniform manner so as not to break the translational invariance), only the second term on the right hand side of this equation contributes, and the solution is a simple monotonic evolution of the condensate phase $\Psi(\mathbf{r},t)$ in time and the magnitude of "wave function" $\Psi(\mathbf{r},t)$ remains constant. In lieu of a better simple alternative, many authors have used this approach to characterize dynamics of Fermi superfluids at essentially zero temperatures, even though the LG/GP description is only justified near the critical temperature.

Another approach is to use the zero-temperature limit of Landau's two fluid hydrodynamics, which reduces to the following two equations at zero temperature

$$\dot{n}(\mathbf{r},t) + \nabla\cdot[\mathbf{v}(\mathbf{r},t)n(\mathbf{r},t)] = 0, \quad m\dot{\mathbf{v}}(\mathbf{r},t) + \nabla\left\{\frac{m\mathbf{v}^2(\mathbf{r},t)}{2m} + \mu[n(\mathbf{r},t)]\right\} = 0.$$
$$(9.112)$$

Here $\mathbf{v}(\mathbf{r},t)$ is the hydrodynamic velocity and $\mu[n(\mathbf{r},t)]$ is the local thermodynamic potential. Since there are no spatial gradients, these two equation simply predict that the number density will remain constant and nothing else will happen.

Apart from the fact that the number density will remain constant and spatially uniform, these three different naïve pictures lead to drastically different predictions. The actual time evolution of the system, shown in Fig. 9.17, is qualitatively different from any individual picture, but demonstrates a combination of the expected features. The pairing gap does increase from almost zero towards the equilibrium value, and it oscillates, but it never crosses the minimum equilibrium value Δ_0 of the "Mexican hat" potential. At the same time, the phase of the pairing gap increases monotonically in time and the number density is constant.

By preparing the initial state slightly differently one can excite different types of these modes that have been dubbed "Higgs" modes of the pairing field. One can vary the upper and the lower values between which the pairing field oscillates, and also adjust the period of these oscillations. It is remarkable, however, that the frequencies of these modes are always smaller than $2\Delta_0$, where Δ_0 is the equilibrium value of the pairing gap at unitarity, even though the excitation energy is large. These are indeed very collective excitations of the system, of extremely low frequency, but with an excitation energy per particle significantly less than pairing gap.

It is still an unresolved question of how these modes will eventually decay and how the system will thermalize. It is also instructive to examine the time dependent population of the various single-particle momentum states of these collective modes as shown in Fig. 9.18. When the value of the pairing gap is very small the occupation probabilities are essentially those of a system in equilibrium. However, when the system reaches a pairing gap essentially equal to the equilibrium value Δ_0, the occupation probabilities are clearly very different from those in the ground state,
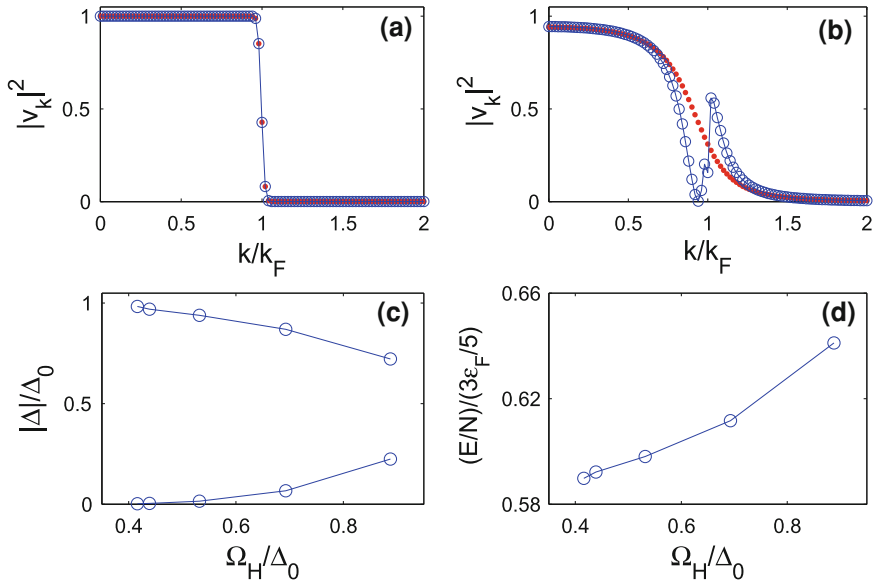
Fig. 9.18 Panels *a* and *b* display the instantaneous occupation probabilities of the mode shown in upper panel of Fig. 9.17 corresponding to times $t > 0$ when the pairing field is at its minimum and maximum values respectively with circles joined by a solid (*blue with circles*) line. With (*red*) dots we plotted the equilibrium occupation probabilities corresponding to the same instantaneous values of the pairing gap. In panels *c* and *d* we show the maximum and minimum values of the oscillating pairing field and the corresponding excitation energy as a function of the frequency of the Higgs-like modes, see Fig.9.17 *a* and *b*

which clearly points to a non-equilibrium state. This aspect should clarify why neither LG/GP nor quantum hydrodynamics are valid as both assume local equilibrium is maintained.

9.4.4 Generation and Dynamics of Vortices

A number of results concerning the generation and dynamics of vortices in a unitary Fermi gas by an external time-dependent perturbation can be found at [191]. As far as we are aware, this problem has been studied in one paper for a pure 2D systems [192]. As in the previous example, we do not yet consider entropy production in these simulations.

In order to illustrate further the power of the TD-SLDA as well as the limitations of traditional approaches such as superfluid hydrodynamics or a LG/GP analysis, we now consider the quantum dynamics of a stirred unitary Fermi gas [191]. We start with the gas in its ground state in a cylindrical trap, uniform and with periodic boundary conditions in the third spatial direction. We then subject the system to a time-dependent external stirring field which breaks the cylindrical symmetry. When implemented numerically [193], if one places the system on a spatial lattice with N_s

spatial lattice points in one direction, one can show that the size of the problem scales as $\propto N_s^5$. When the limitation of spatial homogeneity in the z-direction is lifted the size of the problem scales as $\propto N_s^6$, which as a rule requires an implementation on the largest leadership class supercomputers available. For example, if $N_s = 50$ an efficient solution of the TD-SLDA equations becomes possible only on the JaguarPF Cray XT5,[6] which we are currently utilizing to its full extent.

When homogeneity along the z-direction is enforced, the quasiparticle wave functions have the structure $(u_n(x, y, t) \exp(ikz), v_n(x, y, t) \exp(ikz))$ while self-energy $U(x, y, t)$ and the pairing potential $\Delta(x, y, t)$ are translationally invariant along z. We adiabatically introduce a vertical rod into this "soup can" and stir the gas with a constant angular velocity. One can vary both the stirring radius R and stirring angular frequency ω to control the speed $v_{\text{rod}} = R\omega$ of the rod.

One might expect that if $v_{\text{rod}} \ll v_c$, where v_c is the critical velocity of a unitary Fermi gas, then the system will return to its initial state after the stirring is turned off. However, if $v_{\text{rod}} > v_c$, then one might destroy the superfluid order, resulting in a normal Fermi gas. If $v_1 < v_{\text{rod}} < v_c$, where v_1 is some minimal stirring velocity, one expects that vortices will be created. Unfortunately, none of the simple theories can shed much light on the outcome: superfluid hydrodynamics cannot describe quantum vortices as there is no intrinsic quantization or Planck's constant in its formulation: vortex quantization must be imposed by hand, and there is nothing in principle to prevent decay of a quantized vortex into two fractionally quantized vortices. The time dependent LG/GP approach will also fail to describe the normal state and the transition from superfluid to normal state, as it is formulated explicitly in terms of the order parameter alone, which vanishes in the normal state. Thus, it seems that the only viable solution is to forgo a reduction in the degrees of freedom and deal directly with the quasiparticles included in the DFT.

A unitary Fermi gas is a special system in quite a number of ways: in particular, it appears to have the highest critical velocity of all known superfluids [194, 195]. On the BCS side of the Feshbach resonance, if stirred fast enough, the system can loose superfluidity by the breaking of the Cooper pairs $v_{qp} = \min(E_k, k)$. On the BEC side of the Feshbach resonance, the dominant mechanism for the loss of superfluidity is the excitation of the Anderson-Bogoliubov sound modes $c = v_F \sqrt{\xi/3}$. In the a unitary Fermi gas, these two different critical velocities appear to be essentially identical, and exactly at unitarity one obtains

$$v_c = \min(c, v_{qp}) = v_F \min\left(\sqrt{\frac{\xi}{3}}, \sqrt{\alpha\sqrt{(\bar{\beta} - \xi)^2 + \eta^2} + (\bar{\beta} - \xi)}\right) \approx 0.365 v_F.$$

Since the amount of information one extracts in a TD-SLDA simulation of this type is very large, it is not sufficient to display only a few pictures such as those in Figs. 9.19 and 9.20. We invite the interested reader to explore some of the movies made of these simulations [191]. We shall comment here only on a few selected aspects of these results, most of which will be prepared for a publication at a later time.

---

[6] JaguarPF is a Cray XT5 supercomputer with 224,256 processing cores, see http://ww.nccs.gov.
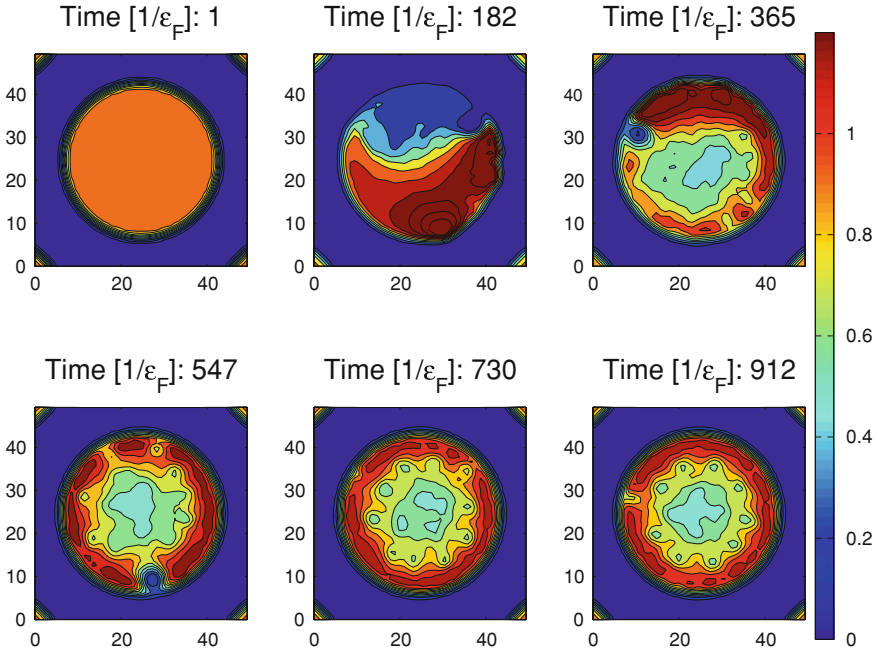
Fig. 9.19 The contour density profiles of a unitary Fermi gas in a cylindrical container, stirred with a uniformly rotating rod, which is inserted and extracted adiabatically from the system. The position (and intensity) of the rod can be inferred as the deepest density depletion in the system, and it is actually visible only in panels 2–4. Initialy the gas shows an almost uniform density distribution, and subsequently it is gathered almost entirely in front of the stirring rod. The magnitude of the density is in units of the unperturbed central initial density of the cloud and the colorbar on the right decodes the meaning of each color used. By the end of the simulation there are 13 vortices forming an almost perfect triangular Abrikosov lattice in this confined geometry

Our expectation that, under gentle stirring, the unitary Fermi gas will return to its initial superfluid state is supported by the simulations [191], and is in line with how one would expect a superfluid to respond to such an external probe. The other expectation, that vigorous stirring can destroy the superfluid order is also confirmed. Within TD-SLDA, the dynamic generation of vortices as well as formation of the celebrated Abrikosov vortex lattice are also readily demonstrated. By varying shape, the number and the stirring velocity we generated a plethora of quantized vortices in this "soup can" of superfluid unitary Fermi gas [191].

While we expected to generate a relatively small number of vortices at low stirring velocity, and that the number of vortices will increase with more vigorous stirring, many of the features of dynamic vortex generation are quite surprising. The fact that this system is compressible results in surprisingly large time-dependent variations of the local number density. Often the entire mass of the system is gathered in front of the stirrer, leaving little matter behind it: The gas can occupy less than half of the available volume, even though the volume excluded by the stirrer is quite small. It also comes as
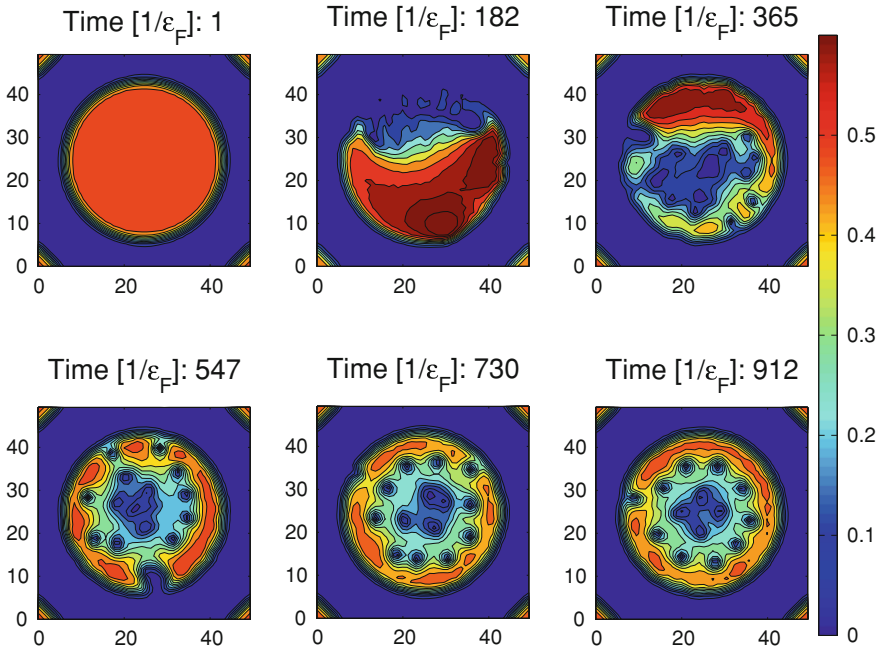
Fig. 9.20 The corresponding contour profiles of the pairing field $|\Delta(x, y, t)|$ a unitary Fermi gas in a cylindrical container, stirred with a uniformly rotating rod. A plot (not shown here) of the phase of the pairing field $\arg \Delta(x, y, t)$ shows that as one circles a vortex core the phase changes by 2π, thus each of these vortices carries exactly $\hbar/2$ units of angular momentum per particle and both the number (normal) density and the pairing field are significantly depleted in the core of the vortex [60]

a great surprise that the system does not loose quantum coherence under such a violent perturbation. Moreover, it organizes itself in an almost perfect vortex lattice after the stirring is turned off. Even more surprising is that the system remains superfluid, *even when stirred at supercritical speeds!* We have observed that the system forms a vortex lattice even if stirred with speeds up to $v_s = 0.60 v_F > v_c \approx 0.365 v_F$ (see the case of 7 vortices with a large radius stirrer at [191]). We attribute this behavior to the fact that an increased density of the cloud during the stirring process corresponds to an increased local critical velocity, since the local Fermi velocity increases as well accordingly.

These two cases of exciting and monitoring the unitary Fermi gas by two drastically different methods illustrate both the power and flexibility of this framework, as well as the richness of the phenomena waiting to be fully explored. One potential topic to be explored by these techniques that has mesmerized the low temperature community during the past few decades is quantum turbulence [196–198]. Hopefully this can also be replicated in experiments with cold atomic fermionic gases. Due to the complexity of the full 3D time-dependent Bogoliubov-de Gennes equations, this

aspect has never been theoretically addressed for fermionic systems. The TD-SLDA appears as a framework of choice in this respect. In particular one can address on a fully microscopic basis for vortex reconnection dynamics, which is likely at the heart of quantum turbulence at zero temperature, where dissipative processes are greatly inhibited.

9.5 Concluding Remarks

We have reviewed here three methods to describe the properties of many-body systems starting from the bare Hamiltonian, and building a practical framework for studying nontrivial properties of mesoscopic systems and quantum dynamics.

The QMC method is particularly suited to calculate properties of the homogeneous phase of matter in an unbiased fashion. It also can be used for inhomogeneous systems, but is limited by system size and can not handle large number of Fermions. It is also generally plagued by the infamous sign problem (except in exceptionally symmetric contexts) and so far has not been used to describe systems in the time dependent domain.

The complimentary approach of DFT through the use of the SLDA and ASLDA can be applied to extend these results to mesoscopic systems with larger number of particles and a wide variety of geometries. The time dependent TDDFT (TD-SLDA) extension brings these techniques to bear on time-dependent quantum dynamics. The main difficulty with the DFT is that there is no well defined procedure to construct the functional. However, in the particular case of a unitary Fermi gas, the form of the SLDA and ASLDA functionals is sufficiently restricted by dimensional analysis, QMC results, and Galilean invariance as to be able to make testable predictions with relatively small uncertainties. This has been validated with both ab initio theoretical and experimental results.

The next step is to use such tools to make predictions about the properties of the unitary gas under various conditions: by changing the geometry and even the Hamiltonian as a function of time, by probing the system with a variety of external probes and exciting a plethora of modes—both linear and nonlinear—and by studying both the equilibrium and non-equilibrium dynamics. We have illustrated a few of these applications, but it is clear that we have barely scratched the surface of this subject.

The Fermi gas in the unitary regime proves to be an extraordinarily rich physical system to study, not only because one can both theoretically and experimentally address many of its properties with both precision and accuracy, but because it has so many truly unexpected phases and dynamical phenomena.

Many fascinating features of this systems are still waiting to be revealed in experiments in their full glory, including: the pseudogap phase, the supersolid LOFF phase, p-wave superfluidity [199, 200], the Higgs mode of the pairing field, the behavior and response to various spatial and time varying trapping fields and probes, the dynamics of vortices which opens a window to quantum turbulence both theoretically and

experimentally, the existence of supercritical superflow, and its kinetic properties—in particular its viscosity. One can safely state that the most extraordinary features of the unitary gas are still waiting to be demonstrated.

Perhaps the most captivating part of the story of the unitary Fermi gas is that it provides a link to an abundance of widespread fields of physics, from optics and atomic physics, to condensed matter physics, to nuclear physics and the physics of neutron stars, color superconductivity in QCD and dark matter, relativistic heavy ion collisions, and the AdS/CFT approaches in quantum field theory.

Appendix

Formal Description of the DFT

Here we present a somewhat formal derivation of the variational property of the Kohn-Sham equations. Consider a general free-energy functional of the following form

$$F = E(n_A, n_B, \cdots) + T \operatorname{Tr}(\rho \ln \rho) \qquad (9.113)$$

where

$$n_A = \operatorname{Tr}\left(\rho A^T\right),$$
$$n_B = \operatorname{Tr}\left(\rho B^T\right),$$
$$\vdots$$

are the various densities, anomalous densities, etc. expressed linearly in terms of the one-body density matrix ρ. By varying the functional with respect to the density

matrix ρ subject to the appropriate constraints on density matrix form (discussed in 'Fermions'), one obtains a solution of the form

$$\rho = f_\beta(\mathbf{H}[\rho]) \qquad (9.114)$$

where $f_\beta(E)$ is the appropriate thermal distribution for the particles of interest, and $\mathbf{H}$ is a single-particle Hamiltonian that depends on ρ:

$$\mathbf{H}[\rho] = \partial En_A \mathbf{A} + \partial En_B \mathbf{B} + \cdots . \qquad (9.115)$$

The typical Kohn-Sham equations follow by diagonalizing the self-consistency condition (9.114) with a set of normalized Kohn-Sham eigenfunctions of definite energy:

$$\mathbf{H}|n\rangle = E_n|n\rangle. \qquad (9.116)$$

The density matrix is diagonal in this basis and expressed in terms of the appropriate distribution functions $f_\beta(E)$:

$$\rho = \sum_n f_\beta(E_n)|n\rangle\langle n|. \qquad (9.117)$$

All of the functionals considered in this chapter may be expressed in this form. Once the appropriate matrix structures $\mathbf{A}$, $\mathbf{B}$ etc. are described, the form of the Kohn-Sham equations and potentials follows directly from these expressions.

Fermions

The only remaining complication is to impose the appropriate constraint on the density matrix ρ. This ensures that the appropriate statistics of the particles is enforces. As we shall be interested in 'Fermions', the relevant constraint on the density matrix (dictated by the canonical commutation relationships) is

$$\rho + \mathbf{C}\rho^T\mathbf{C} = 1 \qquad (9.118)$$

where $\mathbf{C} = \mathbf{C}^T$ is the charge conjugation matrix:

$$\mathbf{C}|\psi\rangle = |\psi\rangle^*. \qquad (9.119)$$

This follows from the anti-commutation relationship for fermions and is discussed further in the 'Single Particle Hamiltonian'. The constrained minimization of the functional $F(\rho)$ results in the standard Fermi distribution[7]

---

[7] Formally, this constraint can be implemented using a Lagrange multiplier, but it is much easier to see the results by letting $\rho = 1/2 + \mathbf{x} - \mathbf{C}\mathbf{x}^T\mathbf{C}$ where $\mathbf{x}$ is unconstrained, and then performing the variation with respect to $\mathbf{x}$.

$$\rho = \frac{1}{1 + e^{\beta(\mathbf{H}[\rho] - \mathbf{C}\mathbf{H}^T[\rho]\mathbf{C})}}, \tag{9.120}$$

which is the fermionic form of the self-consistency condition (9.114) for the density matrix ρ. In practise, one does not iterate the entire density matrix. Instead, one stores only the densities n_A, n_B, etc. Through (9.115), these define the Kohn-Sham Hamiltonian $\mathbf{H}$, which is then diagonalized to form the new density matrix and finally the new densities. If, for example, symmetries allow the Hamiltonian $\mathbf{H}$ to be block diagonalized, then one can construct and accumulate the densities in parallel over each block. Finally, the densities represent far fewer parameters than the full density matrix. Thus, more sophisticated root-finding techniques such as Broyden's method [201] may be efficiently employed: Applying these techniques to the full density matrix would be significantly more expensive.

Single Particle Hamiltonian

It is convenient to express these concepts in the language of second quantization. The Hamiltonian will appear as a quadratic operator of the form

$$H_s = \frac{1}{2}\Psi^\dagger \mathscr{H}_s \Psi \tag{9.121}$$

where Ψ has several components and $\mathscr{H}_s$ is a matrix. The factor of $1/2$ accounts for the double counting to be discussed below. For a two component system, the most general Ψ that allows for all possible pairings has four components:

$$\Psi = \begin{pmatrix} a \\ b \\ a^\dagger \\ b^\dagger. \end{pmatrix}. \tag{9.122}$$

In terms of components of the wavefunction, we will write $\mathscr{H}_s \psi = E\psi$ where:

$$\psi = \begin{pmatrix} u_a \\ u_b \\ v_a \\ v_b \end{pmatrix}. \tag{9.123}$$

The naming of these components is conventional (see for example [117]) and the functions u and v are typically called "Coherence Factors". Note that the convention is that $v_{a,b}^*(\mathbf{r}, t)$ are the wavefunctions of the particles. In this formulation the Hamiltonian has the form presented in (9.100):

$$\mathscr{H}_s = \begin{pmatrix} h_a + U_a & 0 & 0 & \Delta \\ 0 & h_b + U_b & -\Delta & 0 \\ 0 & -\Delta^* & -h_a^* - U_a & 0 \\ \Delta^* & 0 & 0 & -h_b^* - U_b \end{pmatrix} \tag{9.124}$$

Four-Component Formalism

We shall start with this full four-component formalism but soon utilized a reduction: If the superfluid pairing $\Delta \sim \langle ab \rangle$ channel is attractive, then often the "Fock" channel is repulsive so we can take $\langle a^\dagger b \rangle = 0$. In combination with the double-counting discussed below, this will allow us to fully express the system in terms of two components.

The four-component formalism double counts the degrees of freedom: Ψ contains both a and $a^\dagger$. This degeneracy is described in terms of the charge conjugation matrix $\mathscr{C}$:

$$\Psi^\dagger = \mathscr{C}\Psi \quad \text{where} \quad \mathscr{C} = \begin{pmatrix} 0 & 1 \\ 1 & 0 \end{pmatrix}. \tag{9.125}$$

The operator Ψ will satisfy the single-particle Shrödinger equations

$$H_s |\Psi\rangle = E|\Psi\rangle \tag{9.126}$$

where the Hamiltonian $H_s = \Psi^\dagger \mathscr{H}_s \Psi$ can be chosen to satisfy (the sign implements Fermi statistics)

$$\mathscr{C} \mathscr{H}_s^T \mathscr{C} = -\mathscr{H}_s. \tag{9.127}$$

In this form, the charge conjugation symmetry ensures that the eigenstates will appear in $\pm E$ pairs.[8] Keeping only one set of pairs will ensure that we do not double count. Using this symmetry, we can formally diagonalize the Hamiltonian by a unitary transformation $\mathscr{U}$ such that:

$$\mathscr{U}^\dagger \mathscr{H}_s \mathscr{U} = \frac{1}{2} \begin{pmatrix} \mathbf{E} & \mathbf{0} \\ \mathbf{0} & -\mathbf{E} \end{pmatrix} \tag{9.128}$$

where $\mathbf{E} = \text{diag}(E_i)$ is diagonal. The columns of the matrix $\mathscr{U}$ are the (ortho) normalized wave-functions and describe the "coherence" factors. To determine the correct expressions for the densities in terms of the wavefunctions we form them in the diagonal basis and then transform back to the original basis using $\mathscr{U}$.

Despite this formal degeneracy of eigenstates, we are not aware of a general technique to block-diagonalize the original Hamiltonian in the presence of non-zero terms of the form $\langle a^\dagger b \rangle$, though perhaps the symmetry might be incorporated into the eigensolver.

---

[8] Suppose $\mathscr{H}_s \psi = \epsilon \psi$. Applying (9.127), using $\mathscr{C}^2 = 1$, and taking the transpose imply that $\psi^T \mathscr{C}^T \mathscr{H}_s = -\epsilon \psi^T \mathscr{C}^T$. Since left and right eigenvalues are the same, this implies that there is some other state such that $\mathscr{H}_s \tilde{\psi} = -\epsilon \tilde{\psi}$. For Hermitian Hamiltonians, $\mathscr{H}_s = \mathscr{H}_s^\dagger$, hence, the other state can be directly constructed as $\tilde{\psi} = \mathscr{C}\psi^*$.

Two-Component Formalism

If $\langle a^\dagger b \rangle = 0$, however, then the Hamiltonian is naturally block diagonal:

$$\mathscr{H}_s = \frac{1}{2}\begin{pmatrix} \mathbf{H}_s & \mathbf{0} \\ \mathbf{0} & -\mathbf{H}_s^T \end{pmatrix}, \qquad H_s = \psi^\dagger \mathbf{H}_s \psi + \text{const}, \tag{9.129}$$

and one may consider only a single block in terms of the reduced set of operators

$$\psi = \begin{pmatrix} a \\ b^\dagger \end{pmatrix}. \tag{9.130}$$

This directly avoids any double counting issues. This system may be diagonalized:

$$\mathbf{H}_s \mathbf{U} = \mathbf{U}\mathbf{E}. \tag{9.131}$$

The matrix $\mathbf{U}$ defines the single "quasi"-particle operators ϕ as linear combination of the physical particle operators contained in ψ:

$$\phi = \mathbf{U}^\dagger \psi. \tag{9.132}$$

The Hamiltonian is diagonal in this basis

$$H_s = \phi^\dagger \cdot \mathbf{E} \cdot \phi \tag{9.133}$$

and hence expectation values may be directly expressed

$$\langle \phi\phi^\dagger \rangle = \theta_\beta(\mathbf{E}) = \begin{pmatrix} \theta_\beta(E_0) & & & \\ & \theta_\beta(E_1) & & \\ & & \ddots & \\ & & & \theta_\beta(E_n) \end{pmatrix}$$

where $1 - \theta_\beta(E) = f_\beta(E)$ is the appropriate distribution function: For fermions we have

$$\theta_\beta(E) = \frac{1}{1 + e^{-\beta E}}. \tag{9.134}$$

At $T = 0$ this reduces to $\theta_0(E) = \theta(E)$ and is equivalent to the zero-temperature property that negative energy states are filled while positive energy states are empty. This may be simply transformed back into the original densities (on the diagonal) and anomalous densities (off-diagonal):

$$\mathbf{F}_+ = \langle \psi\psi^\dagger \rangle = \begin{pmatrix} \langle aa^\dagger \rangle & \langle ab \rangle \\ \langle b^\dagger a^\dagger \rangle & \langle b^\dagger b \rangle \end{pmatrix} = \mathbf{U}\theta_\beta(\mathbf{E})\mathbf{U}^\dagger,$$

$$\mathbf{F}_-^T = \langle \psi^*\psi^T \rangle = \begin{pmatrix} \langle a^\dagger a \rangle & \langle a^\dagger b^\dagger \rangle \\ \langle ba \rangle & \langle bb^\dagger \rangle \end{pmatrix} = \mathbf{U}^*\theta_\beta(-\mathbf{E})\mathbf{U}^T.$$

Fermi statistics demands $\mathbf{F}_- + \mathbf{F}_+ = 1$ but we may have to relax this requirement somewhat in order to regulate the theory in terms of an energy cutoff $\theta_c(E)$. The columns of $\mathbf{U}_n$ of $\mathbf{U}$ correspond to the single-particle "wavefunctions" for the state with energy E_n. We partition these into two components sometimes referred to as "coherence factors"

$$\mathbf{U}_n = \begin{pmatrix} \mathbf{u}_n \\ \mathbf{v}_n \end{pmatrix}. \tag{9.135}$$

The unitarity of $\mathbf{U}$ imposes the conditions that

$$\mathbf{u}_m^\dagger \mathbf{u}_n + \mathbf{v}_m^\dagger \mathbf{v}_n = \delta_{mn} \tag{9.136a}$$

$$\sum_n \mathbf{u}_n \mathbf{u}_n^\dagger = \sum_n \mathbf{v}_n \mathbf{v}_n^\dagger = 1, \tag{9.136b}$$

$$\sum_n \mathbf{u}_n \mathbf{v}_n^\dagger = \sum_n \mathbf{v}_n \mathbf{u}_n^\dagger = 0. \tag{9.136c}$$

From this we may read off the expressions for the densities

$$\mathbf{n}_a = \langle a^\dagger a \rangle = \sum_n \mathbf{u}_n^* \mathbf{u}_n^T \theta_\beta(-E_n), \tag{9.137a}$$

$$\mathbf{n}_b = \langle b^\dagger b \rangle = \sum_n \mathbf{v}_n \mathbf{v}_n^\dagger \theta_\beta(E_n), \tag{9.137b}$$

$$\nu = \langle ab \rangle = \sum_n \mathbf{u}_n \mathbf{v}_n^\dagger \theta_\beta(E_n) \tag{9.137c}$$

$$= -\sum_n \mathbf{u}_n \mathbf{v}_n^\dagger \theta_\beta(-E_n) \tag{9.137d}$$

$$= \sum_n \mathbf{u}_n \mathbf{v}_n^\dagger \frac{\theta_\beta(E_n) - \theta_\beta(-E_n)}{2}. \tag{9.137e}$$

The last form for ν must be used if the regulator is implemented such that $\theta_c(E) + \theta_c(-E) \neq 1$, in particular, if $\theta_c(E) = 0$ for $|E > E_c|$. Note that these expressions are basis independent, e.g. in position space:

$$n_a(\mathbf{r}, \mathbf{r}') = \sum_n u_n(\mathbf{r})^* u_n(\mathbf{r}')^T \theta_\beta(-E_n). \tag{9.138}$$

The energy E_n here is the energy determined by solving these equations and will contain both positive and negative energies.

References

1. Eagles, D.M.: Phys. Rev. **186**(2), 456 (1969). doi:10.1103/PhysRev.186.456
2. Leggett, A.J.: In: Pekalski, A., Przystawa, J. (eds.) Modern Trends in the Theory of Condensed Matter, Lecture Notes in Physics. Proceedings of the XVI Karpacz Winter School of Theoretical Physics, pp. 13–27. Springer, Berlin (1980)
3. Nozières, P., Schmitt-Rink, S. J.: Low Temp. Phys. **59**, 195 (1985). doi:10.1007/BF00683774
4. Sá de Melo, C.A.R., Randeria, M., Engelbrecht, J.R.: Phys. Rev. Lett. **71**(19), 3202 (1993)
5. Engelbrecht, J.R., Randeria, M., Sáde Melo, C.A.R.: Phys. Rev. B **55**(22), 15153 (1997)
6. Randeria, M.: In: Griffin, A., Snoke, D.W., Stringari, S. (eds.) Bose–Einstein Condensation, pp. 355–392. Cambridge University Press, Cambridge (1995). Chap. 15
7. Haussmann, R.: Zeitschrift fur Physik B Condens. Matter **91**, 291 (1993)
8. Haussmann, R.: Phys. Rev. B **49**(18), 12975 (1994)
9. Pistolesi, F., Strinati, G.C.: Phys. Rev. B **49**(9), 6356 (1994)
10. Pistolesi, F., Strinati, G.C.: Phys. Rev. B **53**(22), 15168 (1996)
11. Pieri, P., Strinati, G.C.: Phys. Rev. B **61**(22), 15370 (2000)
12. Abrikosov, A.A., Gorkov, L.P., Dzyaloshinski, I.E.: Methods of Quantum Field Theory in Statistical Physics. Dover, New York (1975)
13. Gorkov, L., Melik-Barkhudarov, T.: Sov. Phys.–JETP **13**(5), 1018 (1961)
14. Petrov, D.S., Salomon, C., Shlyapnikov, G.V.: Phys. Rev. Lett. **93**(9), 090404 (2004)
15. Bulgac, A., Bedaque, P.F., Fonseca, A.C.: arXiv:cond-mat/0306302v2 (2003)
16. Brodsky, I.V., Kagan, M.Y., Klaptsov, A.V., Combescot, R., Leyronas, X.: Phys. Rev. A **73**(3), 032724 (2006)
17. Levinsen, J., Gurarie, V.: Phys. Rev. A **73**(5), 053607 (2006)
18. Carlson, J., Chang, S.Y., Pandharipande, V.R., Schmidt, K.E.: Phys. Rev. Lett. **91**, 050401 (2003)
19. Bulgac, A., Drut, J.E., Magierski, P.: Phys. Rev. Lett. **96**(9), 090404 (2006)
20. Bertsch, G.F.: The Many-Body Challenge Problem (MBX) (1999). See also [22,23]
21. Ho, T.L.: Phys. Rev. Lett. **92**(9), 090402 (2004)
22. Baker, G.A.: Phys. Rev. C **60**(5), 054311 (1999)
23. Baker, G.A.: Int. J. Mod. Phys. B **15**(10–11), 1314 (2001)
24. Heiselberg, H.: Phys. Rev. A **63**(4), 043606 (2001)
25. O'Hara, K.M., Hemmer, S.L., Gehm, M.E., Granade, S.R., Thomas, J.E.: Science **298**, 2179 (2002)
26. Giorgini, S., Pitaevskii, L.P., Stringari, S., Rev. Mod. Phys. **80**, 1215 (2008)
27. Bloch, I., Dalibard, J., Zwerger, W.: Rev. Mod. Phys. **80**(3), 885 (2008). doi:10.1103/RevModPhys.80.885
28. Ketterle, W., Zwierlein, M.W.: In: Inguscio, M. et al. [29], pp. 95–287. doi:10.3254/978-1-58603-846-5-9
29. Inguscio, M., Ketterle, W., Salomon, C. (eds.): Ultra-Cold Fermi Gases, International School of Physics "Enrico Fermi", vol. 64, IOS Press, Amsterdam (2007)
30. Luo, L., Thomas, J.E.: J. Low Temp. Phys. **154**(1), 1 (2009). doi:10.1007/s10909-008-9850-2
31. Grimm, R., in Inguscio et al.: [29], pp. 413–462. doi:10.3254/978-1-58603-846-5-413
32. Nishida, Y., Son, D.T.: Phys. Rev. Lett. **97**(5), 050403 (2006)
33. Son, D.T.: Phys. Rev. D **78**(4), 046003 (2008)
34. Stoof, H.T.C., Koelman, J.M.V.A., Verhaar, B.J.: Phys. Rev. B **38**(7), 4688 (1988)
35. Tiesinga, E., Kuppens, S.J.M., Verhaar, B.J., Stoof, H.T.C.: Phys. Rev. A **43**(9), 5188 (1991)
36. Tiesinga, E., Moerdijk, A.J., Verhaar, B.J., Stoof, H.T.C.: Phys. Rev. A **46**(3), R1167 (1992)
37. Tiesinga, E., Verhaar, B.J., Stoof, H.T.C.: Phys. Rev. A **47**(5), 4114 (1993)
38. Moerdijk, A.J., Verhaar, B.J., Axelsson, A.: Phys. Rev. A **51**(6), 4852 (1995)
39. Köhler, T., Góral, K., Julienne, P.S.: Rev. Mod. Phys. **78**(4), 1311 (2006)
40. Duine, R.A., Stoof, H.T.C.: Phys. Rep. **396**, 115 (2004)
41. Timmermans, E., Tommasini, P., Hussein, M., Kerman, A.: Phys. Rep. **315**(1–3), 199 (1999)

42. Forbert, H.A., Chin, S.A.: Int. J. Mod. Phys. B **15**, 1752 (2001)
43. Suzuki, M.: Phys. Lett. A **146**(6), 319 (1990)
44. Yoshida, H.: Phys. Lett. A **150**(5–7), 262 (1990)
45. Creutz, M., Gocksch, A.: Phys. Rev. Lett. **63**(1), 9 (1989)
46. Bulgac, A., Drut, J.E., Magierski, P.: Phys. Rev. A **78**(2), 023625 (2008)
47. Negele, J.W., Orland, H.: Quantum Many-particle Systems. Westview Press, Reading, MA (1998)
48. Hirsch, J.E.: Phys. Rev. B **28**(7), 4059 (1983)
49. Koonin, S.E., Dean, D.J., Langanke, K.: Phys. Rep. **278**(1), 1 (1997)
50. Alhassid, Y.: Int. J. Mod. Phys. B **15**, 1447 (2001)
51. Wlazłowski, G., Magierski, P.: Int. J. Mod. Phys. E **18**, 919 (2009)
52. Bulgac, A., Drut, J.E., Magierski, P.: Int. J. Mod. Phys. B **20**, 5165 (2006)
53. Barber, M.N.: In: Domb, C., Lebowitz, J.L. (eds.) Phase Transitions and Critical Phenomena, Phase Transitions and Critical Phenomena, vol. 8, pp. 146. Academic Press, New York (1983)
54. Tan, S.: Annals of Physics **323**(12), 2971 (2008)
55. Braaten, E., Platter, L.: Phys. Rev. Lett. **100**(20), 205301 (2008)
56. Chang, S.Y., Pandharipande, V.R., Carlson, J., Schmidt, K.E.: Phys. Rev. A **70**(4), 043602 (2004)
57. Astrakharchik, G.E., Boronat, J., Casulleras, J., Giorgini, S.: Phys. Rev. Lett. **93**, 200404 (2004)
58. Carlson, J., Reddy, S.: Phys. Rev. Lett. **95**, 060401 (2005)
59. Gezerlis, A., Carlson, J.: Phys. Rev. C **77**(3), 032801 (2008)
60. Bulgac, A., Yu, Y.: Phys. Rev. Lett. **91**(19), 190404 (2003)
61. Magierski, P., Wlazłowski, G., Bulgac, A., Drut, J.E.: Phys. Rev. Lett. **103**(21), 210403 (2009)
62. Heiselberg, H., Pethick, C.J., Smith, H., Viverit, L.: Phys. Rev. Lett. **85**(12), 2418 (2000)
63. Carlson, J., Morales, J., Pandharipande, V.R., Ravenhall, D.G.: Phys. Rev. C **68**(2), 025802 (2003)
64. Lobo, C., Recati, A., Giorgini, S., Stringari, S.: Phys. Rev. Lett. **97**(20), 200403 (2006)
65. Leggett, A.J.: J. Phys. Colloques **41**, C7–19 (1980). doi:10.1051/jphyscol:1980704
66. Perali, A., Pieri, P., Pisani, L., Strinati, G.C.: Phys. Rev. Lett. **92**(22):220404 (2004)
67. Carr, L.D., Shlyapnikov, G.V., Castin, Y.: Phys. Rev. Lett. **92**(15), 150404 (2004)
68. Luo, L., Clancy, B., Joseph, J., Kinast, J., Thomas, J.E.: Phys. Rev. Lett. **98**(8), 080402 (2007)
69. Bulgac, A., Drut, J.E., Magierski, P.: Phys. Rev. Lett. **99**, 120401 (2007)
70. Fetter, A.L., Walecka, J.D.: Quantum Theory of Many-Particle Systems. McGraw-Hill, San Fransisco (1971)
71. Jaynes, E.T.: In: Levine, R.D., Tribus, M. (eds.) Maximum Entropy Formalism, vol. 8, pp. 15–118. MIT Press, Cambridge (1979)
72. Silver, R.N., Sivia, D.S., Gubernatis, J.E.: Phys. Rev. B **41**(4), 2380 (1990)
73. Silver, R.N., Gubernatis, J.E., Sivia, D.S., Jarrell, M.: Phys. Rev. Lett. **65**(4), 496 (1990)
74. White, S.R.: Phys. Rev. B **44**(9), 4670 (1991)
75. Bertero, M., Mol, C.D., Pike, E.R.: Inverse Probl. **1**(4), 301 (1985)
76. Bertero, M., Mol, C.D., Pike, E.R.: Inverse Probl. **4**(3), 573 (1988)
77. Creffield, C.E., Klepfish, E.G., Pike, E.R., Sarkar, S.: Phys. Rev. Lett. **75**(3), 517 (1995)
78. de Villiers, G.D., McNally, B., Pike, E.R.: Inverse Probl. **15**(2), 615 (1999)
79. Magierski, P., Wlazłowski, G.: in preparation.
80. Burovski, E., Prokof'ev, N., Svistunov, B., Troyer, M.: Phys. Rev. Lett. **96**(16), 160402; erratum ibid. **97**(23), 239902 (2006)
81. Burovski, E., Prokof'ev, N., Svistunov, B., Troyer, M.: New J. Phys. **8**(8), 153 (2006)
82. Burovski, E., Kozik, E., Prokof'ev, N., Svistunov, B., Troyer, M.: Phys. Rev. Lett. **101**(9), 090402 (2008). doi:10.1103/PhysRevLett.101.090402
83. Stajic, J., Milstein, J.N., Chen, Q., Chiofalo, M.L., Holland, M.J., Levin, K.: Phys. Rev. A **69**(6), 063610 (2004)

84. Chen, Q., Stajic, J., Tan, S., Levin, K.: Phys. Rep. **412**(1), 1 (2005)
85. Levin, K., Chen, Q.: In: Inguscio, M. et al.: [29], pp. 751–778
86. He, Y., Chien, C.C., Chen, Q., Levin, K.: Phys. Rev. B **76**(22), 224516 (2007)
87. Chin, C., Bartenstein, M., Altmeyer, A., Riedl, S., Jochim, S., Denschlag, J.H., Grimm, R.: Science **305**(5687), 1128 (2004)
88. Greiner, M., Regal, C.A., Jin, D.S.: Phys. Rev. Lett. **94**(7), 070403 (2005)
89. Schunck, C.H., Shin, Y., Schirotzek, A., Zwierlein, M.W., Ketterle, W.: Science **316**(5826), 867 (2007)
90. Kinnunen, J., Rodríguez, M., Törmä, P.: Science **305**, 1131 (2004)
91. He, Y., Chen, Q., Levin, K.: Phys. Rev. A **72**(1), 011602 (2005)
92. Yu, Z., Baym, G.: Phys. Rev. A **73**(6), 063601 (2006)
93. Baym, G., Pethick, C.J., Yu, Z., Zwierlein, M.W.: Phys. Rev. Lett. **99**(19), 190407 (2007)
94. Punk, M., Zwerger, W.: Phys. Rev. Lett. **99**(17), 170404 (2007)
95. Perali, A., Pieri, P., Strinati, G.C.: Phys. Rev. Lett. **100**(1), 010402 (2008)
96. Gaebler, J.P., Stewart, J.T., Drake, T.E., Jin, D.S., Perali, A., Pieri, P., Strinati, G.C.: Nat. Phys. **6**(8), 569 (2010)
97. Stewart, J.T., Gaebler, J.P., Jin, D.S.: Nature **454**, 744 (2008)
98. Kuhnle, E.D., Dyke, P., Mark, M., Hannaford, P., Vale C.J.: Bragg spectroscopy of the BEC–BCS crossover in lithium-6. Poster at BEC 2009 (2009)
99. Magierski, V, Wlazłowski, G., Bulgac, A.: work in progress
100. Thomas, J.E., Kinast, J., Turlapov, A.: Phys. Rev. Lett. **95**(12), 120402 (2005)
101. Bulgac, A., Forbes, M.M.: Phys. Rev. A **75**(3), 031605(R) (2007)
102. Bartenstein, M., Altmeyer, A., Riedl, S., Geursen, R., Jochim, S., Chin, C., Denschlag, J.H., Grimm, R., Simoni, A., Tiesinga, E., Williams, C.J., Julienne, P.S.: Phys. Rev. Lett. **94**(10), 103201 (2005)
103. Kinast, J., Turlapov, A., Thomas, J.E., Chen, Q., Stajic, J., Levin, K.: Science **307**(5713), 1296 (2005)
104. Nascimbène, S., Navon, N., Jiang, K.J., Chevy, F. Salomon, C.: Nature **463**, 1057 (2010)
105. Horikoshi, M., Nakajima, S., Ueda, M., Mukaiyama, T.: Science **327**(5964), 442 (2010)
106. Nascimbène, S., Navon, N., Chevy, F., Salomon, C.: New J. Phys. **12**, 103026 (2010). arXiv:1006.4052, doi:10.1088/1367-2630/12/10/103026
107. Hohenberg, P., Kohn, W.: Phys. Rev. **136**(3B), B864 (1964)
108. Kohn, W., Sham, L.J.: Phys. Rev. **140**(4A), A1133 (1965)
109. Dreizler, R.M., Gross, E.K.: Density Functional Theory: An Approach to the Quantum Many–Body Problem. Springer, Berlin (1990)
110. Parr, R.G., Weitao, Y.: Density-Functional Theory of Atoms and Molecules. No. 16 in International Series of Monographs on Chemistry. Oxford University Press, New York (1989)
111. Drut, J.E., Furnstahl, R.J., Platter, L.: Prog. Part. Nucl. Phys. **64**(1), 120 (2010). doi:10.1016/j.ppnp.2009.09.001
112. Chevy, F.: Phys. Rev. A **74**(6), 063628 (2006)
113. Kohn, W.: Rev. Mod. Phys. **71**(5), 1253 (1999)
114. Papenbrock, T.: Phys. Rev. A **72**(4), 041603 (2005)
115. Rupak, G., Schaefer, T.: Nucl. Phys. A **816**(1–4), 52 (2009)
116. Bulgac, A., Yu, Y.: Phys. Rev. Lett. **88**(4), 042504 (2002)
117. de Gennes, P.G.: Superconductivity of Metals and Alloys. Benjamin, New York (1966)
118. Papenbrock, T., Bertsch, G.F.: Phys. Rev. C **59**, 2052 (1999)
119. Tan, S.: Ann.Phys. **323**(12), 2952 (2008)
120. Blatt, J.M., Weisskopf, V.F.: Theoretical Nuclear Physics, pp. 74–76. Wiley, New York (1952)
121. Huang, K.: Statistical Mechanics, pp. 230–238. Wiley, New York (1987)
122. Huang, K., Yang, C.N.: Phys. Rev. **105**(3), 767 (1957)
123. Lee, T.D., Yang, C.N.: Phys. Rev. **105**(3), 1119 (1957)
124. Bulgac, A., Forbes, M.M.: arXiv:0808.1436 (2008)

125. A. Bulgac, M.M. Forbes, Phys. Rev. Lett. **101**(21), 215301 (2008). doi:10.1103/PhysRevLett.101.215301
126. Cohen, T.D.: Phys. Rev. Lett. **95**, 120403 (2005)
127. Bulgac, A.: Phys. Rev. A **76**, 040502 (2007)
128. Carlson, J., Reddy, S.: Phys. Rev. Lett. **100**(15), 150403 (2008)
129. Bhattacharyya, A., Furnstahl, R.J.: Phys. Lett. B **607**(3-4), 259 (2005)
130. Bhattacharyya, A., Furnstahl, R.J.: Nucl. Phys. A **747**(2-4), 268 (2005)
131. Combescot, R., Giraud, S.: Phys. Rev. Lett. **101**(5), 050404 (2008)
132. Pilati, S., Giorgini, S.: Phys. Rev. Lett. **100**(3), 030401 (2008)
133. Shin, Y.: Phys. Rev. A **77**(4), 041603 (2008)
134. Nascimbène, S., Navon, N., Jiang, K.J., Tarruell, L., Teichmann, M., McKeever, J., Chevy, F., Salomon, C.: Phys. Rev. Lett. **103**(17), 170402 (2009)
135. Chang, S.Y., Bertsch, G.F.: Phys. Rev. A **76**(2), 021603 (2007)
136. Blume, D., von Stecher, J., Greene C.H.: Phys. Rev. Lett. **99**(23), 233201 (2007)
137. Blume, D.: Phys. Rev. A **78**(1), 013635 (2008)
138. Forbes, M.M., Gandolfi, S., Gezerlis, A.: Phys. Rev. Lett. **106**(23), 235303 (2011)
139. Baksmaty, L.O., Lu, H., Bolech, C.J., Pu, H.: Phys. Rev. A **83**(2), 023604 (2010)
140. Pei, J.C., Dukelsky, J., Nazarewicz, W.: Phys. Rev. A **82**(2), 021603 (2010). doi:10.1103/PhysRevA.82.021603
141. Belyaev, S.T., Smirnov, A.V., Tolokonnikov, S.V., Fayans, S.A.: Sov. J. Nucl. Phys. **45**, 783 (1987)
142. Fayans, S.A., Tolokonnikov, S.V., Trykov, E.L., Zawischa, D. Nucl. Phys. A **676**(1–4), 49 (2000)
143. Zwierlein, M.W., Abo-Shaeer, J.R., Schirotzek, A., Schunck, C.H., Ketterle, W.: Nature **435**, 1047 (2005)
144. Combescot, R., Recati, A., Lobo, C., Chevy, F.: Phys. Rev. Lett. **98**(18), 180402 (2007)
145. Yoshida, N., Yip, S.K.: Phys. Rev. A **75**(6), 063601 (2007)
146. Fulde, P., Ferrell, R.A.: Phys. Rev. **135**, A550 (1964)
147. Larkin, A.I., Ovchinnikov, Y.N.: Sov. Phys. JETP **20**, 762 (1965)
148. Larkin, A.I., Ovchinnikov, Y.N.: Zh. Eksper. Teoret. Fiz. **47**, 1136 (1964)
149. Dewel, G., Borckmans, P., Walgraef, D.: J. Phys. C **12**(13), L491 (1979)
150. Radzihovsky, L., Vishwanath, A.: Phys. Rev. Lett. **103**(1), 010404 (2009)
151. Bowers, J.A., Rajagopal, K.: Phys. Rev. D **66**, 065002 (2002)
152. Son, D.T., Wingate, M.B.: Ann. Phys. **321**, 197 (2006)
153. Engel, Y.M., Brink, D.M., Goeke, K., Krieger, S.J., Vautherin, D.: Nucl. Phys. A **249**(2), 215 (1975)
154. Dobaczewski, J., Dudek, J.: Phys. Rev. C **52**(4), 1827 (1995)
155. Nesterenko, V.O., Kleinig, W., Kvasil, J., Vesely, P., Reinhard, P.: Int. J. Mod. Phys. E **17**, 89 (2008)
156. Bender, M., Heenen, P.H., Reinhard, P.G.: Rev. Mod. Phys. **75**(1), 121 (2003)
157. Rajagopal, A.K. Callaway, J.: Phys. Rev. B **7**(5), 1912 (1973)
158. Peuckert, V.: J. Phys. C Solid State Phys. **11**(24), 4945 (1978)
159. Runge, E., Gross, E.K.U.: Phys. Rev. Lett. **52**(12), 997 (1984)
160. http://www.tddft.org/
161. Bulgac, A., Lewenkopf, C., Mickrjukov, V.: Phys. Rev. B **52**(23), 16476 (1995)
162. Andreev, A.F., Bashkin, E.P.: Sov. Phys. JETP **42**, 164 (1975)
163. Andreev, A.F., Bashkin, E.P.: Zh.Éksp. Teor. Fiz. **69**, 319 (1975)
164. Bulgac, A., Yoon, S.: Phys. Rev. Lett. **102**(8), 085302 (2009)
165. Volkov, A.F., Kogan, S.M.: Sov. Phys. JETP **38**, 1018 (1974)
166. Volkov, A.F., Kogan, S.M.: Zh.Éksp. Teor. Fiz. **65**, 2038 (1973)
167. Barankov, R.A., Levitov, L.S., Spivak, B.Z.: Phys. Rev. Lett. **93**(16), 160401 (2004)
168. Barankov, R.A., Levitov, L.S.: Phys. Rev. Lett. **96**(23), 230403 (2006)
169. Andreev, A.V., Gurarie, V., Radzihovsky, L.: Phys. Rev. Lett. **93**(13), 130402 (2004)

170. Szymańska, M.H., Simons, B.D., Burnett, K.: Phys. Rev. Lett. **94**(17), 170402 (2005)
171. Tomadin, A., Polini, M., Tosi, M.P., Fazio, R.: Phys. Rev. A **77**(3), 033605 (2008)
172. Barankov, R.A., Levitov, L.S.: Phys. Rev. A **73**(3), 033614 (2006)
173. Warner, G.L., Leggett, A.J.: Phys. Rev. B **71**(13), 134514 (2005)
174. Yi, W., Duan, L.M.: Phys. Rev. A **73**(1), 013609 (2006)
175. Nahum, A., Bettelheim, E.: Phys. Rev. B **78**(18), 184510 (2008)
176. Teodorescu, R.: J. Phys. A **39**(33), 10363 (2006)
177. Robertson, A., Jiang, L., Pu, H., Zhang, W., Ling, H.Y.: Phys. Rev. Lett. **99**(25), 250404 (2007)
178. Yuzbashyan, E.A., Altshuler, B.L., Kuznetsov, V.B., Enolskii, V.Z.: J. Phys. A **38**(36), 7831 (2005)
179. Dzero, M., Yuzbashyan, E.A., Altshuler, B.L., Coleman, P.: Phys. Rev. Lett. **99**(16), 160402 (2007)
180. Yuzbashyan, E.A., Altshuler, B.L., Kuznetsov, V.B., Enolskii, V.Z.: Phys. Rev. B **72**(22), 220503 (2005)
181. Yuzbashyan, E.A., Dzero, M.: Phys. Rev. Lett. **96**(23), 230404 (2006)
182. Yuzbashyan, E.A.: Phys. Rev. B **78**(18), 184507 (2008)
183. Yuzbashyan, E.A., Tsyplyatyev, O., Altshuler, B.L.: Phys. Rev. Lett. **96**(9), 097005 (2006)
184. Dzero, M., Yuzbashyan, E.A., Altshuler, B.L.: Europhys. Lett. **85**, 20004 (2009)
185. Bulgac, A.: J. Phys. G **37**(6), 064006 (2010)
186. Babaev, E.: Phys. Rev. B **79**(10), 104506 (2009)
187. Babaev, E.: Phys. Rev. Lett. **103**(23), 231101 (2009)
188. Babaev, E., Jäykkä, J., Speight, M.: Phys. Rev. Lett. **103**(23), 237002 (2009)
189. Rupak, G., Schäfer, T., Kryjevski, A.: Phys. Rev. A **75**(2), 023606 (2007)
190. Khalatnikov, I.M.: An introduction to the theory of superfluidity. Advanced Book Program, Perseus Pub, Cambridge, Mass (2000)
191. Bulgac, A., Luo, Y.-L., Magierski, P., Roche, K.J., Yu, Y.: Science **332**, 1288 (2011)
192. Tonini, G., Werner, F., Castin, Y.: Eur. Phys. J. D **39**, 283 (2006)
193. Bulgac, A., Roche, K.J.: J. Phys. Conf. Ser. **125**(1), 012064 (2008)
194. Sensarma, R., Randeria, M., Ho, T.L.: Phys. Rev. Lett. **96**(9), 090403 (2006)
195. Combescot, R., Kagan, M.Y., Stringari, S.: Phys. Rev. A **74**(4), 042717 (2006)
196. Vinen, W.F., Donnelly, R.J.: Phys. Today **60**(4), 43 (2007)
197. Vinen, W.F.: J. Low Temp. Phys. **145**(1–4), 7 (2006). doi:10.1007/s10909-006-9240-6
198. Tsubota, M.: J. Phys. Soc. Jpn. **77**(11), 111006(1 (2008)
199. Bulgac, A., Forbes, M.M., Schwenk, A.: Phys. Rev. Lett. **97**(2), 020402 (2006)
200. Bulgac, A., Yoon, S.: Phys. Rev. A **79**(5), 053625 (2009). doi:10.1103/PhysRevA.79.053625
201. Baran, A., Bulgac, A., Forbes, M.M., Hagen, G., Nazarewicz, W., Schunck, N., Stoitsov, M.V.: Phys. Rev. C **78**(1), 014318 (2008)

Chapter 10
Scaling Flows and Dissipation in the Dilute Fermi Gas at Unitarity

T. Schäfer and C. Chafin

Abstract We describe recent attempts to extract the shear viscosity of the dilute Fermi gas at unitarity from experiments involving scaling flows. A scaling flow is a solution of the hydrodynamic equations that preserves the shape of the density distribution. The scaling flows that have been explored in the laboratory kflccare the transverse expansion from a deformed trap ("elliptic flow"), the expansion from a rotating trap, and collective oscillations. We discuss advantages and disadvantages of the different experiments, and point to improvements of the theoretical analysis that are needed in order to achieve definitive results. A conservative bound based on the current data is that the minimum of the shear viscosity to entropy density ration is $\eta/s \leq 0.5\hbar/k_B$.

10.1 Introduction

A cold, dilute Fermi gas of non-relativistic spin 1/2 particles interacting via a short range interaction tuned to infinite scattering length, commonly referred to as the unitary Fermi gas, provides a new paradigm for many strongly correlated quantum systems [1, 2]. In this contribution we focus on non-equilibrium aspects of the unitary Fermi gas, in particular its shear viscosity [3]. The shear viscosity of a liquid composed of weakly coupled quasi-particles can be estimated as

$$\eta = \frac{1}{3}npl_{mfp},$$

(10.1)

T. Schäfer (✉) · C. Chafin
Department of Physics, North Carolina State University,
Raleigh, NC 27695, USA
e-mail: tmschaef@unity.ncsu.edu

C. Chafin
e-mail: cechafin@ncsu.edu

where n is the density, p is the average momentum of the particles, and l_{mfp} is the mean free path. The mean free path can be written as $l_{mfp} = 1/(n\sigma)$ where σ is the transport cross section. Eq. 10.1 implies that the shear viscosity decreases as the strength of the interaction increases. In the unitary gas the cross section saturates the s-wave unitarity bound $\sigma = 4\pi/k^2$, where k is the scattering momentum, and we expect the shear viscosity to be unusually small.

Danielewicz and Gyulassy pointed out that the Heisenberg uncertainty relation imposes a bound on the product of the average momentum and the mean free path, $p l_{mfp} \geq \hbar$, and concluded that $\eta/n \geq \hbar$ [4]. This is not a precise statement: The kinetic estimate in Eq. 10.1 is not valid if the mean free path is on the order of the mean momentum. A more precise bound has recently emerged from holographic dualities in string theory. In this context the natural quantity to consider is not the ratio η/n, but η/s, where s is the entropy density. Policastro, Son and Starinets showed that in $\mathcal{N} = 4$ supersymmetric QCD the strong coupling limit of η/s is equal to $\hbar/(4\pi k_B)$ [5]. It was later shown that the strong coupling limit is universal in a large class of field theories, and it was conjectured that $\eta/s \geq \hbar/(4\pi k_B)$ is a general lower bound, valid for all fluids [6].

Are there any fluids in nature that attain or possibly violate the proposed bound? A fluid that saturates the bound has to be a quantum fluid (because η is on the order of $\hbar s$), and it has to be strongly interacting (because in a weakly interacting system the mean free path is large). It is also known that many of the model field theories that attain the bound in the strong coupling limit are scale invariant. All of these properties point to the unitary Fermi gas as a plausible candidate for a "perfect fluid".

Almost ideal hydrodynamic flow in the unitary Fermi gas was first observed in [7]. Since then, a number of experiments have been performed that provide constraints on the shear viscosity of the unitary gas [8–15]. In this work we will provide an overview of the hydrodynamic analysis of these experiments, and compare some of the estimates that have been obtained. We emphasize the uncertainties of these results, and point to improvements that need to be implemented.

10.2 Scaling Flows

We begin by studying the ideal (Eulerian) fluid dynamics of a non-relativistic gas in the normal phase. We will introduce dissipative effects in Sects. 10.3.1–10.3.3. In this contribution we will not discuss superfluid hydrodynamics. We will briefly comment on dissipative effects in the superfluid phase in Sect. 10.3.1. The equations of continuity and of momentum conservation are given by

$$\frac{\partial n}{\partial t} + \vec{\nabla} \cdot (n\vec{v}) = 0, \tag{10.2}$$

$$mn\frac{\partial \vec{v}}{\partial t} + mn\left(\vec{v} \cdot \vec{\nabla}\right)\vec{v} = -\vec{\nabla}P - n\vec{\nabla}V, \tag{10.3}$$

where n is the number density, m is the mass of the atoms, $\vec{v}$ is the fluid velocity, P is the pressure and V is the external potential. In the unitarity limit the equation of state at zero temperature is of the form

$$P(n, T) = \frac{n^{5/3}}{m} f\left(\frac{mT}{n^{2/3}}\right), \tag{10.4}$$

where $f(y)$ is a universal function. We note that $y = const \cdot (T/T_F^{hom})$, where $T_F^{hom} = (3\pi^2 n)^{2/3}/(2m)$ is the Fermi temperature of a homogeneous Fermi gas. In the high temperature limit, $y \gg 1$, we have $f(y) \simeq y$ and in the low temperature limit $f(y) \simeq (3\pi^2)^{2/3}\xi/5$, where the parameter $\xi = 0.40(2)$ has been determined in quantum Monte Carlo calculations [16]. Monte Carlo methods have also been used to determine $f(y)$ for all values of y [17, 18]. The critical temperature for superfluidity is $T_c/T_F^{hom} \simeq 0.15$, corresponding to $y_c \simeq 0.72$. An alternative representation of the pressure is

$$P(\mu, T) = \mu^{5/2} m^{3/2} g\left(\frac{T}{\mu}\right), \tag{10.5}$$

where $g(z)$ is a universal function, related to $f(y)$ by thermodynamic identities. In the high temperature limit $g(z) \simeq 2z^{5/2}e^{1/z}/(2\pi)^{3/2}$ and in the low temperature limit $g(z) \simeq 2^{5/2}/(15\pi^2\xi^{3/2})$. The density is

$$n(\mu, T) = \mu^{3/2}m^{3/2}h\left(\frac{T}{\mu}\right), \quad h(z) = \frac{5}{2}g(z) - zg'(z). \tag{10.6}$$

The high and low temperature limits of the function $h(z)$ are $h(z) \simeq 2z^{3/2}e^{1/z}/(2\pi)^{3/2}$ ($z \gg 1$) and $h(z) \simeq 2^{3/2}/(3\pi^2\xi^{3/2})(z \ll 1)$. The equilibrium distribution n_0 of a trapped atomic gas follows from the hydrostatic equation $\vec{\nabla}P_0 = -n_0\vec{\nabla}V$. The trapping potential is approximately harmonic

$$V(x) = \frac{m}{2}\sum_i \omega_i^2 x_i^2. \tag{10.7}$$

Using the Gibbs-Duhem relation $dP = nd\mu + sdT$ together with the fact that the equilibrium configuration is isothermal we can write the equation of hydrostatic equilibrium as $\vec{\nabla}\mu = -\vec{\nabla}V$. This implies that the equilibrium density is $n_0(x) = n(\mu(x), T)$ with

$$\mu(x) = \mu_0 - V(x) = \mu_0\left(1 - \sum_i \frac{x_i^2}{R_i^2}\right), \quad R_i^2 = \frac{2\mu_0}{m\omega_i^2}. \tag{10.8}$$

A scaling flow is a solution of the hydrodynamic equations in which the shape of the density distribution is preserved. Consider the ansatz $n(x, t) = n(\mu(x, t), T(t))$ where

$$\mu(x, t) = \mu_0(t) \left(1 - \frac{x^2}{R_x(t)^2} - \frac{y^2}{R_y(t)^2} - \frac{z^2}{R_z(t)^2} - \frac{xy}{R_{xy}(t)} \right), \qquad (10.9)$$

and $T(t)/T(0) = \mu_0(t)/\mu_0(0)$. Without loss of generality we have restricted the ansatz to rotations in the xy-plane. We note that the fluid remains isothermal during the expansion. Scale invariance implies that properties of the fluid only depend on the dimensionless ratio T/μ. For any given fluid element this ratio does not change during the expansion. In particular, if the fluid element was in the superfluid or normal phase initially, it will stay in that phase throughout the expansion.

The velocity field created by the scaling expansion in Eq. 10.9 is linear in the coordinates. We can write

$$\vec{v}(x, t) = \frac{1}{2} \vec{\nabla} \left(\alpha_x(t) x^2 + \alpha_y(t) y^2 + \alpha_z(t) z^2 + 2\alpha(t) xy \right) + \Omega(t) \hat{z} \times \vec{x}. \quad (10.10)$$

The parameters α_i, α and Ω are related to the parameters R_i, R_{xy} and μ_0 by the continuity equation. Remarkably, the continuity equation is independent of the universal function $h(z)$ in Eq. 10.6. Introducing the dimensionless scale parameters

$$\bar{\mu}(t) = \frac{\mu_0(t)}{\mu_0(0)}, \quad b_i(t) = \frac{R_i(t)}{R_i(0)}, \quad a(t) = \frac{R_x(0)^2}{R_{xy}(t)}, \qquad (10.11)$$

the continuity equation can be written as

$$\bar{\mu} + \frac{2}{3}\bar{\mu} \left(\alpha_x + \alpha_y + \alpha_z \right) = 0, \qquad (10.12)$$

$$\dot{a} + \frac{2(\alpha - \Omega)}{b_x^2} + \frac{2(\alpha + \Omega)}{\lambda^2 b_y^2} + a(\alpha_x + \alpha_y) = 0, \qquad (10.13)$$

$$\dot{b}_x - b_x \alpha_x - \frac{b_x^3 a}{2}(\alpha + \Omega) = 0, \qquad (10.14)$$

$$\dot{b}_y - b_y \alpha_y - \frac{b_y^3 \lambda^2 a}{2}(\alpha - \Omega) = 0, \qquad (10.15)$$

$$\dot{b}_z - b_z \alpha_z = 0, \qquad (10.16)$$

where $\lambda = R_y(0)/R_x(0) = \omega_x/\omega_y$. These equations can be solved directly in the case that there is no rotation, $a(t) = 0$. Then $\alpha = \Omega = 0$ and

$$(\alpha_x, \alpha_y, \alpha_z) = \left(\frac{\dot{b}_x}{b_x}, \frac{\dot{b}_y}{b_y}, \frac{\dot{b}_z}{b_z} \right), \quad \bar{\mu} = \frac{1}{(b_x b_y b_z)^{2/3}}. \qquad (10.17)$$

The velocity field is a simple "Hubble flow", $\vec{v} = (\alpha_x x, \alpha_y y, \alpha_z z)$. Finally, we note that the entropy density is given by $s = (m\mu)^{3/2} g'(T/\mu)$. Since the entropy density

has the same functional form as the particle density we conclude that, in the case of scaling flows, the continuity equation implies entropy conservation,

$$\frac{\partial s}{\partial t} + \vec{\nabla} \cdot (\vec{v}s) = 0. \tag{10.18}$$

10.3 Elliptic Flow

The simplest scaling flow is the expansion of the cloud after the trapping potential is removed [19]. Since the cloud remains isothermal the Euler equation can be derived using the Gibbs-Duhem relation $dP = nd\mu$. This implies that the equation of motion is independent of the universal function $f(y)$ defined in Eq. 10.4. We get

$$\ddot{b}_i = \frac{\omega_i^2}{(b_x b_y b_z)^{2/3}} \frac{1}{b_i}, \tag{10.19}$$

The total energy of the expanding system is given by the sum of internal energy and kinetic energy,

$$E = E_{int} + E_{kin} = \int d^3x \left(\mathscr{E}(x) + \frac{1}{2}mn\vec{v}^2 \right). \tag{10.20}$$

For the Fermi gas at unitarity the energy density $\mathscr{E}$ is related to the pressure by $\mathscr{E} = \frac{3}{2}P$. We find

$$E = E_{int}(0) \left\{ \frac{1}{(b_x b_y b_z)^{2/3}} + \frac{1}{3}\left(\frac{\dot{b}_x^2}{\omega_x^2} + \frac{\dot{b}_y^2}{\omega_y^2} + \frac{\dot{b}_z^2}{\omega_z^2} \right) \right\}, \tag{10.21}$$

where $E_{int}(0)$ is the internal energy at $t=0$. Conservation of energy immediately follows from the equation of motion, Eq. 10.19. We note that the equation of hydrostatic equilibrium, $\vec{\nabla}P = -n\vec{\nabla}V$, implies the Virial theorem $\langle \mathscr{E} \rangle = \langle V \rangle$ [20], where $\langle V \rangle$ denotes the integral of the potential energy over the trap. This means that the total energy of the trapped gas is $E_0 = 2E_{int}(0)$, where the factor 2 is due to the contribution of the potential energy.

We are interested in an axially symmetric trap with $\omega_y = \omega_z = \omega_\perp$ and $\omega_x = \lambda\omega_\perp$. In this case we end up with two coupled equations for $b_\perp$ and b_x. If $\lambda \gg 1$ the evolution in the transverse direction is much faster and the equation for $b_\perp$ can be approximately decoupled,

$$\ddot{b}_\perp = \frac{\omega_\perp^2}{b_\perp^{7/3}}. \tag{10.22}$$

This equation has to be integrated numerically. The behavior at early and late times can be found analytically. We get

$$b_\perp(t) \simeq \begin{cases} 1 + \frac{1}{2}\omega_\perp^2 t^2 + O(t^4) & \omega_\perp t \ll 1, \\ \frac{\omega_\perp t}{\sqrt{\gamma}} + c_0 + O(t^{-1/3}) & \omega_\perp t \gg 1, \end{cases} \tag{10.23}$$

where $\gamma = 2/3$ and c_0 is a constant that can be determined by matching the early and late time behavior. Numerically, we find $c_0 \simeq -1.3$. For the longitudinal expansion the early time behavior is $b_x(t) \simeq 1 + (\lambda\omega_\perp t)^2/2$, and at late times $b_x(t) \simeq const \cdot \lambda^2\omega_\perp t$.

The signature effect of hydrodynamics is that transverse pressure gradients cause the transverse radius to expand much faster than the longitudinal radius. This means that the two radii will eventually cross. This happens at a time

$$t_{cross} = \frac{\sqrt{\gamma}}{\omega_x} (1 + O(\lambda)). \tag{10.24}$$

We note that the crossing time only depends on the trap parameters, and is independent of the initial energy or the number of particles. We also note that at $t \simeq t_{cross}$ the expansion is still two-dimensional, that means the volume of the system grows as $vol \sim t^2$. The expansion becomes three-dimensional, $vol \sim t^3$, at $t_{3d} \sim (\lambda^2\omega_\perp)^{-1}$.

10.3.1 Energy Dissipation

We wish to understand how the expansion is affected by dissipation. The energy momentum tensor of a dissipative fluid is $\Pi_{ij} = P\delta_{ij} + mnv_iv_j + \delta\Pi_{ij}$ with

$$\delta\Pi_{ij} = \eta\left(\nabla_i v_j + \nabla_j v_i - \frac{2}{3}\delta_{ij}\nabla \cdot v\right) + \zeta\delta_{ij}(\nabla \cdot v). \tag{10.25}$$

The energy current is $j_i^\varepsilon = v_i(w + \frac{1}{2}mnv^2) + \delta j_i^\varepsilon$ with $w = \mathcal{E} + P$ and $\delta j_i^\varepsilon = \delta\Pi_{ij}v_j - \kappa\nabla_i T$. The unitary gas is scale invariant and $\zeta = 0$ [21]. Also, for an isentropic scaling expansion the temperature remains independent of position, and there is no contribution from the thermal conductivity κ. We will therefore concentrate on the role of shear viscosity.

Since the shear viscosity is small, we can take it into account perturbatively. The simplest idea it compute the amount of kinetic energy that is converted to heat. We have

$$\dot{E} = -\frac{1}{2}\int d^3x\, \eta\left(\nabla_i v_j + \nabla_j v_i - \frac{2}{3}\delta_{ij}\nabla \cdot v\right)^2. \tag{10.26}$$

For the scaling expansion given in Eq. 10.10 the result is particularly simple. We get

$$\dot{E} = -\frac{4}{3}\left(\frac{\dot{b}_\perp}{b_\perp} - \frac{\dot{b}_x}{b_x}\right)^2 \int d^3x\, \eta(x). \tag{10.27}$$

The total energy dissipated is given by the integral of Eq. 10.27 over time. We first show that the spatial integral over $\eta(x)$ does not depend on time. In the local density approximation $\eta(x) = \eta(\mu(x), T)$. Scale invariance implies that

$$\eta(\mu, T) = n(\mu, T)\alpha_n\left(\frac{T}{\mu}\right), \tag{10.28}$$

where $\alpha_n(z)$ is a universal function, and we have set $\hbar = 1$. In order to compare with the string theory bound it is also useful to define $\eta(\mu, T) = s(\mu, T)\alpha_s(T/\mu)$, where we have also set $k_B = 1$. We can write

$$\int d^3x\, \eta(x) = N\langle\alpha_n\rangle, \tag{10.29}$$

where

$$\langle\alpha_n\rangle = \frac{1}{N}\int d^3x\, n(x, t)\alpha_n\left(\frac{T(t)}{\mu(x, t)}\right) = \frac{1}{N}\int d^3x\, n_0(x)\alpha_n\left(\frac{T_0}{\mu(x, 0)}\right) \tag{10.30}$$

is an average of α_n over the initial density distribution. Analogously, we can write the integral over $\eta(x)$ as $S\langle\alpha_s\rangle$, where S is the total entropy and $\langle\alpha_s\rangle$ is an average of α_s over the initial entropy density.

The time integral over $(\dot{b}_\perp/b_\perp - \dot{b}_x/b_x)^2$ is dominated by the regime $\omega_\perp t \sim 1$ and converges rapidly – the integral reaches 80% of its asymptotic value at $t_{diss} \simeq 5.9\omega_\perp^{-1}$. In the limit $\lambda \ll 1$ we can neglect the contribution from $\dot{b}_x$. On dimensional grounds the integral over $(\dot{b}_\perp/b_\perp)^2$ must be proportional to $\omega_\perp$. The constant of proportionality can be determined numerically. We find

$$\int_0^\infty dt\left(\frac{\dot{b}_\perp}{b_\perp}\right)^2 = 0.87\omega_\perp. \tag{10.31}$$

We can now compute the ratio $\Delta E/E_{int}$ of the dissipated energy to the initial internal energy of the system. In order to express the result in terms of experimentally measured quantities it is useful to introduce the energy $E_F = N\varepsilon_F$ where $\varepsilon_F = \bar{\omega}(3N)^{1/3}$ is the Fermi energy of the trapped gas and $\bar{\omega} = (\omega_x\omega_y\omega_z)^{1/3}$. We find

$$\frac{\Delta E}{E_{int}(0)} = -\frac{8}{3}\cdot 0.87\cdot\beta = -2.32\cdot\beta \tag{10.32}$$

where the parameter β is defined given by

$$\beta = \frac{\langle\alpha_n\rangle}{(3N\lambda)^{1/3}}\frac{1}{(E_0/E_F)} = \frac{\langle\alpha_s\rangle}{(3N\lambda)^{1/3}}\frac{(S/N)}{(E_0/E_F)}. \tag{10.33}$$
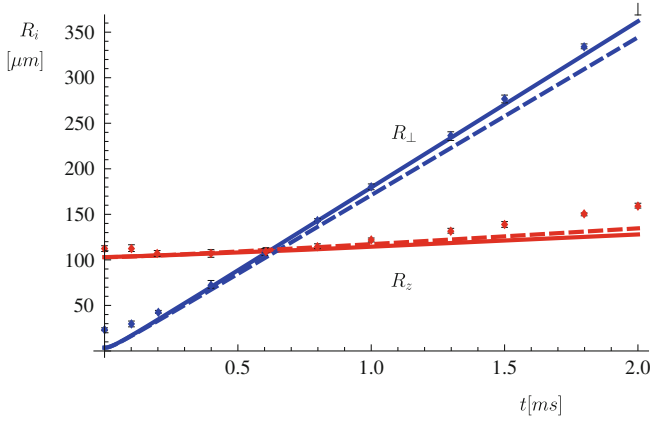
Fig. 10.1 Expansion of the transverse and longitudinal radii after release from a harmonic trap. The data points are taken from [7]. The *solid* and *dashed lines* correspond to solutions of the Navier–Stokes equation with $\langle \alpha_s \rangle = 0$ (*solid lines*) and $\langle \alpha_s \rangle = 0.5$ (*dashed lines*)

Dissipation slows down the transverse expansion of the system. For $(\omega_\perp t) \gg 1$ we have $(\delta \dot{b}_\perp / \dot{b}_\perp) = (\Delta E / E)/2$ and, up to terms that are higher order in λ, the change in the crossing time is directly related to the change in the expansion rate, $(\delta t / t)_{cross} = (\delta \dot{b}_\perp / \dot{b}_\perp)$.

The thermodynamic quantities S/N and E_0/E_F as a function of T/T_F were determined experimentally in [22]. Just above the critical temperature $S/N \simeq 2.2$ and $E_0/E_F \simeq 0.83$. The double ratio $[(S/N)/(E_0/E_F)]$ is only weakly dependent on T, changing by less than 15% between T_c and $4T_c$. In the flow experiment carried out by O'Hara et al. [7] the cloud contained $N = 2 \cdot 10^5$ atoms and the asymmetry parameter was $\lambda = 0.045$. The predicted sensitivity of the crossing time to dissipative effects is

$$\left(\frac{\delta t}{t} \right)_{cross} = 0.008 \left(\frac{\langle \alpha_s \rangle}{1/(4\pi)} \right) \left(\frac{2 \cdot 10^5}{N} \right)^{1/3} \left(\frac{0.045}{\lambda} \right)^{1/3} \left(\frac{S/N}{2.2} \right) \left(\frac{0.83}{E_0/E_F} \right).$$
(10.34)

For $\langle \alpha_s \rangle = 1/(4\pi)$ this is at the limit of what can be resolved experimentally, but for $\langle \alpha_s \rangle = 0.5$ the effect reaches about 5%. An example is shown in Fig. 10.1. The solid lines show the solution of the Euler equation (10.19), and the dashed lines show a solution of the Navier–Stokes equation (see Sect. 10.3.2) with $\langle \alpha_s \rangle = 0.5$. The main effect of shear viscosity is a suppression of the transverse expansion of the system. We find $(\delta t / t)_{cross} = 6.5\%$, in fairly good agreement with the estimate $(\delta t / t)_{cross} = 5\%$ from Eq. 10.34.

The best fit to the data is provided by ideal hydrodynamics with $\langle \alpha_s \rangle = 0$. This is probably related to the fact that the data were taken significantly below T_c, at $T/T_F = 0.13 \pm 0.05$. In this regime the system is described by two-fluid hydrodynamics. The superfluid component has no shear viscosity but the viscosity of

the normal component becomes very large as $T/T_F \rightarrow 0$ [23]. In a finite system, however, the large viscosity of the normal phase is likely to be suppressed by relaxation time effects, see Sect. 10.3.5. As a consequence one observes perfect superfluid hydrodynamics. The data in Fig. 10.1 show some deviations from hydrodynamics at very early and very late times. Discrepancies at early times are probably related to experimental resolution [7], while the differences at late times may be connected to the breakdown of hydrodynamics in the late stages of the expansion.

We can also compute the amount of entropy generated by dissipative effects. Using $dS = dQ/T$ we find

$$\frac{\Delta S}{N} = \frac{4}{3} \frac{\langle \alpha_n \rangle}{(3N\lambda)^{1/3}} \frac{1}{(T_0/T_F)} I_S \tag{10.35}$$

with

$$I_S = \omega_\perp^{-1} \int_0^\tau dt \, b_\perp^{-2/3} \left(\dot{b}_\perp \right)^2 . \tag{10.36}$$

For $\tau \simeq t_{diss}$ we find $I_s \simeq 2.6$ and the produced entropy is small, $(\Delta S/N) \simeq 0.27$ for the conditions given above. However, the integral diverges as $I_s \sim (\omega_\perp \tau)^{1/3}$ for $\tau \rightarrow \infty$. This result is not reliable since we expect hydrodynamics to break down at late times, see Sect. 10.3.4.

10.3.2 Moments of the Navier–Stokes Equation

It is clearly desirable to study the role of dissipation more directly by solving the Navier–Stokes equation. The Navier–Stokes equation differs from the Euler equation by an extra term on the right hand side,

$$mn \left(\frac{\partial v_i}{\partial t} + \left(\vec{v} \cdot \vec{\nabla} \right) v_i \right) = -\nabla_i P - \nabla_j \delta \Pi_{ij} . \tag{10.37}$$

We will assume that the viscosity is small, so that derivatives with respect to thermodynamic variables can be computed at constant entropy. We will also assume that the entropy conservation equation, Eq. 10.18, is not modified. Physically, this implies that we assume that there is a reservoir that removes the heat generated by dissipative effects. In this case, the only correction to the equations of hydrodynamics is the viscous force in the Navier–Stokes equation.

In general the inclusion of the Navier–Stokes term will break the simple scaling form of the flow. The Navier–Stokes equation also depends on the functional form of the pressure and the viscosity, that means we have to specify the functions $f(y)$ in Eq. 10.4 and $\alpha_n(z)$ in Eq. 10.28. A simple approach that avoids extensive numerical work as well as model assumptions about $f(y)$ and $\alpha_n(z)$ is to take moments of the Navier–Stokes equation. Consider the linear moments

$$m \int d^3x x_k n(x) \left(\frac{\partial v_i}{\partial t} + \left(\vec{v} \cdot \vec{\nabla} \right) v_i \right) = - \int d^3x x_k \left(\nabla_i P + \nabla_j \delta \Pi_{ij} \right), \quad (10.38)$$

with $k = 1, 2, 3$. Since the velocity field is linear in the coordinates we find that the ideal fluid terms involve second moments of the density. These moments are related to the potential energy in a harmonic trap and, by the virial theorem, to the total energy of the system. The Navier–Stokes term can be integrated by parts and is proportional to the integral over $\eta(x)$. As a consequence, the first moment of the Navier–Stokes equation depends only on the parameter β defined in Eq. 10.33. We get

$$\ddot{b}_\perp = \frac{\omega_\perp^2}{(b_\perp^2 b_x)^{2/3} b_\perp} - \frac{2\beta\omega_\perp}{b_\perp} \left(\frac{\dot{b}_\perp}{b_\perp} - \frac{\dot{b}_x}{b_x} \right) \qquad (10.39)$$

$$\ddot{b}_x = \frac{\omega_x^2}{(b_\perp^2 b_x)^{2/3} b_x} + \frac{4\beta\lambda\omega_x}{b_x} \left(\frac{\dot{b}_\perp}{b_\perp} - \frac{\dot{b}_x}{b_x} \right). \qquad (10.40)$$

These equations of motion are consistent with the result in the previous section. We can compute the amount of energy dissipated from Eqs. 10.21 and (10.39, 10.40). We find

$$\dot{E} = -\frac{8}{3} \beta E_{int}(0) \left(\frac{\dot{b}_\perp}{b_\perp} - \frac{\dot{b}_x}{b_x} \right)^2. \qquad (10.41)$$

We note that $b_\perp(t)$ and $b_z(t)$ are solutions of the Navier–Stokes equation and have an implicit dependence on β. As long as this dependence is smooth, $b_i(t, \beta) \to b_i(t, 0)$ as $\beta \to 0$, Eq. 10.41 reduces to Eq. 10.27 at leading order in β. Since typical values of β are quite small, we expect the estimates in the previous section to be very accurate. This is studied in more detail in Fig. 10.2. We observe that the dissipated energy $(\Delta E)/E$ is very linear in β even for values of $(\Delta E)/E$ as large as 25%. We note that because of turbulence solutions of the Navier–Stokes equation do not in general approach solutions of the Euler equation in the limit that the shear viscosity goes to zero. Turbulence is not present in our analysis because we do not consider small fluctuations. We also note that there is no continuous forcing in the case of an expanding gas and it is not clear whether turbulence can develop even if fluctuations are included. We will estimate the Reynolds number of the flow in Sect. 10.3.4.

10.3.3 Scaling Solution of the Navier–Stokes Equation

In this section we discuss a specific model for the density dependence of the shear viscosity that preserves the scaling nature of the flow even if the viscosity is not zero. This model allows to compute the local amount of heat that is generated by
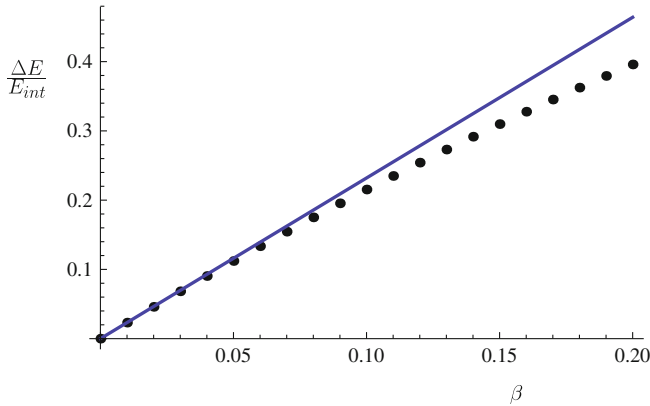
Fig. 10.2 This figure show the ratio $(\Delta E)/E_{int}$ of the dissipated energy to the initial internal energy as a function of the parameter β defined in Eq. 10.33. The dots show the result of a numerical solution of the Navier–Stokes equation (10.39, 10.40) in the limit $\omega_z/\omega_\perp \to 0$ and the line shows the estimate given in Eq. 10.32

dissipation, and to understand some of the shortcomings of the method discussed in Sects. 10.3.1 and 10.3.2. Consider

$$\eta(n, T) = \eta_0 (mT)^{3/2} + \eta_1 \frac{P(n, T)}{T}, \tag{10.42}$$

where $\eta_{0,1}$ are constants and $P(n,T)$ is the pressure. The first term dominates in the low density, high temperature limit. This is the regime in which a kinetic description in terms of weakly coupled atoms is applicable. Kinetic theory gives [24, 25]

$$\eta_0 = \frac{15}{32\sqrt{\pi}}. \tag{10.43}$$

The second term dominates in the high density, low temperature regime. The functional form of this term is not motivated by kinetic theory. We note, however, that η/n has a minimum as a function of T, as expected on theoretical [23] and phenomenological grounds [3].

The model given in Eq. 10.42 has two remarkable features: first, the η_0 term does not contribute to the Navier–Stokes equation at all. The Navier–Stokes term $\nabla_j[\eta_0(mT)^{3/2}(\nabla_i v_j + \cdots)]$ vanishes since both T and $\nabla_i v_j$ are constant. Second, the η_1 term preserves the scaling flow. Using $T, \nabla_i v_j \sim const$ we see that $\nabla_j[\eta_1 P(n, T)/T(\nabla_i v_j + \cdots)]$ scales like the contribution from the pressure of an ideal fluid, $\nabla_i P(n, T)$. We get

$$\ddot{b}_\perp = \frac{\omega_\perp^2}{(b_\perp^2 b_x)^{2/3} b_\perp} - \frac{2\eta_1 \omega_\perp^2}{3 T_0 b_\perp} \left(\frac{\dot{b}_\perp}{b_\perp} - \frac{\dot{b}_x}{b_x} \right) \tag{10.44}$$

$$\ddot{b}_x = \frac{\omega_x^2}{(b_\perp^2 b_x)^{2/3} b_x} + \frac{4\eta_1 \omega_x^2}{3T_0 b_x}\left(\frac{\dot{b}_\perp}{b_\perp} - \frac{\dot{b}_x}{b_x}\right). \tag{10.45}$$

We observe that these equations are identical to the moment Eqs. 10.39, 10.40 with $\beta = \eta_1 \omega_\perp/(3T_0)$. This is not a surprise – the η_1 contribution to $\eta(n, T)$ vanishes as $n \to 0$ and the assumptions underlying the moment method are satisfied. The η_0 term, on the other hand, does not vanish as $n \to 0$, and it cannot be included in the moment equations (it makes an infinite contribution to the integral over $\eta(x)$).

Using the identification $\beta = \eta_1 \omega_\perp/(3T_0)$ we can write

$$\beta = \frac{\eta_1}{3(3\lambda N)^{1/3}} \frac{1}{(T_0/T_F)}, \tag{10.46}$$

which shows that any bound on $\langle \alpha_n \rangle$ obtained using the methods of Sect. 10.3.2 can be translated into an estimate of η_1, $\eta_1 = 3(T_0/E_0)\langle \alpha_n \rangle$. Near T_c this implies that $\eta_1 \simeq 0.76\langle \alpha_n \rangle$. We note that the relation between η_1 and $\langle \alpha_n \rangle$ is precisely what one obtains if the trap average of $\eta(x)$ is computed from the η_1-term only. The situation is more complicated if the contribution from η_0 is taken into account. The ratio η/n is given by

$$\frac{\eta(n, T)}{n} = \eta_0 y^{3/2} + \frac{\eta_1}{y} f(y) \tag{10.47}$$

with $y = (mT)/n^{2/3}$. Since $f(0) = const$ and $f(y) \simeq y$ for $y \gg 1$ this function has a minimum, see Fig. 10.3. The figure also shows that $(\eta/n)_{min}$ receives significant contributions from η_0. It is clearly unsatisfactory that our analysis has no sensitivity to this term. We will return to this issue in Sect. 10.3.5.

Using the explicit form of $\eta(n, T)$ we can also address the question where the energy is being dissipated and how much reheating is taking place. We first consider the contribution from η_1. The energy dissipated is

$$\dot{\mathscr{E}} = -\frac{4\eta_1}{3}\left(\frac{\dot{b}_\perp}{b_\perp}\right)^2 \frac{P(n, T)}{T}. \tag{10.48}$$

For a Fermi gas at unitarity the energy density is related to the pressure by $\mathscr{E}(n, T) = (3/2)P(n, T)$. Equation (10.48) implies that the energy dissipated is proportional to the local internal energy density. The source of the dissipated energy is the reduction in the kinetic energy density relative to its value in ideal hydrodynamics. The local kinetic energy density is

$$\mathscr{E}_{kin} = \frac{m}{2}n\left(\frac{\dot{b}_\perp}{b_\perp}\right)^2 x_\perp^2. \tag{10.49}$$

Since the kinetic energy density differs from the spatial distribution of the dissipated energy there has to be a dissipative contribution to the energy current. This current is given by $\delta \vec{j}^{\,\varepsilon} = (0, \delta j_y^\varepsilon, \delta j_z^\varepsilon)$ with
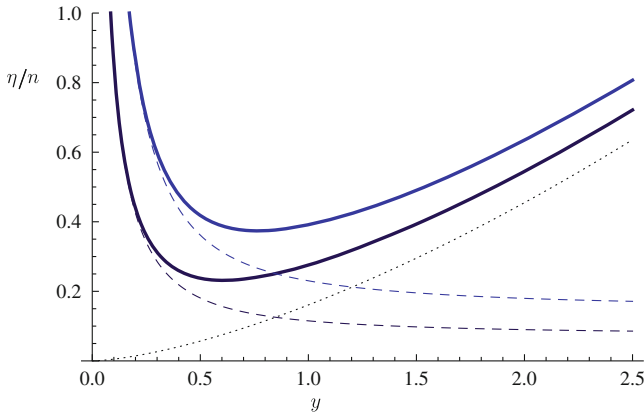
Fig. 10.3 Ratio η/n as a function of $y = (mT)/n^{2/3}$ for the model defined in Eq. 10.42. The two curves correspond to (from *bottom* to *top*) $\eta_1 = 1/(4\pi)$, $2/(4\pi)$ with $\eta_0 = 15/(32\sqrt{\pi})$. The *dashed line* shows the contribution from η_1, which is the term that contributes directly to the Navier–Stokes equation, and the *dotted line* is the contribution from η_0. Note that the critical point for the onset of superfluidity is $y_c \simeq 0.72$

$$\delta j_z^\varepsilon = v_z \delta \Pi_{zz} = - z \frac{2\eta_1 P(n, T)}{3T} \left(\frac{\dot{b}_\perp}{b_\perp} \right)^2, \tag{10.50}$$

and $\delta j_y^\varepsilon = \delta j_z^\varepsilon (z \leftrightarrow y)$. The dissipative current flows from the outer edge of the cloud, where the kinetic energy is peaked, to the center of the cloud, where the pressure is largest.

Energy dissipation leads to reheating. The change in temperature is $\Delta T = (\Delta \mathscr{E})/c_V$. The time evolution of the temperature is governed by

$$\dot{T} = - \frac{4T_0}{3b_\perp^{4/3}} \left(\frac{\dot{b}_\perp}{b_\perp} \right) + \frac{\eta_1 P}{c_V T} \left(\frac{\dot{b}_\perp}{b_\perp} \right)^2, \tag{10.51}$$

where the first term is related to the adiabatic expansion of the system, and the second term is the dissipative correction. Note that if $c_V \sim \mathscr{E}/T$, which is the case in the high temperature limit, then reheating will preserve the fact that the cloud is isothermal. In general the behavior of the specific heat is more complicated and dissipation produces a temperature gradient. The relative importance of reheating is governed by the parameter $(\eta_1 \omega_\perp / T_0)(P/(c_V T))$. In the high temperature limit we can use $P \sim c_V T$ and this expression reduces to the parameter β defined in Eq. 10.46. Reheating becomes important at a time $\omega_\perp t \sim \beta^{-3}$. Since β is typically very small, this occurs very late during the evolution of the system.

A similar analysis of the effects of η_0 leads to a number of puzzles. The energy dissipated is independent of density, and the total energy dissipated over all space is infinite. There is no change in the kinetic energy, and the source of the dissipated energy is the viscous correction to the energy current. This current flows into the

system from spatial infinity. The relative importance of reheating is governed by the parameter $(\eta_0 \omega_\perp / T_0)((mT)^{3/2}/n)$, which is always large in the dilute region of the cloud.

10.3.4 Breakdown of Hydrodynamics

The constant term $\eta \sim \eta_0 (mT)^{3/2}$ in the shear viscosity dominates in the dilute outer regions of the cloud, and the difficulty in understanding the effects of this term must be related to the breakdown of hydrodynamics in the dilute regime. A standard criterion for the applicability of hydrodynamics is the condition that the Knudsen number $Kn = l_{mfp}/L$, the ratio of the mean free path to the system size, is much less than one. In the dilute regime the mean free path is given by

$$l_{mfp} = \frac{1}{n\sigma} = \frac{3}{4\pi} \frac{mT}{n}. \tag{10.52}$$

The density is given by Eq. 10.6. In the dilute regime we can use the high temperature limit of $h(z)$, but the scaling arguments in the following are independent of the functional form of $h(z)$. For a comoving observer the density scales as $n \sim (m\mu)^{3/2}$, and the mean free path scales as $l_{mfp} \sim T/(m^{1/2}\mu^{3/2})$. The evolution of T and μ is governed by the scaling relations discussed in Sect. 10.2. We may use, in particular, that $T/\mu \sim const$ and $\mu \sim \mu(0)/(b_\perp^2 b_x)^{2/3}$. We conclude that in a comoving fluid cell

$$Kn = \frac{l_{mfp}}{L} \sim \left(\frac{b_x}{b_\perp} \right)^{1/3}. \tag{10.53}$$

During the two-dimensional expansion the Knudsen number is dropping, which implies that the hydrodynamic description is becoming more accurate. In the late, three-dimensional stage, the Knudsen number is constant.

A more accurate criterion can be obtained by using a characteristic length or time scale derived from the flow profile. Hydrodynamics is based on a derivative expansion of the energy momentum tensor, and the validity of hydrodynamics requires that $\delta \Pi_{ij}$ is small compared to the ideal fluid stress tensor. Consider the ratio of the moments of the ideal and dissipative terms on the RHS of the Navier–Stokes equation

$$\frac{\langle x_k \nabla_k P \rangle}{\langle x_k \nabla_j \delta \Pi_{kj} \rangle} = \frac{\langle P \rangle}{\langle \frac{4}{3} \eta (\nabla_k v_k) \rangle} \tag{10.54}$$

where $\langle . \rangle$ denotes an integral over d^3x and the index k is fixed. The ratio $(\eta/P)(\nabla \cdot v)$ has a simple interpretation in kinetic theory. For a dilute gas $\eta \sim n p l_{mfp} \sim \rho u^2 \tau_{mft}$ and $P \sim \rho u^2$, where n is the particle density, ρ is the mass density, p is the average quasi-particle momentum, u the average velocity, and τ_{mft} the mean free time. The ratio $\nabla \cdot v \sim \tau_{exp}^{-1}$ defines a characteristic expansion time. The quantity

$$\frac{\eta}{P}(\nabla \cdot v) \sim \frac{\tau_{mft}}{\tau_{exp}} \tag{10.55}$$

measures the ratio of the mean free time over the expansion time. Hydrodynamics is valid if $\tau_{mft} \ll \tau_{exp}$. We observe that for $\eta \sim P$ the freezeout criterion is independent of position and only a function of time. We get

$$\frac{\eta}{P}(\nabla_z v_z) = \frac{\eta_1}{T_0}(b_x b_\perp)^{1/3}\dot{b}_\perp \simeq \frac{\eta_1}{(3N)^{1/3}\lambda^{1/3}}\frac{1}{(T_0/T_F)}(\omega_\perp t)^{1/3}, \tag{10.56}$$

where we have assumed that the expansion is two-dimensional. We note that the relevant parameter is the quantity β defined in Eq. 10.46. Freezeout occurs at $(\omega_\perp t_{fr}) \sim \beta^{-3}$. For typical values of β we find that $t_{fr} \gg t_{cross} \gg t_{diss}$, where $t_{cross} \sim (\omega_\perp \lambda)^{-1}$ is the crossing time, and $t_{diss} \sim 5.9\omega_\perp^{-1}$ is the characteristic time for dissipative effects.

The freezeout time defined by Eq. 10.56 is very long, and the physical freezeout is determined by the viscous effects in the dilute part of the cloud. In the case of a spatially constant shear viscosity we find

$$\frac{\eta}{P}(\nabla_z v_z) = \frac{\eta_0(mT)^{3/2}}{P}\left(\frac{\dot{b}_\perp}{b_\perp}\right) \simeq \frac{45\pi}{8\sqrt{2}}\frac{(T_0/T_F)^2}{(3\lambda N)^{1/3}}b_\perp^{1/3}\dot{b}_\perp \exp\left(\sum_i \frac{x_i^2}{b_i^2 \bar{R}_i^2}\right), \tag{10.57}$$

where we have used $P = nT$ as well as the low density (high temperature) limit of $n_0(x)$, see Eq. 10.6. The radius parameter $\bar{R}_i$ is defined as $\bar{R}_i^2 = 2T_0/(m\omega_i^2)$. The condition $(\eta/P)(\nabla_z v_z)$ determines a freezeout surface $x_{fr}(t)$. This surface is initially at $x_i \gg R_i$, but it moves inward as time increases and reaches the origin at a time $t_{fr} \sim \omega_\perp^{-1}(3\lambda N)(T_F/T_0)^6$. This time is also parametrically very long, but the freezeout time at a characteristic distance $x_i \simeq b_i \bar{R}_i$ is significantly smaller.

Finally, we wish to mention one more quantity that characterizes a viscous flow. The Reynolds number Re is defined as the ratio of inertial and viscous forces in the system. In the case of a scaling flow with $\eta \sim P$ this ratio is independent of position and only a function of time. We find

$$Re = \frac{T_0}{\eta_1 \omega_\perp^2}b_\perp \dot{b}_\perp \simeq \frac{\omega_\perp t}{\beta}. \tag{10.58}$$

The Reynolds number is zero initially, but it grows quickly, reaching $Re \simeq \beta^{-1}$ at $(\omega_\perp t) = 1$. For typical experimental parameters $\beta^{-1} \sim 100$, which is large but not large enough to cause instabilities. At later times even larger values of Re are reached, but at these late times the system is simply free streaming. A constant contribution to the viscosity does not lead to a viscous force, and does not directly contribute to the Reynolds number.

10.3.5 Relaxation Time Approach

The discussion in the previous section does not fully resolve the problems caused by the dilute regions of the cloud. If the shear viscosity is proportional to the pressure then the system freezes out at some time t_{fr}. For values of η/P implied by the data this time is much larger than the characteristic time for dissipative effects in the evolution of the system, and the estimates in Sects. 10.3.1–10.3.3 are internally consistent. If the shear viscosity is constant then there is a freezeout surface which moves inward as a function of time. This implies that the integral in Eqs. 10.27 and 10.38 should be restricted to the region enclosed by the freezeout surface. However, in order for energy to be conserved, and for viscosity to have an effect on the evolution of the system, we would have to include an external force on the freezeout surface.

An approach that can describe the effects of freezeout without the need to introduce an artificial surface is second order viscous hydrodynamic [26]. The second order formalism takes into account terms with two derivatives of the thermodynamic variables in the dissipative correction to the stress tensor and energy current. In general, the second order formalism contains a large number of new transport coefficients. A phenomenological ansatz that has proven to be useful in many different applications is to treat the viscous part of the stress tensor as an independent hydrodynamical variable which satisfies a relaxation equation

$$\tau_R \frac{\partial}{\partial t} \delta \Pi_{ij} = -\delta \Pi_{ij} + \delta \Pi_{ij}^{NS}, \tag{10.59}$$

where τ_R is the relaxation time and $\delta \Pi_{ij}^{NS}$ is the Navier–Stokes expression for the viscous contribution to the stress tensor, Eq. 10.25. An equation of this type was first introduced by Maxwell and Cattaneo in the context of heat transport. More recently, time or frequency dependent viscosities were considered in the study of Bose condensed gases in [27, 28]. In relativistic hydrodynamics relaxation equations for the viscous stress tensor are used in order to restore causality, see the review [29].

Scale invariance implies that $\tau_R(n, T) = w(mT/n^{2/3})/T$ where $w(y)$ is a universal function. In the dilute limit $y \gg 1$ the function $w(y)$ can be calculated in kinetic theory which gives $\tau_R = \eta/(nT)$ [30]. This result corresponds to the estimate for τ_{mft} given in Eq. 10.55. The relaxation equation (10.59) requires an initial condition for the viscous stress $\delta \Pi_{ij}$. If is natural to assume that $\delta \Pi_{ij} = 0$ at $t = 0$. In the center of the cloud τ_R is small and the viscous stress quickly relaxes to the Navier–Stokes result. In the dilute region $\tau_R \to \infty$ and the viscous contribution to the stress tensor remains zero. This implies that even a spatially constant shear viscosity leads to a spatially varying $\delta \Pi_{ij}$ and a non-zero drag force. This drag force is largest near the freezeout surface and breaks the scaling nature of the flow. This means that a detailed study of the Israel-Stewart equations will require numerical solutions of the hydrodynamic equations. We can estimate the effect of the relaxation time by computing the energy dissipation. We have

$$\dot{E} = -\frac{1}{2} \int d^3x \, \delta \Pi_{ij} \left(\nabla_i v_j + \nabla_j v_i - \frac{2}{3} \delta_{ij} \nabla \cdot v \right), \tag{10.60}$$
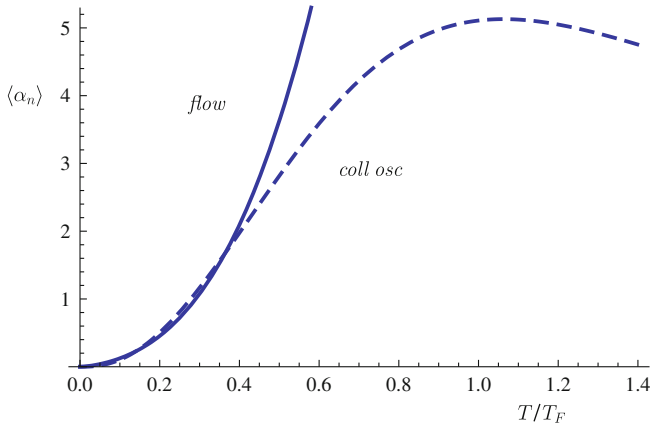
Fig. 10.4 Trap average $\langle \alpha_n \rangle = \langle \eta \rangle / N$ computed from a relaxation time equation with $\eta = \eta_0 (mT)^{3/2}$ and $\tau_R = \eta / (nT)$. Contrary to the pure Navier–Stokes case $\tau_R \to 0$ the ratio $\langle \eta \rangle / N$ depends on the number of particles and the trap geometry. Here we have chosen $N = 2 \cdot 10^5$ and $\lambda = 0.045$. The *solid* shows the result for the elliptic flow field, and the *dashed line* corresponds to the transverse collective mode, see Sect. 10.5

where $\delta \Pi_{ij}$ is determined by Eq. 10.59. The simplest approximation is to set $\delta \Pi_{ij} = \delta \Pi_{ij}^{NS}$ inside the freezeout surface and $\delta \Pi_{ij} = 0$ outside.

In order to obtain more accurate estimates we have to solve the differential equation (10.59). As in Sect. 10.3.1 we may compute $\delta \Pi_{ij}^{NS}$ from the solution of ideal hydrodynamics. The relaxation time can be calculated using the high temperature result for the density profile. We find

$$\omega_\perp \tau_R = \frac{45\pi}{8\sqrt{2}} \frac{1}{(3\lambda N)^{1/3}} \left(\frac{T}{T_F} \right)^2 b_\perp^{4/3} \exp\left(\frac{x_\perp^2}{b_\perp^2 \bar{R}_\perp^2} + \frac{x_z^2}{\bar{R}_z^2} \right), \tag{10.61}$$

which has the same functional form as the freezeout criterion in Eq. 10.57. The viscous stress tensor $\delta \Pi_{ij}$ is determined by integrating Eq. 10.59 and the dissipated energy can be computed from Eq. 10.60. By comparing ΔE with Eq. 10.27 we can express the result in terms of an effective $\langle \alpha_n \rangle$. This quantity is shown in Fig. 10.4. We observe that $\langle \alpha_n \rangle$ grows with temperature as $\langle \alpha_n \rangle \sim T^3$, much faster than one would expect from the relation $\eta \sim T^{3/2}$.

There are no data for elliptic flow at temperatures above T_c, but we will compare the relaxation time result to collective mode data in Sect. 10.5. We note that at low temperature the effective $\langle \alpha_n \rangle$ is the same for expanding and oscillating systems, but that at high temperature the two systems behave differently. In the expanding system the hydrodynamic expansion time τ_{exp} continues to increase during the expansion, whereas the period of the oscillation provides a fixed hydrodynamic time scale in the case of the collective mode. The viscous relaxation time τ_R increases with temperature. This implies that for the collective mode we eventually get $\tau_R > \tau_{exp}$ and the effective $\langle \alpha_n \rangle$ starts to decrease. In the expanding system, on the other hand, the

relaxation time can always match the expansion time and $\langle \alpha_n \rangle$ continues to grow with temperature.

10.4 Expansion From a Rotating Trap

The expansion from a rotating trap was studied in [14]. Rotating gases are of interest for a number of reasons. The quenching of the moment of inertia in a superfluid Bose gas was used as a signature of superfluidity [31]. The remarkable discovery in [14] is that in a Fermi gas at unitarity the suppression of the moment of inertia is also observed in the normal phase. It is clearly of interest to determine to what extent this discovery places constraints on the shear viscosity [32].

10.4.1 Ideal Fluid Dynamics

The Euler equations for a Bose gas with $P \sim n$ were derived in [31]. The result is easily generalized to a Fermi gas at unitarity [14]. As in the case of a non-rotating trap the equations are independent of the temperature and the universal function $f(y)$ in Eq. 10.4. We have

$$\dot{\alpha}_x + \alpha_x^2 + \alpha^2 - \Omega^2 = \frac{\bar{\mu}\omega_x^2}{b_x^2} \tag{10.62}$$

$$\dot{\alpha}_y + \alpha_y^2 + \alpha^2 - \Omega^2 = \frac{\bar{\mu}\omega_y^2}{b_y^2} \tag{10.63}$$

$$\dot{\alpha}_z + \alpha_z^2 = \frac{\bar{\mu}\omega_z^2}{b_z^2} \tag{10.64}$$

$$\dot{\alpha} + \alpha \left(\alpha_x + \alpha_y \right) = \frac{\bar{\mu}a\omega_x^2}{2} \tag{10.65}$$

$$\dot{\Omega} + \Omega \left(\alpha_x + \alpha_y \right) = 0. \tag{10.66}$$

These equations have to be solved together with the continuity Eqs. (10.12–10.16). In all there are ten coupled equations. In the case of a rotating trap there is no initial expansion, $\alpha_i(0) = 0$, but either $\alpha(0)$ or $\Omega(0)$ (or both) are non-zero. If the initial flow is purely irrotational then $\alpha(0) = \omega_{rot}$, where ω_{rot} is the angular velocity of the trap. If the flow corresponds to rigid rotation then $\Omega(0) = \omega_{rot}$. Below the critical temperature the flow of the superfluid component must be irrotational, but above T_c both rotational and irrotational flows are possible.

The equations simplify in the experimentally relevant case of strongly deformed, slowly rotating traps, $\omega_{rot} < \omega_x \ll \omega_\perp$ with $\omega_\perp = \omega_y \simeq \omega_z$. In this limit the motion of the fluid is dominated by the transverse expansion of the system. Up to corrections of order $O(\lambda^2)$ or $O((\omega_{rot}/\omega_\perp)^2)$ we have

$$b_\perp(t) \simeq \begin{cases} 1 + \frac{1}{2}\omega_\perp^2 t^2 + O(t^4) & \omega_\perp t \ll 1, \\ \frac{\omega_\perp t}{\sqrt{\gamma}} + c_0 + O(t^{-1/3}) & \omega_\perp t \gg 1, \end{cases} \tag{10.67}$$

as in the case of a stationary trap. The orientation of the expanding cloud is described by the parameter a defined in Eq. 10.11. We find

$$a(t) \simeq \begin{cases} -\frac{2\omega_{rot} t}{\lambda^2} & \omega_\perp t \ll 1, \\ -\frac{c_a \omega_{rot}}{\lambda^2 \omega_\perp^2 t} & \omega_\perp t \gg 1 \; (t < t_{3d}), \end{cases} \tag{10.68}$$

where c_a is a constant. Below we will show that $c_a = \gamma$. At very late times, $t > t_{3d} \sim 1/(\lambda^2 \omega_\perp)$, we find $a(t) \sim 1/t^2$. The result (10.68) holds irrespective of the nature of the initial rotational flow. The parameter $a(t)$ can be related to the angle of the cloud with respect to the x-axis,

$$\tan(2\theta) = -\frac{a\lambda^2 b_x^2 b_y^2}{b_x^2 - \lambda^2 b_y^2}. \tag{10.69}$$

At early times, $\omega_x t \ll 1$, the angle is proportional to the rotational frequency of the trap, $\theta = \omega_{rot} t$. The angular motion speeds up as $b_y \lambda$ approaches b_x. The angle goes through $45°$ at

$$t_{45°} = \frac{\sqrt{\gamma}}{\omega_x} \tag{10.70}$$

which is the identical to the crossing time in Eq. 10.24. At late times, and up to corrections of $O(\omega_{rot}/\omega_\perp)$, the angle approaches $90°$. The velocity field is dominated by the transverse expansion of the system. In the limit $\omega_{rot} < \omega_x \ll \omega_\perp$ the velocity fields α_i are identical to those in the non-rotating case. We have

$$\alpha_{y,z} \simeq \begin{cases} \omega_\perp^2 t & \omega_\perp t \ll 1, \\ 1/t & \omega_\perp t \gg 1, \end{cases} \tag{10.71}$$

and $\alpha_x = O(\lambda^2)$. The rotational components of the velocity field decay quickly. If the initial flow is irrotational, $\alpha(0) = \omega_{rot}$, then

$$\alpha(t) \simeq \omega_{rot}\left(1 - \omega_\perp^2 t^2\right) \tag{10.72}$$

for $(\omega_\perp t) < 1$. For $(\omega_\perp t) > 1$ the rotational component of the flow is small, $(\alpha/\omega_{rot}) \ll 1$, but the remaining flow decays slowly, $\alpha \sim t^{-1}$ for $t < t_{3d}$ and $\alpha \sim t^{-2}$

for $t > t_{3d}$. In ideal hydrodynamics an initially irrotational flow will remain irrotational, $\Omega(t) = 0$, for all t. If the initial flow corresponds to rigid rotation, $\Omega(0) = \omega_{rot}$, then the early time behavior is given by

$$\Omega(t) \simeq \omega_{rot} \left(1 - \frac{1}{2}\omega_\perp^2 t^2\right). \tag{10.73}$$

An initially rigid rotating flow induces a non-zero irrotational flow. For $(\omega_\perp t) > 1$ both components of the velocity field become much smaller than ω_{rot}.

The angular momentum is given by

$$L_z = \alpha m \langle n(x^2 - y^2)\rangle + \Omega m \langle n(x^2 + y^2)\rangle + \left(\alpha_x - \alpha_y\right) m \langle nxy\rangle, \tag{10.74}$$

where n is the density and $\langle . \rangle$ is an integral over the cloud. The moment of inertia of a rigid rotor is $I_{rig} = m\langle x^2 + y^2\rangle$, and the irrotational moment of inertia is $I_{irr} = m\langle x^2 - y^2\rangle$. We have

$$m\langle nx^2\rangle = \frac{b_x^2}{1 - \frac{\lambda^2}{4}(ab_x b_y)^2} \frac{L_0}{\omega_x}, \tag{10.75}$$

$$m\langle ny^2\rangle = \frac{\lambda^2 b_y^2}{1 - \frac{\lambda^2}{4}(ab_x b_y)^2} \frac{L_0}{\omega_x}, \tag{10.76}$$

$$m\langle nxy\rangle = \frac{-\frac{\lambda^2}{2}ab_x^2 b_y^2}{1 - \frac{\lambda^2}{4}(ab_x b_y)^2} \frac{L_0}{\omega_x}, \tag{10.77}$$

where the scale is set by

$$L_0 = \frac{N}{6} \frac{(3N)^{1/3}}{\lambda^{2/3}} \left(\frac{E_0}{E_F}\right). \tag{10.78}$$

In the experiment of Clancy et al. $(\omega_{rot}/\omega_x) \simeq 0.4$ and $L_0/N \simeq 131(E_0/E_F)$. For $E_0/E_F = 1$, which is in the normal phase, the angular momentum per particle is $50\hbar$.

At early times the trap is strongly deformed and $I_{rig} \simeq I_{irr}$. When the cloud becomes almost spherical the irrotational moment is much smaller than the rigid moment of inertia, $I_{irr} \ll I_{rig}$. However, at times $(\omega_\perp t) > 1$ the angular momentum is mainly carried by the last term in Eq. 10.74, which is related to the transverse expansion of the system. This is true irrespective of the nature of the initial rotational flow. For $(\omega_\perp t) > 1$ we have $\alpha_y m \langle nxy\rangle \simeq (c_a/\gamma)(\omega_{rot}/\omega_x)L_0$. Angular momentum conservation then fixes the constant c_a in Eq. 10.68, $c_a = \gamma$. At very late time, $t > t_{3d}$, the angular momentum is shared among all the terms in Eq. 10.74, and the relative size of the different contributions depends on the initial conditions. In practice, of course, hydrodynamics is no longer applicable at $t > t_{3d}$.

10.4.2 Dissipation

The effects of dissipation on the expansion from a rotating trap can be studied in close analogy with Sects. 10.3.1–10.3.5. The rate of energy dissipation is

$$\dot{E} = -\frac{4}{3}\left(\alpha_x^2 + \alpha_y^2 + \alpha_z^2 - \alpha_x\alpha_y - \alpha_x\alpha_z - \alpha_y\alpha_z + 3\alpha^2\right)\int d^3x\,\eta(x). \quad (10.79)$$

For $\alpha_x \simeq \alpha_y \gg \alpha_z, \alpha$ this expression reduces to the energy dissipated by the transverse expansion of cloud, see Eq. 10.27. This implies that the main effect of dissipation is to slow the transverse expansion of the cloud, and to delay the time $t_{45°}$. This delay is exactly the same as the delay in the crossing time in Eq. 10.34. We have

$$\left(\frac{\delta t}{t}\right)_{45°} = 0.009 \left(\frac{\langle\alpha_s\rangle}{1/(4\pi)}\right)\left(\frac{1.3\cdot 10^5}{N}\right)^{1/3}\left(\frac{0.3}{\lambda}\right)^{1/3}\left(\frac{S/N}{4.8}\right)\left(\frac{2.1}{E_0/E_F}\right). \quad (10.80)$$

We can confirm this estimate by solving the Navier–Stokes equation. The Navier–Stokes equation can be derived using the moment method described in Sect. 10.3.2. As before, an equivalent set of equations can be obtained from the viscosity model given in Eq. 10.42. We get [33]

$$\dot{\alpha}_x + \alpha_x^2 + \alpha^2 - \Omega^2 = \frac{\omega_x^2}{b_x^2}\left\{\bar{\mu} - \frac{6\beta}{\omega_\perp}\left[\frac{2}{3}\alpha_x - \frac{1}{3}\left(\alpha_y + \alpha_z\right) + \frac{1}{2}ab_x^2\alpha\right]\right\} \quad (10.81)$$

$$\dot{\alpha}_y + \alpha_y^2 + \alpha^2 - \Omega^2 = \frac{\omega_y^2}{b_y^2}\left\{\bar{\mu} - \frac{6\beta}{\omega_\perp}\left[\frac{2}{3}\alpha_y - \frac{1}{3}\left(\alpha_x + \alpha_z\right) + \frac{1}{2}a\lambda^2 b_y^2\alpha\right]\right\} \quad (10.82)$$

$$\dot{\alpha}_z + \alpha_z^2 = \frac{\omega_z^2}{b_z^2}\left\{\bar{\mu} - \frac{6\beta}{\omega_\perp}\left[\frac{2}{3}\alpha_z - \frac{1}{3}\left(\alpha_x + \alpha_y\right)\right]\right\} \quad (10.83)$$

$$\dot{\alpha} + \alpha\left(\alpha_x + \alpha_y\right) = \omega_x^2\left\{\frac{\bar{\mu}a}{2} - \frac{3\beta}{\omega_\perp}\left[\frac{a}{6}\left(\alpha_x + \alpha_y - 2\alpha_z\right) + \frac{b_x^2 + \lambda^2 b_y^2}{\lambda^2 b_x^2 b_y^2}\alpha\right]\right\} \quad (10.84)$$

$$\dot{\Omega} + \Omega\left(\alpha_x + \alpha_y\right) = \frac{3\beta\omega_x^2}{\omega_\perp}\left[\frac{a}{2}\left(\alpha_x - \alpha_y\right) + \frac{b_x^2 - \lambda^2 b_y^2}{\lambda^2 b_x^2 b_y^2}\alpha\right]. \quad (10.85)$$

These equations are independent of the functional form of the pressure. A solution of the Navier–Stokes equation for the trap parameters and initial conditions in [14] is shown in Fig. 10.5. The experimental data were taken at $E/E_F = 0.56$ which is in the superfluid phase, and $E/E_F = 2.1$ which is significantly above the phase transition. Similar to the low temperature data for pure transverse expansion in Fig. 10.1 the
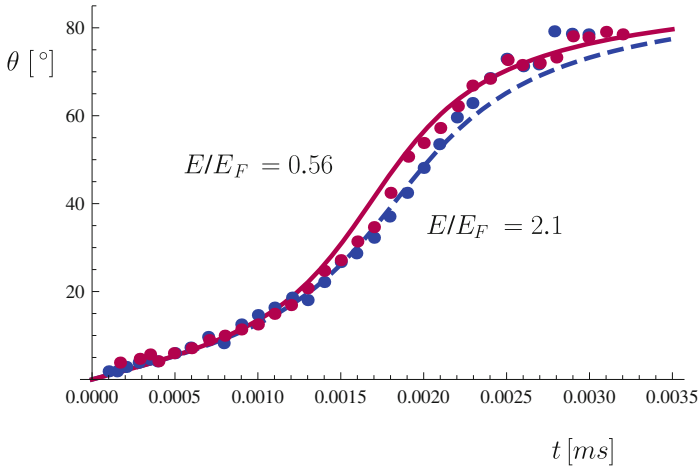
Fig. 10.5 Time evolution of the angle of the major axis of a rotating expanding cloud after release from the trapping potential. The data are taken from [14]. The two data sets were obtained with initial energies $E/E_F = 0.56$ and 2.1. The *solid line* shows the prediction of ideal fluid dynamics, and the *dashed lines* shows the solution of the Navier–Stokes equation for $\beta = 0.061$. Using an entropy per particle $S/N \simeq 4.8$ this value of β implies a shear viscosity to entropy density ratio $\langle \alpha_s \rangle = 0.60$

low temperature result for a rotating cloud shows no dissipative effects, and the best fit to the data is provided by ideal fluid dynamics.

The data for $E/E_F = 2.1$ clearly show a delayed expansion. We find $(\delta t/t)_{45°} \simeq 0.063$. Using $(\delta t/t) \simeq 1.16\beta$ from Eq. 10.32 we estimate $\beta \simeq 0.057$. This estimate is quite accurate, the best fit of the Navier–Stokes solution to the data is obtained for $\beta = 0.061$. Using $N = 1.3 \cdot 10^5$, $\lambda = 0.03$ [14] and $(S/N) \simeq 4.8$ [22] we obtain $\langle \alpha_s \rangle \simeq 0.60$. The measurements were extended to values of E/E_F between 0.56 and 2.1 in [32]. This work reports values of η/s as small as $\langle \alpha_s \rangle \simeq (0.0 - 0.4)$. Note that in this regime it becomes very difficult to measure the viscosity accurately. A value of $\langle \alpha_s \rangle = 0.1$ affects the measured angle of the cloud by less than the with of the lines in Fig. 10.5.

A more detailed study of viscous effects on the evolution of the system is shown in Figs. 10.6, 10.7 10.8. We observe that viscosity slows down the evolution of the scale parameters b_y, b_z and a. More interesting is the effect on the velocity fields α and Ω. Viscosity converts a fraction of the irrotational velocity field α into the rotational velocity field Ω. This is also seen in the breakdown of the angular momentum, see Fig. 10.8. The rotational component of L_z is not large, but it does lead to an observable effect in the angular velocity of the cloud. Figure 10.9 shows that viscosity leads to a decrease in $\dot{\Theta}$. During most of the evolution this effect is dominated by the delayed expansion, but for $t \simeq t_{45°}$ there is an extra reduction which is due to an increase of the effective moment of inertia $I = L/\dot{\Theta}$ caused by the rotational
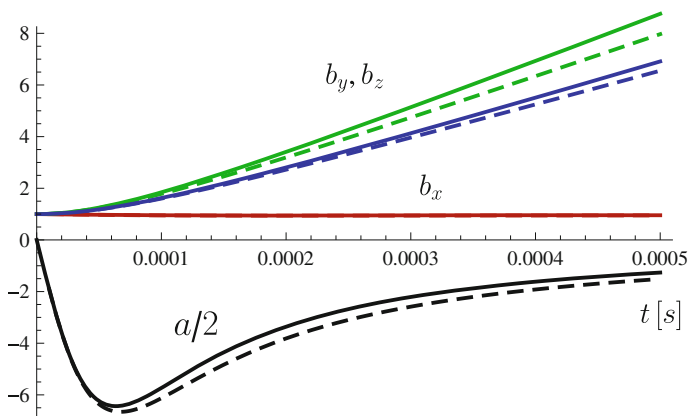
Fig. 10.6 Time evolution of the parameters a, b_x, b_y, b_z that characterize the scaling expansion out of a rotating trap. Note that in this case ω_y and ω_z are not exactly equal, and that the time scale is different from Fig. 10.5. Here, we only show the early evolution of the system. *Solid lines* show the solution of the Euler equation, and *dashed lines* show the solution of the Navier–Stokes equation for $\beta = 0.077$
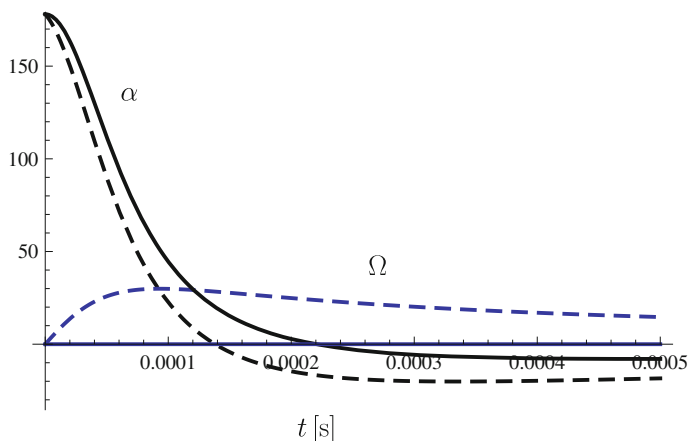
Fig. 10.7 Time evolution of the parameters α and Ω which control the irrotational and rotational components of the velocity field. Parameters were chosen as in Fig. 10.6. *Solid lines* show the solution of the Euler equation, and *dashed lines* show the solution of the Navier–Stokes equation for $\beta = 0.077$

flow. Unfortunately, the experimental data are for $\Theta(t)$ are not sufficiently accurate to demonstrate this effect.
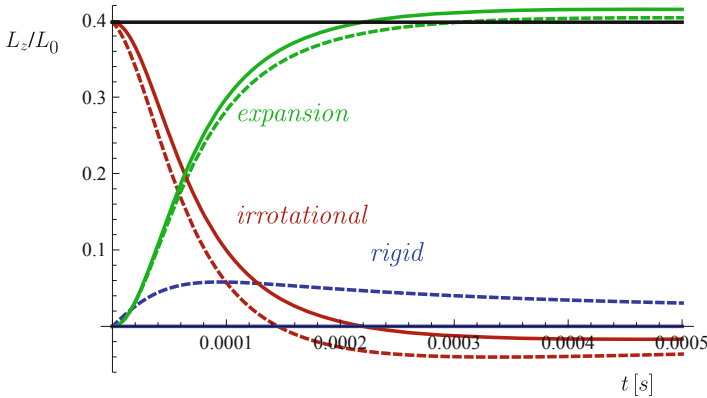
Fig. 10.8 This figure shows different contribution to the total angular momentum of the expanding cloud as a function of time. The angular momentum is given in units of the quantity L_0 defined in the text. The curves labeled irrotational, rigid, and expansion show the $\langle x^2 - y^2 \rangle$, $\langle x^2 + y^2 \rangle$, and $\langle xy \rangle$ contributions. The *solid* and *dashed lines* correspond to ideal and viscous hydrodynamics, respectively. The *solid black line* shows the (conserved) total angular momentum
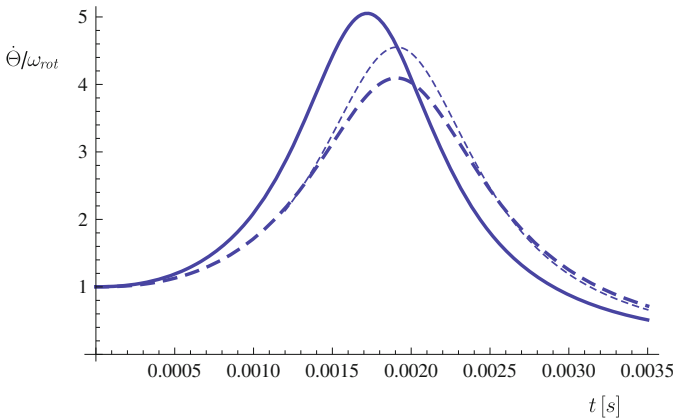
Fig. 10.9 This figure shows the angular velocity of the rotating cloud as a function of time. The *solid line* shows the solution of the Euler equation, and the *dashed line* is the solution of the Navier–Stokes equation for $\beta = 0.077$. The *thin dashed line* shows the result for the angular velocity obtained by rescaling the solution of the Euler equation by a factor $1 + (\delta t/t)_{45°} \simeq 1.1$. The discrepancy between the Navier–Stokes prediction and the rescaled Euler result in the regime where $\dot{\Theta}$ is large is due to the rotational component of the flow. We note that $I = L/\dot{\Theta}$ is the moment of inertia

10.5 Collective Oscillations

In order to study collective oscillations we consider the Euler equation (10.19) in the presence of the trapping potential. The equation of motion is

$$\ddot{b}_i = \frac{\omega_i^2}{(b_x b_y b_z)^{2/3}} \frac{1}{b_i} - \omega_i^2 b_i. \qquad (10.86)$$

The equilibrium solution is $b_x = b_y = b_z = 1$. We now consider small oscillations around the equilibrium, $b_i(t) = 1 + a_i e^{i\omega t}$. The linearized equation of motion gives

$$\omega^2 a_i = \omega_i^2 \left(2a_i + \gamma \sum_j a_j \right), \qquad (10.87)$$

which was derived in [34, 35, 36] using slightly different methods. For the radial breathing mode $a_y = a_z = a_\perp, a_x = 0$ we get $\omega^2 = 2(1 + \gamma)\omega_\perp^2 = (10/3)\omega_\perp^2$. The energy dissipated can be computed from Eq. 10.27. We find

$$\frac{\Delta E}{E_{osc}} = - 4\pi \sqrt{\frac{3}{10}} \beta \simeq - 6.88 \cdot \beta, \qquad (10.88)$$

where ΔE is the energy dissipated per period, E_{osc} is the energy of the collective mode, and β is the parameter defined in Eq. 10.33. We note that the amount of energy dissipated in one period of the transverse breathing mode is about three times larger than the energy dissipated by transverse expansion, see Eq. 10.32.

We can also derive a Navier–Stokes equation, either by taking moments as in Sect. 10.3.2, or by using a simple scaling form of the shear viscosity as in Sect. 10.3.3. For the transverse breathing mode we find

$$\ddot{b}_\perp = \frac{\omega_\perp^2}{b_\perp^{7/3}} - \omega_\perp^2 b_\perp - \frac{2\beta \omega_\perp \dot{b}_\perp}{b_\perp^2}. \qquad (10.89)$$

If β is small then this equation is approximately solved by a damped oscillating function. We have

$$b_\perp(t) = 1 + a_\perp \cos(\omega t) \exp(-\Gamma t). \qquad (10.90)$$

Comparison with Eq. 10.88 gives $\Gamma = \beta \omega_\perp$. The main feature of collective modes is that the viscous term exponentiates so that even very small values of β are experimentally accessible. In Fig. 10.10 we show a comparison between an exact solution of Eq. 10.89 for $\beta = 0.05, a_\perp(0) = 0.25$ and the approximate solution (10.90). We observe that the approximate solution is extremely accurate.

The experimentally measured damping rate can be used to estimate $\langle \alpha_s \rangle$. We have

$$\langle \alpha_s \rangle = (3\lambda N)^{1/3} \left(\frac{\Gamma}{\omega_\perp} \right) \left(\frac{E_0}{E_F} \right) \left(\frac{N}{S} \right). \qquad (10.91)$$

In Fig. 10.11 we show an analysis of the data obtained by Kinast et al. [9] using Eq. 10.91. This plot is very similar to our earlier analysis [37] (see also [38, 39]),
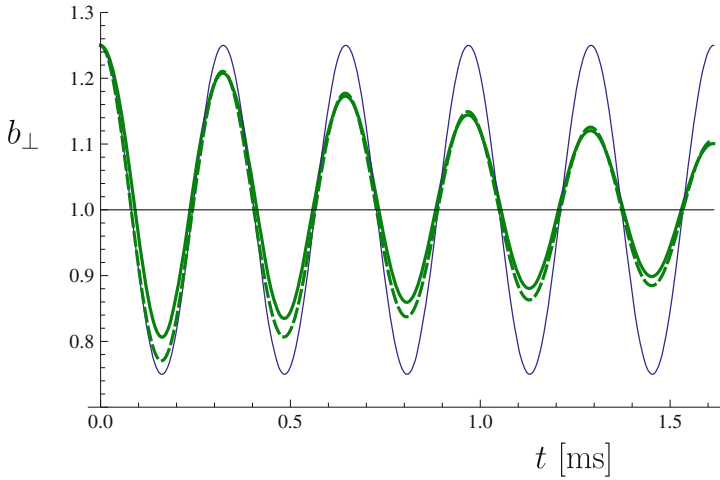
Fig. 10.10 Time evolution of the amplitude of the transverse breathing mode. The *black line* shows the solution of the Euler equation and the *solid green line* is the solution of the Navier–Stokes equation for $\beta = 0.05$. The *dashed green line* is the damped cosine function given in Eq. 10.90. The trap frequency was chosen to be $\omega_\perp = 1696$ Hz as in [10]
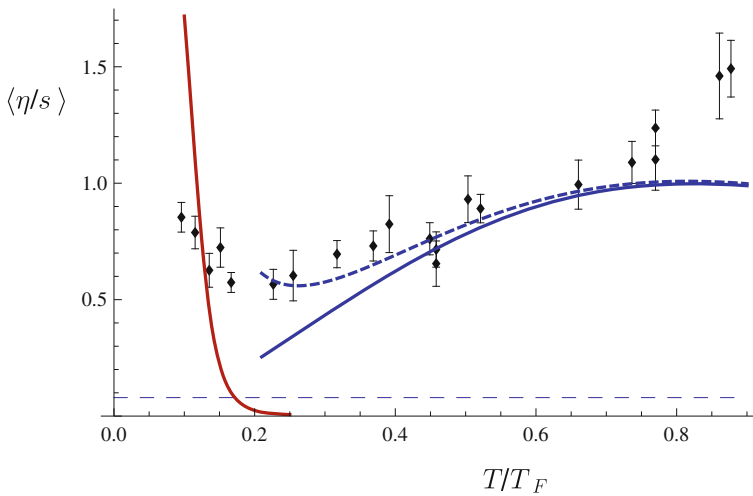
Fig. 10.11 Trap average $\langle \alpha_s \rangle = \langle \eta/s \rangle$ extracted from the damping of the radial breathing mode. The data points were obtained using Eq. 10.91 to analyze the data published by Kinast et al. [9]. The thermodynamic quantities (S/N) and E_0/E_F were taken from [22]. The *solid red* and *blue lines* show the expected low and high temperature limits. Both theory curves include relaxation time effects. The *blue dashed curve* is a phenomenological two-component model explained in the text

except that the temperature calibration and thermodynamic data have been updated using the recent analysis published in [22].

There are a number of important checks on the interpretation of the damping date in terms of viscous hydrodynamics that should be, or have already been, performed. Viscous hydrodynamics predicts that the monopole mode in a spherical trap is not damped at all. This prediction is quite striking, but it has never been tested. Viscous hydrodynamics also predicts simple relationships between the damping constant of the radial breathing mode and the radial quadrupole as well as the scissors mode [37]. These predictions agree qualitatively with the data obtained by the Innsbruck group, but there are some structures in the data that do not fit a simple hydrodynamic description. Finally, hydrodynamics predicts that the damping rate decreases as $N^{-1/3}$. This prediction does not agree with the data published in [9]. We note, however, that Kinast et al. only checked the scaling behavior at very low temperature, and that relaxation time effects may modify the particle number scaling.

We can also compare the results in Fig. 10.11 to theoretical prediction for the shear viscosity in the low and high temperature limit. In the high temperature limit the viscosity is independent of density and the main source of dissipation is the finite relaxation time, see Sect. 10.3.5. In the case of periodic motion the relaxation time equation (10.59) is easily solved. The dissipated energy is given by Eqs. 10.33, 10.88 with

$$\langle \alpha_n \rangle = \eta_0 (mT)^{3/2} \int d^3 x \frac{1}{1 + \omega^2 \tau_R (n(x))^2}. \tag{10.92}$$

We will use the kinetic theory result $\tau_R(n) = \eta/(nT)$ with $\eta = \eta_0 (mT)^{3/2}$. In the high temperature (low density) limit we can use the classical expression for the density profile $n(x)$. In this case the integral over x can be done analytically. We find

$$\langle \alpha_n \rangle = -\frac{45\pi}{32} \left(\frac{T}{T_F} \right)^3 Li_{3/2} \left(-\left[\frac{const}{(\lambda N)^{2/3}} \left(\frac{T}{T_F} \right)^4 \right]^{-1} \right), \tag{10.93}$$

where $const = 1125 \cdot 3^{1/3} \pi^2 / 64 \simeq 250.1$, and $Li_\alpha(x)$ is the polylogarithm function. In the limit $T \ll T_F$ the result scales as $\langle \alpha_n \rangle \sim y^3 \log(y)^{3/2}$ with $y = T/T_F$. For $T \gg T_F$ we get $\langle \alpha_n \rangle \sim y^{-1}$. These results imply that both the temperature scaling and the particle number scaling differ from naive expectations. The shear viscosity scales as $\eta \sim T^{3/2}$, but $\langle \alpha_n \rangle \sim T^3 \log(T)^{3/2}$ at low T, and $\langle \alpha_n \rangle \sim T^{-1}$ at high T. Also, the scaling of the damping rate with N is $\Gamma \sim N^{-1/3} \log(N)^{3/2}$ at low T and $\Gamma \sim N^{1/3}$ at high T, see Fig. 10.12. This implies that there are temperature regions in which the dependence of the damping rate on N is small.

The prediction of Eq. 10.93 is shown as the solid blue line in Fig. 10.11. We observe that the relaxation time model agrees well with the data for $T \sim (0.5 - 0.8)T_F$. For temperature less than $0.5T_F$ the observed damping rate is bigger than the prediction of the relaxation model. At very low temperature the shear viscosity is expected to be dominated by the phonon contribution [23]

$$\eta = 0.018 n \left(\frac{n^{2/3}}{mT} \right)^5. \tag{10.94}$$
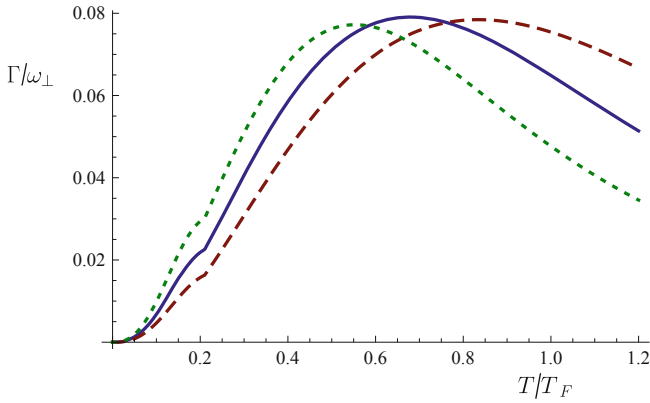
Fig. 10.12 Damping rate of the radial breathing mode in units of the transverse trapping frequency. This figure only shows the contribution from the dilute corona, computed using the relaxation time approach. The *solid line* corresponds to $N \equiv N_0 = 2 \cdot 10^5$, $\lambda = 0.045$ as in [9]. The *long dashed* and *short dashed lines* corresponds to $N = 5N_0$ and $N = 0.2N_0$, respectively

At low temperature we can compute the trap average by using the zero temperature profile. We find $\langle \alpha_n \rangle \simeq 1.5 \cdot 10^{-5}(T_F/T)^5$. This result becomes large for $T/T_F < 0.1$. In this regime relaxation time effects are important, and $\langle \alpha_n \rangle$ at finite frequency goes to zero as $T \to 0$.

Neither the low temperature nor the high temperature result provide a good description of the data in the regime $T \simeq (0.15 - 0.40)T_F$. The dashed blue line in Fig. 10.11 shows a purely phenomenological fit based on the functional form $\eta = \eta_0(mT)^{3/2} + \eta_1 n^{5/3}/(mT)$ with $\eta_0 = 15/(32\sqrt{\pi}) \simeq 0.264$ and $\eta_1 \simeq 0.06$. In this case the minimum value of η/n is 0.24 which occurs below the phase transition at $mT/n^{2/3} \simeq 0.47$.

10.6 Summary and Outlook

A special feature of the hydrodynamics of a unitary Fermi gas is the existence of simple scaling solutions of the equations of ideal fluid dynamics. These solutions are independent of the equation of state, the initial temperature and the number of particles. The only time scales in the problem are the trap frequencies, see Fig. 10.13. The existence of scaling solutions is related to the constraints imposed by scale invariance on the equation of state, and to the harmonic character of the confinement potential.

The properties mentioned above make scaling flows an ideal class of solution to study the effects of shear viscosity. In this contribution we focused on three classes of experiments, expansion from a deformed trap ("elliptic flow"), expansion from a rotating trap, and damping of collective oscillations. These experiments provide
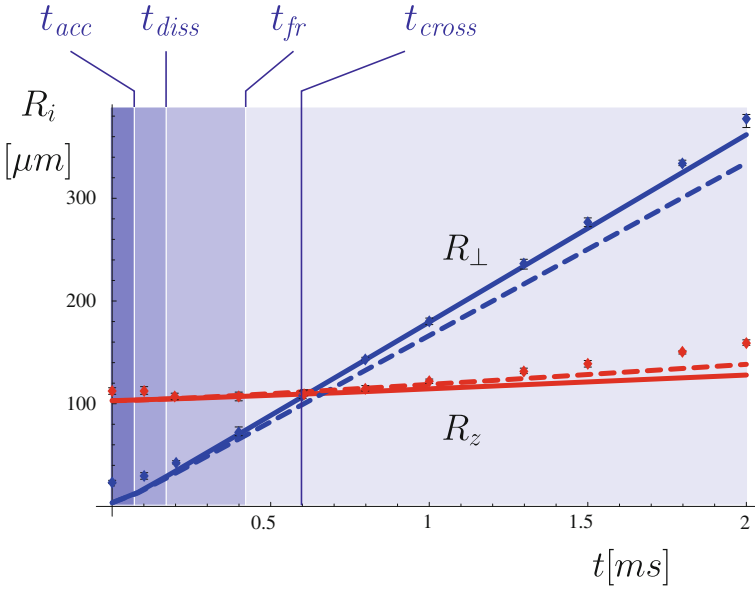
Fig. 10.13 Time scales relevant to the expansion of a unitary Fermi gas from a deformed trap. The inverse trap frequency is $\omega_\perp^{-1} = 0.024$ ms. The scale t_{acc} is the characteristic time for hydrodynamic acceleration, where we have defined $t = t_{acc}$ to be the time when 80% of the initial internal energy has been converted to kinetic energy. The characteristic time for viscous effects, t_{dis}, is determined by the condition that the dissipated energy ΔE has reached 80% of its asymptotic value. The freezeout time t_{fr} is quite uncertain. Here, we show the time at which, for $T_0/T_F = 0.21$, the freezeout surface reaches the point $x_\perp = b_\perp R_\perp$. The crossing time t_{cr} is the time at which the system becomes spherical. The time t_{3d} at which the expansion becomes three-dimensional is bigger by another factor λ^{-1}

somewhat complementary information, and they have different advantages and disadvantages:

- In the case of collective modes the effect of shear viscosity exponentiates, and as a consequence the damping of collective modes is sensitive to very small values of the shear viscosity. Collective modes also have the advantage that qualitatively the effect of dissipation is very simple: The kinetic energy of the collective mode is converted to heat, so that at the end of the evolution the system is again stationary, but the temperature is increased. In the case of flow experiments the situation is more complicated. Dissipation converts kinetic energy into heat but unless the system freezes out first, the internal energy is eventually converted back to kinetic energy. Because of the second law of thermodynamics, the final state of viscous hydrodynamics must differ from that of ideal hydrodynamics, but the differences can be subtle, manifesting themselves in violations of the simple scaling formulas for the density and the velocity field.

- The transverse expansion experiments provide detailed information about the time dependence of the density and flow profiles. This information can be used to understand the breakdown of hydrodynamics, for example by studying deviations from the simple linear velocity profile predicted by ideal fluid dynamics. Transverse flow experiments may also show a different, and possibly smaller, sensitivity to relaxation effects. Figure 10.4 shows that, for $T/T_F < 0.4$, the relaxation time estimate of the trap averaged dissipation due to the spatially constant part of the shear viscosity is similar for transverse flow and transverse collective modes. However, the local response of a rapidly expanding cloud is likely to be different from that of an oscillating system.
- The expansion of a rotating cloud is sensitive to a new viscous effect, the conversion of an irrotational flow $\vec{v} \sim \vec{\nabla}(xy)$ to a rotational flow $\vec{v} \sim \hat{z} \times \vec{x}$. Contrary to the slowdown of the transverse expansion, which could in principle be due to scale-breaking terms in the pressure or residual external potentials, this is a genuine dissipative effect, since vorticity is conserved in ideal hydrodynamics.

The main difficulty in extracting the shear viscosity from the analysis of scaling flows is associated with the role of the dilute corona of the cloud. Kinetic theory predicts that in the dilute limit the shear viscosity is independent of density and only depends on temperature. A simple analysis of the type presented in Sect. 10.3.3 then implies that the dilute corona does not generate a dissipative force. It nevertheless dissipates a large amount of energy. The analysis also suggests that freezeout only occurs very late, see Sect. 10.3.4. There are a number of aspects of this analysis that need to be improved:

- The Navier–Stokes equation is based on the assumption that the viscous correction to the stress tensor appears instantaneously. This is particularly problematic in the case of scaling flows, because the viscous contribution is spatially constant. The fact that the ideal stresses propagate outward with the expansion of the system whereas the dissipative stresses appear immediately indicates that causality is violated. This problem can be addressed by including a finite relaxation time, or by solving a more complete set of second order hydrodynamic equations.
- We have studied the effect of dissipative forces in the Navier–Stokes equations, but we have computed the non-dissipative forces (pressure gradients) based on an approximately isentropic expansion. This procedure neglects reheating, and violates energy conservation. Reheating is important in the dilute corona, and breaks the scaling nature of the expansion.

In addition to implementing these technical improvements it is important to consider other experimental setups that are directly sensitive to the spatially constant part of the shear viscosity. One option would be to measure the attenuation of sound propagating in a very long elongated trap. Another idea would be to directly measure the decay of a shear flow in a long channel.

Finally, we summarize the existing experimental constraints on the shear viscosity of the unitary Fermi gas:

- The damping of collective oscillations constrains the trap average $\langle\eta\rangle/S \equiv \langle\alpha_s\rangle$. We find that this quantity varies between $\langle\alpha_s\rangle \simeq 1$ at $T/T_F \simeq 0.8$ and $\langle\alpha_s\rangle \simeq 0.5$ at $T/T_F \simeq 0.2$. In the regime $0.4 \leq T/T_F \leq 0.8$ the temperature dependence is consistent with $\eta \sim (mT)^{3/2}$ and a relaxation time that scales as $\tau_R \sim \eta/(nT)$. At lower temperatures an additional contribution is needed. In a simple model the minimum of the shear viscosity to density ratio is $\eta/n \simeq 0.2$.

- The expansion of a rotating cloud gives $\langle\alpha_s\rangle \simeq 0.8$ at $T/T_F \simeq 0.8$, and $\langle\alpha_s\rangle \simeq (0.0-0.4)$ at $T/T_F \simeq 0.2$ [32]. The latter results are smaller than the values extracted from collective oscillations, although the errors are also somewhat larger. It will be important to determine whether this discrepancy is due to the effects of the dilute corona, and whether the smaller values of $\langle\alpha_s\rangle$ are more representative of the shear viscosity to entropy density ratio in the core.

Note added: After the initial version of this contribution was finished dissipative effects in the expansion of a dilute Fermi gas at temperatures $T \gg T_F$ were studied experimentally by Cao et al. [40]. This work nicely demonstrates the scaling $\langle\alpha_n\rangle \sim T^3$ predicted in Fig. 10.4. Numerical solutions to the equations of dissipative hydrodynamics were studied in [41]. This work shows that quantitative estimates of the shear viscosity have to take into account the effects of reheating.

References

1. Bloch, I., Dalibard J., Zwerger, W.: Rev. Mod. Phys. **80**, 885 (2008) [arXiv:0704.3011]
2. Giorgini, S., Pitaevskii, L.P., Stringari, S.: Rev. Mod. Phys. **80**, 1215 (2008) [arXiv:0706.3360]
3. Schäfer, T., Teaney, D.: Rept. Prog. Phys. **72**, 126001 (2009) [arXiv:0904.3107 [hep-ph]]
4. Danielewicz, P., Gyulassy, M.: Phys. Rev. D **31**:53 (1985)
5. Policastro, G., Son, D.T., Starinets, A.O.: Phys. Rev. Lett. **87**, 081601 (2001) [arXiv:hep-th/0104066]
6. Kovtun, P., Son, D.T., Starinets, A.O.: Phys. Rev. Lett. **94**, 111601 (2005) [arXiv:hep-th/0405231]
7. O'Hara, K.M., Hemmer, S.L., Gehm, M.E., Granade, S.R., Thomas, J.E.: Science. **298**, 2179 (2002) [cond-mat/0212463]
8. Kinast, J., Hemmer, S.L., Gehm, M.E., Turlapov, A., Thomas, J.E.: Phys. Rev. Lett. **92**, 150402 (2004) [cond-mat/0403540]
9. Kinast, J., Turlapov, A., Thomas, J.E.: Phys. Rev. A **70**, 051401(R) (2004) [cond-mat/0408634]
10. Kinast, J., Turlapov, A., Thomas, J.E.: Phys. Rev. Lett. **94**, 170404 (2005) [cond-mat/0502507]
11. Altmeyer, A., Riedl, S., Kohstall, C., Wright, M., Geursen, R., Bartenstein, M., Chin, C., Hecker Denschlag, J., Grimm, R.: Phys. Rev. Lett. **98**, 040401 (2007) [cond-mat/0609390]
12. Altmeyer, A., Riedl, S., Kohstall, C., Wright, M., Hecker Denschlag, J., Grimm, R.: Phys. Rev. Lett. **98**, 103602 (2007) [cond-mat/0611285]
13. Wright, M.J., Riedl, S., Altmeyer, A., Kohstall, C., Sanchez Guajardo, E.R., Hecker Denschlag, J., Grimm, R.: Phys. Rev. Lett. **99**, 150403 (2007) [arXiv:0707.3593[cond-mat.other]]

14. Clancy, B., Luo, L., Thomas, J.E.: Phys. Rev. Lett. **99**, 140401 (2007) [arXiv:0705.2782 [cond-mat.other]]
15. Riedl, S., Sanchez Guajardo, E.R., Kohstall, C., Altmeyer, A., Wright, M.J., Hecker Denschlag, J., Grimm, R., Bruun, G.M., Smith, H. Phys. Rev. A **78**, 053609 (2008) [arXiv:0809.1814[cond-mat.other]]
16. Carlson, J., Reddy, S.: Phys. Rev. Lett. **95**, 060401 (2005) [cond-mat/0503256]
17. Bulgac, A., Drut, JE., Magierski, P.: Phys. Rev. A **78**, 023625 (2008) [arXiv:0803.3238 [cond-mat.stat-mech]]
18. Nascimbene, S., Navon, N., Jiang, K., Chevy, F., Salomon, C. [arXiv:0911.0747[cond-mat.quant-gas]]
19. Menotti, C., Pedri, P., Stringari, S.: Phys. Rev. Lett. **89**, 250402 (2002) [cond-mat/0208150]
20. Thomas, J.E., Kinast, J., Turlapov, A.: Phys. Rev. Lett. **95**, 120402 (2005) [cond-mat/0503620]
21. Son, D.T.: Phys. Rev. Lett. **98**, 020604 (2007) [arXiv:cond-mat/0511721]
22. Luo, L., Thomas, J.E.: J. Low Temp. Phys. **154**, 1 (2009) [arXiv:0811.1159[cond-mat.other]]
23. Rupak, G., Schäfer, T.: Phys. Rev. A **76**, 053607 (2007) [arXiv:0707.1520 [cond-mat.other]]
24. Bruun, G.M., Smith, H.: Phys. Rev. A **72**, 043605 (2005) [cond-mat/0504734]
25. Bruun, G.M., Smith, H.: Phys. Rev. A **75**, 043612 (2007) [cond-mat/0612460]
26. Garcia-Colina, L.S., Velascoa, R.M., Uribea, F.J.: Phys. Rep. **465**, 149 (2008)
27. Nikuni, T., Griffin, A.: Phys. Rev. A **69**, 023604 (2004) [cond-mat/0309269]
28. Griffin, A., Nikuni, T., Zaremba, E.: Bose-condensed gases at finite temperature. Cambridge University Press, Cambridge (2009)
29. Romatschke, P.: Int. J. Mod. Phys. E **19**, 1–53 (2010) [arXiv:0902.3663 [hep-ph]]
30. Bruun, G.M., Smith, H.: Phys. Rev. A **76**, 045602 (2007) [arXiv:0709.1617]
31. Edwards, M., Clark, C.W., Pedri, P., Pitaevskii, L., Stringari, S.: Phys. Rev. Lett. **88**, 070405 (2002)
32. Thomas, J.E.: Nucl. Phys. A **830**, 665C–672C (2009) [arXiv:0907.0140v2 [cond-mat.quant-gas]]
33. Clancy, B.: Ph.D. thesis, Duke University (2008)
34. Heiselberg, H.: Phys. Rev. Lett. **93**, 040402 (2004) [cond-mat/0403041]
35. Stringari, S.: Europhys. Lett. **65**, 749 (2004) [cond-mat/0312614]
36. Bulgac, A., Bertsch, G.F.: Phys. Rev. Lett. **94**, 070401 (2005) [cond-mat/0404687]
37. Schäfer, T.: Phys. Rev. A **76**, 063618 (2007) [arXiv:cond-mat/0701251]
38. Gelman, B.A., Shuryak, E.V., Zahed, I.: Phys. Rev. A **72**, 043601 (2005) [nucl-th/0410067]
39. Turlapov, A., Kinast, J., Clancy, B., Luo, L., Joseph, J., Thomas, J.E.: J. Low Temp. Phys. **150**, 567 (2008) [arXiv:0707.2574]
40. Cao, C., Elliott, E., Joseph, J., Wu, H., Petricka, J., Schäfer, T., Thomas, J.E.: Science **331**, 5 (2011) [arXiv:1007.2625 [cond-mat.quant-gas]]
41. Schäfer, T.: Phys. Rev. A **82**, 063629 (2010) [arXiv:1008.3876 [cond-mat.quant-gas]]

Chapter 11
Thermodynamics of Fermi Gases

F. Chevy and C. Salomon

11.1 Introduction

Recently, ultra-cold atoms have established a very fruitful connection with condensed matter physics, nuclear physics, astrophysics, and high energy physics on many-body problems in strongly correlated systems. Starting from the pioneering work of Popov and Eagles in the 1970s [1], the connection between superfluidity in a fermionic system with attractive interaction and superfluidity of bosonic pairs of fermions has been the subject of intense theoretical activity (See for instance [2, 3] and other contributions in this book). While the two limiting cases, weakly attractive Fermi gas and weakly repulsive Bose gas are well described by mean field theories, the so-called BEC–BCS crossover region where the gas is strongly correlated poses a challenging theoretical problem. A flurry of theoretical works (see for instance [2, 4–9]) have been developed in order to address the properties of this seemingly simple many-body system of a fermionic species with two spin states interacting with purely s-wave contact potential, but with tunable strength.

On the experimental side the field of ultracold Fermi gases started soon after Bose–Einstein condensation in dilute gases was first observed in 1995 [10]. Quantum degeneracy in a gas of fermionic atoms was obtained in 1999 [11]. Spectacular progress has been achieved since then because strong interactions in a stable system could be produced thanks to the Fano-Feshbach resonance mechanism and the unexpected stability of the gas provided by the Pauli exclusion principle [2, 12, 13]. In these systems, the strong interactions within the gas required the development of

F. Chevy (✉) · C. Salomon
Laboratoire Kastler Brossel, École Normale Supérieure,
CNRS, UPMC, 75005 Paris,
France
e-mail: frederic.chevy@lkb.ens.fr

C. Salomon
e-mail: salomon@lkb.ens.fr

new probes. For instance, the usual thermometry used in dilute Bose gases based on time of flight expansion could no longer be used because of the strongly hydrodynamic behavior of the gas [14, 15]. The transition from the normal phase to a superfluid state could not be observed as easily as in Bose gases and superfluidity was first produced for diatomic molecules formed for positive values of the scattering length [16–19]. In a strongly interacting, spin balanced Fermi gas, the formation of the superfluid is accompanied only by minute changes of the density profile of the trapped sample [20]. The pair-projection method has been used to study the condensation of fermionic pairs by projection onto molecular states [21, 22]. A direct proof of superfluidity was beautifully given by the observation of vortex lattices produced by stirring the gas into rotation [23]. Collective excitation modes have also been a very useful probe of the system to identify deviations from mean-field predictions across the BEC–BCS crossover [24, 25]. Radio-frequency spectroscopy has also revealed the formation of pairs [20, 26] and provided information on the pairing gap. Momentum resolved radio-frequency (RF) spectroscopy has been used to measure the spectral function in the strongly interacting gas [27]. Bragg spectroscopy has probed the short-range pair correlation function in the strongly interacting regime [28] and checked the universality of Tan's relations [29] through measurements of the static structure factor in the BEC–BCS crossover. Tan's universal relations have also been checked by RF spectroscopy and measurement of the high momentum tail of the k distribution [28, 30].

The possibility to prepare imbalanced spin systems (polarized superfluid) has revealed the robustness of Cooper pairs to the mismatch of the Fermi surfaces and the Clogston–Chandrasekhar limit of superfluidity. Phase separation of the superfluid core and the polarized normal phase has been observed [31, 32] unveiling in the dilute normal phase Fermi polaron physics directly comparable with theoretical models [33, 34].

In this Chapter, we focus on the macroscopic probes of strongly interacting Fermi gases. These techniques give access to the thermodynamics of these systems, and allow in particular the determination of their equation of state. Recent progress has led to a detailed and quantitative comparison with advanced theoretical models. We show that these quantities have close connections with microscopic properties of the cloud, such as the momentum distribution or the low energy excitation spectrum.

This chapter is organized as follows. We first introduce the experimental scheme used to measure the equation of state of the gas in the Grand-Canonical Ensemble. We then focus on the zero temperature regime and show that this method reveals the Lee-Yang and Lee-Huang-Yang corrections. We then address the effect of spin imbalance and the robustness of the superfluid against spin polarizing fields. We show that the macroscopic thermodynamic properties of the spin imbalanced Fermi gas can be simply described from the properties of the Fermi-polaron. Finally, we describe the finite temperature phase diagram and discuss the Fermi Liquid nature of the normal phase. Considering the amount of theoretical work on the subject on the last three decades, it is impossible to refer accurately to all contributions. Additional information can be found in the other chapters of this book.

11.2 Thermodynamics of Strongly Interacting Fermi Gases

Thermodynamic properties of this gas in the crossover have been explored through specific heat, entropy, collective mode, sound velocity, critical velocity, and moment of inertia studies [19, 24, 35–41].In these measurements only quantities that are averaged over the inhomogeneous density in the trap have been derived making comparison with many-body theories developed for a uniform system often difficult. A further difficulty resides, as stated above, in the precise determination of the gas temperature, and in particular of the superfluid critical temperature. This has been solved by different means. A first solution uses spin imbalanced gases where the in-trap phase separation enabled a fit of the temperature on the wings of the Thomas-Fermi distribution of the majority spin component [20]. A second solution implemented in [42–44] uses as a thermometer a third species that is is thermal contact with, but minimally disturbs, the strongly interacting gas. Recently, a new probe for these ultracold Fermi gases has been introduced. It is based on the study of local density [45, 46] or spin fluctuations [47]. This probe was first validated on weakly interacting Fermi gases providing an independent measure of temperature. The spin fluctuations provide access to the gas magnetic susceptibility and pair formation, and are vastly reduced in the paired SF phase [47].

A particularly interesting case is achieved for resonant interaction, the so-called unitary limit where $1/a = 0$. In this situation the scattering length is irrelevant. As first pointed out in [48], the only energy scale is the Fermi energy E_F and distance scale the average inter particle distance k_F^{-1}. Thermodynamic properties of the gas such as entropy, energy, compressibility, and specific heat, are universal and depend only on the ratio μ/T where μ is the chemical potential and T the temperature. In particular, in the limit of very low temperature, the relation between μ and E_F should read:

$$\mu = \xi_s E_F, \tag{11.1}$$

where ξ_s is a pure number and the index s refers to the superfluid phase. Several measurements and theoretical predictions for this important parameter have been reported with increasing precision pointing, as we will see below, towards a value of 0.40(2). This universality is valid under the assumption that no short range parameter other than a is involved in the description of the interactions.

11.2.1 Thermodynamics in the Grand Canonical Ensemble and the Local Density Approximation

The thermodynamic equation of state (EoS) is a central quantity for describing the macroscopic properties of a system in thermal equilibrium. Thermodynamic potentials contain all global information over the system and we will see below that

expressing the EoS in the grand canonical ensemble enables a very simple connection with experimental quantities such as the in-trap position distribution.

In the local density approximation (LDA), one assumes the existence of a mesoscopic length ℓ, smaller than the size of the system, but larger than the interparticle distance, over which the system can be considered homogeneous and at thermodynamical equilibrium. Let us consider an imaginary box of size ℓ centered on a position r. According to the local equilibrium hypothesis, it is possible to define local intensive properties such as pressure, temperature or chemical potential. This box can exchange energy and atoms with the rest of the cloud which acts as a reservoir, suggesting that the grand canonical ensemble is the most suitable formalism to describe the properties of a trapped system.

The equilibrium state in the mesoscopic volume is given by the minimization of the grand-potential $\Omega(T, \mu, V) = E - TS - \sum_i \mu_i N_i$, where V is the volume, E the energy, S the entropy, and N_i the number of particles of species i. Differentiating this relation using well known thermodynamical identities

$$d\Omega = - SdT - PdV - \sum_i N_i d\mu_i \tag{11.2}$$

According to this identity, T, μ_i and V are the natural variables characterizing the grand-potential. Interestingly, among them, V is the only extensive quantity. Moreover, using the extensivity of the grand potential, we know that if the size of the system is multiplied by λ, Ω is scaled by the same factor. Using Euler's relation, it is then possible to show that

$$\Omega = V \frac{\partial \Omega}{\partial V}\bigg|_{\mu_i, T} = - PV. \tag{11.3}$$

In other words, the pressure is proportional to the grand-potential and minimizing Ω is equivalent with maximizing P. Another consequence is the celebrated Gibbs-Duhem relation that we obtain by plugging $\Omega = - PV$ into Eq. 11.2, that is

$$V dP = SdT + \sum_i N_i d\mu_i. \tag{11.4}$$

Let us now go back to the case of a trapped system and we define $U_\sigma(r)$ as the local potential trapping particles of spin σ. Locally, we can assume that the gas contained by the mesoscopic volume centered on r is homogeneous and its energy spectrum is simply shifted by $\sum_\sigma U_\sigma(r) N_\sigma$. In that case the grand canonical partition function is simply

$$\Xi = \sum_\alpha e^{-\beta(E_\alpha^0 - \sum_\sigma [(\mu_\sigma - U_\sigma(r)) N_{\sigma,\alpha}]}, \tag{11.5}$$

where the sum spans the eigenstates $|\alpha\rangle$ of the grand-canonical Hilbert space and E_α^0 is the spectrum of the untrapped system. Just like the energy, the chemical potential

of the system is simply shifted by the trapping potential, and using the identity $-PV = \Omega = -k_{\mathrm{B}} T \ln \Xi$, we can write the grand-potential as

$$P = P_{\mathrm{h}}(T, \mu_\sigma - U_\sigma(\boldsymbol{r})), \qquad (11.6)$$

where P_{h} is the pressure of the untrapped homogeneous system.

To calculate the density of spin σ particles, we use the Gibbs-Duhem identity $n_\sigma = (\partial P/\partial \mu_\sigma)_T$ thus yielding

$$n_\sigma(\boldsymbol{r}) = n_{\sigma,\mathrm{h}}(T, \mu_\sigma - U_\sigma(\boldsymbol{r})), \qquad (11.7)$$

with $n_{\sigma,\mathrm{h}} = (\partial P_{\mathrm{h}}/\partial \mu_\sigma)_T$. Knowing the EoS of the homogeneous system, this equation allows one to reconstruct the density profile of the trapped gas. This equation is usually written in a more transparent form by introducing $\mu_{\sigma,\mathrm{h}}(n_\sigma, T)$ as the chemical potential of a homogeneous untrapped system of density n_σ and temperature T. Inverting Eq. 11.7 thus yields the condition

$$\mu_\sigma = \mu_{\mathrm{h},\sigma}(n_\sigma(\boldsymbol{r}), T) + U_\sigma(\boldsymbol{r}), \qquad (11.8)$$

which can be interpreted as stating that the total chemical potential μ_σ is the sum of that of a homogeneous gas and the trapping potential. This approximation is known as the Local Density Approximation and its validity ranges from trapped Fermi gases [44, 49], as described here, to bosonic systems, mixtures, and optical lattices [50]. In the last case, it is at the origin of the now famous wedding cake structure characterizing Mott insulator phases, with a particularly simple EoS in the grand canonical ensemble [50].

11.2.2 Measuring the Local Pressure of a Trapped Fermi Gas

In situ absorption images are particularly well suited to accessing the local pressure of a harmonically trapped gas when assuming the LDA is valid. Let $\omega_x, \omega_y, \omega_z$ be the trap frequencies. Assume the absorption of a two component Fermi gas ($\sigma = 1, 2$) is imaged by a probe beam propagating along the y direction onto a CCD camera in the z, x plane. The two spin states are imaged independently by two successive short ($10\,\mu s$) pulses of resonant light. Let us introduce the doubly-integrated optical density:

$$\bar{n}_\sigma(z) = \int dx\, dy\, n(x, y, z), \qquad (11.9)$$

and

$$\mu_{\sigma z} = \mu_{\sigma z}^0 - \frac{1}{2} m \omega_z^2 z^2 \qquad (11.10)$$

Then, it was shown in [51–53] that the local pressure of the gas along the z axis is simply given by:

$$P(\mu_{1z}, \mu_{2z}, T) = \frac{m\omega_x \omega_y}{2\pi}(\bar{n}_1(z) + \bar{n}_2(z)) \qquad (11.11)$$

In contrast to the Abel transform method introduced first in [54] to derive an equation of state, the pressure along the z axis results from a double integration that considerably reduces technical noise. When the temperature T and the chemical potentials at the trap center μ_1^0, μ_2^0 are known, each abscissa z provides a realization of the equation of state $P(\mu_{1z}, \mu_{2z}, T)$. Thus a single image provides a large number of realizations of the EoS over the interval $[-\infty, \mu_1^0]$ and $[-\infty, \mu_2^0]$. Further averaging of successive images can be performed leading to a low noise equation of state of the homogeneous gas. Several methods can be employed to measure μ_1^0 and μ_2^0 and T and we refer the reader to [44] and [50] for further details. Many systematic errors can be compensated when using this method so that the overall accuracy (statistical + systematic) of the method currently reaches the 5% level. The method can also be generalized to anharmonic potentials. Quantitative comparisons with advanced theoretical models and numerical calculations developed for homogeneous gases can now readily be performed.

11.3 The Zero Temperature Phase Diagram

11.3.1 The BEC–BCS Crossover

We first study the low temperature equation of state of an unpolarized two component Fermi gas. In the weakly attractive limit (a small and negative), the system is described by the celebrated BCS theory that was introduced first by Bardeen, Cooper and Schrieffer to understand the microscopic mechanisms of superconductivity in metals [55]. This mean-field theory stipulates that superfuidity arises from the pairing of opposite-spin fermions into so-called Cooper pairs. In the early 80's an extension to the strongly attractive regime was proposed by Leggett [56], Nozières and Schmitt-Rink [57]. In this BEC–BCS crossover theory, they suggested that by changing the strength of interactions, it would be possible to connect the BCS regime to the strongly attractive limit where the Cooper pairs turn into tightly bound dimers and the system behaves at low temperature as a Bose-Einstein Condensate of molecules.

Since it is difficult to change the interaction strength between electrons in metals, this theory remained untested for twenty years, despite a revival of interest in the 90's with the study of high critical temperature superconductors which are thought to operate in an intermediate regime of interaction similar to that of the BEC–BCS crossover.

The equation of state of an unpolarized, two component Fermi gas is presented in Fig. 11.1 (taken from [49]). Dimensionally, the grand canonical equation of state
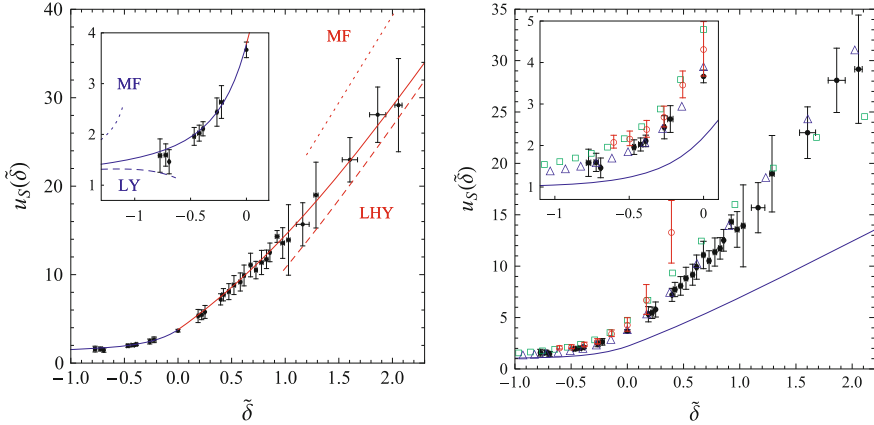
Fig. 11.1 Equation of state of a $T = 0$ Fermi gas in the BEC–BCS crossover, data: *black circles*; *blue and red solid lines*: Padé expansion. *Left* Comparison with analytical expansions: MF: mean-field, LY: Lee-Yang, LHY: Lee-Huang-Yang. *Right* comparison with advanced many-body calculations: quantum Monte-Carlo (*red open circles*) [7]; Diagrammatic (*green open square*) [8]; Nozières-Schmitt-Rink (*blue triangle*) [9]; mean-field theory (*blue solid line*)

of the gas can be parameterized by a single universal function u_S defined by

$$P(\mu) = 2P_F^0(\mu)u_S(\tilde{\delta}), \tag{11.12}$$

where

$$P_F^0(\mu) = \frac{1}{15\pi^2}\left(\frac{2m}{\hbar^2}\right)^{3/2}\mu^{5/2} \tag{11.13}$$

is the pressure of a zero temperature, single component, ideal Fermi gas of chemical potential μ given by $\tilde{\delta} = \hbar/\sqrt{2m\tilde{\mu}a}$ and $\tilde{\mu} = \mu + E_b$ is the chemical potential corrected by the binding energy of the dimers,[1] when they exist (*i.e.* for $a > 0$ in which case $E_b = \hbar^2/2ma^2$). $\tilde{\delta}$ measures the strength of the interactions, and generalizes $1/k_F a$ in the grand canonical ensemble. In particular, the two quantities are equal for an ideal Fermi gas at zero temperature for which $\tilde{\mu} = E_F$, and $\tilde{\delta} = 1/k_F a$.

The dimensionless function u_S was measured using the experimental scheme presented above and is displayed in Fig. 11.1, where it is compared with advanced theoretical calculations. As predicted, the transition between the two limiting cases is smooth and confirms the BEC–BCS crossover scenario. We now discuss its different limits.

Let us start with the weakly attractive BCS regime where a is small and negative. In this regime, the condensation energy (defined as the difference between the energies of the normal and superfluid phases) is proportional to Δ^2, where Δ is the gap

---

[1] This guarantees that $\tilde{\mu}$ stays positive, by contrast with μ which becomes negative in the BEC limit due to the large contribution of the binding energy.

which vanishes exponentially in the BCS limit. As a consequence, the correction
to the energy of the superfluid is essentially the same as that of the normal gas and
can be obtained from a perturbative expansion in the weakly interacting limit [58].
The expansion to second order of the Fermi gas was obtained for the first time by
Lee and Yang [59] and was extended to third order in Baker [60]. At this level of
approximation, the energy E of an ensemble of $N = N_\uparrow + N_\downarrow$ spin 1/2 particles in a
box of volume V is given by

$$\frac{E}{N} = \frac{3}{5} E_F \left[1 + \frac{10}{9\pi} k_F a + \frac{4}{21\pi^2} (11 - 2 \ln 2) (k_F a)^2 + 0.03(k_F a)^3 + ... \right],$$
(11.14)

where $k_F = (3\pi^2 n)^{1/3}$ is the Fermi wave-vector, $n = N/V$ is the total particle density
and $E_F = \hbar^2 k_F^2 / 2m$ is the Fermi energy. In the far BEC limit where the size of the
dimers becomes small compared to the interparticle distance, the gas behaves as a
Bose gas of point-like particles. The equation of state of a gas of weakly interacting
bosons was first obtained by Lee, Huang and Yang who demonstrated that up to
second order in the boson-boson scattering length a_{bb}, the energy E of an ensemble
of N_b repulsive bosons of mass m_b is [61]

$$\frac{E}{N_b} = \frac{g_{bb} n_b}{2} \left(1 + \frac{128}{15\sqrt{\pi}} \sqrt{n_b a_{bb}^3} + ... \right),$$
(11.15)

with $n_b = N_b/V$ the density of bosons and $g_{bb} = 4\pi \hbar^2 a_{bb}/m_b$. Beyond the Lee-
Huang-Yang correction, the equation of state is no longer universal and depends
on the microscopic details of the potential, in particular the characterization of
the 3-body interactions [62, 63]. Using diagrammatic techniques, one can show
that the equation of state of the fermionic superfluid in the BEC limit is given by
Eq. 11.15 [64] with the correct value of the dimer-dimer scattering length $a_{bb} \sim 0.6a$
[12, 65], $N_b = N/2$ and the mass $m_b = 2m$. This result is confirmed by analysis of
the equation state obtained using Fixed Node Monte Carlo simulations [6].

As displayed in Fig. 11.1, the two limiting cases corresponding to Eq. 11.14 and
11.15 can be recast in the grand canonical ensemble and compared to experimental
data obtained by the scheme presented above. In the two cases, we find that the
mean-field corrections are not sufficient to interpret the data and the Lee-Yang and
Lee-Huang-Yang corrections are necessary to recover agreement between theory and
experiment.

The third region of interest is unitarity where $|a| = \infty$, and hence $\tilde\delta = 0$. In this
case, Eq. 11.12 takes a remarkably simple form, since we have

$$P(\mu) = \frac{P_F^0(\mu)}{\xi_S^{3/2}},$$
(11.16)

where $\xi_S^{-3/2} = u_S(0)$ is a numerical constant.[2] We see that the equation of state of
the unitary gas is thus very simple, since within a numerical factor, it is identical

---

[2] The definition is chosen so as to write the chemical potential as $\mu = \xi_s E_F$ as discussed above.

to that of an ideal gas. Despite the high microscopic complexity of the unitary gas, the value of ξ_S is thus the only ingredient necessary to the understanding of its macroscopic behavior. As a consequence, its precise determination has attracted an intense theoretical [6, 66–68] and experimental [14, 19, 31, 36, 49, 69] effort, and its accepted value is now $\xi_S = 0.40(2)$.

We conclude our discussion of the BEC–BCS crossover at zero temperature by noting that, although the equation of state presented in Fig. 11.1 gives information on the macroscopic behavior of the system, it can be related to microscopic properties of the system using an intriguing relationship between the energy of the gas and its momentum distribution as uncovered by S. Tan [70]. Indeed, in the case of a contact potential, the momentum distribution n_k of the gas scales at large momenta like

$$n_{\boldsymbol{k}} \sim \frac{C}{k^4}. \tag{11.17}$$

S. Tan demonstrated that C could be related to several macroscopic quantities of the system, with in particular

$$C = -\frac{4\pi m}{\hbar^2} \frac{\mathrm{d}E}{\mathrm{d}(1/a)}. \tag{11.18}$$

The knowledge of the thermodynamic equation of state thus gives access to some microscopic features of the equation of state of the system which can be compared to experiments measuring directly the momentum distribution or the static structure factor [28, 30]. The figure presents several determinations of the contact coefficient in the limit of zero temperature in the crossover. This relationship between macroscopic and microscopic properties was also confirmed by the analysis of photoassociation measurements [71, 72] (Fig. 11.2).

11.3.2 Spin Imbalanced Gases and the Clogston–Chandrasekhar Limit

The most salient feature of fermionic superfluidity is the existence of a pairing gap which is responsible for most properties of these systems. In principle, its experimental determination requires using microscopic probes (such as tunneling microscopes in solid state devices or radio-frequency spectroscopy with cold atoms [26, 73]). However, Clogston and Chandrasekhar pointed out a subtle relationship between the gap and the spin susceptibility of the system [74, 75]. Indeed, in the presence of a chemical potential imbalance $h = (\mu_\uparrow - \mu_\downarrow)/2 > 0$, it is in principle more favorable to spin flip down atoms into spin up state. However, this also breaks a Cooper pair and thus costs an energy Δ corresponding to the pairing gap. A careful thermodynamic study shows that, as a consequence, a spin imbalanced superfluid remains a local energy minimum at low temperature as long as $|h|$ stays smaller than Δ (see section 9.1). Beyond that limit, it is no longer locally stable and the ground state must
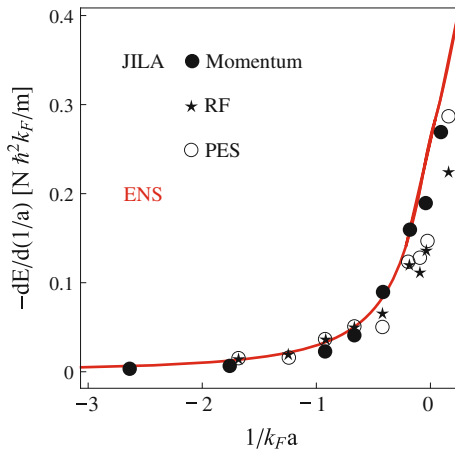
Fig. 11.2 Comparison between thermodynamic and microscopic determination of Tan's contact in the limit of zero temperature. The JILA data include momentum distribution, radiofrequency (RF) spectroscopy and photoemission spectroscopy (PES) and are measured over the whole trapped sample. The ENS data is taken from the homogeneous gas equation of state (from Fig. 11.1) and averaged over the harmonic trap following the approach of [72]

become spin-polarized. This phase transition can be illustrated in the far BEC limit where the polarized system behaves like a Bose-Fermi mixtures of nearly point-like dimers and unpaired atoms, as demonstrated in [76, 77] and observed experimentally in [78]. Assuming $N_\uparrow > N_\downarrow$, we can form $N_b = N_\downarrow$ bosonic dimers, leaving thus $N_a = N_\uparrow - N_\downarrow$ unpaired atoms. In the far BEC limit where interactions can be treated within mean-field approximation, the equation of state of the corresponding Bose-Fermi mixture is [79]

$$\frac{E}{V} = -n_b \frac{\hbar^2}{ma^2} + \frac{g_{bb}n_b^2}{2} + g_{ab}n_a n_b + \frac{3n_a}{5}E_{Fa}, \quad (11.19)$$

where V is the volume of the system, $n_\alpha = N_\alpha/V$ is the density of particles $\alpha \in \{a, b\}$, E_{Fa} is the Fermi energy of the remaining atoms and g_{ab} is the coupling constant describing s-wave atom-dimer interactions, with a scattering length $a_{ab} = 1.2a$ [80]. As discussed already, it is natural to describe the Clogston–Chandrasekhar limit in the grand canonical ensemble by introducing two chemical potentials $\mu_\uparrow$ and $\mu_\downarrow$ as well as the grand potential $\Omega = E - \sum_\sigma \mu_\sigma N_\sigma$. In terms of the chemical potential imbalance h and $\bar{\mu} = (\mu_\uparrow + \mu_\downarrow)/2$, the grand potential is thus given by

$$\frac{\Omega}{V} = -n_b \frac{\hbar^2}{ma^2} + \frac{g_{bb}n_b^2}{2} + g_{ab}n_a n_b + \frac{3n_a}{5}E_{Fa} - 2\bar{\mu}n_b - (\bar{\mu} + h)n_a. \quad (11.20)$$

At given chemical potentials $(\bar{\mu}, h)$, the equilibrium configuration of the system is given by the pair (n_a, n_b) minimizing Ω. Following the aforementioned argument,

we first discuss the *local* stability of the unpolarized superfluid, corresponding to $n_a = 0$. A first equilibrium condition is given by $\partial_{n_b} \Omega = 0$, yielding

$$\bar{\mu} = -\frac{\hbar^2}{2ma^2} + \frac{g_{bb}n_b}{2}, \qquad (11.21)$$

which sets the relation between the chemical potential $\bar{\mu}$ and the density of molecules in an unpolarized system.

Let us now study the stability of the pairing against spin polarization by considering the addition of a small amount of unpaired atoms in the system. In this case, the energy can be expanded as

$$\frac{\Omega}{V}(n_a, n_b) = \frac{\Omega}{V}(0, n_b) - (h + \bar{\mu} - g_{ab}n_b)n_a + \frac{3n_a}{5}E_{Fa} + \dots \qquad (11.22)$$

The coefficient between parenthesis can be written as $h - \Delta$, where by definition $2\Delta = \hbar^2/ma^2 + 2g_{ab}n_b - g_{bb}n_b$ is the energy required to break a dimer including the variation of mean-field energy due to the different scattering lengths associated with atom-dimer and dimer-dimer interactions. As a consequence, we see first that, as described in the Appendix Spin Susceptibility of a Gapped System at Zero Temperature, the molecular BEC is locally stable against an external magnetic field as long as $h \leq \Delta$. Moreover, close to threshold, the polarization of the sample obtained by looking for the minimum of $\Omega(n_a, n_b)$ is given by the asymptotic behavior $n_a \sim (h - \Delta)^{3/2}$ and confirms the second-order nature of the transition.

Up to now, we have only discussed the local stability of the paired superfluid. As a matter of fact this second-order transition between the unpolarized and polarized superfluids occurring at $h = \Delta$ exists only in the far-BEC limit and turns into a first order transition somewhere in the BEC–BCS crossover. Indeed, following Clogston and Chandrasekhar's original argument, we study now the *global* stability of the unpolarized superfluid in the far *BCS* limit. In this regime, the energy difference between the superfluid and normal phases is given by $E_{SF} = E_0 - N_0 \Delta^2/2$, with N_0 the density of state at the Fermi level, while the energy of a polarized normal gas is $E = E_0 - N_0 h^2$. The comparison of the two formulas shows that for $h > h'_c = \Delta/\sqrt{2}$, the superfluid is no longer the absolute ground state of the system. Since $h'_c < \Delta$, the unpolarized state is nevertheless still a local minimum of the energy landscape.

To confirm the existence of this transition between the first and second order Clogston–Chandrasekhar limits and locate its position in the BEC–BCS crossover, we turn back to the mean-field BEC equation of state 11.19, and we compare the grand-potentials of the paired superfluid ($n_a = 0$) and of the ideal Fermi gas ($n_b = 0$) for $h = \Delta = g_{ab}n_b - \bar{\mu}$. As for the molecular condensate, the atom density of the non interacting Fermi gas is given by the condition $\partial_{n_a}\Omega = 0$ for $n_b = 0$, and hence $E_{Fa} = \bar{\mu} + h$. Using this condition, we see that the energy difference between the superfluid (Ω_{SF}) and the normal phase (Ω_F^0) is given by

$$\left(\frac{\Omega_{SF}}{V} - \frac{\Omega_{NIFG}}{V}\right)_{h=\Delta} = -\frac{g_{bb}n_b^2}{2} + \frac{1}{15\pi^2}\left(\frac{2m}{\hbar^2}\right)^{3/2}(g_{ab}n_b)^{5/2}, \qquad (11.23)$$
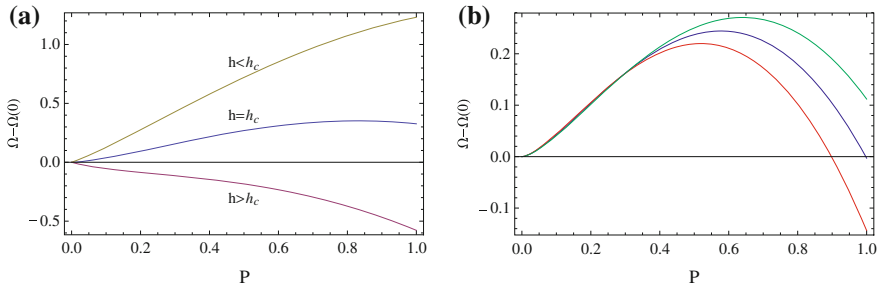
Fig. 11.3 Dependence of the grand-potential with spin population imbalance $P = M/N$, with $M = N_\uparrow - N_\downarrow$ and $N = N_\uparrow + N_\downarrow$. **a** For $1/k_F a > (1/k_F a)_c$ the Clogston–Chandrasekhar limit corresponds to a second order transition where the paired superfluid becomes *locally* unstable for $h > h_c = \Delta$. **b** Grand potential as a function of polarisation at $h = h_c$ for different values of $1/k_F a$. From *top to bottom*, $1/k_F a > (1/k_F a)_c$, $1/k_F a = (1/k_F a)_c$ and $1/k_F a < (1/k_F a)_c$. The transition becomes first order and the CC-limit located at $h'_c \leq \Delta$ is associated with a phase transition between a fully paired superfluid (P=0) and a fully polarized ideal gas (P=1)

which is negative as long as

$$1/k_F a > \left(\frac{1}{k_F a}\right)_c = \left[\frac{36 a_{ab}^5}{25\pi^3 a^3 a_{bb}^2}\right]^{1/3} \simeq 0.66, \qquad (11.24)$$

where k_F is the Fermi wave-vector in the unpolarized superfluid. From this argument, we see that in the strongly interacting regime, although the paired superfluid is still a local energetic minimum at $h = \Delta$, it is no longer the absolute minimum of the Hilbert space. As a consequence, the critical field is lowered at a value h_c smaller than Δ, and the transition becomes first order. The existence of this transition between first and second order is confirmed by a more accurate determination using Fixed Node Monte-Carlo simulations [76]. This calculation locates the transition at $(1/k_F a)_c = 0.53$, which, using the equation of state of the unpolarized supefluid corresponds to $\delta = \hbar/\sqrt{2m\bar{\mu}} a = 1.4$ in the grand canonical ensemble.

In the regime where the transition is first order, the nature of the polarized phase is still debated. Based on general argument by Kohn and Luttinger [81], the system should stay superfluid at zero temperature. Several exotic superfluid mechanisms were proposed to described the weakly interacting polarized superfluid, from inhomogeneous Fulde-Ferrell-Larkin and Ovshinikov phases [82, 83] to Sarma phases [84] or p-wave superfluids [85] (Fig. 11.3).

To test this prediction with solid state systems, one might suggest to spin polarize electrons in superconductors using an external magnetic field in which case Zeeman shifts would play the role of the chemical potential imbalance. However, magnetic field also acts on the center of mass motion of the electrons. Unfortunately, the resulting electric current expels the magnetic field out of the superconductors (the Meissner Effect) and thus prevents spin polarization. As a consequence, signature of the Clogston–Chandrasekhar limit could only be observed in exotic heavy fermion
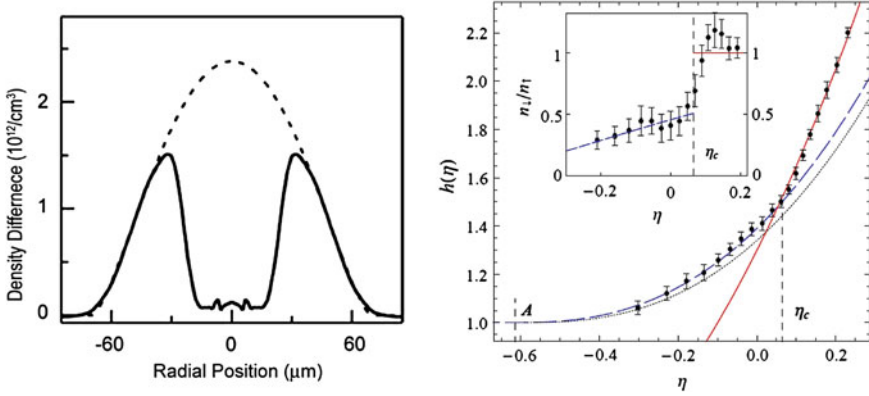
Fig. 11.4 *Left* Density profile $n_\uparrow - n_\downarrow$ measured using inverse Abel transform techniques at MIT (Fig. from [90]). Despite a spin population imbalance, the center of the cloud stays fully paired with $n_\uparrow = n_\downarrow$. *Right* equation of state of a spin imbalanced Fermi gas measured using the doubly integrated density profile (data from [44]). $h = P/P_F^0(\mu_\uparrow)$ is the pressure normalized to the zero temperature ideal gas. $\eta = \mu_\downarrow/\mu_\uparrow$ is the chemical potential imbalance. *Full line* superfluid phase Eq. 11.26; *Dashed line* Normal Fermi mixture Eq. 11.35; *Dotted line* Landau Pomeranchuck equation of state Eq. 11.36. *Inset* density ratio $x = n_\downarrow/n_\uparrow$ deduced from the Gibbs-Duhem relation $n_\sigma = \partial_{\mu_\sigma} P$. The density jump occuring at $\mu_\downarrow/\mu_\uparrow = \eta_c \simeq 0.06$ shows that at unitarity the Clogston–Chandrasekhar limit corresponds to a first order transition between a polarized an an unpolarized phase. $\eta = A \simeq -0.6$ marks the disappearance of the last spin down atom

materials, like UPt$_3$ where the large electron effective mass reduces the effect of the external magnetic field on their motion [86], in aluminium films of thickness smaller than the coherence length [87] or by proximity effects at the frontier with ferromagnetic compounds [88].

In cold atoms, the Clogston–Chandrasekhar limit of fermionic superfluidity was observed experimentally by the groups of Rice and MIT [31, 89] which demonstrated that in a trap the cloud was organized in shells, with at center a superfluid core with equal spin densities, surrounded by a spin imbalanced rim (see Fig. 11.4a for a density profile obtained at MIT using an inverse Abel transform [90]). From these density profiles, it is possible to extract the equation of state of a spin imbalanced Fermi case. In Fig. 11.4, we present the corresponding dimensionless equation of state at unitarity obtained at ENS using this method and presented in ref. [44]. In this regime, the equation of state is rather simple. Indeed, since the superfluid cannot be polarized, it equation of state satisfies the constraint $n_\uparrow = n_\downarrow$ or, using the Gibbs-Duhem relation $n_\sigma = \partial_{\mu_\sigma} P$,

$$\frac{\partial P}{\partial \mu_\uparrow} = \frac{\partial P}{\partial \mu_\downarrow}. \tag{11.25}$$

According to this condition, P is thus a function of $\mu = (\mu_\uparrow + \mu_\downarrow)/2$ only [34]. In the particular case $\mu_\uparrow = \mu_\downarrow$, we should recover the spin balanced unitary equation

of state (11.16), yielding thus

$$P(\mu_\uparrow, \mu_\downarrow) = \frac{1}{15\pi^2} \left(\frac{m}{\xi \hbar^2} \right)^{3/2} \left(\mu_\uparrow + \mu_\downarrow \right)^{5/2}, \qquad (11.26)$$

which is represented in Fig. 11.4 (solid red line) and fits the experimental data down to $\eta_c \sim 0.06$. This point marks the Clogston–Chandrasekhar limit. Indeed, using the experimental equation of state, one can calculate the density ratio $n_\downarrow / n_\downarrow$: above η_c, the two spin densities are equal, showing that, as expected, the fully paired superfluid is stabilized by the pairing gap. At $\eta = \eta_c$, the density varies abruptly (See inset of Fig. 11.9), which indicates the presence of the first order transition mentioned above that we locate here at $h_c \sim 0.9 \bar{\mu}$.

   As discussed previously, the intermediate phase at zero temperature is expected to be a polarized superfluid. However, vortex nucleation experiments indicate that the imbalanced phase is normal [89] and suggest that the critical temperature of these exotic superfluids is probably smaller than the one currently achieved experimentally ($T/T_F \lesssim 0.05$). For a review of imbalanced gases in cold atomic systems, see [91, 92].

11.4 Beyond the Clogston–Chandrasekhar Limit

As we have seen in the previous section, an attractive Fermi gas starts to polarize only when the spin polarizing field h becomes larger than a critical value h_c. In this section, we discuss the phase diagram of the system beyond the Clogston–Chandrasekhar limit. This topic is very vast and is not yet fully understood. As a consequence, the determination of the phase diagram of a zero temperature Fermi gas at zero temperature has triggered a heap of theoretical works based on various approximation schemes, from general qualitative considerations on the topology of the phase diagram [93] to more quantitative mean-field techniques [94–96] and diagrammatic Monte-Carlo simulations [76]. We will not be able to address here all its aspects, and for additional details, we refer the reader to more comprehensive reviews such as [91, 92].

   We describe here the phase diagram in the grand canonical ensemble. In this description, the state of the system can be characterized by two dimensionless numbers $\tilde{h} = h/\mu_\uparrow$ and $\delta = \hbar/\sqrt{2m\mu_\uparrow} a$ describing respectively the chemical potential imbalance and the interaction strength. From the previous section, we know that for $h < h_c(\delta)$, the system is an unpolarized superfluid (SF$_0$). The behavior of h_c in the BEC and BCS limits are rather simple. Indeed, as we have seen earlier, in the BEC region of the phase diagram, the CC-limit is a second order transition taking place at $h_c = \Delta \sim \hbar^2/2ma^2$, yielding $\tilde{h}_c(\delta) \propto \delta^2$. Conversely, in the BCS sector, the gas polarizes through a first order transition taking place at $h_c = \Delta/\sqrt{2}$. Since in this limit the gap is exponentially small, $\tilde{h}_c$ vanishes. The transition from first order to

second order CC limit takes place at a point that Monte-Carlo simulations locate at $\delta = 1.4$.

11.4.1 The Impurity Problem and the Polaron/Molecule Transition

As stated earlier, for $\tilde{h} > \tilde{h}_c$, the gap no longer protects the superfluid against spin polarization. At very high "magnetic field", the system becomes fully polarized. We call $h_S(\delta)$ the corresponding value of the chemical potential imbalance at which the last spin down atom vanishes. By definition, the value of h_S can be obtained by the study of the chemical potential μ_p of a single spin down impurity immersed in an Fermi sea of spin-up particles. Indeed, since the majority atoms are only weakly perturbed by the presence of the impurity, the chemical potential of the majority satisfies $\mu_\uparrow = E_{F\uparrow}$, hence $\tilde{h}_S = (1 - A)/2$, with $A = \mu_p / E_{F\uparrow}$.

Let us start by the BCS limit. In this case the spin down atom dresses with particle/hole excitations of the surrounding Fermi sea. Its forms a quasi-particle called a Fermi polaron, in analogy with condensed matter where the polaron is an electron dressed by excitations of the crystal lattice.

The properties of the Fermi polaron were studied theoretically by Monte-Carlo simulations [97, 98] and a variational ansatz restricted to one [99, 100] and two [101] particle/hole pairs. These studies of the Fermi polaron have demonstrated that its dispersion relation in the limit of small momenta was very similar to that of a free particle with renormalized parameters [97, 98, 100]

$$\varepsilon_{k,\downarrow}(p) = \mu_p + \frac{\hbar^2 k^2}{2m^*} + \ldots \tag{11.27}$$

where m^* is the effective mass and μ_p corresponds to a "Hartree" term shifting the overall impurity spectrum. At unitarity, the values obtained by the various theoretical estimates are consistent with $A \simeq -0.61$ and agree with a study of the Fermi-polaron at MIT made by measuring the shift of radio-frequency resonances induced by the interaction with majority atoms [102]. As shown in Fig. 11.5, we see that this agreement can be extended to the BCS side of the BEC–BCS crossover. The effective mass can be probed experimentally by the study of the collective modes of the system [97]. Indeed, in the regime of strong polarizations, the Fermi polarons are independent from each other and evolve as free particles. From Eq. 11.27 the dynamics of the Fermi polaron in a trap can be described by the quasi-classical Hamiltonian

$$H(\boldsymbol{r}, \boldsymbol{p}) \sim A E_{F\uparrow}(\boldsymbol{r}) + \frac{p^2}{2m^*} + U_{\text{trap}}(\boldsymbol{r}), \tag{11.28}$$

where U_{trap} is the trapping potential and is supposed identical for the two internal states. In the local density approximation, and under the assumption that the spin
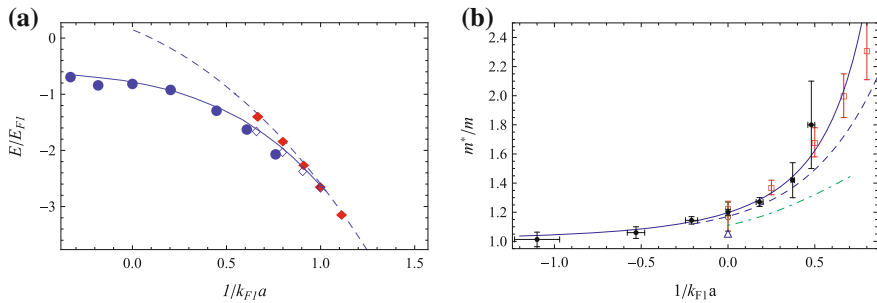
Fig. 11.5 a Chemical potential of an impurity immersed in a Fermi sea. *Circles* experimental measurements of Schirotzek et al. [102] compared to various theoretical predictions for the polaron and molecule energies. *Full* (*empty*) *diamonds* Monte-Carlo simulations of the molecule (polaron). *Full* (*dashed*) *line*, variational ansatz in the fermionic [99, 100] (bosonic [103–105]) sector. **b** Effective mass of the Fermi polaron in the BEC–BCS crossover measured at ENS (*black dots*). The *blue dashed line* is a calculation from [100], *red open squares* [98], *green dot-dashed line* [76], and *blue solid line* [104]. Measurements at unitarity through density profile analysis (*blue triangle* [54]) and collective modes study (*brown empty circle* [106]) are also displayed

imbalance is large enough that majority atoms are not affected by the minority, we can write that $E_{F\uparrow}(\boldsymbol{r}) = E_{F\uparrow}^0 - U_{\text{trap}}(\boldsymbol{r})$. We then see readily that the Hamiltonian (11.28) is equivalent to that of a particle of mass m^* trapped in a renormalized potential $U_{\text{trap}}^*(\boldsymbol{r}) = (1 - A)U_{\text{trap}}(\boldsymbol{r})$. Moreover, if the trapping potential is harmonic, then the effective frequency in the direction i is simply

$$\omega_i^* = \omega_i \sqrt{\frac{m}{m^*}(1 - A)}, \tag{11.29}$$

where ω_i is the "bare" oscillation frequency of a single particle in the potential U_{trap}. This relation shows that, combined with the knowledge of A, a measurement of the oscillation frequency of an impurity immersed in a Fermi sea gives access to the polaron effective mass. Such an experiment is presented in Nascimbène et al. [106] in the case of the lowest lying breathing mode, and gave at unitarity $m^* = 1.17(10)m$, in agreement with theoretical estimates.

This description of the impurity problem in terms of a fermionic quasi-particle fails in the BEC limit. Indeed, in the strongly attractive regime, the spin down atom forms a dimer by binding with a spin-up particle. When the scattering length is small and positive, the size of the molecule is vanishingly small and as in the BEC–BCS crossover, the dimer can be considered as a point-like bosonic object weakly interacting with the surrounding Fermi sea. Using approaches similar to those developed in the study of the Fermi polaron, it was possible to extract the properties of the molecule dressed by the particle/hole excitations of the Fermi sea [98, 103–105, 107]. These studies show that for a large range of values of the scattering length, the energy of the molecule is simply
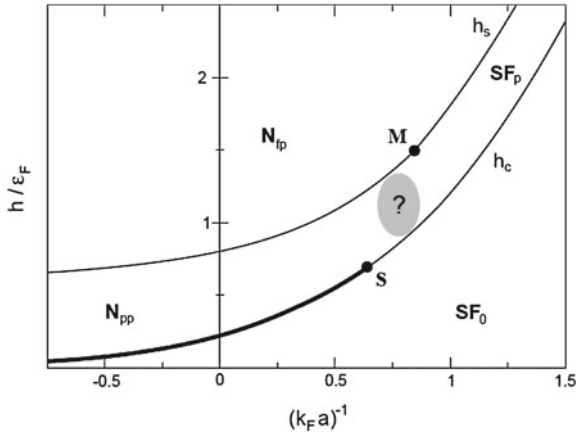
Fig. 11.6 Zero temperature phase diagram from [105]. When the spin polarizing field h is below h_c, the fully paired superfluid SF$_0$ is stable. For $h > h_c$ the gas starts to polarize. At point S, the fully paired/partially polarized transition turns from first order (for $1/k_F a \lesssim 0.5$ to second order (for $1/k_F a \gtrsim 0.5$. In the BCS limit the partially polarized phase N$_{PP}$ is a mixture of ideal gases of majority atoms and polarons. In the BEC limit, this phase can be described as a mixture between a Bose-Einstein condensate of molecules and a Fermi Sea of remaining atoms (SF$_P$). The nature of the frontier between the two phases is not yet clarified. Above the h_s line, the system becomes fully polarized (N$_{fp}$). Note that in M the partially polarized/fully polarized turns from first order in the BCS limit to second order in the BEC regime. Point M is also an endpoint of a finite temperature tricritical line

$$E = -\frac{\hbar^2}{ma^2} - E_{F\uparrow} + g_{ab}n_\uparrow, \tag{11.30}$$

where the first term is the binding energy of the free molecule, the second is the energy required to remove one spin up atom from the Fermi surface to create the dimer and the last one is the mean-field energy describing the interaction between the bosonic dimer and the Fermi sea.

The comparison between the energies of the polaron and the molecule shows that they cross at $1/k_{F\uparrow}a \simeq 0.91(2)$, marking the transition between the molecular and fermionic behavior of the impurity (Fig. 11.6).

11.4.2 The Polarized Superfluid

Between the h_c and h_s lines, the system is partially polarized. According to Kohn and Luttinger's argument [81], attractive interactions between fermions lead to the formation of a superfluid at zero temperature. As we have discussed earlier, in the BEC limit, the equation of state is the same as that of a Bose-Fermi mixture Eq. (11.19) [77] and we can use it to address the stability of the atom/dimer mixture. Thermodynamically, the gas is stable against demixion if the compressibility matrix $\partial_{N_\alpha N_\beta} E$

is positive. After some straightforward algebra, we see that the molecule can stay immersed inside the majority Fermi sea as long as

$$\frac{1}{k_{F\uparrow}a} \geq \frac{9}{4\pi}\left(\frac{a_{ab}^2}{aa_{bb}}\right) \simeq 1.7. \tag{11.31}$$

Above this threshold, the transition between the polarized superfluid and the fully polarized Fermi gas is second order, meaning that the density of molecules goes smoothly to zero across the critical line. Below this point, the transition becomes first order and the density of molecules drops from a finite value to zero on the critical line. Monte-Carlo simulations [76] suggest that this first order behavior disappears again at $1/k_{Fa} \simeq 0.73$, when it meets the polaron line. One consequence is that around the polaron/molecule transition, the single molecule immersed in the Fermi sea is actually unstable against demixion. The transition between the fermionic and bosonic behaviors of the impurity is thus driven by a thermodynamic instability and not the microscopic behavior.

Interestingly, RF studies at MIT show that the fermionic behavior of the impurity vanishes at $1/k_{F\uparrow}a = 0.74(1)$ [102], in good agreement with the value calculated for the position of the endpoint of the polaron line and confirming the collective nature of the polaron/molecule transition.

In the BCS region, the nature of the superfluid and the structure of the phase diagram is still debated, the reason being that the standard Cooper pairing mechanism requires equal densities of spin up and spin down particles. One can then imagine a pairing between same spin atoms, using interactions mediated by the opposite spin Fermi sea [85]. Other proposals suggest the formation of singlet pairs of zero momentum (Sarma phases [84]), or with non-zero momentum - the Fulde-Ferrell-Larkin and Ovchinikov state [82, 83].

11.5 The Normal Phase

Rotation experiments show that the partially polarized region of the cloud is normal around unitarity, suggesting that in practice the critical temperature towards superfluidity is lower than the critical temperature of the (balanced)unpolarized superfluid.

11.5.1 Landau's Fermi Liquid Theory

Fermi Liquid's Theory is a powerful phenomenological model allowing one to describe complex strongly correlated systems in terms of a nearly ideal gas of fermionic excitations [108]. As such, it provides a precise description of properties of systems such as liquid helium 3 or electron in metals above the critical temperature. In a nutshell, this model assumes that the excitations of an interacting system can be obtained from those of a non-interacting Fermi by adiabatically switching on the

interactions. In a non-interacting system, the elementary excitations are either particles (of momentum $k > k_{F\sigma}$) or holes (of momentum $k < k_{F\sigma}$), with $k_{F\sigma}^3 = 6\pi^2 n_\sigma$ and n_σ is the density of particles carrying a spin σ. Since particle number, spin, and linear momentum are conserved by interactions, the excitations of the interacting system will therefore also be characterized by particle (hole) excitations for $k > k_{F\sigma}$ ($k < k_{F\sigma}$), implying in particular that the Fermi level, separating the particle/hole excitations is located at the same value as for a non-interacting system.[3] At low temperatures, the system is weakly excited and the number $\delta N_{k,\sigma}$ of quasiparticles of momentum k and spin σ is small. The energy of the system can thus be expanded in n_k. As demonstrated below, a self-consistent description of the thermodynamic properties of the system requires one to work up to second order in excitation population, and we thus write to this approximation

$$E[n_k] = E_0 + \sum_{k,\sigma} \varepsilon_{k,\sigma} \delta N_{k,\sigma} + \frac{1}{2V} \sum_{kk'} f_{\sigma,\sigma'}(k, k') \delta N_{k,\sigma} \delta N_{k',\sigma'} + ..., \quad (11.32)$$

where E_0 is the energy of the normal ground state, ε_k the dispersion relation of the quasi-particles and the coefficients $f_{\sigma,\sigma'}(k, k')$ describe effective interactions between quasi-particles. Since particle/hole pairs can be arbitrarily created, the number of excitations is not conserved and the system must be described in the grand canonical ensemble. In this case, the grand potential takes the form

$$\Omega[n_k] = E - \sum_{\sigma} \mu_\sigma N_\sigma \quad (11.33)$$

$$= \Omega_0 + \sum_{k,\sigma} (\varepsilon_{k,\sigma} - \mu_\sigma) \delta N_{k,\sigma} + \frac{1}{2V} \sum_{kk'} f_{\sigma,\sigma'}(k, k') \delta N_{k,\sigma} \delta N_{k',\sigma'} + ... \quad (11.34)$$

This form justifies the necessity of pursuing the expansion up to second order. Indeed, at low temperature, excitations are located close to the Fermi level. As a consequence, the $(\varepsilon_k - \mu_\sigma)$ term is small, and the term linear in δN_k is actually of second order.

In general, the properties of the excitations depend on the number of spin up and spin down particles, and here we will study two extreme cases for which $N_\downarrow \ll N_\downarrow$ (strongly polarized limit) and $N_\uparrow = N_\downarrow$ (unpolarized limit).

11.5.2 The Gas of Polarons

The full understanding of the equation of state of the mixed normal phase requires the study of the behavior of an ensemble of Fermi polarons, and can be interpreted within the framework of the Fermi liquid formalism described above. At unitarity, where the

---

[3] This argument constitutes a heuristic demonstration of the Luttinger theorem [109].
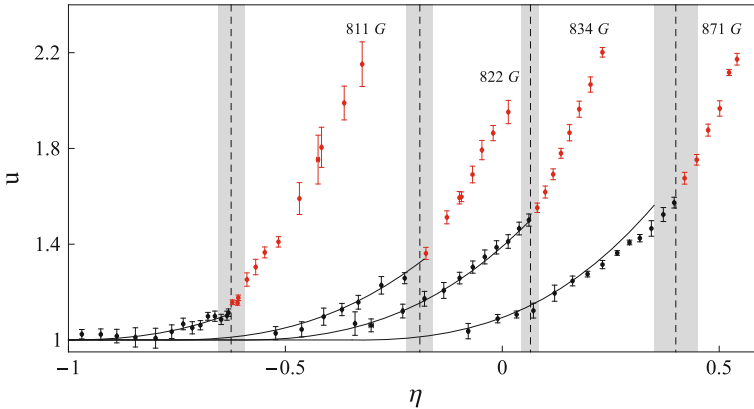
Fig. 11.7 Samples of Equation of State $u = P(\mu_\uparrow, \mu_\downarrow)/P_0(\mu_\uparrow)$ of a spin imbalanced Fermi gas as a function of the ratio $\eta = \frac{\mu_\downarrow}{\mu_\uparrow}$ for various values of the scattering length (Figure from [49]). Unitarity is at $834G$; lower field values correspond to positive a values, higher field values correspond to negative a values. The *gray area* marks the SF/normal phase transition. The *black solid lines* correspond to Eq. 11.35 without adjustable parameter

Fermi wavelength is the only length scale in the problem, the size of the particle-hole cloud shrouding the Fermi polaron is of the order of $1/k_{F\uparrow}$. In other words, if the distance between two impurities is bigger than $1/k_{F\uparrow}$, or equivalently if the ratio $n_\downarrow/n_\uparrow$ is small, then the Fermi polarons do not overlap and can be considered as independent point-like fermions obeying Fermi-Dirac statistics. This intuitive picture was confirmed first by the analysis of Fixed Node Monte Carlo simulations [97] and later on by an analytic expansion of the equation of state in the low impurity density limit [110]. The grand canonical equation of state of the system is in this case

$$P(\mu_\uparrow, \mu_\downarrow) = \frac{1}{15\pi^2} \left[\left(\frac{m}{\hbar^2}\right)^{3/2} \mu_\uparrow^{5/2} + \left(\frac{m^*}{\hbar^2}\right)^{3/2} (\mu_\uparrow - \mu_p)^{5/2} \right], \quad (11.35)$$

where, in the spirit of Fermi Liquid Theory, the pressure of the gas is the sum of the pressures of ideal gases of spin up and down particles, the former being expressed in terms of the renormalized physical quantities m^* and μ_p. This equation of state was confirmed experimentally in [49] using the values of A and m^* calculated from the different theoretical approaches described above, as seen in Fig. 11.4b at unitarity and Fig. 11.7 in the BEC–BCS crossover.

Interestingly, the equation of state (11.35) can be recast in the canonical form $E(n_\uparrow, n_\downarrow)$ as a Landau-Pomeranchuk functional [97]

$$E(N_\uparrow, N_\downarrow) = \frac{3}{5} N_\uparrow E_{F\uparrow} \left(1 + \frac{5A}{3} x + \frac{m}{m^*} x^{5/3} + F x^2 \right), \quad (11.36)$$

with $x = N_\downarrow/N_\uparrow$ and $A = \frac{\mu_p}{E_{F\uparrow}}$ as defined above. The first three terms describe an ideal mixture of non-interacting fermions, while the last one can be interpreted as

an effective interaction between polarons. In [110], it is shown that, using Eq. 11.36, the interaction parameter F is simply given by

$$F = \frac{5}{9} \left(\frac{d\mu_p}{d\mu_\uparrow} \right)^2, \tag{11.37}$$

a relationship that can also be derived from a direct Fermi-liquid analysis of the problem [111] and that was confirmed by comparison with Monte-Carlo simulations [112].

We can reinterpret these results in the language of the Fermi liquid [113, 114]. Indeed, in the case $\delta N_{\downarrow,k} = 0$, we simply recover an ideal gas of majority atoms, for which $\varepsilon_{k,\uparrow} = \hbar^2 k^2 / 2m$. Conversely, the dispersion relation of the spin down particle can be obtained by adding a single spin down impurity, in which case $\varepsilon_{k\downarrow}$ is simply given by the polaron dispersion relation (11.27).

Thanks to Eq. 11.36, it is possible to determine the interaction parameters of the Fermi liquid models (the f coefficients). First, we see that, as aforementioned, for x = 0, we have an ideal gas of spin up particles, meaning an absence of interactions between them and implying $f_{\uparrow\uparrow} = 0$. For the other interaction parameters, we make use of the fact that k' (the momentum of the minority) is small, and k (the momentum of the majority excitations) remains close to the Fermi level. Using rotational invariance, we see that, at leading order, the $f_{\sigma\sigma'}$ are actually constant, and we can thus simplify Fermi liquid formula (11.32) as

$$E[n_k] = E_0(N_\uparrow) + \sum_{k,\sigma} \varepsilon_{k,\sigma} \delta N_{k,\sigma} + \frac{1}{2V} \sum_{\sigma,\sigma'} f_{\sigma,\sigma'}^0 \delta N_\sigma \delta N_{\sigma'} + ..., \tag{11.38}$$

where $E_0(N_\uparrow) = 3N_\uparrow E_{F\uparrow}/5$ is the energy of an ideal gas of spin up particles, the $f_{\sigma\sigma'}^0$ coefficients depend on spin only and $\delta N_\sigma = \sum_k \delta N_{k,\sigma}$ is the variation of the spin σ atom number.[4] Let us consider first a situation where we add polarons without adding majority atoms. In this case, we have $\delta N_\uparrow = 0$ and we recover the Landau-Pomeranchuk equation of state, with

$$f_{\downarrow\downarrow}^0 = \frac{6F}{5} \left(\frac{E_{F\uparrow}}{n_\uparrow} \right). \tag{11.39}$$

Finally, we determine the crossed term by considering a variation of the majority atom number, without perturbing the minority distribution. By considering the equilibrium configuration containing $N_\uparrow + \delta N_\uparrow$, we can then write on the one hand that

$$E = E_0(N_\uparrow + \delta N_\uparrow) + \sum_k \varepsilon_{k\downarrow}(N_\uparrow + \delta N_\uparrow)\delta N_{k,\downarrow} + \frac{f_{\downarrow\downarrow}^0}{2V} \delta N_\downarrow^2. \tag{11.40}$$

---

[4] Since we start the expansion from $N_\downarrow = 0$, $\delta N_\downarrow$ is actually the number of minority atoms.

On the other hand, one can obtain the same situation starting from a system containing $N_\downarrow$ and adding $\delta N_\uparrow$ particle excitations, which in the second case would yield

$$E = E_0(N_\uparrow) + \sum_{\mathbf{k}_1 \sigma} \varepsilon_{\mathbf{k}\sigma}(N_\uparrow) \delta N_{\mathbf{k}\sigma} + \frac{1}{2v} \sum_{\sigma \sigma'} f^0_{\sigma \sigma'} \delta N_\sigma N'_\sigma \qquad (11.41)$$

By definition, Eq. 11.40 and 11.41 must give the same answer up to second order in excitation number. Focusing on the cross terms, we see that we have within this approximation

$$\sum_{\mathbf{k}} \frac{\partial \varepsilon_{\mathbf{k},\downarrow}}{\partial N_\uparrow} \delta N_{\mathbf{k},\downarrow} = \frac{f^0_{\uparrow\downarrow}}{V} \delta N_\downarrow. \qquad (11.42)$$

The characteristic momentum k of the impurities is fixed by the Fermi wavevector $k_{F\downarrow}$ which vanishes in the limit of small impurity densities. This implies that to leading order in spin down excitation number, one can replace $\varepsilon_{\mathbf{k},\downarrow}$ by its zero momentum value μ_p, hence

$$f^0_{\uparrow\downarrow} = \frac{\partial \mu_p}{\partial n_\uparrow}. \qquad (11.43)$$

Beyond providing an intuitive microscopic justification of the equation of state (11.35), the Fermi-Liquid model gives access to some of the out of equilibrium properties of the system. For instance, in the case of ^{3}He, it was used originally to predict the temperature dependence of thermal conductivity or viscosity in the normal phase [115]. In ultra cold fermions, it can be used to study the damping of excitations, such as Fermi polarons [113], or also to address recent measurements of the viscosity of a strongly interacting Fermi gas performed at Duke University [116].

11.5.3 The Fermi Liquid in the Unpolarized Limit

Let us consider now the case of a spin balanced system with $N_\uparrow = N_\downarrow$ which constitutes the usual framework of the Fermi liquid theory.

Compared to the previous paragraph, spin up and spin down particles have now a symmetric behaviour, and in particular both possess a well defined Fermi surface at $k = k_F$.

In the absence of an excitation gap, the particle and hole dispersion branches merge at $k = k_F$, and for $k \sim k_F$ the dispersion relation can be expanded as

$$\varepsilon_{\mathbf{k},\sigma} = \varepsilon_{k_F} + \frac{\hbar k_F (k - k_F)}{m^*} + ...,$$

where m^* is called the *effective mass* of the quasi-particle, defined in analogy with the dispersion relation of a free particle. Similarly to the strongly imbalanced

situation, one can expand the interaction parameters around the Fermi surface. Using again the fact that at low temperature excitations remain close to the Fermi surface, one can make the assumption $|\mathbf{k}| = |\mathbf{k}'| = k_F$, in which case, $f_{\sigma,\sigma'}(\mathbf{k}, \mathbf{k}')$ depends only on the angle θ between $\mathbf{k}$ and $\mathbf{k}'$ and can be expanded as

$$f_{\sigma\sigma'}(\mathbf{k}\mathbf{k}') = \frac{1}{2N_F} \sum_{\ell=0}^{\infty} \left(F_\ell^s + \sigma\sigma' F_\ell^a \right) P_\ell(\cos\theta), \tag{11.44}$$

where P_ℓ is a Legendre polynomial, N_F is the density of states at the Fermi level, $\sigma\sigma' = 1$ for parallel spin and -1 for anti-parallel spins.

As aforementioned, at low temperature, the system is weakly perturbed and a small number of quasi-particles are excited. In this limit, the population of each mode $(\mathbf{k}, \sigma)$ is given by the Fermi-Dirac distribution and leads to the following macroscopic properties[5]:

1. The specific heat C_V varies linearly with temperature and $C_V/C_V^0 = m^*/m$, where C_V^0 is the specific heat of the ideal gas.
2. The compressibility κ_T of the system is finite at $T = 0$, with

$$\kappa_T = \kappa_T^0 \frac{m^*/m}{1 + F_0^s}, \tag{11.45}$$

   where κ_T^0 is the compressibility of an ideal gas.
3. The magnetic susceptibility χ is finite at zero temperature, with

$$\chi = \chi_0 \frac{m^*/m}{1 + F_0^a}, \tag{11.46}$$

   where as above χ_0 is the spin susceptibility of an ideal Fermi gas.

As we have seen at the beginning of the chapter, the grand canonical ensemble provides a natural description of trapped gases. In this framework, the three macroscopic properties given above translate into the following equation of state at low temperature and weak chemical potential imbalance (see Appendix Fermi Liquid Theory in the Grand Canonical Ensemble)

$$P = P_0(\bar{\mu}) + \frac{\chi h^2}{2} + \frac{\gamma T^2}{2}, \tag{11.47}$$

and is thus quadratic in chemical potential imbalance and temperature. We recall that $\bar{\mu} = (\mu_\uparrow + \mu_\downarrow)/2$.

At unitarity, dimensional analysis yields an even simpler form since one can parameterize Eq. 11.46 using universal dimensionless numbers generalizing ξ_S. We can indeed write

---

[5] As a comparison, for an ideal Boltzmann gas of distinguishable particles, the specific heat is constant, while the susceptibility and the compressibility diverge at low temperature as $1/T$

$$P = 2P_F^0(\bar{\mu})\left(\frac{1}{\xi_N^{3/2}} + \frac{\tilde{\chi}b^2}{2} + \frac{\tilde{\gamma}t^2}{2}\right), \tag{11.48}$$

with $b = h/\bar{\mu}$, $t = k_B T/\bar{\mu}$ and ξ_N, $\tilde{\chi}$ and $\tilde{\kappa}$ are three numerical coefficients. $\tilde{\gamma}$ and $\tilde{\chi}$ are related to the specific heat and spin susceptibility by

$$\frac{C_V}{T} = \frac{\tilde{\gamma}\bar{\mu}^2}{2k_B^2 P_F^0(\bar{\mu})}, \tag{11.49}$$

$$\chi = \frac{\tilde{\chi}\bar{\mu}^2}{2P_F(\bar{\mu})}. \tag{11.50}$$

The measurement of the equation of state of the unitary normal phase using the experimental scheme described in the previous version is presented in Fig. 11.8 from Ref. [44, 50] for a spin balanced system at finite temperature, and a spin imbalanced gas at zero temperature. We see that the quadratic dependence with chemical potential and temperature is indeed satisfied and supports the Fermi liquid description of the normal phase. These measurements yield for the universal coefficient, $\xi_N = 0.51$ in agreement with the Fixed Node Monte-Carlo result of ref. [97], $\tilde{\gamma} = 19$ and $\tilde{\chi} = 2.8$, to be compared with the ideal gas values $\xi_N^0 = 1$, $\tilde{\chi}_0 = 15/4 = 3.75$ and $\tilde{\gamma}_0 = 5\pi^2/4 \sim 12$. The determination of these dimensionless numbers gives access to the parameters of the underlying Fermi liquid. For instance, the effective mass is obtained from the specific heat and is given by

$$\frac{m^*}{m} = \xi_N^{1/2}\frac{\tilde{\gamma}}{\tilde{\gamma}_0} = 1.1. \tag{11.51}$$

11.5.4 The Normal/Superfluid Transition Line

The knowledge of the equation of state of both the superfluid and normal phases gives access to the position of the critical line separating the two regime. We can extend the discussion to the full temperature/imbalance phase diagram. In that case the normal to superfluid transition is represented by a critical line joining the second order phase transition of the unpolarized gas and the first order Clogston–Chandrasekhar limit (Fig. 11.9). Assuming the Fermi-liquid behavior (11.46), it is possible to bound the critical region at unitarity.

Indeed, the critical line is given by the equality of pressure and chemical potentials in the normal and superfluid phases

$$P_N(\mu_\uparrow, \mu_\downarrow, T) = P_{SF}(\mu_\uparrow, \mu_\downarrow, T). \tag{11.52}$$

Using Gibbs-Duhem relation, $\partial_T P = S$ and is thus positive according to the Second Law of Thermodynamics. Applying this property to the equation of state of the
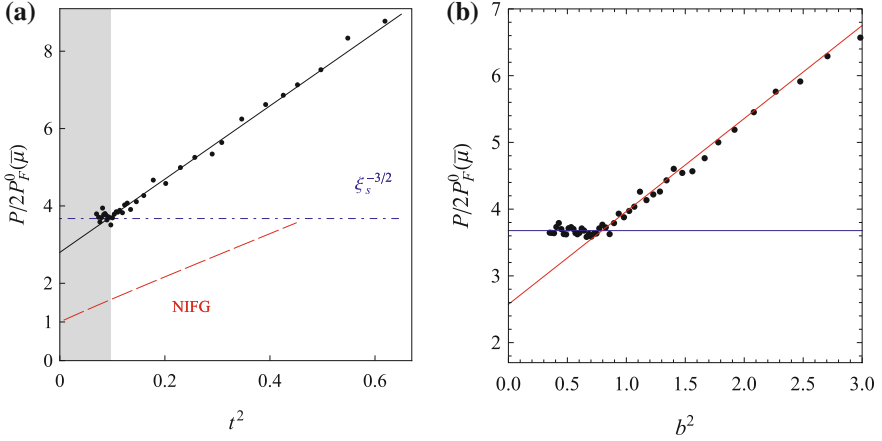
Fig. 11.8 Fermi liquid behavior at unitarity. **a** Specific heat. **b** Spin susceptibility at very low temperature from [117] $t = k_B T / \mu$ and $b = \mu_\uparrow - \mu_\downarrow / \mu_\uparrow + \mu_\downarrow$
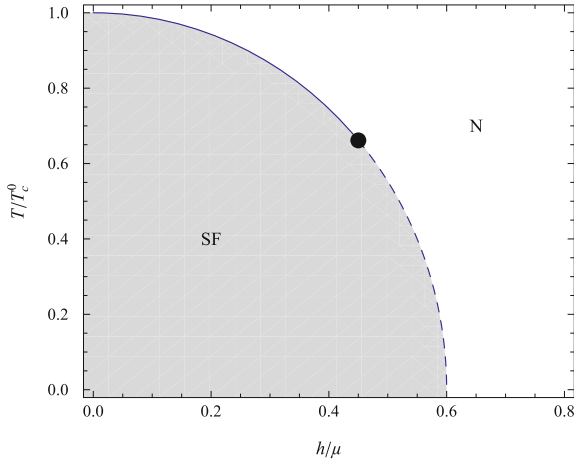
Fig. 11.9 Sketch of the finite temperature phase diagram in $(T/T_c^0, h/\mu)$, where T_c^0 is the critical temperature of the spin balanced gas. The *grey region* is the superfluid region. The second order phase transition line (*solid line*) between the superfluid (SF) and normal (N) phases stops at a tricritical point and turns into a first order critical line (*dashed line*). Note that in this graph we did not represent the FFLO phase

superfluid, we have $P_{SF}(\mu_\uparrow, \mu_\downarrow, T) > P_{SF}(\mu_\uparrow, \mu_\downarrow, 0)$. Since we know that, according to the Clogston–Chandrasekhar scenario, the pairing gap renders the superfluid insensitive to chemical potential imbalance, we have

$$P_{SF}(\mu_\uparrow, \mu_\downarrow, T) \geq P_{SF}^0(\bar{\mu}), \tag{11.53}$$

with P_{SF}^0 given by Eq. 11.26, and $\bar{\mu} = (\mu_\uparrow + \mu_\downarrow)/2$. Using the expression of the equation of state of the Fermi liquid we thus have on the critical line

$$P_{\text{N}}^0(\bar{\mu}) + \frac{\gamma T^2}{2} + \frac{\chi b^2}{2} \geq P_{\text{SF}}^0(\bar{\mu}), \tag{11.54}$$

where this inequality becomes an equality at $T = 0$. Writing this zero-temperature equation, we see that $P_{\text{SF}}^0 - P_{\text{N}}^0$ is simply $\chi b_c^2/2$, where b_c is the dimensionless chemical potential at the Clogston–Chandrasekhar limit.[6] This allows one to write the inequality as

$$\frac{\gamma T^2}{\chi b_c^2} + \frac{b^2}{b_c^2} \geq 1. \tag{11.55}$$

Interestingly, the knowledge of χ, γ and b_c from the Fermi liquid parameters yields the following lower bound for the spin balanced gas

$$\left(\frac{k_{\text{B}}T}{\mu}\right)_c \geq b_c \sqrt{\frac{\tilde{\chi}}{\tilde{\gamma}}} \simeq 0.32. \tag{11.56}$$

This value is actually very close to the one obtained directly from the analysis of the equation of state of the finite temperature balanced gas [44] or by Monte-Carlo simulations [7, 118, 119]. The inequality in Eq. 11.55 is therefore nearly an equality, which suggests that P_{SF} depends only weakly on temperature. This feature is actually not surprising. Indeed, excitations in the superfluid are of two kinds. First, single-particle excitations are exponentially suppressed below T_c by the pairing gap. Second, collective excitations associated with phonons follow at low temperature a Rayleigh-Jeans behavior and give a contribution $\propto T^4$ to the energy. Both of them vary slowly with T and are then strongly suppressed at low temperature.

11.5.5 The Tricritical Point

Since the two limiting cases of the critical lines correspond to phase transitions of different orders, there is a point (called a tricritical point) where the order of the phase transition changes from first to second.

A similar phenomenon is present in ^{3}He-^{4}He mixtures the phase diagram of which attracted a lot of attention in the 1970s for the development of dilution refrigerators [120–122]. This work was then extended to cold atoms in [123] using Nozières-Schmitt-Rink approximation and at unitarity using a renormalization scheme [124]. Experimentally, the tricritical point was observed at unitarity in [125], with $T_3 \simeq 0.09 T_{\text{F}\uparrow}$, in agreement with the prediction of [124].

---

[6] This relations is similar to the the one existing between the condensation energy and the critical magnetic field in superconductors.

Mean-field analysis of the phase diagram unveils an intriguing connection between the tricritical point and the inhomogeneous FFLO phase [84, 126] since in the weakly attractive limit, the tricritical point corresponds also to the disappearance of the FFLO phase.

When varying interactions from the BCS to the BEC region of the phase diagram, the temperature of the tricritical point decreases [123] and for some particular value of the interaction parameter $1/k_{F\uparrow}a \sim 1.7$, T_3 even vanishes. As a consequence, the critical line of Fig. 11.9 becomes fully second order, and the first order Clogston–Chandrasekhar transition disappears. The physical interpretation of this zero-temperature phase transition is actually rather intuitive. Indeed, in this regime, the system behaves as a Bose-Fermi mixture of atoms and molecules repelling each other with a scattering length $a_{ad} = 0.6a$ [80]. Using a mean-field description of the mixture it was demonstrated that, in the low bosonic density limit, a demixing instability can happen at large density of fermions [79], in our case for $1/k_{F\uparrow}a = 1.88$.

11.6 Fermi Liquid Versus Non-Fermi Liquid

11.6.1 Molecular Limit

As mentioned earlier for the superfluid or the impurity, in the far BEC limit the physics of the gas is dominated by the existence of dimers imparting a bosonic nature to the excitations of the systems and as such invalidating the Fermi-liquid picture used to describe the normal phase in the BCS and unitarity regimes. Indeed, on the one hand molecules start to form at a temperature T^* of the order of the binding energy $\hbar^2/ma^2$ which goes to infinity when a vanishes. On the other hand for a weakly interacting Bose gas, the critical temperature does not depend on the temperature. As a consequence, when a is large enough, T^* becomes larger than T_c and pre-formed molecules exist in the normal phase. This scenario was confirmed by theoretical studies of the normal phase in a lattice using the Dynamic Mean-Field Theory (DMFT) [127, 128], as well as Fixed Node Monte-Carlo simulations of the normal Fermi gas [117].

Experimentally, it is possible to address this transition by studying the spin susceptibility of the system which is reduced by the presence of the molecules. Indeed, being spin singlet, the dimers are not affected by the spin polarizing field h and, just like Cooper pairs, are protected by their molecular binding energy. In the far BEC limit, the spin susceptibility can be calculated using a chemical balance model showing that indeed, the spin susceptibility decreases exponentially as soon as $T/T^* \lesssim 1$, where a significant number of dimers start to form. In contrast with its fermionic counterpart, the Bose liquid is thus characterized by a cancelation of the zero temperature spin susceptibility. Although this Fermi to Bose liquid transition has not yet been observed, experimental evidence as well as Fixed Node Monte-Carlo simulations indicate that such transition should happen around $1/k_{Fa} = 0.7$ [117]. Interestingly,
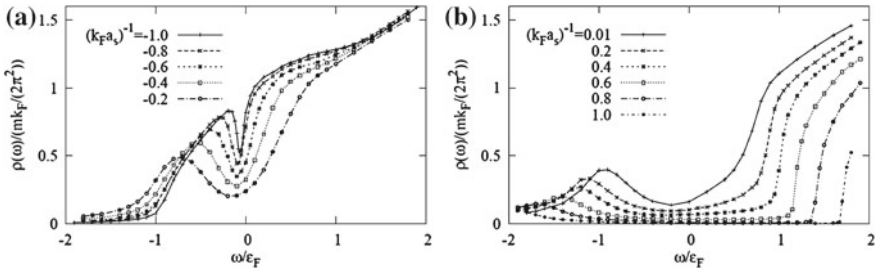
Fig. 11.10 Density of states at $T = T_c$ calculated within the self-consistent T-matrix approximation in the BCS (**a**) and BEC (**b**) sectors—Figure from [130]

this value is close to the one for which the polaron vanishes (see section 1). This coincidence supports the fact that the properties of quasi-particles depend relatively little on the spin imbalance. Let us illustrate this point in the case where $T^* \ll T_F$. In the quantum degenerate regime $T/T_F \ll 1$, the susceptibility of an ideal Fermi gas is proportional to the density of states at the Fermi level. At finite temperature, the excitations span an energy range T around E_F. If $T \gg T^*$, the distribution is only weakly sensitive to the energy states in the pseudogap dip. On the contrary, for $T \ll T^*$, the quasi-particles are mostly inside the dip and the spin susceptibility is thus sensitive to the reduction of the density of state at the Fermi level.

11.6.2 Pseudogap

The cancellation of the spin susceptibility of the low temperature normal phase in the BEC limit is a consequence of the existence of a gap in the density of states of the molecular gas associated with the binding energy of the dimers. At $1/k_F a = 0.7$ this gap vanishes but a dip remains in the density of states and smears out when one varies the interaction strength towards the BCS-limit of the BEC–BCS crossover (see Fig. 11.10). This dip is sometimes called a pseudogap, in analogy with a characteristic feature of the normal phase of high-critical temperature superconductors where a gap starts to open at the Fermi surface in precise crystallographic directions even above T_c [129]. By analogy with the molecular behavior we call T^* the characteristic width of the dip, which will quantify the energy scale of the pseudogap features [7] (see for instance [130–132]).

Most naturally, the first proposals to study this pseudo gap physics involved microscopic probes, in particular RF-spectroscopy [27, 133]. We show here that this physics can also be explored by the study of the thermodynamic properties of

---

[7] Note that here our definition of the pseudo-gap characteristic energy T^* is based on the properties of the normal phase at $T = 0$. Another definition is the temperature T^{**} at which the dip vanishes [130].

Fig. 11.11 Spin susceptibility in the BEC–BCS crossover χ normalized to the zero temperature susceptibility χ_0 of an ideal Fermi gas. *Full line* ideal Fermi gas; *Dotted line* Curie's law $(1/T)$; *Dashed line* ideal molecular mixture (see Appendix Susceptibility of a Molecular Gas) for $T^* = 2T_F$
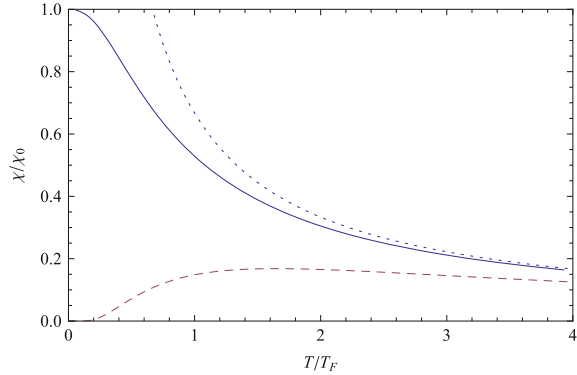
the normal phase, and in particular the temperature dependence of the spin susceptibility. Indeed, in the BEC–BCS crossover, $\chi(T)$ evolves between the two limits displayed in Fig. 11.11. In the BEC limit, we recover that the spin susceptibility is zero at $T = 0$, with a maximum located at $T \propto T^*$. In the BCS limit, the system behaves like an ideal Fermi gas, with a saturation of Curie's Law when $T \lesssim T_F$. In between, we expect a crossover between the two behaviors, with a non monotonous evolution, and a maximum at $T \sim T^*$, and a finite susceptibility at $T = 0$. The temperature dependence of the spin susceptibility has been very recently measured in [134] and further investigation will be required to clarify the existence of a pseudogap.

11.7 High Temperature Expansion

In the non degenerate regime, the Fermi liquid description is no longer valid. In this limit, an asymptotic expansion of the equation of state can be obtained using a virial expansion based on the analyticity of the grand canonical partition function with the fugacity $z = \exp(\beta\mu)$. Generally speaking, it is indeed possible to write (see Appendix Virial Expansion)

$$P(\mu, T) = \sum_{n \geq 1} b_n z^n \tag{11.57}$$

where b_n is related to the properties of the n-body system. As a consequence, $n = 1$ corresponds to the ideal gas and interaction effects enter the game for $n \geq 2$. For an ideal gas, quantum correlations impose $b_n^0 = (-1)^{n+1}/n^{5/2}$. To study the effect of interactions we thus set $b_n = b_n' + b_n^0$. The coefficient b_2' was calculated first in [48, 135] and gives $b_2' = 1/\sqrt{2}$. The calculation of higher order terms is more involved and is related to the study of the few-body problem whose interest was renewed by the recent observation of Efimov trimers in cold atoms [136] (for a review see [137]). Two contradicting theoretical values of b_3' can be found in literature $b_3' = -0.355$ [138] and $b_3' = 1.05$ [139]. Experimental data of Fig. 11.12 yielding a value $b_3' = -0.35(2)$

Fig. 11.12 High temperature equation of state of the normal phase. We plot here the dimensionless pressure $u_N = P/P_0(\mu)$ versus the inverse of fugacity. Comparison between experimental points of ref. [44] and virial expansions of second (*dotted*), third (*dashed*) and fourth (*solid*) order
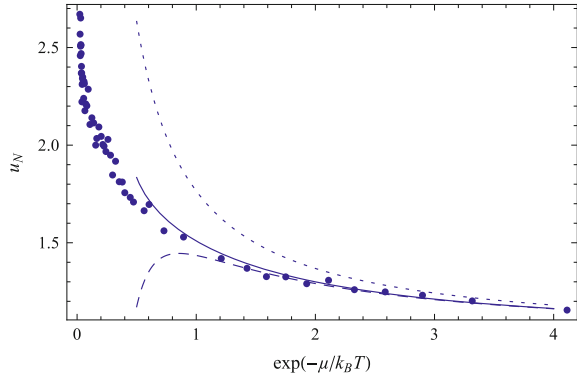
validates the result of ref. [138]. The analysis of the Fig. 11.12 allows in addition to extract the value of fourth virial coefficient the value of which is $b_4' = 0.096(15)$. As already mentioned, the *ab-initio* calculation of b_4 involves the full resolution of the 4-body problem, a challenging task that has been addressed in some specific cases (calculation of the dimer-dimer scattering length [12, 65] or the equation of state of a dilute BEC of dimers [64]) but has not been undertaken for a normal gas at high temperature.

The virial expansion is valid only in the high temperature regime. To make the connexion with the low temperature behavior discussed in the Fermi Liquid section, more advanced calculations are required [8, 40, 108]. Detailed comparison with experiment is presented in ref. [44].

11.8 Conclusion

In this contribution we have shown that the study of the thermodynamics of a strongly interacting spin-1/2 system is a powerful tool to address its macroscopic properties as well as its low energy excitations. *In situ* absorption images provide direct access to the gas pressure and to the equation of state at thermal equilibrium. We have presented several simple models to analyze this EoS in various limiting cases and could perform a quantitative comparison with more advanced theoretical models. A number of open issues remain on this seemingly simple many-body system. For instance the predicted FFLO (Fulde-Ferrell-Larkin and Ovshinikov) inhomogeneous superfluid phases in the imbalanced gas are yet to be observed [82, 83], the investigation of critical phenomena, and the complete phase diagram as a function of temperature and spin imbalance would reveal additional features. The measurement of the spin susceptibility as a function of temperature and interaction strength, and the precise determination of the critical temperature would enable one to further test advanced theoretical models. The measurement of the EoS through the local pressure is not restricted to Fermi gases [50]. It applies equally well to ultracold bosons, Bose-Fermi mixtures and atoms confined in optical lattices [50], provided the local

density approximation is valid. We believe that the simplicity of implementation of this measurement scheme will help in the understanding of challenging many-body problems in the future, deepening the connection between this research on cold atoms and that on condensed matter.

Appendix

Spin Susceptibility of a Gapped System at Zero Temperature

Let us consider a system containing $N_\uparrow$ and $N_\downarrow$ spin up and spin down particles. We define $M = N_\uparrow - N_\downarrow$ and $N = N_\uparrow + N_\downarrow$ the polarization and the total atom number and we denote $E(N,M)$ as the energy of the system. If one assumes that the energy can be expanded in M then by symmetry the linear term vanishes and one gets $E(N, M) = E(N, 0) + M^2/2\chi + ...$ (see also below). With this definition, χ is then the spin susceptibility of the system. Indeed, adding a magnetic field h contributes to a $-hM$ term to the energy and we immediately see that the energy minimum is shifted from $M = 0$ to $M = \chi h$.

This argument is no longer true in the case of a gapped system. Indeed, polarizing a spin balanced system costs the binding energy of the broken pairs. This definition applies to any system composed of spin-singlet dimers, from a fermionic superfluid composed of Cooper pairs, or a pure gas of uncondensed molecules, and leads to the following leading order expansion

$$E(N, M) = E(N, 0) + |M|\Delta + ...$$

To evaluate the spin susceptibility, we add as above a magnetic field h changing the energy into $E - hM$. We see that for $h \neq 0$, the potential is tilted but the energy minimum stays located at $M = 0$, as long as $|h| < \Delta$ corresponding to the Pauli limit below which pairing can resist spin polarization (see Fig. 11.13).

Fermi Liquid Theory in the Grand Canonical Ensemble

At the macroscopic level, the Fermi liquid is characterized by three properties

1. *The specific heat C_V varies linearly with temperature and $C_V/C_V^0 = m^*/m$, where C_V^0 is the specific heat of the ideal gas.* By definition, the heat transfer

Fig. 11.13 Energy E of a
gapped system versus spin
polarization M. *Solid line*:
the spin polarizing field h is
0 and the slope of the energy
is given by the gap Δ.
Dotted line: non zero spin
polarizing field. The energy
is tilted but as long as
$|h| < \Delta$, the ground state
remains unpolarized
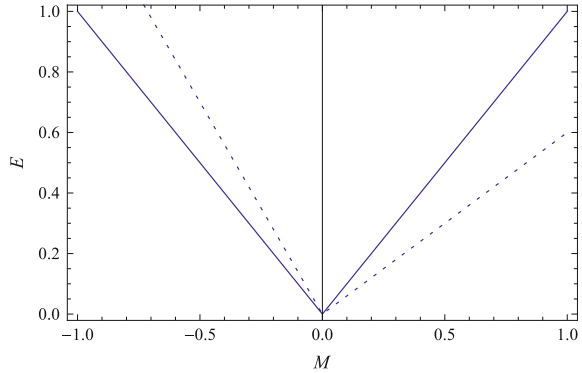
δQ at constant volume and atom number reads $\delta Q = C_V dT + h dV$, and we
thus have

$$dS = \frac{\delta Q}{T} = \frac{C_V}{T} dT + \frac{h}{T} dV. \tag{11.58}$$

Using the thermodynamic identity $dF = -SdT - PdV + \sum_\sigma \mu_\sigma dN_\sigma$ for the
free energy F, we have finally

$$C_V = -T \left(\frac{\partial^2 F}{\partial T^2} \right). \tag{11.59}$$

2. *The compressibility of the system is finite at T = 0.* We have by definition of
pressure

$$P = -\left(\frac{\partial F}{\partial V} \right)_{T,N,M}, \tag{11.60}$$

hence for a compression at constant temperature and atom number

$$dP = -\left(\frac{\partial^2 F}{\partial V^2} \right)_{T,N,M} dV \tag{11.61}$$

From the definition of the isotherme compressibility, we have

$$\kappa_T = \frac{-1}{V} \left(\frac{\partial V}{\partial P} \right)_{T,N,M}, \tag{11.62}$$

and we have finally

$$\kappa_T^{-1} = V \left(\frac{\partial^2 F}{\partial V^2} \right)_{T,N,M}. \tag{11.63}$$

3. *The magnetic susceptibility is finite at zero temperature.* This calculation is very similar to the previous one. Indeed, we have

$$h = \left(\frac{\partial F}{\partial M}\right)_{N,T,V}, \tag{11.64}$$

with $M = (N_\uparrow - N_\downarrow)/2$ and $N = (N_\uparrow + N_\downarrow)/2$. Polarizing the system at constant atom number, we have

$$dh = \left(\frac{\partial^2 F}{\partial M^2}\right)_{N,V,T} dM. \tag{11.65}$$

Defining the susceptibility of the gas has

$$\chi = \frac{1}{V}\left(\frac{\partial M}{\partial h}\right)_{N,T,V}, \tag{11.66}$$

and we have the identity

$$\chi^{-1} = V\left(\frac{\partial^2 F}{\partial M^2}\right) \tag{11.67}$$

At low temperature and spin imbalance, we can expand the free energy with respect to T and M. To second order, we have

$$F(T, V, N, M) = F_0(T, V, N) + T\left(\frac{\partial F}{\partial T}\right)_0 + M\left(\frac{\partial F}{\partial M}\right)_0$$
$$+ \frac{T^2}{2}\left(\frac{\partial^2 F}{\partial T^2}\right)_0 + \frac{M^2}{2}\left(\frac{\partial^2 F}{\partial M^2}\right)_0 + MT\left(\frac{\partial^2 F}{\partial T \partial M}\right)_0. \tag{11.68}$$

According to the Third Law of Thermodynamics, entropy is zero at zero temperature. From the previous expansion, we thus have

$$S = -\left(\frac{\partial F}{\partial T}\right)_{V,N,M} = \left(\frac{\partial F}{\partial T}\right)_0 + T\left(\frac{\partial^2 F}{\partial T^2}\right)_0 + M\left(\frac{\partial^2 F}{\partial T \partial M}\right)_0 = 0. \tag{11.69}$$

We then obtain readily

$$\left(\frac{\partial F}{\partial T}\right)_0 = \left(\frac{\partial^2 F}{\partial T \partial M}\right)_0 = 0, \tag{11.70}$$

and thus

$$F(T, V, N, M) = F_0(T, V, N) + \frac{T^2}{2}\left(\frac{\partial^2 F}{\partial T^2}\right)_0 + \frac{M^2}{2}\left(\frac{\partial^2 F}{\partial M^2}\right)_0. \tag{11.71}$$

Let us set $C_V = V\gamma T$ at low temperature. According to the previous discussion we therefore have

$$F = F_0 - \frac{\gamma T^2}{2} + \frac{M^2}{2\chi} + \dots \tag{11.72}$$

Let us now consider the grand potential $\Omega = F - \mu N - hM$. We have using the relation $h = \chi M$ in the weakly polarized limit

$$\Omega(\mu, h, T, V) = F_0 - \mu N - V\frac{\gamma T^2}{2} - V\frac{\chi h^2}{2}, \tag{11.73}$$

which can be recast as

$$\Omega(\mu, h, T, V) = \Omega_0(\mu, V) - \left(\frac{\gamma T^2}{2} + \frac{\chi h^2}{2}\right) V, \tag{11.74}$$

where Ω_0 is the value of the grand potential for $T = h = 0$. Let us introduce $P_1(\mu)$ the pressure of a single species Fermi gas at zero temperature. We then have using $\Omega = -PV$

$$\frac{P}{P_1} = \frac{P_0(\mu)}{P_1(\mu)}\left[1 + \frac{\gamma T^2}{2P_0} + \frac{\chi h^2}{2P_0}\right]. \tag{11.75}$$

Susceptibility of a Molecular Gas

Let us consider a mixture of spin-1/2 fermions in the BEC side of a Feshbach resonance and in this regime $a > 0$, so two atoms can form a stable dimer of energy $\hbar^2/ma^2$. Let us consider the free energy $F(N_\uparrow, N_\downarrow, N_b)$. Since the formation of δN_b dimers requires the disappearance of a same number of spin-up and down atoms, the free energy varies at fixed temperature as

$$\delta F = \left(\partial_{N_b}F - \partial_{N_\uparrow}F - \partial_{N_\downarrow}F\right)\delta N_b. \tag{11.76}$$

At equilibrium, $\delta F = 0$ to first order, yielding the condition

$$\mu_b = \mu_\uparrow + \mu_\downarrow = 2\bar{\mu}, \tag{11.77}$$

where as before $\bar{\mu} = (\mu_\uparrow + \mu_\downarrow)/2$. Let us consider the BEC limit, where the binding energy of the dimers is $-\hbar^2/ma^2$ and the atom-atom, atom-dimer and dimer-dimer interactions are negligible. In this case we can describe the system as a mixture of ideal gases. Moreover, if we work above the quantum degenerate regime, we can use classical thermodynamics to describe the system. In this regime the partition function of an ensemble of N non-interacting particles described by a dispersion

relation $E(p) = E_\alpha^0 + p^2/2m_\alpha$, where the α encapsulates the nature and the internal state of the particle, is given by

$$Z = \frac{1}{N!} \left[\int \frac{V d^3 p}{(2\pi \hbar)^3} e^{-\beta E(p)} \right] = \frac{1}{N!} \left(\frac{V e^{-\beta E_0}}{\lambda_{\text{th}}^3} \right)^N, \quad (11.78)$$

where $\lambda_{\text{th}} = \sqrt{2\pi \hbar^2/m_\alpha k_B T}$ is the thermal wavelength and the factor $N!$ was introduced to take into account the classical indiscernibility of the particles.[8] We deduce the chemical potential from the definition $\mu = \partial_N F$ with $F = -k_B T \ln Z$. After a straightforward calculation we obtain

$$\mu = E_0 + k_B T \left(\ln(n\lambda_{\text{th}}^3) - 1 \right). \quad (11.79)$$

for the gases of atom ($m_\alpha = m$, $E_\alpha^0 = 0$) and molecules ($m_\alpha = 2m$ and $E_\alpha^0 = -\hbar^2/ma^2$), we have

$$\mu_\sigma = k_B T \left[\ln \left(n_\sigma \lambda_T^3 \right) - 1 \right] \quad (11.80)$$

$$\mu_b = -\frac{\hbar^2}{ma^2} + k_B T \left[\ln \left(n_\sigma \lambda_T^3/2^{3/2} \right) - 1 \right], \quad (11.81)$$

where λ_{th} is the thermal wavelength of the atoms.

Let us consider first the balanced case, $n_\uparrow = n_\downarrow = n_a$. Writing the condition (11.75), we recover the law of mass action

$$\frac{n_a^2}{n_b} = \frac{e^{-T^*/T}}{2^{3/2}\lambda_{\text{th}}^3}, \quad (11.82)$$

with $k_B T^* = \hbar^2/ma^2$. As expected, we see that this ratio goes to zero when the temperature becomes much smaller than T^*. In this limit, we have in particular $N = N_\uparrow + N_\downarrow + 2N_b \sim 2N_b$, hence

$$n_a^2 \sim \frac{2n e^{-T^*/T}}{2^{3/2}\lambda_{\text{th}}^3}. \quad (11.83)$$

Let us now consider the imbalanced case. Using Eq. 11.78, we see that

$$h = \frac{k_B T}{2} \ln \left(\frac{n_\uparrow}{n_\downarrow} \right). \quad (11.84)$$

---

[8] Note that without this factor the free energy is not an extensive quantity.

Inverting this relation, we see that when h is small we have

$$n_\uparrow - n_\downarrow = \frac{2n_a}{k_B T} h, \tag{11.85}$$

where n_a is given by (11.81) and is exponentially small in the low temperature limit $T/T^* \ll 1$. The spin susceptibility is thus given by

$$\chi = \frac{1}{V}\left(\frac{\partial M}{\partial h}\right)_N \propto \frac{e^{-T^*/2T}}{T}. \tag{11.86}$$

In the opposite limit $T/T^* \gg 1$, we have $n_b \ll n_a$ hence $n_a \sim n/2$ and

$$\chi \propto \frac{1}{T}, \tag{11.87}$$

where we recover Curie's law.

Virial Expansion

Let us consider the Grand canonical partition function of a many-body system

$$Z = \sum_{\alpha \in \mathcal{H}} e^{-\beta(E_\alpha - \mu N_\alpha)},$$

where the $|\alpha\rangle$ are the eigenstates of the hamiltonian H and span the whole grand canonical Hilbert space $\mathcal{H}$. Let us now decompose this sum over Fock states of fixed atom number N. We thus have

$$Z = \sum_N \left(e^{\beta \mu N} \sum_{\alpha \in \mathcal{H}_N} e^{-\beta(E_\alpha)} \right).$$

We see in this case that the partition function can be expanded with the fugacity $z = \exp(\beta\mu)$, a result known as the Virial expansion. The grand-potential $\Omega = -PV = -k_B T \ln Z$ is also analytical with fugacity z and can therefore be expanded as

$$P(\mu, T) = \sum_{n \geq 1} b_n z^n \tag{11.88}$$

where b_n can be obtained from the knowledge of the spectrum of the Hamiltonian at a number $n' \leq n$ 0 of particles.

References

1. Eagles, D.M: Phys. Rev. **186**(2), 456–463 (1969)
2. Inguscio, M., Ketterle, W., Salomon, C. (eds.): Proceedings of the International School of Physics Enrico Fermi on Ultracold Fermi gases, Course CLXIV, Varenna. Società Italiana di Fisica (2006)
3. Giorgini, S., Pitaevskii, L.P, Stringari, S.: Rev. Mod. Phys. **80**(4), 1215–1274 (2008)
4. Holland, M., Kokkelmans, S.J.J.M.F., Chiofalo, M.L., Walser, R.: Phys. Rev. Lett. **87**(12), 120406 (2001)
5. Heiselberg, H.: Phys. Rev. A **63**(4), 043606 (2001)
6. Astrakharchik, G.E, Boronat, J., Casulleras, J., Giorgini, S.: Phys. Rev. Lett. **93**(20), 200404 (2004)
7. Bulgac, A., Drut, J.E., Magierski, P.: Phys. Rev. A **78**(2), 23625 (2008)
8. Haussmann, R., Rantner, W., Cerrito, S., Zwerger, W.: Phys. Rev. A **75**(2), 023610 (2007)
9. Hu, H., Liu, X.J., Drummond, P.D.: Europhys. Lett. **74**, 574–580 (2006)
10. Cornell, E.A., Wieman, C.E.: Rev. Mod. Phys. **74**(3), 875–893 (2002)
11. DeMarco, B., Jin, D.S: Science **285**(5434), 1703 (1999)
12. Petrov, D.S., Salomon, C., Shlyapnikov, G.V.: Phys. Rev. Lett. **93**(9), 090404 (2004)
13. Cubizolles, J., Bourdel, T., Kokkelmans, S.J.J.M.F., Shlyapnikov, G.V., Salomon, C.: Phys. Rev. Lett. **91**(24), 240401 (2003)
14. O'Hara, K.M., Hemmer, S.L., Gehm, M.E., Granade, S.R., Thomas, J.E.: Science **298**(5601), 2179 (2002)
15. Bourdel, T., Cubizolles, J., Khaykovich, L., Magalhães, K.M.F., Kokkelmans, S.J.J.M.F., Shlyapnikov, G.V., Salomon, C.: Phys. Rev. Lett **91**(2), 020402 (2003)
16. Jochim, S., Bartenstein, M., Altmeyer, A., Hendl, G., Riedl, S., Chin, C., Hecker Denschlag, J., Grimm, R.: Science **302**(5653), 2101 (2003)
17. Greiner, M., Regal, C.A., Jin, D.S.: Nature **426**(6966), 537–540 (2003)
18. Zwierlein, M.W., Stan, C.A., Schunck, C.H., Raupach, S.M.F., Gupta, S., Hadzibabic, Z., Ketterle, W.: Phys. Rev. Lett. **91**(25), 250401 (2003)
19. Bourdel, T., Khaykovich, L., Cubizolles, J., Zhang, J., Chevy, F., Teichmann, M., Tarruell, L., Kokkelmans , S.J.J.M.F., Salomon, C.: Phys. Rev. Lett. **93**(5), 050401 (2004)
20. Ketterle W., Zwierlein, M.: Making, probing and understanding ultra-cold fermi gases in Proceedings of the International School of Physics "Enrico Fermi", course CLXIV, Varenna. Società Italiana di Fisica (2008)
21. Regal, C.A., Greiner, M., Jin, D.S.: Phys. Rev. Lett. **92**, 040403 (2004)
22. Zwierlein, M.W., Stan, C.A., Schunck, C.H., Raupach, S.M.F., Kerman, A.J., Ketterle, W.: Phys. Rev. Lett., **92**, 120403 (2004)
23. Zwierlein, M.W., Abo-Shaeer, J.R., Schirotzek, A., Schunck, C.H., Ketterle, W.: Nature **435**(7045), 1047–1051 (2005)
24. Bartenstein, M., Altmeyer, A., Riedl, S., Jochim, S., Chin, C., Hecker-Denschlag, J., Grimm, R.: Phys. Rev. Lett. **92**, 203201 (2004)
25. Pitaevskii, L., Stringari, S.: Bose-Einstein condensation. Clarendon Press, UK (2003)
26. Chin, C., Bartenstein, M., Altmeyer, A., Riedl, S., Jochim, S., Hecker Denschlag, J., Grimm, R.: Science **305**(5687), 1128 (2004)
27. Stewart, J.T., Gaebler, J.P., Jin, D.S.: Nature **454**(7205), 744–747 (2008)
28. Kuhnle, E.D., Hu, H., Liu, X.-J., Dyke, P., Mark, M., Drummond, P.D., Hannaford, P., Vale, C.J.: Phys. Rev. Lett. **105**(7), 070402 (2010)
29. Shina, T.a.n.: Ann. Phys. **323**(12), 2952–2970 (2008)
30. Stewart, J.T., Gaebler, J.P., Drake, T.E., Jin, D.S.: Phys. Rev. Lett. **104**(23), 235301 (2010)
31. Partridge, G.B., Li, W., Kamar, R.I., Liao, Y., Hulet, R.G.: Science **311**(5760), 503–505 (2006)
32. Zwierlein, M.W., Schunck, C.H., Schirotzek, A., Ketterle, W.: Nature **442**(7098), 54–58 (2006)

33. Schirotzek, A., Shin, Y.I., Schunck, C.H., Ketterle, W.: Phys. Rev. Lett. **101**(14), 140403 (2008)
34. Chevy, F.: Phys. Rev. Lett. **96**(13), 130401 (2006)
35. Stewart, J.T., Gaebler, J.P., Regal, C.A., Jin, D.S.: Phys. Rev. Lett. **97**(22), 220406 (2006)
36. Kinast, J., Turlapov, A., Thomas, J.E., Chen, Q., Stajic, J., Levin, K.: Science **307**(5713), 1296 (2005)
37. Kinast, J., Hemmer, S.L., Gehm, M.E., Turlapov, A., Thomas, J.E.: Phys. Rev. Lett. **92**(15), 150402–150402 (2004)
38. Miller, D.E., Chin, J.K., Stan, C.A., Liu, Y., Setiawan, W., Sanner, C., Ketterle, W.: Phys. Rev. Lett. **99**(7), 070402 (2007)
39. Riedl, S., Sánchez Guajardo, E.R., Kohstall, C., Hecker Denschlag, J., Grimm, R.: Phys. Rev. A **79**(5), 053628 (2009)
40. Luo, L., Thomas, J.E.: J. Low Temp. Phys. **154**(1), 1–29 (2009)
41. Horikoshi, M., Nakajima, S., Ueda, M., Mukaiyama, T.: Science **327**(5964), 442 (2010)
42. Jin D.S., Regal, C.A. Fermi Gas experiments In: Proceedings of the International School of Physics "Enrico Fermi", Course CLXIV, Varenna. Società Italiana di Fisica (2008)
43. Spiegelhalder, F.M., Trenkwalder, A., Naik, D., Hendl, G., Schreck, F., Grimm, R.: Phys. Rev. Lett. **103**(22), 223203 (2009)
44. Nascimbène, S., Navon, N., Jiang, K., Chevy, F., Salomon, C.: Nature **463**, 1057–1060 (2010)
45. Müller, T., Zimmermann, B., Meineke, J., Brantut, J.-P., Esslinger, T., Moritz, H.: Phys. Rev. Lett. **105**(4), 040401 (2010)
46. Sanner, C., Su, E.J., Keshet, A., Gommers, R., Shin, Y.-I., Huang, W., Ketterle, W.: Phys. Rev. Lett. **105**(4), 040402 (2010)
47. Sanner, C., Su, E.J., Keshet, A., Huang, W., Gillen, J., Gommers, R., Ketterle, W.: Phys. Rev. Lett. **106**(1), 010402 (2011)
48. Ho, T.L.: Phys. Rev. Lett. **92**(9), 90402 (2004)
49. Navon, N., Nascimbène, S., Chevy, F., Salomon, C.: Science **328**, 729 (2010)
50. Nascimbène, S., Navon, N., Chevy, F., Salomon, C.: New J. Phys. **12**, 103206 (2010)
51. Ho, T., Zhou, Q.: Nat. Phys. **6**, 131 (2009)
52. Cheng, C.-H., Yip, C.-H.: Phys. Rev. B **75**(1), 014526 (2007)
53. Fuchs, J.N., Leyronas, X., Combescot, R.: Phys. Rev. A **68**(4), 043610 (2003)
54. Shin, Y.I.: Phys. Rev. A **77**(4), 041603 (2008)
55. Bardeen, J., Cooper, L.N., Schrieffer, J.R.: Phys. Rev. **108**(5), 1175–1204 (1957)
56. Leggett, A.J.: J. Phys. Colloq. **41**(C7), 19–26 (1980)
57. Nozières, P., Schmitt-Rink, S.: J. Low Temp. Phys. **59**(3), 195–211 (1985)
58. Diener , R.B., Sensarma, R., Randeria, M.: Phys. Rev. A **77**(2), 23626 (2008)
59. Lee, T.D., Yang, C.N.: Phys. Rev. **105**(3), 1119–1120 (1957)
60. Baker, G.A. Jr: Rev. Mod. Phys. **43**(4), 479–531 (1971)
61. Lee, T.D., Huang, K., Yang, C.N.: Phys. Rev. **106**(6), 1135–1145 (1957)
62. Wu, T.T.: Phys. Rev. **115**(6), 1390–1404 (1959)
63. Braaten, E., Hammer, H.W., Mehen, T.: Phys. Rev. Lett. **88**(4), 40401 (2002)
64. Leyronas, X., Combescot, R.: Phys. Rev. Lett. **99**(17), 170402 (2007)
65. Brodsky, I.V., Kagan, M.Y., Klaptsov, A.V., Combescot, R., Leyronas, X.: Phys. Rev. A **73**(3), 032724 (2006)
66. Carlson, J., Chang, S.-Y., Pandharipande, V.R., Schmidt, K.E.: Phys. Rev. Lett. **91**(5), 050401 (2003)
67. Perali, A., Pieri, P., Strinati, G.C.: Phys. Rev. Lett. **93**(10), 100404 (2004)
68. Carlson, J., Reddy, S.: Phys. Rev. Lett. **95**(6), 060401 (2005)
69. Bartenstein, M., Altmeyer, A., Riedl, S., Jochim, S., Chin, C., Hecker Denschlag, J., Grimm, R.: Phys. Rev. Lett. **92**(12), 120401 (2004)
70. Tan, S.: Ann. Phys. **323**(12), 2971–2986 (2008)
71. Partridge, G.B., Strecker, K.E., Kamar, R.I., Jack, M.W., Hulet, R.G.: Phys. Rev. Lett. **95**(2), 020404 (2005)

72. Werner, F., Tarruell, L., Castin, Y.: Eur. Phys. J. B **68**(3), 401–415 (2009)
73. Schirotzek, A., Shin, Y., Schunck, C.H., Ketterle, W.: Phys. Rev. Lett. **101**(14), 140403 (2008)
74. Clogston, A.M.: Phys. Rev. Lett. **9**(6), 266–267 (1962)
75. Chandrasekhar, B.S.: App. Phys. Lett. **1**(1), 7–8 (1962)
76. Pilati, S.k, Giorgini, S.: Phys. Rev. Lett. **100**(3), 030401 (2008)
77. Alzetto, F., Leyronas, X.: Phys. Rev. A **81**(4), 043604 (2010)
78. Shin, Y., Schirotzek, A., Schunck, C.H., Ketterle, W.: Phys. Rev. Lett. **101**(7), 070404 (2008)
79. Viverit, L., Giorgini, S.: Phys. Rev. A **66**(6), 063604 (2002)
80. Skorniakov G.V., and Ter-Martirosian K.A.: Sov. Phys. JETP, **4** (1957)
81. Kohn, W., Luttinger, J.M.: Phys. Rev. Lett. **15**(12), 524–526 (1965)
82. Larkin, A.I., Ovchinnikov, Y.N.: Zh. Eksp. Teor. Fiz. **47**, 1136 (1964)
83. Fulde, P., Ferrell, R.A.: Phys. Rev. **135**, A550 (1964)
84. Sarma, G.: J. Phys. Chem. Solids **24**(8), 1029–1032 (1963)
85. Bulgac, A., Forbes, M.M.N., Schwenk, A.: Phys. Rev. Lett. **97**, 020402 (2006)
86. Heffner, R.H., Norman, M.R.: Comments Cond. Matt. Phys. **17**, 361 (1996)
87. Tedrow, P.M., Meservey, R., Schwartz, B.B.: Phys. Rev. Lett. **24**(18), 1004–1007 (1970)
88. Kontos, T., Aprili, M., Lesueur, J., Grison, X.: Phys. Rev. Lett. **86**(2), 304–307 (2001)
89. Zwierlein, M.W., Schirotzek, A., Schunck, C.H., Ketterle, W.: Science **311**(5760), 492–496 (2006)
90. Shin, Y., Zwierlein, M.W., Schunck, C.H., Schirotzek, A., Ketterle, W.: Phys. Rev. Lett. **97**(3), 030401 (2006)
91. Radzihovsky, L., Sheehy, D.E: Rep. Prog. Phys. **73**, 076501 (2010)
92. Chevy, F., Mora, C.: Rep. Prog. Phys. **73**, 112401 (2010)
93. Son, D.T., Stephanov, M.A.: Phys. Rev. A **74**, 013614 (2006)
94. Mora, C., Combescot, R.: Europhys. Lett. **68**(1), 79 (2004)
95. Sheehy, D.E., Radzihovsky, L.: Phys. Rev. Lett. **96**(6), 60401 (2006)
96. Sheehy, D.E., Radzihovsky, L.: Ann. Phys. **322**(8), 1790–1924 (2007)
97. Lobo, C., Recati, A., Giorgini, S., Stringari, S.: Phys. Rev. Lett. **97**(20), 200403 (2006)
98. Prokof'ev, N., Svistunov, B.: Phys. Rev. B **77**(2), 020408 (2008)
99. Chevy, F.: Phys. Rev. A **74**(6), 063628 (2006)
100. Combescot, R., Recati, A., Lobo, C., Chevy, F.: Phys. Rev. Lett. **98**(18), 180402 (2007)
101. Combescot, R., Giraud, S.: Phys. Rev. Lett. **101**(5), 050404 (2008)
102. Schirotzek, A., Wu, C.-.H., Sommer, A., Zwierlein, M.W: Phys. Rev. Lett. **102**(23), 230402 (2009)
103. Mora, C., Chevy, F.: Phys. Rev. A **80**(3), 033607–033617 (2009)
104. Combescot, R., Giraud, S., Leyronas, X.: Europhys. Lett. **88**(6), 6007 (2009)
105. Punk, M., Dumitrescu, P.T., Zwerger, W.: Phys. Rev. A **80**, 053605–053615 (2009)
106. Nascimbène, S., Navon, N., Jiang, K., Tarruell, L., Teichmann, M., McKeever, J., Chevy, F., Salomon, C.: Phys. Rev. Lett. **103**(17), 170402 (2009)
107. Bruun G., Massignan, P.: Phys. Rev. Lett. **105** (2010)
108. Pines, D., Nozières, P.: The Theory of Quantum Liquids, vol.I: Normal Fermi Liquids. WA Benjamin, New York (1966)
109. Luttinger, J.M., Ward, J.: Phys. Rev. **118**(5), 1417–1427 (1960)
110. Mora, C., Chevy, F.: Phys. Rev. Lett. **104**(23), 230402 (2010)
111. Yu, Z., Zöllner, S., Pethick, C.J.: Phys. Rev. Lett. **105**(18), 188901 (2010)
112. Bertaina, G., Giorgini, S.: Phys. Rev. A **79**(1), 013616 (2009)
113. Bruun, G.M., Recati, A., Pethick, C.J., Smith, H., Stringari, S.: Phys. Rev. Lett. **100**(24), 240406 (2008)
114. Chevy, F., Nascimbène, S., Navon, N., Kaijun, J., Lobo, C., Salomon, S.: J. Phys.: Conf. Ser. **264**, 012012 (2011)
115. Abrikosov, A.A., Khalatnikov, I.M.: Rep. Prog. Phys **22**, 329 (1959)
116. Cao, C., Elliott, E., Joseph, J., Wu, H., Petricka, J., Schäfer, T., Thomas, J.E.: Science **331**(6013), 58 (2011)

117. Nascimbène S., Navon N., Pilati S., Chevy F., Giorgini S., Georges A., Salomon, C.: A new Fermi liquid: the normal phase of a strongly interacting gas of cold atoms. (2010) Arxiv preprint arXiv:1012.4664
118. Burovski, E., Prokof'ev, N., Svistunov, B., Troyer, M.: Phys. Rev. Lett. **96**(16), 160402 (2006)
119. Goulko, O., Wingate, M.: Phys. Rev. A **82**(5), 053621 (2010)
120. Riedel, E.K.: Phys. Rev. Lett. **28**(11), 675–678 (1972)
121. Riedel, E.K., Wegner, F.J.: Phys. Rev. Lett. **29**(6), 349–352 (1972)
122. Wegner, F.J., Riedel, E.K.: Phys. Rev. B **7**(1), 248–256 (1973)
123. Parish, M.M., Marchetti, F.M., Lamacraft, A., Simons, B.D.: Nat. Phys. **3**(2), 124–128 (2007)
124. Gubbels, K.B., Stoof, H.T.C.: Phys. Rev. Lett. **100**(14), 140407 (2008)
125. Shin, Y., Schunck, C.H., Schirotzek, A., Ketterle, W.: Nature **451**(4), 689–693 (2008)
126. Combescot, R., Mora, C.: Eur. Phys. J. B **28**(4), 397–406 (2002)
127. Capone, M., Castellani, C., Grilli, M.: Phys. Rev. Lett. **88**(12), 126403 (2002)
128. Toschi, A., Barone, P., Capone, M., Castellani, C.: New J. Phys. **7**, 7 (2005)
129. Fischer, Ø., Kugler, M., Maggio-Aprile, I., Berthod, C., Renner, C.: Rev. Mod. Phys. **79**(1), 353–419 (2007)
130. Tsuchiya, S., Watanabe, R., Ohashi, Y.: Phys. Rev. A **80**(3), 33613 (2009)
131. Perali, A., Pieri, P., Strinati, G.C., Castellani, C.: Phys. Rev. B **66**(2), 024510 (2002)
132. Chen, Q., Stajic, J., Tan, S., Levin, K.: Phys. Rep. **412**(1), 1–88 (2005)
133. Dao, T.L., Ferrero, M., Georges, A., Capone, M., Parcollet, O.: Phys. Rev. Lett. **101**(23), 236405 (2008)
134. Sommer, A., Ku, M., Roati, G., Zwierlein, M.W.: Nature **472**, 201–204 (2011)
135. Ho, T.L., Mueller, E.J.: Phys. Rev. Lett. **92**(16), 160404 (2004)
136. Kraemer, T., Mark, M., Waldburger, P., Danzl, J.G., Chin, C., Engeser, B., Lange, A.D., Pilch, K., Jaakkola, A., Nägerl, H.C. et al.: Nature **440**(7082), 315–318 (2006)
137. Braaten, E., Hammer, H.W.: Ann. Phys. **322**(1), 120–163 (2007)
138. Liu, X.J., Hu, H., Drummond, P.D.: Phys. Rev. Lett. **102**(16), 160401 (2009)
139. Rupak, G.: Phys. Rev. Lett. **98**(9), 90403 (2007)
140. Bulgac, A., Drut, J.E., Magierski, P.: Phys. Rev. Lett. **96**(9), 90404 (2006)

Chapter 12
Normal Phase of Polarised Strongly Interacting Fermi Gases

Alessio Recati and Sandro Stringari

Abstract The theory of the normal phase of strongly interacting polarized atomic Fermi gases at zero temperature is reviewed. We use the formalism of quasi-particles to build up the equation of state of the normal phase with the relevant parameters calculated via Monte-Carlo. The theory is used to discuss the phase diagram of polarized Fermi gases at unitarity. The Fermi liquid nature of these configurations is pointed out. The theory provides accurate predictions for many different quantities experimentally measured, like the Chandrasekhar–Clogston limit of critical polarization, the density profiles and the Radio-Frequency spectrum.

12.1 Introduction

The observation of superfluidity in ultra-cold Fermi gases has built a new bridge between the field of atomic gases and condensed matter. Moreover the flexibility one has in cold gases gives the possibility to explore new regimes and investigate new phases [1–3]. Remarkably in cold gases it is also possible to change the strength of the interatomic force between atoms. Due to the very low temperature and the diluteness of the gas the interaction can be described as a contact potential with strength $g = 4\pi\hbar^2 a/m$ where m is the mass of the atoms and a the scattering length. The latter depending on the atomic species can be changed by applying an external magnetic field profiting of the so-called Fano-Feshbach resonances (see e.g., [2], the article by Ketterle and Zwierlein in [1] and reference therein). Such a knob is one of

A. Recati (✉) · S. Stringari
Dipartimento di Fisica,
Università di Trento and CNR-INO BEC Center,
Povo 38121, Trento Italy
e-mail: recati@science.unitn.it

S. Stringari
e-mail: stringar@science.unitn.it

the key feature in the recent development of the field of cold gases and in particular has allowed to experimentally confirm the existence of a smooth crossover between the so-called Bardeen–Cooper–Schrieffer (BCS) regime of weakly attractive fermions and the Bose–Einstein condensation (BEC) of deeply bound pairs. The idea of a crossover, rather than a phase transition, was proposed in the early 80s by Leggett [4], Nozières and Schmitt-Rink [5].

While at $T = 0$ the state of a spin-1/2 Fermi gas with attractive interaction is a superfluid, a very interesting issue is what happens in the presence of spin population imbalance. In the standard BCS theory, superconductivity arises from Cooper pairing of opposite spin fermions, and is therefore sensitive to a mismatch between the Fermi surfaces of the two spin species. Indeed in a superconducting metal when we apply a magnetic field the coupling to the orbital motion (responsible for the Meissner effect) is negligible and the important effect is the coupling to the electron spins. The field can lower the energy of the spin-polarized normal state and, if it is strong enough, make the normal state energetically more favourable than the superconducting spin-singlet state. The value of the field at which this transition takes place is known as the Chandrasekhar–Clogston (CC) limit [6, 7] and, in a BCS superconductor, it requires that the field (or, in neutral systems, the chemical potential difference between the two spin states) be larger than $\Delta/\sqrt{2}$ where Δ is the superconductor gap. Crucially, this estimate assumes that the change in energy of the normal state due to polarization is only kinetic in origin and neglects changes in the interaction energy. However, if the system is strongly interacting, the value of the Chandrasekhar–Clogston field can also depend on the interactions in the normal state, an effect that must be accurately taken into account if we wish to study normal/superfluid coexistence.

Experimentally, the phase diagram of a polarized Fermi gas remained unexplored until recent work at MIT [8–10], Rice University [11, 12] and ENS [13–15] on ultra-cold Fermi gases, where experiments in the strongly interacting unitary limit of two-component atomic Fermi gases have been carried out. Such gases can be polarised leading to a state most naturally described as phase separated between a normal and a superfluid component.

In what follows we review the Fermi liquid theory of the normal state which was first introduced in [16] and its building block the Fermi polaron, i.e., a single impurity in an otherwise non-interacting Fermi gas. The normal phase has received a number of quite stringent experimental test. Its predictions for the critical polarization (related to the CC limit), the detailed structure of the density profiles agree very well with the experimental data obtained at MIT and ENS. The calculated value of the polaron parameters also agree with the ones found in very recent experiments [15, 17].

The same theory provides explicit predictions for the frequencies of the spin excitations in the normal phase and experiments in this direction would provide a crucial test of the applicability of Landau theory to the dynamics of these strongly interacting normal Fermi gases. We discuss this issue briefly at the end of the review.

In this review we do not follow the historical development of the understanding of the phase diagram for strongly interacting imbalanced Fermi gases. We rather start with the single impurity problem, then we consider the equation of state (EoS) for

finite concentration and the resulting nature and properties of the superfluid/normal phase transition. When possible we make comparison with experiments.

12.2 The $N + 1$ or Polaron Problem

12.2.1 Homogeneous Case

In this section we consider the extreme polarised case of a single impurity interacting attractively with a bath of N non-interacting fermions. It is worth mentioning that such a problem is the simplest realisation of the moving impurity problem, and it bears a strong similarity with other old and notoriously difficult condensed matter problems, such as the Kondo problem, the x-ray singularity in metals [18], the mobility of ions [19] and ^{4}He atoms in ^{3}He [20].

For later purpose let us identify with $\uparrow$ the atoms in the bath and with $\downarrow$ the impurity atom. Pictorially the bath will dress the impurity. Since the interaction is attractive, the impurity $\downarrow$ prefers staying in the bath, gaining an energy $\mu_\downarrow$ and acquires a renormalised mass m^*. Sometimes $\mu_\downarrow$ is also called in literature binding energy for the simple fact that it is negative. The dressed particle is called Fermi-polaron or simply polaron in analogy with solid state physics concepts used to describe electrons dressed by optical phonons, hence a bath of bosons.

For weak interaction one can easily calculate within perturbation theory the two relevant parameters $\mu_\downarrow$ and m^*. Introducing the Fermi momentum of the bath $k_F = (6\pi^2 n)^{1/3}$, with n the density of the bath, one finds to second order in $k_F a$ the expressions

$$\mu_\downarrow = E_F \left(\frac{4k_F a}{3\pi} + \frac{2(k_F a)^2}{\pi^2} \right) \tag{12.1}$$

$$m^* = m \left(1 + \frac{4}{3\pi^2} (k_F a)^2 \right), \tag{12.2}$$

where $E_F = \hbar^2 k_F^2/(2m)$ is the Fermi energy. They are the analogue of the Galitskii correction for the energy and the effective mass for a balanced weakly interacting Fermi gas [21]. Usually it is not easy to do much better than this, but for the present problem the fact that we are dealing with a single impurity in a non-interacting fermionic bath allows to obtain reliable results till unitarity using a simple variational approach. The starting point is to write the simplest non-trivial variational many-body wave-function for such a system, namely the sum of a non-interacting system with single particle-hole excitations. The trial wave function $|\psi\rangle$ for a system of total momentum **p** is the following momentum eigenstate [22, 23]

$$|\psi\rangle = \phi_0^p |\mathbf{p}\rangle_\downarrow |0\rangle_\uparrow + \sum_{q<k_F}^{k>k_F} \phi_{\mathbf{qk}}^p |\mathbf{p}+\mathbf{q}-\mathbf{k}\rangle_\downarrow\, c_{\mathbf{k}_\uparrow}^\dagger c_{\mathbf{q}_\uparrow} |0\rangle_\uparrow \qquad (12.3)$$

where $c_{\mathbf{k}_\uparrow}$ and $c_{\mathbf{k}_\uparrow}^\dagger$ are annihilation and creation operators of atoms in the bath with momentum $\mathbf{k}$. In the first term the free Fermi sea is in its ground state $|0\rangle_\uparrow = \prod_{k<k_F} c_{\mathbf{k}_\uparrow}^\dagger |v\rangle$ ($|v\rangle$ is the vacuum) and the impurity atom is in the plane-wave state $|\mathbf{p}\rangle_\downarrow$, while the second term is an excited state corresponding to the creation of a particle-hole pair in the Fermi sea with momentum $\mathbf{k}$ and $\mathbf{q}$ respectively and the $\downarrow$-spin atom carrying the rest of the momentum. The first part corresponds to free propagation and, thus, $|\phi_0^p|^2$ is to the quasi-particle residue Z_p [24]. The coefficients ϕ_0^p and $\phi_{\mathbf{qk}}$ are found by minimizing the total energy. In the minimisation procedure one has to handle, as usual, with the zero range interaction potential and the corresponding regularisation in terms of the scattering length (see, e.g., [21]). In this way one gets for the energy change:

$$E = \epsilon_{\downarrow p} + \sum_{q<k_F} f(E, \mathbf{p}, \mathbf{q}) \qquad (12.4)$$

$$\frac{1}{f(E,\mathbf{p},\mathbf{q})} = \frac{m}{4\pi a} - \sum_k \frac{m}{k^2} + \sum_{k>k_F} \frac{1}{\epsilon_{\uparrow k} + \epsilon_{\downarrow \mathbf{p}+\mathbf{q}-\mathbf{k}} - \epsilon_{\uparrow q} - E}$$

where $\epsilon_{\uparrow,\downarrow k} = k^2/2m$ is the kinetic energy of the $\uparrow$ and $\downarrow$ atoms. For $\mathbf{p} = 0$ we have $E = \mu_\downarrow$, while the variation of E for small $\mathbf{p}$ gives the effective mass. In Fig. 12.1 we report the results for the energy of the polaron as a function of the inverse of the interaction $1/k_F a$. In the same figure we report the perturbative result (12.2) as well as the results (Stefano Giorgini, private communication) obtained by using Fixed-Node Diffusion Monte-Carlo (FN-DMC) simulations. The latter technique is a zero-temperature Monte-Carlo technique based on a trial wave function which fixes the nodal surface, used as an ansatz in the DMC. We restrict the analysis to the case where there are no bound states between the $\uparrow$ and the $\downarrow$ atoms. Such a bound state clearly exists in the BEC limit $1/k_F a \to +\infty$, where molecules are present. While the present approach recovers this limiting behavior, the effect of a bound state in the intermediate regime has to be properly taken into account [25–27] and it is not well described by the variational ansatz (12.3). The point is that, as it was first shown in [28], the polaron is not the lowest energy state any more for $1/k_F a \leq 1$. At the many-body level this would imply that at $T = 0$ one has a BEC of molecule almost for any polarization of the system. It is worth noticing that moreover as soon as the molecules are formes the the ssystem prefers to phase separate in a BEC of molecule and an ideal Fermi gas [29]. Thus the study of the physics of the molecular state embedded in an ideal Fermi gas [25–27] is experimentally challenging.

Going back to the results at unitarity ($k_F a \to \infty$), as can be seen from Fig. 12.1, the impurity chemical potential appraches the value $\sim 3/5 E_F$ which means that the bath "dresses" the impurity with just a single atom. The effect on the mass is even
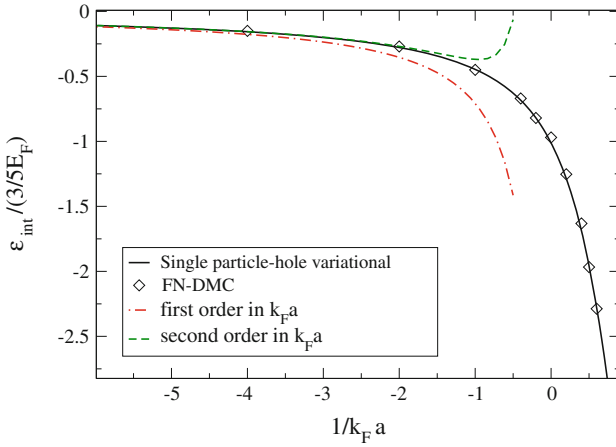
Fig. 12.1 Polaron energy as a function of the inverse of the interaction between the impurity and the fermionic bath $k_F a$, with k_F the Fermi momentum of the ideal Fermi gas and a the scattering length between ↑ and ↓ atoms. *Solid (black) line*: the variational result solving Eq. 12.5; *dot-dashed (red) line*: first order correction; *dashed (green) line*: second order perturbation theory; diamonds: Fixed-Node Monte-Carlo
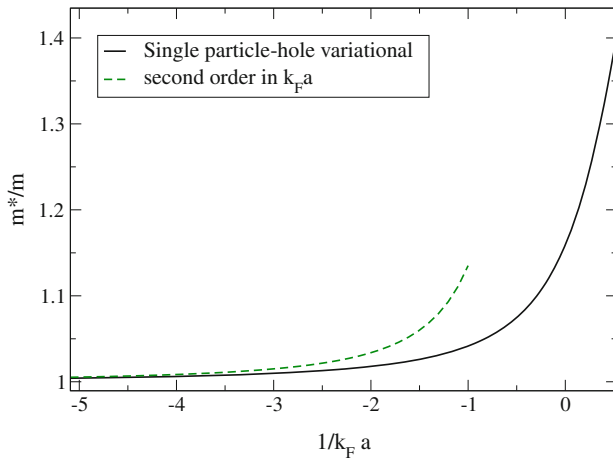
Fig. 12.2 Polaron effective mass m^* as a function of the inverse of the interaction between the impurity and the fermionic bath $k_F a$, with k_F the Fermi momentum of the ideal Fermi gas and a the scattering length between ↑ and ↓ atoms. *Solid (black) line*: the variational result solving Eq. 12.5; *dashed (green)* line: second order perturbation theory; diamonds: Fixed-Node Monte-Carlo

smaller, being the effective mass less than 20% bigger than the bare one. In Fig. 12.2 we report the variational and perturbative results (12.2) for the effective mass.

The fact that we can thrust the variational calculation is many-fold. Indeed, as can be seen in Fig. 12.1, it agrees very well with the Monte-Carlo calculation, further-

more it has been shown that the inclusion of essentially any number of particle-hole excitation does not significantly change the results [30]. Finally where applied to a one-dimensional system [23, 31] it gives results that are in very good agreement with the exact solution explored by McGuire [32]. It is also worth mentioning that the variational approach is equivalent to a more standard many-body treatment via a *T*-matrix approximation also known as Brueckner-Hartree-Fock [23, 33].

12.2.2 Non-Homogeneous/Trapped Case

Up to now we have considered the system as being homogeneous. In a real experiment the atoms are trapped by an external electromagnetic field, which in most of the cases can be included in the Hamiltonian by means of a harmonic potential of the form

$$V_{ho}(\mathbf{x}) = \frac{1}{2}m(\omega_x^2 x^2 + \omega_y^2 y^2 + \omega_z^2 z^2). \tag{12.5}$$

The bath can be considered not altered by the presence of the impurity and can be described by an ideal Fermi gas in an harmonic trap. Moreover, most of the times, local density approximation (LDA) [2] is applicable. In such approximation one defines the local chemical potential as $\mu_\uparrow(\mathbf{x}) = (6\pi^2 n_\uparrow)^{2/3} = \mu_\uparrow - V(\mathbf{x})$, where $\mu_\uparrow$ is fixed by the number of $\uparrow$-atoms, i.e., $\mu_\uparrow = (6N_\uparrow)^{1/3}\hbar\bar{\omega}$, with $\bar{\omega}^3 = \omega_x\omega_y\omega_z$ the frequency geometrical average. The impurity is dressed by the bath as described above and can be described by a particle of mass m^* in an effective external potential. Its Hamiltonian is easily written as [34]

$$H_{sp} = \frac{p^2}{2m^*} + V_{ho}(\mathbf{x})\left(1 + \frac{3}{5}A\right), \tag{12.6}$$

where, for later convenience, we have introduced the dimensionless polaron energy parameter $A = -\mu_\downarrow/(3/5E_F) > 0$, which is $\simeq 1$ at unitarity. The impurity feels a potential stronger than the bare one with the renormalised oscillator frequencies

$$\widetilde{\omega}_i = \omega_i\sqrt{\left(1 + \frac{3}{5}A\right)\frac{m}{m^*}}. \tag{12.7}$$

This means, e.g., that the dipole (sloshing) mode of the impurity along, let us say, the *x*-axis has a larger frequency with respect to the one of the harmonic confinement ω_x, namely

$$\omega_D^{(s)} = \omega_x\sqrt{\left(1 + \frac{3}{5}A\right)\frac{m}{m^*}}. \tag{12.8}$$

For example taking the values obtained by the variational ansatz at unitarity, i.e., $A \simeq 1.01$ and $m^*/m \simeq 1.17$ we have $\omega_D^{(s)}/\omega_x \simeq 1.2$, i.e., an increase of 20% with respect to the bare harmonic oscillator frequency.

It is clear from the above equation that the frequency of the impurity dipole mode (or *(s)*pin-*D*ipole) provides information about the polaron parameters. First measurements along this line have been reported in [13] and are discussed in Sect. 12.6.

In most of the present chapter we assume that the atoms forming the bath and the impurity atom are just different hyperfine levels of the same atomic specie, thus they are both fermions, have the same mass and they feel the same external potential. It is worth mentioning that the discussion is easily generalised to different atomic species. The value of the polaron parameters A (or $\mu_\downarrow$) and $m_\downarrow^*/m_\downarrow$ depend on the mass ratio $m_\downarrow/m_\uparrow$ [23], which eventually affect the possible configuration in the trap when considering the many-polaron case as we briefly discuss in the Sect. 12.3.3.

12.3 Unbalanced Fermi Gas or Many-Polaron Problem

In this section we discuss what does happen when the concentration of the impurities is finite and the atoms are trapped by an harmonic confinement. We stress that the impurities are also fermions. This fact does not affect clearly the $N+1$ problem, but it makes a huge difference for the kind of phase one has in the finite concentration case. We define the concentration as $x = n_\downarrow/n_\uparrow$ where $n_\downarrow$ and $n_\uparrow$ are the densities of the minority spin-$\downarrow$ atoms and of the majority spin-$\uparrow$ atoms, respectively. We also introduce the polarisation of the system as

$$P = \frac{N_\uparrow - N_\downarrow}{N_\uparrow + N_\downarrow}, \tag{12.9}$$

where $N_\uparrow$ ($N_\downarrow$) is the number of spin-$\uparrow$ ($-\downarrow$) atoms. Moreover we mainly discuss the case when the gas is at unitarity, i.e., $a \to \infty$.

12.3.1 Homogeneous Case

The main assumption in describing a system with finite concentration is that even at unitarity the impurities behave as a (almost) non interacting Fermi gas of polarons, or in other words they preserve they fermionic nature and the dressed particles are weakly interacting [16]. Let us start again considering a homogeneous system. The energy functional of the system can be written in the form of the Landau-Pomeranchuk Hamiltonian [16]

$$\frac{E(x)}{N_\uparrow} = \frac{3}{5}E_{F\uparrow}\left(1 - Ax + \frac{m}{m^*}x^{5/3} + Bx^2\right)$$

$$\equiv \frac{3}{5}E_{F\uparrow}\epsilon(x), \tag{12.10}$$

where $N_\uparrow$ is the number of spin-$\uparrow$ atoms and $E_{F\uparrow} = \hbar^2/2m(6\pi^2 n_\uparrow)^{2/3}$ is the Fermi energy of the spin-$\uparrow$ gas. We repeat again that the first term in Eq. 12.10 corresponds
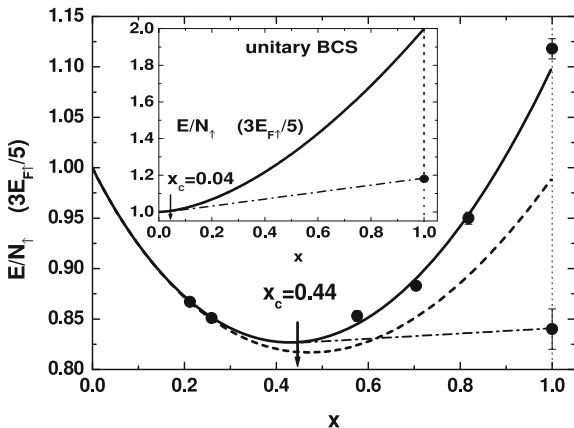
Fig. 12.3 Equation of state of a normal Fermi gas as a function of the concentration x (*circles*), from [16]. The *solid line* is a best fit to the FN-DMC results, from which the value B of the energy (12.10) is extracted. The *dashed line* corresponds to the non interacting gas of polaron, i.e., Eq. 12.10 with $B = 0$. The *dot-dashed line* is the coexistence line between the normal and the unpolarized superfluid states and the *arrow* indicates the critical concentration x_c above which the system phase separates. For $x = 1$, both the energy of the normal and of the superfluid (*diamond*) states are shown. In the inset we report the results of a "naive-BCS" theory (see text), in which the superfluid is much more robust

to the energy per particle of the non-interacting gas. The linear term in x gives the single-particle energy of the spin-down particles, while the $x^{5/3}$ term represents the quantum pressure of a Fermi gas of quasi-particles with an effective mass m^*. Eventually, the last term includes the corrections to the free polaron energy. The form of the latter term has been first found by fitting the Monte-Carlo results for finite concentration up to $x = 1$ [16, 29]. The (fitted) energy functional (12.10) is shown in Fig. 12.3, together with the Monte Carlo data and the free polaron energy functional, $B = 0$ (dashed line). The physical interpretation of the x^2 term is still not clear, but it can be thought as a quasi-particle forward interaction [35, 36]. It is worth remarking that, while Eq. 12.10 is thought as an expansion of the normal state energy for small concentration, it agrees very well with Monte-Carlo calculations for any values of x [16]. In the present work we use the values $A = 0.99(1)$, $m^* = 1.09(2)$ and $B = 0.14$ calculated in [29], using Fixed-Node Monte-Carlo techniques.

On the other hand we know in the balance case, $x = 1$, and at $T = 0$, the system is superfluid. The equation of state of a homogeneous unpolarized superfluid at unitarity is simply given by the energy of an ideal Fermi gas multiplied by an universal parameter (see, e.g., [2, 3])

$$\frac{E_S}{N_S} = \xi_S \frac{3}{5} \frac{\hbar^2}{2m} (6\pi^2 n_S)^{2/3} \equiv \epsilon_S(n_S), \qquad (12.11)$$

where N_S is the number of atoms in the superfluid phase and the universal parameter ξ_S has been calculated by different techniques, e.g., employing Quantum Monte Carlo simulations [37, 38] or diagrammatic techniques [39]. It has been also measured experimentally. We rely in what follows on the Monte Carlo value $\xi_S \simeq 0.42$. It means that if we assume that the system admits only these two phases, namely the unpolarized superfluid and the partially polarized normal phase, there exists a critical value of the concentration, x_c, at which the superfluid starts to be nucleated in the normale state. The transition between the normal and the superlfluid phase is of first order nature and the equilibrium of the two phases is found by imposing chemical and mechanical equilibrium. At constant volume V a further increase of the number of the minority atoms turns in a increase of the superfluid part. The equilibrium pressure reads

$$\frac{\partial E(x)}{\partial V} = \frac{\partial E_S}{\partial V} \tag{12.12}$$

and using Eqs. 12.11 and 12.10, it provides the relation between the superfluid density and the majority atom density in the normal phase

$$\frac{n_S}{n_\uparrow} = \left(\frac{\epsilon(x)}{2\xi_S} \right)^{3/5}. \tag{12.13}$$

The chemical potential equilibrium is equivalent to state that the chemical potential of the superfluid is equal to the sum of the chemical potential of the majority, $\mu_\uparrow$, and of the minority, $\mu_\downarrow$, atoms. From Eq. 12.11 one has $\xi_S \hbar^2/(2m)(6\pi^2 n_S)^{2/3} = \mu_\uparrow + \mu_\downarrow$. Eventually one finds that the critical concentration is given by the solution of the equation

$$\frac{3}{5}(x_c - 1)\epsilon'(x_c) = \epsilon(x_c) - 2\xi_S \left(\frac{\epsilon(x_c)}{2\xi_S} \right)^{2/5}, \tag{12.14}$$

where the prime means the derivative with respect to the concentration x. In this way we determine the critical concentration to be $x_c \simeq 0.44$ and interestingly enough the density jump between the superfluid and the majority component is almost not existent being $n_S/n_\uparrow \simeq 1.02$. This is peculiar of the equal mass case, while for different masses the jump can be pretty large (see Sect. 12.3.3). The coexistence line, shown also in Fig. 12.3 by the dashed-dot line, is obtained by minimizing the energy at a constant volume of a superfluid coexisting with a normal phase with concentration x_c. To show the importance of properly including the interaction in the normal phase, in the inset of Fig. 12.3 we report the same results but using the most "naive-BCS" theory. Namely we take the BCS result for the superfluid energy at unitarity (i.e., without any Hartree term) and the normal phase is just a two-component unbalance free Fermi gas. The normal phase would be practically never realised.

   Before moving to the trapped case, a couple of remarks on the unstable strongly interacting normal phase at $x = 1$. are due. Such a phase has an energy which, being at unitarity, can be written as the one for the superfluid

$$\frac{E_\mathrm{n}}{N} = \xi_\mathrm{n} \frac{3}{5} \frac{\hbar^2}{2m} (6\pi^2 n)^{2/3} \equiv \epsilon_\mathrm{n}(n), \tag{12.15}$$

with a different universal interaction parameter ξ_n that was also calculated via Monte-Carlo technique in [37, 38]. Such a phase is difficult to get in the lab, although it was suggested that it could emerge as an equilibrium phase in a rotating trap [40–42]. However, such a phase is not just of academic interest. Indeed it turns out that it is possible to probe such a phase experimentally, being connected to the $T \neq 0$, $P = 0$ and to the $T = 0$, $P \neq 0$ normal phase of the gas. This has been shown by the very recent analysis of some extrapolated quantities measured by the ENS group (C. Salomon, private communication).

12.3.2 Non-Homogeneous/Trapped Case

In a trap the local chemical potential fixes the sequence of phases present as a function of the distance from the trap centre. A good way to understand this feature is to convert the density relations to the chemical potential ones, i.e., to draw the grand canonical phase diagram in terms of total chemical potential $\mu = (\mu_\uparrow + \mu_\downarrow)/2$ and effective magnetic field $h = (\mu_\uparrow - \mu_\downarrow)/2$ as sketched in Fig. 12.4. In this respect the superfluid to normal phase transition is characterise by $(h/\mu)_c = 0.96$ (continuous red line in Fig. 12.4) or $\eta_c = (\mu_\downarrow/\mu_\uparrow)_c = 0.02$. The earlier value is precisely the Chandrasekhar–Clogston limit for our unitary Fermi gas. We also draw the line of the transition between the normal mixed phase and the fully polarised one which corresponds to the chemical potential ratio for a single impurity $h/\mu = (1 - 3/5A)/(1 + 3/5A) = 3.94$ (dashed green line in Fig. 12.4). We call $\mu^0_{\uparrow,\downarrow}$ the chemical potentials in the centre of the trap. The chemical potential $\mu = (\mu^0_\uparrow + \mu^0_\downarrow)/2 - V(\mathbf{x})$ decreases going outward in the trap, while $h = (\mu^0_\uparrow - \mu^0_\downarrow)/2$ is constant, and thus in a trap we explore the phase diagram along a straight line parallel to μ. In other words we can explore the whole phase diagram in a single shot and this represents a very stringent test for any theory. It is clear that it could be that some of these phases occupy a very narrow space region that are not detectable in actual experiments.

We see from Fig. 12.4 that if h is not too large we expect to have a superfluid in the centre of the trap surrounded by a shell of normal phase with decreasing concentration x going outward in the trap. When h is large enough no superfluid is present. This $T = 0$ behaviour is in agreement with what has been found experimentally [8–10, 13, 15, 43].

A quantitative comparison with experiments can be done by calculating the density profiles, which in a trap are given by the following LDA expression

$$\frac{\mu^0_\uparrow + \mu^0_\downarrow}{2} = \xi_\mathrm{S} \frac{\hbar^2}{2m} (6\pi^2 n_\mathrm{S})^{2/3} + V(\mathbf{r}) \tag{12.16}$$

in the superfluid region and by
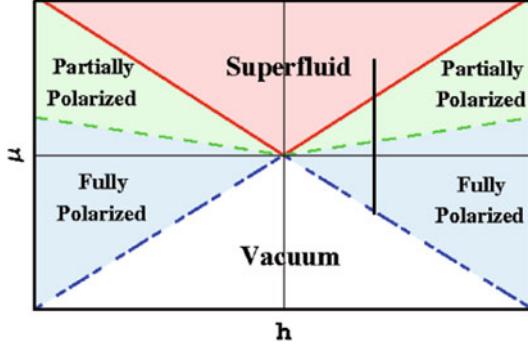
Fig. 12.4 The $\mu - h$ phase diagram. The first order phase transition is indicated by a *continuous line* and where we report also the second order transition between the mixed normal phase and the fully polarised gas. The straight *black line* are the phases present in the trapped gas. The total chemical potential μ decreases moving outward in the trap, while h is constant and fixed by the polarization P. If P is not too large one has a superfluid in the center of the trap, then a normal mixed phase and eventually a fully polarised Fermi gas of the majority atoms

$$\mu_\uparrow^0 = \left(\epsilon(x) - \frac{3}{5}x\epsilon'(x)\right)\frac{\hbar^2}{2m}(6\pi^2 n_\uparrow)^{2/3} + V(\mathbf{r}), \qquad (12.17)$$

$$\mu_\downarrow^0 = \frac{3}{5}\epsilon'(x)\frac{\hbar^2}{2m}(6\pi^2 n_\uparrow)^{2/3} + V(\mathbf{r}), \qquad (12.18)$$

in the region occupied by the normal phase. The value of $\mu_\uparrow^0$ and $\mu_\downarrow^0$ are determined, as usual, by fixing the number of atoms $N_\uparrow$ and $N_\downarrow$. The border between the superfluid and the normal phase region is given by the locus of points $\mathcal{R}$ satisfying

$$\frac{\mu_\downarrow^0 - V(\mathcal{R})}{\mu_\uparrow^0 - V(\mathcal{R})} = \eta_c. \qquad (12.19)$$

In a spherical trap ($\omega_x = \omega_y = \omega_z = \omega_0$) we can identify $\mathcal{R}$ with the radius of the superfluid, R_S. The first result one can get is the critical polarization above which the superfluid disappears from the trap. It happens when the density ratio in the centre of the trap is equal to the critical value x_c. It turns out that $P_c = 0.77$ and this prediction is in very good agreement with experiments. An even stronger test for the theory is the direct comparison of the density profiles, which can be obtained experimentally via the so called Abel transform [44]. In Fig. 12.5 we show the comparison between theory and experiment. The agreement is extremely good and the jump in going from the equal density superfluid to the mixed normal phase is evident and in agreement with the CC limit $x_c \simeq 0.44$.

A deeper insight in the density profiles and a link with the single polaron problem can be obtained by solving Eqs. 12.17 and 12.18 in the high polarisation case, i.e., $N_\uparrow \gg N_\downarrow$. To the leading order in x, we get

Fig. 12.5 Density profiles
for a polarization $P = 44\%$.
Theory: *solid black line*
(*dashed red line*) is the
spin-↑ (spin-↓) density.
Experiment: the *black* (*red*)
line is the spin-↑ (spin-↓)
density as reported in [10].
The density jump in the ↓
component is clearly visible
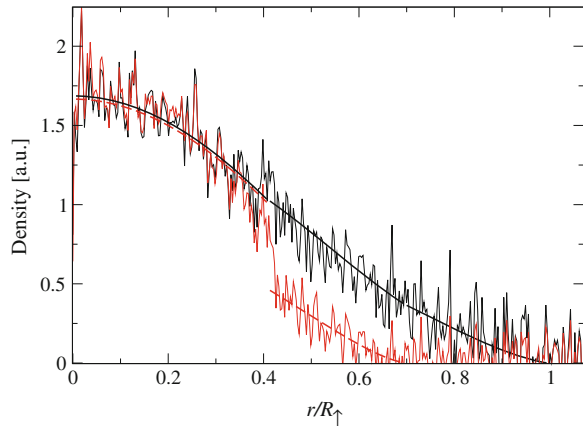
$$\mu_\uparrow^0 = \frac{\hbar^2}{2m}(6\pi^2 n_\uparrow)^{2/3} + V(\mathbf{r}), \tag{12.20}$$

$$\mu_\downarrow^0 + \frac{3}{5}A\mu_\uparrow^0 = \frac{\hbar^2}{2m^*}(6\pi^2 n_\downarrow)^{2/3} + V(\mathbf{r})\left(1 + \frac{3}{5}A\right), \tag{12.21}$$

yielding the non-interacting value $\mu_\uparrow^0 = (6N_\uparrow)^{1/3}\hbar\omega_0$ for the chemical potential of
the majority component. The above equations show that both the majority and the
minority components have an ideal Fermi gas profile, the latter being described by a
renormalised mass m^* and feeling a renormalised external potential. The radius of
the minority component is hence quenched by the interaction to the value

$$R_\downarrow = R_\downarrow^0 \left[\frac{m^*}{m}\left(1 + \frac{3}{5}A\right)\right]^{-1/4}, \tag{12.22}$$

where $R_\downarrow^0 = (48N_\downarrow)^{1/6}\sqrt{\hbar/(m\omega_0)}$ is the Thomas-Fermi radius of the ideal Fermi
gas. These results are easily understood in terms of the effective single quasi-particle
Hamitonian (12.6).

12.3.3 Different Mass Case: Fermi Mixture

The analysis developed in the previous sections can be extended to Fermi mixtures,
where the two spin species correspond to different atoms, as, e.g., $^6\text{Li} - ^{40}\text{K}$ [45, 46].
We will focus mainly on the unitarity regime. Since we are interested in describing
the normal phase of the system, we assume again that the only two possible phases
are an unpolarised superfluid and a mixed normal phase [47], whose description is

based on the polaron concept. The calculation of the polaron parameters is the same as the one explained in Sect. 12.2 just with the impurity mass $m_\downarrow$ different from the mass $m_\uparrow$ of the atoms forming the bath. In this case we have a new parameter given by the mass ratio $r = m_\downarrow/m_\uparrow$.

Let us here make two remarks on the polaron energy. First of all there exists an approximate easy expression for the binding energy as a function of $k_F a$ and r, which is obtained in the limit for large ratio $\rho = |\mu_\downarrow|/\mu_\uparrow$ [23]

$$\frac{1}{k_F a} = \sqrt{\frac{\rho r}{1+r}} - \frac{2}{3\pi}\frac{1+r}{\rho r}, \tag{12.23}$$

Althuogh it has been obtained in the large ρ limit, the above expression (i) recovers the weakly interacting result (12.2) (with the proper reduced mass), (ii) is in pretty good agreement with the known value at unitarity where it reads $\rho = (1+1/r)(2/3\pi)^{2/3}$ and (iii) recovers the correct two-body binding energy $\rho = (1+1/r)(1/k_F a)^2$ for small positive-a. Second, the infinite mass ratio case admits an exact solution. Indeed, since the impurity is static in this case we can use the Fumi's theorem [48] which relates the impurity energy to an integral over the phase shifts δ_l of the scattering states of the atoms in the bath:

$$\mu_\downarrow = -\frac{\hbar^2}{m\pi}\int_0^{k_F} k \sum_l \delta_l(k)dk. \tag{12.24}$$

For low energy atoms only s-wave phase shifts are relevant and $\tan(\delta_0(k)) = -ka$. From (12.24) we get

$$\rho = \frac{1}{\pi}\left(\frac{1}{k_F a} - \left(1 + \frac{1}{(k_F a)^2}\right)\arctan(k_F a)\right). \tag{12.25}$$

In Figs. 12.6 and 12.7 the absolute value of the polaron energy and effective mass, respectively, are shown for different values of r. The main message is that the lighter is the impurity, the larger the effect of the bath on it. This behaviour is shown at unitarity in the insets, where for the polaron energy we show also the approximate result obtained from Eq. 12.23 for $k_F a \to \infty$.

Once the polaron parameters are known one can write a Landau-Pomeranchuck energy as for the equal mass case

$$\frac{E(x,\kappa)}{N_\uparrow} = \frac{3}{5}E_{F\uparrow}\left(1 - A(\kappa)x + \frac{F(\kappa)^{-1}}{\kappa}x^{5/3} + B(\kappa)x^2\right)$$
$$= \frac{3}{5}E_{F\uparrow}g(x,\kappa) \equiv \epsilon_n(x,\kappa), \tag{12.26}$$

where the term in x^2 has been added in analogy with the equal mass case, and its coefficient determined by imposing that at $x = 1$ Eq. 12.26 reduces to the energy of the normal (balanced) state Eq. 12.15. Indeed for both the unpolarised superfluid
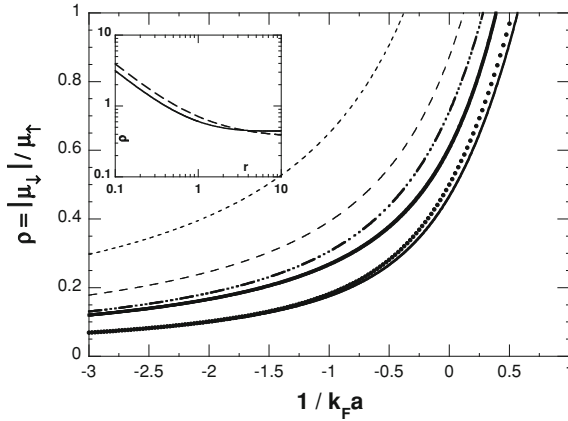
Fig. 12.6 Polaron energy as a function of $1/k_F a$ for various mass ratios r. *Black curves* from *top* to *bottom*: polaron energy for mass ratio $r = 0.25, 0.5, 1$ (*solid thick line*), and ∞ (*lower solid line*). The *dashedtriple dotted blue line* above the equal mass line is the interpolating approximation Eq. 12.23. The *dotted red line* just above the infinity mass impurity line is the exact result Eq. 12.25. The inset compares, at unitarity, the approximation Eq. 12.23 (*dashed line*) with the numerical results (*solid line*) as a function of the mass ratio r

Fig. 12.7 Relative effective mass $m^*/m_\downarrow$ as a function of $1/k_F a$ for various mass ratios r. Same conventions as in Fig. 12.6 for $r = 0.25, 0.5$, and 1. The *dashed-dotted line* is $r = 4$, and the *dashedtriple-dotted line* is $r = 10$. The inset shows the effective mass as a function of r at unitarity
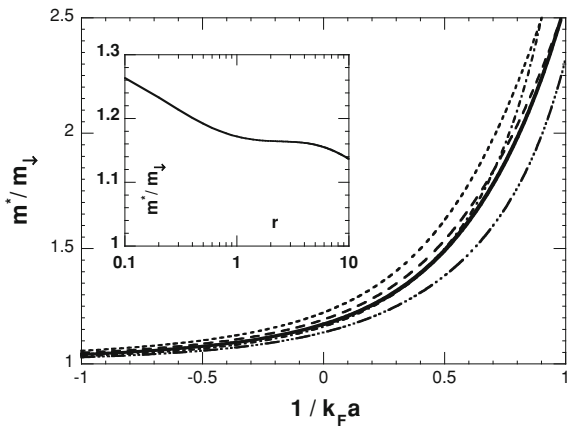
phase at unitarity and the normal $x = 1$ phase the universal parameter $\xi_{S,n}$ depends very weakly on the mass ratio once the free Fermi gas energy is expressed in terms of the reduced mass.

Following the procedure explained in Sect. 12.3 one finds the critical concentration at which the system starts nucleating a superfluid. The results are reported in Fig. 12.8. For comparison we also report the result obtained by the naive-BCS mean-field calculation, as discussed in the previous section, where the interaction in the normal phase is not taken into account and the BCS value $\xi_{S(BCS)} = 0.59$ for the superfluid phase is consistently used. Interesting enough, within the present

Fig. 12.8 Critical concentration $x_c(\kappa)$ for a homogeneous system as a function of the mass ratio κ: *upper line* is obtained using the equation of state (12.26), while the *lower dashed line* is derived from the BCS mean-field solutions at unitarity (see text)
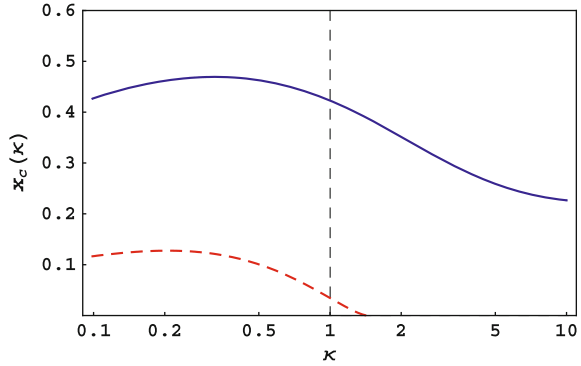
Fig. 12.9 (Color online) For $\kappa = 2.2$ the phase diagram is asymmetric. Shown are the superfluid S (*solid red lines*), partially polarized PP (*dashed green*) and fully polarized FP (*dot-dashed blue*) regions
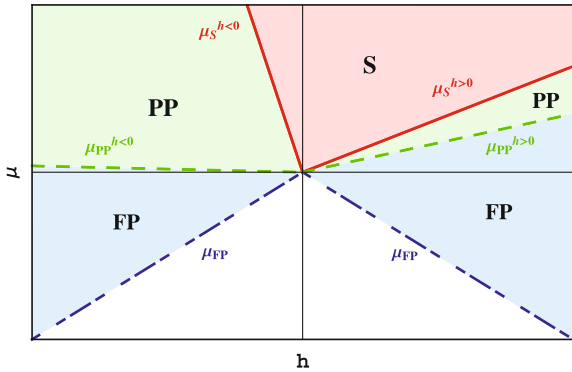
approach—and also within BCS mean-field theory—the critical concentration has a non-monotonic behaviour. The range of values is also pretty limited. It is more interesting the behaviour of the density change between the superfluid and the normal phase. For the equal mass case is given by Eq. 12.13 and it is very close to unity. For the unequal mass case Eq. 12.13 reads

$$\frac{n_\uparrow(x,\kappa)}{n_S(\kappa)} = \left(\frac{(1 + \frac{1}{\kappa})\xi_S}{g(x,\kappa)} \right)^{3/5}. \tag{12.27}$$

For instance for a mixture $^6\text{Li} -^{40}$ K with more Lithium present, i.e., $\kappa \simeq 6.67$, one has $x_c(6.67) = 0.24$ and a density jump $n_{\text{Li}}/n_S = 0.71$.

The grand-canonical phase diagram is in this case asymmetric with respect to the change $h \to -h$ and for $\kappa = 2.2$ is shown in Fig. 12.9. This feature together with the possibility to have different confinement potentials for the two atomic species, i.e., different trapping frequencies for a harmonic confinement $\omega_{i,\uparrow} \neq \omega_{i,\downarrow}$, $i = x$, y, z, allows for more available configurations for trapped gases, with respect to the homonuclear case described before [47]. Even for equal trapping potentials interesting configurations can appear. As an example here we consider the case of a $^6\text{Li} -^{40}$ K

Fig. 12.10 (Color online) **a**
Phase diagram for $\kappa = 6.7$,
corresponding to a
^{40}K $- ^6$Li mixture. **b**
Density profiles in units of
the central density of the
noninteracting ↑-gas (*dashed
line*) for $P = -0.13$. The
inset shows a zoom of the
outer superfluid-"light"
normal border
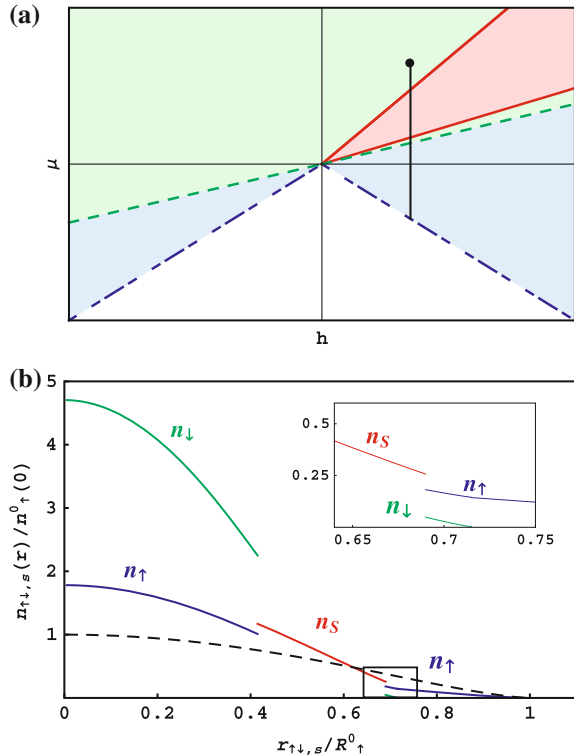
mixture. Generally if $\mu_\downarrow/\mu_\uparrow > 1/\eta_c(1/\kappa)$ the trapped system will consist of a three-shell configuration, where the superfluid is sandwiched between a "heavy" normal phase (heavy spin-↓ are the majority) at the center of the trap, and a "light" normal phase (light spin-↑ are the minority) in the outer trap region [47, 49–51].

The phase diagram and the relative density profiles of the system are shown in Fig. 12.10, for a polarization $P = -0.13$. The density jump between the superfluid and both normal phases previously discussed are clearly visible.

Another interesting case, in view of studying the normal phase of a strongly interacting Fermi mixture, is when one of the component is not trapped, but just confined due to interatomic forces as shown in Fig. 12.11.

In order to get a better insight into such configuration we can again refer to the highly unbalanced case $N_\downarrow \gg N_\uparrow$ (black solid line in Fig. 12.11a). The densities are easily found to be

$$\mu_\downarrow^0 = \frac{\hbar^2}{2m}(6\pi^2 n_\downarrow(\mathbf{r}))^{2/3} + V_\downarrow(\mathbf{r}), \tag{12.28}$$

$$\mu_\uparrow^{0'} = \frac{\hbar^2}{2m^*}(6\pi^2 n_\uparrow(\mathbf{r}))^{2/3} + V_\uparrow'(\mathbf{r}), \tag{12.29}$$

Fig. 12.11 (Color online)
No trapping for the spin-↑
component, i.e., $\omega_{\uparrow, i} = 0$
and $\kappa = 1$. **a** Phase diagram.
b Density profiles in units of
the central density of the
noninteracting gas for a
polarization $P = -0.5$
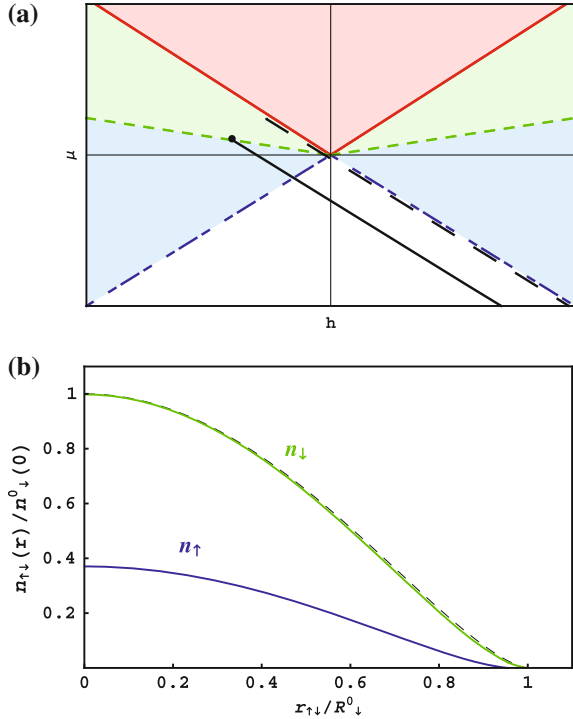
where $\mu_{\uparrow}^{0'} = \mu_{\uparrow}^{0} + \frac{3}{5}A\mu_{\downarrow}^{0}$, $V_{\uparrow}'(\mathbf{r}) = V_{\uparrow}(\mathbf{r}) + \frac{3}{5}AV_{\downarrow}(\mathbf{r})$ and $A \equiv A(\kappa = 1)$. From these equations it is clear that if $V_{\uparrow} \to 0$, the ↑-atoms feel neverthelsess the renormalized potential $\frac{3}{5}AV_{\downarrow}(\mathbf{r})$ and are confined due to the interaction with the ↓-component.

12.4 RF Spectroscopy

An invaluable tool to prepare, manipulate and probe ultracold gases is the RF spectroscopy. There have been quite a number of experimental and theoretical papers discussing it to which the reader is refer to for all the details and subtleties (see [52] and references therein). In the following we present a short digression on RF spectroscopy as a tool to probe polaron properties.

Let us consider as usual in this review that the bath and the impurity are labelled by $| \uparrow \rangle$ and $| \downarrow \rangle$, respectively, and that the RF field couples the latter with a third state $|3\rangle$ which does not interact with the bath. Since the RF field has a very long wavelength (zero momentum transferred) and is constant over the size of the atomic cloud the RF operator reads

$$\hat{O} = \hbar\Omega_R \int d^3\mathbf{x}\, \hat{\psi}_3^\dagger(\mathbf{x})\hat{\psi}_\downarrow(\mathbf{x}) + h.c., \tag{12.30}$$

where Ω_R is the Rabi frequency and $\hat{\psi}_3(\mathbf{x})$ and $\hat{\psi}_\downarrow(\mathbf{x})$ are the field operators for the atoms in the internal state $|3\rangle$ and $|\downarrow\rangle$, respectively. According to Fermi's golden rule the RF spectrum $\Gamma(\omega)$ for the system prepared in the state $|\Phi\rangle$ is

$$\Gamma(\omega) = \frac{2\pi}{\hbar} \sum_f |\langle f|\hat{O}|\Phi\rangle|^2 \delta(\hbar\omega - E_f + E_i), \tag{12.31}$$

where the sum is over all the possible final states $|f\rangle$ and ω is measured with respect to the bare frequency $\omega_{\downarrow 3}$ of the $|\downarrow\rangle \rightarrow |3\rangle$ atomic transition. The spectrum is easily calculated assuming a single impurity and the variational state Eq. 12.3. We are left with two contribution for the spectrum [17]

$$\Gamma(\omega) = 2\pi\hbar\Omega_R^2 \left[|\phi_0^p|^2 \delta\left(\hbar\omega + \epsilon_\downarrow + \frac{p^2}{2m^*} - \frac{p^2}{2m}\right) \right. \tag{12.32}$$

$$\left. + \sum_{\substack{k>k_F \\ q<k_F}} |\phi_{\mathbf{q}k}^p|^2 \delta\left(\hbar\omega + \epsilon_\downarrow + \frac{p^2}{2m^*} - \epsilon_{\uparrow k} + \epsilon_{\uparrow q} - \epsilon_{\downarrow\mathbf{p}+q-k}\right) \right], \tag{12.33}$$

where $\epsilon_\downarrow$ is the single polaron energy. The first contribution is a delta-peak at $\epsilon_\downarrow - (1 - m/m^*)p^2/2m$ [34], i.e., at the polaron rest energy plus the contribution due to the fact that the effective mass is different from the bare one, and with a weight given by the quasi-particle residue $|\phi_0^p|^2 = Z_p$. Since $\epsilon_\downarrow < 0$ the RF field has to supply additional energy for the transition to occur with respect to the bare one $\hbar\omega_{\downarrow 3}$. The second term instead consists of a continuum of frequencies. Such a structure is typical in Landau theory of Fermi liquids. Indeed for free particles one has only the first term, since the spectral function is simply a delta function. For an interacting Fermi system the spectral function of a quasi-particle in the limit of infinite life-time can be written as a coherent delta-function term plus an incoherent part. In actual experiments one has always a finite concentration of the minority component and, due to the effective mass this leads to a broadening of the delta peak. Indeed, as we have seen in the previous sections, the system can be described as a free Fermi gas of polarons. The spectrum is then just the sum of the single polaron spectrum (12.33). The coherent part reads [17]

$$\Gamma^{\text{coh}}(\omega) = 2\pi\hbar\Omega_R^2 \sum_{p<k_{F\downarrow}} |\phi_0^p|^2 \delta\left(\hbar\omega + \mu_\downarrow + \frac{p^2}{2m^*} - \frac{p^2}{2m}\right). \tag{12.34}$$

where $p_{F\downarrow}$ is the Fermi momentum of the minority component. Thus the spectrum starts at $\epsilon_\downarrow$ and goes again to zero at $\hbar\omega = -\epsilon_\downarrow + (1 - m/m^*)p_{F\downarrow}^2/2m$. A more detailed and refine description of the behaviour of RF-spectrum at finite concentration

can be found in, e.g., [53, 54]. The RF-spectrum measurement has been indeed carried out and in this way was possible to obtain the first observation of Fermi polaron physics with the measurement of its energy, effective mass and quasi-particle residue [17].

12.5 Collisional Properties of the Normal Phase

In the previous sections we introduced the polaron concept as an infinite life-time quasi-particle. In the same spirit we have briefly discussed the *out of phase* oscillations of the impurity with respect to the ideal Fermi gas (that are be extensively discussed in Sect. 12.6) and we extended the analysis to finite concentration. We considered the system as being perfectly collisionless, by assuming that the only effect of the bath is to renormalise the potential and the mass of the impurity. Generally this is not the case and when the impurity moves with a relative speed in the bath we have a damping of the counterflow determined by the rate at which momentum is transferred between the two components. Such a rate is related to the quasi-particle scattering amplitude which, in the weakly interacting regime, is proportional to the scattering length a. In the strongly interacting case one expects that the system is more easily in a collisional (hydrodynamic) regime. At finite temperature even the polaron at rest has a finite life-time since real collisions can take place. A finite life-time changes the delta-peak in the coherent part of the spectral function to just a function peaked around the polaron energy and, thus, it could be extracted from RF measurements as described in the previous Section.

In this section we use the concepts of Fermi liquid theory to describe the scattering amplitude and the momentum relaxation time (see e.g., [55]). The elementary excitations of our system are quasi-particles with effective mass $m^*_\downarrow$. We take the minority component to have a mean velocity $\mathbf{v}$ with respect to the majority component corresponding to a total momentum per unit volume $\mathbf{P}_\downarrow = n_\downarrow m^*_\downarrow \mathbf{v}$.

We define the momentum relaxation time τ_P by the relation

$$\frac{d\mathbf{P}_\downarrow}{dt} = -\frac{\mathbf{P}_\downarrow}{\tau_P}. \tag{12.35}$$

and calculate τ_P by assuming that both components are in thermal equilibrium. Introducing the single particle energies $\epsilon_{\mathbf{p}'\uparrow} = p'^2/2m_\uparrow$ and $\epsilon_{\mathbf{p}\downarrow} = p^2/2m^*_\downarrow$ the thermal equilibrium is described by the distribution functions $n_{\mathbf{p}'\uparrow} = f[\beta(\epsilon_{\mathbf{p}'\uparrow} - \mu_\uparrow)]$ and $n_{\mathbf{p}\downarrow} = f[\beta(\epsilon_{\mathbf{p}\downarrow} - \mathbf{p}\cdot\mathbf{v} - \mu_\downarrow)]$ with $\beta = 1/k_B T$ and where $f(x) = 1/(e^x + 1)$ is the Fermi distribution function. The term $\mathbf{p}\cdot\mathbf{v}$ boosts the $\downarrow$-atom distribution function by a velocity $\mathbf{v}$. The momentum of the impurities changes due to collisions with the majority atoms according to

$$\mathbf{p}\downarrow + \mathbf{p}'\uparrow \longrightarrow (\mathbf{p} - \mathbf{q})\downarrow + (\mathbf{p}' + \mathbf{q})\uparrow \tag{12.36}$$

If we call U the momentum independent scattering amplitude for such a process the rate of change of the minority momentum may be written as

$$\frac{d\mathbf{P}\downarrow}{dt} = -\frac{2\pi|U|^2}{V^3} \sum_{\mathbf{p},\mathbf{p}',\mathbf{q}} \mathbf{p}[n_{\mathbf{p}\downarrow}n_{\mathbf{p}'\uparrow}(1-n_{\mathbf{p}-q\downarrow})(1-n_{\mathbf{p}'+q\uparrow})$$

$$- n_{\mathbf{p}-q\downarrow}n_{\mathbf{p}'+q\uparrow}(1-n_{\mathbf{p}\downarrow})(1-n_{\mathbf{p}'\uparrow})]\delta(\epsilon_{\mathbf{p}\downarrow} + \epsilon_{\mathbf{p}'\uparrow} - \epsilon_{\mathbf{p}-q\downarrow} - \epsilon_{\mathbf{p}'+q\uparrow}), \tag{12.37}$$

where V is the volume of the system. The second term on the right hand side of (12.37) correspond to the inverse of the process (12.36).

The effective interaction U may be estimated from thermodynamic arguments. Since the momenta of the $\downarrow$-atoms are assumed to be much less than the Fermi momentum of the $\uparrow$-atoms, the quasiparticle interaction may be taken to be independent of the angle between the quasiparticle momenta. To estimate the scattering amplitudes in terms of Landau parameters it is generally necessary to allow for additional processes due to screening by particle–hole pairs [56]. However, since we assume that $n_\downarrow \ll n_\uparrow$, these processes may be neglected, and we take the scattering amplitude to be independent of the direction of the momenta of the quasiparticles and equal to the Landau quasiparticle interaction averaged over the angle between the momenta of the two quasiparticles, i.e., $U = f^0_{\uparrow\downarrow}$ in the standard notation of Landau Fermi liquid theory. The latter may be determined from the energy as a function of the densities of the two components:

$$U = f^0_{\uparrow\downarrow} = \frac{\partial^2 E(x)/V}{\partial n_\uparrow \partial n_\downarrow} = \frac{\partial \mu_\downarrow}{\partial n_\uparrow} \longrightarrow U = \frac{2\pi^2}{m_\uparrow k_{\mathrm{F}\uparrow}}\gamma, \tag{12.38}$$

where $E(x)$ is the energy (12.10) of the polarised system, $k_{\mathrm{F}\sigma} = (6\pi^2 n_\sigma)^{1/3}$ and we define

$$\gamma = -\frac{3}{5}A\left(1 + \frac{3n_\uparrow}{2A}\frac{\partial A}{\partial n_\uparrow}\right). \tag{12.39}$$

For the case of a resonant interaction, $\gamma = -3/5A$ and $U = -(6\pi^2 A/5)/(m_\uparrow k_{\mathrm{F}\uparrow})$. This is very different from the effective interaction at low densities (weak interacting case), which is proportional to a. The previous result tell us already that there exists a range of temperature for which the unitary polarised Fermi gas is collisionless.

It is convenient to rewrite the expression (12.37) in terms of response function. By introducing the quantity $\omega_{\mathbf{q}} = \mathbf{q}\cdot\mathbf{v}$, using the relation $n_{\mathbf{p}}(1-n_{\mathbf{p}-\mathbf{q}}) = (n_{\mathbf{p}} - n_{\mathbf{p}-\mathbf{q}})/\{1 - \exp[\beta(\epsilon_{\mathbf{p}} - \epsilon_{\mathbf{p}-\mathbf{q}})]\}$, and taking the continuum limit we obtain

$$\frac{d\mathbf{P}\downarrow}{dt} = -|U|^2 \int \frac{d^3q\,\mathbf{q}}{(2\pi)^2} \int_{-\infty}^{\infty} d\omega \frac{\mathrm{Im}\chi_\downarrow(q,\omega_{\mathbf{q}}\omega)\mathrm{Im}\chi_\uparrow(q,\omega)}{(1 - e^{\beta(\omega-\omega_{\mathbf{q}})})(1 - e^{-\beta\omega})}, \tag{12.40}$$

where

$$\mathrm{Im}\,\chi_\sigma(q,\omega) = \int \frac{d^3p}{(2\pi)^3}(n_{\mathbf{p}\sigma} - n_{\mathbf{p}+\mathbf{q}\sigma})\delta(\omega + \epsilon_{\mathbf{m}\sigma} - \epsilon_{\mathbf{p}+\mathbf{q}\sigma}) \tag{12.41}$$

is, apart from a factor of π, the imaginary part of the Lindhard function, and the distribution functions are now global equilibrium ones without the boost for the down-atoms.

12.5.1 $T = 0$

Let us start by considering the zero-temperature momentum relaxation rate. Due to the Bose factors in (12.40) one has the condition $0 \le \omega \le \omega_{\mathbf{q}}$. Depending on the ratio between the momentum of the minority cloud and its Fermi momentum, i.e., $m_{\downarrow}^* v / k_{F\downarrow}$, it is possible to distinguish two important limiting regimes for which simple expressions for τ_P can be obtained.

12.5.1.1 Low Velocity Regime, $m_{\downarrow}^* v \ll k_{F\downarrow}$

In this case the significant contribution to (12.40) comes from $q \le 2k_{F\downarrow}$ with a small energy transfer $\omega_{\mathbf{q}} \ll k_{F\downarrow}^2 / 2m_{\downarrow}^*$ We can then use $\mathrm{Im}\chi_{\sigma}(q, \omega) = m_{\sigma}^{*2}\omega / (4\pi^2 q)$ and the resulting integrals in (12.40) yield

$$\frac{1}{\tau_P} = \frac{4\pi}{25}|\gamma|^2 \left(\frac{k_{F\downarrow}}{k_{F\uparrow}}\right)^2 m_{\downarrow}^* v^2 = \frac{4\pi}{25}\frac{1}{\tau_0}\left(\frac{m_{\downarrow}^* v}{k_{F\downarrow}}\right)^2, \qquad (12.42)$$

where $1/\tau_0 = |\gamma|^2 k_{F\downarrow}^4 / m_{\downarrow}^* k_{F\uparrow}^2$.

12.5.1.2 High Velocity Regime, $k_{F\downarrow} \ll m_{\downarrow}^* v \ll k_{F\uparrow}$

In this case we can again carry out the integrations in (12.40) and obtain

$$\frac{1}{\tau_P} = \frac{2\pi}{35}|\gamma|^2 \frac{m_{\downarrow}^{*3} v^4}{k_{F\uparrow}^2} = \frac{2\pi}{35}\frac{1}{\tau_0}\left(\frac{m_{\downarrow}^* v}{k_{F\downarrow}}\right)^4. \qquad (12.43)$$

More generally, the scaled relaxation time $\tilde{\tau}_P \equiv \tau_P / \tau_0$ depends only on the variable $\tilde{v} = m_{\downarrow}^* v / k_{F\downarrow}$ provided $m_{\downarrow}^* v \ll k_{F\uparrow}$ and its dependence, aside from the prefactors, is the same as the one obtained for a (balanced) neutral Fermi liquid (see, e.g., [55]).

12.5.2 $T \ne 0$

We now turn to non-zero temperature. Although current experiments on polarised gases achieve very low temperatures in the highly polarised case it can happen that

the actual temperature is much smaller than the larger Fermi temperature, related to the majority component, but still of the same order or larger than the smaller one, related to the polaron gas. In the following we analyse only the case when both components are degenerate, i.e., $T \ll T_{F\downarrow} \ll T_{F\uparrow}$ with $k_B T_{F\downarrow} = k_{F\downarrow}^2/2m_\downarrow^*$ and $k_B T_{F\uparrow} = k_{F\uparrow}^2/2m_\uparrow$. For a discussion on the high-temperature and intermediate regimes the reader can consult Ref. [57].

For small relative velocities, $v k_{F\downarrow} \ll kT$, it is sufficient to expand the integrand in (12.40) to first order in $\beta\omega_{\mathbf{q}}$. Using the symmetry property $\mathrm{Im}\chi_\sigma(q,\omega) = -h\chi_\sigma(q,-\omega)$ we obtain

$$\frac{d\mathbf{P}\downarrow}{dt} = -\mathbf{v}\frac{\pi |U|^2}{3kT} \int \frac{d^3 q}{(2\pi)^3} q^2$$
$$\times \int_{-\infty}^{\infty} d\omega \frac{\mathrm{Im}\chi_\downarrow(q,-\omega)\mathrm{Im}\chi_\uparrow(q,\omega)}{(1-e^{\beta\omega})(1-e^{-\beta\omega})}. \tag{12.44}$$

Since $T \ll T_{F\downarrow}$, we can again use the result $\mathrm{Im}\chi_\sigma(q,\omega) = m_\sigma^{*2}\omega/(4\pi^2 q)$ which yields for the relaxation rate in the limit of low velocities the expression

$$\frac{1}{\tau_P} = \frac{4\pi^3}{9}|\gamma|^2 \frac{m_\downarrow^*}{k_{F\uparrow}^2}(kT)^2 = \frac{\pi^3}{9}\frac{1}{\tau_0}\left(\frac{T}{T_{F\downarrow}}\right)^2. \tag{12.45}$$

The T^2-dependence is due to the fact that the phase space for scattering increases with temperature and it is also the same as for a Fermi liquid [55]. Equation (12.45) shows that for equal masses of the two components and at unitarity $1/\tau_P \sim kT^2/T_{F\uparrow}$, as one would expect on dimensional grounds because the effective interaction measured in terms of the density of states of the up-atoms is of the order of unity.

12.5.3 Experimental Consequences for Collective Modes

The previous sections considered the momentum relaxation time for a homogeneous gas. In this section we study the possible consequences on experiments devoted to measure collective mode frequencies in harmonically confined systems. For the sake of concreteness let us analyse the spin dipole mode of a Fermi gas above the critical polarisation where, as previously discussed, the system is normal. We assume that the cloud of minority atoms is displaced by a distance δX from the centre equilibrium position in the harmonic trap. Depending on the amplitude of the displacement (and consequently on the velocity acquired by the minority component due to the external force) as well as on the value of temperature, the cloud either oscillates with weak damping around $\delta X = 0$ (collisionless regime) or it relaxes towards equilibrium without any oscillations (hydrodynamic regime).

In the collisionless limit $\omega_D \tau_P \gg 1$ the dipole mode is well defined and its frequency ω_D can be derived within Landau theory of Fermi liquid (see Sect. 12.6).

Fig. 12.12 The quantity $1/\omega_0\tau_P$ determining the damping of the dipole mode as a function of the amplitude of the oscillation for $T = 0$ and $T = 0.03T_{F\uparrow}$ (For details see text.)
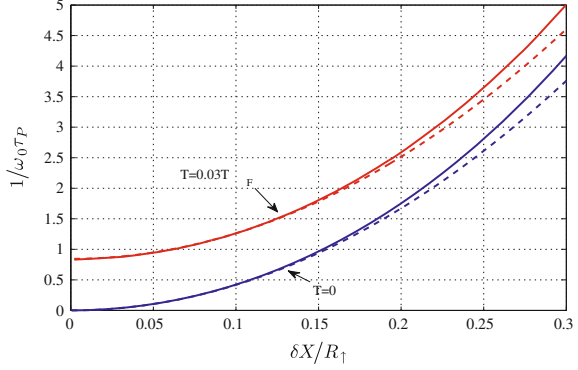
The latter coincides with (12.8) in the extreme imbalance case. The mode becomes over-damped in the hydrodynamic regime $\omega_D\tau_P \ll 1$ since the spin current is not conserved by collisions [58].

In order to estimate $\omega_D\tau_P$ we assume that the displacement of the $\downarrow$-atom cloud is sufficiently small with respect to the majority cloud size, $R_\uparrow$, i.e., we consider $\delta X \ll R_\uparrow$, such that the density of $\uparrow$-atoms may be regarded as uniform when estimating the relaxation rate. Moreover we consider that both component are degenerate and a highly polarised case such that the majority cloud remains essentially at rest during the motion of minority component. The relative velocity of the two components is in this case given by $v = \omega_D\delta X$. Within our assumption we can use the low-speed Eq. 12.42 and low-temperature Eq. 12.45 results which, expressed in terms of the new quantities, read

$$\frac{1}{\omega_0\tau_P} = \frac{81\pi}{25^2}(6N_\uparrow)^{1/3}A^2\frac{m_\downarrow^*}{m_\uparrow}\left(\frac{T_{F\downarrow}}{T_{F\uparrow}}\right)^2\left(\frac{\delta X}{R_\uparrow}\right)^2, \tag{12.46}$$

$$\frac{1}{\omega_0\tau_P} = \frac{2\pi^3}{25}(6N_\uparrow)^{1/3}A^2\frac{m_\downarrow^*}{m_\uparrow}\left(\frac{T}{T_{F\uparrow}}\right)^2, \tag{12.47}$$

respectively, where we have used the result $\gamma = -3/5A$ for a resonant interaction, the fact that $kT_{F\uparrow} = k_{F\uparrow}^2/2m_\uparrow = (6N_\uparrow)^{1/3}\omega_0$ and that ω_D is close to ω_0.

In Fig. 12.12 we report the full result for the relaxation time of the dipole mode at zero (lower full line) and finite (upper full line) temperature using the values $N_\uparrow = 10^7$, and $N_\downarrow/N_\uparrow = 0.026$ (correspondingly $T_{F\downarrow}/T_{F\uparrow} = 0.3$) which are the conditions achieved in the MIT experiment [9] for a mixture of ^{6}Li-atoms in two different hyperfine states. The lower dashed line is the expression (12.46), while the upper dashed line is the sum of the results (12.46) and (12.47) in the spirit of Landau theory [55]. We see that the analytical results are a good approximation to those obtained by direct numerical integration in the regimes of experimental interest.

The calculated values of $\omega_0\tau_P$ demonstrate that, for the experimental conditions now attainable, the polarised normal phase is easily in a regime intermediate between

collisionless and hydrodynamic behaviour, implying significant damping of the spin dipole mode. At lower temperature, the gas enters the collisionless regime. Indeed such behaviour has been experimentally seen at ENS as reported in [13] (see also Sect. 12.6).

How important collisions are in a given mode is sensitive to the anisotropy of the trap, which we have neglected so far. For instance, cigar-shaped trap ($\omega_z < \omega_\perp$) the transverse mode will be more collisionless, the value of $1/\omega_D \tau_P$ being multiplied by a factor $\omega_z/\omega_\perp$ for a fixed value of τ_P and by a factor $(\omega_z/\omega_\perp)^{1/3}$, for a fixed value of the trapping frequency geometric average $(\omega_\perp^2 \omega_z)^{1/3}$. When the two atomic species are different, the value of $\omega_0 \tau_P$ will be depend on the trapping potentials of the two species, which can be varied independently of each other.

For low velocity, $m_\downarrow^* v \ll k_{F\downarrow}$, one sees from (12.42) and (12.45) that the momentum relaxation rate scales as $m_\downarrow^*$. Consequently, since $m_\downarrow^* \approx m_\downarrow$ the spin motion can be made more collisionless by trapping an atom mixture with a lighter minority component. However, calculations indicate that this effect is reduced due to the fact that, at unitarity, the scattering amplitude for the case of extreme imbalance increases with decreasing $m_\downarrow/m_\uparrow < 1$ [23]. For $m_\downarrow/m_\uparrow > 1$ the scattering amplitude is predicted to be approximately constant and therefore $1/\tau_P \propto m_\downarrow$ in this regime. Thus, the spin motion becomes more hydrodynamic for $m_\downarrow/m_\uparrow > 1$.

12.6 Collective Oscillations: The Quadrupole Mode

We have seen that there exists a very good agreement between experiments and the theory developed for the polarised normal phase, when static properties are considered. The theory is essentially based on Landau theory of Fermi liquid, which was built mainly for describing dynamical properties of an interacting Fermi system. Thus a crucial question is whether Landau theory is applicable to the dynamics of strongly interacting normal Fermi gases. In the previous sections we have practically considered only the single particle *out of phase* motion. The aim of the present section is to study the collective mode frequencies of the unitary normal phase as a function of the polarisation. To this purpose we develop the proper Landau formalism to describe the collisionless regime of the polarised Fermi gas.

We face the problem by a lagrangian variational principle to derive the collective modes in the collisionless regime. Such a method has been widely used in nuclear physics to describe collective excitations in an elastic theory of nuclei (see e.g., [59] and reference therein). The variational principle $\delta S = 0$ is applied to the action integral

$$
\begin{aligned}
S &= \int dt \langle \Psi | H - i\hbar\partial_t | \Psi \rangle \\
&= \int dt (E - \langle \Psi | i\hbar\partial_t | \Psi \rangle),
\end{aligned} \tag{12.48}
$$

where $|\Psi\rangle$ is a multi-parameter many-body wave-function and $E = \langle\Psi|H|\Psi\rangle$ is the energy functional of the system. The latter on the basis of the Landau-Pomeranchuk energy (12.10) can be written in the form

$$E = \sum_\sigma \int d\mathbf{x} \left(\frac{\tau_\sigma}{2m} + \frac{m}{2}(\omega_\perp^2 r^2 + \omega_z^2 z^2)n_\sigma \right)$$

$$+ \frac{3}{5}A\frac{\hbar^2(6\pi^2)^{2/3}}{2m}\int d\mathbf{x}n_\downarrow n_\uparrow^{2/3} + a\int d\mathbf{x}\left(\frac{\tau_\downarrow}{2m} - \frac{n_\downarrow}{2m}\frac{j_\uparrow^2}{n_\uparrow^2} \right), \quad (12.49)$$

where $\tau_\sigma/2m$ is the kinetic energy density of the species σ. The functional (12.49) accounts for the interaction between the majority and the minority component through the local term in A and the last integral, which is necessary in order to keep into account that the polarons ($\downarrow$-particles) acquires an effective mass due to interaction effects and that galilean invariance implies the presence of a counter current term $j_\uparrow^2$ of the majority component. We include the latter term for completeness, although, since the effective mass is just $10-20\%$ larger than the bare one, the effect of the current term on the frequencies turns out to be fairly small. Expression (12.49) corresponds to a typical energy functional to be used in time-dependent Hartree-Fock approaches in the context of small amplitude and low energy oscillations. It is worth noticing that this approach is equivalent to Landau's theory of Fermi liquid.

At equilibrium the kinetic energy density in Eq. 12.49 reduces to $\tau_\sigma = \hbar^2(6\pi^2 n_\sigma)^{2/3}n_\sigma$ and $j_\uparrow = 0$ and, thus, the energy functional Eq. 12.49 can be used to calculate the density profiles using standard variational procedures. The calculation at equilibrium shows that at very high polarization the majority component is scarcely affected by the interaction and, in particular, its radius is in practice given by the ideal gas value

$$R_{\uparrow,i}^0 = (48N_\uparrow)^{1/6}\sqrt{\frac{\hbar\bar{\omega}}{m\omega_i^2}}, \quad i = x, \; y, \; z \quad (12.50)$$

with $\bar{\omega}^3 = \omega_x\omega_y\omega_z$. Instead the radius of the minority component is quenched with respect to the non interacting gas due to the attractive nature of the force. By taking a Thomas-Fermi description for the minority component (which holds with good accuracy for a large class of experimentally available configurations), one finds that the radius of the minority component is given by the simple expression

$$R_\downarrow/R_\uparrow^0 = \left(\frac{1-P}{1+P} \right)^{1/6}\left(\left(1 + \frac{3}{5}A\right)\frac{m^*}{m} \right)^{-1/4}. \quad (12.51)$$

From Eq. 12.51 it is seen that the minority radius is quite flat as a function of P except at very high polarization when it goes to zero as the inset of Fig. 12.13 shows. We find that this behavior is reflected in the collective mode frequencies.

The proper variational ansatz for the wave function depends on the modes we want to study. We focus on the compressional modes, since the easiest experimental
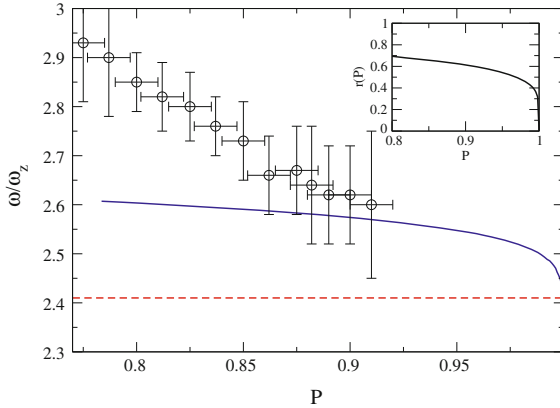
Fig. 12.13 Frequency of the axial compressional mode as a function of the polarization P. *Dashed line*: the single polaron mode frequency. *Solid line*: the collisionless value of the mode frequency obtained via the variational principle described in the present work. Points: experimental data reported in [13]. Inset: the behaviour of the minority radius as a function of P, $r(P) = ((1 - P)/(1 + P))^{1/6}$ (see (12.51))

way of exciting the spin modes in trapped Fermi gases is through a sudden change of the value of scattering length. This procedure, which mainly affects the motion of the impurities, is not able to excite other important oscillations like, e.g., the dipole mode of the minority component and it is the actual procedure employed in the recent experiment reported in Ref. [13]. The starting point are variational single-particle wavefunctions that are then used to built the many-body state as a Slater determinant. In order to study the compressional modes and assuming that the equilibrium configuration is axially symmetric we write the scaling transformation

$$\psi_\sigma(r, z, t) = e^{-1/2(2\alpha_\sigma + \beta_\sigma)} \psi_\sigma^0(e^{-\alpha_\sigma} r, e^{-\beta_\sigma} z) e^{i(\chi_\sigma r^2 + \xi_\sigma z^2)}. \tag{12.52}$$

applied to the single particle wave-functions ψ_σ of the two spin species $\sigma = \uparrow, \downarrow$, and where $r^2 = x^2 + y^2$ and z are the radial and the axial coordinate, respectively. The scaling transformation depends on $4 + 4$ time-dependent parameters and the corresponding equations are obtained by imposing the variation $\delta S = 0$ with S as in (12.48) with $\langle \Psi | H | \Psi \rangle$ given by Eq. 12.49. With respect to a typical hydrodynamic energy functional, Eq. 12.49 accounts for the deformation of the Fermi surface produced by the scaling ansatz. This effect arises from the kinetic energy density term τ_σ and exploits the elastic nature exhibited by a Fermi liquid in the collisionless regime. The use of hydrodynamic theory would actually yield wrong predictions for the oscillations of these Fermi gases.

The collective modes are small oscillations around equilibrium, i.e., solutions of the equations of motion derived from the action expanded to second order in the scaling parameters. The first order expansion of the action S with respect to the scaling parameters takes contribution only from the energy functional Eq. 12.49. Then, the

condition $\delta S = 0$ provides a relation between the kinetic and the interaction energy equivalent to the virial theorem. Defining the effective mass as $m/m^* = (1+a)$ and the averages $N_\sigma \langle f \rangle_\sigma = \int f(r,z) n_\sigma(r,z)$, we obtain

$$-\frac{4}{3} \int \frac{\tau_\uparrow}{2m} + N_\uparrow m\omega_\perp^2 \langle r^2 \rangle_\uparrow - N_\downarrow \frac{\hbar^2 (6\pi^2)^{2/3}}{2m} A \left(\langle r\partial_r n_\uparrow^{2/3} \rangle_\downarrow + \frac{4}{3} \langle n_\uparrow^{2/3} \rangle_\downarrow \right) = 0,$$

$$-\frac{2}{3} \int \frac{\tau_\uparrow}{2m} + N_\uparrow m\omega_z^2 \langle z^2 \rangle_\uparrow - N_\downarrow \frac{\hbar^2 (6\pi^2)^{2/3}}{2m} A \left(\langle z\partial_z n_\uparrow^{2/3} \rangle_\downarrow + \frac{4}{3} \langle n_\uparrow^{2/3} \rangle_\downarrow \right) = 0,$$

$$-\frac{4}{3} \int \frac{\tau_\downarrow}{2m^*} + N_\downarrow m\omega_\perp^2 \langle r^2 \rangle_\downarrow + N_\downarrow \frac{\hbar^2 (6\pi^2)^{2/3}}{2m} A \langle r\partial_r n_\uparrow^{2/3} \rangle_\downarrow = 0,$$

$$-\frac{2}{3} \int \frac{\tau_\downarrow}{2m^*} + N_\downarrow m\omega_z^2 \langle z^2 \rangle_\downarrow + N_\downarrow \frac{\hbar^2 (6\pi^2)^{2/3}}{2m} A \langle z\partial_z n_\uparrow^{2/3} \rangle_\downarrow = 0, \qquad (12.53)$$

where all the densities are to be calculated at equilibrium. Note that in the low-concentration or high polarisation limit $N_\downarrow/N_\uparrow \to 0$ Eq. 12.53 decouples and one recover correctly the result for the free polaron case. Defining $E_{K\sigma}$ the kinetic energy of the σ-component (including the mass m^* for the minority spin-$\downarrow$ component), Eq. 12.53 becomes the standard virial theorem for the majority component

$$-\frac{2}{3} E_{K\uparrow} + N_\uparrow m\omega_\perp^2 \langle r^2 \rangle_\uparrow = 0, \qquad (12.54)$$

$$-\frac{1}{3} E_{K\uparrow} + N_\uparrow m\omega_z^2 \langle z^2 \rangle_\uparrow = 0 \qquad (12.55)$$

and the virial theorem for a free gas of particles of mass m^* feeling an effective potential for the minority component

$$-\frac{2}{3} E_{K\downarrow} + N_\downarrow m\omega_\perp^2 \left(1 + \frac{3}{5} A \right) \langle r^2 \rangle_\downarrow = 0, \qquad (12.56)$$

$$-\frac{1}{3} E_{K\downarrow} + N_\downarrow m\omega_z^2 \left(1 + \frac{3}{5} A \right) \langle z^2 \rangle_\downarrow = 0. \qquad (12.57)$$

The term in the action which depends on the time derivative of the wave-function does not give rise to linear terms due to time reversal symmetry. The corresponding quadratic term reads

$$\langle \Psi | i\hbar \partial_t | \Psi \rangle^{(2)} = 2 \sum_\sigma N_\sigma (\langle r^2 \rangle_\sigma \alpha_\sigma \dot{\xi}_\sigma + \langle z^2 \rangle_\sigma \beta_\sigma \dot{\chi}_\sigma). \qquad (12.58)$$

Summing up all the contributions and imposing the variational procedure $\delta S = 0$, we get eight coupled equations of motion. Four of them represent continuity equations and are relations between the current parameters ξ_σ, χ_σ and the density ones α_σ, β_σ. In this way we are left to solve a linear system of 4 equations.

We find that the two lowest frequency are almost independent of the ratio $N_\downarrow/N_\uparrow$ and they are very close to the ideal gas values $\omega = 2\omega_\perp$ and $\omega = 2\omega_z$. We call

them the in phase modes since the majority and the minority components move in phase. The frequencies of the other two modes, that we name out of phase or spin modes, can be written as $\omega = 2C_1\omega_\perp$ and $\omega = 2C_2\omega_z$, where the renormalization factors are very close to each other, i.e., $C_1 \simeq C_2$. Such modes correspond to the radial and axial motion of the minority component moving in opposite phase with respect to the majority one. In the limit of a single impurity we recover the value $C_1 = C_2 = \sqrt{(1 + 3/5A)\, m/m^*}$ of Eq. 12.7.

In Fig. 12.13 we report (solid blue line) the result for the axial spin mode as a function of the polarisation of the system as calculated with the above described variational approach, using for the polaron parameters the values $A = 1.01$ and $m^*/m = 1.17$ [23]. We notice that at high polarisation the correction to the polaron frequency Eq. 12.7, as a function of the polarisation, follows the law $(1 - P)^{1/6}$ characterising the radius of the minority component (see inset in Fig. 12.13 and Eq. 12.51). In Fig. 12.13 we also put the experimental data of [13] and one sees that there is a qualitative difference between the present theory and the experiment [13]. A possible explanation is by invoking the collisional properties of the strongly interacting system even at the lowest achievable temperature as we have discussed in Sect. 12.5. Indeed our prediction was derived in the collisionless regime, while the experiment clearly shows that the in phase mode frequency is strongly affected by collisions even for the highest polarisation available. Understanding the discrepancy between theory and experiment in terms of collisional effects is not however obvious. In fact collisions usually reduce the value of the frequencies with respect to their collisionless values. Thus the question of how the observed frequency in Fig. 12.13 can be compared with our prediction has not an obvious answer.

The Landau theory prediction agrees better with the experimental data at the highest polarisation points, where the collisionless approximation is better satisfied as it can also be inferred from the measurement of the majority component compressional mode frequency reported in [13]. One would then expect that a measurement of the radial compressional mode, would give a much better insight into the problem, since, as we pointed out in Sect. 12.5 for a fixed relaxation time τ, if the radial frequency is much higher than the axial one, the collisions for the radial dipole mode are less effective, being $\omega_\perp \tau \gg \omega_z \tau$. As a last comment, we should remind that the energy functional (12.49) is strictly valid only at high polarization, being an expansion in the concentration $n_\downarrow/n_\uparrow$. It works however quite well when applied to investigate the static properties even till the critical concentration. For instance the inclusion of the next term proportional to $(n_\downarrow/n_\uparrow)^2$ introduces only small corrections to the values of the radii, even close to the critical polarization limit $P_C = 0.77$. Thus one can think that such a term does not change the picture previously described.

References

1. Inguscio, M., Ketterle, W., Salomon, C.: Ultracold Fermi Gases. In: Proceedings of the International School of Physics "Enrico Fermi", Course CLXIV, Varenna (2006)
2. Giorgini, S., Pitaevskii, L., Stringari, S.: Rev. Mod. Phys, **80**, 1215 (2008)
3. Bloch, I., Dalibard, J., Zwerger, W.: Rev. Mod. Phys. **80**, 885 (2008)
4. Leggett, A.J.: J. Phys. C. **41**, 7 (1980)
5. Nozieres, P., Schmitt-Rink, S.: J. Low Temp. Phys. **59**, 195 (1985)
6. Chandrasekhar, B. S.: Appl. Phys. Lett. **1**, 7 (1962)
7. Clogston, A. M.: Phys. Rev. Lett. **9**, 266 (1962)
8. Zwierlein, M.W., Schirotzek, A., Schunck, C.H., Ketterle, W.: Science **311**, 492 (2006)
9. Shin, Y., Zwirlein, M.W., Schunck, C.H., Schirotzek, A., Ketterle, W.: Phys. Rev. Lett. **97**, 030401 (2006)
10. Shin, Y., Schunck, C.H., Schirotzek, A., Ketterle, W.: Nature **451**, 689 (2008)
11. Partridge, G.B., Li, W., Kamar, R.I., Liao, Y.A., Hulet, R.G.: Science **311**, 503 (2006)
12. Partridge, G.B., Li, W., Liao, Y.A., Hulet, R.G., Haque, M., Stoof, H.T.C.: Phys. Rev. Lett. **97**, 190407 (2006)
13. Nascimbene, S., Navon, N., Jiang, K.J., Tarruell, L., Teichmann, M., McKeever, J., Chevy, F., Salomon, C.: Phys. Rev. Lett. **103**, 170402 (2009)
14. Nascimbene, S., Navon, N., Jiang, K., Chevy, F., Salomon, C.: Nature **463**, 1057 (2010)
15. Navon, N., Nascimbne, S., Chevy, F., Salomon, C.: Science **328**, 5979 (2010)
16. Lobo, C., Recati, A., Giorgini, S., Stringari, S.: Phys. Rev. Lett. **97**, 200403 (2006)
17. Schirotzek, A., Wu, C.-H., Sommer, A., Zwierlein, M. W.: Phys. Rev. Lett. **102**, 230402 (2009). Online supplemental material at http://prl.aps.org/supplemental/PRL/v102/i23/e230402
18. Mahan, G.D.: Many-Particle Physics. Kluwer Academic, Dordrecht (2000)
19. Prokofev, N.V.: Phys. Rev. Lett. **74**, 2748 (1995) (and references therein)
20. Arias de Saavedra, F., Boronat, J., Polls, A., Fabrocini, A.: Phys. Rev. B **50**, 4248 (1994) (and references therein)
21. Lifshitz, E.M., Pitaevski, L.P.: Statistical Physics Part 2. Pergamon Press, New York (1980)
22. Chevy, F.: Phys. Rev. A **74**, 063628 (2006)
23. Combescot, R., Recati, A., Lobo, C., Chevy, F.: Phys. Rev. Lett. **98**, 180402 (2007)
24. Pines, D.: The Many-Body Problem. W. A. Benjamin Inc, New York (1962)
25. Combescot, R., Giraud, S., Leyronas, X.: Eur. Phys. Lett. **88**, 60007 (2009)
26. Mora, C., Chevy, F.: Phys. Rev. A **80**, 033607 (2009)
27. Punk, M., Dumitrescu, P.T., Zwerger, W.: Phys. Rev. A **80**, 053605 (2009)
28. Prokof'ev, N., Svistunov, B.: Phys. Rev. B **77**, 020408 (2008)
29. Pilati, S., Giorgini, S.: Phys. Rev. Lett. **100**, 030401 (2008)
30. Combescot, R., Giraud, S.: Phys. Rev. Lett. **101**, 050404 (2008)
31. Giraud, S., Combescot, R.: Phys. Rev. A **79**, 043615 (2009)
32. McGuire, J.B.: J. Math. Phys. (N.Y.) **7**, 123 (1966)
33. Lipparini, E.: Modern many-particle physics: atomic gases, nanostructures and quantum liquids, 2nd edn. World Scientific Publishing Company, Singapore (2008)
34. Recati, A., Lobo, C., Stringari, S.: Phys. Rev. A **78**, 023633 (2008)
35. Mora, C., Chevy, V.: Phys. Rev. Lett. **104**, 230402 (2010)
36. Yu, Z., Zöllner, S., Pethick, C. J.: http://arxiv.org/abs/1006.4723
37. Carlson, J., Chang, S.Y., Pandharipande, V.R., Schmidt, K.E.: Phys. Rev. Lett. **91**, 050401 (2003)
38. Astrakharchik, G.E., Boronat, J., Casulleras, J., Giorgini, S.: Phys. Rev. Lett. **93**, 200404 (2004)
39. Haussmann, R., Rantner, W., Cerrito, S., Zwerger, W.: Phys. Rev. A **75**, 023610 (2007)
40. Bausmerth, I., Recati, A., Stringari, S.: Phys. Rev. Lett. **100**, 070401 (2008)
41. Bausmerth, I., Recati, A., Stringari, S.: Phys. Rev. A **78**, 063603 (2008)
42. Urban, M., Schuck, P.: Phys. Rev. A **78**, 011601(R) (2008)

43. The fact that the results obtained at RICE [10,11] showed the presence of a superfluid at any value of the polarization, i.e., of h, is still quite puzzling.
44. Bracewell, R.N.: The Fourier Transform and Its Applications. McGraw-Hill, New York (1986)
45. Wille, E. et al.: Phys. Rev. Lett. **100**, 053201 (2008)
46. Taglieber, M., Voigt, A.-C., Aoki, T., Hänsch, T.W., Dieckmann, K.: Phys. Rev. Lett. **100**, 010401 (2008)
47. Bausmerth, I., Recati, A., Stringari, S.: Phys. Rev. A **79**, 043622 (2009)
48. Fumi, F.G.: Phil. Mag. **46**, 1007 (1955)
49. Wu, S.-T., Pao, C.-H., Yip, S.-K.: Phys. Rev. B **74**, 224504 (2006)
50. Pao, C.-H., Wu, S.-T., Yip, S.-K.: Phys. Rev. A **76**, 053621 (2007)
51. Parish, M.M., Marchetti, F.M., Lamacraft, A., Simmons, B.D.: Phys. Rev. Lett. **98**, 160402 (2007)
52. Ketterle, W., Zwierlein, M.: In: Inguscio, M., Ketterle, W., Salomon, C. (eds.) Proceedings of the International School of Physics Enrico Fermi, Course CLXIV, p. 95. IOS Press, Amsterdam (2008)
53. Punk, M., Zwerger, W.: Phys. Rev. Lett. **99**, 170404 (2007)
54. Schneider, W., Shenoy, V. B., Randeria, M.: http://arxiv.org/abs/0903.3006
55. Pines, D., Noziéres. P.: Theory of Quantum Liquids Volume I: Normal Fermi Liquids. W. A. Benjamin, New York (1966)
56. Baym, G., Pethick, C.J.: Landau Fermi-liquid Theory: Concepts and Applications. Wiley, New York (1991)
57. Bruun, G., Recati, A., Pethick, C., Smith, H., Stringari, S.: Phys. Rev. Lett. **100**, 240406 (2008)
58. Vichi, L., Stringari, S.: Phys. Rev. A **60**, 4734 (1999)
59. Stringari, S.: Ann. Phys. **151**, 35 (1983)

Chapter 13
Thermodynamics of Trapped Imbalanced Fermi Gases at Unitarity

J. M. Diederix and H. T. C. Stoof

Abstract We present a theory for the low-temperature properties of a resonantly interacting Fermi mixture in a trap, that goes beyond the local-density approximation. The theory corresponds essentially to a Landau–Ginzburg-like approach that includes self-energy effects to account for the strong interactions at unitarity. We show diagrammatically how these self-energy effects arise from fluctuations in the superfluid order parameter. Gradient terms of the order parameter are included to account for inhomogeneities. This approach incorporates the state-of-the-art knowledge of the homogeneous mixture with a population imbalance exactly and gives good agreement with the experimental density profiles of Shin et al. (Nature 451:689 (2008)). This allows us to calculate the universal surface tension of the interface between the equal-density superfluid and the partially polarized normal state of the mixture. We also discuss the possibility of a metastable state to explain the deformation of the superfluid core that is seen in the experiment of Partridge et al. (Science 311:503 (2006)).

13.1 Introduction

Ultracold atom experiments are always performed in a trap to avoid contact of the atoms with the 'hot' material walls that would heat up the cloud. Due to this trapping potential the atomic cloud is never homogeneous. However, typically the energy splitting of the trap corresponds to a small energy scale, so that the inhomogeneity is not very severe. In this case, we may use the so-called local-density approximation

J. M. Diederix · H. T. C. Stoof (✉)
Institute for Theoretical Physics, Utrecht University,
Leuvenlaan 4, 3584 CE Utrecht,
The Netherlands
e-mail: H.T.C.Stoof@uu.nl

J. M. Diederix
e-mail: J.M.Diederix@uu.nl

(LDA). It physically implies that the gas is considered to be locally homogeneous everywhere in the trap. The density profile of the gas is then fully determined by the condition of chemical equilibrium, which causes the edge of the cloud to follow an equipotential surface of the trap.

But even if the trap frequency is small, the LDA may still break down. An important example occurs when an interface is present in the trap due to a first-order phase transition. For a resonantly interacting Fermi mixture with a population imbalance in its two spin states [1, 2], such interfaces were encountered in the experiments by Partridge et al. [2] and Shin et al. [3] at sufficiently low temperatures. Here the LDA predicts the occurrence of a discontinuity in the density profiles of the two spin states, which cost an infinite amount of energy when gradient terms are taken into account. Experimental profiles are therefore never truly discontinuous, but are always smeared out. An important goal of this chapter is to address this interesting effect, which amounts to solving a strongly interacting many-body problem beyond the LDA. Due to the rich physics of the interface, new phases can be stabilized that are thermodynamically unstable in the bulk. This exciting aspect shares similarities with the physics of superfluid helium-3 in a confined geometry [4] and spin textures at the edge of a quantum Hall ferromagnet [5].

Note that the presence of an interface also can have further consequences. Namely, in a very elongated trap, Partridge et al. observed a strong deformation of the minority cloud at their lowest temperatures. At higher temperatures the shape of the atomic clouds still followed the equipotential surfaces of the trap [6]. A possible interpretation of these results is that only for temperatures sufficiently far below the tricritical point [3, 7–11], the gas shows a phase separation between a balanced superfluid in the center of the trap and a fully polarized normal shell around this core. The superfluid core is consequently deformed from the trap shape due to the surface tension of the interface between the two phases [6, 12, 13]. This causes an even more dramatic breakdown of the LDA. Although the above interpretation leads to a good agreement with the experiments of Partridge et al. [6], a microscopic understanding of the value of the surface tension required to explain the observed deformations has still not been obtained. Presumably closely related to this issue are a number of fundamental differences with the study by Shin et al. [3]. Most importantly, the latter observes no deformation and finds a substantially lower critical polarization, which agrees with Monte Carlo calculations combined with a LDA. It appears that the interfaces between the superfluid core and the normal state are fundamentally different for the two experiments, which might play an important role in resolving the remaining discrepancies. In order to investigate this interface we need to go beyond the local-density approximation.

To study the details of the superfluid-normal interface we need a theory that can describe the inhomogeneous and population imbalanced unitarity Fermi gas. For this, we first need a theory that includes in the homogeneous case both the normal state and the superfluid state in one quantitative correct description. Secondly, we need to incorporate the inhomogeneous effects of the trapping potential. The aim of this chapter is to give a simple and elegant way to achieve this. In the following two sections, we fist arrive at an accurate, and to a large extent analytical descrip-

tion of the thermodynamics of a population imbalanced unitarity Fermi gas. This is achieved by constructing an appropriate thermodynamic potential Ω for the Fermi mixture at unitarity. All desired thermodynamic quantities can then be obtained by performing the appropriate differentiations of the thermodynamic potential that are well known from statistical physics. The inhomogeneity effects of the trapping potential are included by taking the energy penalty for large variations in the order parameter into account. These gradient terms smoothen the jump of the order parameter that is predicted by the LDA at the location of the first-order phase transition. We will see that this gives a more detailed explanation of the experimental data of Shin et al. [3]. In the last section we then show how the surface tension can be computed with this more detailed description of the interface. This surface tension turns out to be relatively small. This does, therefore, not explain the dramatic deformation seen in the experiment of Partridge et al. [6]. An alternative explanation may be that there exists a metastable state with a deformed superfluid core [14]. At the end of this chapter we briefly discuss this possibility. We find that the Landau–Ginzburg-like theory derived here does not appear to contain such a metastable state.

13.2 Ultracold Quantum Fields

In order to properly study the unitary Fermi mixture, we derive a single thermodynamic potential that in a quantitative correct manner describes both the normal and the superfluid phases. As we will see, the normal state of the unitarity Fermi mixture is straightforwardly incorporated by introducing two mean-field-like self-energies. In particular, it is possible in this manner to completely reproduce the equation of state known from Monte-Carlo calculations. However, including also the possibility of superfluidity at low temperatures and low polarizations turns out to be more difficult. To understand better how this can nevertheless be achieved, we first give an exact diagrammatic discussion of the superfluid state that is then in the next section used to arrive at the desired thermodynamic potential of the unitarity Fermi mixture.

13.2.1 Bardeen-Cooper-Schrieffer Theory

In this section we outline the basic ingredients of a field-theoretical description for the superfluid state of the imbalanced Fermi mixture [15]. We start with the essentially exact action for such an atomic two-component mixture,

$$
\begin{aligned}
S[\phi^*, \phi; J^*, J] = &\sum_{\sigma=\pm} \int d\tau\, d\mathbf{x}\, \phi_\sigma^*(\mathbf{x}, \tau) \left(\hbar \frac{\partial}{\partial \tau} - \frac{\hbar^2 \nabla^2}{2m} - \mu_\sigma \right) \phi_\sigma(\mathbf{x}, \tau) \\
&+ \int d\tau\, d\mathbf{x}\, V_0 \phi_+^*(\mathbf{x}, \tau) \phi_-^*(\mathbf{x}, \tau) \phi_-(\mathbf{x}, \tau) \phi_+(\mathbf{x}, \tau) \\
&- \hbar \sum_{\sigma=\pm} \int d\tau\, d\mathbf{x}\, \left(J_\sigma^*(\mathbf{x}, \tau) \phi_\sigma(\mathbf{x}, \tau) + \phi_\sigma^*(\mathbf{x}, \tau) J_\sigma(\mathbf{x}, \tau) \right).
\end{aligned}
$$

(13.1)

Here ϕ_σ is the fermion field of the atomic species in the hyperfine state $|\sigma\rangle$, μ_σ is the associated chemical potential, J_σ is a Grassmann-valued current source that is convenient in the following, but which is put equal to zero at the end of the calculations, and V_0 is the strength of the unitarity-limited attractive interactions between the two species. The grand-canonical partition function is then given by

$$Z[J, J^*] = \int \prod_\sigma d[\phi_\sigma^*]d[\phi_\sigma] \exp\left\{-\frac{1}{\hbar}S[\phi^*, \phi; J^*, J]\right\}. \qquad (13.2)$$

This represents a functional integral over all the fermion fields that are antiperiodic on the imaginary time interval $[0, \hbar\beta]$, with $\beta = 1/k_B T$ the inverse thermal energy. The thermodynamic potential is ultimately given in terms of the partition function as

$$\Omega(\mu_+, \mu_-, T, V) = -\frac{1}{\beta}\log Z[0, 0], \qquad (13.3)$$

with V the total volume of the system. To make the connection with thermodynamics explicit, we note that the thermodynamic potential is related to the pressure p of the gas by means of $\Omega = -pV$.

In order to describe pairing of the fermions, we perform a Hubbard–Stratonovich transformation to the complex pairing field Δ. For this field we have that

$$\langle\Delta(\mathbf{x}, \tau)\rangle = V_0\langle\phi_-(\mathbf{x}, \tau)\phi_+(\mathbf{x}, \tau)\rangle. \qquad (13.4)$$

This transformation makes the action quadratic in the fermion fields. More precisely, we have that

$$\begin{aligned}
S[\Delta^*, \Delta, \phi^*, \phi; J^*, J] = &-\int d\tau d\mathbf{x} \frac{|\Delta(\mathbf{x}, \tau)|^2}{V_0} \\
&- \hbar \int d\tau d\mathbf{x} \, d\tau' \, d\mathbf{x}' \, \Phi^\dagger(\mathbf{x}, \tau) \cdot \mathbf{G}_{BCS}^{-1}(\mathbf{x}, \tau; \mathbf{x}', \tau'; \Delta) \cdot \Phi(\mathbf{x}', \tau') \\
&+ \hbar \int d\tau d\mathbf{x} \, \left(J^\dagger(\mathbf{x}, \tau) \cdot \Phi(\mathbf{x}, \tau) + \Phi^\dagger(\mathbf{x}, \tau) \cdot J(\mathbf{x}, \tau)\right),
\end{aligned}$$
$$(13.5)$$

where we defined $\Phi^\dagger = [\phi_+^*, \phi_-]$ and $J^\dagger = [J_+^*, J_-]$, which are vectors in a two-dimensional space, known as Nambu space. In this space the 2×2 Green's function matrix is given by $\mathbf{G}_{BCS}^{-1}(\mathbf{x}, \tau; \mathbf{x}', \tau'; \Delta) = \mathbf{G}_0^{-1}(\mathbf{x}, \tau; \mathbf{x}', \tau') - \Sigma_{BCS}(\mathbf{x}, \tau; \mathbf{x}', \tau')$. The first term in the right-hand side represents the noninteracting part and is given by

$$\mathbf{G}_0^{-1}(\mathbf{x}, \tau; \mathbf{x}', \tau') = \begin{bmatrix} G_{0;+}^{-1}(\mathbf{x}, \tau; \mathbf{x}', \tau') & 0 \\ 0 & -G_{0;-}^{-1}(\mathbf{x}', \tau'; \mathbf{x}, \tau) \end{bmatrix}, \qquad (13.6)$$

with $G_{0;\sigma}$ the noninteracting Green's function of species σ. The second term corresponds to the BCS self-energy, which has only off-diagonal terms and reads

$$\hbar\Sigma_{\text{BCS}}(\mathbf{x}, \tau; \mathbf{x}', \tau') = \begin{bmatrix} 0 & \Delta(\mathbf{x}, \tau) \\ \Delta^*(\mathbf{x}, \tau) & 0 \end{bmatrix} \delta(\mathbf{x} - \mathbf{x}')\delta(\tau - \tau'). \quad (13.7)$$

The action now only contains quadratic terms in the fermion fields, which is something we can handle exactly. However, the tradeoff is an extra functional integral over the Δ field. Starting with the easy part, we perform the functional integral over the fermion fields. Since this is a standard Gaussian integral, we immediately obtain

$$S^{\text{eff}}[\Delta^*, \Delta; J^*, J] = -\int d\tau d\mathbf{x} \frac{|\Delta(\mathbf{x}, \tau)|^2}{V_0} - \hbar \text{Tr}\left[\log\left(-\mathbf{G}_{\text{BCS}}^{-1}\right)\right]$$
$$+ \hbar \int d\tau d\mathbf{x} d\tau' d\mathbf{x}' J^\dagger(\mathbf{x}, \tau) \cdot \mathbf{G}_{\text{BCS}}(\mathbf{x}, \tau; \mathbf{x}', \tau'; \Delta) \cdot J(\mathbf{x}', \tau'),$$
$$(13.8)$$

where the trace implies a summation over the Nambu space indices as well as an integral over position and imaginary time. The second term in the action contains all orders in $|\Delta|^2$ and as a result the theory is thus still very complex and impossible to solve completely. In BCS theory, we make a saddle-point approximation and replace the pairing field by its expectation value. In other words, we write $\Delta = \Delta_0 + \delta\Delta$, with Δ_0 the expectation value $\langle\Delta\rangle$ and $\delta\Delta$ representing the fluctuations, and subsequently neglect these fluctuations. The actual value of the BCS gap Δ_0 can then be determined by the gap equation in Eq. 13.4, which is equivalent to $\delta S^{\text{eff}}[\Delta^*, \Delta; 0, 0]/\delta\Delta^*|_{\Delta=\Delta_0} = 0$, and is to be solved selfconsistently. This procedure is of course only valid when the interaction strength is sufficiently small.

13.2.2 Fluctuations

But what happens when the interaction strength is not small, as is the case at unitarity? In that case we cannot neglect the fluctuations. To deal with that situation we use in Sect. 13.3.2 an approach inspired by Landau–Ginzburg theory, in which we try to find an accurate self-energy matrix for the fermions that effectively takes all fluctuation effects into account. In particular we need two self-energies that contribute to the diagonal part of the exact inverse Green's function matrix $\mathbf{G}^{-1}$, because otherwise the normal state would correspond to an ideal Fermi mixture, which at unitarity is not an accurate starting point for a discussion of the instability towards superfluidity. However, the effective interaction between the two atomic species is not the same in the normal and superfluid states of the gas. Therefore, also this diagonal part of the self-energy must sufficiently deep in the superfluid state depend on the expectation value of the pairing field or gap Δ_0 and it is important to understand how this dependence precisely comes about. In this section we show that in principle all interaction effects can indeed be included in a self-energy matrix, and that also the diagonal part of this self-energy depends explicitly on the gap. A nice and insightful way to achieve this is by considering the appropriate Feynman diagrams.

The diagonal parts of the Green's function matrix, i.e., $G_{\text{BCS};11}$ and $G_{\text{BCS};22}$, are dressed by the pairing field Δ. This is described by the Dyson equation. This Dyson equation follows from inverting the relation $\mathbf{G}_{\text{BCS}}^{-1} = \mathbf{G}_0^{-1} - \Sigma_{\text{BCS}}$ and can be written as

$$\mathbf{G}_{\text{BCS}} = \mathbf{G}_0 + \mathbf{G}_0 \cdot \Sigma_{\text{BCS}} \cdot \mathbf{G}_{\text{BCS}}. \tag{13.9}$$

Diagrammatically the diagonal part of this equation can be represented in the following way,

$$\tag{13.10}$$

Here the dashed line represents the pairing field Δ and the direction of the arrow depicts the difference between Δ and Δ^*. The solid line represents the noninteracting fermionic propagators $G_{0;\sigma}$, where in this case the direction of the arrow depicts alternatingly the propagator of the two different fermion species. The first line of the equation shows the recurrence relation for the full diagonal propagator and the second line shows the first three elements originating from this Dyson equation by iteration.

In the superfluid state, the pairing field Δ has a nonzero expectation value Δ_0. In a mean-field approximation we neglect the fluctuations and replace Δ by its expectation value Δ_0. In this approximation the diagonal propagators reduces to the standard form known from BCS theory. However, when we take fluctuations into account we also get self-energy corrections on the noninteracting fermion propagators in the Dyson equation. This follows directly from the definition of the exact fermionic propagators,

$$
\begin{aligned}
\mathbf{G}_{11}(\mathbf{x}, \tau; \mathbf{x}', \tau') &= -\langle \phi_+(\mathbf{x}, \tau)\phi_+^*(\mathbf{x}', \tau') \rangle \\
&= \frac{1}{Z[0,0]} \frac{\delta}{\delta J_+^*(\mathbf{x}, \tau)} \frac{\delta}{\delta J_+(\mathbf{x}', \tau')} Z[J^*, J] \Big|_{J^*=J=0} \\
&= \frac{1}{Z[0,0]} \int \mathrm{d}[\Delta^*]\mathrm{d}[\Delta]\mathbf{G}_{\text{BCS};11}(\mathbf{x}, \tau; \mathbf{x}', \tau'; \Delta)e^{-\frac{1}{\hbar} S^{\text{eff}}[\Delta^*, \Delta; 0, 0]} ,
\end{aligned}
$$
$$\tag{13.11}$$

and similarly for $\mathbf{G}_{22}$. In BCS mean-field theory we thus have $\mathbf{G}_{11}(\mathbf{x}, \tau, \mathbf{x}', \tau') = \mathbf{G}_{\text{BCS};11}(\mathbf{x}, \tau, \mathbf{x}', \tau'; \Delta_0)$, but at unitarity we still have to perform a functional integral over the pairing field to obtain the exact results.

We can represent this functional integral over the fluctuations diagrammatically by connecting some of the Δ fields with the pair propagator, which is determined by the effective action $S^{\text{eff}}[\Delta^*, \Delta; 0, 0]$, put the other fields equal to the expectation value Δ_0, and then sum over all possible diagrams. Because of the U(1) symmetry of the effective action, we can only draw a pair propagator between a Δ and a Δ^*, as suggested by the arrows. The fully dressed diagonal propagators now become,

$$\text{(13.12)}$$

Here the connected dashed lines represent the pair propagator and the cross represents the expectation value. This series can be resummed such that we get the exact Dyson equation

$$\mathbf{G} = \mathbf{G}_0 + \mathbf{G}_0 \cdot \Sigma \cdot \mathbf{G}, \tag{13.13}$$

but now with an exact 2×2 self-energy matrix Σ, which contains both diagonal (normal) and off-diagonal (anomalous) elements. For instance, the second and fifth terms drawn in the right-hand side of Eq. 13.12 contribute to the diagonal self-energy, whereas the last term leads to an additional contribution to the off-diagonal self-energy. These terms thus renormalize the BCS self-energy that is obtained from Eq. 13.7 by replacing Δ by Δ_0. From the expectation values of the gap inside the loops in Eq. 13.12, we explicitly see that the normal self-energies can be written as a series expansion in $|\Delta_0|^2$. The same is in fact also true for the first diagram in the right-hand side of Eq. 13.12, because the nonlinearities in the effective action make sure that the pair propagator already contains all orders of $|\Delta_0|^2$. These nonlinearities also lead to more complicated Feynman diagrams containing higher-order (connected) correlation functions of the pair field that are not shown here, but this does not affect our main conclusions.
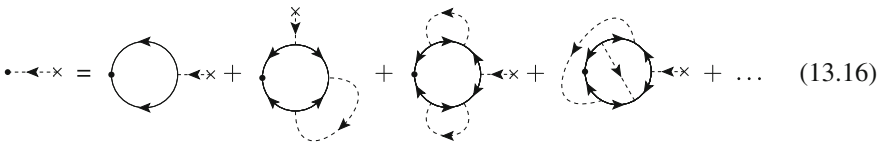
We just showed that fluctuation effects of the pair field can be incorporated in an effective self-energy. The same discussion can be carried out for the gap equation. This can also be very nicely illustrated diagrammatically. The gap equation in Eq. 13.4 is an equation between the expectation value of the gap and the off-diagonal or anomalous propagator. We can again use the Dyson equation in Eq. 13.9 for the anomalous propagator to study the effects of the fluctuations on the gap equation,

$$\text{(13.14)}$$

Here the small dot on the left of all diagrams represents the fact that the gap only depends on one space-time point, i.e., $\langle \Delta(\mathbf{x}, \tau) \rangle = V_0 G_{12}(\mathbf{x}, \tau; \mathbf{x}, \tau)$ due to the point-like and instantaneous nature of the attractive interaction.

The fluctuation effects follow again from performing the functional integral over the Δ field, since from Eq. 13.4 we have that

$$
\langle \Delta(\mathbf{x}, \tau) \rangle = \frac{V_0}{Z[0, 0]} \frac{\delta}{\delta J_-^*(\mathbf{x}, \tau)} \frac{\delta}{\delta J_+^*(\mathbf{x}, \tau)} Z[J^*, J] \Big|_{J^* = J = 0}
$$

$$
= \frac{V_0}{Z[0, 0]} \int d[\Delta^*] d[\Delta] \mathbf{G}_{\mathrm{BCS};12}(\mathbf{x}, \tau; \mathbf{x}, \tau; \Delta) e^{-\frac{1}{\hbar} S^{\mathrm{eff}}[\Delta^*, \Delta, 0, 0]} .
$$

$$(13.15)$$

The diagrammatic representation of this equation follows from connecting some of the pair lines in Eq. 13.14. Again also higher-order correlation functions of the pair field contribute, but for simplicity we do not consider these as they do not change our results. When we carry out this procedure we obtain

$$(13.16)$$

Notice that all terms are now proportional to Δ_0 instead of $|\Delta_0|^2$. The first three terms in the right-hand side can again be incorporated in a fully dressed fermion propagator by resumming this series. The last term, which for the gap equation behaves as a vertex correction, is then again incorporated into the anomalous self-energy.

In the unitarity limit, these vertex corrections are important to find the correct gap equation and, therefore, the expectation value for the gap. Also the diagonal part of the self-energy is important for a determination of the energy and the densities of the Fermi mixture. There is, however, no clear-cut way do derive these full self-energies from first principles for the unitarity case. In this chapter, we therefore use a more top–down approach. We will use the fact that these self-energies exist and can be expanded in powers of $|\Delta_0|^2$. Moreover, our previous renormalization group theory [11] has shown that for thermodynamic quantities the self-energies can in a good approximation be considered to be momentum and frequency independent. Combining these observations we are ultimately able to derive an accurate approximation to the thermodynamic potential Ω of the unitarity Fermi mixture.

13.3 The Thermodynamic Potential

In the previous section we showed that interaction effects in the unitary Fermi gas can be described by including appropriate normal and anomalous self-energies into the theory. We also discussed that this, in principle well-known fact, can be understood

as an effect of pair fluctuations. As a result the self-energies, and in particular the normal self-energies, depend on the gap Δ_0. In addition, we showed also that the gap equation contains vertex corrections, which cannot be incorporated by dressing the diagonal propagators alone. This is one important reason for deriving also the gap equation from the thermodynamic potential, because the minimization condition then automatically generates the correct vertex corrections. For our purposes it is therefore crucial to realize that in principle there exists an exact thermodynamic potential that describes the full thermodynamics of the unitarity-limited Fermi gas. It is, however, impossible to derive this from first principles for this strongly interacting system, and we therefore have to find an appropriate approximation. In this section we will show how to arrive at such an accurate approximation to the exact thermodynamic potential.

13.3.1 Normal State

Despite the strong interaction, it is now rather well established that BCS mean-field theory gives the correct qualitative description of the unitarity limit, at least at the temperatures accessible to the state-of-the-art experiments. Therefore a reasonable starting point for the approximation of the thermodynamic potential is this mean-field theory. From experiments, renormalization group theory, and several Monte-Carlo calculations it is found that the phase diagram has the following features, as illustrated in Fig. 13.1. At zero temperature both experiments and theoretical calculations find a first-order phase transition at a local critical polarization $P_c \simeq 0.4$. In the balanced situation $P = 0$ both find a second-order transition at a critical temperature of about $T_c \simeq 0.15T_F$ [16]. These second- and first-order transition lines should then be connected by a tricritical point, which is confirmed in experiments and by renormalization group theory.

The thermodynamic potential in BCS theory leads to exactly the same qualitative behavior of the phase diagram, although the critical temperatures and critical polarizations are off by almost an order of magnitude and would not be visible in the window shown in Fig. 13.1. We therefore start with BCS theory, after which we systematically include the dominant interaction effects that are still missing. At unitarity the BCS energy functional is

$$
\begin{aligned}
\Omega_{\mathrm{BCS}}[\Delta; \mu, h] = &\sum_{\mathbf{k}} \left(\varepsilon_{\mathbf{k}} - \mu - \hbar\omega_{\mathbf{k}} + \frac{|\Delta|^2}{2\varepsilon_{\mathbf{k}}} \right) \\
&- k_{\mathrm{B}}T \sum_{\sigma,\mathbf{k}} \log\left(1 + e^{-\hbar\omega_{\mathbf{k},\sigma}/k_{\mathrm{B}}T} \right),
\end{aligned}
\tag{13.17}
$$

where $\varepsilon_{\mathbf{k}} = \hbar^2\mathbf{k}^2/2m$, m is the atomic mass, and the superfluid dispersion is given by the well-known BCS formula, $\hbar\omega_{\mathbf{k}} = \sqrt{(\varepsilon_{\mathbf{k}} - \mu)^2 + |\Delta|^2}$. The second term in the right-hand side contains also a sum over the pseudospin projection $\sigma = \pm$, and
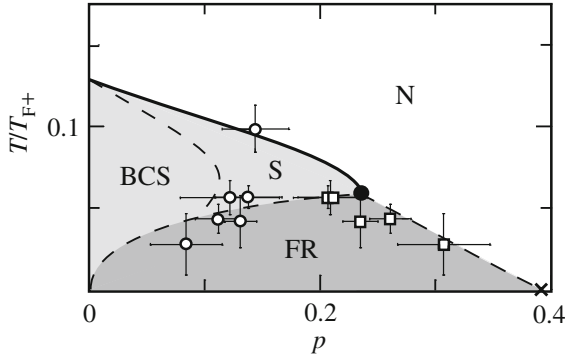
Fig. 13.1 The phase diagram of the unitary Fermi mixture in the temperature-polarization plane. The Fermi temperature of the majority species is denoted by T_{F+} and the polarization P equals $(N_+ - N_-)/(N_+ + N_-)$ with N_σ the number of atoms in hyperfine state $|\sigma\rangle$. The phase diagram consists of the normal phase (N), a forbidden region (FR) where phase separation takes place, and the superfluid phase in which a crossover occurs between the gapless Sarma phase (S) and the gapped BCS phase. The *solid line* depicts the line of second-order phase transitions [11], the *dashed line* gives the boundary of the forbidden region associated with the first-order phase transitions, and the *black dot* represents the tricritical point. The *open squares* and *circles* are experimental data points [3]

represents the contribution due to an ideal gas of quasiparticles with the quasiparticle dispersion of the two spin states given by $\hbar\omega_{\mathbf{k},\sigma} = \hbar\omega_{\mathbf{k}} - \sigma h$. Finally, we introduced the average chemical potential $\mu = (\mu_+ + \mu_-)/2$ and half the chemical potential difference $h = (\mu_+ - \mu_-)/2$ that acts as an effective magnetic field on the pseudospin as the quasiparticle dispersion $\hbar\omega_{\mathbf{k},\sigma}$ clearly shows.

In BCS theory, the normal state is treated as an ideal Fermi gas, thus no interactions are taken into account. This is not correct in the unitarity limit. As discussed above, these interaction effects can be described by two self-energies. The imbalanced normal phase in the unitary limit, has been studied with Monte-Carlo methods [17]. From this, the equation of state can be determined. If we can find the self-energies such that it reproduces the same equation of state for the theory, we have effectively taken all interaction effect in the normal phase into account.

For momentum and frequency independent self-energies, the self-energies can be incorporated in the theory of an ideal Fermi gas, by just changing the chemical potential. We thus replace the chemical potentials as

$$\mu'_\sigma = \mu_\sigma - \hbar\Sigma_\sigma. \tag{13.18}$$

Here μ'_σ is the effective chemical potential and Σ_σ the self-energy for species σ. Inspired by Hartree–Fock theory we would write down an *ansatz* for the self-energy of species σ that is proportional to the density of species $-\sigma$ [10]. However, the densities are in a grand-canonical setting calculated by taking the derivative of Ω with respect to the chemical potentials, i.e., $N_\sigma = -\partial\Omega/\partial\mu_\sigma$. It is therefore preferable to write the self-energies as a function of the chemical potentials only. By considering
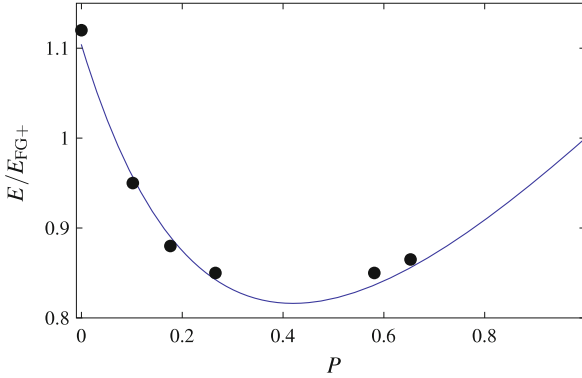
Fig. 13.2 The equation of state of the normal phase at zero temperature, with on the horizontal axis the polarization and on the vertical axis the energy. The *dots* are the Monte-Carlo data from Ref. [17] and the *line* is the equation of state found with the use of the effective chemical potentials as defined in Eq. 13.20. The energy is given by $E = \Omega + \mu_+ N_+ + \mu_- N_-$ and is scaled with the ideal gas energy of the majority component of the mixture $E_{\mathrm{FG}+} = \frac{3}{5} E_{\mathrm{F}+} N_+$ and $E_{\mathrm{F}+}$ the Fermi energy of the majority species

terms with the correct units that incorporate the Hartree–Fock-like feature mentioned above, we find that the following self-energies gives rise to the correct equation of state of the strongly interacting normal phase,

$$\mu'_\sigma = \mu_\sigma + \frac{3}{5} A \frac{(\mu'_{-\sigma})^2}{\mu'_+ + \mu'_-} . \tag{13.19}$$

The prefactor can be determined from the self-energy of a single minority atom in the presence of a Fermi sea of majority atoms and equals $A \simeq 0.96$ [11, 17–19]. Explicitly in terms of μ and h, these relations imply that

$$\mu' = \mu \left(1 - \frac{5 - 3A}{10 - 3A} + \frac{5\sqrt{(5 + 3A)^2 + 3A(10 - 3A)(h/\mu)^2}}{(10 - 3A)(5 + 3A)} \right) ,$$

$$h' = h \left(1 - \frac{3A}{5 + 3A} \right) . \tag{13.20}$$

In Fig. 13.2 the resulting energy of the mixture determined from the thermodynamic potential $\Omega(\mu, h, T, V) = \Omega_{\mathrm{BCS}}[0; \mu', h']$ at zero temperature is plotted as a function of the polarization. This figure shows the excellent agreement between the Monte-Carlo data and the *ansatz* from Eq. 13.20. In the next section we discuss how these self-energies can be further improved when we also consider the effects of pairing in the superfluid state.

13.3.2 Superfluid State

When the temperature is low enough and the imbalance not too large, the unitary Fermi gas becomes superfluid. In the unitarity limit, the scattering length goes to infinity and is no longer a relevant length scale. In fact, in the homogeneous situation, the (average) Fermi energy is the only energy scale in the problem. This makes the system universal and as a result, we can write most thermodynamic properties of the system in terms of this Fermi energy [18].

In Sect. 13.2 we showed that the self-energies can be explicitly written as a power series in $|\Delta|^2$. The straightforward first step to incorporate these superfluid gap corrections to the self-energy is to take the first term in $|\Delta|^2$ into account [20]. We subtract this from the effective chemical potential in Eq. 13.20 as

$$\mu'(\mu, h, \Delta) = \mu'(\mu, h, 0) - B \frac{|\Delta|^2}{\mu'(\mu, h, 0)} \tag{13.21}$$

and B a constant to be determined next. For this we use one simple but important piece of information, namely the value of the thermodynamic potential in the balanced superfluid minimum. From experiments and Monte-Carlo calculations this minimum is known to be

$$\Omega = -\frac{4\sqrt{2}\mu^{5/2}m^{3/2}}{15\pi^2\hbar^3(1+\beta)^{3/2}}V \equiv \Omega_{\mathrm{cr}}, \tag{13.22}$$

with V the volume and $\beta \simeq -0.58$ a universal number. Matching the energy in the minimum is important, because this ensures a correct energy balance between the (imbalanced) normal state and the superfluid state and therefore the correct location of the first-order phase transition at low temperature. From experiments and several theoretical calculations, it is now believed that at low temperatures the superfluid state is balanced. Thus, to find the transition we should compare the energy in the balanced superfluid with the normal state energy, for which we have already a description that agrees with the Monte-Carlo equation of state and thus has the correct energy. This condition fixes the unknown constant to $B \simeq 0.21$, which follows directly from the zero-temperature minimum of $\Omega_{\mathrm{BCS}}[\Delta; \mu', 0]$ in Eq. 13.17 with both self-energy corrections subtracted from the chemical potential.

At this point our construction, where everything is explicitly written in terms of the chemical potentials μ and h, gives rise to a problem: The superfluid in the minimum of the thermodynamic potential turns out not to be balanced at low temperatures for $h \neq 0$. This problem originates from the normal self-energies in Eq. 13.20 which explicitly depends on the chemical potential difference h. It is in particular the renormalization of the average chemical potential which depends on h, thus $\mu'(\mu, h, \Delta)$. This problem could have been avoided by making an *ansatz* in terms of the densities instead of the chemical potentials, which would automatically have resulted in a balanced superfluid [21]. This follows directly from the fact that BCS theory already gives a balanced superfluid at low temperature and the dependence on imbalance

in the self-energies is thus suppressed in the superfluid state. Physically, the problem is that the formation of a Bose–Einstein condensate of Cooper pairs gives the superfluid state a strong preference for equal densities of the two spin states, which is not present in the normal state. To incorporate this extra piece of physics into the theory, we need to add an extra $|\Delta|^2$ dependence to the model to ensure a balanced superfluid in the minimum of the thermodynamic potential. There are several ways to achieve this, but an exponential suppression of the h dependence in μ' turns out to give the best interpolation between the various known regimes. Technically this is achieved, by replacing h in $\mu'(\mu, h, \Delta)$ by $h \exp{(-|4\Delta|^2/\mu^2)}$. The factor of 4 in the exponent is somewhat arbitrary, but should be large enough to make the h dependence in the ground-state superfluid minimum negligible.

We now have included the self-energy effects in both the normal state as well as in the superfluid state. This results in an approximation for the thermodynamic potential which has the correct equation of state in the normal phase, the correct energy minimum for the superfluid phase, and interpolates between these two in a manner that incorporates all the known physical properties of the system. In Fig. 13.3 the resulting thermodynamic potential is plotted for several values of h and at zero temperature. As a check we can compute the critical polarization which gives about $P \simeq 0.4$ as desired. Also the universal number $\zeta = \Delta_0/\mu$ of the balanced superfluid ground state has a very reasonable value. Here we find 0.97 while Monte-Carlo gives 1.07 ± 0.15 [22, 23]. In principle, we can easily correct for this difference by including a small correction to the anomalous self-energy, but in view of the already rather good agreement with the Monte-Carlo results we refrain from doing so in the following.

A large region of the trapped unitary Fermi gas can be well described using the local-density approximation. However, near the interface of a first-order phase transition, this approximation always breaks down, as it leads to an unphysical discontinuity in the density profiles. The thermodynamic potential we constructed so far also describes the system out of equilibrium, i.e., with Δ not in a minimum of the thermodynamic potential, which is precisely what happens near the interface. But in order to describe the interface properly, we need to go beyond the LDA by including also a gradient term for Δ in the thermodynamic potential,

$$\Omega[\Delta; \mu, h] = \int d\mathbf{x} \left(\frac{1}{2} \gamma(\mu, h) |\nabla \Delta(\mathbf{x})|^2 + \omega_{\mathrm{BCS}}[\Delta(\mathbf{x}); \mu', h'] \right), \quad (13.23)$$

where ω_{BCS} denoted the homogeneous thermodynamic potential density Ω_{BCS}/V and $\hbar\gamma(\mu, h)\sqrt{\mu/m}$ is a positive function of the ratio h/μ only, due to the universal nature of the Fermi mixture at unitarity. The functional minimum of this new thermodynamic potential gives a smooth transition at the interface, instead of the discontinuous step obtained within the LDA. A careful inspection of the interface in the data of Shin et al. [3], cf. Fig. 13.4, also reveals that the interface is not a sharp step. This is most clear in the data for the density difference, since the noise in the density difference is much smaller than in the total density. This has to do with the experimental procedure used, which only measures the density difference directly.
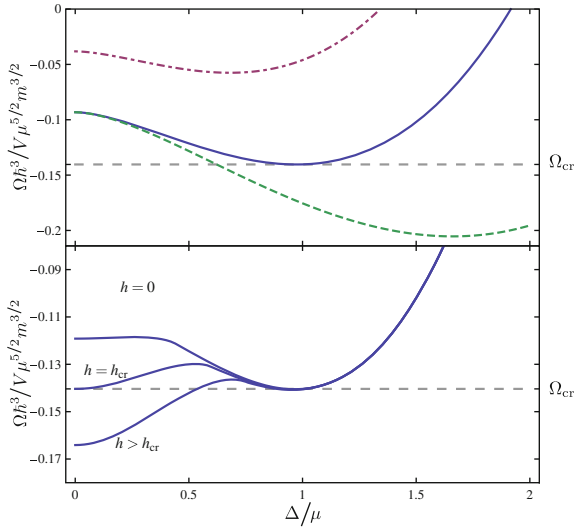
Fig. 13.3 The zero-temperature thermodynamical potential functional as a function of the order parameter Δ. The *upper panel* illustrates the balanced case, where the *dash-dotted line* is the usual BCS result, the *dashed line* incorporates only the normal-state self-energy effects, and the *solid line* includes also the superfluid self-energy correction. In the *lower panel* the energy functional is shown for various values of the chemical potential difference h, with $h_{cr} \simeq 0.94\mu$ its critical value

Such a smooth transition arises also in the self-consistent Bogoliubov–de Gennes equations. But these lead then also to oscillations in the order parameter and the densities, due to the proximity effect [24]. This is not observed experimentally. Oscillations will also occur in our Landau–Ginzburg approach if $\gamma(\mu, h) < 0$. However, we have checked both with the above theory as well as with renormalization group calculations [11] that $\gamma(\mu, h)$ is positive. This agrees with the phase diagram of the imbalanced Fermi mixture containing a tricritical point and not a Lifshitz point in the unitarity limit [25].

We restrict ourselves here to a gradient term that is of second order in Δ and also of second order in the gradients. There are of course higher-order gradient terms that may contribute quantitatively [26], but the leading-order physics is captured in this way due to the absence of a Lifshitz transition. One way to compute the coefficient $\gamma(\mu, h)$ is to use the fact that in equilibrium this coefficient can be exactly related to the superfluid stiffness, and therefore the superfluid mass density ρ_s, by $\gamma = \hbar^2 \rho_s / 4m^2 |\langle\Delta\rangle|^2$. At zero temperature it gives the simple result that $\gamma(\mu, h) = \sqrt{m/2\mu}/6\pi^2\hbar^2\zeta(1+\beta)^{3/2}$, with β and ζ universal constants as defined earlier. With this result for γ our thermodynamic potential functional in Eq. 13.23 contains no longer any free parameters and can now be confronted with experiments. The result of this comparison, at a realistic temperature of about one third the tricritical temperature T_{c3}, is shown in Fig. 13.4 and turns out to be excellent.
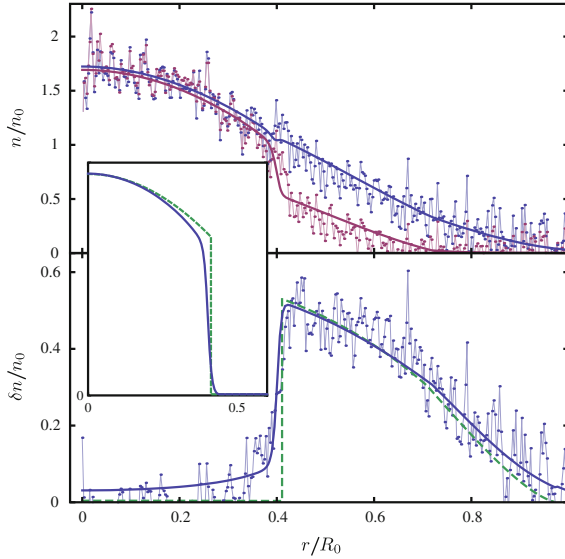
Fig. 13.4 (Color online) The density profiles of a unitary mixture with polarization $P \simeq 0.44$ in a harmonic trap. The *upper* figure shows the majority and minority densities as a function of the position in the trap. The *lower* figure shows the density difference, where the theoretical *curves* show the results both within the LDA (*dashed line*) and for our theory (*solid line*) that goes beyond this approximation and, therefore, allows for a substantial better agreement with experiment. The *inset* shows the BCS gap parameter $\Delta_0(r)/\Delta_0(0)$ both for the LDA (*dashed line*) and our theory (*solid line*). The experimental data points and scaling are from Shin et al. [3]

13.4 Applications

We have thus constructed an accurate approximation to the exact thermodynamic potential of the imbalanced Fermi mixture at unitarity. With a simple *ansatz* for the self-energies we can describe both the homogeneous normal and superfluid phase at zero and nonzero temperatures. Moreover, the description is also valid out of equilibrium, i.e., when the value of the gap is not in a minimum of the thermodynamic potential. By including also the energy cost for gradients of the gap parameter we have a Landau–Ginzburg-like theory that can describe the inhomogeneous situation that is used in experiments [2, 3] in a manner that goes beyond the local-density approximation.

In this section we use the thermodynamic potential $\Omega[\Delta; \mu, h]$ from Eq. 13.23 to investigate the properties of the superfluid-normal interface. First, we consider the trap to be spherically symmetric and in that case calculate the surface tension of the interface. This is an important quantity that has been put forward [2, 12] as a possible explanation for the deformations of the superfluid core observed by Partridge et al. [2]. Second, we then show how the anisotropy of the trap can be incorporated and study the effect of this anisotropy on the equilibrium gap profile $\Delta_0(\mathbf{x})$. In this section

we for simplicity always take the gap $\Delta_0(\mathbf{x})$ to be real, which does not lead to any loss of generality for the applications that we consider here.

13.4.1 Interface and Surface Tension

The fact that we are able to study the superfluid-normal interface beyond the LDA, makes it possible for us to also determine the surface tension. The surface tension is determined by the difference in thermodynamic potential between a one-dimensional LDA result with a discontinuous step in $\Delta_0(\mathbf{x})$ and our Landau–Ginzburg theory with a smooth profile for the order parameter $\Delta_0(\mathbf{x})$. In actual experiments, however, the width of the interface is rather small compared to the size of the whole atomic cloud. This makes it possible to compute the surface tension by considering a flat interface in a homogeneous system rather than a curved interface in the trap. In the homogeneous case, such an interface occurs only when the imbalance is critical, i.e., when $h = h_{\mathrm{cr}}(\mu) = \kappa\mu$ with κ another universal number, for which we have obtained $\kappa \simeq 0.94$. This means that the thermodynamic potential of the normal state minimum is exactly equal to the thermodynamic potential of the superfluid state minimum. The surface tension is then the difference in thermodynamic potential between a system that stays in one minimum and one that goes near the interface from one minimum to the other.

How the system achieves the latter is determined by minimizing the thermodynamic potential,

$$\left.\frac{\delta\Omega[\Delta;\mu,h_{\mathrm{cr}}]}{\delta\Delta(z)}\right|_{\Delta=\Delta_0} = \frac{\partial\omega_{\mathrm{BCS}}[\Delta_0(z);\mu',h']}{\partial\Delta} - \gamma(\mu,h_{\mathrm{cr}})\frac{\partial^2}{\partial z^2}\Delta_0(z) = 0.$$
(13.24)

In principle, this highly nonlinear equation can be numerically solved, to get a hyperbolic tangent-like function for $\Delta_0(z)$ that on the normal side of the interface approaches zero and on the superfluid side approaches the equilibrium position of the superfluid minimum that we simply denote by Δ_0. Fortunately, however, this solution is not needed to compute the surface tension, because the surface tension can be conveniently written as

$$\sigma(\mu) = \int\limits_{-\infty}^{\infty} dz\,\left(\omega[\Delta_0(z);\mu,h_{\mathrm{cr}}] - \omega[0;\mu,h_{\mathrm{cr}}]\right),$$
(13.25)

where $\omega = \Omega/V$ is the thermodynamic potential density. This equation can be rewritten as an integral over Δ, knowing that $\Delta_0(z)$ is a monotonically increasing function between zero and Δ_0. Using also the first integral of Eq. 13.24, we end up with

$$\sigma(\mu) = \sqrt{2\gamma(\mu,h_{\mathrm{cr}})} \int\limits_{0}^{\Delta_0} d\Delta\sqrt{\omega_{\mathrm{BCS}}[\Delta;\mu',h'] - \omega_{\mathrm{BCS}}[0;\mu',h']}\,.$$
(13.26)
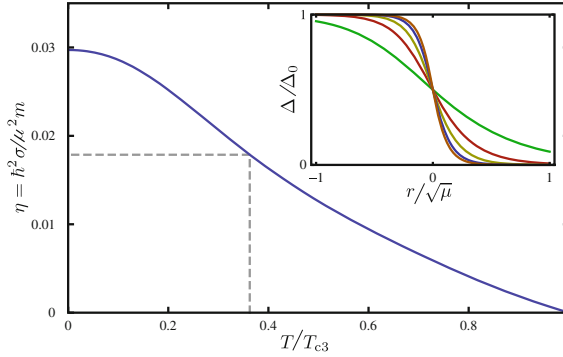
Fig. 13.5 The surface tension as a function of the temperature, computed in the homogeneous case at unitarity. The temperature is scaled by the temperature of the tricritical point T_{c3}. The *dashed line* shows the value used to compare with experiments in Fig. 13.4. The *inset* shows the gap around the interface for several temperatures 0.9, 0.7, 0.5, 0.25 and 0.01 T_{c3}, respectively

This is clearly independent of the actual shape of the interface. The surface tension thus only depends directly on $\sqrt{\gamma(\mu, h_{cr})}$ and on the shape of the barrier in between the two minima of the thermodynamic potential. It is useful to write the surface tension in a dimensionless form. We define this as $\sigma(\mu) = \eta(m/\hbar^2)\mu^2$, with η a dimensionless number. This number depends only on the temperature. In a trap, the relevant chemical potential is the one at the position of the interface. This location is also dependent on the polarization of the mixture and in that manner also the surface tension will inherit in a trap a dependence on the polarization [13].

The surface tension of this model is plotted in Fig. 13.5 as a function of the temperature. Here the surface tension is plotted in its dimensionless form. In this form it was previously found that for the experiment of Partridge et al. $\eta \simeq 0.6$ [6]. This was extracted from the large deformations of the superfluid core observed in that experiment. The experiment of Shin et al. does not show any deformation, which puts an upper bound on η of about 0.1 [13, 27]. At the tricritical point the surface tension vanishes and at zero temperature it is about $\eta \simeq 0.03$. For a more realistic temperature of about $0.3T_{c3}$ we find $\eta \simeq 0.02$ which is significantly smaller than the surface tension that would cause a substantial deformation. This is thus in agreement with the experiment of Shin et al. [3].

We now give a more detailed discussion of our analysis of the density profiles observed by Shin et al. In experiments the cloud is trapped in an anisotropic harmonic potential, which is cigar shaped, and in the axial direction less steep than in the radial direction. However, since the atomic cloud shows no deformations in this case we can in a good approximation take the trap to be spherically symmetric. The order parameter then depends only on the radius, and the total thermodynamic potential is given by integrating our Landau–Ginzburg-like thermodynamic potential density over the trap volume. To account for the trap potential in the energy functional we let the average chemical potential depend on the radius, such that we have $\mu(r) = \mu - V(r)$, with $V(r)$ the effectively isotropic harmonic potential.

To find the order parameter as a function of the radius we have to minimize the energy functional with respect to the order parameter, or $\delta\Omega[\Delta; \mu, h]/\delta\Delta(r)|_{\Delta=\Delta_0} = 0$. This gives a second-order differential equation for $\Delta_0(r)$ as we have seen. Solving this Euler-Lagrange equation, with the proper boundary conditions in the center of the trap, gives a profile for Δ_0 that is shown in the inset of Fig. 13.4. This profile of the order parameter is much smoother than the discontinuous step one obtains within the LDA that is also shown in Fig. 13.4. Besides this, there are two more aspects that deserve some attention. First, we notice that the value of the gap at the original LDA-interface is decreased by almost a factor of three and, second, the gap penetrates into the area originally seen as the normal phase. This behavior makes the gap for a small region smaller than h', giving locally rise to a gapless superfluid, which implies a stabilization of the Sarma phase.

Before discussing this particular physics, we focus first on the density difference. To obtain the density profiles within our theory, the thermodynamic relation $n_\sigma(r) = \partial\omega_{BCS}/\partial\mu_\sigma(r)$ is used, where $n_\sigma = N_\sigma/V$ is the density of particles in state $|\sigma\rangle$ and $\mu_\sigma(r) = \mu_\sigma - V(r)$ the associated local chemical potential. It is important that, because of the self-energy effects, we cannot use the standard BCS formulas for the density, but really have to differentiate the thermodynamic potential. In BCS theory this would of course be equivalent. Given the density profiles, the comparison between theory and experiment can be made and is ultimately shown in Fig. 13.4. Overall the agreement is very good. Theoretically the interface appears to be somewhat sharper than observed. This can be due to higher-order gradient terms, that are neglected in the calculation and that would give an additional energy penalty for a spatial variation of the order parameter. There are also experimental effects that could make the interface appear broader, for instance, the spatial resolution of the tomographic reconstruction or the accuracy of the elliptical averaging (Ketterle W., Shin Y., Private communication).

The Landau–Ginzburg-like approach presented here, shows some new features compared to the LDA. One interesting feature is the kink, that is visible in the majority density profile shown in Fig. 13.4. Notice that this kink appears *before* the original (LDA) phase transition from the superfluid to the normal phase. This kink signals a crossover to a new exotic phase, namely the gapless Sarma phase. Note that at zero temperature this crossover becomes a true quantum phase transition. At the crossover, the order parameter becomes smaller than the renormalized chemical potential difference h' and the unitarity limited attraction is no longer able to fully overcome the frustration induced by the imbalance. As a result the gas becomes a polarized superfluid. Because the gap Δ is smaller than h' this corresponds to a gapless superconductor. In a homogeneous situation this can, far below the tricritical temperature, never be a stable state as shown in Fig. 13.1. However, because of the inhomogeneity induced by the confinement of the gas, the gap is at the interface forced to move away from the local minimum of the thermodynamic potential and ultimately becomes smaller than h'. The Sarma state is now locally stabilized even at these low temperatures. Notice that this is a feature of the smooth behavior of the gap and that the presence of the Sarma phase thus does not depend on the quantitative details of the energy functional $\Omega[\Delta; \mu, h]$.

13.4.2 Deformation

When the surface tension is sufficiently small or when the aspect ratio of the external potential of the system is close to one, the gap profile $\Delta_0(\mathbf{x})$ will closely follow the equipotential surfaces of the external trap and can be reasonably well approximated by a function of a single variable only. This can be achieved by scaling away the anisotropy of the external potential and introducing the effective radius

$$R^2 = x^2 + y^2 + \left(\frac{z}{\alpha}\right)^2 , \tag{13.27}$$

with α the aspect ratio of the trap. However, when the aspect ratio is large, this might not always be valid. In the experiment of Partridge et al. [6], an aspect ratio of about 45 is used, and dramatic deviations between the equipotential surfaces and the shape of the superfluid core are observed. This can be explained by a large surface tension [13], but as we have just seen the required large value of η cannot yet be understood from a microscopic theory. Another possibility is that the gas has ended up in a metastable state in which the shape of the gap parameter differs from the equipotential surfaces of the external potential [14].

The latter possibility is something that can also be investigated using the thermodynamic potential that we have just derived. To do so, we first study the linear response of the system when we also allow the gap profile to depend on more (angular) variables then the effective radius R. After that we also look at gap profiles with a different aspect ratio than the external potential. It appears from our analysis that our present Landau–Ginzburg-like approach gives indeed rise to small deviations in the gap shape. However, it does not exhibit a metastable state with a deviation that is as large as seen in the experiment of Partridge et al.

13.4.2.1 Linear Response

The harmonic potential used in the experiments has an elliptical symmetry, which means that it can be written as a function of a single coordinate R as defined in Eq. 13.27. As a consequence, the local thermodynamic potential also only depends explicitly on this R. Therefore, in the local-density approximation, the gap parameter can only depend on R as well. When we go beyond the LDA, by including gradient terms in the theory, this symmetry is explicitly broken.

In this section we first perform the above-mentioned scaling of the axial coordinate. After that we can treat the beyond-LDA corrections of the gap profile as perturbations on the symmetric solution that can be expanded in the form of spherical harmonics as

$$\Delta_0(\mathbf{x}) = \sum_l \frac{D_l(R)}{R} Y_{l0}(\theta, \phi) . \tag{13.28}$$

Since the trap is rotationally symmetric around the z-axis, the gap profile does not depend on the azimuthal angle ϕ and we are allowed to take $m = 0$ in the expansion in Eq. 13.28. Also the mirror symmetry in the x–y plane causes all coefficients with odd l to be zero. We will now assume that the elliptically symmetric part $D_0(R)$ is much larger than the part with coefficients $l > 0$ and for simplicity only look at the first anisotropic perturbation $D_2(R)$.

To describe the deformations we have thus chosen spherical coordinates, but with the z-coordinate defined as $z = \alpha R \cos\theta$. This coordinate system is not orthogonal and gives rise to a coupling between the spherical harmonics due to the gradient terms. The Jacobian is given by $\alpha R^2 \sin\theta$. The gradient terms in the thermodynamic potential can be written in these coordinates as

$$
\Omega_{\mathrm{gr}}[\Delta_0] \equiv \int dx \frac{\gamma(\mathbf{x})}{2} |\nabla\Delta_0(\mathbf{x})|^2
$$

$$
\simeq -\frac{\alpha}{2} \int_0^\infty dR \left\{ \gamma_0 D_0(R) \frac{d^2}{dR^2} D_0(R) + \gamma_2 D_2(R) \left(\frac{d^2}{dR^2} D_2(R) - \frac{6}{R^2} D_2(R) \right) \right.
$$

$$
\left. + \gamma_{02} D_0(R) \left(2\frac{d^2}{dR^2} D_2(R) + \frac{6}{R}\frac{d}{dR} D_2(R) + \frac{3}{R^2} D_2(R) \right) \right\} .
$$

$$(13.29)$$

Here we suppressed for convenience the dependence on the chemical potentials and approximated the stiffness $\gamma(\mathbf{x})$ by its value at the location of the interface, that we from now on denote simply by γ. The latter is a very good approximation in practice, because for the traps of interest the width of the superfluid-normal interface is much smaller that the typical length scale on which the trapping potential varies. Furthermore, we defined the various different effective stiffnesses as

$$
\gamma_0 = \left(\frac{2}{3} + \frac{1}{3}\frac{1}{\alpha^2} \right) \gamma, \quad \gamma_2 = \left(\frac{10}{21} + \frac{11}{21}\frac{1}{\alpha^2} \right) \gamma, \quad \gamma_{02} = -\frac{2}{3\sqrt{5}}\left(1 - \frac{1}{\alpha^2} \right) \gamma.
$$

$$(13.30)$$

This can naturally be extended to general l, where every D_l is coupled to D_{l+2}, but we do not need that extension here.

As indicated above, we want to treat D_2 as a small perturbation in linear-response theory. To achieve this we need to expand the local part of the thermodynamic potential in terms of D_2. This is straightforward and is given by,

$$
\Omega_{\mathrm{loc}}[\Delta_0] = \alpha \int_0^\infty dR \left\{ 4\pi R^2 \omega_{\mathrm{BCS}}[\Delta_0(R); R] + \frac{1}{2}\frac{\partial^2 \omega_{\mathrm{BCS}}[\Delta_0(R); R]}{\partial\Delta_0^2} D_2(R)^2 + \ldots \right\} .
$$

$$(13.31)$$

We find the elliptical symmetric part $\Delta_0(R) = D_0(R)/R\sqrt{4\pi}$ of the gap by neglecting the D_2 contribution and minimizing the thermodynamic potential with respect to $\Delta_0(R)$. This gives a spherical symmetric equation similar to Eq. 13.24, but now with a slightly smaller gradient coefficient, given by γ_0 in Eq. 13.30. When we have obtained a solution for D_0 we can minimize the thermodynamic potential with respect to D_2, which gives the following linear-response equation

$$\mathscr{L} D_2(R) = S\left(D_0(R); R\right),\tag{13.32}$$

with the linear operator

$$\mathscr{L} = \frac{1}{2}\frac{\partial^2\omega_{\mathrm{BCS}}[\Delta_0(R); R]}{\partial\Delta_0{}^2} - \frac{\gamma_2}{2}\left(\frac{d^2}{dR^2} - \frac{6}{R^2}\right)\tag{13.33}$$

and the inhomogeneous term that acts as a source for the quadrupole deformations

$$S\left(D_0(R); R\right) = \frac{\gamma_{02}}{2}\left(\frac{d^2}{dR^2}D_0(R) - \frac{3}{R}\frac{d}{dR}D_0(R) + \frac{3}{2R^2}D_0(R)\right).\tag{13.34}$$

In Dirac notation the solution of this equation is formally given by $|D_2\rangle = \mathscr{L}^{-1}|S(D_0)\rangle$. Inverting the operator $\mathscr{L}$ can be accomplished by first diagonalizing this operator, which we can do by finding all its eigenfunctions and eigenvalues. Interestingly, these are determined by a Schrödinger equation

$$\left\{-\frac{\hbar^2}{2m^*}\frac{d^2}{dR^2} + V^{\mathrm{eff}}(R)\right\}\phi_n(R) = E_n\phi_n(R),\tag{13.35}$$

with an effective mass given by $m^* = \hbar^2/\gamma_2$ and an effective potential $V^{\mathrm{eff}}(R)$

$$V^{\mathrm{eff}}(R) = \frac{1}{2}\frac{\partial^2\omega_{\mathrm{BCS}}[\Delta_0(R); R]}{\partial\Delta_0{}^2} + \frac{\hbar^2}{2m^*}\frac{6}{R^2}.\tag{13.36}$$

A typical example of this effective potential with its eigenstates and energies is shown in Fig. 13.6. Given these eigenfunctions the solution for D_2 can in Dirac notation finally be written as $|D_2\rangle = \sum_n(1/E_n)|\phi_n\rangle\langle\phi_n|S(D_0)\rangle$, which amounts to

$$D_2(R) = \sum_n \frac{\phi_n(R)}{E_n}\int_0^\infty dR'\,\phi_n(R')S\left(D_0(R'); R'\right).\tag{13.37}$$

In Fig. 13.6 also the corresponding solution for D_2 is shown. This solution is centered around the interface and is also roughly of the same width as the interface. This is as expected, since the terms in the thermodynamic potential that do not obey the elliptical symmetry and are the source for the quadrupole deformations, are most significant near the interface. Formally, this comes about because the sum in the right-hand side of Eq. 13.37 is, due to the energy denominator, dominated by the eigenstates with low energies that are localized in the dimple of the effective potential $V^{\mathrm{eff}}(R)$.

The outcome of our linear-response analysis gives only rise to small deformations from the elliptical symmetry. In fact, this *a posteriori* makes this approach self-consistent and confirms the assumption that the gap can be well described with a solution that has the same symmetry as the trap. While this symmetric solution gives roughly speaking the average shape of the interface, the small quadrupole
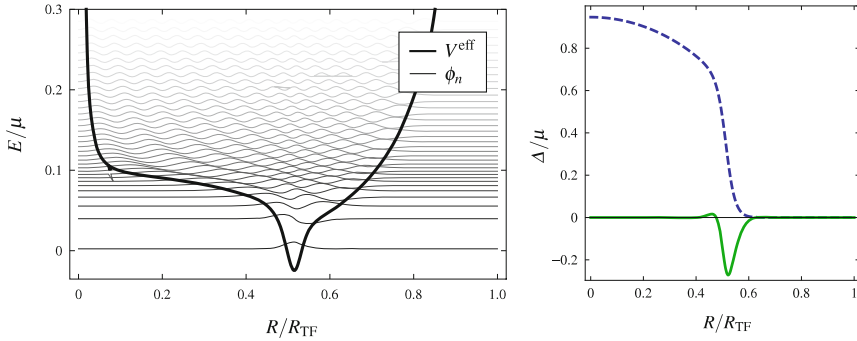
Fig. 13.6 The *left panel* shows the solutions for the eigenfunctions (*thin lines*) and eigenvalues (*line height*) of Eq. 13.36. The *thick line* is the effective potential in Eq. 13.36, which shows a pronounced dimple at the location of the interface. The *right panel* shows the elliptically symmetric solution $\Delta_0(R)$ (*dashed line*) and the quadrupole correction $D_2(R)$ (*solid line*). Here we have taken $\alpha = 45$ and $P = 0.4$, which are typical values for the experiments of Partridge et al. [6]

deformations correct for this and widen the interface in the radial direction and shrink it in axial direction. This effect becomes bigger for larger aspect ratios, but never gives rise to such large deformations as is seen in the experiments of Partridge et al. For an aspect ratio of one, the deformation disappears, because the source term $S(\Delta_0(R), R)$ is proportional to γ_{02}, which becomes zero at $\alpha = 1$. In principle, a deformation could then occur spontaneously, if one or more eigenvalues E_n become negative. However, for typical experimental parameters, this never happens.

In this section we discussed the linear response of the superfluid-normal interface shape. This is a nice application for our Landau–Ginzburg-like thermodynamic potential functional that can be used to study in detail the effect of the aspect ratio of the trap on the experiment of Shin et al. However, we cannot use it to describe the large deformations observed by Partridge et al. A possible way to handle this situation requires beyond linear-response methods that are covered in the next section.

13.4.2.2 Metastable States

In the previous section we assumed that the deviations from the elliptically symmetric solution for the gap are small and therefore validates the use of linear response. But since we have the full thermodynamic potential at our disposal we can also consider large deviations by using a variational approach. In the experiment of Partridge et al. the observed deformation of the superfluid core is indeed large. This deformation can be modelled by giving the superfluid core a different aspect ratio than that of the trap [13] and by letting the polarized normal shell follow the shape of the trap. It is still unclear whether this represents the true energy minimum of the system or corresponds to a metastable state [14]. We can use our thermodynamic potential to

investigate this, and we will see that there appears to be no metastable state in the Landau–Ginzburg-like theory presented in this chapter.

The superfluid core is described by a nonzero gap function, which is determined by minimizing the thermodynamic potential. The case of a metastable state then corresponds to a local, but not a global minimum of the thermodynamic potential. We want to find such minima by using a variational approach. This implies that we somehow have to parameterize a likely functional form of the gap, and then vary the thermodynamic potential with respect to these parameters. To find a appropriate trial function that describes the gap well, let us start with the following function that very accurately describes the gap in the elliptically symmetric case

$$\Delta_0(R) = \Delta_0 \left(1 - \frac{R^2}{\rho R_{\text{TF}}^2} \right) \frac{\tanh\left(\frac{R_0 - R}{\Delta R}\right) + 1}{2} . \tag{13.38}$$

Here ρ, R_0 and ΔR are variational parameters. These parameters can be understood as follows. In the homogeneous theory the gap is proportional to the chemical potential $\Delta_0 = \zeta \mu \simeq 0.97\mu$, as discussed before, and in the trap the chemical potential is given by $\mu - V(\mathbf{x}) \equiv \mu(1 - R^2/R_{\text{TF}}^2)$. This explains the first factor in the right-hand side of Eq. 13.38, where the parameter ρ is needed to incorporate beyond-LDA effects. The function $[\tanh((R_0 - R)/\Delta R) + 1]/2$ with center R_0 and width ΔR describes the interface profile, since this is approximately equal to the usual soliton solution for an interface in Landau–Ginzburg theory. For specific temperatures and polarizations a minimum of the thermodynamic potential with respect to these variational parameters can easily be found numerically.

Let us now also include the aspect ratio in this variational approach. We want to see how the thermodynamic potential changes when the superfluid core has a smaller aspect ratio than the normal shell. Since we consider this in a variational manner, we need a proper function with a parameter to describe this. Let us first simply vary the aspect ratio of the gap profile. This can be achieved by performing in Eq. 13.38 the substitution $R \to R_{\text{sf}}$, with R_{sf} the scaled coordinate of Eq. 13.27 with aspect ratio α_{sf}. This then results in

$$\Omega(\alpha_{\text{sf}}) = \int d\mathbf{x} \left(\frac{1}{2} \gamma(\mathbf{x}) |\nabla \Delta_0(R_{\text{sf}})|^2 + \omega_{\text{BCS}}[\Delta_0(R_{\text{sf}}); \mathbf{x}] \right). \tag{13.39}$$

In Fig. 13.7 the solid line (curve A) shows the total thermodynamic potential as a function of α_{sf}. For this plot, we choose the trap aspect ratio to be $\alpha = 45$, because this is a typical value for the experiments of Partridge et al. where deformation is clearly visible. Also a polarization should be taken and we choose $P = 0.4$ in the elliptically symmetric case for these figures. The thermodynamic potential, however, does not show any signs of a dramatic metastable deformation. Yet the energy minimum is at a slightly smaller aspect ratio for the superfluid core then the trap. We find that for these parameters we have $\alpha_{\text{sf}} \simeq 0.99\alpha$. This very small deformation is consistent with the linear-response result from the previous section.
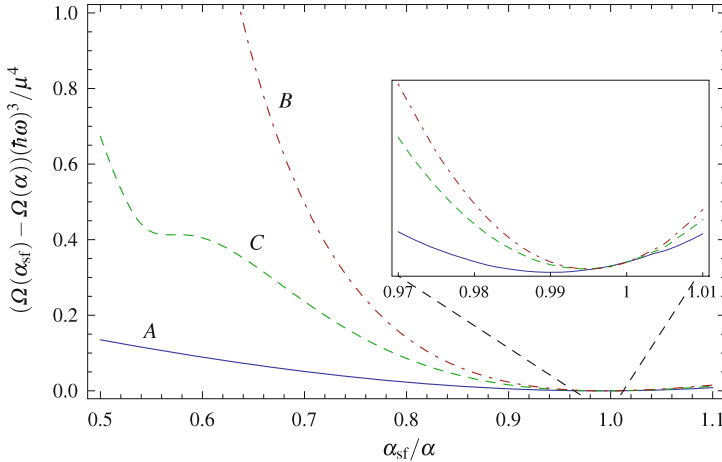
Fig. 13.7 The total thermodynamic potential of the system as a function of the deformation α_{sf}/α of the superfluid core. The different lines correspond to different choices for the deformation of the superfluid core as discussed in the text. The *solid line* shows a simple change in aspect ratio for the superfluid core only, as in Eq. 13.39. This corresponds to a change in the axial direction only. For the *dashed* and *dash-dotted line* the gap profile also changes in the radial direction. For an appropriate scaling of the thermodynamic potential we have introduced the radial trap frequency ω

In the experiment of Partridge et al., not only the superfluid-normal interface deforms, but also the partially polarized shell appears to be absent. To some extent, this can be reproduced with a gap parameter that is nonzero further to the outside of the trap in a region where the LDA would predict it to be zero. Since a nonzero gap forces the system to be balanced, the majority species will be forced to the outside, and the gas resembles what is seen in the experiment. In order to look for a metastable state that does exactly this, we can parameterize a gap function in different ways. One possibility (option B) is to change the aspect ratio of the gap, not by shrinking it in the axial direction, but by enlarging it in the radial direction. This means we replace the radius R_{sf} in Eq. 13.39 by

$$(R_{sf})^2 = \left(\frac{\alpha_{sf}}{\alpha}\right)^2 (x^2 + y^2) + \left(\frac{z}{\alpha}\right)^2, \tag{13.40}$$

with again α_{sf} the variational parameter that we can change. An even better option (option C) is to actually shift the location of the interface while changing the aspect ratio simultaneously. This can be done by using again R_{sf} as in Eq. 13.39 and substituting $R_0 \rightarrow R_0\alpha/\alpha_{sf}$ in Eq. 13.38.

The thermodynamic potential for both options is again plotted in Fig. 13.7, with the same aspect ratio α and polarization as for option A. The thermodynamic potential for option B has clearly no features and only one minimum near the elliptically symmetric solution. The result for option C, however, seems to have a feature that looks like a metastable point near $\alpha_{sf} = 0.57\alpha$. A closer look reveals that it is

not a local minimum but a saddle point. This point is a result of our choice of parametrization, since this is exactly the point where the center of the interface in Eq. 13.38 is equal to the point where the factor $1 - R_{\mathrm{sf}}^2/\rho R_{\mathrm{TF}}^2$ becomes zero. At this value of α_{sf} the interface thus disappears.

For the different trial functions of the gap that we considered here, we can conclude that there is no metastable solution with a dramatic deformation in this system. There are of course many more possible trial functions conceivable, but at present it appears unlikely that any of these contain a clear and deep enough metastable solution that can explain the dramatic deformation of Partridge et al. [2]. Because of the large deformations that we are looking for, higher-order gradient effects in the gap, or even density gradient effects, may be very important. We can therefore not conclude that we should reject metastability as the solution to this outstanding problem, but it remains a challenge to find such metastable solutions in a theory that is simultaneously also able to accurately describe the experiments of Shin et al.

13.5 Conclusions

In this chapter we discussed a Landau–Ginzburg-like approach to the unitarity Fermi gas problem, that we believe is both simple and elegant. This approach is based on the existence of an exact thermodynamic potential functional. By taking the most important interaction contributions into account, we showed that in this way all known thermodynamic properties of the homogeneous imbalanced Fermi mixture can be accounted for. When also the gradient energy of the gap is incorporated, the theory can be extended to describe inhomogeneity effects of a Fermi mixture trapped in an external potential in a manner that goes beyond the usual local-density approximation.

We showed in the first part of this chapter that the interactions can be incorporated in two frequency and momentum independent self-energies. We showed that these self-energies naturally depend on the superfluid gap. The topology of the phase diagram of the unitary Fermi mixture is correctly captured by the mean-field BCS-theory. The self-energy corrections do not change this topology, but change the critical lines in the phase diagram quantitatively. The results from experiments and various Monte-Carlo calculations uniquely determine the two parameters in the self-energy. This results in a parameter free thermodynamic potential that contains all known features and has the correct energies and equation of state for the homogeneous Fermi mixture.

The homogeneous result can be used in a local-density approximation. To go beyond this approximation, the energy cost of gradients in the gap needs to be taken into account. With this additional contribution to the thermodynamic potential we can describe the superfluid-normal interface in more detail. The experimental data from Shin et al. [3], which shows a rather smooth interface, is very well explained in this way. The smooth interface leads also to a local stabilization of a gapless superfluid, the Sarma phase. This interesting prediction of the theory, however, still needs to

be corroborated by further experiments. The surface tension of the interface can be calculated and turns out to be rather small. This is consistent with the observation of Shin et al., who see experimentally no deformation of the superfluid core, but it is in sharp contrast with the observations of Partridge et al. [6], who see a dramatic deformation. This deformation actually suggests a much larger surface tension, but another explanation may be that in their case the system is in a metastable minimum of the thermodynamic potential. In a variational approach we showed, however, that the Landau-Ginzburg-like model derived in this chapter, most likely does not contains such a local minimum. Because the deformation is large, higher-order gradient effects in the gap, or even density gradient effects, may be very important. These effects are more complicated to include in the thermodynamic potential, and are beyond the scope of this chapter.

References

1. Zwierlein, M.W., Schirotzek, A., Schunck, C.H., Ketterle, W.: Science **311**, 492 (2006)
2. Partridge, G.B., Li, W., Kamar, R.I., Liao, Y.a., Hulet, R.G.: Science **311**, 503 (2006)
3. Shin, Y., Schunck, C., Schirotzek, A., Ketterle, W.: Nature **451**, 689 (2008)
4. Fetter, A.L.: Phys. Rev. B **14**, 2801 (1976)
5. Karlhede, A., Kivelson, S.A., Lejnell, K., Sondhi, S.L.: Phys. Rev. Lett. **77**, 2061 (1996)
6. Partridge, G.B., Li, W., Liao, Y.A., Hulet, R.G., Haque, M., Stoof, H.T.C.: Phys. Rev. Lett. **97**, 190407 (2006)
7. Sarma, G.: J. Phys. Chem. Solids **24**, 1029 (1963)
8. Combescot, R., Mora, C.: Europhys. Lett. **68**, 79 (2004)
9. Parish, M.M., Marchetti, F.M., Lamacraft, A., Simons, B.D.: Nat. Phys. **3**, 124 (2007)
10. Gubbels, K.B., Romans, M.W.J., Stoof, H.T.C.: Phys. Rev. Lett. **97**, 210402 (2006)
11. Gubbels, K.B., Stoof, H.T.C.: Phys. Rev. Lett. **100**, 140407 (2008)
12. De Silva, T.N., Mueller, E.J.: Phys. Rev. Lett. **97**, 070402 (2006)
13. Haque, M., Stoof, H.T.C.: Phys. Rev. Lett. **98**, 260406 (2007)
14. Baksmaty, L.O., Hong Lu, H.P., Bolech, C.J.: Phys. Rev. A **83**, 023604 (2011)
15. Stoof, H.T.C., Gubbels, K.B., Dickerscheid, D.B.M.: Ultracold quantum fields. Theoretical and Mathematical Physics. Springer, Dordrecht (2009)
16. Burovski, E., Prokof'ev, N., Svistunov, B., Troyer, M.: Phys. Rev. Lett. **96**, 160402 (2006)
17. Lobo, C., Recativ, A., Giorgini, S., Stringari, S.: Phys. Rev. Lett. **97**, 200403 (2006)
18. Chevy, F.: Phys. Rev. A **74**, 063628 (2006)
19. Combescot, R., Recati, A., Lobo, C., Chevy, F.v: Phys. Rev. Lett. **98**, 180402 (2007)
20. Bulgac, A., Forbes, M.: Phys. Rev. Lett. **101**, 215301 (2008)
21. Diederix, J.M., Gubbels, K.B., Stoof, H.T.C.: arXiv:0907.0127 (2009)
22. Carlson, J., Reddy, S.: Phys. Rev. Lett. **100**, 150403 (2008)
23. Carlson, J., Reddy, S.: Phys. Rev. Lett. **95**, 060401 (2005)
24. McMillan, W.L.: Phys. Rev. **175**, 559 (1968)
25. Gubbels, K.B., Baarsma, J.E., Stoof, H.T.C.: Phys. Rev. Lett. **103**, 195301 (2009)
26. Stoof, H.T.C.: Phys. Rev. B **47**, 7979 (1993)
27. Baur, S.K., Basu, S., De Silva, T.N., Mueller, E.J.: Phys. Rev. A **79**, 063628 (2009)

Chapter 14
BCS–BEC Crossover and Unconventional Superfluid Order in One Dimension

A. E. Feiguin, F. Heidrich-Meisner, G. Orso and W. Zwerger

Abstract In this chapter we discuss the BCS–BEC crossover in one-dimensional Fermi gases. We present exact results using the Bethe Ansatz as well as numerical calculations of the correlation functions and the complete phase diagram. In a balanced gas, a continuous crossover occurs from a BCS-type fermionic superfluid to a BEC of pairs that are described by the Lieb-Liniger model. In the case of a finite imbalance, superfluidity persists in the form of a Fulde-Ferrell-Larkin-Ovchinnikov (FFLO) state with finite-momentum pairs on the weak coupling side. For strong attractive interactions, it is replaced by a Bose-Fermi mixture. The perspectives to observe an FFLO-state with ultracold fermions in a harmonic trap are discussed.

A. E. Feiguin
Department of Physics and Astronomy,
University of Wyoming,
Laramie, WY 82071,
USA
e-mail: afeiguin@uwyo.edu

F. Heidrich-Meisner · G. Orso
Department of Physics,
Arnold Sommerfeld Center for Theoretical Physics,
Ludwig-Maximilians-Universität München,
D-80333 München,
Germany
e-mail: heidrich-meisner@lmu.de

G. Orso
e-mail: giuliano.orso@univ-paris-diderot.fr

W. Zwerger
Physik Department, Technische Universität München,
D-85747 Garching,
Germany
e-mail: zwerger@ph.tum.de

14.1 Introduction

Starting with the historic controversy between Bardeen and Schafroth about the proper explanation of superconductivity, the crossover from a Bardeen–Cooper–Schrieffer (BCS) superfluid with Cooper pairs, whose size is much larger than the inter-particle spacing, to a Bose–Einstein Condensate (BEC) of molecules composed of fermions tightly bound into pairs has been a fundamental issue in many-body physics. The realization of fermionic superfluids with ultracold gases near a Feshbach resonance has turned this more or less academic, fifty-year-old problem into one that can be studied experimentally [1–3]. In the 3D situation, the crossover is well understood for the balanced gas, despite the fact that no analytical results are available for even the most basic quantities such as the ground-state energy or the critical temperature of the superfluid to normal gas transition in the most interesting regime near unitarity. In the situation with a finite imbalance, many questions are still open, in particular, the issue of unconventional superfluids that are expected in some parts of the phase diagram (see the chapters by Bulgac, Forbes and Magierski, by Diederix and Stoof and by Recati and Stringari). It is therefore of considerable interest to have an analytically solvable model of the BCS–BEC crossover that provides quantitative results in a particular case and, moreover, a better understanding of the conditions under which unconventional superfluid pairing may appear. Such an exact solution of the problem is possible in one dimension (1D), both for the balanced [4, 5] and the imbalanced gas [6, 7]. The importance of this solution goes beyond the generic interest in solvable many-body problems because

1. 1D Fermi gases with a tunable attractive interaction and arbitrary values of the imbalance have been realized experimentally [8, 9] and
2. the imbalanced 1D Fermi gas exhibits unconventional superfluid order of the FFLO type [10, 11] in a wide range of the phase diagram [12–19].

In the FFLO state, the pairs that form the superfluid acquire a finite center-of-mass momentum and thus lead to an order parameter that oscillates in real space. Such an unconventional superfluid has been predicted by Fulde and Ferrell [10] and—in a more general form—by Larkin and Ovchinnikov [11]. Despite intense research over several decades, this state has never been seen unambiguously, neither in condensed matter nor in the more exotic context of QCD at high densities, where FFLO-type phases based on pairing of quarks are predicted [20]. There is only some indirect evidence for an FFLO state from specific heat data on organic superconductors in a very strong magnetic field parallel to the layer structure [21]. As will be shown below, ultracold Fermi gases in 1D with a finite imbalance provide a rather simple realization of a state with finite-momentum Cooper pairs and thus give rise to the hope that this elusive unconventional superfluid can eventually be observed experimentally.

This chapter provides an introduction to FFLO-physics in one dimension and to exactly solvable 1D Fermi gases with attractive interactions in general (see also the recent reviews by Sheehy and Radzihovsky [22, 23]).

14.2 BCS–BEC Crossover of a Balanced One-Dimensional Fermi Gas

In a 3D gas, the BCS–BEC crossover is realized by changing the attractive contact interaction between two different hyperfine states through a Feshbach resonance, beyond which a bound state appears in the two-particle problem in free space. On the BCS side of the crossover, pairs only exist in the many-body system due to the Pauli blocking of states below the Fermi energy, which gives rise to a finite density of states at effectively zero energy. In one and also in two dimensions, the situation is quite different because any purely attractive interaction produces a bound state already at the two particle level. In fact, the existence of a two-body bound state is both a necessary and sufficient condition for a BCS instability [24]. At first sight, this seems to exclude a crossover with a proper BCS-limit in 1D because a two-body bound state is always present. Moreover, the BEC limit of tightly bound pairs is very special in 1D, because the Pauli principle for the constituent fermions makes these pairs behave like hard-core bosons. The bound pairs thus form a strongly interacting Tonks–Girardeau gas, very different from the weakly interacting gas of dimers that appears on the BEC side of the crossover in 3D. Remarkably, the situation in a real physical context, where atoms are confined to individual 'quantum wires' of finite width $\ell_\perp$ by, e.g., a strong 2D optical lattice, is different. In this case, an analog of the 3D crossover can be achieved in 1D by exploiting a confinement induced resonance (CIR) in a tight trap where the effective 1D scattering length exhibits a resonance caused by the mixing with a closed-channel bound state in the trap [25].

The microscopic Hamiltonian that describes a Fermi gas with two different components is the Gaudin–Yang (GY) model [26, 27]

$$H = -\frac{\hbar^2}{2m} \left(\sum_{i=1}^{N_\uparrow} \frac{\partial^2}{\partial x_i^2} + \sum_{j=1}^{N_\downarrow} \frac{\partial^2}{\partial y_j^2} \right) + g_1 \sum_{i,\,j=1}^{N_\uparrow,\,N_\downarrow} \delta(x_i - y_j). \tag{14.1}$$

Here, x_i and y_j denote the coordinates of up- and down-spin fermions respectively, whose total numbers $N_\uparrow$, $N_\downarrow$ are fixed but, in general, different. The interaction between fermions of opposite spin is described by a contact potential $g_1 \delta(x - y)$. Note that fermions of the same spin, which are never at the same point in space, have no interaction whatsoever in this model. In a situation where the atoms are subject to a transverse confinement, the strictly 1D model (14.1) is applicable provided that only the lowest eigenstate of the quantized motion in the transverse direction is occupied. For a harmonic confinement with radial frequency $\omega_\perp/2\pi$ and associated oscillator length $\ell_\perp = \sqrt{\hbar/m\omega_\perp}$, this requires $\varepsilon_F \ll \hbar\omega_\perp$ or—equivalently— $n\ell_\perp \ll 1$, where $n \equiv N/L$ is the 1D density at total particle number $N = N_\uparrow + N_\downarrow$. In this low density regime, the replacement of the actual interaction between ultracold atoms by a 1D contact potential turns out to be valid over a rather wide range of coupling constants. Indeed, the momenta for the scattering of two fermions are of the order of the Fermi momentum $k_F = \pi n/2$. The reflection amplitude

$$f(k) = \frac{-1}{1 + i\cot(\delta(k))} \simeq \frac{-1}{1 + ika_1 + \mathcal{O}\left((k\ell_\perp)^3\right)} \tag{14.2}$$

that describes two-particle scattering in 1D [1] can thus be replaced by its low-energy limit $-1/(1 + ika_1)$ as long as $k_F^2 \ll a_1/\ell_\perp^3$. Here, a_1 is the 1D scattering length, which is the single parameter that describes low-energy scattering in 1D. For a δ-function potential $V(x) = g_1\delta(x)$, the low-energy expression $-1/(1 + ika_1)$ for the reflection amplitude holds for arbitrary k, with scattering length $a_1 = -2\hbar^2/mg_1$, which is positive for attractive interactions $g_1 < 0$. The replacement of the actual inter-atomic potential by an effective contact interaction in 1D thus requires the density to be small enough such that the condition $(n\ell_\perp)^2 \ll a_1/\ell_\perp$ is obeyed. Since $n\ell_\perp \ll 1$ in the single transverse mode limit, this condition is satisfied in a rather wide range, except very close to the confinement induced resonance, where a_1 vanishes (see Eq. 14.4).

In the case of a uniform, balanced gas with total density n, the Hamiltonian (14.1) is characterized by a single dimensionless coupling constant $\gamma \equiv mg_1/\hbar^2 n$, which is inversely proportional to the density. In 1D, the strong coupling limit $|\gamma| \gg 1$ is therefore reached at *low* densities. This initially counterintuitive fact can be understood by noting that low densities imply small momenta. Moreover, the 1D scattering amplitude (14.2) has its maximum phase shift $\delta(0) = \pi/2$ as $k \to 0$ because 1D potentials become impenetrable at zero energy, i.e. $f(k \to 0) = -1$. At low densities, therefore, the interaction is strongest, quite in contrast to the 3D case where the s-wave phase shift $\tan\delta_0(k) = -ka + \ldots$ vanishes in the low-energy limit. The dimensionless coupling constant $\gamma = -\pi/(k_F a_1)$ is therefore large when the 1D scattering length is much smaller than the Fermi wave-length.

For weak attractive interactions $\gamma \to 0^-$, the ground state of the Gaudin–Yang model in the balanced case $N_\uparrow = N_\downarrow$ is a BCS-like state with Cooper pairs, whose size is much larger than the average inter-particle spacing. This is a direct consequence of the fact that the binding energy of these pairs (or—more precisely—the so called spin gap that separates the singlet ground state from the first triplet excited state) [4]

$$\Delta = \varepsilon_F \cdot \frac{16}{\pi}\sqrt{\frac{|\gamma|}{\pi}}e^{-\pi^2/2|\gamma|} \tag{14.3}$$

is much smaller than the Fermi energy ε_F in the weak coupling limit $k_F a_1 \gg 1$. At a given strength a_1 of the attractive interaction, this gap decreases exponentially as $\Delta \sim \exp(-\pi k_F a_1/2)$ with increasing density $n \sim k_F$, in contrast to the 3D case, where $\Delta \sim \exp(-\pi/2k_F|a|)$ strongly increases as the density and therefore, k_F grows. This fundamental difference is the basic reason for the fact that the unbalanced superfluid appears at the *edge* of a trapped gas with a finite overall imbalance and not in its center, as in 3D (see Sect. 14.3.2). The origin of this can be understood as a simple density-of-states effect. Indeed, the formation of pairs due to weak attractive interactions in a Fermi gas is favored by a large density of states $\nu(\varepsilon_F)$ at the Fermi energy. In 3D, $\nu_{3D}(\varepsilon_F) \sim \sqrt{\varepsilon_F} \sim k_F$ increases linearly with k_F while in 1D, due to $\nu_{1D}(\varepsilon_F) \sim 1/\sqrt{\varepsilon_F} \sim 1/k_F$, the situation is reversed and pairing is strong at *low*

densities. In the strong coupling regime $k_F a_1 \ll 1$, the attractive interaction leads to the formation of tightly bound molecules, whose binding energy coincides with the binding energy of the two-body problem $\Delta \equiv \varepsilon_b$. These pairs behave like a hard-core Bose gas. In a strictly 1D situation, therefore, the BEC limit of the crossover corresponds to a Tonks–Girardeau gas of dimers and one never reaches a weakly interacting BEC as in 3D.

A rather different situation, however, is encountered for the physically relevant case of 3D fermions that are confined in a quasi-1D geometry, such that their transverse degrees of freedom are completely frozen. For simplicity, we assume the atoms to be trapped in a harmonic waveguide with radial frequency $\omega_\perp/2\pi$ and oscillator length $\ell_\perp$. As shown by Bergeman et al. [28], the exact solution of the two-body scattering problem in such a waveguide always exhibits one and only one two-body bound state with energy $\tilde{\varepsilon}_b$, *whatever* the 3D scattering length a. Apart from this bound state, the low energy scattering properties can be described by an effective 1D delta potential $g_1 \delta(x)$ with strength [25]

$$g_1(a) = \frac{2\hbar\omega_\perp a}{1 - Aa/\ell_\perp} \quad \leftrightarrow \quad \frac{a_1(a)}{\ell_\perp} = -\frac{\ell_\perp}{a} + A. \tag{14.4}$$

Here, $A = -\zeta(1/2)/\sqrt{2} \simeq 1.0326$ is a numerical constant. As naively expected, an attractive 3D interaction $a < 0$ implies a negative value of g_1. The associated two-particle bound state has energy $\varepsilon_b = mg_1^2/4\hbar^2$ and coincides with the exact bound state energy $\tilde{\varepsilon}_b$ in the limit $a/\ell_\perp \to 0$. Remarkably, g_1 and also the binding energy $\tilde{\varepsilon}_b = 0.606\hbar\omega_\perp$ remain finite at a Feshbach resonance $a = \pm\infty$, a prediction that has been verified experimentally [9]. Entering the positive side $a > 0$, the vanishing of the 1D scattering length a_1 at $\ell_\perp/a = A \simeq 1.0326$ leads to a CIR, where g_1 jumps from $-\infty$ to $+\infty$ just as in a standard 3D Feshbach resonance. For $g_1 > 0$, the short-range potential $g_1 \delta(x)$ no longer has a bound state. It is still present, however, in the quasi-1D problem and its energy $\tilde{\varepsilon}_b$ is always larger than its value $2\hbar\omega_\perp$ at the CIR [28].

For a 1D gas with a finite density, the condition that only the lowest eigenstate of the transverse motion is occupied requires $\hbar\omega_\perp$ to be much larger than the Fermi energy ε_F. Beyond the CIR at $1/\gamma = 0$, the true bound-state energy $\tilde{\varepsilon}_b \geq 2\hbar\omega_\perp$ is therefore the largest energy scale in the problem and the dimers in this regime are essentially unbreakable bosons. In order to describe the resulting 1D Bose gas, one needs to know the effective interaction between these composite bosons. This has been studied by Mora et al. [29], who have solved the four-body scattering problem in 1D with delta-function interactions between the particles in the presence of a harmonic, transverse confinement. It turns out that the effective interaction of the dimers can again be described by a pseudo-potential $g_{dd} \delta(x)$, with a *repulsive* interaction constant $g_{dd} > 0$. Far away from the CIR, were the dimer size $a \ll \ell_\perp$ is much smaller than the scale $\ell_\perp$ of the transverse confinement, this interaction coincides with that expected from the free space result for the dimer-dimer scattering length $a_{dd} \simeq 0.6a$ in 3D, which has been derived by Petrov et al. [30]. As a result, $g_{dd} \to 2\hbar\omega_\perp a_{dd}$ vanishes in the deep BEC limit $a \to 0$ and one recovers—as in

3D—a weakly interacting Bose gas of dimers. Close to the resonance, the effective g_{dd} diverges, consistent with the expectation that the dimers near the CIR form a Tonks–Girardeau gas of hard-core bosons. In a waveguide geometry, therefore, there is a full BCS–BEC crossover in one dimension [4, 5] that is described by a Gaudin–Yang model of attractively interacting fermions up to the CIR and a Lieb–Liniger model [31] of repulsive bosons beyond the CIR. On a formal level, the continuous evolution from an attractive Fermi to a repulsive Bose gas in one dimension is implicit in the Bethe-ansatz equations of these models, as noted already by Gaudin [26]. Indeed, the ground-state energy per particle

$$\frac{E_0}{N} = \frac{\varepsilon_b}{2} + 2 \int\limits_{-B}^{B} \frac{d\lambda}{n} \sigma(\lambda) \frac{\hbar^2 \lambda^2}{2m} \tag{14.5}$$

of the attractive Fermi gas is obtained from the solution of the Bethe-ansatz integral equation

$$\pi \sigma(\lambda) = 1 + \int\limits_{-B}^{B} \frac{dq}{n} \frac{\gamma \sigma(q)}{\gamma^2 + [(\lambda - q)/n]^2}. \tag{14.6}$$

Here, $\sigma(\lambda)$ is the distribution function of the quasi-momenta (rapidities). They appear in complex conjugate pairs $k^{\pm} = \lambda \pm i/a_1$ and describe the $N/2$ bound states of the balanced gas. The value of B is fixed by the normalization $\int_{-B}^{B} d\lambda \sigma(\lambda) = n/2$. For the fermionic Gaudin–Yang problem, γ is negative. Remarkably, the identical equation applies for the Lieb–Liniger gas of dimers, where γ is positive. Since one is now dealing with dimers of mass $2m$ and density $n/2$, the dimensionless parameter $\gamma = 4mg_{dd}/\hbar^2 n = -4/(na_{1,dd})$ depends on the coupling constant g_{dd} or the associated scattering length $a_{1,dd}$ of the dimer-dimer interaction. Its dependence on the experimentally accessible parameters a and $\ell_{\perp}$ is determined by the exact solution of the 1D dimer-dimer scattering problem in the presence of a transverse confinement by Mora et al. [29]. As a function of the experimentally tunable ratio $\ell_{\perp}/a$, the resulting parameter $1/\gamma$, which replaces the standard inverse coupling constant $1/k_F a$ for the 3D crossover problem, smoothly grows from $1/\gamma = 0$ at the CIR $a \simeq \ell_{\perp}$ to $1/\gamma \gg 1$ in the BEC limit $a \ll \ell_{\perp}$, where the size of the dimers is much smaller than the transverse confinement length. More precisely, the effective dimer-dimer interaction g_{dd} that determines the dimensionless coupling constant $\gamma > 0$ on the BEC-side, does not diverge at the CIR of the atoms but close to the 3D Feshbach resonance, where the exact two-particle binding energy is close to $\tilde{\varepsilon}_b \simeq 0.6\hbar\omega_{\perp}$, see Fig. 1 in [29].

The qualitative physics of the BCS–BEC crossover in a balanced 1D Fermi gas is now easy to understand: in the high-density, BCS limit $-\pi/\gamma = k_F a_1 \gg 1$, the system consists of weakly bound Cooper pairs. In this regime, there is a gap between the singlet ground state and the first excited triplet state that increases strongly with decreasing density. In addition, there are gapless density fluctuations, describing

Fig. 14.1 Velocity of the Bogoliubov sound mode along the 1D BCS–BEC crossover
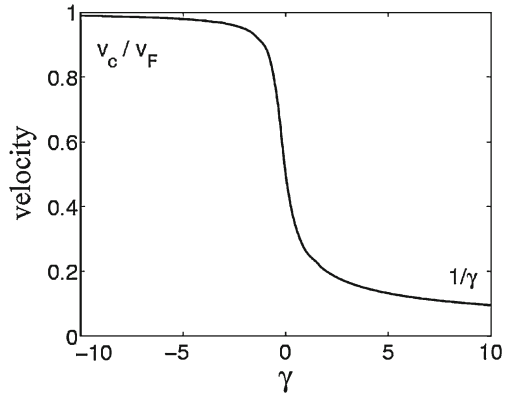
the Bogoliubov-Anderson mode of a neutral superfluid. The attractive Fermi gas is thus a so called Luther-Emery liquid [32, 33]. At the confinement induced resonance, when $k_F a_1 = 0$, the system is a Tonks–Girardeau gas of tightly bound dimers. It still exhibits sound modes with a linear spectrum, however, the spin excitations have disappeared because the spin gap is effectively infinite. For positive 3D scattering lengths $0 < a \simeq \ell_\perp$, the system is an interacting Bose gas of tightly bound molecules. Its excitations are the standard Bogoliubov sound modes, whose velocity vanishes asymptotically in the weak coupling (BEC) limit $1/\gamma \gg 1$, as shown in Fig. 14.1. The possibility of separating the BCS–BEC crossover into a purely fermionic problem on one side of the CIR and a purely bosonic one on the other side of the resonance is a peculiar property of one dimension. It relies on the assumption of a dilute system $n\ell_\perp \ll 1$, whose Fermi energy is much smaller than the binding energy at resonance. Defining a characteristic length scale $r^\star$ by the two-particle binding energy $\varepsilon^\star = \hbar^2/m(r^\star)^2$ at resonance, the low density condition $k_F r^\star \ll 1$ in 1D is completely equivalent to the condition $k_F r^\star \ll 1$ of a broad Feshbach resonance in 3D [1]. In this form, the condition applies more generally also for a two-channel, Bose-Fermi resonance model [34]. In the opposite, narrow Feshbach resonance limit $k_F r^\star \gg 1$, the physics near the CIR becomes more complicated. In particular, a new phase appears where atoms and dimers, both in a superfluid state with algebraically decaying correlations, coexist [35, 36].

14.3 Spin-Imbalanced Fermi Gas in One Dimension

In this section we discuss the extension of the Gaudin–Yang solution for a balanced attractive Fermi gas to the situation with a finite imbalance, as presented in [6, 7]. We first discuss the quantum phase diagram for the homogeneous system, where the underlying model is integrable by means of the Bethe ansatz. We then include a longitudinal trapping potential via the local density approximation and derive the

shell-structure of the density profiles of the two components. Effects of finite temperature have been investigated using the Bethe ansatz in [37, 38] and will not be covered here. A similar behavior at zero temperature is found for the case of optical lattices at filling factors below one. This case is covered in [39].

14.3.1 Bethe-Ansatz Solution for the Homogeneous Gas

The Hamiltonian (14.1) can be diagonalized exactly also in the presence of a finite spin polarization. For fixed values of the linear number densities $n_\uparrow = N_\uparrow/L$ and $n_\downarrow = N_\downarrow/L$, where L is the size of the system, the ground state energy E is given by

$$\frac{E}{L} = \frac{4\hbar^2}{ma_1^3}\left[\int_{-B}^{B}\left(2\lambda^2 - \frac{1}{2}\right)\sigma(\lambda)d\lambda + \int_{-Q}^{Q} k^2\rho(k)dk\right], \quad (14.7)$$

where $a_1 = -2\hbar^2/mg_1$ is the effective 1D scattering length, and B and Q are non-negative numbers related to the particle densities by $n_\downarrow a_1 = 2\int_{-B}^{B}\sigma(\lambda)d\lambda$ and $n_\uparrow a_1 - n_\downarrow a_1 = 2\int_{-Q}^{Q}\rho(k)dk$. The spectral functions $\sigma(\lambda)$ and $\rho(k)$ appearing in Eq. 14.7 are solutions of two coupled integral equations [26]

$$\sigma(\lambda) = \frac{1}{\pi} - \int_{-B}^{B} K_1(\lambda, \lambda')\sigma(\lambda')d\lambda' - \int_{-Q}^{Q} K_2(\lambda, k)\rho(k)dk,$$

$$\rho(k) = \frac{1}{2\pi} - \int_{-B}^{B} K_2(\lambda, k)\sigma(\lambda)d\lambda, \quad (14.8)$$

where the kernels are given by $\pi K_1(\lambda, \lambda') = 1/[1 + (\lambda' - \lambda)^2]$ and $\pi K_2(\lambda, k) = 2/[1 + 4(k - \lambda)^2]$. The need for a second distribution function $\rho(k)$ beyond the function $\sigma(\lambda)$ introduced in Sect. 14.1 for the balanced gas is due to the presence of uncompensated spins in the imbalanced case $n_\uparrow \neq n_\downarrow$. These uncompensated spins are not bound in pairs and are thus described by real rapidities k_j. In the thermodynamic limit, this gives rise to a distribution function $\rho(k)$. It is only for $n_\uparrow = n_\downarrow$ that no uncompensated spins exist. In this case, we have $Q = 0$ and the coupled set of equations (14.8) reduces to a single integral equation for $\sigma(\lambda)$ which is identical to Eq. 14.6 discussed in Sect. 14.1 by a trivial rescaling.

For a fixed value of the total density $n \equiv n_\uparrow + n_\downarrow$, the density difference $s \equiv n_\uparrow - n_\downarrow$ can vary in the range $0 \leq s \leq n$. For $s = 0$, the ground state of the Hamiltonian (14.1) is *fully paired* with a spin gap Δ, corresponding to the energy needed to break a pair in the many-body system, whereas in the opposite limit $s = n$,
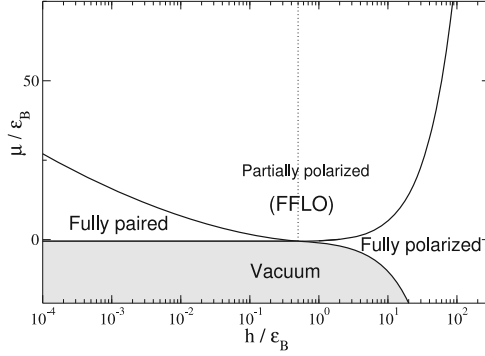
Fig. 14.2 Quantum phase diagram of attractively interacting fermions obtained from the Bethe-ansatz solution of the Gaudin model. Here $\mu, h = (\mu_\uparrow \pm \mu_\downarrow)/2$, where $\mu_{\uparrow,\downarrow}$ are the chemical potentials of the two components, and ε_b is the binding energy of the pair. Reproduced from [7]

the system is a *fully polarized* gas of $\uparrow$ fermions. For $0 < s < n$, the gas is *partially polarized* and is a superfluid of the FFLO type [12–19].

Using the mean chemical potential μ and the *effective* magnetic field h, defined as

$$\mu = \frac{\partial(E/L)}{\partial n}, \quad h = \frac{\partial(E/L)}{\partial s} \tag{14.9}$$

as new independent variables, one obtains the universal phase diagram shown in Fig. 14.2, where $\varepsilon_b = \hbar^2/ma_1^2$ is the binding energy of the molecule.

The phase boundary $h = h_c(\mu)$ between the partially polarized and the fully paired regions is calculated by setting $s = 0$ in Eq. 14.9. We see that h_c is a *decreasing* function of the chemical potential, being exponentially small at large particle density and reaching its maximum value $h_c = \varepsilon_b/2$ in the zero density limit. This behavior can be understood by noticing that the critical magnetic field is related to the spin gap Δ of the *unpolarized* gas by $h_c = \Delta/2$, and therefore, it increases when one enters into the low density regime (μ decreases), where interaction effects become stronger. We emphasize that in higher dimensions the situation is completely reversed [40] (see also the discussion in the previous section).

The boundary $h = h_s(\mu)$ between the partially polarized and the fully polarized phases in Fig. 14.2 is obtained by setting $s = n$ in Eq. 14.9. This yields the implicit formula $h_s = 2\varepsilon_b[Q^2(1 - \arctan(2Q)/\pi) + (2Q - \arctan(2Q) + \pi)/4\pi]$, with $Q = \sqrt{(\mu + h_s)/2\varepsilon_b}$. The fully paired and fully polarized phases correspond, respectively, to the paramagnetic and ferromagnetic states of a superconductor in a magnetic field [41, 42].

The presence of a two-body bound state leads to a direct boundary $\mu = -\varepsilon_B/2$ between the fully paired phase and the vacuum. In the fully polarized phase the atom density vanishes in correspondence to $\mu_\uparrow = (\mu + h)/2 = 0$, as for the 3D case [40]. We stress that the partially polarized phase has no direct boundary with the vacuum,

implying the absence of n-body bound states with $n > 2$. This feature will change in the presence of a mass asymmetry, as we shall discuss in Sect. 14.5.

We see from Fig. 14.2 that the fully paired and fully polarized phases *cannot* coexist for a fixed value of the magnetic field. In particular, for $h < \varepsilon_b/2$, only the fully paired phase is allowed, whereas for $h > \varepsilon_b/2$, only the fully polarized phase can occur. This property determines the shell structure of a trapped gas, as we shall see next.

14.3.2 Phase Separation in a Trap

We now assume that particles are trapped longitudinally by a shallow harmonic potential $V_{ho}(z) = m\omega_z^2 z^2/2$, where ω_z is the trapping frequency, and we calculate the density profiles of the two components via the local density approximation (LDA). This is done by imposing the local equilibrium condition $\mu_\sigma[n_\uparrow(z), n_\downarrow(z)] + V_{ho}(z) = \mu_\sigma^0$, where $\mu_\sigma[n_\uparrow, n_\downarrow]$ are the corresponding chemical potentials of the homogeneous system and μ_σ^0 are constants fixed by the normalization $N_\sigma = \int n_\sigma(z)dz$. Taking into account that $\mu, h = (\mu_\uparrow \pm \mu_\downarrow)/2$, this reduces to

$$\mu[n_\uparrow(z), n_\downarrow(z)] = \mu^0 - V_{ho}(z),$$
$$h[n_\uparrow(z), n_\downarrow(z)] = h^0, \tag{14.10}$$

where $\mu^0, h^0 = (\mu_\uparrow^0 \pm \mu_\downarrow^0)/2$. Equation 14.10 shows that the LDA trajectories correspond to vertical lines in the phase diagram of Fig. 14.2, implying that the trapped one-dimensional gas phase-separates into *two* shells: a partially polarized core and either fully paired or fully polarized wings. This is a key difference with respect to three-dimensional systems, where the trap induces a three-shell structure [40].

In Fig. 14.3 we show the calculated Thomas–Fermi radii R_{in} and $R_\uparrow$ of the inner and outer shells, respectively. These are plotted as a function of the spin polarization $P \equiv (N_\uparrow - N_\downarrow)/N$, where $N = N_\uparrow + N_\downarrow$ is the total number of particles, and for different values of the interaction parameter $\lambda = N a_1^2/a_z^2$. In the absence of interactions, we find $R_\uparrow, R_{in} = \sqrt{1 \pm P} a_z N^{1/2}$ which are monotonic functions of P (*top curves*). For finite attractive interactions, the two radii show instead a non-monotonic behavior as a function of P, signaling the appearance of fully paired wings at low polarizations. In particular, the cloud size ($R_\uparrow$) first decreases as P increases because the density profiles of majority and minority components must match at the edge of the cloud. Beyond a critical value $P = P_c$ of the spin polarization, the outer shell becomes fully polarized, implying that the cloud size must increase steadily for $P > P_c$, as shown in Fig. 14.3. The critical spin polarization P_c increases going towards the strongly interacting dilute regime, where it eventually saturates at $P_c(\lambda = 0) = 1/5$ (see [6, 7] for details).
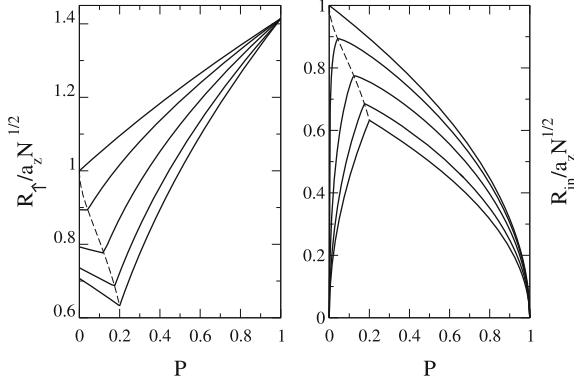
Fig. 14.3 Thomas–Fermi radii of the outer ($R_\uparrow$) and of the inner ($R_{\rm in}$) shell computed via LDA from the exact solution for the homogeneous system. Radii versus P for values of the interaction parameter $\lambda = \infty, 10, 1, 0.1, 0$ (*bottom to top*). The non-monotonic behavior is a signature of the fully paired wings at low spin polarization. Reproduced from [7] with permission of the author

14.4 FFLO Correlations in the Partially Polarized Phase

14.4.1 Predictions From Bosonization

So far, we have only discussed the thermodynamics of attractive 1D fermions at zero temperature. As shown in the previous section, this allows one to determine the density profiles of trapped gases within LDA. A detailed understanding of the order that is present in the balanced and imbalanced attractive Fermi gas, however, requires to calculate correlation functions. Of particular interest is the nature of superfluid order in the ground state. It follows from the pair correlation

$$\rho_{ij}^{\rm pair} = \left\langle c_{i,\uparrow}^\dagger c_{i,\downarrow}^\dagger c_{j,\uparrow} c_{j,\downarrow} \right\rangle, \tag{14.11}$$

which describes the tendency for singlet pairing as a function of separation $x = i - j$ (we use a continuum or discrete notation interchangeably, in particular since quantitative results for correlation functions at arbitrary distances require using a lattice model with discrete sites i, see the following section). In a standard singlet superconductor, the pair correlation function approaches a finite constant at large separation $x \to \infty$, which is proportional to the square of the gap parameter in weak coupling. In one dimension, long-range order is destroyed by quantum fluctuations even in the ground state and at most algebraically decaying correlations may exist. For the balanced gas, the correlation exponent Δ_{SS} for singlet pairing, defined by $\rho_{ij}^{\rm pair} \sim |i - j|^{-\Delta_{SS}}$, turns out to be the inverse $\Delta_{SS} = 1/K_c$ of the (charge) Luttinger exponent K_c [32]. For attractive interactions, this implies $\Delta_{SS} < 1$. The singlet pairing correlations thus decay very slowly. They are, in fact, the dominant correlations in the system, i.e., those with the smallest value of the correlation exponent Δ in the two-particle

channel. In the case with a finite imbalance $P \neq 0$, superfluid pairing still persists in the ground state, however it changes both its nature and also decays more quickly with distance. The fact that the nature of pairing is different can be understood most easily from a mean-field description of pairing in the weak coupling limit. At finite imbalance $P = (n_\uparrow - n_\downarrow)/n > 0$, the two components have different Fermi wave vectors $k_{F,\sigma} = \pi n_\sigma$. A BCS-instability of the free Fermi gas, which pairs an up-spin fermion with a down-spin one at opposite sides of the respective Fermi 'surfaces' will thus lead to pairs with a finite total momentum

$$Q = k_{F\uparrow} - k_{F\downarrow} = \pi n P. \tag{14.12}$$

This results in an oscillating superfluid correlation function of the form

$$|\rho_{ij}^{\mathrm{pair}}| \propto |\cos(Qx)|/x^{\Delta(p)} \tag{14.13}$$

which is characteristic of states of the FFLO-type (sometimes also denoted LOFF in the literature) order. Fermionic superfluids with pairs that have a finite momentum in the ground state were initially suggested for superconductors in the presence of strong internal magnetic fields [10, 11]. In the present context of imbalanced Fermi gases, the Hamiltonian is time-reversal invariant. The ground state therefore necessarily has a vanishing net current. Pairs with net momentum Q and $-Q$ are thus equally probable and the superfluid order parameter is a real function $\sim \cos(Qx)$, up to an arbitrary overall phase. A peculiar feature of the situation in one dimension is the fact that FFLO-type order is the dominant correlation (i.e. the one with the smallest value of the correlation exponent Δ) at arbitrary polarizations $P > 0$, up to $P = 1$ where the system is a trivial fully polarized and non-interacting Fermi gas [13, 16, 17]. (for early mean-field studies, see [43, 44]).

A convenient method to calculate the long-distance behavior of correlations in 1D quantum liquids is bosonization [32]. The attractive Fermi gas in the presence of a finite effective field h that couples to the imbalance in a Zeeman-like form $H' = -h(N_\uparrow - N_\downarrow)$ can thus be reduced to a sine-Gordon model for the spin-density field $\phi_s(x)$ that determines the imbalance via $p(x) \sim \partial_x \phi_s(x)$ [12]. The imbalance remains zero up to a critical value $h_c = \Delta/2$ of the effective field that is determined by the spin gap Δ of the balanced gas. Beyond this critical field, a finite density $n_{sol} = n_\uparrow - n_\downarrow = Q/\pi$ of solitons arises in $\phi_s(x)$ where the superfluid order parameter changes by π at each soliton. The associated pair correlation function has the form given in Eq. 14.13 with a correlation exponent $\Delta_{SS}(p) = \Delta_{SS}(p=0) + 1/2$. It is larger than the one of the balanced gas by an additional contribution $1/2$ that arises from the fluctuations around the average periodic order of the soliton lattice [12]. The appearance of an order parameter that is periodic in space can be understood in simple physical terms by noting that the additional up-spins in the imbalanced gas prefer to sit at the zeroes of the order parameter (naively associated with a locally vanishing pairing gap), which are $1/n_{sol}$ apart on average. These results are supported by detailed numerical investigations of correlation functions in the attractive Hubbard model on a 1D lattice, using density matrix renormalization

Fig. 14.4 Exponents of density-density correlations and (s-wave) pair-pair correlations functions, calculated numerically from the Bethe-ansatz, as a function of polarization and for several densities [16]
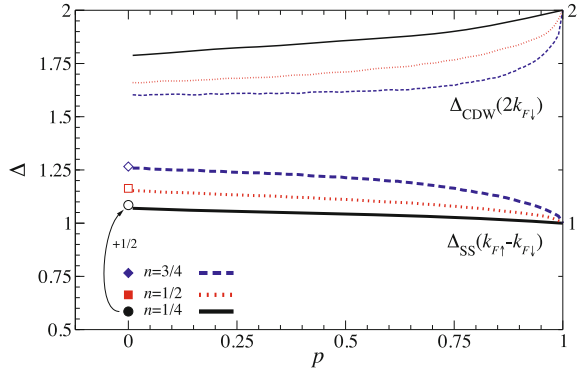
group (DMRG) or Quantum Monte Carlo (QMC) methods [12–19]. In particular, the values of the correlation exponents for density-density correlations (denoted by Δ_{CDW}) which are dominant for repulsive interactions and those for superfluid pairing of the FFLO-type are shown in Fig. 14.4. These results were obtained in [16] by numerically solving the respective Bethe-ansatz equations [45, 46]. It is evident that for attractive interactions, FFLO is the dominant instability at arbitrary values of the polarization, also compared to other algebraically decaying correlation functions such as, e.g., triplet superfluidity [16]. It is favored by small filling fractions on the lattice. Moreover, there is hardly any dependence of the exponents on polarization P beyond the initial jump by 1/2, in agreement with the predictions of bosonization. There is one major caveat, however, of this method, which will be discussed in the following.

The exact Bethe-ansatz solution of the imbalanced gas shows that the finite polarization $P(h) \sim (h - h_c)$ which appears beyond the critical field $h_c = \Delta/2$ starts *linearly* with the deviation from the critical field. By contrast, bosonization predicts a square root behavior $P(h) \sim \sqrt{h - h_c}$ of the polarization near the critical field [12]. This behavior is characteristic for the appearance of solitons in a Sine-Gordon model with a finite tilt, as was found by Pokrovsky and Talapov [47] in the context of 2D commensurate-incommensurate transitions. The failure of bosonization in this context has been discussed by a number of authors [48–51] and is due to a breakdown of spin-charge separation in this problem. To understand the physics behind this effect, it is convenient to consider the strong coupling limit $k_F a_1 \rightarrow 0^+$ of the attractive Fermi gas at given values of the total density n and density difference $s = n_\uparrow - n_\downarrow$. The ground-state is effectively a gas of dimers with density $n_d = n_\downarrow = (n - s)/2$ that coexists with a gas of unpaired fermions with density s. Since the dimers are hard-core bosons, the ground-state energy density is of the form [7]

$$e_0(n, s) = -\varepsilon_b n_d + e_0^{TG} + e_0^F = -\varepsilon_b n_d + \frac{\hbar^2 \pi^2}{12m} \frac{1}{8} (n - s)^3 + \frac{\hbar^2 \pi^2}{6m} s^3. \quad (14.14)$$

Here e_0^{TG} is the energy density of the Tonks–Girardeau gas of dimers with mass $2m$ while e_0^F is that of a free Fermi gas. Note that there is no contribution $g_{ad} n_d s$ from the

atom-dimer repulsion here, because in one dimension the effective coupling constant g_{ad} turns out to vanish like s^2 [52]. Using $h = \partial e_0/\partial s$ and the strong coupling result $2h_c(n) = \varepsilon_b - \varepsilon_F/2 + \ldots$ for the critical field, Eq. 14.14 leads to

$$h - h_c = \frac{\varepsilon_F}{2} P - \frac{\varepsilon_F}{4} P^2 + 4\varepsilon_F P^2 + \ldots. \tag{14.15}$$

As a result, the dimensionless polarization $P = 2(h - h_c)/\varepsilon_F + \ldots$ vanishes linearly with $h - h_c$, consistent with the Bethe-ansatz solution (see also [50, 53]). The linear behavior is a result of a contribution $\varepsilon_F P^2/4$ to the ground-state energy density e_0^{TG} of the Tonks–Girardeau gas in Eq. 14.14. For small polarization $P \to 0$, this term dominates the kinetic energy $e_0^F \sim P^3$ of the Fermi gas of unpaired atoms that gives rise to the last, irrelevant contribution on the rhs of Eq. 14.15. The failure of bosonization is that it does not account for the change in the energy density e_0^{TG} that is associated with the creation of unpaired fermions from the gas of bound pairs. Bosonization pretends they are created out of a vacuum state whose energy is unaffected by a finite polarization. Only the kinetic energy $\sim P^3$ due to the filling of an initially empty band in the spin sector is included. A different way to see that bosonization cannot describe the correct linear dependence $P(h) = 2(h - h_c)/\varepsilon_F + \ldots$ is that it does not account for an energy scale of order ε_F, 'knowing' only about the Fermi momentum, which is proportional to $\sqrt{\varepsilon_F}$. Also note that the coupling between spin and charge that results from the nontrivial dependence of e_0^{TG} on n and s changes the effective interaction between individual unpaired fermions (i.e., the solitons of the Sine-Gordon theory) from the standard $1/x^3$-behavior discussed in the context of 2D commensurate-incommensurate transitions [47] to a longer range $1/x^2$-dependence.

14.4.2 Exact Numerical Results

In this section we wish to demonstrate that the FFLO correlations predicted from bosonization [12] indeed exist in the partially polarized phase of 1D systems of attractively interacting fermions. While both the Gaudin–Yang and the 1D Hubbard model, the lattice version, are integrable models, the calculation of correlation functions is notoriously difficult, and one therefore has to resort to numerically exact methods such as DMRG or QMC.

For concreteness, we consider the 1D attractive Hubbard model:

$$H_0 = -t \sum_{i=1,\sigma}^{L-1} \left(c_{i\sigma}^\dagger c_{i+1\sigma} + h.c. \right) + U \sum_{i=1}^{L} n_{i\uparrow} n_{i\downarrow} \tag{14.16}$$

with an attractive onsite interaction U and open boundary conditions. Here $c_{i\sigma}$ annihilates a fermion with spin σ at site i and $n_{i\sigma}$ is the local density of the fermions with spin σ. The phase diagram for the 1D attractive Hubbard model for $n \le 1$ has the
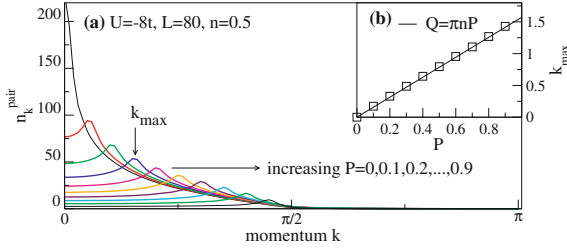
Fig. 14.5 Momentum distribution function of pairs in the 1D Hubbard model with $U = -8t$ and $n = 0.5$. In Eq. 14.18, $i_0 = L/2$. Inset: the position of the maximum in n_k^{pair} shows the expected scaling with $Q = k_{F\uparrow} - k_{F\downarrow} = \pi n P$. Compare also [14, 17] for the case of optical lattices and [15] for the case of the continuum

same phases as the continuum model: vacuum, partially polarized phase, fully paired phase, fully polarized phase [39, 54]. Additional phases emerge at larger densities that, however, are related to the aforementioned ones by means of a particle-hole transformation.

We use DMRG [55, 56] to compute the pair-pair correlation functions Eq. 14.11 [13, 17, 18]. Similar results can be obtained with QMC for both optical lattices [14] (there, the particle numbers are smaller than what can be accessed with DMRG [39], though) and the continuum case [15].

It is illustrative to go to momentum space by computing the associated momentum distribution function:

$$n_k^{pair} = (1/L) \sum_{lm} \exp[ik(l-m)]\rho_{lm}^{pair}. \tag{14.17}$$

Typical results for a homogeneous system with open boundary conditions are shown in the main panel of Fig. 14.5. At zero polarization $P = 0$, the MDF has a maximum at zero momentum, which, upon polarizing the system, shifts to finite momenta. The smoking gun for the presence of FFLO correlations is the scaling of the position Q of the finite-momentum maximum with polarization: in the case of 1D we expect Eq. 14.12 to hold. This is verified in the inset of Fig. 14.5, where we find $Q = \pi n P$, as expected (compare [13–15, 17, 18]). Note that this behavior is seen up to full polarization.

The next questions to address are the actual functional form of the spatial decay of pair correlations and the stability of FFLO correlations in the presence of a harmonic trap. We address both points by considering a trapped system

$$H = H_0 + V \sum_i n_i (i - i_0)^2, \tag{14.18}$$

summarizing key results from [13, 39] (see also [15, 18, 57]).

In Sect. 14.3, we emphasized that in the case of one dimension, the partially polarized phase always (i.e., at all U and $P > 0$) sits in the core of a trapped two-component Fermi gas, which can be predicted by applying LDA to the exactly known
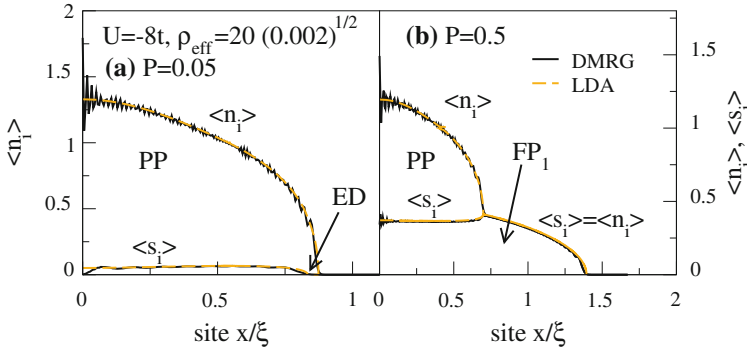
Fig. 14.6 Phase separation in an optical lattice with $U = -8t$, $N = 160$ fermions and (a) $P = 0.05$ and (b) $P = 1/2$ (reproduced from [39] with permission from the authors). Solid lines are DMRG results, dashed lines are LDA. If the main interest is in the behavior in the wings of a trapped Fermi gas, then it is computationally advantageous to use $i_0 = 0$ in Eq. 14.18 [39]

phase diagram of either the continuum [6, 7] or the lattice case [39]. This prediction was verified by exact numerical DMRG results in the case of an optical lattice [13, 18] and QMC simulations for the continuum [15] case. For illustration, we show DMRG results for the particle and the spin density profiles of a trapped Fermi gas at small polarizations $P < P_c$ and large polarizations $P > P_c$ in Fig. 14.6 [39], for which we have numerically obtained the ground-state of Eq. 14.18 with H_0 from Eq. 14.16 and realistic particle numbers of $N = 160$. Note that we display the spatial coordinate in units of the oscillator length $\xi = 1/\sqrt{V}$. Figure 14.6 clearly shows that the core is partially polarized and that the wings are fully paired for $P < P_c$ and fully polarized for $P > P_c$. Furthermore, for this particle number, the corresponding LDA result obtained from the exact Bethe-ansatz solution for the 1D attractive Hubbard model agrees quantitatively with the exact DMRG results (see [39] for a discussion and [15] for a similar analysis of the continuum case).

Turning now to the question of pair correlations in the trapped system, Fig. 14.8 shows the pairs' MDF for a trapped Fermi gas: similar to the homogeneous case, a finite-momentum instability emerges upon polarizing the system. In order to verify the relation Eq. 14.12 in the trapped case, one has to take into account that for $P > P_c$, part of the total polarization goes into the fully polarized wings. In other words, the FFLO correlations are driven by a smaller effective polarization $P_{\text{eff}} < P$. In order to extract $P_{\text{eff}} < P$, we explain the strategy of [13]: the spatial extension L_{eff} of the quasi-condensate can be extracted by computing the highest occupied natural orbital ϕ_0 of the matrix ρ_{ij}^{pair} Eq. 14.11 (i.e., the eigenvector corresponding to the largest eigenvalue). An example for the spatial form of $|\phi_0|^2$, taken from [13], is shown in Fig. 14.7, which yields an illustration of the node structure in the 1D FFLO state. Note that the spin density takes maxima in the nodes of the quasi-condensate [44] (an analogous result for the spin density was obtained with QMC for the continuum case [15]).
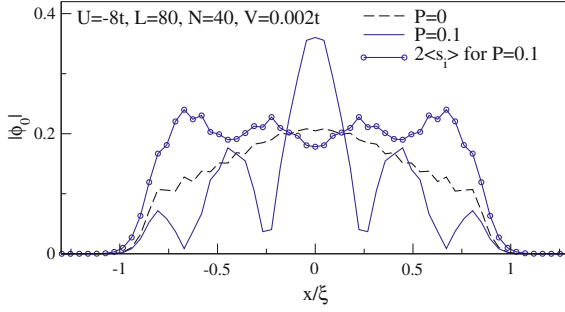
Fig. 14.7 Highest occupied natural orbital $|\phi_0|$ of a trapped 1D Fermi gas in an optical lattice for $P = 0, 0.1$ and $U = -8t$ (*lines*). The spin density is displayed with stars. The natural orbital yields a visualization of the 1D FFLO quasi-condensate. DMRG data taken from [13]
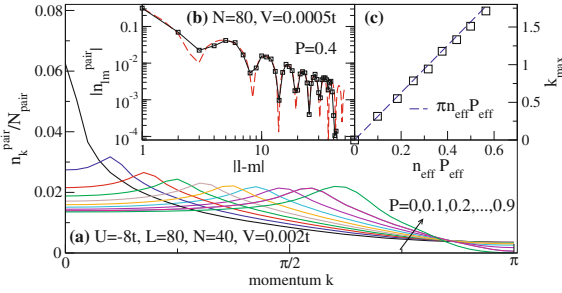
Fig. 14.8 a Momentum distribution function of pairs of a trapped, two-component Fermi gas with $U = -8t$ (see the legends for further parameters) described by the Hamiltonian Eq. 14.18. **b** Decay of pair correlations in real space and comparison of DMRG results (symbols) to the prediction from bosonization [12], Eq. 14.13 (*lines*). **c** The position of the maximum in n_k^{pair} shows the expected scaling with $Q = k_{F\uparrow} - k_{F\downarrow} = \pi n_{\text{eff}} P_{\text{eff}}$, where P_{eff} is the effective polarization in the partially polarized core (see the discussion in [13]). Reproduced from [13]

The effective polarization is then obtained by integrating $\langle s_i \rangle = \langle n_{i\uparrow} - n_{i\downarrow} \rangle$ over the spatial extent of $|\phi_0.|$ By plotting the position Q of the maximum in n_k^{pair} vs $n_{\text{eff}} P_{\text{eff}}$, one recovers the expected linear dependence in agreement with Eq. 14.12 (see Fig. 14.8c). Finally, the spatial decay of pair correlations at large $|U|$ indeed follows the prediction from bosonization, Eq. 14.13 [12], as we show in Fig. 14.8b.

Using DMRG, a variety of other correlation functions can be obtained as well in the partially polarized phase, including spin-spin correlations [17, 58], density-density correlations [17], and noise correlations [16]. The FFLO state leaves distinct fingerprints in these correlations and their respective Fourier transforms. For instance, the $2k_F$ peak/kink present in the structure factor for density-density correlations in the unpolarized case splits into two peaks at $2k_{F\uparrow}$ and $2k_{F\downarrow}$ [17]. The spin structure factor, as a consequence of the $2Q$ spin density wave that accompanies the FFLO state (see Fig. 14.7) has a pronounced kink at $2Q = 2(k_{F\uparrow} - k_{F\downarrow})$ [58]. A proposal

for the experimental measurement of spin correlations in a spin-polarized Fermi gas has been put forward in [58]. Finally, the FFLO correlations induce the presence of peaks in noise correlations whose distance is given by Q (for a detailed discussion, see [16]).

14.5 Spin- and Mass-Imbalanced Fermi Mixtures

So far we have discussed situations in which up and down fermions have the same mass (or effective mass) and are described by integrable models. In this section we address the more general problem in which pairing occurs between particles of different species, for example ^{6} Li and ^{40} K atoms [59–61]. In this case the masses of spin up and down fermions are different and the underlying Hamiltonian is no longer integrable. For lattice systems, the simplest model is the 1D asymmetric Fermi-Hubbard:

$$H = - \sum_{i\sigma} t_\sigma \left(c_{i,\sigma}^\dagger c_{i+1,\sigma} + h.c. \right) + U \sum_i n_{i\uparrow} n_{i\downarrow}, \qquad (14.19)$$

where t_σ are spin-dependent tunneling rates. The model (14.19) has been studied recently by the bosonization method in [62], assuming equal densities of the two components, $n_\uparrow = n_\downarrow$. The extension to spin-imbalanced gases was first investigated numerically in [63, 64].

For equal masses, $t_\downarrow = t_\uparrow$, the exact solution of the Hubbard model shows that fermions can bind in pairs, but n-body bound states with $n > 2$ are generally forbidden. For unequal masses, it has recently been shown [65, 66] that three-body bound states, hereafter called trimers, exist and can considerably affect the many-body picture. Here we outline the key results of [65, 66].

The trimer gap, namely the energy needed to break a single trimer at finite density, is defined as

$$\Delta_{\mathrm{tr}} = - \lim_{L\to\infty} \Big[E_L(N_\uparrow + 1, \ N_\downarrow + 2) + E_L(N_\uparrow, N_\downarrow)$$

$$- E_L(N_\uparrow + 1, \ N_\downarrow + 1) - E_L(N_\uparrow, \ N_\downarrow + 1) \Big], \qquad (14.20)$$

where $E_L(N_\uparrow, N_\downarrow)$ is the ground state energy of a system with atom numbers $N_\uparrow$, $N_\downarrow$ in a chain of size L. The limit in Eq. 14.20 is taken assuming $N_\sigma \to \infty$ with $n_\sigma \equiv N_\sigma / L$ being fixed. Equation 14.20 has been evaluated by DMRG on lattices of up to $L = 160$ sites and the thermodynamic limit was extrapolated via finite-size scaling.

For equal masses, $t_\downarrow = t_\uparrow$, no trimers exist and therefore, $\Delta_{\mathrm{tr}} = 0$. For $t_\downarrow < t_\uparrow$, the trimer gap (14.20) is finite only when the two concentrations are commensurate, i.e., $n_\downarrow = 2n_\uparrow$. It is plotted in Fig. 14.9 as a function of $n_\downarrow$ and for different values of the interaction strength. We see that the gap is a decreasing function of the density
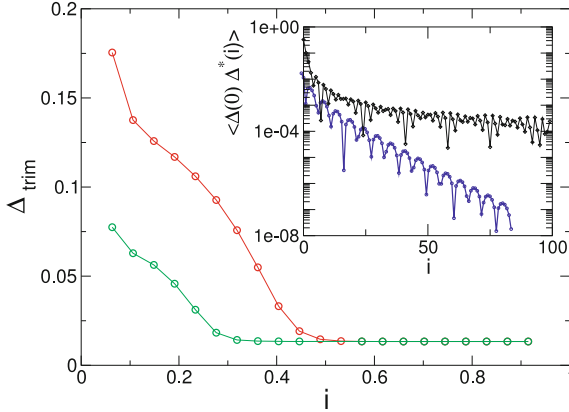
Fig. 14.9 Trimer energy gap (20) in unit of $t_\uparrow$ plotted versus density $n_\downarrow$ and different values of $U = -2t_\uparrow$ (bottom) and $U = -4t_\uparrow$. The mass anisotropy is $t_\downarrow = 0.3$. *Inset*: superconducting correlations as a function of the distance from the center of the chain for different values of the density $n_\downarrow = 0.7$ (upper curve), where $\Delta_{tr} = 0$, *and* $n_\downarrow = 0.3$, where $\Delta_{tr} > 0$. The parameters used are $U = -4t_\uparrow$, $t_\downarrow = 0.3t_\uparrow$ and $L = 200$ and the densities are commensurate, $n_\uparrow = n_\downarrow/2$. Notice the change from an algebraic to an exponential decay. Reproduced from [66]

and vanishes at a critical concentration $n_\downarrow = n_\downarrow^{cr}$—in sharp contrast with the case of equal densities, $n_\uparrow = n_\downarrow$, where the associated pairing gap is *always* positive for any filling. This result is consistent with the bosonization analysis performed in [65]. In particular, for densities satisfying the constraint $pn_\uparrow - qn_\downarrow = 0$, with p, q integer numbers, the bosonized action includes the following interaction term

$$H_{int} = A \int \cos 2(p\phi_\uparrow(z) - q\phi_\downarrow(z)), \qquad (14.21)$$

where A is an amplitude and $\phi_\sigma(z)$ the phase operator of each component. For $p = q = 1$, the operator (14.21) describes pair superconductivity and is a relevant perturbation, implying that the pairing gap opens at any $U < 0$. For trimers, corresponding to $p = 1, q = 2$, the perturbation (14.21) is instead irrelevant, and the trimer gap only opens beyond a critical interaction strength, $U < U_c < 0$ or, equivalently, only at sufficiently low density.

The phase with $\Delta_{tr} \neq 0$ corresponds to a Luttinger liquid of trimers. Since pairs are bound into these composite objects and cannot propagate freely, the long distance behavior of the superconducting FFLO correlations changes from algebraic to exponential decay, as shown in the inset of Fig. 14.9.

Next, we discuss the grand-canonical phase diagram of the asymmetric Hubbard model, which is obtained by replacing the densities $n_\uparrow$ and $n_\downarrow$ by two new variables, corresponding to the mean chemical potential $\mu = \partial E / \partial(N_\uparrow + N_\downarrow)$ and the *effective magnetic field* $h = \partial E / \partial(N_\uparrow - N_\downarrow)$, where E is the ground state energy calculated by DMRG. This is shown in Fig. 14.10, for fixed parameters $t_\downarrow/t_\uparrow = 0.3$ and $U = -4t_\uparrow$.
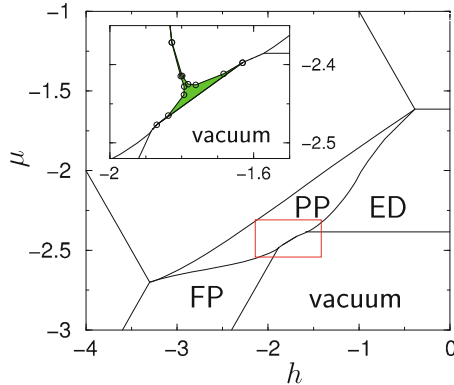
Fig. 14.10 Phase diagram of the asymmetric Hubbard model for $t_\downarrow = 0.3t_\uparrow$ and $U = -4t_\uparrow$. The novel line boundary between partially polarized phase and vacuum is a consequence of the existence of n-body bound states with $n > 2$. Inset: a zoom-in of the low density region of the PP phase. The locus of commensurate densities $n_\uparrow = n_\downarrow/2$ is shown by the shaded area. Reproduced from [66]

For clarity, only the $h < 0$ part of the phase diagram is displayed, corresponding to a majority of heavy ($\downarrow$) fermions.

The evolution of the overall shape of the phase diagram with changing $t_\downarrow$ has been presented in [64]. Here we concentrate on the topological changes induced by trimers. In particular, the boundary with the vacuum is given by the formula

$$\mu_{vac} = \min_{p,q} \frac{E(p,q) - (p-q)h}{p+q}, \qquad (14.22)$$

where p, q are non negative integers and the size of the chain is sufficiently large. At the integrable point, where no trimer exists, the boundary (14.22) reduces to two lines, $E(0,1) - \mu + h = 0$ and $E(1,1) - 2\mu = 0$, separating the vacuum from the fully polarized (FP) and fully paired (ED) phases, respectively. The existence of additional bound states in the asymmetric Hubbard model implies that the partially polarized phase (PP) has a direct line boundary with the vacuum, as shown in Fig. 14.10. In particular, trimers are represented by the line $E(1,2) - 3\mu + h = 0$.

It is also instructive to consider the locus of $n_\uparrow = n_\downarrow/2$ on the phase diagram. At low density ($n_\downarrow < n_\downarrow^{cr}$), the trimer gap is non-zero and the locus corresponds to the shaded area in the inset of Fig. 14.10. At higher density ($n_\downarrow > n_\downarrow^{cr}$), the energy gap closes and the locus shrinks to a single line.

Finally, we would like to mention that trimers, though of a different origin, appear also in three-component Fermi gases [67–70] and in Bose gases [71, 72], leading to equally interesting many-body effects.

14.6 A Two-Channel Model: The Bose-Fermi Resonance Model

The previous sections focussed on one-channel models, i.e., attractively interacting fermions described by either the Gaudin–Yang model Eq. 14.1 or the 1D Hubbard model Eq. 14.16. Several aspects of the one-dimensional BCS–BEC crossover, though, cannot be captured by one-channel models. First, in the BEC limit, such models result in a Tonks–Girardeau gas of dimers. Therefore, the regime of weakly interacting bosons, which is reached when the characteristic length scale of the two-body bound state is smaller than the transverse oscillator length, is not captured. Second, models of attractively interacting fermions, in the case of a population imbalance, always feature the 1D FFLO state, for any interaction strength. In reality, both close to and beyond resonance, i.e., upon entering the BEC regime, minority fermions get bound into closed-channel molecules, and are thus not available anymore for pairing that would result in the FFLO state. Therefore, one expects a competition between the FFLO phase, stable on the BCS side, with a Bose-Fermi mixture in which the bosons are composite molecules in the closed channel, immersed into a fully polarized gas of fermions.

This second aspect can be incorporated in the framework of the so-called Bose-Fermi resonance (BFRM) model [73, 74]:

$$
\hat{H}' = \hat{H} - \mu \hat{N} = \int dx \left(\sum_{\sigma = \uparrow, \downarrow} \hat{\psi}_\sigma^\dagger \left[-\frac{\hbar^2}{2m} \partial_x^2 - \mu \right] \hat{\psi}_\sigma \right.
$$
$$
\left. + \hat{\psi}_B^\dagger \left[-\frac{\hbar^2}{4m} \partial_x^2 - 2\mu + v \right] \hat{\psi}_B + g \left(\hat{\psi}_B^\dagger \hat{\psi}_\uparrow \hat{\psi}_\downarrow + h.c. \right) \right) \tag{14.23}
$$

where $\hat{\psi}_\sigma(x)$ (resp. $\hat{\psi}_B(x)$) are fermionic (resp. bosonic) field operators describing atoms (resp. the bound state in the closed channel, i.e., bare dimers), μ is the chemical potential, m (resp. $2m$) is the mass of the atoms (resp. of the bare dimers), v is the detuning in energy of one bare dimer with respect to two atoms and g is the coupling constant for the conversion of two atoms into a bare dimer and vice-versa. In principle, there is also a direct background interaction between fermions of opposite spin. Our key interest here is in the behavior close to resonance, where the interactions mediated by the Feshbach coupling g dominate any background interaction. For a negative detuning $v < 0$ of the molecular level, g gives rise to an attractive two-particle interaction $g^2/v < 0$ between the fermions [34].

An important insight into the properties of the BCS–BEC crossover of a spin imbalanced gas in 1D was gained by Baur et al. [75], who studied the associated three-body problem. In the Sec. 14.2, we pointed out that the BCS–BEC crossover of a balanced Fermi gas is smooth. This changes once one goes to a finite imbalance, which can be captured already on the three-body level, as pointed out by Baur et al. [75]. By writing the wave function as

$$|\psi\rangle = \left(\sum_K f_K b_K^\dagger c_{-K}^\dagger + \sum_{k,K} g_{k,K} c_{K\downarrow}^\dagger c_{k-K/2\uparrow} c_{-k-K/2\uparrow} |0\rangle\right) \qquad (14.24)$$

where $b_K^\dagger$ creates a molecule with momentum K, one can show that the function f_K is either symmetric, namely on the BEC side, or antisymmetric, namely on the BCS side, upon exchanging the position of the molecule and the fermion [75]. This change in the symmetry of the wave-function occurs at $v' = v/g^{4/3} \approx 0.635$, i.e., on the BEC side of the resonance, and can be traced back to a level-crossing of the symmetric and anti-symmetric wave-functions [75]. Baur et al. further used Quantum Monto Carlo simulations to compute the thermal density matrix on the three-body level, finding results consistent with their analytical predictions.

14.6.1 Phase Diagram of the Bose-Fermi Resonance Model at Finite Imbalance

The analytical results by Baur et al. suggest that a phase transition could be present in the many-body case at a finite imbalance, separating the FFLO phase from a Bose-Fermi mixture. Such a transition would eventually be characterized by a complete depletion of the minority fermions and consequently, the corresponding Fermi volume vanishes. A general discussion of the possible phases along the crossover depending on the number of Fermi surfaces is given in [76].

The BFRM, unlike the one-channel model discussed before, does not allow for an analytically exact solution. One therefore has to resort to numerical approaches, which in one dimension can still provide us with exact results. In the present case, DMRG can be applied, yet it requires a discretization of the model (14.23). Thus, we rewrite the Hamiltonian in a real-space version:

$$\begin{aligned}
H = &-t \sum_{i=1}^{L-1} (c_{i,\sigma}^\dagger c_{i+1,\sigma} + h.c.) \\
&- t_{\mathrm{mol}} \sum_{i=1}^{L-1} (m_i^\dagger m_{i+1} + h.c.) - (v + 3t) \sum_{i=1}^{L} m_i^\dagger m_i \qquad (14.25) \\
&+ g \sum_{i=1}^{L} (m_i^\dagger c_{i,\uparrow} c_{i,\downarrow} + h.c.).
\end{aligned}$$

Here, $m_i^\dagger$ creates a composite boson on site i. The boson energy is shifted with respect to that of single fermions by an effective detuning $v + 3t$. It is chosen such that the energies for adding two fermions or one boson, each at zero momentum, coincide at resonance $v = 0$. The hopping matrix elements for fermions and molecules are denoted by t and $t_{\mathrm{mol}} = t/2$, respectively. The only conserved particle number is

$N = N_f + 2N_{mol}$, where $N_{mol} = \sum_i \langle n_i^{mol} \rangle$; $n_i^{mol} = m_i^\dagger m_i$ and $N_f = N_\uparrow + N_\downarrow$. We use $n = N/L$ to denote the filling factor. Note that at maximum one molecule can sit on a single site, *i.e.*, the molecules behave as hard-core bosons.

The phase diagram can be obtained by calculating various quantities, including the MDF of pairs, molecules and the fermionic components, as well as polarization curves and the density in the molecular channel as a function of polarization P and detuning v. While details on such calculations are given in [19], we here wish to focus on the discussion of the emergent phases. A typical phase diagram is shown in Fig. 14.11a as magnetic field $h' = h/\varepsilon^*$ versus dimensionless detuning $v' = v/\varepsilon^*$. h is defined as the difference in chemical potential for spin up and down while ε^* is the binding energy at resonance $v = 0$ [19]. For $h' < h_c$, the system remains balanced, and we thus recover the BCS–BEC crossover of a balanced mixture, discussed in Sec. 14.2. For $h' > h_{sat}$, the system is fully polarized with $n_\uparrow = n$. As expected, the FFLO phase is stable on the BCS side in the imbalanced case $h_c < h'$. The system then undergoes two consecutive phase transitions, either at a fixed polarization $P > 0$ or at a fixed detuning in the vicinity of the resonance $v' \lesssim 0$, at two critical fields h_1 and h_2. The phase boundary of the FFLO phase is given by $h' = h_1(v')$ [19], or by $P = P_1'(v')$, respectively. The intermediate phase, labeled *BEC + PP LL* (BEC plus partially polarized Luttinger liquid), still has oscillatory correlations, yet there are instabilities in the pairs' MDF at both finite and zero momentum [19]. While in the FFLO and in the *BEC + PP LL* phase, $n_\downarrow > 0$, the transition into the Bose-Fermi mixture phase *BEC + FP FG* (BEC plus fully polarized Fermi gas) occurs at the point at which $n_\downarrow = 0$ [19]. The *BEC + FP FG* has smooth algebraically decaying dimer-dimer correlations (and consequently, pair-pair correlations), with no oscillatory component. Note that in a one-channel model, in contrast to the BFRM, the line with $n_\downarrow = 0$ is equivalent to full polarization $n = n_\uparrow$. Therefore, the upper limit for the stability of the FFLO state is the maximum polarization possible, suggesting that FFLO is more stable in one-channel models (compare the discussion in Sect. 14.4).

In the example shown here ($g = t$, filling $n = 0.6$), the FFLO phase breaks down before resonance $v' < 0$ on the BCS side and the phase boundary exhibits a significant dependence on polarization. In general, the critical detuning, which is the detuning at which FFLO correlations disappear in the $P \rightarrow 0$ limit, depends on both the filling and the Feshbach coupling g. For instance, at a fixed value of g, sending the density to zero moves the phase boundary towards larger v'. In the example shown in the figure, the critical detuning, approaches $v' \approx 0.97$ as $n \rightarrow 0$ [19], which is beyond resonance on the BEC side, consistent with the results by Baur et al. for the associated three-body problem in the continuum [75].

So far we have not specified a specific realization of the model (14.23) since we have treated v and g as model parameters. It could, for instance, model a resonance due to photoassociation or a confinement-induced resonance (see the discussion in [34]). To allow a discussion of the phase diagram in terms of experimentally accessible parameters, it is useful to replace the detuning v' by the parameter $\gamma = \sqrt{\varepsilon_b(v')/\varepsilon_F}$ where $\varepsilon_b(v)$ is the two-body binding energy and $\varepsilon_F = 2t(1 - \cos(k_F))$ is the Fermi energy of a noninteracting gas at the same density. In the continuum limit, this yields the usual definition of the interaction parameter γ. The corresponding behavior
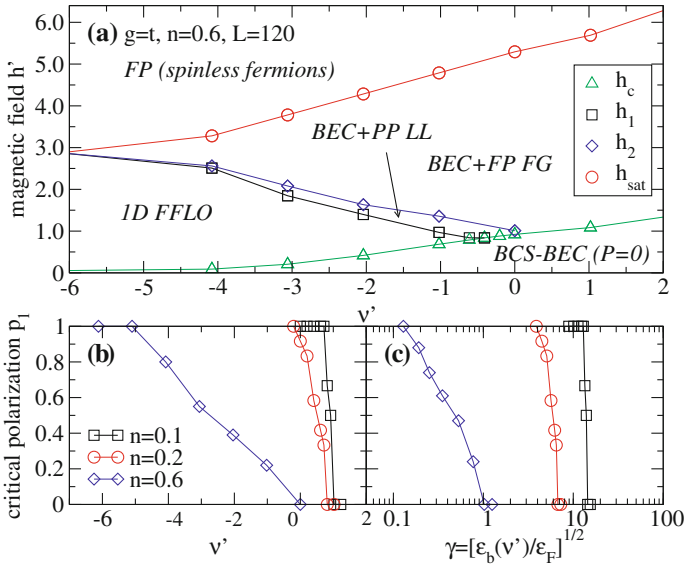
Fig. 14.11 Phase diagram of the Bose-Fermi resonance model Eq. 14.25 for $g = t$: **a** Dimensionless field h' vs dimensionless detuning v'. **b** Critical polarization P_1 vs detuning v' for $n = 0.1, 0.2, 0.6$. **c** Critical polarization P_1 vs ratio of binding energy over Fermi energy $\gamma = \sqrt{\varepsilon_b/\varepsilon_F}$. Figures reproduced from [19]

is displayed in Fig. 14.11c as a polarization vs. γ phase diagram. We only show the phase boundary $P = P_1$ (corresponding to $h' = h_1$) of the 1D FFLO phase, for different densities n. Obviously, for a given n, the ratio of binding energy over Fermi energy determines the range of stability for FFLO. By decreasing n at a fixed g, FFLO becomes stable at arbitrarily large values of γ.

Finally, we emphasize that the limit of a broad resonance, characterized by $nr^* \ll 1$ (compare the discussion of Sec. 14.2) can be reached by either decreasing density or by increasing g such that the binding energy at resonance $\varepsilon_b^* = \varepsilon_b(v = 0)$ increases. For the parameters of Fig. 14.11a ($g = t$, $n = 0.6$), the system is not in this regime since $nr^* \approx 1.21$, yet enters into this limit as n decreases (compare Fig. 14.11b, c).

14.7 Beyond 1D, Other Variations

The FFLO phase occupies a tiny sliver of the $T = 0$ phase diagram in three dimensions and this region shrinks with increasing temperature, making it very difficult for the experimentalist to detect it. In one dimension, on the contrary, nesting effects are pervasive at all fillings and polarization, the FFLO instability becomes enhanced, and the phase more robust. In experiments with cold atoms, low dimensions are now

within reach [1, 8, 9], paving the way to its realization. Strictly in one dimension, the FFLO phase occupies large regions of the phase diagram as we have illustrated in this chapter.

Even though the FFLO phase is more robust in 1D, long-range order is not present, and one can only describe a *quasi* long-range order with algebraically decaying correlations. Moreover, in order to realize this physics one should effectively be able to reach zero temperature. However, this obstacle can be remedied in part by turning on a weak coupling between 1D chains. Cold atoms experiments are carried out by loading the fermions onto 1D tubes, formed by the interference pattern of sets of counter-propagating lasers. By tuning the intensity of the lasers one could adiabatically turn on the coupling between the tubes, allowing one to study the dimensional crossover from 1D to 3D (or 2D) [51, 77]. Unfortunately, this scenario is out of reach for DMRG (at least as far as the crossover from 1D to 3D is concerned) and has so far only been studied within an effective field theory [51], by a mean-field treatment [77], or by feeding in the exactly known instabilities of the 1D system into an RPA analysis [16]. Both approaches [16, 51] show that depending on polarization, interaction strength, and inter-tube coupling, the system is either in the FFLO phase or becomes a polarized Fermi liquid. In [77] the authors raised the possibility of finding two distinct FFLO phases as one increases the tunneling between chains: In a 1D system and within a mean-field description, the order parameter possesses nodes, or domain walls, resembling a soliton-like structure, with the excess fermions concentrated at these nodes. One can imagine coupling chains into a higher dimensional array. The excess Fermions would feel the soliton structure as a superimposed lattice and will form a band of Andreev bound states that is filled, similar to a band insulator. This phase is called a commensurate FFLO phase in [77]. A plausible scenario is that at intermediate inter-chain couplings, the system could undergo a transition to an incommensurate FFLO phase where the band of Andreev bound states is partially filled. This is a mean-field scenario that has not been further explored.

An alternative path was taken in [78]. A "poor man's" version of the dimensional crossover could be achieved by arranging the tubes into a super-lattice, coupling pairs of them into ladders (basically two one-dimensional chains coupled in the transverse direction). Interestingly enough, most of the two-dimensional physics already manifests itself in these systems: At low densities only one band is occupied for each flavor of spin, and the physics reduces to the that of one dimension. This in turn can be associated to the rotational symmetric situation in higher dimensions, in which the Fermi surfaces are spheres, and the order parameter can be described by a single wave vector $|\mathbf{Q}|$. As the density is increased, more bands start being occupied, and multiple Fermi points contribute to pairing. As a consequence, a multi-nodal FFLO order parameter is required to describe the new scenario. The ladder geometry is still highly nested, making the FFLO phase very robust. However, in two dimensions, particularly at high densities or magnetic fields, the nesting between bands with opposite spin is weak, with Fermi surfaces with different shapes, and large mismatch in Fermi velocities. This makes pairing—and the FFLO state—unfavorable, giving room for a normal polarized phase.

As discussed in earlier sections, in a trapped gas in 3D and also in 2D [79], the partially polarized phase and thus the FFLO phase is in the core of the trapped cloud, according to mean-field calculations. This behavior can already be seen on the two-leg geometry at small polarizations [78], suggesting this one as a useful toy system to understand aspects of the dimensional crossover in a model that allows for a numerically exact solution.

An additional motivation for studying the attractive Hubbard model comes from the fact that the knowledge on the phases of the spin-imbalanced, attractive model also gives information on the ground states of the repulsive model via a particle-hole transformation. This could become relevant for 2D systems where in general, the ground states are not known, calling for experiments in this direction (see the discussion in [80, 81]).

Interesting possibilities arise when multi-band pairing is considered [82]. Consider a setup with anisotropic Fermi surfaces, in which the tunnelling along the x direction is much weaker than the other two (transverse) directions. This leads to a multi-band scenario in which one spin species populates only the s-band, while the other partially occupies the p_x band directly above, with Fermi surfaces lying on different bands. This gives rise to a new unconventional FFLO-like paired state, with the main difference that the pairs have p-wave center-of-mass momenta, and an order parameter modulated by a wave-vector $\mathbf{Q} = \mathbf{k}_F^\uparrow + \mathbf{k}_F^\downarrow$.

Remarkably, optical lattices can potentially be tuned independently for both hyperfine species [83]. This technique could provide another knob for tuning their relative masses, or changing the shape and relative orientation of the Fermi surfaces. For instance, in [84], the authors proposed rotating the Fermi surfaces for each spin flavor by 90 degrees with respect to one another. Then, FFLO-like physics with a modulated order parameter can be realized in *unpolarized* mixtures. A similar idea has been discussed to realize exotic unpolarized phases in 1D, using a multi-band setup [85].

Other authors [70, 86–90] have also considered multi-flavor systems, in which three hyperfine species are present, interacting via attractive interactions. This gives rise to a rich variety of possibilities beyond FFLO, such as molecules (trions), and a competition between three pairing tendencies with different center-of-mass momenta. Moreover, the BCS–BEC crossover of a balanced mixture of a four-component gas has recently been discussed in [91]. Finally, FFLO-like phases can also be stable in the case of repulsive interactions on the ladder geometry [92, 93].

14.8 Proposals for the Experimental Observation of FFLO Correlations

One of the main open experimental challenges is the actual characterization of the partially polarized phase as the FFLO phase. While the phase-separated profiles observed in the Rice experiment [8] show a remarkable agreement with the theoretical

predictions obtained from the Bethe ansatz combined with LDA [6, 7], experiments have not unambiguously demonstrated that the phase indeed corresponds to a paired state with a finite center-of-mass momentum. This is not a trivial task, since the number of available techniques to probe cold atomic systems remains limited. However, the quest for the FFLO state has certainly presented an extraordinary motivation and the breeding ground for novel and clever ideas. The most straightforward possibility is to take snapshots trying to resolve the spin density modulations [13, 15, 44]. Another possibility is to probe the spin–spin correlations using spatially resolved quantum polarization spectroscopy [58]. While the spin modulations are characteristic of the FFLO state, they are no direct evidence of pairing. One way to identify pairing may be using a time-of-flight (TOF) measurement to observe the velocity distribution of the condensate. Since the pairs have finite center-of-mass momenta, they would imprint a characteristic signature [94].

The latter work also has proposed to use noise correlations, and mean-field [95] and DMRG studies [16] show that this technique would indeed produce a clear and unambiguous signal. Although spectroscopic techniques to probe cold atomic systems are under development and are not widely available [96], FFLO signatures should also be evident in the rf-spectra [97, 98] and angle resolved photo-emission spectra [84]. An interesting recent proposal consists of studying the response of the system to time-dependent potentials [99], which would excite the spin-dipole modes. When the oscillation of the potential is in resonance with the excitations, a dramatic response at the proper momenta would indicate FFLO physics. Another idea exploiting time-dependent perturbations using modulation spectroscopy [100] consists of measuring the response of the double occupancy [101]. At present, the only relevant experiment is the one by Yiao et al. [8], which realizes 1D tubes in the continuum. Therefore, for this particular system, proposals that assume the presence of an optical lattice along the 1D direction may not be applicable [101]. It should further be stressed that some of the ideas put forward here have only been substantiated by mean-field theory [95, 97, 99]. While one may argue that mean-field theory gives qualitatively reasonable results for the phase diagram of attractively interacting fermions in 1D [22, 102], there are considerable quantitative deficiencies already on the level of density profiles [98] and it is by no means obvious that mean-field theory is valid for the description of time-dependent detection schemes [97, 99].

Finally, for the question of whether FFLO can be observed in an actual experiment, the accessible temperatures may play a crucial role [15, 37, 103, 104]. The effect of temperature on density profiles in traps was studied with Bethe-ansatz methods in [37] and numerically using QMC in [15, 104]. In [104], the visibility of the finite-momentum peak in the pairs' MDF was also discussed as a function of temperature.

In conclusion, while all these ideas can potentially provide the smoking gun that would signal the presence of the FFLO phase in experiments, their implementation still remains challenging, and some have shortcomings. However, it is very likely that some of these techniques may routinely be used in the future.

14.9 Summary

The recent realization of 1D Fermi gases with ultracold atoms in the vicinity of a
Feshbach resonance [8] opens the possibility to investigate the physics of strongly
correlated fermions in a situation, where exact analytical or numerical results are
available. As shown above, this makes accessible the physics of solvable models
such as those of Gaudin, Yang, Lieb and Wu and others. It also provides a means to
study unconventional pairing of the FFLO-type in a simple example. Compared to
the BCS–BEC crossover in 3D, where a number of open questions still exists for the
imbalanced gas, the 1D case is rather well understood, at least as far as equilibrium
quantities are concerned. Issues such as equilibration or the expansion dynamics,
or the effects of finite temperature are, however, still open and topics of ongoing
research. The physics of 1D fermions will thus remain of interest for some time to
come, in particular, because ultracold atoms provide an experimental realization that
allows one to investigate physics in one dimension over a wide range of parameters.

References

1. Bloch, I., Dalibard, J., Zwerger, W.: Rev. Mod. Phys. **80**, 885 (2008)
2. Giorgini, S., Pitaevskii, L.P., Stringari, S.: Rev. Mod. Phys. **80**, 1215 (2009)
3. Ketterle, W., Zwierlein, M.: In: Inguscio, M. (ed.) Ultracold Fermi Gases, Proceedings of the
   International School of Physics "Enrico Fermi", Course CLXIV, Varenna, 20–30 June 2006,
   (2008)
4. Fuchs, J.N., Recati, A., Zwerger, W.: Phys. Rev. Lett. **93**, 090408 (2004)
5. Tokatly, I.V.: Phys. Rev. Lett. **93**, 090405 (2004)
6. Hu, H., Liu, X.J., Drummond, P.D.: Phys. Rev. Lett. **98**, 070403 (2007)
7. Orso, G.: Phys. Rev. Lett. **98**, 070402 (2007)
8. Liao, Y.A., Rittner, A.S.C., Paprotta, T., Li, W., Partridge, G.B., Hulet, R.G., Baur, S.K.,
   Mueller, E.J.: Nature **467**, 567 (2010)
9. Moritz, H., Stöferle, T., Günter, K., Köhl, M., Esslinger, T.: Phys. Rev. Lett. **94**, 210401 (2005)
10. Fulde, P., Ferrell, A.: Phys. Rev. **135**, A550 (1964)
11. Larkin, A., Ovchinnikov, Y.: Zh. Eksp. Teor. Fiz. **47**, 1136 (1964)
12. Yang, K.: Phys. Rev. B **63**, 140511 (2001)
13. Feiguin, A., Heidrich-Meisner, F.: Phys. Rev. B **76**, 220508(R) (2007)
14. Batrouni, G.G., Huntley, M.H., Rousseau, V.G., Scalettar, R.T.: Phys. Rev. Lett. **100**, 116405
    (2008)
15. Casula, M., Ceperley, D.M., Mueller, E.J.: Phys. Rev. A **78**, 033607 (2008)
16. Lüscher, A., Noack, R., Läuchli, A.: Phys. Rev. A **78**, 013637 (2008)
17. Rizzi, M., Polini, M., Cazalilla, M., Bakhtiari, M., Tosi, M., Fazio, R.: Phys. Rev. B **77**, 245105
    (2008)
18. Tezuka, M., Ueda, M.: Phys. Rev. Lett. **100**, 110403 (2008)
19. Heidrich-Meisner, F., Feiguin, A.E., Schollwöck, U., Zwerger, W.: Phys. Rev. A **81**(023629),
    023629 (2010)

20. Casalbuoni, R., Nardulli, G.: Rev. Mod. Phys. **76**, 263 (2004)
21. Lortz, R., Wang, Y., Demuer, A., Böttger, P.H.M., Bergk, B., Zwicknagl, G., Nakazawa, Y., Wosnitza, J.: Phys. Rev. Lett. **99**, 187002 (2007)
22. Sheehy, D.E., Radzihovsky, L.: Ann. Phys. **322**, 1790 (2007)
23. Radzihovsky, L., Sheehy, D.: Rep. Prog. Phys. **73**, 076501 (2010)
24. Randeria, M., Duan, J.M., Shieh, L.Y.: Phys. Rev. Lett. **62**, 98 (1989)
25. Olshanii, M.: Phys. Rev. Lett. **81**, 938 (1998)
26. Gaudin, M.M.: Phys. Lett. **24A**, 55 (1967)
27. Yang, C.N.: Phys. Rev. Lett. **19**, 1312 (1967)
28. Bergeman, T., Moore, M.G., Olshanii, M.: Phys. Rev. Lett. **91**, 163201 (2003)
29. Mora, C., Egger, R., Gogolin, A.O.: Phys. Rev. A **71**, 052705 (2005)
30. Petrov, D.S.: Phys. Rev. A **67**, 010703 (2003)
31. Lieb, E.: Phys. Rev. **130**, 1605 (1963)
32. Giamarchi, T., Nattermann, T., LeDoussal, P.: Fundamental problems of mesoscopic physics. Nato Science Series II **154**, 275 (2004)
33. Luther, A., Peschel, I.: Phys. Rev. B **74**, 002911 (1974)
34. Recati, A., Fuchs, J., Zwerger, W.: Phys. Rev. A **71**, 033630 (2005)
35. Citro, R., Orignac, E.: Phys. Rev. Lett. **95**, 130402 (2005)
36. Sheehy, D.E., Radzihovsky, L.: Phys. Rev. Lett. **95**, 130401 (2005)
37. Kakashvili, P., Bolech, C.J.: Phys. Rev. A **79**, 041603 (2009)
38. Zhao, E., Guan, X.W., Liu, W.V., Batchelor, M.T., Oshikawa, M.: Phys. Rev. Lett. **103**, 140404 (2009)
39. Heidrich-Meisner, F., Orso, G., Feiguin, A.E.: Phys. Rev. A **81**, 053602 (2010)
40. Silva, T.N.D., Mueller, E.J.: Phys. Rev. A **73**, 051602 (2006)
41. Woynarovich, F., Eckle, H., Trunng, T.: J. Phys. A Math. Gen. **22**, 4207 (1989)
42. Guan, X.W., Batchelor, M.T., Lee, C., Bortz, M.: Phys. Rev. B **76**, 085120 (2007)
43. Buzdin, A.I., Tugushev, V.V.: Zh. Eksp. Teor. Fiz. **85**, 735 (1983)
44. Machida, K., Nakanishi, H.: Phys. Rev. B **30**, 122 (1984)
45. Frahm, H., Korepin, V.E.: Phys. Rev. B **42**, 10553 (1990)
46. Frahm, H., Korepin, V.E.: Phys. Rev. B **43**, 56532 (1991)
47. Pokrovsky, V.L., Talapov, A.L.: Phys. Rev. Lett. **42**, 65 (1979)
48. Feiguin, A.E., Huse, D.A.: Phys. Rev. B **79**, 100507(R) (2009)
49. Frahm, H., Vekua, T.: J. Stat. Mech. P01007 (2008)
50. Vekua, T., Matveenkov, S., Shlyapnikov, G.: JETP Lett. **90**, 289 (2009)
51. Zhao, E., Liu, W.V.: Phys. Rev. A **78**, 063605 (2008)
52. McGuire, J.B.: J. Math. Phys. **7**, 123 (1965)
53. He, J., Foerster, A., Guan, X., Batchelor, M.T.: New J. Phys. **11**, 073009 (2009)
54. Essler, F., Frahm, H., Göhmann, F., Klümper, A., Korepin, V.E.: The One-Dimensional Hubbard Model. Cambridge University Press, Cambridge (2005)
55. Schollwöck, U.: Rev. Mod. Phys. **77**, 259 (2005)
56. White, S.R.: Phys. Rev. Lett. **69**, 2863 (1992)
57. Tezuka, M., Ueda, M.: New J. Phys. **12**, 055029 (2010)
58. Roscilde, T., Rodriguez, M., Eckert, K., Romero-Isart, O., Lewenstein, M., Polzik, E., Sanpera, A.: New J. Phys. **11**, 055041 (2009)
59. Wille, E., Spiegelhalder, F.M., Kerner, G., Naik, D., Trenkwalder, A., Hendl, G., Schreck, F., Grimm, R., Tiecke, T.G., Walraven, J.T.M., Kokkelmans, S.J.J.M.F., Tiesinga, E., Julienne, P.S.: Phys. Rev. Lett. **100**, 053201 (2008)
60. Voigt, A.C., Taglieber, M., Costa, L., Aoki, T., Wieser, W., Hänsch, T.W., Dieckmann, K.: Phys. Rev. Lett. **102**, 020405 (2009)
61. Orso, G., Pitaevskii, L.P., Stringari, S.: Phys. Rev. A **77**, 033611 (2008)
62. Cazalilla, M.A., Ho, A.F., Giamarchi, T.: Phys. Rev. Lett. **95**, 226402 (2005)
63. Batrouni, G.G., Wolak, M.J., Hebert, F., Rousseau, V.G.: EPL **86**, 47006 (2009)
64. Wang, B., Chen, H.D., Sarma, S.D.: Phys. Rev. A **79**, 051604(R) (2009)

65. Burovski, E., Orso, G., Jolicoeur, T.: Phys. Rev. Lett. **103**, 215301 (2009)
66. Orso, G., Burovski, E., Jolicoeur, T.: Phys. Rev. Lett. **104**, 065301 (2010)
67. Azaria, P., Capponi, S., Lecheminant, P.: Phys. Rev. A **80**, 041604 (2009)
68. Guan, X.W., Batchelor, M.T., Lee, C., Zhou, H.-Q.: Phys. Rev. Lett. **100**, 200401 (2008)
69. Kantian, A., Dalmonte, M., Diehl, S., Hofstetter, W., Zoller, P., Daley, A.J.: Phys. Rev. Lett. **103**, 240401 (2009)
70. Lüscher, A., Läuchli, A. arXiv:0906.0768 (unpublished)
71. Keilmann, T., Cirac, I., Roscilde, T.: Phys. Rev. Lett. **102**, 255304 (2009)
72. Valiente, M., Petrosyan, D., Saenz, A.: Phys. Rev. A **81**, 011601 (2010)
73. Timmermans, E., Furuyab, K., Milonnia, P.W., Kermanc, A.K.: Phys. Lett. A **285**, 228 (2001)
74. Holland, M., Kokkelmans, S.J.J.M.F., Chiofalo, M.L., Walser, R.: Phys. Rev. Lett. **87**, 120406 (2001)
75. Baur, S.K., Shumway, J., Mueller, E.J.: Phys. Rev. A **81**, 033628 (2010)
76. Sachdev, S., Yang, K.: Phys. Rev. B **73**, 174504 (2006)
77. Parish, M.M., Baur, S.K., Mueller, E.J., Huse, D.A.: Phys. Rev. Lett. **99**, 250403 (2007)
78. Feiguin, A., Heidrich-Meisner, F.: Phys. Rev. Lett. **102**, 076403 (2009)
79. Conduit, G.J., Conlon, P.H., Simons, B.D.: Phys. Rev. A **77**, 053617 (2008)
80. Ho, A.F., Cazalilla, M.A., Giamarchi, T.: Phys. Rev. A **79**, 033620 (2009)
81. Moreo, A., Scalapino, D.J.: Phys. Rev. Lett. **98**, 216402 (2007)
82. Zhang, Z., Hung, H.H., Ho, C.M., Zhao, E., Liu, W.V.: Phys. Rev. A **82**, 033610 (2010)
83. Liu, W.V., Wilczek, F., Zoller, P.: Phys. Rev. A **70**, 033603 (2004)
84. Feiguin, A.E., Fisher, M.P.A.: Phys. Rev. Lett. **103**, 025303 (2009)
85. Zapata, I., Wunsch, B., Zinner, N.T., Demler, E.: Phys. Rev. Lett. **105**, 095301 (2010)
86. Cherng, R.W., Refael, G., Demler, E.: Phys. Rev. Lett. **99**, 130406 (2007)
87. Rapp, A., Zaránd, G., Honerkamp, C., Hofstetter, W.: Phys. Rev. Lett. **98**, 160405 (2007)
88. Capponi, S., Roux, G., Lecheminant, P., Azaria, P., Boulat, E., White, S.R.: Phys. Rev. A **77**, 013624 (2008)
89. Capponi, S., Roux, G., Azaria, P., Boulat, E., Lecheminant, P.: Phys. Rev. B **75**, 100503 (2007)
90. Roux, G., Capponi, S., Lecheminant, P., Azaria, P.: Eur. Phys. J. B **68**, 293 (2009)
91. Nishida, Y., Son, D.: Phys. Rev. A **82**, 043606 (2010)
92. Roux, G., White, S.R., Capponi, S., Poilblanc, D.: Phys. Rev. Lett. **97**, 087207 (2006)
93. Roux, G., Orignac, E., Pujol, P., Poilblanc, D.: Phys. Rev. B **75**, 245119 (2007)
94. Yang, K.: Phys. Rev. Lett. **95**, 218903 (2005)
95. Paananen, T., Koponen, T.K., Törmä, P., Martikainen, J.P.: Phys. Rev. A **77**, 053602 (2008)
96. Stewart, J., Gaebler, J., Jin, D.: Nature **454**, 744 (2008)
97. Bakhtiari, M.R., Leskinen, M.J., Törmä, P.: Phys. Rev. Lett. **101**, 120404 (2008)
98. Molina, R.A., Dukelsky, J., Schmitteckert, P.: Phys. Rev. Lett. **102**, 168901 (2009)
99. Edge, J.M., Cooper, N.R.: Phys. Rev. Lett. **103**, 065301 (2009)
100. Kollath, C., Iucci, A., Giamarchi, T., Hofstetter, W., Schollwöck, U.: Phys. Rev. Lett. **97**, 050402 (2006)
101. Korolyuk, A., Massel, F., Törma, P.: Phys. Rev. Lett. **104**, 236402 (2010)
102. Liu, X.J., Hu, H., Drummond, P.D.: Phys. Rev. A **75**, 023614 (2007)
103. Liu, X.J., Hu, H., Drummond, P.D.: Phys. Rev. A **76**, 043605 (2007)
104. Wolak, M.J., Rousseau, V.G., Miniatura, C., Gremaud, B., Scalettar, R.T., Batrouni, G.G.: Phys. Rev. A **82**, 013614 (2010)